frontiers | Research Topics

Quantification of immunological memory

Edited by
Antonella Prisco, Filippo Castiglione, Uri Hershberg
and Francesca Di Rosa

Published in
Frontiers in Immunology

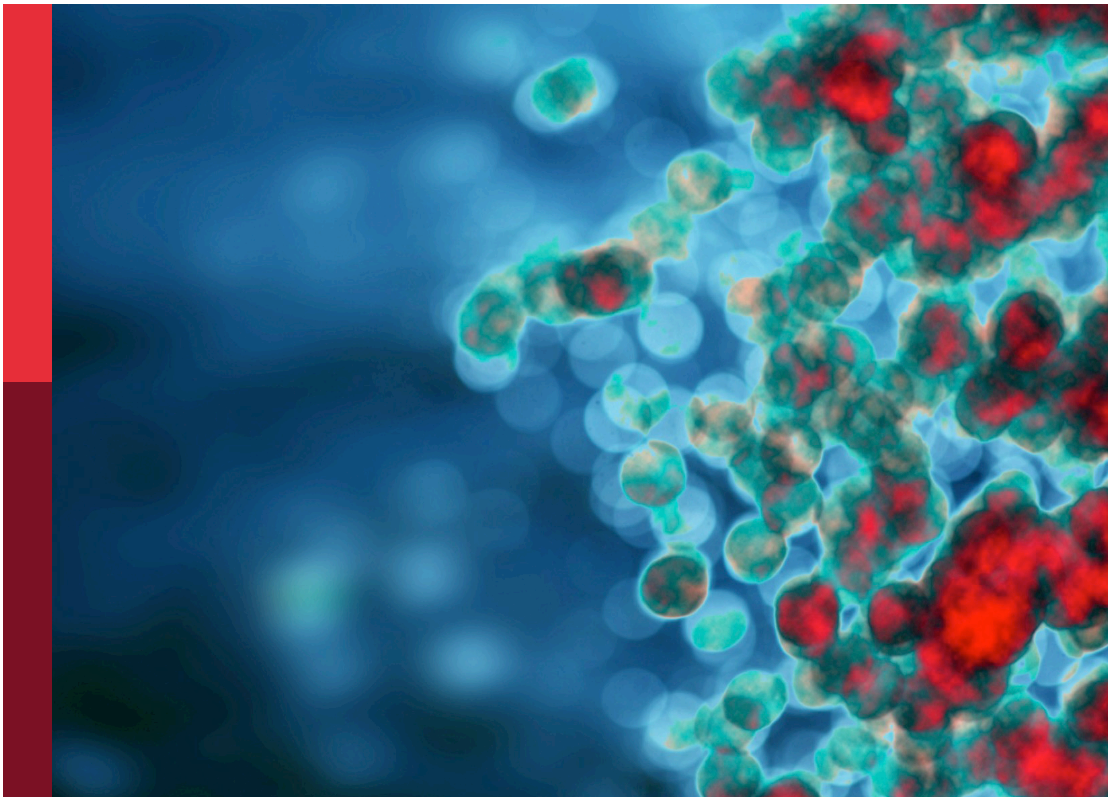

ISSN 1664-8714
ISBN 978-2-8325-2755-9
DOI 10.3389/978-2-8325-2755-9

About Frontiers

Frontiers is more than just an open access publisher of scholarly articles: it is a pioneering approach to the world of academia, radically improving the way scholarly research is managed. The grand vision of Frontiers is a world where all people have an equal opportunity to seek, share and generate knowledge. Frontiers provides immediate and permanent online open access to all its publications, but this alone is not enough to realize our grand goals.

Frontiers journal series

The Frontiers journal series is a multi-tier and interdisciplinary set of open-access, online journals, promising a paradigm shift from the current review, selection and dissemination processes in academic publishing. All Frontiers journals are driven by researchers for researchers; therefore, they constitute a service to the scholarly community. At the same time, the *Frontiers journal series* operates on a revolutionary invention, the tiered publishing system, initially addressing specific communities of scholars, and gradually climbing up to broader public understanding, thus serving the interests of the lay society, too.

Dedication to quality

Each Frontiers article is a landmark of the highest quality, thanks to genuinely collaborative interactions between authors and review editors, who include some of the world's best academicians. Research must be certified by peers before entering a stream of knowledge that may eventually reach the public - and shape society; therefore, Frontiers only applies the most rigorous and unbiased reviews. Frontiers revolutionizes research publishing by freely delivering the most outstanding research, evaluated with no bias from both the academic and social point of view. By applying the most advanced information technologies, Frontiers is catapulting scholarly publishing into a new generation.

What are Frontiers Research Topics?

Frontiers Research Topics are very popular trademarks of the *Frontiers journals series*: they are collections of at least ten articles, all centered on a particular subject. With their unique mix of varied contributions from Original Research to Review Articles, Frontiers Research Topics unify the most influential researchers, the latest key findings and historical advances in a hot research area.

Find out more on how to host your own Frontiers Research Topic or contribute to one as an author by contacting the Frontiers editorial office: frontiersin.org/about/contact

Quantification of immunological memory

Topic editors

Antonella Prisco — Institute of Genetics and Biophysics Adriano Buzzati-Traverso, Department of Biomedical Sciences, National Research Council (CNR), Italy

Filippo Castiglione — Technology Innovation Institute (TII), United Arab Emirates

Uri Hershberg — University of Haifa, Israel

Francesca Di Rosa — Institute of Molecular Biology and Pathology, Department of Biomedical Sciences, National Research Council (CNR), Italy

Citation

Prisco, A., Castiglione, F., Hershberg, U., Di Rosa, F., eds. (2023). *Quantification of immunological memory*. Lausanne: Frontiers Media SA.
doi: 10.3389/978-2-8325-2755-9

Table of contents

Frontiers in Immunology

TYPE Editorial
PUBLISHED 05 June 2023
DOI 10.3389/fimmu.2023.1219067

Editorial: Quantification of immunological memory

Francesca Di Rosa[1], Filippo Castiglione[2], Uri Hershberg[3] and Antonella Prisco[4]*

[1]Institute of Molecular Biology and Pathology, Department of Biomedical Sciences, National Research Council (CNR), Rome, Italy, [2]Biotech Research Center, Technology Innovation Institute, Masdar City, Abu Dhabi, United Arab Emirates, [3]Department of Human Biology, Faculty of Sciences University of Haifa, Haifa, Israel, [4]Institute of Genetics and Biophysics Adriano Buzzati-Traverso, Department of Biomedical Sciences, National Research Council (CNR), Naples, Italy

EDITED AND REVIEWED BY
Scott N Mueller,
The University of Melbourne, Australia

*CORRESPONDENCE
Antonella Prisco
antonella.prisco@igb.cnr.it

RECEIVED 08 May 2023
ACCEPTED 22 May 2023
PUBLISHED 05 June 2023

CITATION
Di Rosa F, Castiglione F, Hershberg U and Prisco A (2023) Editorial: Quantification of immunological memory.
Front. Immunol. 14:1219067.
doi: 10.3389/fimmu.2023.1219067

KEYWORDS

recall memory, anamnestic response, memory persistence, B cell memory, T cell memory, modeling, vaccine

Editorial on the Research Topic
Quantification of immunological memory

Quantification of immunological memory requires a diversity of approaches to accurately collect data on all the relevant cell types and molecules, identify the correlates of protection, and model the kinetics of the immune response. This collection of articles reports studies performed in humans, in mouse, and *in silico* models, that altogether emphasize the strength of integrating diverse methodologies for investigating the complexity of immunological memory.

1 Memory lymphocyte subtypes

Several contributors to this topic emphasized memory T and B cell heterogeneity. Humphries et al. offered a comprehensive overview of non-human primate and human studies on pulmonary-Resident Memory T (T_{RM}) and B (B_{RM}) lymphocytes in respiratory infections. These authors highlighted the need for improving vaccination strategies to induce T_{RM} and B_{RM}, and methods to quantify these cells; they also discussed some promising novelties in the techniques to assess respiratory airways immunity. Yordanova et al. investigated memory T cell heterogeneity in recall responses to *H. polygyrus*, a strictly enteric nematode, in a mouse model. The peculiarity of this model is that memory T cells were found in *H. polygyrus*-cured mice in the peritoneal cavity and lungs, in addition to intestinal lamina propria and mesenteric lymph nodes (LNs). Distinct transcriptional profiles characterized T cells from each tissue. Upon *H. polygyrus* challenge, parasite-specific OX40$^+$ Th2 cells expanded as early as day 3 in the peritoneum, coincident with the presence of abundant OX40L$^+$ dendritic cells and eosinophils in this organ, while Th2 cells increased only at day 14 in mesenteric LNs.

The memory T cell compartment comprises both foreign antigen (Ag)-specific "authentic" memory and memory-phenotype (MP) cells, whose function is unclear. Kawabe et al. identified a set of markers distinguishing Ag-specific from MP cells in the mouse CD44hi CD62Llow memory CD4$^+$ T cell compartment. Thus, the "authentic" memory cells, that in this study were elicited by infection with lymphocytic choriomeningitis virus (LCMV), were mostly CD127hi Sca1hi, while the MP cells were more heterogeneous in terms of CD127 and Sca1 expression. Notably, Bcl2 expression was significantly higher in CD127hi Sca1hi Ag-specific cells than in CD127hi Sca1hi MP cells. Further experiments demonstrated that CD127hi Sca1hi MP cells had a Th1-signature, consistent with a pro-inflammatory 'innate-type' function that can either protect at early times after encounter with a new Ag, before the development of Ag-specific immunity, or mediate immunopathology.

2 Ag receptor-repertoires and Ag-specificity of memory lymphocytes

Huisman et al. sequenced the TCR-repertoires of 190 purified memory CD8 T-cell populations from 29 healthy human donors, directed against 21 epitopes of Cytomegalovirus, Epstein-Barr virus, and Adenovirus, looking for so-called "public" TCR sequences shared among different individuals. The authors found that a large part of the sequenced TCRs contained Identical (I-PUB) and Highly Similar (HS-PUB) CDR3β, confirmed their results in an independent cohort, and proposed that the shared TCR sequences may be attractive candidates for innovative anti-viral therapies, e.g., based on TCR gene transfer. Although "public" TCRs may derive from a subset of memory T cells selected for their ability to control viral reactivation in chronic infections, they have been identified also in the TCR-repertoires of T cells specific for non-latent viruses. Ohm-Laursen et al. used Adaptive Immune Receptor Repertoire sequencing (AIRR-seq) to analyse the Ig repertoire from the respiratory tract of atopic asthma patients and controls and to investigate B cell clone dissemination in the airways. This study reported that atopic asthma patients had distinct Ig repertoires, and that B cell clones trafficked more prominently from the nasal to the bronchial mucosa, than between right and left bronchial trees. Furthermore, heavily mutated IgD-only B cells were found in the asthmatic bronchial mucosa, and their Ig sequences were consistent with the hypothesis of bacteria/superantigen-driven stimulation (e.g. in terms of IGHV-genes, CDR3 length, etc.). Neuman et al. presented IgTreeZ (Immunoglobulin Tree analyZer), a new tool to analyze Ig gene lineage trees and Ig repertoires, and showed that their method of lineage tree-based analysis was instrumental to account for mutations in the CDR3. For example, analysis of samples from COVID-19 patients by IgTreeZ demonstrated that extensive Ig somatic hypermutation (SHM) occurred between the second and fourth week after the onset of clinical symptoms, while affinity-maturated, structurally stable antibodies (Abs) appeared at about one month from clinical symptom onset.

The persistence of virus-specific Abs and their potential cross-reactions are topics of renewed interest in the context of COVID-19 pandemic. Tanunliong et al. performed a longitudinal study on the SARS-CoV-2 serostatus of long-term care residents living in a facility that experienced two COVID-19 outbreaks, one in April and the other in October 2020. The authors demonstrated persistence of Abs directed against the Spike Ag of SARS-CoV-2 over seven months, with a gradual waning of anti-Nucleocapsid Abs. They also found, among SARS-CoV-2 seropositive individuals, elevated Abs against human seasonal coronaviruses OC43 and HKU1, which may be attributed to a heterologous boosting effect by SARS-CoV-2 infection and/or cross-reaction.

3 Regulation of immunological memory

Immunological memory is generally associated with the concept of protective long-term immunity, e.g., post-vaccination, even though memory T cell responses may be insufficient or even detrimental in some diseases. Barnaba gave an extensive overview of the mechanisms supporting durable T cell memory and preventing excessive T cell activation and immunopathology, e.g., effector T cell exhaustion and suppression by regulatory T cells. The author critically discussed recent findings on immuno-regulatory cellular and molecular mechanisms, highlighting the remaining gaps, and proposing innovative strategies to improve T cell-mediated protection against infectious agents and cancer cells, and to inhibit the development and progression of autoimmune diseases. Using a network-based bioinformatics approach, Onisiforou and Spyrou described the effects of microbiota-host and microbiota-virus interactions on the regulation of immune response in neurodegenerative diseases. Their findings pointed out a marked impact of microbiota-mediated-immune effects on Multiple Sclerosis.

4 Vaccine-induced immunological memory

A better understanding of immunological memory can be highly beneficial to optimize vaccine formulations and vaccination protocols. Duhen et al. examined the extent to which OX40L:Ig, an OX40 agonist, enhanced T and B cell responses to either a protein and adjuvant-based or a self-amplifying mRNA-based vaccine against SARS-CoV-2 in mouse models. They tested OX40L:Ig according to different vaccination schemes (e.g., single or repeated OX40L:Ig injection, at the time of prime, boost, third booster, etc.) and found that it consistently increased both humoral and cellular responses. Natalini et al. investigated the impact of the time interval between vaccine doses on CD8 T cell immunity induced by prime with HIV-1 gag-encoding Chimpanzee adenovector and boost with HIV-1 gag-encoding Modified Vaccinia virus Ankara in a mouse model. A delayed boost (i.e., at day 100 post-prime) was more effective than an early one (i.e., at day 30 post-prime), as evaluated by multi-lymphoid organ assessment of gag-specific CD8 T cell frequency, cytotoxicity, and IFN-γ production. Cell number estimation showed that boost at day 100 yielded a ~3-fold higher number of gag-specific CD8 T cells in the sum of spleen and bone marrow (BM) than boost at day 30, and a ~15-fold higher number than prime only. The authors described a splenic memory CD8 T cell molecular signature associated with enhanced response to delayed boost that trended toward a central memory phenotype, and was characterized by shut off of several proliferative genes, and up-regulation of stem cell genes previously implicated in setting the equilibrium between quiescence and proliferation. Interestingly, gag-specific CD8 T cell frequency selectively diminished in the blood at day 100 post-prime, but not in the spleen, LNs, and BM, coincidently with the improved responsiveness to boost. Stolfi et al. used a stochastic agent-based immune simulation platform to explore the impact of the time interval between vaccine doses on the immunological memory elicited by a SARS-CoV-2 Spike-encoding adenoviral vaccine in humans. The computational model was calibrated to reproduce the serological results of an observational study and of a clinical trial, whereby longer intervals resulted in higher Ab responses as compared to shorter intervals (i.e., 45>20>10 weeks) (1). Stolfi et al. showed that, although the magnitude of the Ab response to boost depended on the number of pre-existing memory B cells, the difference among protocols was mainly due to Ag availability, which was reduced in the shorter interval protocols due to higher levels of pre-existing Abs and memory cytotoxic T cells. Interestingly, two groups of vaccinees emerged in the simulations, i.e., *sustainers* and *decayers*, with distinct kinetics of Ab decline due to differences in long-lived plasma cells. Repeated vaccine injections could rescue Ab levels in *decayers*, with possible implications for individuals having reduced serological memory in real life. In the simulations by Stolfi et al., memory CD8 T cells peaked after the first vaccine dose and then slowly declined, with only minor expansion after any second dose, in agreement with the few available data on human CD8 response to COVID-19 adenoviral vaccines (2). This is quite different from the experimental findings by Natalini et al. Such apparent discrepancy may derive from one or more of the following differences between the study by Stolfi et al. and that by Natalini et al.: i) a homologous versus heterologous prime/boost protocol was used; ii) model parameters were adjusted based on human vaccination results versus data obtained in mice; iii) the shortest and intermediate intervals analysed in the computational model (i.e. 10 and 20 weeks, respectively) were in the same range of the longest one in the mouse study (i.e. 100 days), and the additional interval of 45 weeks was lacking in the mouse study. Other possible differences include, for example, distinct Ag-specific naïve CD8 T cell frequencies, and diversities in Ag availability. It should be noted that the identification of similarities and discrepancies between simulations and real experiments appears greatly fruitful for further advancements in the immunological memory field (3).

5 Modeling memory T cell homeostasis

Swain et al. modeled *in silico* in a hypothetical laboratory mouse two classic hypotheses on the mechanisms regulating memory T cell homeostasis, i.e., 'global' competition for cytokines, and 'cognate' competition for Ag. Over time, the former led to a skewed T cell repertoire dominated by the first immune responses, while the latter to a more realistic scenario of high TCR diversity in the memory population. However, given the limited experimental evidence for 'cognate' competition, the authors worked on the 'global' competition model to improve it. They found that introducing 'cellular aging', along with a small continual source of memory T cells (either from stem-cell-like memory T cells or from naive T-cell recruitment into the memory pool) lead to a more convincing model of memory T cell homeostasis. The concept of 'cellular aging' took into account the declining cell fitness depending on the number of cell divisions, considering that there is a maximal number of divisions a somatic cell can go through, i.e., the so-called 'Hayflick limit'. Strikingly, recent experiments in mouse models demonstrated that memory CD8 T cells specific for a single Ag were able to mount a fully functional response *in vivo* after 16 serial adoptive transfers and >50 immunizations, with no apparent limit to the number of cell divisions. The surprising results of these beautiful experiments suggested that memory CD8 T cells maintained their proliferation potential for about 10 years, a time about 3-times longer than mouse lifespan (4). Once again, experimental results and data obtained from simulations challenge each other, thus stimulating further studies, and opening new promising opportunities to improve our understanding of immunological memory.

Author contributions

AP and FD wrote the first draft, which was integrated with insightful contributions by UH and FC. All authors approved the text for submission.

Funding

The authors acknowledge support by the following grants: Italian Minister of Research and University (MIUR) grant PRIN 2017K55HLC_006 to FD; EU funding within the Next Generation EU-MUR PNRR Extended Partnership initiative on Emerging Infectious Diseases (PE00000007 INF-ACT) to FD and AP. UH was funded by NIH P01 AI106697 and the European Union's Horizon 2020 research and innovation program, under grant agreement No 825821.

Conflict of interest

The authors declare that the research was conducted in the absence of any commercial or financial relationships that could be construed as a potential conflict of interest.

Publisher's note

References

1. Flaxman A, Marchevsky NG, Jenkin D, Aboagye J, Aley PK, Angus B, et al. Reactogenicity and immunogenicity after a late second dose or a third dose of ChAdOx1 nCoV-19 in the UK: a substudy of two randomised controlled trials (COV001 and COV002). *Lancet* (2021) 398:981–90. doi: 10.1016/S0140-6736(21)01699-8

2. Sette A, Crotty S. Immunological memory to SARS-CoV-2 infection and COVID-19 vaccines. *Immunol Rev* (2022) 310:27–46. doi: 10.1111/imr.13089

3. Natalini A, Simonetti S, Sher C, D'Oro U, Hayday AC, Di Rosa F. Durable CD8 T cell memory against SARS-CoV-2 by Prime/Boost and multi-dose vaccination: considerations on inter-dose time intervals. *Int J Mol Sci* (2022) 23:1–20. doi: 10.3390/ijms232214367

4. Soerens AG, Künzli M, Quarnstrom CF, Scott MC, Swanson L, Locquiao J, et al. Functional T cells are capable of supernumerary cell division and longevity. *Nature* (2023) 614:762–66. doi: 10.1038/s41586-022-05626-9

frontiers in Immunology

REVIEW
published: 17 September 2021
doi: 10.3389/fimmu.2021.738955

Pulmonary-Resident Memory Lymphocytes: Pivotal Orchestrators of Local Immunity Against Respiratory Infections

Duncan C. Humphries[1,2*], *Richard A. O'Connor*[1], *Daniel Larocque*[2], *Martine Chabaud-Riou*[2], *Kevin Dhaliwal*[1*] *and Vincent Pavot*[2]

[1] *Centre for Inflammation Research, Queen's Medical Research Institute, Edinburgh BioQuarter, The University of Edinburgh, Edinburgh, United Kingdom,* [2] *Sanofi Pasteur, R&D, Marcy l'Etoile, Lyon, France*

OPEN ACCESS

Edited by:
Francesca Di Rosa,
Italian National Research Council,
Italy

Reviewed by:
Wolfgang Kastenmüller,
Julius Maximilian University of Würzburg, Germany
Rita Carsetti,
Bambino Gesù Children Hospital (IRCCS),
Italy

Correspondence:
Duncan C. Humphries
Duncan.Humphries@ed.ac.uk
Kevin Dhaliwal
Kev.Dhaliwal@ed.ac.uk

Specialty section:
This article was submitted to Immunological Memory, a section of the journal Frontiers in Immunology

Received: *09 July 2021*
Accepted: *01 September 2021*
Published: *17 September 2021*

Citation:
Humphries DC, O'Connor RA, Larocque D, Chabaud-Riou M, Dhaliwal K and Pavot V (2021) Pulmonary-Resident Memory Lymphocytes: Pivotal Orchestrators of Local Immunity Against Respiratory Infections. Front. Immunol. 12:738955. doi: 10.3389/fimmu.2021.738955

There is increasing evidence that lung-resident memory T and B cells play a critical role in protecting against respiratory reinfection. With a unique transcriptional and phenotypic profile, resident memory lymphocytes are maintained in a quiescent state, constantly surveying the lung for microbial intruders. Upon reactivation with cognate antigen, these cells provide rapid effector function to enhance immunity and prevent infection. Immunization strategies designed to induce their formation, alongside novel techniques enabling their detection, have the potential to accelerate and transform vaccine development. Despite most data originating from murine studies, this review will discuss recent insights into the generation, maintenance and characterisation of pulmonary resident memory lymphocytes in the context of respiratory infection and vaccination using recent findings from human and non-human primate studies.

Keywords: lung, resident memory T cells, resident memory B cells, infection, vaccination, *in situ* optical imaging, EVLP

INTRODUCTION

Respiratory tract infections remain the leading overall cause of death in developing countries, contributing to 5.4 million deaths annually (1) despite advances in vaccination uptake and technology. Recent evidence has revealed resident memory lymphocyte populations play a key role in the response to reinfection and the development of immune "memory". Two populations of circulating memory T cells with distinct effector and migratory properties were initially described: central memory T cells (T_{CM}) and effector memory T cells (T_{EM}). Mechanistic studies in mice demonstrated that T_{EM} were more prevalent in tissues, while T_{CM} were more prevalent in lymph nodes (LN) and persisted following infection (2). T_{CM} access and survey the LN for pathogens using the LN homing receptors C-C chemokine receptor type 7 (CCR7) and CD62-L and have a high proliferative capacity but exhibit low cytotoxicity (2–4). T_{EM} lack or express low levels of CCR7 and CD62-L but express receptors enabling access to peripheral tissues, where upon reencounter with cognate antigen they rapidly exhibit high cytotoxicity (2–4). This concept has since been refined after it was found that T_{EM} are largely excluded from tissue and are restricted to the spleen and intravascular compartment (4). A novel subset of memory T cells that share similarities to both T_{CM}

and T_{EM}, termed peripheral memory T cells (T_{PM}), have been identified as the predominant subset that re-circulate between blood and peripheral tissues (4). It is now recognised that additional subset designations exist, and memory T cells fall on a continuum, rather than rigid subsets, based on their localisation, trafficking, metabolism, longevity, and phenotypic characteristics (5).

During the last decade, a memory T cell subgroup found to reside long-term in tissues without recirculating in blood has been identified. Lacking CD62-L and CCR7, resident memory T cells (T_{RM}) function as a first line of adaptive immune defence against subsequent re-infection and constitute the majority of T cells within the lung (5, 6). Lung-resident memory B cells (B_{RM}) have also been recently recognised for their critical role in immunity to respiratory infection (7). Maintained in a quiescent state, B_{RM} await secondary challenge where they accelerate secondary B cell responses.

Humans frequently develop respiratory infections throughout life and the current global coronavirus disease 2019 (COVID-19) pandemic has highlighted the need to develop and distribute effective vaccines to prevent/reduce key infectious respiratory diseases. Therefore, the development of new vaccines (e.g. COVID-19, respiratory syncytial virus, Middle East Respiratory Syndrome coronavirus) and the improvement of existing vaccines (e.g. tuberculosis, pertussis, pneumococcal and influenza) able to induce long-lasting immunity and prevent such diseases is urgently needed. The role of T_{RM} and B_{RM} in the control of respiratory infections has been highlighted recently in human and animal models (7, 8). Vaccination strategies that enhance either pre-existing memory T and B cells or promote the establishment of new antigen-specific T_{RM}/B_{RM} populations and their maintenance, alongside novel techniques for their *in situ* detection and functional characterisation, will be important tools for developing vaccines that provide long-lasting immunity against heterosubtypic infection. Here, we discuss the current knowledge of pulmonary T_{RM} and B_{RM} in human and animal models in the context of infection, highlighting knowledge gaps and opportunities in vaccine development.

FORMATION AND MAINTENANCE OF PULMONARY T_{RM} AND B_{RM}

Generation of Pulmonary T_{RM}

Professional antigen presenting cells (APCs) including dendritic cells (DCs) are key regulators of innate and adaptive immune responses. During primary viral/bacterial respiratory infection, lung-resident DCs process and present the pathogen's antigens and migrate to the mediastinal lymph node (MLN) to prime naïve T cells and stimulate their proliferation (**Figure 1**). Migratory lung DCs within the MLN imprint T cell lung homing through site-specific surface molecular signatures (15, 16) and help influence pulmonary T_{RM} generation. In human and humanized mice, pulmonary CD1c$^+$ and CD141$^+$ DCs have both been shown to present viral antigens, however only CD1c$^+$ DCs drive the expression of CD103 (a key marker of T_{RM} – see "Phenotypic Characterisation") on both naïve and memory CD8$^+$ T cells (17). Multiple chemokine receptors involved in lung trafficking are expressed by T_{RM} including C-X-C Motif Chemokine Receptor 3 (CXCR3), CXCR6 and CCR5 (11, 18–20). Although no specific combination of homing markers have been identified for pulmonary T_{RM}, CD4$^+$ are likely recruited to the airway during Respiratory Syncytial Virus (RSV) infection in human *via* C-X-C motif chemokine 10 (CXCL10 - the ligand for CXCR3), as chemokine levels correlated with activated CD4$^+$ T cell recruitment in bronchoalveolar lavage (BAL) (18).

Shortly after activation in the MLN, effector T cells migrate to the lungs and contribute towards pathogen clearance. The majority of pathogen-specific T cells then undergo apoptosis, however a minority differentiate into T_{RM} in response to environmental cues (21), with the number of T cells persisting in the lung following infection correlating with the efficiency of T_{RM} differentiation (22).

Effector T cells entering the lung express sphingosine-1-phosphate receptor (S1PR1), sensing increasing sphingosine-1-phosphate (S1P) gradients in blood and lymph, leading to tissue egress (10). S1PR1 expression is regulated by local cytokine-induced transcriptional downregulation and early activation marker CD69-mediated post-transcriptional antagonism (10). CD69 is a cell-surface receptor that is rapidly and transiently expressed on all recently activated T cells. Induction of the membrane-bound type II C-lectin receptor CD69 by antigen stimulation and inflammatory cytokine exposure leads to downregulation of S1PR1, which when combined with inflammation-induced chemotactic signalling, supports effector T cell retention and T_{RM} generation (10, 23). Transition of recruited effector T cells to T_{RM} in murine lung requires simultaneous tissue damage and T cell receptor (TCR) activation by pulmonary cognate antigen encounter (24–27). Overlapping TCR genes from human T_{RM} and non-T_{RM} indicate that environment, rather than epitope specificity, drives T_{RM} formation (19). Antigen-dependent cross-competition however does promote T_{RM} formation, with effector T cells recognising antigen presented by infected tissue cells preferentially entering the local T_{RM} pool (28). Although demonstrated in murine skin, it is possible the same rules also apply to the lung. Naïve T cells in LNs may also be epigenetically preconditioned during steady state conditions by migratory DCs to differentiate into T_{RM} upon exposure to cognate antigen (29). Dependent on DC-driven, transforming growth factor β (TGF-β), altering local or systemic TGF-β activity prior to vaccination may help promote T_{RM} formation (29).

Once established, T_{RM} remain lung-resident and contribute towards immunosurveillance and homeostasis (6). Maintained in a quiescent state, human transplant studies have demonstrated donor CD4$^+$ and CD8$^+$ T_{RM} to persist in the lungs for over 15 months, with single cell transcriptome analysis confirming *de novo* T_{RM} generation *via* the identification of a "mature T_{RM}" and an immature "T_{RM}-like" population that gradually acquire T_{RM} markers (CD69, CD103 and CD49a) over time (30, 31). Pulmonary CD8$^+$ T_{RM} are however more short-lived than those found in other tissues such as the skin and intestine (32, 33). As microbes are constantly being inhaled, the limited longevity of

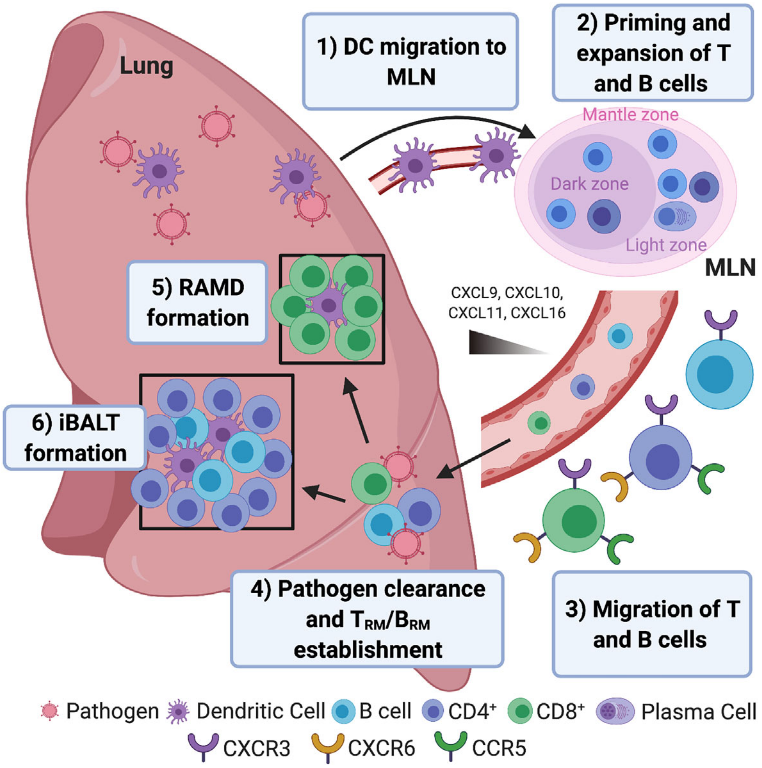

FIGURE 1 | Pulmonary resident memory lymphocyte formation. **1)** Inhaled respiratory pathogen (viral/bacterial) antigens are processed and presented by dendritic cells (DCs) that migrate to the mediastinal lymph node (MLN). **2)** DCs prime naïve CD4$^+$ and CD8$^+$ T cells in MLN with cognate antigen expressed on MHC II and MHC I, respectively, resulting in T cell proliferation. B cells interact with cognate CD4$^+$ T cells at the border between the B and T cell zones within Germinal Centres (GCs), becoming short-lived, antibody-secreting plasma cells or early memory B cells (IgM$^+$) or enter the GC and undergo somatic hypermutation and isotype switching, with low affinity B cells differentiating into memory cells to ensure a degree of poly-reactivity. High affinity B cells differentiate into long-lived plasma cells and migrate to the bone marrow where they secrete antibodies for decades (9). **3)** Stimulation within the MLN leads to the expression of chemokine receptors CXCR3, CXCR6 and CCR5 that enable T cell trafficking to the lung and airways following CXCL9/CXCL10/CXCL11/CXCL16 chemokine gradients. Pulmonary epithelial cells, DCs and macrophages secrete CCR5 and CXCR3 binding chemokines following respiratory infection (10). The CXCR6 ligand, CXCL16, is also expressed by lung bronchial epithelial cells and may also play a role in T cell homing (11). Memory B cells also migrate to the infected lung, following interferon-inducible chemokines CXCL9, CXCL10 and CXCL11 *via* CXCR3 (12, 13) where they are strategically located for subsequent reinfection. **4)** Once entered the lung, effector T cells and short-lived plasma cells help clear infection and undergo apoptosis. A minority of effector T cells differentiate into pulmonary-resident memory T cells (T_{RM}). IgM$^+$ pulmonary-resident memory B cells (B_{RM}) seed the lung early after infection, followed by isotype-switched B_{RM} (7). **5)** CD8$^+$ T_{RM} accumulate and self-renew in areas undergoing tissue regeneration following infection known as repair-associated memory depots (RAMD) where they seed airway CD8$^+$ T_{RM}, which are ideally located for pathogen clearance in the case of reinfection. **6)** CD4$^+$ T_{RM} and B_{RM} reside within GCs of inducible bronchus-associated lymphoid tissue (iBALT). Associated with prolonged persistence of antigens, iBALT GCs in infected lungs serve as sites for exaggerated B cell proliferation and cross-reactive clonal selection of plasma cells/memory progenitors following B cell/CD4$^+$ T_{RM} interactions (14).

pulmonary CD8$^+$ T_{RM} may provide a mechanism for avoiding unnecessary inflammation and pathogenesis in this tissue (34).

Gene Regulation in T_{RM}

In human, Notch signalling alongside low levels of T-bet and Eomesodermin (EOMES) are required for the development and maintenance of CD4$^+$/CD8$^+$ T_{RM}, with Notch regulating T_{RM} metabolic programs (11, 20). Human pulmonary CD8$^+$ T_{RM} display elevated levels of the transcription factors Hobit (encoded by the gene *ZNF683*) and Runx3, that may be involved in T_{RM} generation and/or maintenance (30). Interestingly, despite showing elevated mRNA levels, Hobit protein expression was reported absent in human CD4$^+$ T_{RM}, suggesting differences between CD4$^+$/CD8$^+$ T_{RM} formation/maintenance (11).

Heterogeneity in effector function and phenotype is evident within T_{RM} populations, particularly within CD4$^+$ T_{RM} (19). Transcriptome profiling of human lung CD69$^+$ T_{RM} has revealed the differential expression of 31 core genes associated with migration, adhesion and regulatory molecules when compared to CD69$^-$ subsets (19). This transcriptional profile is conserved across CD4$^+$/CD8$^+$ CD69$^+$ lineages as well as tissues (19). Pulmonary T_{RM} exhibit high transcript levels for genes encoding for several chemokine receptors, pro-inflammatory cytokines and cytotoxic mediators, enabling them to be recruited and retained within the lung and undergo rapid, polyfunctional responses (11, 20). T_{RM} respond rapidly with effector functions, however, expression of regulatory genes (e.g. cytotoxic T-lymphocyte-associated protein 4 [CTLA4] and B-and T-lymphocyte attenuator 4 [BTLA4]) in CD8$^+$ T$_{RM}$ may present a safety mechanism to minimise aberrant activation and associated inflammation/tissue damage (20).

Generation of Pulmonary B$_{RM}$

Human antigen-experienced lungs are enriched with B cells containing a resident memory phenotype (35). As human and non-human primate (NHP) B$_{RM}$ data are limited, most findings are derived from mouse studies. During primary respiratory infection, naïve B cells, primed by either free antigen or antigen delivered by subcapsular sinus (SCS) macrophages (36), interact with cognate CD4$^+$ T cells at the T-B border within the MLN (9, 37). Following initial proliferation at the outer follicles, B cells may differentiate into extrafollicular short-lived plasma cells, early (germinal centre (GC)-independent) memory cells or proliferate to form the GC (**Figure 1**). Following somatic hypermutation, B cells can exit as long-lived plasma cells, migrating to the bone marrow where they secrete antibodies for decades, or memory B cells (9, 37). Having migrated to the lungs to participate in pathogen clearance, most of the responding B cells undergo apoptosis, leaving a few resting memory cells in the respiratory tract and lymphoid organs where they wait for the same antigen.

Murine parabiosis studies have demonstrated B$_{RM}$ generation requires local antigen encounter and is dependent on early CD40-interactions with T cells (7). Once established, B$_{RM}$ remain lung resident due to expression of CD69 (7). Here they undergo metabolic reprogramming, switching from anabolic to catabolic pathways to reduce their requirement for high levels of cytokines for their maintenance (37). In mice, B$_{RM}$ are quiescent and long-lived, maintained from precursors within persisting GCs in areas known as inducible bronchus-associated lymphoid tissue (iBALT) (14), however B$_{RM}$ have also been detected in the absence of iBALT (39). Established one week after influenza infection, murine pulmonary B$_{RM}$ have been demonstrated to be phenotypically and functionally distinct from their systemic counterparts (7).

Gene Regulation in B$_{RM}$

Few studies have investigated gene regulation in pulmonary B$_{RM}$, particularly in humans. Although the possibility of a "master transcription factor" for B$_{RM}$ generation has been suggested, no unique transcription factor has been identified so far (9). Increased expression of the transcription factors Bach2, KLF2, ZBTB32, ABF1 and STAT5 are associated with B$_{RM}$ formation in mice, however their exact roles are yet to be understood (9, 40). The transcriptional regulation of pulmonary B$_{RM}$ differentiation is likely to be unique – understanding these transcription factors may help identify methods for modulating their formation (41).

PHENOTYPIC CHARACTERISATION

Human and Non-Human Primate T$_{RM}$ Markers

Due to their similarities to human, NHPs provide an invaluable tool for investigating host response to respiratory infection and vaccination. Although heterogenous within the lung, human and NHP T$_{RM}$ are phenotypically distinct from T$_{CM}$ and T$_{EM}$ and are primarily identified by the high expression of the C-type lectin receptor CD69, and integrins CD103 and CD49a (30). The transmembrane CD69 is a key marker of pulmonary T$_{RM}$, distinguishing memory T cells in tissue from those in circulation (19), however murine evidence suggests its expression is not essential for the establishment and maintenance of T$_{RM}$ in the lung (25, 42, 43). Although considered as an early activation marker for TCR signalling, T$_{RM}$ CD69 expression is not associated with markers of recent activation and appears to be a function of previous antigen exposure (19).

Preferentially expressed on CD8$^+$ T$_{RM}$ compared to CD4$^+$, CD103 promotes adherence to E-cadherin, an adhesion molecule expressed by epithelial cells (22, 30, 44). CD103 expression is driven by membrane-bound TGF-β (mediated by IL-10) on APCs (CD1c$^+$ DCs and monocytes) (17, 45) and is thought to contribute towards initial recruitment and persistence of CD8$^+$ T$_{RM}$ to aide surveillance rather than long-term maintenance (42). CD49a, expressed by both CD4$^+$ and CD8$^+$ T$_{RM}$, is an integrin specific to collagen IV that facilitates locomotion for surveillance and is essential for T$_{RM}$ survival by limiting apoptosis following ligand engagement (42). Other recognised surface markers of pulmonary T$_{RM}$ are outlined in **Table 1** - understanding the full function of these markers, whether they represent different subsets/maturation states and whether they are pathogen-dependent remains to be determined.

B$_{RM}$ Markers

Although no specific marker of B$_{RM}$ residency has been described, pulmonary B$_{RM}$ are phenotypically distinct from their systemic memory and non-memory counterparts (7) – see **Table 2**. As well as lacking CD62-L, murine pulmonary B$_{RM}$ express markers associated with T$_{RM}$, such as CD69, CXCR3 and CD44, which retain B$_{RM}$ within the lung (7, 12, 35, 39). CD69 has also been found on human pulmonary B$_{RM}$ (35). Whether other markers found in mice are also expressed on human and NHP pulmonary B$_{RM}$ requires further investigation.

Functional studies have revealed B$_{RM}$ established early after murine influenza infection are positive for immunoglobulin M (IgM$^+$) which are later followed by isotype-switched B$_{RM}$ (7). Following murine *pneumococcal* infection, the majority of isotype-switched B$_{RM}$ are IgG$^+$, with a small fraction IgA$^+$ (35). The majority of B$_{RM}$ found in healthy human lung are also isotype-switched (35).

ANATOMICAL LOCATION

T$_{RM}$/B$_{RM}$ persist at sites of previous antigen encounter (13). CD8$^+$CD103$^+$ T$_{RM}$ are found at higher frequencies in the airway than in parenchyma due to adhesion to epithelial E-cadherin, making them ideally located to respond to reinfection (30). Murine CD8$^+$ T$_{RM}$ reside and self-renew in peribronchiolar foci in areas undergoing tissue remodelling, known as repair-

TABLE 1 | Human and Non-Human Primate Surface Marker Expression on Pulmonary T$_{RM}$.

Surface Marker	Cell Type	Function	Pathogen/Condition Studied	Species + References
CD69	CD4$^+$ T$_{RM}$	Tissue retention	Lung Donation, *Mtb, RSV, Influenza*	Human (18, 19, 22, 24, 30, 46) NHP (44)
	CD8$^+$ T$_{RM}$		Lung Donation*, Mtb, RSV, Influenza*	Human (8, 18, 19, 22, 24, 30, 45, 46) NHP (21, 44, 45)
CD103 (αE integrin)	CD4$^+$ T$_{RM}$	Adhesion to E-cadherin, initial recruitment, facilitates persistence and surveillance	Lung Donation, *Mtb*, biopsy, *RSV, Influenza*	Human (11, 18, 19, 22, 24, 30, 46)
	CD8$^+$ T$_{RM}$		Lung Donation, *Mtb*, biopsy, *RSV, Influenza*	Human (8, 18, 19, 22, 24, 30, 45, 46) NHP (21, 45)
CD49a ($\alpha_1\beta_1$ integrin/VLA-1)	CD4$^+$ T$_{RM}$	Adhesion to Collagen IV, limits apoptosis, facilitates locomotion for surveillance	Lung Donation, *Mtb*	Human (19, 24, 30)
	CD8$^+$ T$_{RM}$		Lung Donation, *Mtb*	Human (19, 24, 30)
CD49d ($\alpha_4\beta_1$ integrin/VLA-4)	CD4$^+$ T$_{RM}$	Adhesion to Fibronectin	*Mtb*	Human (24, 47)
CD101	CD4$^+$ T$_{RM}$	Inhibits T cell activation, proliferation	Lung Donation	Human (30)
	CD8$^+$ T$_{RM}$		Lung Donation, *Mtb*	Human (19, 24, 30)
PD-1 (CD279)	CD4$^+$ T$_{RM}$	Immune checkpoint and T cell exhaustion marker (prevent aberrant activation)	Lung Donation, *Mtb*	Human (19, 30) NHP (48)
	CD8$^+$ T$_{RM}$		*Influenza*	Human (19, 30, 46) NHP (44)
CXCR3	CD4$^+$ T$_{RM}$	Chemokine receptor	*Mtb, RSV*	Human (11, 18)
	CD8$^+$ T$_{RM}$		Biopsy	Human (20)
CXCR6	CD4$^+$ T$_{RM}$	Chemokine receptor	Lung Donation, biopsy	Human (11, 19, 46)
	CD8$^+$ T$_{RM}$		Lung Donation, biopsy	Human (19, 20, 46)
CCR5	CD4$^+$ T$_{RM}$	Chemokine receptor	Lung Donation/cancer lobectomy, *Mtb*	Human (11, 18, 46)
	CD8$^+$ T$_{RM}$		*Mtb*	Human (46)
CCR6	CD8$^+$ T$_{RM}$	Chemokine Receptor	Lung Resection	Human (20, 49)
CD44	CD8$^+$ T$_{RM}$	Leukocyte rolling and adhesion	*Mtb, influenza*	Human (24)
CD28/CD28H	CD8$^+$ T$_{RM}$	T cell activation	Lung Resection	Human (11, 49)
CD45RO	CD4$^+$ T$_{RM}$	Memory T cell marker	*Influenza*	Human (33)
	CD8$^+$ T$_{RM}$		Lung donation, *Influenza*	Human (22, 33)
CD45RA$^-$	CD4$^+$ T$_{RM}$	Naïve T cell marker	Lung Donation	Human (19, 30)
	CD8$^+$ T$_{RM}$		Lung Donation	Human (19, 30)

Multiple markers relating to adhesion/migration/activation are specifically upregulated on lung T$_{RM}$. Other naive/effector/memory markers help distinguish memory T cells from regular effector T cells (e.g. CD45RA and CD45RO). Mtb, Mycobacterium tuberculosis; RSV, Respiratory Syncytial virus.

TABLE 2 | Surface Marker Expression of Human/Mouse Pulmonary B$_{RM}$.

Surface Marker	Function	Pathogen/Condition Studied	Species + References
CD38	Cell adhesion	*Influenza*	Mouse (12)
CD80	GC-matured memory marker	*Influenza, Pneumococcus*	Mouse (7, 12, 35, 39)
CD27	Post- activation marker, memory B cell marker	Healthy lung resection/lobectomy	Human (35)
CD73	GC-matured memory marker	*Influenza, Pneumococcus*	Mouse (12, 35, 39)
PD-L2 (CD273)	GC-matured memory marker	*Influenza, Pneumococcus*	Mouse (7, 12, 35, 39)
CD20	B cell differentiation	*Pneumococcus*	Mouse (39)
CD69	Tissue retention	Healthy lung resection/lobectomy, *Influenza, Pneumococcus*	Human (35) Mouse (7, 12, 35, 39)
CD44	Leukocyte rolling and adhesion	*Pneumococcus*	Mouse (35, 39)
CD11a	Integrin, cell adhesion	*Pneumococcus*	Mouse (35)
CXCR3	Chemokine receptor	*Influenza*	Mouse (7, 12)

B$_{RM}$ surface markers are mostly associated with activation, GC-maturation and tissue homing and share some similarities with T$_{RM}$.

associated memory depots (RAMDs) (25, 38) (**Figure 2**). Tissue damage is a requirement for RAMDs (25) and may have implications for vaccine design and delivery. The existence of human RAMDs containing CD8$^+$ T$_{RM}$ remains to be confirmed.

CD4$^+$ T$_{RM}$ and B$_{RM}$ are located and maintained around the small airways within iBALT located within the parenchyma (13, 14, 25, 30) (**Figure 2**). iBALT contain GCs that serve as sites for B cell selection and maturation following murine influenza infection (50), generating cross-reactive memory B cells to ensure heterosubtypic humoral protection (14). Formation is associated with inflammation (44) and prolonged antigen persistence (14). B$_{RM}$ have also been observed in non-lymphoid areas below the airway epithelium and airways (13) as well as lungs of *pneumococcal*-recovered mice lacking iBALT,

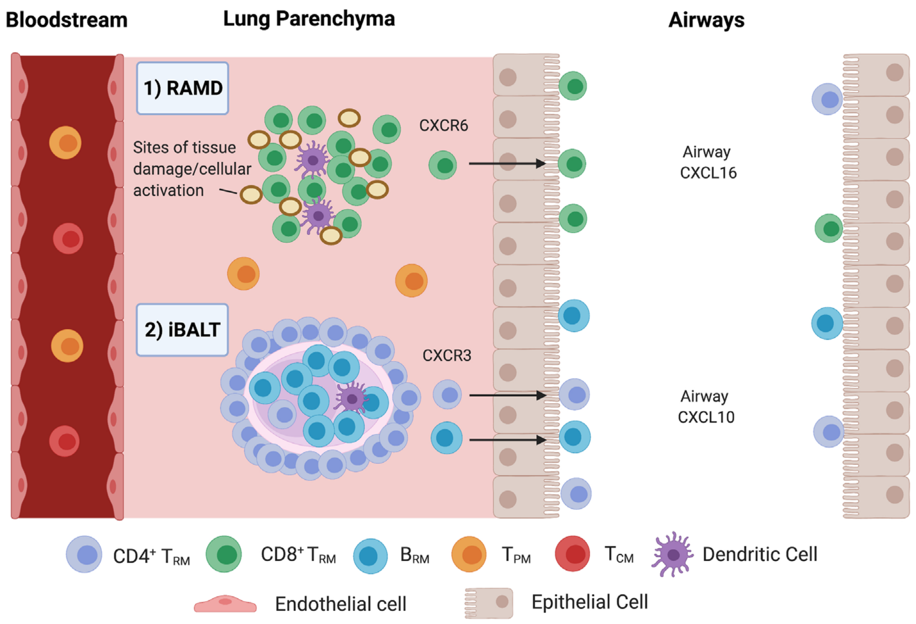

FIGURE 2 | Compartmentalisation of Pulmonary T_{RM} and B_{RM}. **1)** $CD8^+$ T_{RM} are maintained in repair-associated memory depots (RAMDs) located in peribronchiolar foci in areas previously damaged from primary infection. RAMDs can be identified *via* the presence of cytokeratin-expressing cell aggregates which contain distal airway stem cells that help reconstruct damaged lung tissue (10). Murine evidence suggests interstitial $CD8^+$ T_{RM} are primarily maintained by a process of homeostatic proliferation and seed airway T_{RM}, driven by CXCR6 in response to airway CXCL16 (38). **2)** $CD4^+$ T_{RM} surround B_{RM} cell follicles in iBALT located within the pulmonary parenchyma, where prolonged antigen persistence enhances $CD4^+$ T_{RM}/B_{RM} formation. Just like RAMDs, iBALT requires tissue damage/inflammation for their establishment. $CD4^+$ T_{RM} are then recruited to the alveolar space *via* CXCL10/CXCR3.

indicating that they are components of histologically unremarkable lungs that may not require iBALT for their maintenance (35, 39).

FUNCTION

T_{RM} Response to Viral Infection

Growing evidence indicates that virus-specific T cells resident along the respiratory tract are highly effective at providing potent and rapid protection against inhaled pathogens. In human influenza infection, $CD8^+$ T_{RM} have been shown to recognise the internal, conserved proteins of the virus whereas $CD4^+$ T_{RM} recognise both internal and external proteins, with both cell types contributing towards heterosubtypic protection (33). $CD8^+$ T_{RM} have been shown to be cross-reactive against three influenza strains (51), with single cell sequencing revealing diverse TCR profiles “capable of recognising newly emerging viral escape variants” (22).

Influenza-specific $CD8^+$ T_{RM} have a low activation requirement, requiring only cognate antigen in the absence of helper cell-derived signals (52). Once stimulated, they are highly proliferative, producing polyfunctional progeny (producing ≥2 cytokines – IFN-γ, TNF, Granzyme B and IL-2) with effector function superior even to their parent population (22, 44). Polyfunctional T_{RM} offer enhanced protection by producing higher levels of cytokines whilst simultaneously driving effector responses (53) - activated $CD8^+$ T_{RM} exert their cytotoxic function to kill infected cells (10) whilst $CD4^+$ T_{RM} interact with B cells in iBALT to generate new neutralising antibodies (14, 54). A newly identified, long-lived $CD4^+$ T resident helper (T_{RH}) population with functional and phenotypical similarities to lymphoid T follicular helper cells (T_{FH}) has also been described following murine influenza infection. Residing within iBALT, T_{RH} are tightly localised with B_{RM} to support local antibody production following reinfection (55).

In an experimental human RSV infection model, the abundance of RSV-specific, pulmonary $CD8^+$ T_{RM} before infection was associated with reduced symptoms and viral load, implying that $CD8^+$ T_{RM} can confer protection against severe respiratory viral disease when humoral immunity is overcome (8). RSV-specific $CD8^+$ T_{RM} displayed phenotypic changes representative of advanced differentiation, with downregulation of both co-stimulatory and cytotoxicity markers, suggesting cells can respond rapidly to reinfection, but function is restricted to minimise excessive tissue damage (8).

RSV infection in African Green Monkeys (AGM) also induced virus-specific airway $CD8^+$ T_{RM} capable of reducing viral titres, however failed to induce robust $CD4^+$ T_{RM} and humoral responses (21). Previously protective RSV-candidate vaccines in AGM induced a strong T cell response, whilst those eliciting a strong neutralisation antibody response without detectable T cell response were not as effective (56). Similar to influenza, CD8$^+$ T$_{RM}$ recognise internal proteins of RSV, whilst CD4$^+$ T$_{RM}$ recognise external proteins (18). RSV-induced immunopathology relates to a dysregulated T cell response – RSV-specific memory CD8$^+$ T cells in blood display little evidence of multiple cytokine production unlike those seen against influenza (8, 18). CD8$^+$ T$_{RM}$ however appear to be more polyfunctional, generating IFN-γ, IL-2 and TNF (21), however fail to undergo proliferation when activated and express reduced cytotoxicity markers compared to peripheral memory cells (8).

T$_{RM}$ Reponses to Bacterial Infection

Activated CD4$^+$ and CD8$^+$ T$_{RM}$ have been identified in the lungs of patients infected with *Mycobacterium tuberculosis* (*Mtb*), where they help limit intracellular macrophage *Mtb* replication (46). T$_{RM}$ were polyfunctional, expressing IFN-γ, TNF ± IL-2, and exhibited a highly cytotoxic profile, with CD4$^+$ T$_{RM}$ appearing more polyfunctional than CD8$^+$ T$_{RM}$ (46). CD49d is upregulated on airway CD4$^+$ T$_{RM}$ and optimises the localisation of human *Mtb*-specific recall responses (47). *Mtb* infection in macaques drives a cellular T helper 1 (T$_H$1) and humoral response, without protective efficacy, however repeated pulmonary Bacillus Calmette-Guérin (BCG) delivery was shown to induce polyfunctional, T$_H$17 CD4$^+$ T$_{RM}$, leading to airway IgA secretions in BAL (48), presumably through the generation of B$_{RM}$. Interstitial CD4$^+$ depletion with *simian immunodeficiency virus* (SIV) following *Mtb* infection identified CD4$^+$ T$_{RM}$ (57), proliferating CD8$^+$ memory T cells (T$_{CM}$, T$_{EM}$ and likely T$_{RM}$) and B cells within iBALT (58) as critical for suppressing latent *Mtb* reactivation.

T$_H$17 CD4$^+$ T$_{RM}$ are also critical in protecting against murine nasal *Bordetella pertussis* (Bp) colonization (59). Although both capable of protecting against Bp lung infection, whole cell Bp vaccine, unlike the acellular vaccine, induced nasal IL-17-producing CD103$^+$ CD4$^+$ T$_{RM}$ (similar to natural Bp infection) that recruited neutrophils to enhance bacterial clearance.

T$_{RM}$ Bystander Effect

Lung T$_{RM}$ also display "innate-like" behaviour, amplifying inflammation following noncognate bacterial infection. APC-derived IL-12/IL-18 activated virus-specific CD8$^+$ T$_{RM}$ within the lung parenchyma, leading to the rapid synthesis of IFN-γ. This "bystander activation" boosted neutrophil recruitment to improve bacterial clearance. Despite being performed in mice, the authors demonstrated *in vitro* that human CD8$^+$ T$_{RM}$ similarly synthesise IFN-γ in response to IL-12/IL-18 (60).

B$_{RM}$ Response to Viral and Bacterial Infections

Alongside long-lived antibody-secreting plasma cells, B$_{RM}$ contribute towards the protective humoral immune response to pulmonary reinfection (12). The presence of B$_{RM}$ is a common feature of antigen-experienced lungs and is important for acquired immunity (7). B cells in the airways secrete antibodies that act both locally and at mucosal surfaces. These antibodies, predominantly IgM and IgA, bind to glandular epithelial and mucosal surfaces to promote pathogen clearance (61). B cells activated in respiratory lymphoid tissue also differentiate into IgA-secreting plasma cells that predominantly act in the airway. Current knowledge of B cell homing and class switching in the airway remains limited.

Murine parabiosis/adoptive transfer/depletion studies have demonstrated the protective role played by B$_{RM}$ in response to both viral (7, 12, 54) and bacterial lung infection (35). B$_{RM}$ provide rapid antibody-secreting cells (ASC), producing a range of class switched neutralising antibodies (7, 12). Lung B$_{RM}$ produce greater numbers of ASC than splenic memory cells following exposure to drifted virus, indicative of heterosubtypic protection (14). Cross-neutralising antibodies to conserved, internal influenza proteins provide heterosubtypic protection (14, 54). Although IgA is more effective than IgG at preventing upper respiratory infection, in combination they achieve maximal neutralising activity against influenza in mice (12). Following murine *pneumococcal* infection, B$_{RM}$ contribute towards bacterial clearance by rapidly secreting cross-reactive antibodies, even when reactivated by a serotype-mismatched strain (35). In macaques, iBALT persistence is associated with reduced *Mtb* reactivation due to enhanced B-cell and humoral immunity (58). B$_{RM}$ are also potent APC, binding and endocytosing antigen *via* their BCR to increase peptide/MHC II presentation and further enhance CD4$^+$/B cell responses (9, 13).

LOSS OF PULMONARY PROTECTION

Pulmonary immunity to respiratory pathogens wanes over time, meaning individuals are susceptible to recurrent infections throughout their lifetime. Although antigen drift may contribute to loss of protection, the gradual loss of pulmonary CD8$^+$ T$_{RM}$ is a major contributor (32). Murine lung CD8$^+$ T$_{RM}$ are less durable than those found in skin due to an increased susceptibility to apoptosis (32), and have been shown to undergo "retrograde migration" to the MLN where they provide longer-lived regional memory (62). Loss of RAMDs due to tissue repair correlated with a decline in CD8$^+$ T$_{RM}$ number in mice (10, 25), whilst in humans iBALT diminishes with age (6) which may explain why older age groups are more susceptible to respiratory infection due to a reduced ability to mount CD4$^+$ T$_{RM}$/B$_{RM}$ responses.

IMMUNOPATHOLOGY

Although T$_{RM}$-driven immunopathology has been described in other tissues (63), less is known regarding pulmonary T$_{RM}$. Moderate-severe asthma patients display increased numbers of CD4$^+$CD103$^+$ T$_{RM}$ in their airways (64) and vaccine-enhanced disease in children with formalin-inactivated RSV is driven by T$_H$2 CD4$^+$ memory cells that induce excessive inflammation (65). Exacerbations of pulmonary pathology following RSV infection have also been linked to iBALT which stimulate increased, yet detrimental, immune responses (66). CD8$^+$ T$_{RM}$ may impact gas exchange *via* the presence of RAMD or through inflammation induced by bystander activation (60). *In vitro*, CD8$^+$ T cells damage non-infected epithelial cells during influenza infection through TNF and IFN-γ release (67). Although the detrimental effect due to T$_{RM}$/B$_{RM}$ has not been demonstrated *in vivo*, T$_{RM}$/B$_{RM}$ formation may not always be beneficial if accompanied by another immune cell influx such as that found following acute infections.

VACCINATION STRATEGIES TO PROMOTE T$_{RM}$

The presence of pathogen-specific T$_{RM}$ cells in the lungs has been shown to correlate with protection in human and animal models. It has therefore been proposed that T$_{RM}$ represent one of several immune mechanisms that should be harnessed together for optimal vaccine-mediated protection. A better understanding of how lung T$_{RM}$ are generated and maintained is required for optimal vaccine development. Vaccination strategies to promote T$_{RM}$ have been successfully demonstrated in mouse models, including engineered biomaterials that modulate antigen delivery and retention time, adjuvant combinations, viral vectors and virus-like particles, as well as direct APC targeting (68), however studies in human and NHP are limited.

In mice and human, inactivated influenza vaccines induce systemic humoral responses but fail to induce T cell immunity in the lungs (33, 69, 70). Intranasal live-attenuated influenza virus vaccines however generate mucosal IgA, lung CD4$^+$ T$_{RM}$ and virus-specific CD8$^+$ T$_{RM}$ similar in phenotype to those generated by influenza virus infection, providing long term, heterosubtypic protection, independent of circulating T cells and neutralising antibodies (70, 71). Tissue-resident alveolar macrophages have been found to limit CD8$^+$ T$_{RM}$ formation following murine influenza infection and may offer an attractive target for manipulation (72).

Intravascular, but not subcutaneous, administration of an agonistic anti-CD40 antibody alongside poly-IC : LC (a Toll-like receptor 3 activator) with HIV envelope peptide antigen directly stimulated APCs in the blood, MLN and lung to enhance pulmonary CD8$^+$CD103$^+$ T$_{RM}$ formation in macaques (45). Intravenous BCG in macaques induces more antigen responsive pulmonary CD4$^+$ and CD8$^+$ T$_{RM}$ than intradermal administration, with protection lasting 6 months later (73). Intratracheal boosting with BCG however following intradermal BCG vaccination enhances protection (74). Although this study only analysed peripheral blood to correlate increased CD4$^+$ T$_{EM}$ populations with improved protection, it is anticipated that local delivery of antigen to the lungs would also increase T$_{RM}$/B$_{RM}$ populations. Pulmonary mucosal BCG vaccination therefore offers superior protection against *Mtb* compared to standard intradermal vaccination (48, 75, 76).

VPM1002, a live BCG vaccine genetically modified to improve immunogenicity, outperforms live-attenuated BCG in preclinical testing and is undergoing clinical trials (NCT03152903) (77). Aerosol immunization with a mutated *Mtb* strain *Mtb*Δ*sigH* reduced bacterial burden and lung pathology when compared to aerosolised BCG following *Mtb* challenge in macaques (78). *Mtb*Δ*sigH* persisted for longer in the lungs than BCG and generated increased iBALT and CD69$^+$ T cells in BAL, which likely include T$_{RM}$. Since antigen is required for T$_{RM}$/B$_{RM}$ establishment, increasing its persistence enhances generation. Increasing antigen persistence using a cytomegalovirus vector encoding *Mtb* antigen inserts prevented disease in macaques through the establishment and maintenance of lung T$_{RM}$ (79).

It is also possible that skin-resident T$_{RM}$ generated through intradermal vaccination may enhance both local and systemic host responses to *Staphylococcus aureus*, a common commensal of the skin and nasal mucosa, to help minimise Staphylococcal pneumonia (80).

VACCINATION STRATEGIES TO PROMOTE B$_{RM}$

Strategies to induce pulmonary B$_{RM}$ require delivery of antigen to the lung (7). In mice, intranasal vaccination extended antibody specificity to confer heterosubtypic protection by inducing GCs that generated cross-reactive antibody responses (14). In human, the squalene emulsion adjuvants AS03 or MF59 augmented neutralising antibody production when co-administered intramuscularly with influenza vaccine (81). Both adjuvants enhanced antigen uptake and presentation in local tissue leading to increased CD4$^+$ and B cell responses, with AS03 also shown to increase naïve B cell activation and the adaptability of pre-existing memory B cells (82). Despite increasing the breadth of B cell repertoire following seasonal Flu vaccine (83), the impact of adjuvants on pulmonary T$_{RM}$/B$_{RM}$ remains to be demonstrated for such intramuscular vaccine. We could not exclude that a boost from an adjuvanted vaccine in humans previously exposed to a similar antigen encountered in the lung could re-activate and maintain pulmonary T$_{RM}$/B$_{RM}$.

In contrast, certain respiratory viruses such as RSV are known to trigger a T$_H$2-like, dysregulated antiviral response (84). Acute RSV infection limits pulmonary B$_{RM}$ formation (85) and encodes a number of immunomodulatory proteins that impair antigen presentation and type 1 interferon release (18), which may explain why infection is associated with a low level antibody response (21). Similarly, COVID-19 also suppresses MHC I/ MHC II antigen presentation and interferon response (86). These issues of dysregulated T cell responses should be avoided or overcome through vaccination, leading to long-term humoral protection.

QUANTIFYING IMMUNOLOGICAL MEMORY FOLLOWING VACCINATION

Most vaccine studies in humans rely on peripheral blood sampling to evaluate protection. Serum haemagglutination inhibition (HAI), ELISA or ELISpot may indicate the humoral response generated against a given pathogen/vaccine, however does not always reflect immunity, as protection against influenza has been seen despite the absence of HAI titres (87). Nasal IgA is also a better reflector of protection to RSV than serum IgG (85). Circulating memory T and B cells do not always correlate with protection (8, 85) and immune responses can differ from those in lung (44).

Limited peripherally accessible biomarkers have been identified following immunization relating to resident memory lymphocyte generation. Early rises in plasma IL-10 correlated with pulmonary $CD8^{+}CD103^{+}$ T_{RM} generation following immunization in macaques (45). The CXCL10/CXCR3 axis has also been postulated as a potential biomarker for $CD4^{+}$ migration to the lung (18). Further immunization studies correlating peripheral biomarkers with T_{RM}/B_{RM} formation are required.

Airway T_{RM} can be isolated *via* BAL (30). Virus-specific $CD8^{+}$ frequencies have been found to be 10 times higher in BAL than in peripheral blood in AGM, highlighting the quantitative differences between local and systemic T cell responses (21). BAL can be collected multiple times, providing temporal information on airway populations, but not interstitial. Post-mortem analysis is often the only method for assessing T_{EM}/T_{RM}. Tissue sections can be collected for histology or enzymatic tissue digestion, however accessing human/NHP tissue is difficult. Lung tissue is easily contaminated with alveolar/intravascular cells unless the organ is perfused and BAL collected (however this is not 100% effective). Intravenous antibody staining can distinguish tissue resident from circulatory cells, however, is not performed in humans/NHP. T_{RM}/B_{RM} are identified through surface marker expression or gene signature, with pathogen-specificity evaluated through intracellular cytokine staining following exposure to antigen/MHC tetramers (T_{RM}) or binding of labelled-antigen (B_{RM}). Given the limited information gained on pulmonary T_{RM}/B_{RM} populations using current sampling methods, new detection techniques are required.

In Situ Optical Imaging

Optical endomicroscopy imaging (88), recently used for the detection of human alveolar neutrophils *in situ* (89), may provide a valuable tool for assessing pulmonary-resident memory lymphocytes and quantifying immunological memory following vaccination. Fluorescently tagged ligands or antibodies, capable of binding to specific T_{RM}/B_{RM} surface markers, can be delivered to the airways *via* a bronchoscope to enable visualisation (**Figure 3**). The information gained can be combined with systemic data to evaluate vaccine efficacy and expected degree of protection against respiratory pathogens. *In situ* optical imaging may also be used to screen lungs for transplantation, as the presence of T_{RM} in donor tissue is associated with reduced adverse clinical events in the recipient (30).

Ex Vivo Lung Perfusion

The COVID-19 pandemic has highlighted how immune responses in the airways differ from those in the circulation and that it is tissues, not blood, where immune cells function (90). Assessing tissue-based immunity following infection and vaccination is therefore essential. *Ex vivo* lung perfusion (EVLP), using human lungs deemed non-suitable for transplantation,

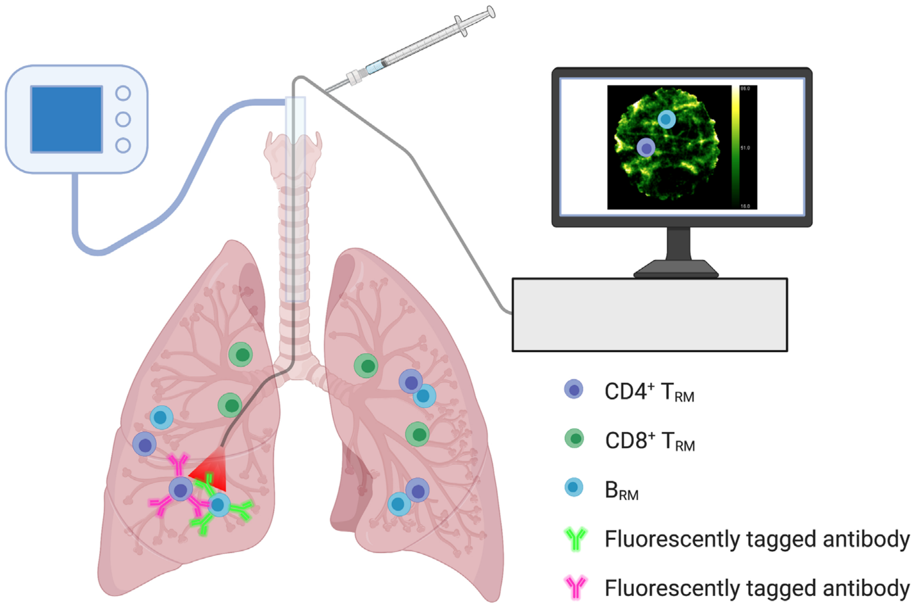

FIGURE 3 | *In Situ* Optical Imaging of Resident Memory Lymphocytes. Optical endomicroscopy imaging within the lungs may allow for the *in situ* detection and quantification of resident memory lymphocyte populations. Monitoring numbers following immunization may help reflect vaccine efficacy and immunological memory. Fluorescently tagged ligands or antibodies, capable of binding to specific T_{RM}/B_{RM} surface markers, can be delivered to the airways *via* a bronchoscope to enable visualisation. Using a combination of fluorescent ligands/antibodies could help differentiate resident memory lymphocyte populations.

provides an ideal model for assessing tissue immunity and optimising *in situ* optical imaging. As well as studying populations *in situ*, EVLP offers the ability to isolate large numbers of human T_{RM}/B_{RM}, far higher than those obtained from a typical BAL, for in-depth analysis (including phenotype, function, and antigen-specificity). Intraperfusate delivery of a fluorescently tagged CD45 antibody can also differentiate circulating (labelled) from tissue-resident (non-labelled) cells. This technique has recently revealed how human lung T_{RM} colocalise with lung-resident macrophages, preferentially around the airways, where they receive costimulatory signals to augment effector cytokine production and degranulation (91).

CONCLUDING REMARKS

Resident memory lymphocytes in the lung enhance immunity against respiratory pathogens. Understanding the mechanisms that drive T_{RM} and B_{RM} formation will improve vaccine design, with the hope of generating long lived, polyfunctional T_{RM} and broadly reactive, neutralising-antibody-secreting B_{RM} in the lung. Targeting respiratory APCs with antigen followed by subsequent “boosts” may establish and maintain these populations. Assessing the local and systemic responses using a combination of *in situ* imaging and peripheral blood sampling may reveal the efficacy of novel vaccines designed specifically to induce resident memory lymphocyte populations in the lung. Human *ex vivo* lung perfusion provides an ideal model for researching T_{RM}/B_{RM} populations and optimising novel methods for their *in situ* detection to help quantify immunological memory.

AUTHOR CONTRIBUTIONS

DH, KD, MC-R, and VP contributed to conception and design of the manuscript. DH wrote the first draft of the manuscript. DH, RO’C, DL, MC-R, and VP wrote sections of the manuscript. All authors contributed to the article and approved the submitted version.

FUNDING

This work was funded by Sanofi Pasteur.

ACKNOWLEDGMENTS

All figures created with BioRender.com.

REFERENCES

1. Ferkol T, Schraufnagel D. The Global Burden of Respiratory Disease. *Ann Am Thorac Soc* (2014) 11:404–6. doi: 10.1513/AnnalsATS.201311-405PS
2. Wherry EJ, Teichgräber V, Becker TC, Masopust D, Kaech SM, Antia R, et al. Lineage Relationship and Protective Immunity of Memory CD8 T Cell Subsets. *Nat Immunol* (2003) 4:225–34. doi: 10.1038/ni889
3. Masopust D, Soerens AG. Tissue-Resident T Cells and Other Resident Leukocytes. *Annu Rev Immunol* (2019) 37:521–46. doi: 10.1146/annurev-immunol-042617-053214
4. Gerlach C, Moseman EA, Loughhead SM, Alvarez D, Zwijnenburg AJ, Waanders L, et al. The Chemokine Receptor CX3CR1 Defines Three Antigen-Experienced CD8 T Cell Subsets With Distinct Roles in Immune Surveillance and Homeostasis. *Immunity* (2016) 45:1270–84. doi: 10.1016/j.immuni.2016.10.018
5. Jameson SC, Masopust D. Understanding Subset Diversity in T Cell Memory. *Immunity* (2018) 48:214–26. doi: 10.1016/j.immuni.2018.02.010
6. Snyder ME, Farber DL. Human Lung Tissue Resident Memory T Cells in Health and Disease. *Curr Opin Immunol* (2019) 59:101–8. doi: 10.1016/j.coi.2019.05.011
7. Allie SR, Bradley JE, Mudunuru U, Schultz MD, Graf BA, Lund FE, et al. The Establishment of Resident Memory B Cells in the Lung Requires Local Antigen Encounter. *Nat Immunol* (2019) 20:97–108. doi: 10.1038/s41590-018-0260-6
8. Jozwik A, Habibi MS, Paras A, Zhu J, Guvenel A, Dhariwal J, et al. RSV-Specific Airway Resident Memory CD8+ T Cells and Differential Disease Severity After Experimental Human Infection. *Nat Commun* (2015) 6:1–15. doi: 10.1038/ncomms10224
9. Palm AKE, Henry C. Remembrance of Things Past: Long-Term B Cell Memory After Infection and Vaccination. *Front Immunol* (2019) 10:1787. doi: 10.3389/fimmu.2019.01787
10. Takamura S. Persistence in Temporary Lung Niches: A Survival Strategy of Lung-Resident Memory CD8+ T Cells. *Viral Immunol* (2017) 30:438–50. doi: 10.1089/vim.2017.0016
11. Oja AE, Piet B, Helbig C, Stark R, van der Zwan D, Blaauwgeers H, et al. Trigger-Happy Resident Memory CD4 + T Cells Inhabit the Human Lungs. *Mucosal Immunol* (2018) 11:654–67. doi: 10.1038/mi.2017.94
12. Onodera T, Takahashi Y, Yokoi Y, Ato M, Kodama Y, Hachimura S, et al. Memory B Cells in the Lung Participate in Protective Humoral Immune Responses to Pulmonary Influenza Virus Reinfection. *Proc Natl Acad Sci USA* (2012) 109:2485–90. doi: 10.1073/pnas.1115369109
13. Allie SR, Randall TD. Resident Memory B Cells. *Viral Immunol* (2020) 44:282–93. doi: 10.1089/vim.2019.0141
14. Adachi Y, Onodera T, Yamada Y, Daio R, Tsuiji M, Inoue T, et al. Distinct Germinal Center Selection at Local Sites Shapes Memory B Cell Response to Viral Escape. *J Exp Med* (2015) 212:1709–23. doi: 10.1084/jem.20142284
15. Mikhak Z, Strassner JP, Luster AD. Lung Dendritic Cells Imprint T Cell Lung Homing and Promote Lung Immunity Through the Chemokine Receptor CCR4. *J Exp Med* (2013) 210:1855–69. doi: 10.1084/jem.20130091
16. Pejoski D, Ballester M, Auderset F, Vono M, Christensen D, Andersen P, et al. Site-Specific DC Surface Signatures Influence CD4+ T Cell Co-Stimulation and Lung-Homing. *Front Immunol* (2019) 10:1650. doi: 10.3389/fimmu.2019.01650
17. Yu CI, Becker C, Wang Y, Marches F, Helft J, Leboeuf M, et al. Human CD1c+ Dendritic Cells Drive the Differentiation of CD103+ CD8+ Mucosal Effector T Cells. *Via Cytokine TGF-β Immun* (2013) 38:818–30. doi: 10.1016/j.immuni.2013.03.004
18. Guvenel A, Jozwik A, Ascough S, Ung SK, Paterson S, Kalyan M, et al. Epitope-Specific Airway-Resident CD4+ T Cell Dynamics During Experimental Human RSV Infection. *J Clin Invest* (2020) 130:523–38. doi: 10.1172/JCI131696
19. Kumar BV, Ma W, Miron M, Granot T, Guyer RS, Carpenter DJ, et al. Human Tissue-Resident Memory T Cells Are Defined by Core Transcriptional and Functional Signatures in Lymphoid and Mucosal Sites. *Cell Rep* (2017) 20:2921–34. doi: 10.1016/j.celrep.2017.08.078
20. Hombrink P, Helbig C, Backer RA, Piet B, Oja AE, Stark R, et al. Programs for the Persistence, Vigilance and Control of Human CD8 + Lung-Resident Memory T Cells. *Nat Immunol* (2016) 17:1467–78. doi: 10.1038/ni.3589
21. Li H, Callahan C, Citron M, Wen Z, Touch S, Monslow MA, et al. Respiratory Syncytial Virus Elicits Enriched CD8+ T Lymphocyte Responses in Lung Compared With Blood in African Green Monkeys. *PloS One* (2017) 12:1–19. doi: 10.1371/journal.pone.0187642

22. Pizzolla A, Nguyen THO, Sant S, Jaffar J, Loudovaris T, Mannering SI, et al. Influenza-Specific Lung-Resident Memory T Cells are Proliferative and Polyfunctional and Maintain Diverse TCR Profiles. *J Clin Invest* (2018) 128:721–33. doi: 10.1172/JCI96957
23. Mackay LK, Braun A, Macleod BL, Collins N, Tebartz C, Bedoui S, et al. Cutting Edge: CD69 Interference With Sphingosine-1-Phosphate Receptor Function Regulates Peripheral T Cell Retention. *J Immunol* (2015) 194:2059–63. doi: 10.4049/jimmunol.1402256
24. Ogongo P, Zachary Porterfield J, Leslie A. Lung Tissue Resident Memory T-Cells in the Immune Response to Mycobacterium Tuberculosis. *Front Immunol* (2019) 10:992. doi: 10.3389/fimmu.2019.00992
25. Takamura S, Yagi H, Hakata Y, Motozono C, McMaster SR, Masumoto T, et al. Specific Niches for Lung-Resident Memory CD8+ T Cells at the Site of Tissue Regeneration Enable CD69-Independent Maintenance. *J Exp Med* (2016) 213:3057–73. doi: 10.1084/jem.20160938
26. McMaster SR, Wein AN, Dunbar PR, Hayward SL, Cartwright EK, Denning TL, et al. Pulmonary Antigen Encounter Regulates the Establishment of Tissue-Resident CD8 Memory T Cells in the Lung Airways and Parenchyma Article. *Mucosal Immunol* (2018) 11:1071–8. doi: 10.1038/s41385-018-0003-x
27. McKinstry KK, Strutt TM, Bautista B, Zhang W, Kuang Y, Cooper AM, et al. Effector CD4 T-Cell Transition to Memory Requires Late Cognate Interactions That Induce Autocrine IL-2. *Nat Commun* (2014) 5:5377. doi: 10.1038/ncomms6377
28. Muschaweckh A, Buchholz VR, Fellenzer A, Hessel C, König P-A, Tao S, et al. Antigen-Dependent Competition Shapes the Local Repertoire of Tissue-Resident Memory CD8+ T Cells. *J Exp Med* (2016) 213:3075–86. doi: 10.1084/jem.20160888
29. Mani V, Bromley SK, Äijö T, Mora-Buch R, Carrizosa E, Warner RD, et al. Migratory DCs Activate TGF-β to Precondition Naïve CD8(+) T Cells for Tissue-Resident Memory Fate. *Science (80-)* (2019) 366(6462):eaav5728. doi: 10.1126/science.aav5728
30. Snyder ME, Finlayson MO, Connors TJ, Dogra P, Senda T, Bush E, et al. Generation and Persistence of Human Tissue-Resident Memory T Cells in Lung Transplantation. *Sci Immunol* (2019) 4:eaav5581. doi: 10.1126/sciimmunol.aav5581
31. Mami-Chouaib F, Tartour E. Editorial: Tissue Resident Memory T Cells. *Front Immunol* (2019) 10:1018. doi: 10.3389/fimmu.2019.01018
32. Slutter B, Van Braeckel-Budimir N, Abboud G, Varga SM, Salek-Ardakani S, Harty JT. Dynamic Equilibrium of Lung Trm Dictates Waning Immunity After Influenza A Infection. *Sci Immunol* (2017) 2:3374–82. doi: 10.1126/sciimmunol.aag2031.Dynamic
33. Pizzolla A, Wakim LM. Memory T Cell Dynamics in the Lung During Influenza Virus Infection. *J Immunol* (2019) 202:374–81. doi: 10.4049/jimmunol.1800979
34. Reagin KL, Klonowski KD. Incomplete Memories: The Natural Suppression of Tissue-Resident Memory CD8 T Cells in the Lung. *Front Immunol* (2018) 9:17. doi: 10.3389/fimmu.2018.00017
35. Barker KA, Etesami NS, Shenoy AT, Arafa EI, Lyon de Ana C, Smith NM, et al. Lung-Resident Memory B Cells Protect Against Bacterial Pneumonia. *J Clin Invest* (2021) 131(11):e141810. doi: 10.1172/JCI141810
36. Carrasco YR. Batista FD. B Cells Acquire Particulate Antigen in a Macrophage-Rich Area at the Boundary Between the Follicle and the Subcapsular Sinus of the Lymph Node. *Immunity* (2007) 27:160–71. doi: 10.1016/j.immuni.2007.06.007
37. Kurosaki T, Kometani K, Ise W. Memory B Cells. *Nat Rev Immunol* (2015) 15:149–59. doi: 10.1038/nri3802
38. Takamura S, Kato S, Motozono C, Shimaoka T, Ueha S, Matsuo K, et al. Interstitial-Resident Memory CD8+ T Cells Sustain Frontline Epithelial Memory in the Lung. *J Exp Med* (2019) 216:2736–47. doi: 10.1084/jem.20190557
39. Barker KA, Smith NM, Shenoy AT, Martin IMC, Jones MR, Quinton LJ, et al. Repeated Respiratory Bacterial Exposures Elicit Lung Resident Memory B Cells in the Absence of Organized Tertiary Lymphoid Tissue. *J Immunol* (2019) 202:66.22.
40. Song S, Matthias PD. The Transcriptional Regulation of Germinal Center Formation. *Front Immunol* (2018) 9:2026. doi: 10.3389/fimmu.2018.02026
41. Laidlaw BJ, Cyster JG. Transcriptional Regulation of Memory B Cell Differentiation. *Nat Rev Immunol* (2021) 21:209–20. doi: 10.1038/s41577-020-00446-2
42. Reilly EC, Emo KL, Buckley PM, Reilly NS, Smith I, Chaves FA, et al. TRM Integrins CD103 and CD49a Differentially Support Adherence and Motility After Resolution of Influenza Virus Infection. *Proc Natl Acad Sci USA* (2020) 117:12306–14. doi: 10.1073/pnas.1915681117
43. Walsh DA, Borges da Silva H, Beura LK, Peng C, Hamilton SE, Masopust D, et al. The Functional Requirement for CD69 in Establishment of Resident Memory CD8 + T Cells Varies With Tissue Location. *J Immunol* (2019) 203:946–55. doi: 10.4049/jimmunol.1900052
44. Pichyangkul S, Yongvanitchit K, Limsalakpetch A, Kum-Arb U, Im-Erbsin R, Boonnak K, et al. Tissue Distribution of Memory T and B Cells in Rhesus Monkeys Following Influenza A Infection. *J Immunol* (2015) 195:4378–86. doi: 10.4049/jimmunol.1501702
45. Thompson EA, Darrah PA, Foulds KE, Hoffer E, Caffrey-Carr A, Norenstedt S, et al. Monocytes Acquire the Ability to Prime Tissue-Resident T Cells *via* IL-10-Mediated TGF-β Release. *Cell Rep* (2019) 28:1127–35. doi: 10.1016/j.celrep.2019.06.087
46. Yang Q, Zhang M, Chen Q, Chen W, Wei C, Qiao K, et al. Cutting Edge: Characterization of Human Tissue-Resident Memory T Cells at Different Infection Sites in Patients With Tuberculosis. *J Immunol* (2020) 204:2331–6. doi: 10.4049/jimmunol.1901326
47. Walrath JR, Silver RF. The α4β1 Integrin in Localization of Mycobacterium Tuberculosis-Specific T Helper Type 1 Cells to the Human Lung. *Am J Respir Cell Mol Biol* (2011) 45:24–30. doi: 10.1165/rcmb.2010-0241OC
48. Dijkman K, Sombroek CC, Vervenne RAW, Hofman SO, Boot C, Remarque EJ, et al. Prevention of Tuberculosis Infection and Disease by Local BCG in Repeatedly Exposed Rhesus Macaques. *Nat Med* (2019) 252:255–62. doi: 10.1038/s41591-018-0319-9
49. Tian Y, Sun Y, Gao F, Koenig MR, Sunderland A, Fujiwara Y, et al. CD28H Expression Identifies Resident Memory CD8 + T Cells With Less Cytotoxicity in Human Peripheral Tissues and Cancers. *Oncoimmunology* (2019) 8: e1538440. doi: 10.1080/2162402X.2018.1538440
50. Tan H-X, Esterbauer R, Vanderven HA, Juno JA, Kent SJ, Wheatley AK. Inducible Bronchus-Associated Lymphoid Tissues (iBALT) Serve as Sites of B Cell Selection and Maturation Following Influenza Infection in Mice. *Front Immunol* (2019) 10:611. doi: 10.3389/fimmu.2019.00611
51. Koutsakos M, Illing PT, Nguyen THO, Mifsud NA, Crawford JC, Rizzetto S, et al. Human CD8 + T Cell Cross-Reactivity Across Influenza A, B and C Viruses. *Nat Immunol* (2019) 20:613–25. doi: 10.1038/s41590-019-0320-6
52. De Bree GJ, Van Leeuwen EMM, Out TA, Jansen HM, Jonkers RE, Van Lier RAW. Selective Accumulation of Differentiated CD8+ T Cells Specific for Respiratory Viruses in the Human Lung. *J Exp Med* (2005) 202:1433–42. doi: 10.1084/jem.20051365
53. Gray JI, Westerhof LM, MacLeod MKL. The Roles of Resident, Central and Effector Memory CD4 T-Cells in Protective Immunity Following Infection or Vaccination. *Immunology* (2018) 154:574–81. doi: 10.1111/imm.12929
54. Rangel-Moreno J, Carragher DM, Misra RS, Kusser K, Hartson L, Moquin A, et al. Randall TD. B Cells Promote Resistance to Heterosubtypic Strains of Influenza. *Via Multiple Mechanisms J Immunol* (2008) 180:454–63. doi: 10.4049/jimmunol.180.1.454
55. Swarnalekha N, Schreiner D, Litzler LC, Iftikhar S, Kirchmeier D, Künzli M, et al. T Resident Helper Cells Promote Humoral Responses in the Lung. *Sci Immunol* (2021) 6(55):eabb6808. doi: 10.1126/sciimmunol.abb6808
56. Eyles JE, Johnson JE, Megati S, Roopchand V, Cockle PJ, Weeratna R, et al. Nonreplicating Vaccines can Protect African Green Monkeys From the Memphis 37 Strain of Respiratory Syncytial Virus. *J Infect Dis* (2013) 208:319–29. doi: 10.1093/infdis/jit169
57. Corleis B, Bucsan AN, Deruaz M, Vrbanac VD, Lisanti-Park AC, Gates SJ, et al. HIV-1 and SIV Infection Are Associated With Early Loss of Lung Interstitial CD4+ T Cells and Dissemination of Pulmonary Tuberculosis. *Cell Rep* (2019) 26:1409–18. doi: 10.1016/j.celrep.2019.01.021
58. Foreman TW, Mehra S, LoBato DN, Malek A, Alvarez X, Golden NA, et al. CD4+ T-Cell-Independent Mechanisms Suppress Reactivation of Latent Tuberculosis in a Macaque Model of HIV Coinfection. *Proc Natl Acad Sci USA* (2016) 113:E5636–44. doi: 10.1073/pnas.1611987113
59. Dubois V, Chatagnon J, Thiriard A, Bauderlique-Le Roy H, Debrie AS, Coutte L, et al. Suppression of Mucosal Th17 Memory Responses by Acellular Pertussis Vaccines Enhances Nasal Bordetella Pertussis Carriage. *NPJ Vaccines* (2021) 6(1):6. doi: 10.1038/s41541-020-00270-8

60. Ge C, Monk IR, Pizzolla A, Wang N, Bedford JG, Stinear TP, et al. Bystander Activation of Pulmonary Trm Cells Attenuates the Severity of Bacterial Pneumonia by Enhancing Neutrophil Recruitment. *Cell Rep* (2019) 29:4236–44. doi: 10.1016/j.celrep.2019.11.103
61. Kiyono H, Fukuyama S. NALT-Versus Peyer's-Patch-Mediated Mucosal Immunity. *Nat Rev Immunol* (2004) 4(9):699–710. doi: 10.1038/nri1439
62. Stolley JM, Johnston TS, Soerens AG, Beura LK, Rosato PC, Joag V, et al. Retrograde Migration Supplies Resident Memory T Cells to Lung-Draining LN After Influenza Infection. *J Exp Med* (2020) 217:e20192197. doi: 10.1084/jem.20192197
63. Sasson SC, Gordon CL, Christo SN, Klenerman P, Mackay LK. Local Heroes or Villains: Tissue-Resident Memory T Cells in Human Health and Disease. *Cell Mol Immunol* (2020) 17:113–22. doi: 10.1038/s41423-019-0359-1
64. Smyth LJC, Eustace A, Kolsum U, Blaikely J, Singh D. Increased Airway T Regulatory Cells in Asthmatic Subjects. *Chest* (2010) 138:905–12. doi: 10.1378/chest.09-3079
65. Christiaansen AF, Knudson CJ, Weiss KA, Varga SM. The CD4 T Cell Response to Respiratory Syncytial Virus Infection. *Immunol Res* (2014) 59:109–17. doi: 10.1007/s12026-014-8540-1
66. Silva-Sanchez A, Randall TD. (2019) Role of iBALT in Respiratory Immunity. In: Kabashima K., Egawa G. (eds) Inducible Lymphoid Organs. Current Topics in Microbiology and Immunology, vol 426. Cham: Springer. doi: 10.1007/82_2019_191
67. Van De Sandt CE, Barcena M, Koster AJ, Kasper J, Kirkpatrick CJ, Scott DP, et al. Human CD8+ T Cells Damage Noninfected Epithelial Cells During Influenza Virus Infection *In Vitro*. *Am J Respir Cell Mol Biol* (2017) 57:536–46. doi: 10.1165/rcmb.2016-0377OC
68. Knight FC, Wilson JT. Engineering Vaccines for Tissue-Resident Memory T Cells. *Adv Ther* (2021) 4(4):2000230. doi: 10.1002/adtp.202000230
69. Koutsakos M, Wheatley AK, Loh L, Clemens EB, Sant S, Nüssing S, et al. Circulating TFH Cells, Serological Memory, and Tissue Compartmentalization Shape Human Influenza-Specific B Cell Immunity. *Sci Transl Med* (2018) 10(428):eaan8405. doi: 10.1126/scitranslmed.aan8405
70. Mohn KGI, Smith I, Sjursen H, Cox RJ. Immune Responses After Live Attenuated Influenza Vaccination. *Hum Vaccines Immunother* (2018) 14:571–8. doi: 10.1080/21645515.2017.1377376
71. Zens KD, Chen JK, Farber DL. Vaccine-Generated Lung Tissue–Resident Memory T Cells Provide Heterosubtypic Protection to Influenza Infection. *JCI Insight* (2019) 1:1–12. doi: 10.1172/jci.insight.85832
72. Goplen NP, Huang S, Zhu B, Cheon IS, Son YM, Wang Z, et al. Tissue-Resident Macrophages Limit Pulmonary CD8 Resident Memory T Cell Establishment. *Front Immunol* (2019) 10:2332. doi: 10.3389/fimmu.2019.02332
73. Darrah PA, Zeppa JJ, Maiello P, Hackney JA, Wadsworth MH, Hughes TK, et al. Prevention of Tuberculosis in Macaques After Intravenous BCG Immunization. *Nature* (2020) 577:95–102. doi: 10.1038/s41586-019-1817-8
74. Sharpe S, White A, Sarfas C, Sibley L, Gleeson F, McIntyre A, et al. Alternative BCG Delivery Strategies Improve Protection Against Mycobacterium Tuberculosis in non-Human Primates: Protection Associated With Mycobacterial Antigen-Specific CD4 Effector Memory T-Cell Populations. *Tuberculosis* (2016) 101:174–90. doi: 10.1016/j.tube.2016.09.004
75. Verreck FAW, Tchilian EZ, Vervenne RAW, Sombroek CC, Kondova I, Eissen OA, et al. Variable BCG Efficacy in Rhesus Populations: Pulmonary BCG Provides Protection Where Standard Intra-Dermal Vaccination Fails. *Tuberculosis* (2017) 104:46–57. doi: 10.1016/j.tube.2017.02.003
76. White AD, Sarfas C, West K, Sibley LS, Wareham AS, Clark S, et al. Evaluation of the Immunogenicity of Mycobacterium Bovis BCG Delivered by Aerosol to the Lungs of Macaques. *Clin Vaccine Immunol* (2015) 22:992–1003. doi: 10.1128/CVI.00289-15
77. Nieuwenhuizen NE, Kulkarni PS, Shaligram U, Cotton MF, Rentsch CA, Eisele B, et al. The Recombinant Bacille Calmette-Guérin Vaccine VPM1002: Ready for Clinical Efficacy Testing. *Front Immunol* (2017) 8:1147. doi: 10.3389/fimmu.2017.01147
78. Kaushal D, Foreman TW, Gautam US, Alvarez X, Adekambi T, Rangel-Moreno J, et al. Mucosal Vaccination With Attenuated Mycobacterium Tuberculosis Induces Strong Central Memory Responses and Protects Against Tuberculosis. *Nat Commun* (2015) 26:8533. doi: 10.1038/ncomms9533
79. Hansen SG, Zak DE, Xu G, Ford JC, Marshall EE, Malouli D, et al. Prevention of Tuberculosis in Rhesus Macaques by a Cytomegalovirus-Based Vaccine. *Nat Med* (2018) 24:130–43. doi: 10.1038/nm.4473
80. Clegg J, Soldaini E, Bagnoli F, McLoughlin RM. Targeting Skin-Resident Memory T Cells *via* Vaccination to Combat Staphylococcus Aureus Infections. *Trends Immunol* (2021) 42(1):6–17. doi: 10.1016/j.it.2020.11.005
81. Jackson LA, Campbell JD, Frey SE, Edwards KM, Keitel WA, Kotloff KL, et al. Effect of Varying Doses of a Monovalent H7N9 Influenza Vaccine With and Without AS03 and MF59 Adjuvants on Immune Response a Randomized Clinical Trial. *JAMA J Am Med Assoc* (2015) 314:237–46. doi: 10.1001/jama.2015.7916
82. Galson JD, Trück J, Kelly DF, van der Most R. Investigating the Effect of AS03 Adjuvant on the Plasma Cell Repertoire Following Ph1n1 Influenza Vaccination. *Sci Rep* (2016) 6:37229. doi: 10.1038/srep37229
83. Lofano G, Mancini F, Salvatore G, Cantisani R, Monaci E, Carrisi C, et al. Oil-In-Water Emulsion MF59 Increases Germinal Center B Cell Differentiation and Persistence in Response to Vaccination. *J Immunol* (2015) 195:1617–27. doi: 10.4049/jimmunol.1402604
84. Openshaw PJ, Chiu C. Protective and Dysregulated T Cell Immunity in RSV Infection. *Curr Opin Virol* (2013) 3:468–74. doi: 10.1016/j.coviro.2013.05.005
85. Habibi MS, Jozwik A, Makris S, Dunning J, Paras A, DeVincenzo JP, et al. Impaired Antibody-Mediated Protection and Defective IgA B-Cell Memory in Experimental Infection of Adults With Respiratory Syncytial Virus. *Am J Respir Crit Care Med* (2015) 191:1040–9. doi: 10.1164/rccm.201412-2256OC
86. Taefehshokr N, Taefehshokr S, Hemmat N, Heit B. Covid-19: Perspectives on Innate Immune Evasion. *Front Immunol* (2020) 11:580641. doi: 10.3389/fimmu.2020.580641
87. Hobson D, Curry RL, Beare AS, Ward-Gardner A. The Role of Serum Haemagglutination-Inhibiting Antibody in Protection Against Challenge Infection With Influenza A2 and B Viruses. *J Hyg (Lond)* (1972) 70:767–77. doi: 10.1017/S0022172400022610
88. Krstajin N, Mills B, Murray I, Marshall A, Norberg D, Craven TH, et al. Low-Cost High Sensitivity Pulsed Endomicrocopy to Visualize Tricolor Optical Signatures. *J Biomed Optics* (2018) 23:1–12. doi: 10.1117-1.JBO.23.7.076005
89. Craven TH, Walton T, Akram AR, Scholefield E, McDonald N, Marshall ADL, et al. Activated Neutrophil Fluorescent Imaging Technique for Human Lungs. *Sci Rep* (2021) 11:976. doi: 10.1038/s41598-020-80083-w
90. Farber DL. Tissues, Not Blood, are Where Immune Cells Function. *Nature* (2021) 593:506–9. doi: 10.1038/d41586-021-01396-y
91. Snyder ME, Sembrat J, Noda K, Myerburg MM, Craig A, Mitash N, et al. Human Lung-Resident Macrophages Colocalize With and Provide Costimulation to PD1(hi) Tissue-Resident Memory T Cells. *Am J Respir Crit Care Med* (2021) 203:1230–44. doi: 10.1164/rccm.202006-2403OC

Conflict of Interest: KD is a founder and shareholder of Edinburgh Molecular Imaging. DH, DL, MC-R and VP were employed by Sanofi Pasteur.

The authors declare that this study received funding from Sanofi Pasteur. The funder had the following involvement in the study: study design, preparation of the manuscript and decision to publish.

The remaining author declares that the research was conducted in the absence of any commercial or financial relationships that could be construed as a potential conflict of interest.

frontiers in Immunology

ORIGINAL RESEARCH
published: 14 October 2021
doi: 10.3389/fimmu.2021.702074

Edited by:
Uri Hershberg,
University of Haifa, Israel

Reviewed by:
Thierry Defrance,
Institut National de la Santé et de la Recherche Médicale (INSERM),
France
Chaim A. Schramm,
National Institute of Allergy and Infectious Diseases (NIH),
United States

***Correspondence:**
Hannah J. Gould
hannah.gould@kcl.ac.uk

† These authors have contributed equally to the work

‡ These authors have contributed equally to the work

Specialty section:
This article was submitted to Immunological Memory,
a section of the journal Frontiers in Immunology

Received: 29 April 2021
Accepted: 06 September 2021
Published: 14 October 2021

Citation:
Ohm-Laursen L, Meng H, Hoehn KB, Nouri N, Jiang Y, Clouser C, Johnstone TG, Hause R, Sandhar BS, Upton NEG, Chevretton EB, Lakhani R, Corrigan CJ, Kleinstein SH and Gould HJ (2021) B Cell Mobilization, Dissemination, Fine Tuning of Local Antigen Specificity and Isotype Selection in Asthma.
Front. Immunol. 12:702074.
doi: 10.3389/fimmu.2021.702074

B Cell Mobilization, Dissemination, Fine Tuning of Local Antigen Specificity and Isotype Selection in Asthma

Line Ohm-Laursen [1,2†], Hailong Meng [3†], Kenneth B. Hoehn [3], Nima Nouri [3,4], Yue Jiang [5], Chris Clouser [5], Timothy G. Johnstone [5], Ron Hause [5], Balraj S. Sandhar [1,2], Nadine E. G. Upton [1,2], Elfy B. Chevretton [6], Raj Lakhani [6], Chris J. Corrigan [2,7], Steven H. Kleinstein [3,8,9‡] and Hannah J. Gould [1,2‡]*

[1] Randall Centre for Cell and Molecular Biophysics and School of Basic and Medical Biosciences, King's College London, London, United Kingdom, [2] Asthma UK Centre in Allergic Mechanisms of Asthma, London, United Kingdom, [3] Department of Pathology, Yale School of Medicine, New Haven, CT, United States, [4] Center for Medical Informatics, Yale School of Medicine, New Haven, CT, United States, [5] Bristol Myers Squibb, Seattle, WA, United States, [6] Department of Ear, Nose and Throat (ENT) Services, Guy's and St Thomas' NHS Foundation Trust, London, United Kingdom, [7] Department of Respiratory Medicine and Allergy and School of Immunology and Microbial Sciences, King's College London, London, United Kingdom, [8] Interdepartmental Program in Computational Biology and Bioinformatics, Yale University, New Haven, CT, United States, [9] Department of Immunobiology, Yale School of Medicine, New Haven, CT, United States

In order to better understand how the immune system interacts with environmental triggers to produce organ-specific disease, we here address the hypothesis that B and plasma cells are free to migrate through the mucosal surfaces of the upper and lower respiratory tracts, and that their total antibody repertoire is modified in a common respiratory tract disease, in this case atopic asthma. Using Adaptive Immune Receptor Repertoire sequencing (AIRR-seq) we have catalogued the antibody repertoires of B cell clones retrieved near contemporaneously from multiple sites in the upper and lower respiratory tract mucosa of adult volunteers with atopic asthma and non-atopic controls and traced their migration. We show that the lower and upper respiratory tracts are immunologically connected, with trafficking of B cells directionally biased from the upper to the lower respiratory tract and points of selection when migrating from the nasal mucosa and into the bronchial mucosa. The repertoires are characterized by both IgD-only B cells and others undergoing class switch recombination, with restriction of the antibody repertoire distinct in asthmatics compared with controls. We conclude that B cells and plasma cells migrate freely throughout the respiratory tract and exhibit distinct antibody repertoires in health and disease.

Keywords: asthma, immunoglobulin, allergy, adaptive immunity, IgD, innate immunity, repertoire and AIRR-seq/sequencing

INTRODUCTION

The respiratory tract is located inside the body but, like the digestive and reproductive tracts, is constantly exposed to the external environment with its plethora of stimuli from microorganisms, proteins including allergens and other particulate matter including particulate pollution. The respiratory tract is divided into upper and lower regions above and below the larynx, the former comprising the nasal cavity, paranasal sinuses and pharynx and the latter the trachea and bronchial tree. It is also contiguous with the skin (*via* the nostrils) and the conjunctiva (*via* the nasolacrimal ducts). The respiratory tract mucosa serves as a physical barrier composed principally of pseudostratified cells, with ciliated columnar epithelial cells resting on a basement membrane along with mucin-producing goblet cells. The cellular composition of the lamina propria underneath the epithelial layer varies according to the site within the respiratory tract but includes blood vessels and lymphatics, structural cells and a range of immune cells including innate immune cells, antigen-presenting and effector cells, cartilage and, in the lower respiratory tract, smooth muscle cells. Lymphoid tissue surrounds the upper respiratory tract (Waldeyer's Ring, which includes the lingual tonsils and the adenoids), while lymph nodes are abundant adjacent to the lower airways in the mediastinum and adjacent to the trachea and bronchi. Lymph flows towards the hilum and ultimately returns to the systemic venous circulation *via* the right lymphatic and left thoracic ducts.

In contrast to this prominent network of lymph nodes outside the lower airways, the question whether or not organized lymphoid tissue exists within the walls of normal airways (bronchial associated lymphoid tissue, or BALT), is still debated, although it is widely accepted that BALT can be "induced" (iBALT) in association with many chronic inflammatory diseases of the airways such as COPD (1–4). In addition, we have shown that the enzyme activation-induced cytidine deaminase (AID), which is necessary for both somatic hypermutation and isotype switching in B cells, is expressed in both healthy and asthmatic lung tissue (5). Both observations support the hypothesis that B cell maturation can take place within the walls of the airways themselves.

While the process of immune cellular migration from the blood vessel capillaries into the tissues and their return to the systemic circulation *via* the lymph nodes and lymphatics is relatively well established, little is known about the capacity of *individual* immune cells such as B cells and plasma cells to migrate freely between the mucosal surfaces and lymphatics of the upper and lower respiratory tracts. According to the concept of the "United Airways Disease" (UAD) treatment of disease at one site in the respiratory tract, such as allergic rhinitis, will result in improvement in symptoms in another, such as the lower respiratory tract in allergic asthma (6). This is consistent with the hypothesis that such B cell migration within the respiratory tract may occur.

We previously characterized the expressed antibody repertoires of the bronchial mucosal B cells at various sites within the lower respiratory tract, obtained at bronchial biopsy, and the peripheral blood in one patient with atopic asthma (AA) and one non-atopic, non-asthmatic (NANA) control subject using Adaptive Immune Receptor Repertoire sequencing (AIRR-seq). Detailed analysis of the sequences provided conclusive evidence that B cells are able to migrate both locally and to more distal sites within the bronchial mucosa of the same lung (7). The study also, for the first time, revealed the presence of so-called IgD-only cells in the bronchial mucosa, i.e. B cells expressing surface IgD but not IgM generated through isotype switching utilizing a cryptic switch region upstream of the ∂ constant region (8, 9). These cells were first described as highly mutated germinal center centroblasts (10). It has been suggested that this switching process is driven by bacteria (8), which could include common commensal bacteria in asthma, making the discovery of bronchial IgD-only cells relevant to our aim to better understand asthma pathogenesis.

In the present study a primary goal was to extend these observations by addressing the hypothesis that B cells in the upper (nasal) and lower (bronchial) respiratory tract mucosa of both lungs are directly related. We compared the repertoires of the B cells obtained near contemporaneously from nasal biopsies (NBx) and bronchial mucosal biopsies (BBx) (including biopsies from both the left and right bronchial trees from one individual) and the peripheral blood from patients with atopic asthma (AA) and non-atopic, non-asthmatic control subjects (NANA). Our secondary aim, through detailed analysis of somatic hypermutation of the B cell antibody genes, was to attempt to align their directions of travel with their maturation history. Thirdly and finally, we wished to confirm and extend our previous observation of IgD-only cells in the bronchial mucosa in a larger cohort and to compare IgD-only cells of the nasal and bronchial mucosa.

MATERIALS AND METHOD

Study Subjects and Sample Collection

Six atopic patients with asthma (AAXX) and nine non-atopic, non-asthmatic controls (NANAXX) were enrolled in the study (**Supplementary Table 1**). The criteria for the diagnosis of asthma and atopy have been described previously (11). From each subject, two biopsies of the nasal mucosa were obtained from the inferior turbinates at anterior rhinoscopy under local anaesthesia and, at a second visit 4-43 days later, 10 bronchial mucosal biopsies from various sites in the lower airways at fibreoptic bronchoscopy under local anaesthesia (**Figure 1**). For subject AA07, 13 bronchial biopsies were collected, as we also obtained three biopsies from the lower lobes of the right lung of this subject. At both visits 30 ml peripheral blood were also collected for PBMC and serum isolation.

RNA Extraction, AbSeq Library Preparation and Sequencing

Total RNA was extracted from one of the paired nasal biopsies and one bronchial biopsy from each of four sites within the bronchial mucosa using a Qiagen RNEasy plus kit. One aliquot of 10^6 PBMCs from each blood sample was carefully thawed and RNA extracted using the Promega Maxwell HT simply RNA custom kit. RNA recovery and quality were estimated using Agilent TapeStation and HSRNA ScreenTapes.

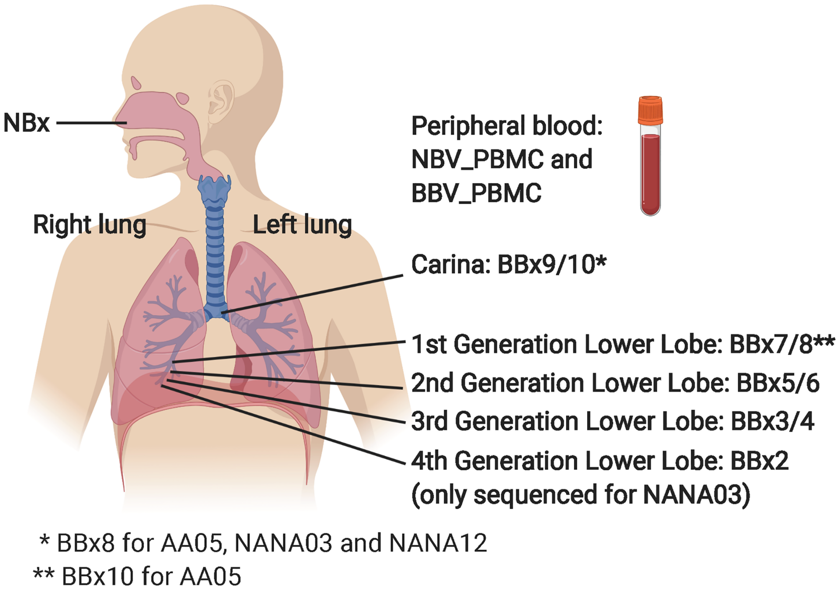

FIGURE 1 | Schematic showing origins of the various samples from the nasal mucosa, the right lung bronchial mucosa and the peripheral blood. The NBV_PBMC and BBC_PBMC peripheral blood sample were collected at the same time as the nasal biopsy (NBx) and the bronchial biopsies (BBx), respectively. For AA07, three biopsies from the left lung were also collected: BBx11 (3rd generation lower lobe), BBx12 (2nd generation lower lobe) and BBx13 (1st generation lower lobe). The carina is at the bottom of the trachea where it divides into the left and right main bronchi. 4th generation lower lobe biopsies were collected from all subjects but only sequenced from NANA03 as this individual lacked a 1st generation lower lobe biopsy sample. This figure was created in BioRender.com.

The RNA was used for heavy chain immunoglobulin amplification and high-throughput sequencing using the previously described AbSeq protocol (12). Briefly, RNA was reverse-transcribed into cDNA using a biotinylated oligo dT primer. An adaptor sequence was added to the 5' end of all cDNA, which contains the Illumina P7 universal priming site and a 17-nucleotide unique molecular identifier (UMI). Products were purified using streptavidin-coated magnetic beads followed by a primary PCR reaction using a pool of primers targeting the IGHA, IGHD, IGHE, IGHG, and IGHM regions, as well as a sample-indexed Illumina P7C7 primer. The immunoglobulin-specific primers contained tails corresponding to the Illumina P5 sequence. PCR products were then purified using AMPure XP beads. A secondary PCR was then performed to add the Illumina C5 clustering sequence to the end of the molecule containing the constant region. The number of secondary PCR cycles was tailored to each sample to avoid entering the plateau phase, as judged by a prior quantitative PCR analysis. Final products were purified, quantified with Agilent Tapestation and pooled in equimolar proportions, followed by high-throughput paired-end sequencing on the Illumina MiSeq platform. For sequencing, the Illumina 600 cycle kit was used with modifications: 325 cycles were used for read 1, 6 cycles for the index reads, 300 cycles for read 2 and a 20% PhiX spike-in to increase sequence diversity.

AbSeq Sequence Analysis

Briefly, data were processed and analyzed using the Immcantation Framework (http://immcantation.org) with the Presto v0.5.7 (13), Change-O v0.4.0 (14), Alakazam v0.2.10 (14), SHazaM v0.1.9 (14, 15), Dowser v0.0.1 (16), IgPhyML v1.1.3 (17) and other custom scripts through the R environment (18). Filtering steps included discarding sequences aligned against the PhiX174 reference genome, sequences with mismatches in the constant region, sequences with more than six mismatches in a 10 nucleotide stretch and sequences with only one single contributing read. Non-functional sequences were also removed from the data, and clonally related sequences were identified using a clustering-based approach as detailed in the **Supplementary Methods**. A detailed description of the various analyses performed can be found in figure legends and **Supplementary Methods**.

AbPair Single Cell Sequencing

From five selected asthmatics and four non-atopic controls (marked in **Table 1**) we also prepared PBMCs to sequence the paired heavy and light chain sequences using the AbPair protocol (19). Selection was based on the finding of shared IgD and/or IgE clones between tissue samples (nasal and/or bronchial mucosa) and a PBMC sample in the data generated by AbSeq. In the analysis of AbPair sequences, the heavy chain sequences from single cell data were extracted and combined with bulk data and then analyzed using the Immcantation pipeline. A detailed description can be found in **Supplementary Methods**.

Statistical Analyses

Unless specifically stated, all statistical analyses throughout the study were performed as two-tailed Wilcoxon rank sum tests to test whether or not samples from two groups were likely to originate from the same population.

TABLE 1 | Numbers of sequences and clones from the various individuals and samples.

Identifier	Days btw. samples	NBx* No. of sequences (No. of clones)	NBV_PBMC* No. of sequences (No. of clones)	BBx* No. of sequences (No. of clones)	BBV_PBMC* No. of sequences (No. of clones)
Atopic Asthmatics (AA)					
AA02	28	19933	7100**	8013	14756**
		(8190)	(4502)	(1534)	(8344)
AA03	23	15508	693	4092	5765**
		(5943)	(191)	(1638)	(3516)
AA04	32	17229	426	13646	1489
		(7936)	(113)	(4356)	(962)
AA05	6	19717	1401**	4126	386
		(8877)	(768)	(1487)	(108)
AA06	21	13623	3916	18852	626
		(6891)	(1898)	(6119)	(293)
AA07	4	13364	2570**	21939***	19
		(6047)	(1859)	(5073)	(9)
Non-Atopic, Non-Asthmatic controls (NANA)					
NANA01	38	13115	28976**	19398	14636**
		(5055)	(21016)	(4807)	(9257)
NANA03	29	27556	640	8809	1618
		(10539)	(528)	(3297)	(859)
NANA04	7	35805	4	17034	8736**
		(10951)	(4)	(5517)	(7060)
NANA05	33	41013	33877	16957	2973
		(11082)	(26559)	(5491)	(2026)
NANA07	26	41549	17250	18994	4532
		(12165)	(2366)	(6141)	(1595)
NANA08	29	16333	2556**	22065	1385
		(8246)	(2086)	(7645)	(518)
NANA10	43	14037	582	10082	713
		(6249)	(401)	(3748)	(282)
NANA11	13	12976	571	14482	410
		(5451)	(215)	(3979)	(99)
NANA12	18	11009	6467	13485	3885
		(5041)	(3272)	(4909)	(1924)

**NBx, nasal mucosal biopsy; NBV_PBMC, peripheral blood cells from a blood sample taken at the same time as the nasal biopsy; BBx, bronchial musical biopsy and BBV_PBMC, peripheral blood cells from a blood sample taken at the time of the bronchoscopy.*

***AbSeq and AbPair data combined.*

****This number includes 958 sequences from the carina, 11093 sequences from biopsies from the right lung mucosa and 9888 sequences from biopsies form the left lung mucosa.*

Study Approval

All 15 study participants provided written, informed consent to take part in the study in accordance with the Declaration of Helsinki. The study had been approved by a local research ethics committee (REC number 15/LO/1800).

RESULTS

Almost 700,000 High-Quality B Cell Receptors From Nasal Biopsies, Bronchial Biopsies and Peripheral Blood B Cells From 15 Individuals Were Sequenced and Analyzed

We enrolled six atopic asthmatics (AA) and nine non-atopic, non-asthmatic control subjects (NANA) into the study (see **Supplementary Table 1**). From each we collected nasal biopsies (NBx), bronchial biopsies (BBx) from multiple sites within the lower airways including the carina and peripheral blood (**Figure 1**). Total RNA was extracted from one of the paired nasal biopsies, one bronchial biopsy from each of the four bronchial sites and an aliquot of PBMCs from each of two blood samples (NBV_PBMC taken at the time of the nasal biopsy and BBV_PBMC taken at the time of the bronchoscopy). The RNA was used for heavy chain immunoglobulin amplification and sequencing using the previously described AbSeq protocol (12). A total of 48,731,069 heavy chain sequences were generated. After multiple steps of quality control (QC), filtering and trimming (see Materials and Methods), a total of 693,700 unique high-quality sequences, ranging from 25,414 to 94,820 per subject, were retained and used for analyses (see **Table 1** for a breakdown). Rarefaction analysis (**Supplementary Figure 1**) showed that, although we had not saturated the diversity for any sample type, the coverage was generally good.

High Degree of Overlap Between the B Cell Repertoires of the Left and Right Lung and Carina Bronchial Mucosa

From one of the atopic asthmatic subjects, AA07, we obtained near contemporaneous biopsies from the bronchial mucosa of the right and left lungs, allowing detailed analysis of the clonal relationships between B cells at the two sites (see **Supplementary Materials and Methods**). We found a high degree of B cell clonal overlap in the left and right bronchial mucosa (38 and 29%, respectively), and many of these clones were also shared with the carina and/or the nose (**Figure 2A**). If a B cell clone was shared between the bronchial mucosa of both lungs and the carina, it was more likely also to have members in the nasal mucosa (171 clones shared between the four sites *versus* 54 only found in the three lung sites). These expanded clones were often large (up to 512 unique sequences) compared to the local clones found in only one site (maximum of 28 unique sequences in the nasal and 58 in the bronchial biopsies). Connectivity analysis (**Figure 2B**) revealed the potential for clonal overlap between all of the sampled sites in the airway mucosa, confirming that the sites are immunologically connected and that no specific connections seem to be favored. Phylogenetic reconstruction of the pattern of accumulated somatic hypermutation (SHM) (**Figures 2C, D**) suggested that individual clones expand and disperse to occupy the bronchial mucosa of both lungs, the carina, nasal mucosa and/or peripheral blood. Isotype switching from IgA to IgG along the pathway of migration was also apparent in some of the lineages (example in **Figure 2C**).

To determine whether the connectivity of B cell clones in the left and right bronchial mucosa were different in this individual (AA07), we analyzed the pattern of trafficking events between tissues along B cell lineage trees (see Materials and Methods). Briefly, given the tissue (e.g., nasal, left or right lung bronchial mucosa) associated with each observed sequence in a lineage tree, the algorithm determines the set of internal node tissue states requiring the fewest number of trafficking events along the tree. The types of trafficking events (e.g., trafficking from left to right lung) that occur within each tree are then compared to those obtained from the same tree topologies with randomized tissue states (16). We first considered only sequences from the left or right lung mucosa and found no significant bias in the directions of trafficking between the two lungs (**Figure 2E**). Next, considering sequences from the nasal, left or right lung mucosa together, we observed a significantly greater proportion of trafficking events from the nasal mucosa to the bronchial mucosa of either lung ($p<0.01$ for both, **Figure 2F** and **Supplemental Table 2**). We also observed fewer total transitions in B cell lineage trees (mean=2949.3) compared to randomized trees (mean=3664.1) in all 100 simulation repetitions ($p<0.01$), showing that sequences from the same tissue were more similar than expected by chance. These results indicated a biased ancestor/descendent relationship within these trees from the nasal mucosa to the bronchial mucosa of both lungs, but not from the left or right bronchial mucosa to the other. This is consistent with biased B cell trafficking from the nose to the lungs, with no evidence for biased trafficking between the mucosa of the two lungs. A number of B cell clones spanning these tissues also had members in the peripheral blood (see example phylogenetic tree in **Figure 2C**) suggesting that this trafficking could take place, at least partially, *via* the circulation.

The clonal sequences confined to the left or right bronchial tree or carina shared similar characteristics in terms of mutation frequency, expansion, isotype distribution and numbers of isotypes within a clone (**Supplementary Figures 2A–D**, respectively). Thus, sampling either lung can provide B cell repertoire data representative of the entire bronchial mucosa. In the rest of the subject cohort (five atopic asthmatics and nine non-atopic controls in total), we sampled only the right lung.

Differences in Clonal and Antigen-Driven Diversity in the Asthmatic Respiratory Tract Mucosa Compared to Non-Atopic Controls

Trafficking is a feature of ongoing humoral immune responses often also characterized by clonal expansion of B cells, which can lead to loss of clonal diversity (20). We used the method of Hill (21) to measure various aspects of diversity and to compare diversity in the mucosa of the upper (nose) and lower (bronchi) respiratory tract and between asthmatics and control subjects (**Supplementary Figure 3**). The Hill plots were made using re-sampling to correct for varying sequencing depth of the analyzed populations and indicated that the diversity in sequences from the bronchial mucosa was more restricted in the asthmatics compared to the non-atopic controls, as confirmed by a significantly lower Shannon diversity index ($p=0.03$) (**Figure 3A**). We observed a similar trend for the Simpson diversity index, but this did not reach statistical significance. No differences in diversity between the groups were observed in the nasal mucosa (**Figure 3B**). Overall, the bronchial, but not the nasal mucosa, of the asthmatic subjects contained fewer unique sequences with greater clonal expansion suggesting an ongoing immune response perhaps with a more restricted number of driving antigens.

BASELINe analyses confirmed a positive selection pressure in the complementarity determining regions (CDRs) and a negative selection pressure in the framework regions (FWR) consistent with antigen-driven selection in both asthmatics and control subjects (**Figure 3C**). Interestingly, the analyses showed statistically significantly lower selection strength scores (Σ) for both the CDRs and FWRs of the tissue samples from atopic asthmatics compared to the non-atopic controls ($p=2.3^{-9}$ and 0.0004, respectively). Estimating the selection strength separately for nasal and bronchial biopsy samples, we still found statistically lower selection pressure scores in the CDRs of asthmatics compared to controls ($p<0.0005$ for both bronchial and nasal samples) (**Figure 3D**), but no differences were seen in the FWRs. We also found that the selection pressure was significantly higher in the nasal biopsies compared to the bronchial biopsies within both groups (atopic asthmatics and non-atopic controls) ($p<0.005$). This confirms that the antigenic selection pressure that the sequences from the bronchial and nasal tissue have encountered is different and also that sequences from atopic asthmatics and non-atopic controls have been exposed to different selection pressure.

Both the Nasal and Bronchial Mucosa B Cell Repertoires Are Dominated by Mutated, Isotype Switched Immunoglobulin Sequences Utilizing a Broad Range of IGHV-Genes

Diversity in antigen specificity and effector function is caused by the recombination of a variety of different IGHV-genes and

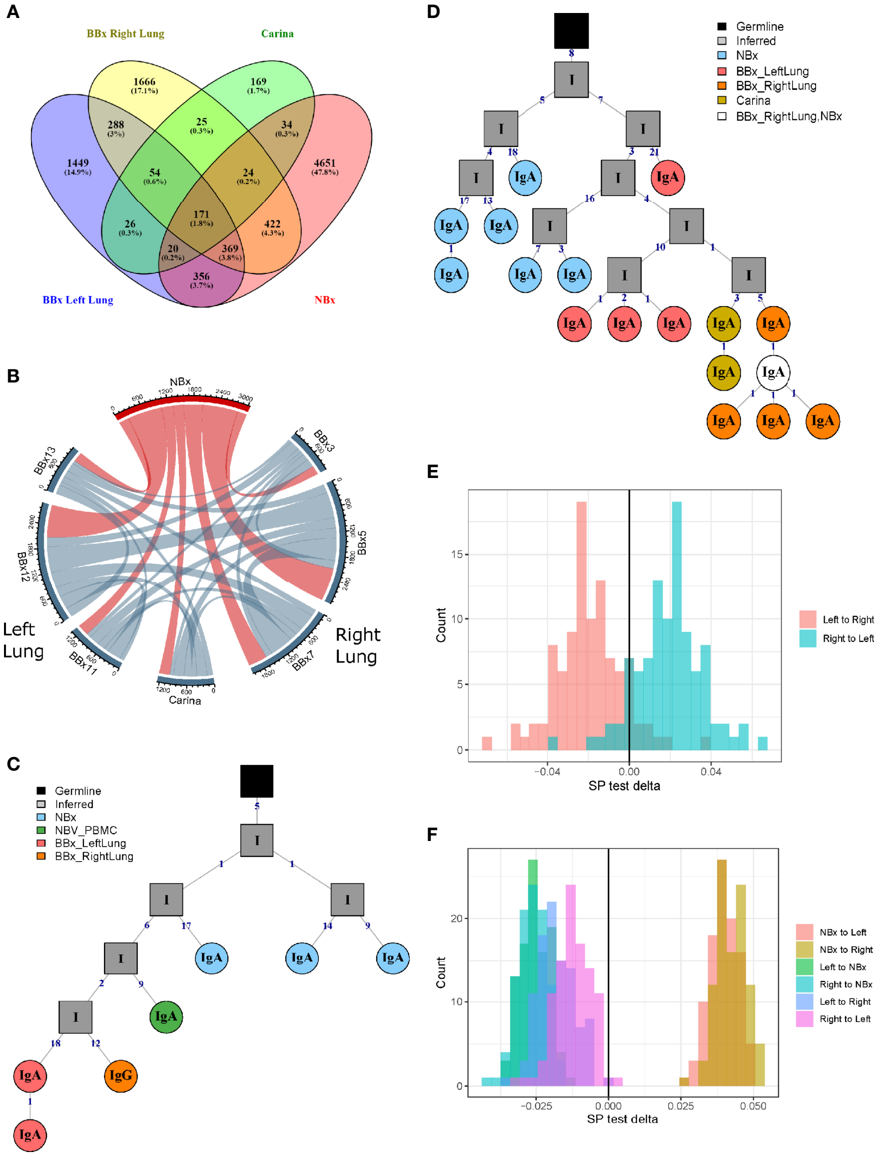

FIGURE 2 | B cells can traffic between the left and the right lungs, as well as from the carina and the nose to the lower airways. **(A)** Venn diagram showing the numbers (and percentages) of clones that overlap in the left and the right lungs, carina and the nose from the asthmatic patient AA07. **(B)** Clonal relationships between all seven bronchial biopsies (BBx) and the nasal biopsy (NBx) from AA07 were calculated and plotted in a Circos plot. The lines between regions indicate a clonal relationship and the numbers around the perimeter indicate counts of overlapped clones between two biopsies. Clones that overlapped more than two biopsies could be duplicated in the Circos plot. **(C, D)** Examples of clonal trees for two clones from AA07 spanning both lungs (right: orange and left: red), the nose (blue) and, for the clones in **(C)**, also the peripheral blood (green). The clone in **(D)** also has members from the carina (yellow). The clone in **(C)** has undergone isotype switching and contains both IgA and IgG sequences. The numbers along each of the branches indicate mutations. **(E)** Maximum parsimony phylogeography analyses show no enrichment for trafficking between the mucosa of the two lungs in either direction. **(F)** When the nasal clones are included, the analyses reveal enrichment for trafficking from the nasal mucosa to either lung (peach and yellow) whereas trafficking between the mucosa of the two lungs (purple and pink) shows no directional bias. There is negative enrichment for travel from either lung to the nasal mucosa (green and blue) confirming the directional preference for B cell trafficking from the nasal to the bronchial mucosa.

constant region gene (IGHC), respectively. We first examined the isotype usage and found that in all subjects, atopic asthmatics as well as non-atopic controls, the nasal mucosa was dominated by IgA (70-90%, mean 85.9% of unique sequences) followed by IgG (mean 10.3% of unique sequences), but also included small amounts of IgM (mean 2.4% of unique sequences) and IgD (mean 1.4% of unique sequences) (**Figure 4A** and **Supplementary Figure 4** for individual samples). In the bronchial mucosa, IgA was still the dominant isotype in most samples (30-80%, mean 67.8% of unique sequences) although the levels were significantly lower than in the nasal mucosa ($p<0.05$). We found more IgG (up to 50%, mean 24.1% at sequence level),

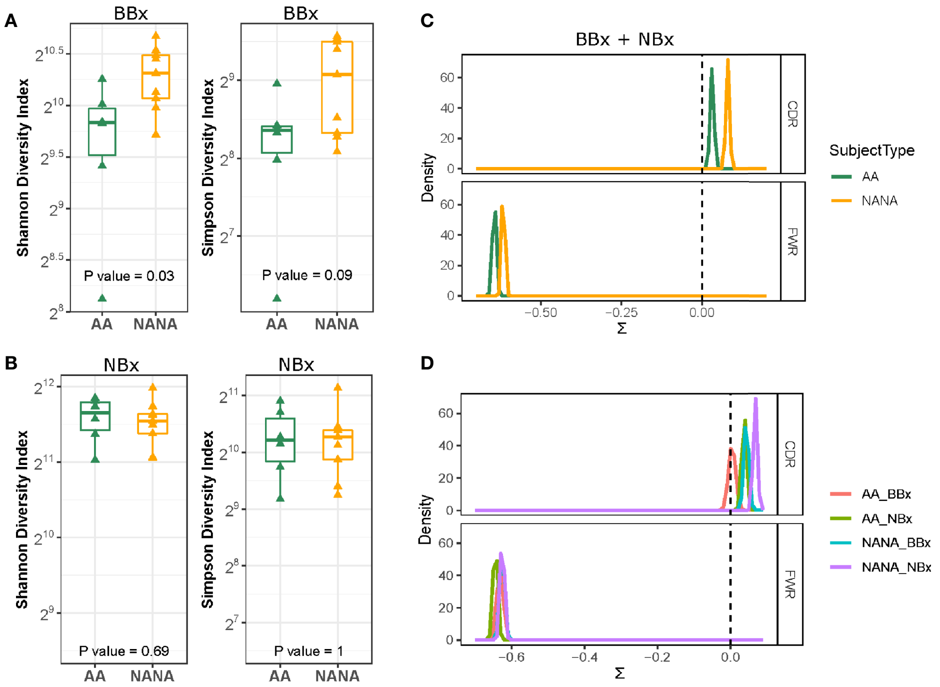

FIGURE 3 | Greater diversity and positive immunoglobulin selection pressure in non-atopic, non-asthmatics (NANA) compared with atopic asthmatics (AA). The Shannon diversity and Simpson diversity indices of immunoglobulin sequences from biopsies from each individual show significantly less diversity in the asthmatics (green) compared with the non-atopic controls (yellow) in the bronchial **(A)** but not the nasal biopsies **(B)**. Comparison of **(C)** pooled bronchial and nasal biopsy immunoglobulin sequences from asthmatics and non-atopic control samples (green and yellow, respectively) and **(D)** bronchial (red) and nasal (green) biopsy sequences from the atopic asthmatics and bronchial (blue) and nasal (purple) sequences from the non-atopic controls shows a higher degree of antigen-driven selection in the complementarity determining regions (CDRs) of the antibodies in the non-atopic controls compared with the atopic asthmatics. Statistically significant differences between the subject groups were found in the framework regions (FWR) when bronchial and nasal biopsy samples were combined **(C)** but not for individual sample types **(D)**.

more IgM (4.2% of unique sequences) and significantly more IgD (3.9% of unique sequences, $p<0.05$) compared to the nasal mucosal samples. This was in contrast to the peripheral blood, where samples were dominated by IgM (30-70% of unique sequences), which was significantly increased compared to the tissue samples ($p<0.05$ for all comparisons). Owing to technical issues with the IgE-specific primers, we identified only small numbers of IgE sequences, which were insufficient for further, detailed analysis. In the lower airways, there were no significant isotype distribution differences between the asthmatic and non-atopic control subjects ($p>0.05$ for all comparisons), but we found it noteworthy that more IgD sequences were present in the lower airways from the asthma patients compared to the non-atopic controls. 99% of these IgD sequences were part of clones that did not include IgM sequences, referred to as IgD-only. We previously reported, for the first time, a high incidence of these IgD-only clones in the bronchial mucosa of a single asthmatic patient (7).

Comparing the degree of SHM in the B cell clones from the asthmatics and non-atopic controls, we found no significant differences in any compartment (tissue or peripheral blood) (**Figure 4B**). However, we found that the clones from both tissues carried significantly more mutations than their isotype-matched blood counterparts ($p<0.05$ for all comparisons) with the exception of IgA from nasal biopsies of asthmatics and IgA from bronchial biopsies of controls, which both exhibited the same trend but were not statistically significant ($p=0.078$ and 0.082, respectively). For IgD the mean SHM frequency was 10-11% in tissue but mostly un-mutated in blood and for IgM mean SHM frequency was 5-6% in tissue and 1% in blood. While these differences might in theory be explained by greater numbers of naïve B cells in the peripheral blood compared to tissue, we also found a difference for IgA (mean SHM 8% in tissue and 6-7% in blood) and IgG (mean SHM 8-9% in tissue and 6% in blood). Thus, there is clear evidence of selection of more somatically mutated clones in the tissues compared to the peripheral blood.

B cells in all samples, tissue as well as blood, utilized a broad spectrum of IGHV-genes (**Figure 4C** and **Supplementary Figure 5**) with IGHV3-23, IGHV3-30 and IGHV4-39, being the most commonly used in all subsets, which is in line with a previous report (22). Each individual had a unique IGHV-gene usage profile as evidenced by the fact that the nasal and bronchial mucosal samples from the same individual clustered with each other in all but one individual (AA02) (**Figure 4C**). No consistent differences were found between the bronchial and nasal samples or between the two subject groups suggesting that

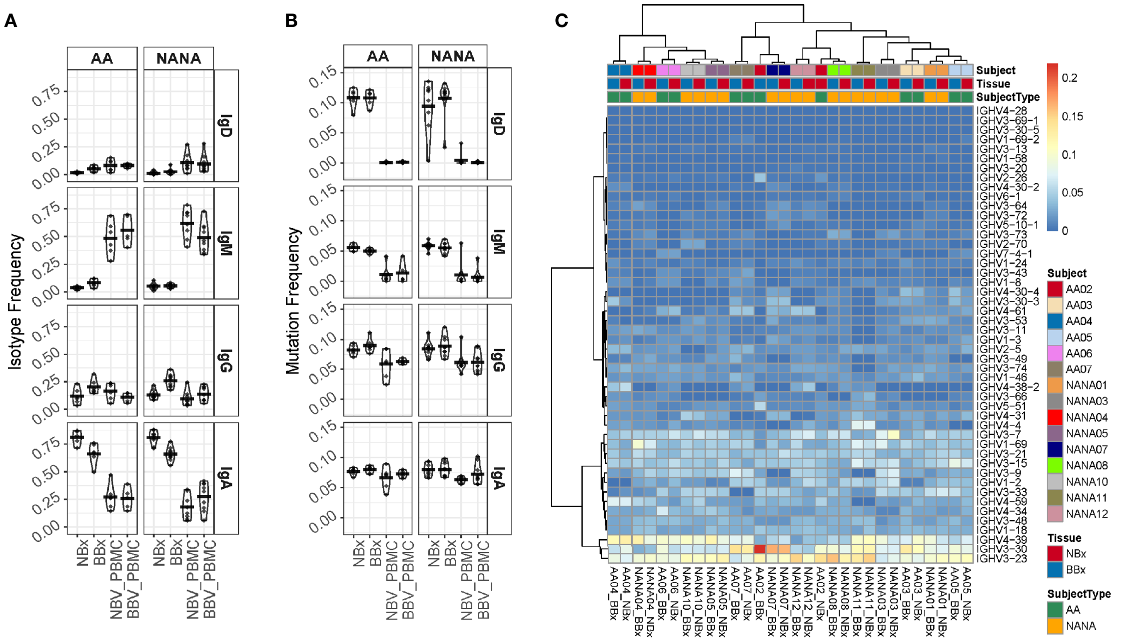

FIGURE 4 | Analysis of isotype frequencies, levels of somatic hypermutation (SHM) and IGHV-gene usage of Ig clones from the bronchial (BBx) and nasal mucosal biopsies (NBx) and peripheral blood mononuclear cells of the atopic asthmatics and non-atopic, controls. **(A)** Isotype frequencies in samples were calculated as fractions of the total sequences expressing a given isotype. Each dot represents an individual. **(B)** SHM frequencies were calculated for each sequence, then means calculated for all the clones of a given isotype and then for each isotype in each tissue type for each individual. Each dot represents an individual. **(C)** Heatmap showing the IGHV-gene usage frequencies in the bronchial and nasal mucosal biopsies from each individual.

the overall IGHV-gene usage is not significantly affected by disease status. A few genes were statistically significantly more (IGHV1-18 and IGHV1-3) or less (IGHV3-23 and IGHV4-34) utilized when comparing tissue with blood samples (FDR<0.05) (data not shown) and the overall pattern of IGHV-gene usage in tissue and peripheral blood differed.

Directional B Cell Trafficking From the Nasal to the Bronchial Mucosa

We have previously shown that B cells can traffic within the local lung mucosa as well as to more distal sites within the mucosa of a single lung (7) and between lungs (here). To extend our previous study, we here included the nasal mucosa as a more distant site within the respiratory tract. Overlap plots showed a high degree of clone sharing between all individual bronchial biopsies and the nasal biopsy but to a lesser degree with the two blood samples (**Figure 5A**). Clones spanning both the nasal and the bronchial mucosa tended to have more mutations in the bronchial members than the nasal clone members, which attained statistical significance in all 6 of the asthmatic subjects and in 4 of the 9 non-atopic controls (see **Supplementary Table 3**).

We further investigated the direction of B cell trafficking between the nasal and bronchial mucosa of all subjects using B cell lineage trees and the approach described in Materials and Methods. Considering only sequences from nasal and bronchial biopsies, we identified fewer total trafficking events along the B cell lineage trees compared to trees with randomized tissue states at the tips in all individuals (p<0.01 for each). This indicates that sequences from the same tissue (nasal or bronchial mucosa) were more similar than would be expected by chance. Using the same method, we further identified a significantly greater proportion of trafficking events from nasal to bronchial mucosa than in randomized trees in 6/6 atopic asthmatics, and in 7/9 non-atopic control individuals (p<0.05 for each; **Supplementary Table 4**). These results confirmed a biased ancestor/descendent relationship from the nasal mucosa to the bronchial mucosa within these trees that was more evident in asthmatics (**Figure 5B**). We found no correlation between the strength of this relationship and either the proportion of sequences from nasal biopsies or the elapsed time between biopsies (**Supplementary Figures 6A, B**, respectively). This confirmed that these results were unlikely to result from either biased sampling (16) or accumulation of additional mutations between biopsies. When analyzing sequences from all tissue samples together (nasal and bronchial mucosa and peripheral blood at two time points), we found a significantly greater proportion of trafficking events from the nasal to the bronchial mucosa in 14/15 individuals (p<0.05 for each; **Supplementary Table 5**). All other directional comparisons only showed a significantly greater proportion of trafficking events in a maximum of two individuals suggesting no general importance. Overall, these results indicate that a biased ancestor/descendant relationship from the nasal to the bronchial mucosa is the dominant pattern in the analyzed trees (*e.g.* in **Figure 5C**), providing further evidence that, particularly in asthmatics, the immune response can be initiated in the nose and that activated B cells can then traffic to the bronchial tissue, accumulating mutations either within the bronchial mucosa or at unknown sites *en route* from the nasal to the bronchial mucosa.

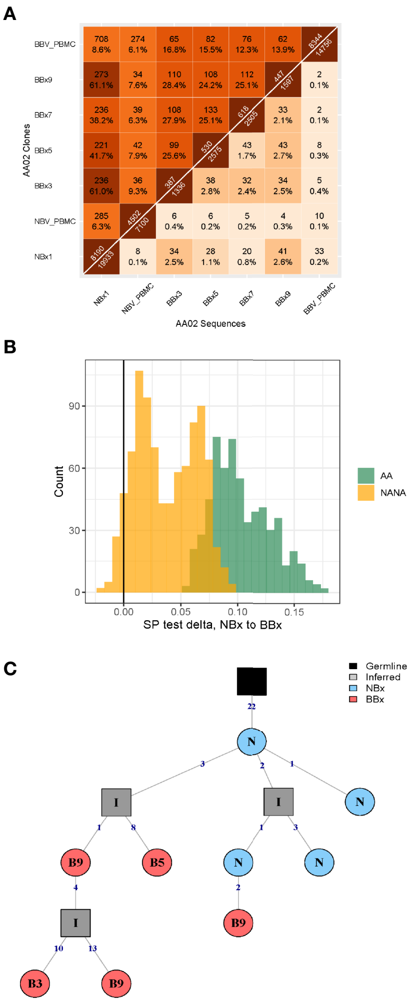

FIGURE 5 | High frequency of immunoglobulin gene clones spanning nasal and bronchial mucosa and evidence of enrichment of trafficking from the nose to the lungs. **(A)** Overlap heatmap showing the numbers and frequencies of sequences (below the diagonal) and clones (above the diagonal) shared between all pairs of samples from subject AA02. Numbers immediately above and below the diagonal indicate the number of sequences and clones in each sample, respectively. There is a high degree of overlap of clones in the nasal biopsy (NBx1) and all the bronchial biopsies (BBx) (38-61% at clonal level) and between individual bronchial biopsies (24-28% at clonal level). Some overlap of clones is also seen in the two blood samples taken at the same times as the nasal and bronchial biopsies (6% at clonal level) as well as between both samples and the nasal biopsy (6% and 9%, respectively) and bronchial biopsy samples (6-9% for the NBV_PBMC taken at the time of the nasal biopsy and 12-19% for BBV_PBMC taken at the time of the bronchoscopy). A lower degree of overlap is found at sequence level, as this requires 100% nucleotide sequence identity. **(B)** Lineage tree analysis by maximum parsimony phylogeography showing an enrichment of switches along B cell lineage trees from nasal to bronchial mucosa compared to randomized trees. The enrichment is significantly more pronounced in the atopic asthmatics (AA, green, p<0.02 for all subjects) compared to the non-atopic controls (NANA, yellow, p<0.05 in 4 of 9 subjects). **(C)** Example of a phylogenetic tree from subject AA06 showing a clear pattern of trafficking from the nose (N, blue) to the lungs (bronchial biopsies B3, B5 and B9, red). N is an abbreviation for nasal biopsy (NBx) and B3, B5 and B9 abbreviations of bronchial biopsies BBx3, BBx5 and BBx9. All the members of this particular clone are of the IgA isotype.

Trafficking of B Cell Clones of All Isotypes Between the Nasal and Bronchial Mucosa Is Linked to Isotype Switching and/or Selection

To analyze the effect of trafficking within the respiratory tissue, we divided the clones and sequences into non-global nasal sequences (NBx_NG) – sequences from clones found in the nasal but not in the bronchial mucosa, global nasal sequences (NBx_G) – the nasal mucosa sequences from clones that spanned the nasal and bronchial mucosa, global bronchial sequences (BBx_G) – the bronchial sequences from clones that spanned the nasal and bronchial mucosa and non-global bronchial sequences (BBx_NG) – sequences from clones found in the bronchial but not nasal mucosa. We used the previous evidence of predominant directional trafficking from the nasal to the bronchial mucosa to track selection working on B cell clones leaving the nasal mucosa and clones entering the bronchial mucosa. We first observed that the B cell clones leaving the nose (NBx_G) are similar to the ones only found in the nasal mucosa (NBx_NG) in terms of isotype composition with a mean of 86% IgA, 10% IgG and smaller amounts IgD and IgM (**Figures 6A, B**). The values were similar in atopic asthmatics and non-atopic controls. However, we found a shift in isotype composition towards more IgG and less IgA in the B cells clones entering the bronchial mucosa (BBx_G) (mean of 74% IgA and 19% IgG), which was even more distinct in the clones found only with the bronchial mucosa (BBx_NG) (mean of 57% IgA but 34% IgG) (**Figures 6A, B**). This trend for a shift in isotype from IgA to IgG was replicated within single B cell clones when comparing the fractions in the nasal and bronchial mucosa, consistent with a possible scenario of B cell migration in concert with local proliferation and class switch recombination (CSR) from the nasal to the bronchial mucosa (**Figure 6C**). Our sequence analysis does not allow distinction of individual immunoglobulin sub-classes, but given the relative 5' to 3' position of the IGHC gene-segments in the immunoglobulin gene-locus and the direction of switching, this would be limited to switching from IgA1 to IgG2 or IgG4. This picture was most distinct in the non-atopic controls.

Somatic hypermutation takes place in activated B cells. The overall mutation frequency was significantly higher in the global clones (both the nasal and bronchial mucosa fractions; NBx_G and BBx_G) compared to the non-global clones from both tissues (NBx_NG and BBx-NG) for IgA and IgG ($p<0.05$; **Figure 6D**) with the exception of IgG clones from the nasal mucosa of asthmatics. For IgD and IgM clones the picture was mixed with significantly more mutations in global IgD and IgM clones in the bronchial mucosa of asthmatics (BBx_G) and significantly more mutation for nasal global (NBx_G) IgM clones in non-atopic controls ($p<0.05$; **Figure 6D**). This strongly suggests the possibility of site-specific, isotype-specific

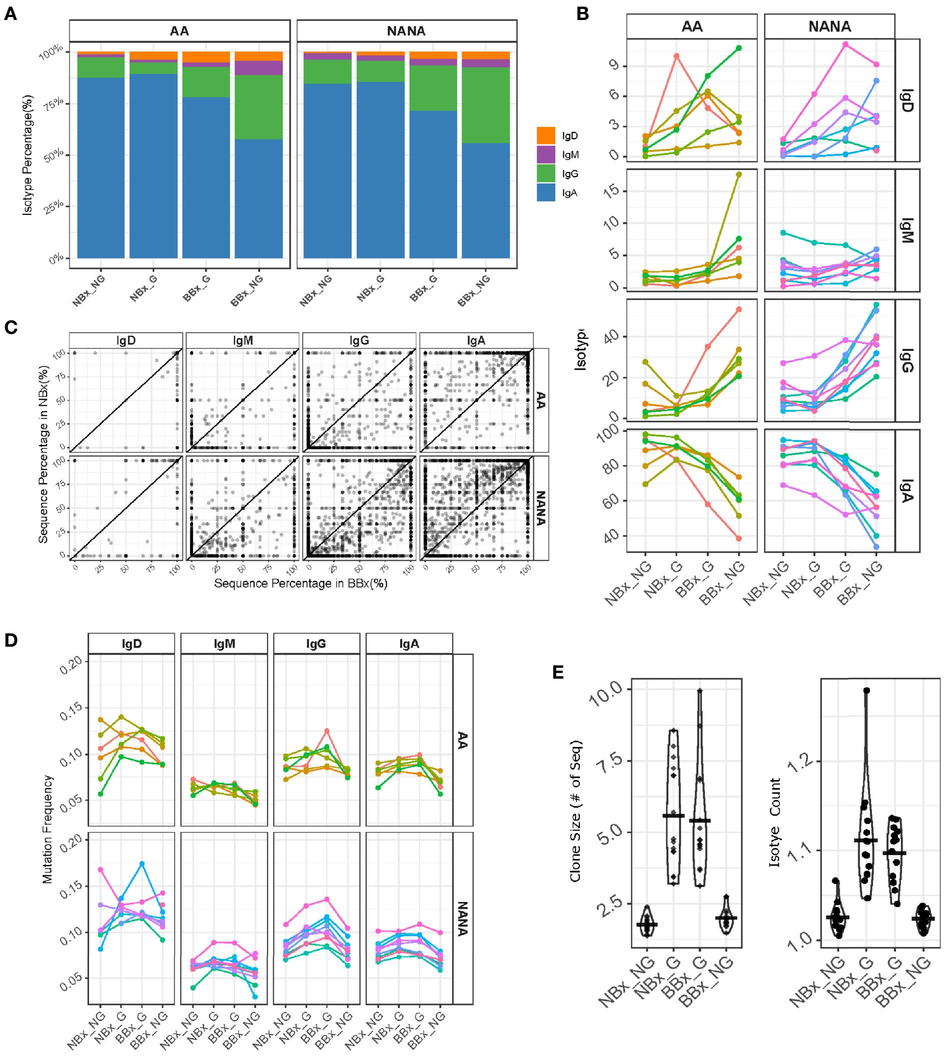

FIGURE 6 | B cells of all isotypes are able to traffic from the nasal to the bronchial mucosa. Global clones are defined as those that contain both nasal and bronchial sequences. We divided the sequences into non-global nasal sequences (NBx_NG) – sequences from clones found in the nasal but not in the bronchial mucosa, global nasal sequences (NBx_G) – the nasal mucosal sequences from global clones, global bronchial sequences (BBx_G) – the bronchial sequences from global clones and non-global bronchial sequences (BBx_NG) – sequences from clones found only in the bronchial mucosa. **(A)** The percentages of the total number of sequences belonging to each isotype (IgD = orange, IgM = purple, IgG = green and IgA = blue) were plotted for each of the four sequence groups for atopic asthmatics (AA) or non-atopic, non-asthmatic controls (NANA). The percentages were calculated for each subject first and then averaged for the asthmatics and non-atopic controls separately. **(B)** Linked changes in the percentage of each isotype from NBx_NG to NBx_G to BBx-G and BBx_NG were plotted for each individual (each line represents an individual, colored the same way as panel **(D)**. **(C)** For each global clone, corresponding to a data point in the plot, the percentages of sequences of a given isotype within the clone found in the nasal mucosa (y-axis) were plotted against the percentages of sequences from the bronchial mucosa (x-axis). **(D)** The mutation frequencies were plotted as the mean of the mutation frequency for sequences of a given isotype for each individual (each line represents an individual, colored the same way as panel **(B)**. **(E)** Left: mean clone size for a given cell subset in each subject for non-global and global clones from either the nasal or bronchial mucosa. Right: mean numbers of isotypes in a clone (right). Each point represents an individual.

variation in B cell mobilization. Compared to local sequences from both the nasal and bronchial mucosa, global B cell clones were significantly larger and tended to comprise greater numbers of isotypes (**Figure 6E**), consistent with the hypothesis that global clones arise from activated B cells.

To look for evidence of differences in selection between the tissues, we further analyzed the heavy chain 3rd complementarity determining region (CDR3). This region is not only the most variable region of an antibody including significant variability in length, but it is also usually critical for antigen binding and therefore a major site for affinity maturation. We found that the CDR3 length was significantly increased in both nasal and bronchial global sequences of IgA and IgG isotype ($p<0.05$ for all comparisons except IgA from the bronchial mucosa in asthmatics) (**Figure 7A**). This may, at least in part, reflect increased usage of the longest IGHJ gene, IGHJ6, and reduced usage of the shorter IGHJ4 gene in global sequences, as compared with both nasal and bronchial non-global clones, although this didn't attain statistical significance (**Figure 7B**). The IgM CDR3 length was consistent between both subsets of non-global and both subsets of global B cell clones (with the exception of one asthmatic outlier). We also note that the CDR3 length increased in IgD, so that the non-global bronchial mucosal IgD clones displayed the longest CDR3 (**Figure 7A**, p=0.034 for NANA), suggesting differences in selection of IgD clones with nasal and bronchial mucosal origin. These observations suggested that some selective forces were influencing which B cells could leave the nasal and enter and/or ultimately survive in the bronchial mucosa. To determine whether the differences in CDR3 length were associated with other physicochemical properties, we analyzed eight amino acid properties of the CDR3 (see **Supplementary Figures 7A–H**). PCA analysis based on the CDR3 amino acid properties showed a separation between the four clonal subsets (non-global and global nasal sequences and non-global and global bronchial sequences) (**Figures 7C–F**). The separations are particularly distinct between global clones in the nasal and bronchial mucosa (**Figure 7E**) and between global and non-global clones within the bronchial mucosa (**Figure 7F**) suggesting that some selective pressure is found in the trafficking between the nasal and the bronchial mucosa and *in to* the bronchial mucosa. This selection also operates on the isotype (**Figure 6B**), mutational

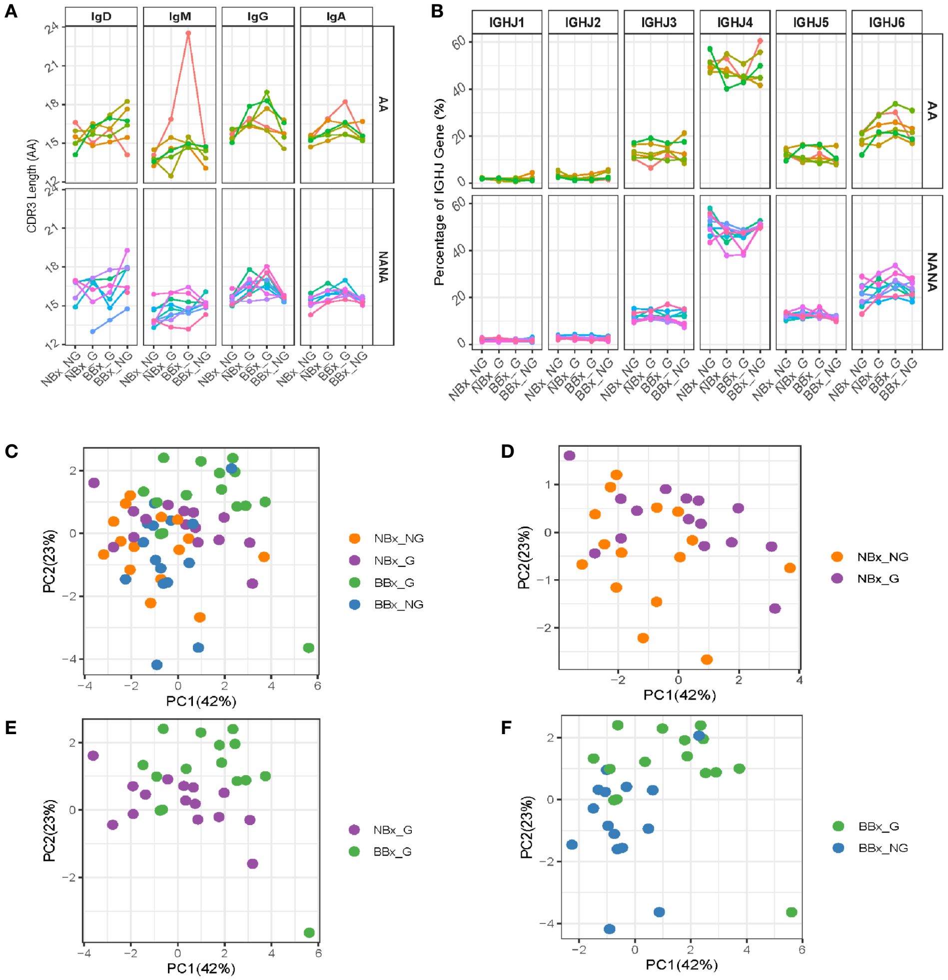

FIGURE 7 | Global clones have longer CDR3 regions with distinct amino acid properties. Sequences from the nasal and bronchial mucosa were divided into groups as described in **Figure 6**. **(A)** The mean lengths (in amino acids) of the CDR3 region of sequences belonging to each group were calculated for each individual (each line represents an individual, colored the same way as panel **(B)** and **Figure 6**). **(B)** The IGHJ-gene usage in sequences of the four sample types was plotted for atopic asthmatics (AA) and non-atopic, non-asthmatic controls (NANA) separately for each individual (each line represents an individual, colored the same way as panel **(A)** and **Figure 6**). Eight different properties of the CDR3 amino acids were calculated (see **Supplementary Figure 7**) and summarized in PCA plots. Each unique sequence was included with the weight of one. The PCA plots were for **(C)** the four sequence subsets together (non-global nasal sequences (orange), global nasal sequences (purple), global bronchial sequences (green) and non-global bronchial sequences (blue), **(D)** non-global (orange) versus global (purple) nasal sequences, **(E)** global nasal (purple) versus bronchial (green) sequences and **(F)** global (green) versus non-global (blue) bronchial sequences.

load (**Figure 6D**), the CDR3 length (**Figure 7A**) and IGHJ-gene usage (**Figure 7B**) showing that the repertoire is progressively shaped as B cells traffic from the upper to the lower respiratory tract.

A Diverse Subset of Heavily Mutated IgD-Only B Cells With Long CDR3 Regions Are More Prevalent in the Bronchial Mucosa of Asthmatic Patients Compared With Non-Atopic Controls

Whereas the nasal mucosal biopsies yielded a higher overall frequency of B cell clones producing IgA, the bronchial mucosal biopsies yielded a higher frequency of clones producing IgD (**Figure 6A**), 99% of these being IgD-only. IgD-only B cell clones were more prevalent (mean 6.3%) in the bronchial mucosa of the atopic asthmatics compared to the non-atopic controls (mean 2.5%), although this difference did not attain statistical significance (p=0.087) (**Figure 8A**). In contrast, in the nasal mucosa the frequency of IgD-only B cell clones was significantly lower (about 1-2%, $p=6.1^{e-05}$) than in the bronchial mucosa and was similar between the asthmatics and the control subjects (p=0.48). A mean of 20% of the IgD-only clones from each individual asthmatic, and 15% in individuals from the control group, were shared between the nasal and bronchial mucosa. The IgD-only mutation frequency was very high (11-12% on average) in both groups and at both sites (**Figure 8B**), higher than for any other isotype (**Figure 4B**).

We and others (7, 23) have previously reported that the IgD from B cells expressing IgD-only have longer heavy chain CDR3 regions compared to IgD from clones also expressing IgM. In the present study, we found that IgD-only B cell clones in the bronchial and nasal mucosa had significantly longer CDR3s than IgM-sequences (p<0.05) with the exception of bronchial IgD-only sequences from atopic asthmatics where the same trend was present, but the difference was not significant owing to one inexplicable outlier (AA02) (p=0.067). No significant differences were found with IgG (p=0.69) and IgA (p=0.08) (**Figure 8C**). IGHJ6 is the longest of the six IGHJ genes and over-usage is often associated with long CDR3 regions. We found a distinct over-usage of IGHJ6 in the IgD-only sequences compared to the IgM, IgG and IgA isotypes in both nasal and bronchial biopsy samples (**Figure 8D**, p<0.05 for all comparisons). However, this overuse of IGHJ6 could not by itself explain the significantly longer CDR3s of IgD-only compared to IgM, as even IgD-only sequences using non-IGHJ6 genes were significantly longer than their IgM counterparts (**Figure 8E**, p<0.05 for both NBx and BBx from asthmatics).

When analyzing individual amino acid properties, as described comparing non-global and global clones, we found several significant differences (**Supplementary Figure 8**). For example, the CDR3 regions of IgD-only sequences from both bronchial and nasal biopsies had a significantly higher GRAVY index (indicative of a more hydrophobic nature of the side chains) and higher aliphatic index compared to IgM in both asthmatics and non-atopic controls. The IgD-only CDR3 regions also had significantly lower contents of aromatic amino acids compared to the three isotypes tested, IgM, IgG and IgA. In the asthmatic patients this was true both in the nasal and bronchial mucosa whereas it only reached significance in the bronchial mucosa of non-atopic controls. This suggests that IgD-only sequences are selected not only for long CDR3 regions but also for certain properties of the amino acids, which they encode. The more hydrophobic, and in particular aliphatic nature of these side chains, may indicate that the antigenic epitopes that are recognized display a similar nature; such hydrophobic interactions generally make the predominant contribution to protein/protein interactions.

IgD-Only Cells Show Evidence of Antigenic Selection That Varies Between Tissue and Sample Type

To further analyze selection in IgD-only, we performed BASELINe analyses of the selection strength (Σ). This revealed that IgD-only B cells from both the bronchial and nasal mucosa showed evidence of a significantly stronger negative selection pressure in the CDR1 and CDR2 regions compared with that of switched isotypes (IgA and IgG) and IgM (p<0.01 for all comparisons) (**Figures 9A, B**). Remarkably, we also uncovered evidence of a significantly elevated selection strength scores in the bronchial, but not the nasal, mucosal IgD-only B cell clones from the non-atopic controls as compared with the asthmatic patients (p=0.01 and 0.28 respectively) (**Figures 9A, B**). No such differences between asthmatics and non-atopic controls were found for the other switched isotypes (p>0.05), but in both tissues the IgM sequences showed significantly higher selection strength in the CDRs compared to the switched isotypes (p<0.00001). All subsets - from both asthmatics and non-atopic control subjects and from both the nasal and bronchial mucosal tissue – showed negative selection strength scores in the framework regions (FWR). This pattern of selection pressure is consistent with antigen-driven selection and it is interesting that these differences in IgD-only selection between the asthmatics and controls were evident only in the bronchial mucosa and not evident for any other antibody isotype.

We previously found that the ratio of replacement to silent mutation rates in the CDRs (a measure of selection strength) was negatively correlated with the number of mutations within a clone (17). This indicated that more mutated clones tended to have a stronger signal of purifying selection; i.e., selection for maintaining the amino acid structure of the BCR. A similar pattern was observed in the present study (**Supplementary Figure 9**). The IgD-only subset tended to have the highest mutation frequency and the most negative selection strength scores compared to all other isotypes. One possible explanation for this relationship is that early replacement mutations are positively selected, but once a significant (optimal) affinity increase is achieved, additional replacement mutations are more likely to be selected against. To explore which amino acid replacements were being selected for (or against) in the IgD-only sequences, we analyzed the amino acid usage at each

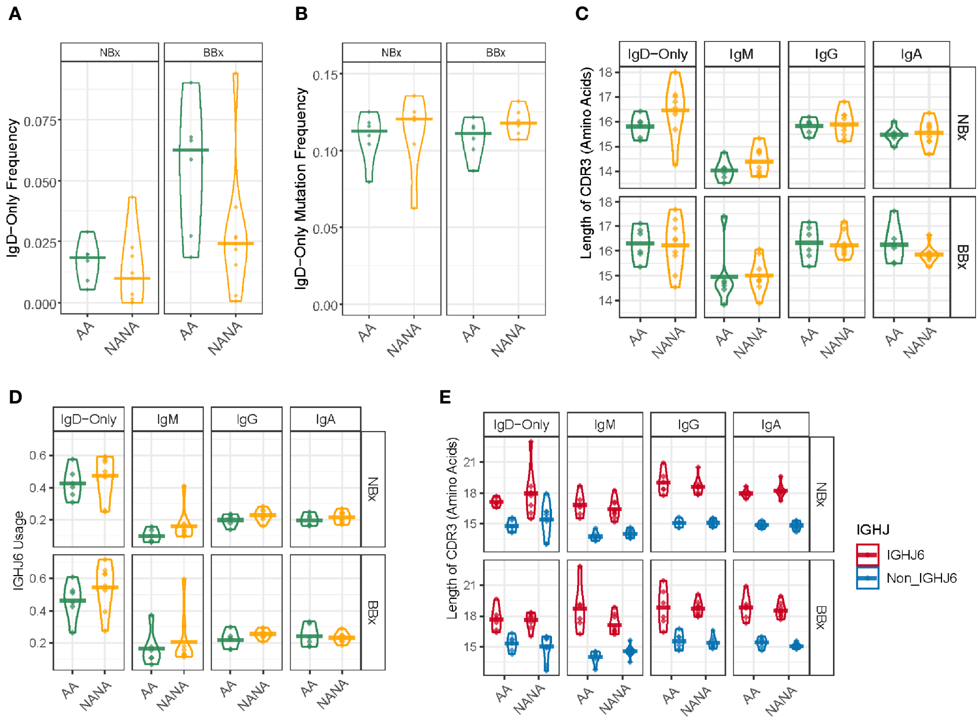

FIGURE 8 | Highly mutated IgD-only sequences with a long CDR3 region and a bias towards IGHJ6 are found in both the bronchial and nasal tissue. **(A)** IgD-only sequences are more commonly found in the bronchial mucosa (BBx) of atopic asthmatics (AA) compared to non-atopic controls (NANA). Lower frequencies of IgD-only sequences are seen in the nasal mucosa (NBx) of both subject groups. NANA03, 07 and 12 have been excluded from this and all subsequent analyses involving the IgD-only cell subset as they have too few IgD-only sequences (< 20 IgD-only sequences). **(B)** IgD-only sequences have a high rate of somatic hypermutation in both atopic asthmatics and non-atopic controls and both bronchial and nasal mucosa. No significant differences were found between groups. **(C)** The CDR3 lengths (given as the numbers of amino acids) of sequences belonging to each sequence type (IgD-only, IgM, IgG and IgA). Each dot represents the sequences from one individual. The IgD-only CDR3s were significantly longer than those from IgM sequences (p=0.05) except in bronchial biopsies from asthmatics which showed only a trend (p=0.067) but not compared to other isotypes (p>0.05 for all other comparisons). No significant differences were found between atopic asthmatics and non-atopic controls. **(D)** IGHJ6 is over-used in IgD-only sequences in both bronchial and nasal tissue (p<0.05 for all comparisons). Each dot represents an individual and the line is the mean for the group. **(E)** Sequences where divided into those using IGHJ6 or other IGHJ genes (Non_IGHJ6), which shows that the significantly longer CDR3 regions of IgD-only sequences compared to IgM sequences are found even in sequences using other IGHJ genes (blue) (p<0.05 in both the nasal and bronchial mucosa of atopic asthmatics). Each dot represents an individual and the line is the mean for the group.

position in the IGHV gene using position weight matrices (PWMs) (see **Supplementary Materials and Methods**) for the most commonly used IGHV genes (defined as more than 2.5% usage in at least three individuals). Compared to sequences of IgM, IgA and IgG isotype, many positions in the CDRs of IgD-only sequences showed a strong preference for (and against) specific against amino acid changes both in the bronchial and nasal mucosa (example for IGHV3-30 in **Figure 9C** top and bottom, respectively). Interestingly, the FWRs also showed a strong preference for particular amino acids at many positions. Many of these preferences were similar in the two tissues (e.g. positions 86 and 64 in FWR2 and CDR2, respectively, see **Figure 9C**) whereas others were tissue specific (e.g. positions 17 and 37 in FWR1 and CDR2, respectively, see **Figure 9C**). There was, however, a general trend for stronger selection in positions in sequences from the bronchial mucosa compared to sequences from the nasal mucosa (**Figure 9C**) confirming that there are differences in the selective pressures on IgD-only B cells in the lower and upper respiratory tract.

DISCUSSION

In this study we employed Adaptive Immune Receptor Repertoire (AIRR) analysis to compare the antibody repertoires of B cells at various sites in the upper (nose) and lower (lung) respiratory tract mucosa of atopic asthmatic patients and non-atopic controls in order to gain deeper insight into the mechanisms underlying immune defense and disease pathogenesis in asthma. In summary, our data and analysis clearly demonstrate passage of B cells between the upper and lower respiratory tract mucosa, dominantly from the nasal to the bronchial mucosa, and mutually between the mucosal surfaces of the right and left bronchial trees. Our observations that B cell clones undergo somatic hypermutation and may undergo isotype switching during the trafficking suggest that it is predominantly activated B cells that traffic. We have also uncovered evidence of site- and maturation-specific selective forces shaping the local B cell repertoire. Furthermore, we confirm the presence of a special subset of IgD-only B cells,

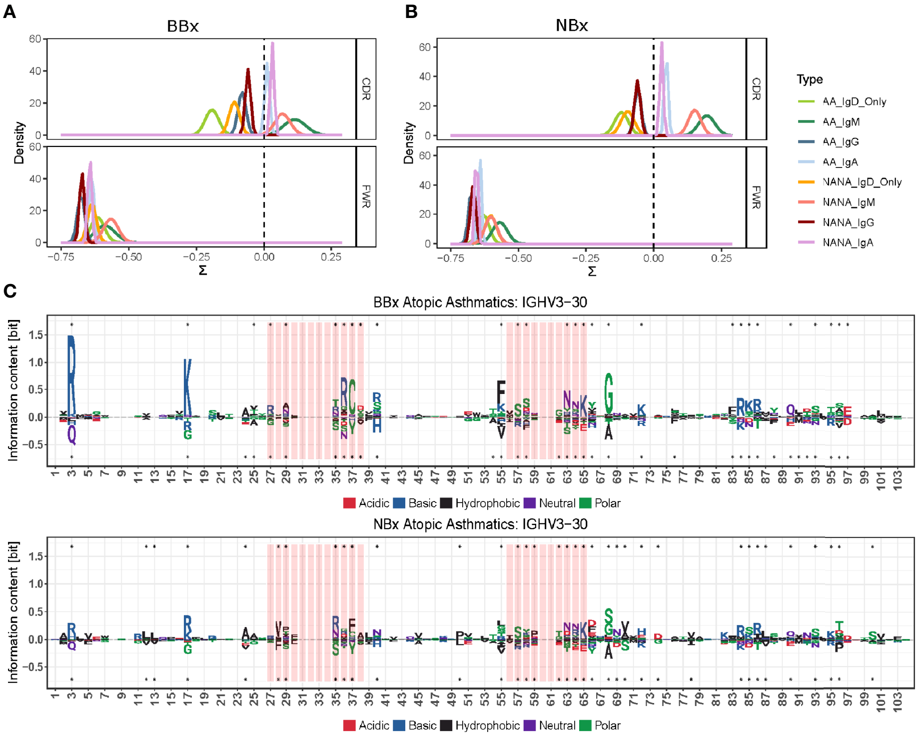

FIGURE 9 | The antigenic selection pressure exerted on IgD-only cell varies between tissues and sample types. **(A, B)** BASELINe estimation of the posterior distribution of selection strengths (Σ) for the complementarity determining regions (CDR) and framework regions (FWR) of IgD-only sequences (light green for atopic asthmatics (AA) and yellow for non-atopic, non-asthmatic controls (NANA)] and those of other switched isotypes: IgA (light blue AA, violet NANA) and IgG (dark blue AA, maroon NANA) and IgM sequences (dark green AA, pink NANA) in **(A)** the bronchial mucosal and **(B)** the nasal mucosa samples. IgD-only sequences display significantly more negative selection strength in the CDRs compared to switched isotypes and IgM in both the bronchial and nasal mucosa. The IgD-only bronchial mucosa also showed a statistically significant difference between atopic asthmatics and non-atopic controls with asthmatics displaying the lowest pressure in the CDRs of all sample types tested. **(C)** Position weight matrix (pwm) analyses of somatic hypermutation generated amino acid substitutions selected for in IgD-only sequences (over the axis) and against (below the axis) in the IGHV3-30 gene in the bronchial (top panel) and nasal (bottom panel) mucosa of atopic asthmatics. The red areas indicate CDR1 and 2 and the white areas are the FWRs. The letters denote the one letter amino acid codes and the colors show the properties of the amino acids selected for or against with red = acidic, blue = basic, black = hydrophobic, purple = neutral and green = polar. The size of the letters shows the strength of selective pressure in the given position. Dots indicate significant differences between IgD-only and the other sequences.

most prominent in the asthmatic bronchial mucosa, characterized by a very high degree of somatic hypermutation and with features of selection pressures distinct from those operating on the B cells of other isotypes.

We have further clarified the practicability of determining the B cell repertoire in the respiratory mucosa from a limited number of mucosal biopsies from the upper and lower respiratory tracts. This corresponds to our previous findings (7, 24), but here we also show that sampling only one lung enables a fair, if incomplete, representation of the total B cell repertoire of the bronchial mucosa tissue (**Supplementary Figure 1**). We also analyzed the B cell repertoire in the peripheral blood. This was less complete than that of the bronchial mucosa, but sufficient to demonstrate that the peripheral blood is a possible route by which B cells are disseminated to other sites in the respiratory tract.

We found that B cell clones could be shared between all of the sites that we sampled, *i.e.* the nasal mucosa, four different sites within the bronchial mucosa ranging from the carina down to the 4th generation bronchi of the lower lobe as well as the peripheral blood. There was no detected directional bias for trafficking between the two lungs but clones shared between the left and right bronchial mucosa were more likely to be related to cells in the nasal mucosa, suggesting that the shared clones were selected for mobilization, most likely following activation by exposure to specific antigen (25). The biological consequence of mobilization of B cell clones would be uniform sensitization to antigens across the respiratory tract following exposure at any site. This would likely facilitate immune defense as well as pathological processes, which was also previously suggested by the "united airways disease" model (6). This could be an advantage in terms of immunological protection but clearly disadvantageous in atopic disease, in that antigen sensitization in one tissue could lead to reaction in another.

Despite many shared clones, the B cell repertoire was more diverse in the nasal compared with the bronchial mucosa. Diversity was also higher in the bronchial (but not nasal) mucosa of non-atopic control subjects compared with the atopic asthmatics (**Supplementary Figure 3**). It is tempting to interpret this observation in relation to the function of B cells in adaptive immunity and/or asthma pathology. As a result of filtering and limitations of particle size in the upper airways, the bronchial mucosa is likely to be exposed to fewer, but conceivably more relevant antigens against which local antibodies, with at least adequate specificity, affinity and isotype, are directed. The more focused repertoire in the patients with atopic asthma compared with the non-atopic controls may reflect differences in the local microbiome and possibly inappropriate (pathological) activation of only limited B cell subsets like IgD-only B cells found to be up-regulated in asthmatics (see below). Another example, although they could not be detected in this study owing to technical issues, would be B cells expressing IgE, also known to be up-regulated in the bronchial mucosa of asthmatics (11).

With regard to isotype distribution, we found IgA to be the dominant antibody isotype in the nasal mucosa. This may reflect an evolutionary adaptation to the local environment, considering that IgA antibodies are secreted into the airways lumen and inhibit contact of their targets with the mucosa. In contrast, although IgA was still the most frequent isotype in the bronchial mucosa, this bias was diminished and compensated by the higher proportions of IgM, IgG and IgD clones lower down in the respiratory tract, where direct contact of the mucosa with particulate antigens is progressively less likely. Since IgA clones cannot undergo isotype switching to IgM, IgD, IgG1 or IgG3, this suggests activation of new cells/clones in the bronchial mucosa. Our sequences do not allow individual sub-class identification, so the observed change from IgA to IgG that was even found in individual clones spanning the nasal and bronchial mucosa (**Figure 6C**) must be from IgA1 to IgG2 or IgG4 as these are the only possible switches due to the location of the individual gene-segments on the chromosome. These findings implicate selective trafficking of certain clones between the two tissues. It was not possible to determine whether CSR occurred *en route* to the bronchial mucosa or following entry, but selection against IgA did not seem to occur at the stage of clones leaving the nasal mucosa. Our observation that global clones tended to have a greater mutational load (driven by SHM and affinity maturation) is fully compatible with a scenario of antigen-driven migration of B cells which have undergone proliferation, isotype switching by CSR and affinity maturation. However, as for CSR, it was not possible to determine whether SHM took place *en route* to the bronchial mucosa, for example in local, draining lymph nodes or other systemic lymphoid tissue, or locally within the mucosa itself. We also searched for directional bias in B cell migration using a parsimony-based phylogenetic test, which takes into account the progressive accumulation of mutations from the germline toward the tips of the clonal linage trees (16). This showed that trafficking of B cell clones between the two lungs is bi-directional and not significantly biased in either direction, whereas there was significant biased trafficking from the nasal to bronchial mucosa. The signature of raised levels of SHM was significantly stronger in the atopic asthmatic patients compared with the non-atopic controls, which might suggest an overall higher degree of B cell activation and directional trafficking in the asthmatic subjects. Of interest, 5 of the 6 asthmatics but none of the 9 control subjects reported suffering from rhinitis consistent with the United Airway Disease Hypothesis (6). We sampled the nasal mucosa biopsies 4-43 days before the bronchial mucosa biopsies and we found that the time between the sampling did not affect the conclusions about directional B cell trafficking.

Our data, while clearly confirming B cell migration throughout the respiratory tract mucosa, do not make it possible precisely to determine the routes of this migration. However, our finding of some clones with members in both tissues and the peripheral blood suggests that the peripheral blood may be involved in the trafficking. Trafficking may however also have included the lymphatics followed by homing back to local lymph nodes and thence back into the lymphatics, or homing to, and migration through local, mucosal blood capillaries or both. This implies a degree of B cell "homing", which is intriguing because, so far as we are aware, there is no established mechanistic basis for this. Sampling of local lymphoid aggregates in the context of mucosal inflammatory diseases ("iBALT") (2) might conceivably shed further light on this conundrum in future studies. There is some precedent for this, as we have previously established that in multiple sclerosis accumulation of SHM takes place in the draining cervical lymph nodes from where the B cells can traffic to the central nervous system (26). A complicating factor for local B cell maturation within the bronchial tissues itself is that, although nasal and bronchial mucosal B cells have been documented in previous studies to express markers of recent SHM (27), the duration and time course of expression of these markers in relation to the dissemination of clones in the respiratory tract remain to be clarified.

The IgD antibodies expressed by the B cells in the respiratory tract mucosa differ from those in PBMCs, which are expressed principally by mature, naive IgM$^+$IgD$^+$ B cells that produce both IgM and IgD with identical VDJ rearrangements through alternative mRNA splicing. These B cells have not yet "experienced" antigen activation, SHM and affinity maturation or CSR, and the vast majority will never do so or survive long enough to be observed. In contrast, the antibodies from IgD-only B cells that we have identified in the bronchial, and to a significantly lesser extent the nasal mucosa, in this and our previous study (7) differ from those of other isotypes. They are more highly mutated (7, 10), and have CDR3s that are significantly longer than those of IgM cells - but similar in length to other switched isotypes – and show greater than two-fold increase in usage of the IGHJ6 gene segment. IgD-only B cells arise by non-canonical switch recombination (9) and are found in both the asthmatic patients and the non-atopic control subjects but are up-regulated in the asthmatics. Compared to other isotypes, bronchial mucosal IgD-only B cells show significantly stronger signature of purifying (negative) selection in the CDR1 and 2 regions (**Figures 9A, B**), particularly in asthmatics. It has previously been reported (17) that clones with large numbers of mutations show a stronger signature of purifying selection. This was hypothesized to be because the benefit of new replacement mutations is expected to decrease once a sufficiently high level of affinity has been reached. This seems possible here as well, because IgD-only clones generally have a high level of SHM. On the other hand, continual exposure and affinity maturation against the same or limited antigens (perhaps from commensal bacteria) could also explain why IgD-only B cells have strong signatures of purifying selection, although a different reason for lower selection pressure in the IgD-only cells cannot be ruled out (see below). The really interesting picture that emerges from our analysis is that CDR selection pressure in asthmatics and non-atopic controls of IgD-only clones differs in the bronchial, but not in the nasal mucosa, suggesting that the selective forces (antigens) driving the affinity maturation are different in the two tissues. This is consistent with the identified differences in the local microbiomes in the upper and lower airways (28) and with the concept of filtering and limitations of particle size when moving down the airways referred to above.

Conservation of sequence is, of course, far greater in the framework regions of all antibody isotypes, since these regions maintain the structural framework in which the CDRs are presented. Surprisingly, however, using position weight matrix analyses we found that some of the IgD-only clones utilizing certain IGHV genes exhibited a particular pattern of framework mutations. Many of these mutations differed from those of antibodies of IgM, IgA or IgG isotypes, and we found differences between the nasal and bronchial mucosa, again suggesting that differences in local stimuli may be reflected in differences in mutation patterns. Such patterns of framework mutations as seen in our IgD-only cell subsets are found in antibodies that to bind to superantigens (29–31).

Having analyzed the FWR and CDR1 and 2, we wanted to focus on the CDR3 region known to be the most important region for antigen-binding. We found that, similarly to other switched isotypes, IgA and IgG, IgD-only antibodies have significantly longer CDR3 regions compared to IgM antibodies. IgD-only antibodies also show a distinct bias towards the expression of the longest of the IGHJ-genes, IGHJ6, which could explain the long CDR3s, however we found that the 5' ends of the IGHJ6-gene were heavily trimmed in the IgD-only rearrangements (data not shown). IGHJ6 harbors 5-6 tyrosine residues at the 5' end and since tyrosine residues are the amino acids most commonly involved in antibody-antigen interactions because of their ability to recognize and interact with antigens both by hydrogen bonding and hydrophobic interactions (32, 33), untrimmed IGHJ6-gene segments could be hypothesized to contribute to CDR3s with strong antigen-binding potential. However, consistent with the heavy trimming, we found a clear and significant selection against aromatic amino acids (**Supplementary Figure 8**) in the CDR3 regions of IgD-antibodies using IGHJ6. We also found higher hydrophobicity (GRAVY index) and higher aliphatic contents of IgD-only CDR3 (**Supplementary Figure 8**). Taken together, this suggested that IgD-only CDR3s were dominated by more aliphatic amino acids (alanine, valine, leucine and isoleucine) and fewer aromatic amino acids (tyrosine, phenylalanine and tryptophan), which is a pattern of amino acid composition that is inconsistent with antigen selection and specificity. In support of this, the BASELINe analyses showing that the selection strength in the CDR1 and 2 of IgD-only sequences was significantly more negative than that of other isotypes, especially in the bronchial mucosa, can also be interpreted as lack of evidence for antigenic selection. This is an alternative, but not mutually exclusive, interpretation of the negative selection pressure being caused by a very high level of SHM, as previously discussed.

In light of our results and reports from clinical studies (34, 35), we suggest that commensal bacteria in the lower and/or upper respiratory tract or recurrent bacterial infections associated with asthma could be involved in driving mutations in the IgD-only cells either in a B-cell superantigen-like manner (explaining the underrepresentation of aromatic side chains in the CDR3) or towards purifying selection due to antigens of aliphatic nature to match the over-representation of aliphatic and hydrophobic side chains in the CDR3. The commensals could also be driving the generation and proliferation of IgD-only cells. There is some precedent for this, as switching to IgD-only in a mouse model has been shown to be stimulated by the microbiota and to occur only in mucosa-associated lymphoid tissue (8). The effect could be restricted to certain IGHV-gene (families) as previously reported for B cell IGHV-family gene expression in antibodies driven by certain enterotoxins from the commensal *Staphylococcus aureus* (36, 37), even though these enterotoxins are better known as T cell superantigens. Staphylococcal protein A (SPA) is also known to specifically bind to a specific IGHV-gene family (IGVH3) (31). Two of the study subjects, one asthmatic and one control, had clinically relevant serum concentrations of IgE antibodies specific for the *S. aureus* enterotoxin toxic shock syndrome toxin-1, TSST-1, as detected by ImmunoCAP, and three other individuals (two asthmatics and one control) had detectable serum concentrations of anti-enterotoxin-specific IgEs, evidence that *S. aureus* had been present in those subjects.

Two species of common commensal bacteria, *Moraxella catarrhalis* and *Haemophilus influenzae* express IgD-binding proteins that can bind to the Cδ1 domain of IgD on naïve IgD-expressing B cells (38, 39), thereby acting as superantigens by stimulating polyclonal B cell proliferation and immunoglobulin class switching (40, 41). The very same bacteria are associated with asthma (34, 35). It is therefore plausible that these commensal bacteria may be involved in driving the generation of IgD-only B cells but, given the findings of this study examining the variable domain of IgD-only B cells, we propose that other bacteria/superantigens might also be involved. While analysis of these hypotheses is beyond the scope of the present study, the data lead us further to hypothesize that IgD has evolved to provide a combination of innate interaction with bacteria through the Cδ-1 region as well as adaptive immunity to bacteria through SHM and selection in the variable regions as we show here. The cost of this is likely increased inflammation and the possibility of autoimmunity by the selection of autoantibodies (23). While these observations are currently speculative, we trust that they may uncover new possible mechanisms of bronchial inflammation in asthma.

DATA AVAILABILITY STATEMENT

The datasets presented in this study can be found in online repositories. The names of the repository/repositories and accession number(s) can be found below: https://www.ncbi.nlm.nih.gov, PRJNA698997.

ETHICS STATEMENT

The studies involving human participants were reviewed and approved by London Central Ethics Committee, REC number 15/LO/1800. The patients/participants provided their written informed consent to participate in this study.

AUTHOR CONTRIBUTIONS

LO-L and HJG designed the research. CJC, RL and EBC collected the samples. LO-L, BSS and NEGU processed the samples. YJ, CC, TGJ and RH performed the sequencing and initial data processing. HM, KBH, NN and SHK analyzed the data and produced the figures in discussion with LO-L and HJG. LO-L, HJG, SHK and CJC. wrote the paper. All authors contributed to the article and approved the submitted version.

FUNDING

LO-L, BS, NU, CC and HG were supported by a research grant from The Medical Research Council, UK (grant number MR/M022943/1) and by the National Institute for Health Research (NIHR) Clinical Research Facility at Guy's & St Thomas' NHS Foundation Trust and NIHR Biomedical Research Centre based at Guy's and St Thomas' NHS Foundation Trust and King's College London. The work of SK was supported in part by the National Institute of Allergy and Infectious Diseases of the National Institutes of Health (award number R01AI104739). The work of HG and LO-L was also supported by the award of a Leverhulme Emeritus Professorship to HG (award number EM-2019 027).

ACKNOWLEDGMENTS

We acknowledge the excellent clinical support provided by Kheem Jones and Isabelle Schelcher. We would like to thank Prof. Brian Sutton for his informed advice on our interpretation of the properties displayed by IgD antibodies in this study. We also thank Anthony Melillo for submission of our data to the SRA and Leverhulme Trust for HJG's Emeritus Professorship.

SUPPLEMENTARY MATERIAL

The Supplementary Material for this article can be found online at: https://www.frontiersin.org/articles/10.3389/fimmu.2021.702074/full#supplementary-material

REFERENCES

1. Richmond I, Pritchard GE, Ashcroft T, Avery A, Corris PA, Walters EH. Bronchus Associated Lymphoid Tissue (BALT) in Human Lung: Its Distribution in Smokers and non-Smokers. *Thorax* (1993) 48(11):1130–4. doi: 10.1136/thx.48.11.1130
2. Hwang JY, Randall TD, Silva-Sanchez A. Inducible Bronchus-Associated Lymphoid Tissue: Taming Inflammation in the Lung. *Front Immunol* (2016) 7:258. doi: 10.3389/fimmu.2016.00258
3. Elliot JG, Jensen CM, Mutavdzic S, Lamb JP, Carroll NG, James AL. Aggregations of Lymphoid Cells in the Airways of Nonsmokers, Smokers, and Subjects With Asthma. *Am J Respir Crit Care Med* (2004) 169(6):712–8. doi: 10.1164/rccm.200308-1167OC
4. Randall TD, Mebius RE. The Development and Function of Mucosal Lymphoid Tissues: A Balancing Act With Micro-Organisms. *Mucosal Immunol* (2014) 7(3):455–66. doi: 10.1038/mi.2014.11
5. Takhar P, Smurthwaite L, Coker HA, Fear DJ, Banfield GK, Carr VA, et al. Allergen Drives Class Switching to IgE in the Nasal Mucosa in Allergic Rhinitis. *J Immunol* (2005) 174(8):5024–32. doi: 10.4049/jimmunol.174.8.5024
6. Licari A, Castagnoli R, Denicolò CF, Rossini L, Marseglia A, Marseglia GL. The Nose and the Lung: United Airway Disease? *Front Pediatr* (2017) 5:44. doi: 10.3389/fped.2017.00044
7. Ohm-Laursen L, Meng H, Chen J, Zhou JQ, Corrigan CJ, Gould HJ, et al. Local Clonal Diversification and Dissemination of B Lymphocytes in the Human Bronchial Mucosa. *Front Immunol* (2018) 9:1976. doi: 10.3389/fimmu.2018.01976
8. Choi JH, Wang KW, Zhang D, Zhan X, Wang T, Bu CH, et al. IgD Class Switching is Initiated by Microbiota and Limited to Mucosa-Associated Lymphoid Tissue in Mice. *Proc Natl Acad Sci U.S.A.* (2017) 114(7):E1196–204. doi: 10.1073/pnas.1621258114
9. Rouaud P, Saintamand A, Saad F, Carrion C, Lecardeur S, Cogné M, et al. Elucidation of the Enigmatic IgD Class-Switch Recombination *via* Germline Deletion of the IgH 3' Regulatory Region. *J Exp Med* (2014) 211(5):975–85. doi: 10.1084/jem.20131385
10. Liu YJ, de Bouteiller O, Arpin C, Brière F, Galibert L, Ho S, et al. Normal Human IgD+IgM- Germinal Center B Cells can Express Up to 80 Mutations in the Variable Region of Their IgD Transcripts. *Immunity* (1996) 4(6):603–13. doi: 10.1016/S1074-7613(00)80486-0
11. Pillai P, Fang C, Chan YC, Shamji MH, Harper C, Wu SY, et al. Allergen-Specific IgE is Not Detectable in the Bronchial Mucosa of Nonatopic Asthmatic Patients. *J Allergy Clin Immunol* (2014) 133(6):1770–2.e11. doi: 10.1016/j.jaci.2014.03.027
12. Di Niro R, Lee SJ, Vander Heiden JA, Elsner RA, Trivedi N, Bannock JM, et al. Salmonella Infection Drives Promiscuous B Cell Activation Followed by Extrafollicular Affinity Maturation. *Immunity* (2015) 43(1):120–31. doi: 10.1016/j.immuni.2015.06.013
13. Vander Heiden JA, Yaari G, Uduman M, Stern JN, O'Connor KC, Hafler DA, et al. pRESTO: A Toolkit for Processing High-Throughput Sequencing Raw Reads of Lymphocyte Receptor Repertoires. *Bioinformatics* (2014) 30 (13):1930–2. doi: 10.1093/bioinformatics/btu138
14. Gupta NT, Vander Heiden JA, Uduman M, Gadala-Maria D, Yaari G, Kleinstein SH. Change-O: A Toolkit for Analyzing Large-Scale B Cell Immunoglobulin Repertoire Sequencing Data. *Bioinformatics* (2015) 31 (20):3356–8. doi: 10.1093/bioinformatics/btv359
15. Yaari G, Vander Heiden JA, Uduman M, Gadala-Maria D, Gupta N, Stern JN, et al. Models of Somatic Hypermutation Targeting and Substitution Based on Synonymous Mutations From High-Throughput Immunoglobulin Sequencing Data. *Front Immunol* (2013) 4:358. doi: 10.3389/fimmu.2013.00358
16. Hoehn KB, Pybus OG, Kleinstein SH. Phylogenetic Analysis of Migration, Differentiation, and Class Switching in B Cells. *bioRxiv* (2020). doi: 10.1101/2020.05.30.124446
17. Hoehn KB, Vander Heiden JA, Zhou JQ, Lunter G, Pybus OG, Kleinstein SH. Repertoire-Wide Phylogenetic Models of B Cell Molecular Evolution Reveal Evolutionary Signatures of Aging and Vaccination. *Proc Natl Acad Sci USA* (2019) 116(45):22664–72. doi: 10.1073/pnas.1906020116

18. R Development Core Team. *R: A Language and Environment for Statistical Computing*. R Foundation for S (2010).
19. Briggs AW, Goldfless SJ, Timberlake S, Belmont BJ, Clouser CR, Koppstein D, et al. Tumor-Infiltrating Immune Repertoires Captured by Single-Cell Barcoding in Emulsion. *bioRxiv* (2017), 134841. doi: 10.1101/134841
20. Meng W, Zhang B, Schwartz GW, Rosenfeld AM, Ren D, Thome JJC, et al. An Atlas of B-Cell Clonal Distribution in the Human Body. *Nat Biotechnol* (2017) 35(9):879–84. doi: 10.1038/nbt.3942
21. Hill M. Diversity and Evenness: A Unifying Notation and its Consequences. *Ecology* (1973) 54:427–32. doi: 10.2307/1934352
22. Brezinschek HP, Brezinschek RI, Lipsky PE. Analysis of the Heavy Chain Repertoire of Human Peripheral B Cells Using Single-Cell Polymerase Chain Reaction. *J Immunol* (1995) 155(1):190–202.
23. Koelsch K, Zheng NY, Zhang Q, Duty A, Helms C, Mathias MD, et al. Mature B Cells Class Switched to IgD are Autoreactive in Healthy Individuals. *J Clin Invest* (2007) 117(6):1558–65. doi: 10.1172/JCI27628
24. Wu YC, James LK, Vander Heiden JA, Uduman M, Durham SR, Kleinstein SH, et al. Influence of Seasonal Exposure to Grass Pollen on Local and Peripheral Blood IgE Repertoires in Patients With Allergic Rhinitis. *J Allergy Clin Immunol* (2014) 134(3):604–12. doi: 10.1016/j.jaci.2014.07.010
25. Pereira JP, Kelly LM, Cyster JG. Finding the Right Niche: B-Cell Migration in the Early Phases of T-Dependent Antibody Responses. *Int Immunol* (2010) 22 (6):413–9. doi: 10.1093/intimm/dxq047
26. Stern JN, Yaari G, Vander Heiden JA, Church G, Donahue WF, Hintzen RQ, et al. B Cells Populating the Multiple Sclerosis Brain Mature in the Draining Cervical Lymph Nodes. *Sci Transl Med* (2014) 6(248):248ra107. doi: 10.1126/scitranslmed.3008879
27. Takhar P, Corrigan CJ, Smurthwaite L, O'Connor BJ, Durham SR, Lee TH, et al. Class Switch Recombination to IgE in the Bronchial Mucosa of Atopic and Nonatopic Patients With Asthma. *J Allergy Clin Immunol* (2007) 119 (1):213–8. doi: 10.1016/j.jaci.2006.09.045
28. Fonkou MD, Dufour JC, Dubourg G, Raoult D. Repertoire of Bacterial Species Cultured From the Human Oral Cavity and Respiratory Tract. *Future Microbiol* (2018) 13:1611–24. doi: 10.2217/fmb-2018-0181
29. Chen JB, James LK, Davies AM, Wu YB, Rimmer J, Lund VJ, et al. Antibodies and Superantibodies in Patients With Chronic Rhinosinusitis With Nasal Polyps. *J Allergy Clin Immunol* (2017) 139(4):1195–204.e11. doi: 10.1016/j.jaci.2016.06.066
30. Mitropoulou AN, Bowen H, Dodev TS, Davies AM, Bax HJ, Beavil RL, et al. Structure of a Patient-Derived Antibody in Complex With Allergen Reveals Simultaneous Conventional and Superantigen-Like Recognition. *Proc Natl Acad Sci U.S.A.* (2018) 115(37):E8707–16. doi: 10.1073/pnas.1806840115
31. Potter KN, Li Y, Capra JD. Staphylococcal Protein A Simultaneously Interacts With Framework Region 1, Complementarity-Determining Region 2, and Framework Region 3 on Human VH3-Encoded Igs. *J Immunol* (1996) 157 (7):2982–8.
32. Koide S, Sidhu SS. The Importance of Being Tyrosine: Lessons in Molecular Recognition From Minimalist Synthetic Binding Proteins. *ACS Chem Biol* (2009) 4(5):325–34. doi: 10.1021/cb800314v
33. Dondelinger M, Filée P, Sauvage E, Quinting B, Muyldermans S, Galleni M, et al. Understanding the Significance and Implications of Antibody Numbering and Antigen-Binding Surface/Residue Definition. *Front Immunol* (2018) 9:2278. doi: 10.3389/fimmu.2018.02278
34. Moffatt MF, Cookson WO. The Lung Microbiome in Health and Disease. *Clin Med (Lond)* (2017) 17(6):525–9. doi: 10.7861/clinmedicine.17-6-525
35. Green BJ, Wiriyachaiporn S, Grainge C, Rogers GB, Kehagia V, Lau L, et al. Potentially Pathogenic Airway Bacteria and Neutrophilic Inflammation in Treatment Resistant Severe Asthma. *PloS One* (2014) 9(6):e100645. doi: 10.1371/journal.pone.0100645
36. Domiati-Saad R, Attrep JF, Brezinschek HP, Cherrie AH, Karp DR, Lipsky PE. Staphylococcal Enterotoxin D Functions as a Human B Cell Superantigen by Rescuing VH4-Expressing B Cells From Apoptosis. *J Immunol* (1996) 156 (10):3608–20.
37. Domiati-Saad R, Lipsky PE. Staphylococcal Enterotoxin A Induces Survival of VH3-Expressing Human B Cells by Binding to the VH Region With Low Affinity. *J Immunol* (1998) 161(3):1257–66.
38. Samuelsson M, Jendholm J, Amisten S, Morrison SL, Forsgren A, Riesbeck K. The IgD CH1 Region Contains the Binding Site for the Human Respiratory Pathogen Moraxella Catarrhalis IgD-Binding Protein MID. *Eur J Immunol* (2006) 36(9):2525–34. doi: 10.1002/eji.200535594
39. Singh K, Nordström T, Mörgelin M, Brant M, Cardell LO, Riesbeck K. Haemophilus Influenzae Resides in Tonsils and Uses Immunoglobulin D Binding as an Evasion Strategy. *J Infect Dis* (2014) 209(9):1418–28. doi: 10.1093/infdis/jit593
40. Nordström T, Jendholm J, Samuelsson M, Forsgren A, Riesbeck K. The IgD-Binding Domain of the Moraxella IgD-Binding Protein MID (MID962-1200) Activates Human B Cells in the Presence of T Cell Cytokines. *J Leukoc Biol* (2006) 79(2):319–29. doi: 10.1189/jlb.0205065
41. Riesbeck K, Nordstrom T. Structure and Immunological Action of the Human Pathogen Moraxella Catarrhalis IgD-Binding Protein. *Crit Rev Immunol* (2006) 26(4):353–76. doi: 10.1615/CritRevImmunol.v26.i4.40

Author Disclaimer: The views expressed are those of the authors and not necessarily those of the NHS, the NIHR or the Department of Health.

Conflict of Interest: SHK receives consulting fees from Northrop Grumman. KBH receives consulting fees from Prellis Biologics. YJ, CC, TGJ and RH are employed by Bristol Myers Squibb.

The remaining authors declare that the research was conducted in the absence of any commercial or financial relationships that could be construed as a potential conflict of interest.

The handling editor has declared past collaborations with one of the authors SHK at the time of this review.

frontiers in Immunology

ORIGINAL RESEARCH
published: 03 January 2022
doi: 10.3389/fimmu.2021.775420

Persistence of Anti-SARS-CoV-2 Antibodies in Long Term Care Residents Over Seven Months After Two COVID-19 Outbreaks

Guadalein Tanunliong [1], ***Aaron Liu*** [2], ***Rohit Vijh*** [3,4], ***Tamara Pidduck*** [5], ***Jesse Kustra*** [5], ***Ana Citlali Márquez*** [5], ***Alexandra Choi*** [3], ***Meghan McLennan*** [5], ***Althea Hayden*** [3], ***Christy Kearney*** [6], ***Soren Gantt*** [7], ***Mel Krajden*** [1,5], ***Muhammad Morshed*** [1,5], ***Agatha N. Jassem*** [1,5] **and** ***Inna Sekirov*** [1,5]*

[1] Department of Pathology and Laboratory Medicine, University of British Columbia, Vancouver, BC, Canada, [2] Department of Experimental Medicine, University of British Columbia, Vancouver, BC, Canada, [3] Office of the Chief Medical Health Officer, Vancouver Coastal Health, Vancouver, BC, Canada, [4] School of Population and Public Health, University of British Columbia, Vancouver, BC, Canada, [5] British Columbia Centre for Disease Control (BCCDC) Public Health Laboratory, Vancouver, BC, Canada, [6] Haro Park Centre, Vancouver, BC, Canada, [7] Centre de Recherche de Centre Hospitalier Universitaire (CHU) Sainte-Justine, Département de microbiologie, infectiologie et immunologie, Université de Montréal, Montréal, QC, Canada

Edited by:
Antonella Prisco,
Institute of Genetics and Biophysics (CNR), Italy

Reviewed by:
Veronika Zarnitsyna,
Emory University, United States
Carlota Dobano,
Instituto Salud Global Barcelona (ISGlobal), Spain

****Correspondence:***
Inna Sekirov
inna.sekirov@bccdc.ca

Specialty section:
This article was submitted to Immunological Memory, a section of the journal Frontiers in Immunology

Received: *14 September 2021*
Accepted: *10 December 2021*
Published: *03 January 2022*

Citation:
Tanunliong G, Liu A, Vijh R, Pidduck T, Kustra J, Márquez AC, Choi A, McLennan M, Hayden A, Kearney C, Gantt S, Krajden M, Morshed M, Jassem AN and Sekirov I (2022) Persistence of Anti-SARS-CoV-2 Antibodies in Long Term Care Residents Over Seven Months After Two COVID-19 Outbreaks. Front. Immunol. 12:775420. doi: 10.3389/fimmu.2021.775420

Background: As part of the public health outbreak investigations, serological surveys were carried out following two COVID-19 outbreaks in April 2020 and October 2020 in one long term care facility (LTCF) in British Columbia, Canada. This study describes the serostatus of the LTCF residents and monitors changes in their humoral response to SARS-CoV-2 and other human coronaviruses (HCoV) over seven months.

Methods: A total of 132 serum samples were collected from all 106 consenting residents (aged 54-102) post-first outbreak (N=87) and post-second outbreak (N=45) in one LTCF; 26/106 participants provided their serum following both COVID-19 outbreaks, permitting longitudinal comparisons between surveys. Health-Canada approved commercial serologic tests and a pan-coronavirus multiplexed immunoassay were used to evaluate antibody levels against the spike protein, nucleocapsid, and receptor binding domain (RBD) of SARS-CoV-2, as well as the spike proteins of HCoV-229E, HCoV-HKU1, HCoV-NL63, and HCoV-OC43. Statistical analyses were performed to describe the humoral response to SARS-CoV-2 among residents longitudinally.

Findings: Survey findings demonstrated that among the 26 individuals that participated in both surveys, all 10 individuals seropositive after the first outbreak continued to be seropositive following the second outbreak, with no reinfections identified among them. SARS-CoV-2 attack rate in the second outbreak was lower (28.6%) than in the first outbreak (40.2%), though not statistically significant ($P>0.05$). Gradual waning of anti-nucleocapsid antibodies to SARS-CoV-2 was observed on commercial (median Δ=-3.7, P=0.0098) and multiplexed immunoassay (median Δ=-169579, P=0.014) platforms;

however, anti-spike and anti-receptor binding domain (RBD) antibodies did not exhibit a statistically significant decline over 7 months. Elevated antibody levels for beta-HCoVs OC43 ($P<0.0001$) and HKU1 ($P=0.0027$) were observed among individuals seropositive for SARS-CoV-2 compared to seronegative individuals.

Conclusion: Our study utilized well-validated serological platforms to demonstrate that humoral responses to SARS-CoV-2 persisted for at least 7 months. Elevated OC43 and HKU1 antibodies among SARS-CoV-2 seropositive individuals may be attributed to cross reaction and/or boosting of humoral response.

Keywords: SARS-CoV-2, COVID-19, serologic testing, outbreak investigation, humoral immune response, long term care facilities, human coronavirus (HCoV)

INTRODUCTION

Long term care facilities (LTCF) have been disproportionately affected by the coronavirus disease 2019 (COVID-19) pandemic. The high risk for respiratory virus transmission and outbreaks within the LTCF setting, in addition to advanced age and multiple co-morbidities, predisposes LTCF residents to a greater susceptibility to severe COVID-19 (1). In British Columbia, one LTCF experienced two COVID-19 outbreaks in April 2020 and October 2020. A lower prevalence following the second outbreak investigation in comparison to the first may be attributed to the refinement of public health infection control measures and the persistence of protective immune responses following the first outbreak (2). Additionally, pre-existing immunity to endemic coronaviruses may also be a contributing factor to the immune response development during SARS-CoV-2 infection.

Severe acute respiratory syndrome coronavirus 2 (SARS-CoV-2), the etiologic agent of COVID-19, emerged in December 2019 and poses an acute public health challenge worldwide; however, seasonal human coronaviruses (HCoV) are endemic and have long been recognized as the cause of ~10-30% of upper respiratory tract infections (3). The endemic HCoVs OC43 and HKU1 (beta-lineage coronavirus) along with NL63 and 229E (alpha-lineage coronavirus) exhibit sequence and structural homology to SARS-CoV-2 (4). Additionally, growing evidence demonstrates cross-reactivity between antibodies against endemic HCoV and SARS-CoV-2 (5). As such, there is interest in understanding the possibility that pre-existing immunity from endemic HCoVs contributes to protection against SARS-CoV-2 infection.

Published findings from our previous serological survey following the first LTCF outbreak demonstrated that serological testing uncovered seropositive cases that were missed during the outbreak investigation (2). Our main objective in this study was to describe the serostatus of residents and monitor the changes in their humoral response to SARS-CoV-2 and endemic HCoVs following the second outbreak. To investigate the persistence of antibody responses over seven months, we compared the sero-survey findings post-first and post-second COVID-19 outbreaks in one LTCF in British Columbia, Canada. Findings may provide better insight into pre-existing protection against SARS-CoV-2 infection, help guide public health infection control measures, and inform vaccination implementation guidelines.

MATERIALS AND METHODS

Study Participants

Sero-surveys were conducted after COVID-19 outbreaks were declared over in the affected LTCF. The first serological survey was administered on May 4th to 14th 2020, and venous blood specimens were collected from residents in the LTCF (N = 87) (2). A second post-outbreak sero-survey was conducted on December 22nd, 2020, following a second outbreak in the fall of 2020, and venous blood specimens were collected from residents in the same LTCF (N = 45).

All LTCF residents (or their substitute decision makers) were informed of the planned investigations, and verbal consent for sample collection and testing was secured from all participants (or their substitute decision makers) who were willing to participate in the study. The investigations in this study were carried out as part of our public health-driven outbreak investigations in LTCF affected by COVID-19 outbreaks, and findings served to inform improvements to our outbreak control strategies. As such, these investigations were part of our practice and undertaken within our practice mandate, institutional ethics review was not required for specimen collection. Serological testing on clinical platforms was done as regular clinical testing. Serological testing on the Meso Scale Discovery (MSD) platform and subsequent analysis was done as part of the assay validation and approved by REB protocol H20-01089.

Nucleic Acid Amplification Tests (NAAT)

Nasopharyngeal swab samples were collected from participants during the two outbreaks in April 2020 and October 2020, in accordance with established clinical and infection control practices in the facilities during the time of each outbreak (practices evolved over time) and all residents were tested by NAAT for active SARS-CoV-2 infection. NAAT testing was performed in accredited clinical laboratories using validated laboratory-developed assay (6) and/or Roche cobas® SARS-CoV-2 commercially available test (7).

Health Canada-Approved Commercial Serology Assays

Serological testing of participants from the first survey was performed using 5 different commercially available SARS-CoV-2 antibody assays in our previous study (2). Sera obtained from the second serological survey were tested in accordance with established clinical protocols using three single-antigen chemiluminescent assays. Specimens were first screened by ADVIA Centaur XP SARS-CoV-2 Total Antibody (Siemens T; Siemens, USA) to detect total antibodies to SARS-CoV-2 S1 RBD. All reactive samples received supplementary testing by ARCHITECT i2000 SARS-CoV-2 IgG (Abbott IgG; Abbott, USA), and VITROS 7600 Anti-SARS-CoV-2 Total Antibody (Ortho T; Ortho Clinical Diagnostics, USA) assays, detecting antibodies against SARS-CoV-2 Nucleocapsid and S1 Spike respectively. All commercial serology assays were carried out according to manufacturers' protocols (8).

Meso Scale Discovery Multiplex Immunoassay

As an additional supplementary test, we utilized a highly sensitive multiplex electrochemiluminescent immunoassay from MSD for the simultaneous detection of antibodies to SARS-CoV-2 and other circulating endemic HCoVs (V-PLEX Coronavirus Panel 2). Multi-spot plates spotted with purified and dried antigens were used for the detection of the following antibodies: spike, S1 RBD, and nucleocapsid of SARS-CoV-2, and spike proteins from circulating alpha-HCoV (229E and NL63) and beta-HCoV (HKU1 and OC43). Assays were performed according to manufacturer's protocol for V-PLEX Coronavirus Panel 2 (9).

Briefly, multi-spot plates were initially incubated with MSD Blocker A for 30 minutes, then washed off. Reference standard, controls, and specimens (sera diluted 1:5000 in Diluent 100) were then added and incubated on the plates for 2 hours. Following incubation, plates were washed, incubated with MSD SULFO-TAG Anti-Human IgG detection antibody for an hour, then washed again. Finally, MSD Gold Read Buffer B was added to the wells and the assay plate was immediately measured on the MSD QuickPlex SQ120 instrument. All incubation steps were carried out in room temperature with shaking at 700rpm, and all wash steps were performed three times with MSD Wash Buffer, prior to addition of the subsequent reagents.

Raw data generated was processed using MSD Discovery Workbench software (Version 4.0), then imported into RStudio (Version 1.2.5033) to interpret signal cut-off values. Cut-off thresholds for reactivity were provided by the manufacturer and are as follows: SARS-CoV-2 spike values above 1960 AU/mL, nucleocapsid values above 5000 AU/mL, and S1 RBD values above 538 AU/mL. Samples above cut-off values for at least two of SARS-CoV-2 S1 RBD, nucleocapsid, and spike were considered serologically reactive using this MSD immunoassay.

Statistical Analysis

Attack rates were calculated by taking the percentage of seropositive participants relative to the total number of susceptible participants for each outbreak. Two attack rates were calculated for outbreak 2 as above, based on two assumptions: A) Individuals seropositive in survey 1 were protected from reinfection during outbreak 2 (10/35), and B) Individuals seropositive in survey 1 were susceptible to reinfection (10/45).

Descriptive statistics of the study population were summarized on R (Version 3.6.2) and RStudio (Version 1.2.5033), and non-parametric statistical tests were carried out using the *ggpubr* (Version 0.6.0) and *stats* (Version 3.6.2) packages to assess attack rates, differences between groups, and changes in humoral responses across surveys. Processed data from the MSD immunoassay was visualized using *ggplot2* (Version 3.3.3) and *ggpubr* packages on RStudio.

RESULTS

Study Population

A total of 132 serum samples were collected from the 106 LTCF residents included in this study. 87 of the serum samples were collected following the first outbreak, while 45 were collected following the second outbreak. Among the 106 residents, 26 of them provided their serum samples following both the first and second outbreaks, thus permitting the longitudinal assessment of SARS-CoV-2 antibodies in this subset of residents. The median age of all study participants included was 85 years, and the age and sex distribution of the LTCF residents included in this study is described in **Supplementary Table 1**.

Seroprevalence and Attack Rates of SARS-CoV-2 in LTCF

A summary of the sero-survey results from both clinical and MSD assays are provided in **Table 1**, with the corresponding NAAT and serology status of each resident listed in **Supplementary Table 2**. Lower attack rates were observed during the second outbreak compared to the first using both clinical and MSD platforms. Specifically, when calculated under the assumption that the individuals who seroconverted in outbreak 1 remain susceptible to reinfection during the second outbreak (10/45), the attack rate during the second outbreak (22.2%) appeared significantly lower than during the first outbreak (40.2%) ($P = 0.036$). However, when calculated under the assumption that the individuals who seroconverted in outbreak 1 were protected from reinfection during the second outbreak (10/35), the attack rate during the second outbreak (28.6%) was lower, but not significantly lower than during the first outbreak (40.2%) ($P > 0.05$). Overall, while there appeared to be slightly greater odds of seroconversion (First assumption: Odds Ratio = 1.68, 95% CI: 0.67-4.42; Second assumption: Odds Ratio = 2.34 95% CI: 0.976-6.01) following the first outbreak compared to the second outbreak, this was not found to be statistically significant. As the first sero-survey was conducted at the beginning of the pandemic, these individuals were presumed to be negative for SARS-CoV-2 prior to the outbreaks. Additionally, comparisons between clinical and MSD interpretations demonstrated a 98.7% (76/77) agreement with negative samples and a 98.2% (55/56) agreement with positive samples (**Supplementary Figure 1**).

TABLE 1 | Summary of sero-survey results.

Assumption	Serology Platform	OB	Positive (N)	Negative (N)	Total (N)	Attack Rate	P-Value
A	Commercial	**1**	35	52	87	40.2%	X^2, P = 0.2274
		2	10	25	35	28.6%	Fisher, P = 0.3002
		Total	45	77	122		OR = 1.68 (0.674-4.42)
	MSD	**1**	35	52	87	40.2%	X^2, P = 0.3643
		2	11	24	35	31.4%	Fisher, P = 0.4137
		Total	46	76	122		OR = 1.46 (0.598-3.76)
B	Commercial	**1**	35	52	87	40.2%	**X^2, P = 0.0386***
		2	10	35	45	22.2%	Fisher, P = 0.0523
		Total	45	77	132		OR = 2.34 (0.976-6.01)
	MSD	**1**	35	52	87	40.2%	X^2, P = 0.0712
		2	11	34	45	32.4%	Fisher, P = 0.0845
		Total	46	76	132		OR = 2.06 (0.879-5.15)

*Assumption A assumes that the 10 individuals seropositive from outbreak 1 were protected from reinfection and were excluded from the attack rate calculation. Assumption B assumes that reinfections are possible within the 10 seropositive from outbreak 1 and were susceptible to reinfection during outbreak 2. *p < 0.05. Bolded values initially indicated significance (p < 0.05).*

A breakdown of the characteristics of the seropositive individuals is shown in **Table 2**. Following the first outbreak, 85.7% (30/35) had a previous positive NAAT test and 14.3% (5/35) of the seropositive cases had no previous NAAT test, as described previously (2). Serological testing was repeated following the second outbreak and 3 of the 26 paired residents were new seroconversions, all of whom were previously confirmed seronegative during the first survey, diagnosed with COVID-19 by NAAT during the second outbreak and identified as seropositive by both commercial serology (**Figure 1A**) and using MSD (**Figure 1B**). Notably, one additional seroconversion was identified by MSD (**Figure 1B**), where the individual was found reactive on MSD for anti-RBD and anti-nucleocapsid antibodies to SARS-CoV-2, but was non-reactive for either antigen on commercial platforms and had no positive NAAT history. No differences were observed in SARS-CoV-2 antibody levels between sexes (**Supplementary Figure 2**). Additionally, all 10 individuals seropositive during the first outbreak remained seropositive and had a negative NAAT test during the second outbreak, indicating no reinfections were identified during the second outbreak.

Duration of SARS-CoV-2 IgG

Individuals positive for SARS-CoV-2 during the first outbreak demonstrated statistically significant waning of anti-nucleocapsid IgG antibodies for SARS-CoV-2 between the first survey and the second survey in both the clinical Abbott IgG assay (median Δ = -3.7, P = 0.0098) (**Figure 1C**), as well as the MSD immunoassay (median Δ = -169579, P=0.014) (**Figure 1D**). Anti-spike and anti-RBD IgG antibodies remained relatively stable when assessed by clinical tests (**Figure 1C**), but a slight decrease was observed on the MSD assays (**Figure 1D**); however, none of these changes were statistically significant (**Figure 1C, D**; **Supplementary Table 3**). Notably, two seropositive individuals were found to have anti-nucleocapsid IgG below reactivity cut-off on MSD. One of the participants was non-reactive for anti-nucleocapsid on both commercial and MSD platforms post-first survey, the other individual was reactive for anti-nucleocapsid on commercial tests but non-reactive on MSD, just below the cut-off (4958 AU/mL) post-second survey.

TABLE 2 | Breakdown of seropositive participants based on clinical serology tests.

	N (%)
Outbreak 1	87
Seropositive	35 (100%)
Negative NAAT result	0 (0%)
Positive NAAT result	30 (85.7%)
No NAAT result	5 (14.3%)
Outbreak 2	45
Seropositive	20 (100%)
Seroconverted in outbreak 1	10 (50%)
Seroconverted in outbreak 2	3 (15%)
No baseline serology results from outbreak 1	7 (35%)

N, Number of participants tested; OB, Outbreak; N/A, Not Available.

Elevation of HCoV-HKU1 and HCoV-OC43 Antibody Levels Among SARS-CoV-2 Positive Persons

Overall, antibody levels to all 4 endemic HCoV (229E, NL63, HKU1, OC43) spike proteins appeared relatively stable between the first and second sero-surveys (**Figure 2A**). Interestingly, anti-spike IgG for 229E was elevated (P = 0.002) following the second outbreak in comparison to the first outbreak, when looking at antibody levels for the 10 individuals that remained seropositive since the first outbreak (**Figure 2A**). While there appeared to be a slight difference in OC43 and HKU1 antibody levels between sexes (**Supplementary Figure 2**), the 10 individuals comprised of 9 females and 1 male; hence, no sex-stratified analysis can be performed.

Individuals seropositive for SARS-CoV-2 were also found to have elevated antibody levels for beta-HCoVs OC43 (P < 0.0001) and HKU1 (P = 0.0027), suggesting an immunologic boosting effect following SARS-CoV-2 infection and/or cross-reaction of anti-SARS-CoV-2 antibodies with beta-HCoV antibodies (**Figure 2B**; **Supplementary Figure 1**).

DISCUSSION

Our study evaluated the serostatus of LTCF residents and monitored changes in their humoral response and antibody

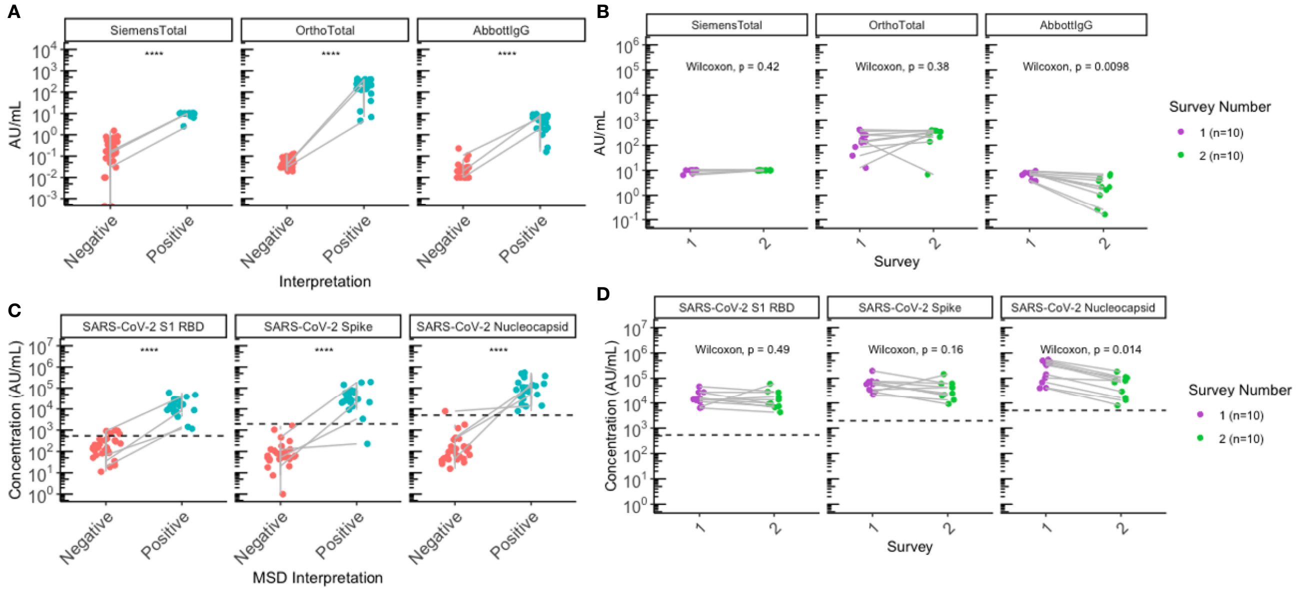

FIGURE 1 | Sero-surveys identified three new seroconversions and demonstrated gradual waning of anti-nucleocapsid antibodies following the second outbreak. **(A, B)** Antibody levels for all residents with paired sera collected (N=26) were plotted by SARS-CoV-2 serostatus to assess SARS-CoV-2 antibodies. **(A)** Commercial serology data plotted according to clinical interpretation. **(B)** MSD data plotted according to MSD interpretation. **(C, D)** All participants (N=10) seropositive for SARS-CoV-2 following the first outbreak (purple) remained seropositive following the second outbreak (green) on both **(C)** commercial and **(D)** MSD platforms. Grey lines indicate paired samples collected from the same individual from both surveys, and lines on **(A, B)** traversing across negative (red) to positive (blue) indicate seroconversion, while vertical lines indicate that the individual's paired serum samples both remained seronegative or seropositive across the two surveys. **(B, D)** Black dashed lines on represent positive signal cut-off for SARS-CoV-2 S1 RBD (538 AU/mL), spike (1960 AU/mL), and nucleocapsid (5000 AU/mL). Statistical analysis was performed using **(A, B)** Wilcoxon's Rank Sum Test and **(C, D)** Wilcoxon's Signed Rank Test. ****p<=0.0001.

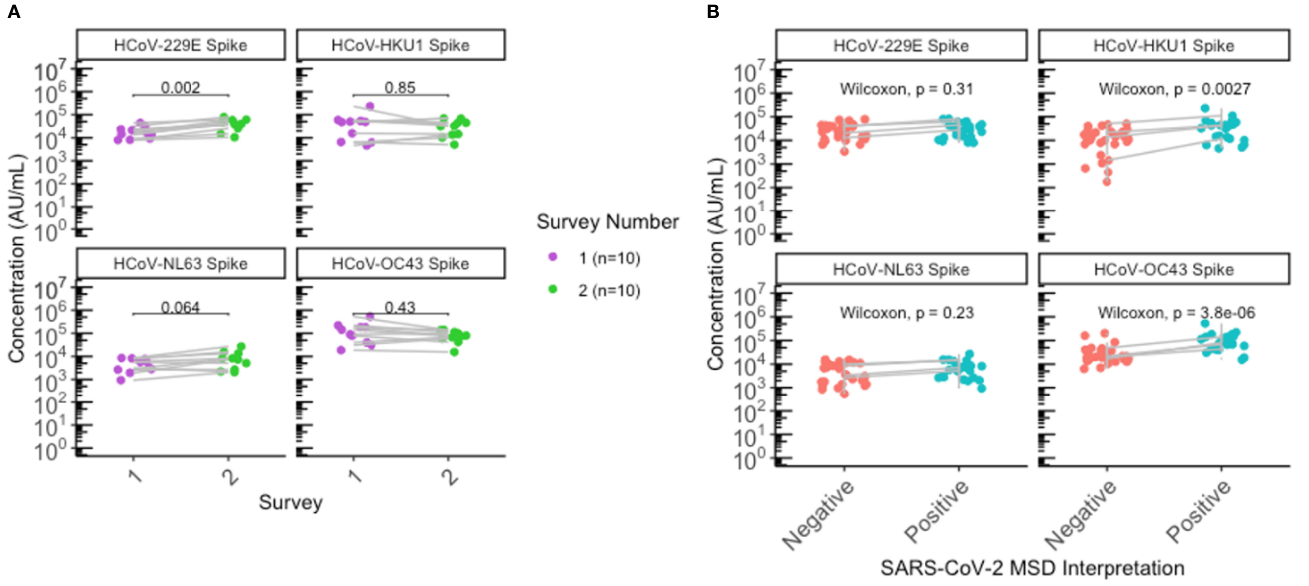

FIGURE 2 | Significant elevation of HKU1 and OC43 antibodies in SARS-CoV-2 positive individuals. **(A)** HCoV antibody levels of residents that were seropositive during the first survey (N=10) were plotted according to the first (purple) and second (green) sero-surveys. **(B)** Antibody levels for all residents with paired sera collected (N=26) were plotted by SARS-CoV-2 negative (red) or positive (blue) status to assess antibody levels to endemic HCoV. Grey lines indicate paired samples collected from the same individual from both surveys, and lines on **(A, B)** traversing across negative (red) to positive (blue) indicate seroconversion, while vertical lines indicate that the individual's paired serum samples both remained seronegative or seropositive across the two surveys. **(A, B)** Statistical analysis was performed using **(A)** Wilcoxon signed-rank test and **(B)** Wilcoxon rank-sum test.

titers over time. The lower attack rate and absence of reinfections observed during the second LTCF outbreak may be attributed to protective effects from herd immunity and/or enhanced public health infection control measures. Additionally, the COVID-19 related case fatality in the facility was 23.6% (13 of 55 residents) during the first outbreak and 6.7% (1 of 15 residents) during the second outbreak, and while our study only included residents that consented to participating in this sero-survey, the lower case fatality during the second outbreak also supports that improved infection control measures and persistent antibody response from the first outbreak (along with improved management of COVID-19 disease by the medical community over the course of the pandemic) may have contributed to the lower attack rate and absence of reinfections during the second outbreak. Moreover, unlike the first outbreak, no additional cases of SARS-CoV-2 infection were uncovered by serological testing post second outbreak. While the MSD assay indicated one additional seroconversion, this individual is less likely to be a true positive because, while they were reactive for anti-RBD and anti-nucleocapsid on MSD, they were non-reactive on commercial assays and have negative NAAT results during the outbreaks. Additionally, reactivity with SARS-CoV-2 RBD and nucleocapsid by the MSD assay could have been due to cross-reactivity from high levels of endemic HCoV antibodies found in this individual's serum.

Due to the recent emergence of SARS-CoV-2, there are limited longitudinal immunologic studies investigating the stability of SARS-CoV-2 and HCoV antibody levels across various population demographics over a longer duration (10–12). Our findings suggest that a SARS-CoV-2 infection in the elderly was able to elicit an immune response lasting at least 7 months. Here, we found persistent antibody titers for SARS-CoV-2 spike and RBD between the first and the second sero-surveys for the 10 individuals infected during the first outbreak, but a statistically significant waning of SARS-CoV-2 nucleocapsid antibodies among these individuals was observed by 2 serological assays. Our results are consistent with multiple published literature describing similar trends, where nucleocapsid antibodies demonstrated faster waning and a shorter half-life, frequently falling to below detectable levels within 4-7 months (12–15). Notably, the individuals from our study all remained seropositive after 7 months and had detectable levels of anti-nucleocapsid antibodies present, despite the significant waning of anti-nucleocapsid IgG levels observed.

There have also been studies that reported declining anti-spike and anti-RBD IgG titers over time. Similar to our study, Dan et al. and Cohen et al. also evaluated SARS-CoV-2 immune responses longitudinally in COVID-19 patients over 6 to 8 months (16, 17). While our results all agree that anti-Spike and anti-RBD were longer lasting than anti-nucleocapsid antibodies in COVID-19 patients, both Dan et al. and Cohen et al. utilized half-life modeling to predict declining antibody kinetics in the general adult population. As described in our **Supplementary Table 3**, our study also demonstrated a declining trend in antibody titers among these 10 individuals for RBD (median Δ=-2906.7, P=0.49) and Spike (median Δ=-24567.3, P = 0.16) using the MSD assay, although unlike Nucleocapsid (median Δ=-169579, P=0.014), we did not find this to be statistically significant.

The differences in antibody durability and protection against reinfection may be attributed to various factors including cohort characteristics and COVID-19 severity (14, 18). Dan et al. found that 90% (36/40) of subjects remained seropositive for Spike IgG while 88% (35/40) remained positive for RBD IgG after 6 to 8 months (16). In contrast, we saw all 10 individuals remain seropositive over the 7 months. As our study was conducted as part of the public health outbreak investigations, we were limited to 10 individuals that were seropositive during the first outbreak and consented to participating in both first and second surveys for our longitudinal comparisons in the same individual. It is possible that observing a larger population over time would allow us to see the same proportion of seropositive individuals that Dan et al. saw in the specified timeframe (16). Interestingly, those with older age and severe COVID-19 were found to exhibit stronger immune responses, higher IgG titers, and seroconvert to negative more slowly than those with mild or asymptomatic disease (14, 17, 19). With this in mind, the 10 individuals in our study comprised of older aged adults that are likely to have more severe disease or worse clinical progression, which may contribute to slower waning in this population in contrast to other studies that evaluated immune durability in healthy adults that primarily have mild or asymptomatic disease (16, 17). As such, the disparity in findings reported across multiple studies investigating the persistence of SARS-CoV-2 antibodies longitudinally is likely attributed to various cohort-specific factors.

Alternatively, the timing of an individual's seroconversion may also contribute to the disparity in findings across published studies on antibody durability. Specifically, the first survey was conducted in May 2020, a month following the facility outbreak in April 2020. Previous studies have shown that it can take 4-5 weeks to reach peak antibody responses following a primary infection (20), and this may even take months in those with severe disease (21). There are studies that describe older age as a predictor of poor seroconversion (22), perhaps due to potential comorbidities or immunosenescence. As such, it is possible that some of the 10 individuals that were seropositive during the first survey had antibody responses that remained on the rising phase and have yet to reach peak IgG levels by the time of the first survey. In this case, if the true decay from peak IgG levels was missed, this may potentially explain the absence of a significant decline in SARS-CoV-2 RBD and Spike antibody levels among our elderly population. This highlights the importance of better understanding how various biological factors may contribute to variation in seroconversion rates and antibody dynamics within the population.

Serological assays do not directly quantify neutralizing antibodies; however, they have been shown to correlate with levels of neutralizing antibodies and may be indicative of protection against reinfection (23). While emerging data has shown that previous infection is not a guarantee for immunity from reinfection (24), our data demonstrated that all residents known to be seropositive post-first outbreak who were also included in the second survey remained seropositive for SARS-

CoV-2 antibodies but negative on NAAT, thus providing evidence that a pre-existing infection-induced serological response to SARS-CoV-2 may contribute protection against reinfection in the elderly for at least 7 months. Notably, 2/10 residents seropositive during the first outbreak appeared to show higher anti-Spike and anti-RBD antibody titers during the second outbreak, but not for nucleocapsid (**Figure 1**). It is possible that this boosting could be attributed to a potential recall response, where re-exposure of these 2 individuals to SARS-CoV-2 during the second outbreak may have not been sufficient to establish a clinically detectable reinfection (NAAT negative), but was enough to elicit a serological memory response that was detectable through sensitive serologic testing. This further supports that previous immunity may offer some protection from reinfection, although more studies need to be conducted to evaluate the degree of protection across individuals, given the heterogeneity of immune responses to SARS-CoV-2 in the population. Taken together, our findings are also consistent with recent evidence showing an 84% reduction in risk of reinfection when observed 7 months following primary infection (25). It has been conclusively shown that vaccine-induced humoral responses are stronger than those from natural infection, and vaccination is superior to natural immunity in protecting from infection (26). However, better understanding of the persistence versus waning dynamic of infection-induced responses may help in allocation of primary and booster vaccine doses in settings where these resources are scarce.

By utilizing a multiplexed immunoassay, we were able to simultaneously detect endemic HCoV antibodies in addition to SARS-CoV-2 antibodies. We found anti-spike IgG to endemic HCoV appear relatively stable overall between the first and second surveys, with a slight elevation in levels of 229E antibodies post-second survey among those seropositive for SARS-CoV-2 from the first survey. While our results found this difference to be statistically significant, there has been limited literature on the relationship between humoral responses to SARS-CoV-2 and alpha-HCoVs and this difference could likely be attributed to our small sample size and intra-assay variability. Additionally, there has been no known HCoV outbreak in British Columbia in the past two years, suggesting that the elevated levels of 229E spike antibodies are unlikely due to recent exposures. Nonetheless, the observed difference in 229E antibody levels can be explored further using larger sample sizes and in the general adult population.

Consistent with multiple published findings (4, 19, 27, 28), we also observed significantly elevated endemic antibody levels for beta-HCoVs OC43 and HKU1 following SARS-CoV-2 infection and seroconversion, unlike alpha-HCoVs. This finding is not unexpected due to the higher sequence and structural homology of beta-HCoVs with SARS-CoV-2 (29). It is unknown whether cross-reactivity or immunologic boosting related to OC43 and HKU1 antibody responses may contribute to protection against COVID-19. Previous studies suggest that endemic HCoV antibodies have poor neutralizing activity against SARS-CoV-2 (4, 30), while other studies describe that higher levels of HCoV-OC43 and HCoV-HKU1 antibodies are associated with less severe course of disease (31, 32). Nonetheless, the clinical significance of pre-existing immunity from endemic HCoV exposure against SARS-CoV-2 infection and COVID-19 severity remains to be determined.

In summary, our study used well-validated assays to provide evidence that humoral responses to SARS-CoV-2 elicited by natural infection persist over at least seven months in the elderly and may confer protection from reinfection. Taken together, our results also suggest the potential effectiveness of the quality improvement efforts in infection control after the first outbreak (2). Limitations of our study include a small sample size of residents from a single LTCF; therefore, it may not be representative of other elderly populations with varying demographic characteristics (i.e., age, sex, geographic region, etc.). Additionally, a natural survival bias is intrinsic to this type of survey, where serological testing is conducted following the outbreaks, as such, those captured in either outbreak would have had to survive to be included in our dataset. Including those that did not participate in our serosurveys, the case fatality during the first and second outbreak was 23.6% (13/55) and 6.7% (1/15) respectively. The lower case fatality during the second outbreak is likely multifactorial in nature. While this does not directly address survival bias, similar to the lower attack rate during the second survey, this decreasing trend could also be attributed to improved infection control measures in the facility following the first outbreak, although additional contributions from improved management of COVID-19 by the time of second outbreak (due to improved knowledge in the medical field) is also likely to contribute. Furthermore, our study only assessed IgG responses longitudinally, which are expected to persist for a longer duration. Recent findings have also demonstrated that SARS-CoV-2 IgA antibodies can persist for over 6 months following infection (16, 32–34), suggesting that quantifying IgA antibodies may potentially be beneficial to sero-surveillance studies and add to its overall sensitivity in identifying past infections. Future studies evaluating other SARS-CoV-2 and HCoV antibody isotypes longitudinally may provide valuable insight in understanding the humoral response to SARS-CoV-2 infections.

The strength of our study includes using multiple serological platforms that are authorized for diagnostic use, as well as MSD's pan-coronavirus multiplex immunoassay that allows for highly sensitive simultaneous detection of IgG against SARS-CoV-2 and HCoV antigens, thus we have the advantage of reporting consistent data reproducible across different platforms that are known to be highly reliable. Additionally, outbreaks in LTCF remain a major concern in the proper management of the COVID-19 pandemic due to higher burden of disease and risk of severe complications among the elderly. Therefore, while plenty of studies investigate the antibody responses longitudinally in the healthy adult population, our study contributes substantially to the field and fills the gap in knowledge of understanding how antibody response change and persist over time in older, high-risk adults.

The findings of our study provide insight into humoral responses to SARS-CoV-2 among LTCF residents and the potential for reinfection. However, additional studies are needed to more extensively characterize the durability of SARS-CoV-2 immune responses following natural infection and vaccination, and their role in protection against SARS-CoV-2 infection and

COVID-19 severity among high-risk groups. In particular, large-scale longitudinal studies from multiple LTCF would provide valuable data on the durability of immune responses among institutionalized older adults.

DATA AVAILABILITY STATEMENT

The raw data supporting the conclusions of this article will be made available by the authors, without undue reservation.

ETHICS STATEMENT

The investigations in this study were carried out as part of our public health-driven outbreak investigations and and undertaken within our practice mandate. Institutional ethics review was not required for specimen collection. Written informed consent for participation was not required for this study in accordance with the national legislation and the institutional requirements. Serological testing on clinical platforms was performed as regular clinical testing. Serological testing on the Meso Scale Discovery (MSD) platform and subsequent analysis was done as part of the assay validation and approved by REB protocol H20-01089.

AUTHOR CONTRIBUTIONS

GT, AL, RV, AC, AH, MMo, AJ, and IS were involved in the study conceptualization and methodology. Data curation was conducted by GT, AL, RV, TP, and JK, and data analysis was performed by GT, AL, and RV. CM assisted in sample management. CK carried out the recruitment of study participants. MMc was involved in experimental organization and sample collection. MK and SG were involved in the supervision of the study. The manuscript was originally drafted by GT and edited by IS, AJ, SG, TP, AC, and MMc. All authors contributed to the article and approved the submitted version.

FUNDING

This work was funded by Genome British Columbia (Grant number COV050). The study sponsor had no role in data collection, analysis, and interpretation.

ACKNOWLEDGMENTS

We would like to thank the families and the staff of the LTCF for all the support in the participant recruitment and specimen collection for this study. We would also like to thank Lisa Liu for her support in this study.

SUPPLEMENTARY MATERIAL

The Supplementary Material for this article can be found online at: https://www.frontiersin.org/articles/10.3389/fimmu.2021.775420/full#supplementary-material

REFERENCES

1. Childs A, Zullo AR, Joyce NR, McConeghy KW, Van Aalst R, Moyo P, et al. The Burden of Respiratory Infections Among Older Adults in Long-Term Care: A Systematic Review. *BMC Geriatr* (2019) 19(1):1–10. doi: 10.1186/s12877-019-1236-6
2. Vijh R, Ghafari C, Hayden A, Schwandt M, Sekirov I, Morshed M, et al. Serological Survey Following SARS-COV-2 Outbreaks at Long-Term Care Facilities in Metro Vancouver, British Columbia: Implications for Outbreak Management and Infection Control Policies. *Am J Infect Control* (2020) 000:2–5. doi: 10.1016/j.ajic.2020.10.009
3. Fung TS, Liu DX. Similarities and Dissimilarities of COVID-19 and Other Coronavirus Diseases. *Annu Rev Microbiol* (2021) 75(1):1–29. doi: 10.1146/annurev-micro-110520-023212
4. Westerhuis BM, Aguilar-Bretones M, Raadsen MP, de Bruin E, Okba NMA, Haagmans BL, et al. Severe COVID-19 Patients Display a Back Boost of Seasonal Coronavirus-Specific Antibodies. *medRxiv* (2020). doi: 10.1101/2020.10.10.20210070
5. Hicks J, Klumpp-Thomas C, Kalish H, Shunmugavel A, Mehalko J, Denson JP, et al. Serologic Cross-Reactivity of SARS-CoV-2 With Endemic and Seasonal Betacoronaviruses. *medRxiv* (2020). doi: 10.1101/2020.06.22.20137695
6. LeBlanc JJ, Gubbay JB, Li Y, Needle R, Arneson SR, Marcino D, et al. Real-Time PCR-Based SARS-CoV-2 Detection in Canadian Laboratories. *J Clin Virol* (2020) 128:104433. doi: 10.1016/j.jcv.2020.104433
7. Roche. *Cobas® SARS-CoV-2 Test*. Available at: https://diagnostics.roche.com/global/en/products/params/cobas-sars-cov-2-test.html.
8. Van Caeseele P, Bailey D, Forgie SE, Dingle TC, Krajden M. SARS-CoV-2 (COVID-19) Serology: Implications for Clinical Practice, Laboratory Medicine and Public Health. *CMAJ* (2020) 192(34):E973–9. doi: 10.1503/cmaj.201588
9. Johnson M, Wagstaffe HR, Gilmour KC, Mai AL, Lewis J, Hunt A, et al. Evaluation of a Novel Multiplexed Assay for Determining IgG Levels and Functional Activity to SARS-CoV-2. *J Clin Virol* (2020) :130. doi: 10.1016/j.jcv.2020.104572
10. Mariën J, Ceulemans A, Michiels J, Heyndrickx L, Kerkhof K, Foque N, et al. Evaluating SARS-CoV-2 Spike and Nucleocapsid Proteins as Targets for Antibody Detection in Severe and Mild COVID-19 Cases Using a Luminex Bead-Based Assay. *J Virol Methods* (2021) 288:114025. doi: 10.1016/j.jviromet.2020.114025
11. Murchu E O, Byrne P, Walsh KA, Carty PG, Connolly M, De Gascun C, et al. Immune Response Following Infection With SARS-CoV-2 and Other Coronaviruses: A Rapid Review. *Rev Med Virol* (2021) 31(2):1–11. doi: 10.1002/rmv.2162
12. Murrell I, Forde D, Tyson L, Chichester L, Garratt A, Vineall O, et al. A Longitudinal Comparison of Spike and Nucleocapsid SARS-CoV-2 Antibody Responses in a Tertiary Hospital's Laboratory Workers With Validation of DBS Specimen Analysis. *MedRxiv* (2020). doi: 10.1101/2020.10.29.20219931
13. Ripperger TJ, Uhrlaub JL, Watanabe M, Wong R, Castaneda Y, Pizzato HA, et al. Orthogonal SARS-CoV-2 Serological Assays Enable Surveillance of Low-Prevalence Communities and Reveal Durable Humoral Immunity. *Immunity* (2020) 53(5):925–33.e4. doi: 10.1016/j.immuni.2020.10.004
14. Van Elslande J, Oyaert M, Ailliet S, Van Ranst M, Lorent N, Vande Weygaerde Y, et al. Longitudinal Follow-Up of IgG Anti-Nucleocapsid

Antibodies in SARS-CoV-2 Infected Patients Up to Eight Months After Infection. *J Clin Virol* (2021) 136:104765. doi: 10.1016/j.jcv.2021.104765

15. Isho B, Abe KT, Zuo M, Jamal AJ, Rathod B, Wang JH, et al. Persistence of Serum and Saliva Antibody Responses to SARS-CoV-2 Spike Antigens in COVID-19 Patients. *Sci Immunol* (2020) 5(52):1–21. doi: 10.1126/sciimmunol.abe5511
16. Dan JM, Mateus J, Kato Y, Hastie KM, Yu ED, Faliti CE, et al. Immunological Memory to SARS-CoV-2 Assessed for Up to 8 Months After Infection. *Science* (2021) 371(6529):eabf4063. doi: 10.1126/science.abf4063
17. Cohen KW, Linderman SL, Moodie Z, Czartoski J, Lai L, Mantus G, et al. Longitudinal Analysis Shows Durable and Broad Immune Memory After SARS-CoV-2 Infection With Persisting Antibody Responses and Memory B and T Cells. *Cell Rep Med* (2021) 2(7):100354. doi: 10.1016/j.xcrm.2021.100354
18. Long Q-X, Tang X-J, Shi Q-L, Li Q, Deng H-J, Yuan J, et al. Clinical and Immunological Assessment of Asymptomatic SARS-CoV-2 Infections. *Nat Med* (2020) 26(8):1200–4. doi: 10.1038/s41591-020-0965-6
19. Aguilar-Bretones M, Westerhuis BM, Raadsen MP, de Bruin E, Chandler FD, Okba NMA, et al. Seasonal Coronavirus–Specific B Cells With Limited SARS-CoV-2 Cross-Reactivity Dominate the IgG Response in Severe COVID-19. *J Clin Invest* (2021) 131(21):e150613. doi: 10.1172/JCI150613
20. Wei J, Matthews PC, Stoesser N, Maddox T, Lorenzi L, Studley R, et al. Anti-Spike Antibody Response to Natural SARS-CoV-2 Infection in the General Population. *Nat Commun* (2021) 12(1):6250. doi: 10.1038/s41467-021-26479-2
21. Wang K, Long Q-X, Deng H-J, Hu J, Gao Q-Z, Zhang G-J, et al. Longitudinal Dynamics of the Neutralizing Antibody Response to Severe Acute Respiratory Syndrome Coronavirus 2 (SARS-CoV-2) Infection. *Clin Infect Dis* (2021) 73 (3):e531–9. doi: 10.1093/cid/ciaa1143
22. Buttiron Webber T, Provinciali N, Musso M, Ugolini M, Boitano M, Clavarezza M, et al. Predictors of Poor Seroconversion and Adverse Events to SARS-CoV-2 mRNA BNT162b2 Vaccine in Cancer Patients on Active Treatment. *Eur J Cancer* (2021) 159:105–12. doi: 10.1016/j.ejca.2021.09.030
23. Suhandynata RT, Hoffman MA, Huang D, Tran JT, Kelner MJ, Reed SL, et al. Commercial Serology Assays Predict Neutralization Activity Against SARS-CoV-2. *Clin Chem* (2021) 67(2):404–14. doi: 10.1093/clinchem/hvaa262
24. Tillett RL, Sevinsky JR, Hartley PD, Kerwin H, Crawford N, Gorzalski A, et al. Genomic Evidence for Reinfection With SARS-CoV-2: A Case Study. *Lancet Infect Dis* (2021) 21(1):52–8. doi: 10.1016/S1473-3099(20)30764-7
25. Hall VJ, Foulkes S, Charlett A, Atti A, Monk EJM, Simmons R, et al. SARS-CoV-2 Infection Rates of Antibody-Positive Compared With Antibody-Negative Health-Care Workers in England: A Large, Multicentre, Prospective Cohort Study (SIREN). *Lancet* (2021) 397(10283):1459–69. doi: 10.1016/S0140-6736(21)00675-9
26. Cavanaugh AM, Spicer KB, Thoroughman D, Glick C, Winter K. Reduced Risk of Reinfection With SARS-CoV-2 After COVID-19 Vaccination. *MMWR Morb Mortal Wkly Rep* (2021) 70(32):1081–3. doi: 10.15585/mmwr.mm7032e1
27. Aydillo T, Rombauts A, Stadlbauer D, Aslam S, Abelenda-Alonso G, Escalera A, et al. Antibody Immunological Imprinting on COVID-19 Patients. *Nat Commun* (2020) 12(1):3871. doi: 10.1101/2020.10.14.20212662
28. Shrock E, Fujimura E, Kula T, Timms RT, Lee IH, Leng Y, et al. Viral Epitope Profiling of COVID-19 Patients Reveals Cross-Reactivity and Correlates of Severity. *Science* (2020) 370(6520):eabd4250. doi: 10.1126/science.abd4250
29. Becker M, Strengert M, Junker D, Kaiser PD, Kerrinnes T, Traenkle B, et al. Exploring Beyond Clinical Routine SARS-CoV-2 Serology Using MultiCoV-Ab to Evaluate Endemic Coronavirus Cross-Reactivity. *Nat Commun* (2021) 12(1):1152. doi: 10.1038/s41467-021-20973-3
30. Poston D, Weisblum Y, Wise H, Templeton K, Jenks S, Hatziioannou T, et al. Absence of SARS-CoV-2 Neutralizing Activity in Pre-Pandemic Sera From Individuals With Recent Seasonal Coronavirus Infection. *Clin Infect Dis* (2021) 73(5):e1208–11. doi: 10.1093/cid/ciaa1803
31. Dugas M, Grote-Westrick T, Vollenberg R, Lorentzen E, Brix T, Schmidt H, et al. Less Severe Course of COVID-19 Is Associated With Elevated Levels of Antibodies Against Seasonal Human Coronaviruses OC43 and HKU1 (HCoV OC43, HCoV Hku1). *Int J Infect Dis* (2021) 105:304–6. doi: 10.1016/j.ijid.2021.02.085
32. Ortega N, Ribes M, Vidal M, Rubio R, Aguilar R, Williams S, et al. Seven-Month Kinetics of SARS-CoV-2 Antibodies and Role of Pre-Existing Antibodies to Human Coronaviruses. *Nat Commun* (2021) 12(1):4740. doi: 10.1038/s41467-021-24979-9
33. Ivanov A, Semenova E. Long-Term Monitoring of the Development and Extinction of IgA and IgG Responses to SARS-CoV-2 Infection. *J Med Virol* (2021) 93(10):5953–60. doi: 10.1002/jmv.27166
34. Gaebler C, Wang Z, Lorenzi JCC, Muecksch F, Finkin S, Tokuyama M, et al. Evolution of Antibody Immunity to SARS-CoV-2. *Nature* (2021) 591 (7851):639–44. doi: 10.1038/s41586-021-03207-w

Conflict of Interest: SG reports having received research support and/or consulting fees from Moderna, Merck, GSK, VBI Vaccines, and Meridian Biosciences. No products of these companies were used in the study.

The remaining authors declare that the research was conducted in the absence of any commercial or financial relationships that could be construed as a potential conflict of interest.

frontiers
in Immunology

REVIEW
published: 03 January 2022
doi: 10.3389/fimmu.2021.811968

T Cell Memory in Infection, Cancer, and Autoimmunity

Vincenzo Barnaba[1,2]*

[1] *Istituto Pasteur Italia, Fondazione Cenci Bolognetti, Rome, Italy,* [2] *Dipartimento di Scienze Cliniche, Interistiche, Anestesiologiche e Cardiovascolari, Sapienza Università di Roma, Rome, Italy*

Long-term immunological memory represents a unique performance of the adaptive immunity selected during evolution to support long-term survival of species in vertebrates, through protection against dangerous "invaders", namely, infectious agents or unwanted (e.g., tumor) cells. The balance between the development of T cell memory and various mechanisms of immunoregulation (namely, T cell effector exhaustion and regulatory T cell suppression) dictates the fate in providing protection or not in different conditions, such as (acute or chronic) infection, vaccination, cancer, and autoimmunity. Here, these different environments are taken in consideration to outline the up-to-date cellular and molecular features regulating the development or damping of immunological memory and to delineate therapeutic strategies capable to improve or control it, in order to address pathological contexts, such as infection, tumor, and autoimmunity.

Keywords: adaptive immunity, immunological memory, infection, vaccination, cancer, autoimmunity

OPEN ACCESS

Edited by:
Antonella Prisco,
Institute of Genetics and Biophysics (CNR), Italy

Reviewed by:
Hidehiro Yamane,
National Institutes of Health (NIH) United States
Mario M. D'Elios,
University of Florence, Italy

****Correspondence:***
Vincenzo Barnaba
vincenzo.barnaba@uniroma1.it

Specialty section:
This article was submitted to Immunological Memory, a section of the journal Frontiers in Immunology

Received: *09 November 2021*
Accepted: *07 December 2021*
Published: *03 January 2022*

Citation:
Barnaba V (2022) T Cell Memory in Infection, Cancer, and Autoimmunity. Front. Immunol. 12:811968. doi: 10.3389/fimmu.2021.811968

INTRODUCTION

Unique and essential properties of the adaptive immune system are the fine specificity towards each type of peptides (epitopes) and the long-term immunological memory. The latter usually develops following resolution of a given infection, through the generation of memory B and T cells, which persist for almost a lifetime and promptly trigger secondary protective responses in the event of reinfection (1–3). The adaptive immune system and the concatenated long-term immunological memory (appearing about 450 million years ago in fish) were selected in the vertebrates in a Darwinian fashion, probably under the evolutive pressure of the significantly higher lifespan and lower reproductive capacity, as compared with the invertebrates only having the innate immunity (present since 1 billion years ago without having had any fundamental changes to date): for instance, insects do not need the long-term memory of an infection, because they have a very short life and a huge number of offspring allowing the species survival. The first description of the immunological memory was probably dated back to Thucydides, who reported, in his writing about the plague outbreak that decimated the Athenians during the Peloponnesian war against Sparta (443–404 BC), that individuals who recovered from the infection no longer get sick.

Abbreviations: APCs, antigen-presenting cells; DC, dendritic cell; MHC, major histocompatibility complex; TCRs, T cell receptors; L, ligand; h, helper; c, cytotoxic; PAMP, pathogen-associated molecular pattern; DAMP, danger-associated molecular pattern; T_N, naïve T; T_{CM}, central memory T; T_{EM}, effector memory T; T_{PM}, peripheral memory T; T_{RM}, resident memory T; HAV, hepatitis A virus; TFs, transcription factors; ICs, immune check-points; Tregs, regulatory T cells; NSCLC, non-small cell lung cancer; TILs, tumor-infiltrating T cells; ICB, IC blockade; T1D, type 1 diabetes.

The generation of effective adaptive immune responses against the "invaders", which come from outside or are aberrantly generated in our body (principally infecting agents or tumors), requires that naïve B or T lymphocytes receive the appropriate signals (i.e., antigenic signal 1 and costimulatory signal[s] 2) provided by professional (p) antigen-presenting cells (APCs) (1–3). In this review, we will focus on T cell responses. pAPCs (principally the myeloid or monocyte-derived dendritic cell [DC] subsets normally patrolling our tissues), mature and convert from tolerogenic into stimulatory (s)DCs, following the exposure to the innate immunity (infectious or danger) signals (signal[s] 3) received within inflamed tissues. sDCs more efficiently phagocytose and process antigens, upregulate both major histocompatibility complex (MHC) and costimulatory molecules, and acquire the capacity to efficiently migrate into draining lymphoid organs, because of the overexpression of appropriate homing chemokine receptors (e.g., CCR7). Once arriving into lymph nodes, sDCs efficiently present or cross-present peptides (generated by the antigen processing) on class II or class I MHC molecules to high avidity T cell receptors (TCRs) of CD4^{+} or CD8^{+} T cells, respectively (signal 1), and provide various costimulatory molecules (e.g., B7.1, B7.2, B7RP1, CD27 ligand [L]) interacting with the corresponding receptors (e.g., CD28, ICOS, CD27) expressed by naïve T cells (signal 2) (**Figure 1**). Only under these conditions, the single antigen-specific naïve T cells, whose frequency ranges between about 1/200,000 and 1/1,000,000 cells in humans according to the type of antigen (4), are primed, proliferate by several logs of magnitude, differentiate into protective effector cells clearing the "invader", and generate long-term memory. Basically, CD4^{+} T helper (h) cells and CD8^{+} T cytotoxic (c) cells divide the labor: the former help B cells to produce long-lived antibody responses, synthesize a wide variety of cytokines (depending on the context) and, in some setting, can acquire cytotoxic function; the latter are primarily antigen-specific cytotoxic cells, and can produce various types of cytokines, such as the CD4. The requirement of third party CD4^{+} T cells in the interaction DCs/CD8^{+} T cells for CD8^{+} T cell priming and long-term CD8^{+} T cell memory development (5–7) is inversely correlated with the level of inflammation and pathogen- or danger-associated molecular pattern (PAMP or DAMP) signals conditioning the priming (3, 8). It is superfluous in high-level inflammatory contexts, in which PAMP or DAMP signals trigger a variety of inflammatory responses and mediate DC activation resulting in CD8^{+} T cell

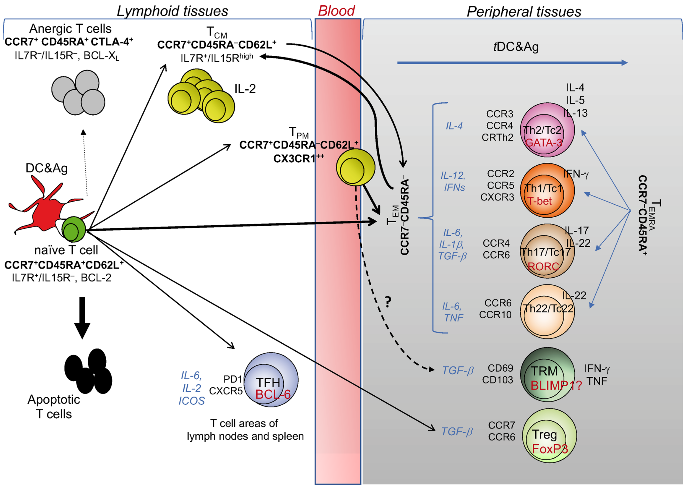

FIGURE 1 | T cell diversity and memory pathways. This cartoon depicts the "one cell, multiple fates" hypothesis proposing that a single naïve (CD4^{+} or CD8^{+}) T cell undergoes multiple fates, according to the strength of signals 1 and 2 received by pAPCs: suboptimal signals (e.g., signal 1 without signal 2) causes T cell anergy; excessive signals (as in the case of response to superantigens, such as some bacterial toxins) cause T cell apoptosis; optimal signal strength induces typically and functionally distinct T$_{EM}$, T$_{CM}$, and T$_{PM}$ cells with the same specificity. T$_{CM}$ cells can also derive from T$_{EM}$: upon performing effector functions, the majority of T$_{EM}$ dye, while a minority is saved and generates T$_{CM}$. T$_{CM}$ cells acquiring the chemokine lymphoid homing receptors (indicated in bold under the T$_{CM}$ subset) continuously recirculate *via* the bloodstream to lymphoid organs, and promptly generate secondary responses. CX3CR1^{+} T$_{PM}$ cells migrate from blood to tissue to lymph nodes, proliferate in a higher fashion than the T$_{CM}$ population, display the ability to perform cytotoxic function, and survey non-lymphoid tissues. The differentiation into the various T$_{EM}$ subsets (Th1, Th2, Th17, Th22, or the cytotoxic T [Tc] cell counterparts) is conditioned by the microenvironmental cytokine milieu (indicated by the cytokines in italics), in which the response takes place. Under these conditions, each of the T$_{EM}$ subsets activates its own specific transcription master regulator (indicated in red within each T$_{EM}$ subset) contributing to establish the gene expression patterns correlated with specific cytokine immune-phenotypes (indicated to the right of each T$_{EM}$ subset), and expresses its own specific pattern of inflamed tissue homing receptors (indicated to the left of each T$_{EM}$ subset). Upon migration into the specific inflamed tissues, each type of T$_{EM}$ subset is ready to differentiate into terminally-differentiated effector cells (T$_{EMRA}$) promptly performing the functions for which they are programmed (Th2, Th1, Th17, etc.), following contact with tissue-resident (*t*)DCs presenting the specific antigens derived from various type of pathogens: that is, the helminths preferentially will condition the Th2, the intracellular pathogens the Th1, the fungi the Th17 differentiation, etc. TFH cell differentiation is regulated by IL-6, IL-2, inducible costimulator receptor (ICOS): if the chemokine receptor CXCR5 is expressed, they will migrate to the border of the B cell follicle and help B cell differentiation, whereas, in the presence of the related cell signals, they differentiate into Th1-, Th2-, or Th17-like cells, exit the lymphoid tissue and traffic to the site of infection or inflammation. Similar cell diversification occurs upon optimal activation of CD8^{+} T cells that also acquire the cytotoxicity function (Tc: T cytotoxic cell). T$_{RM}$ and Treg profiles are conditioned by the antigens they meet directly in the tissues and lymphoid organs, respectively, in the presence of TGF-β.

priming and memory development (9–13). By contrast, the need of CD4$^+$ T cell help for priming CD8$^+$ T cell responses seems to be necessary in chronic infections, where various signals (2 and/or 3) are impaired (3), although it still fails to restore effective CD4$^+$ or CD8$^+$ T cell memory.

The generation of long-term immunological memory is dependent on appropriate level of immunopathology caused by the innate and adaptive effector immune responses addressed to eliminate the "invader" by killing infected host cells and providing tissue inflammation that stop upon pathogen clearance (recovery). The great value of vaccination is based on its capacity, through the administration of "invader" antigens (signal 1) and adjuvants (such as alum, MF59, ASOs, CpG, TLR ligands, viral, RNA or DNA vectors) (14) (signal 3 principally addressed to activate DCs providing signal 2), to elicit strong immune responses and long-term memory mimicking those observed in individuals recovered from a natural infection, without the severe phenomena associated with the disease that can even result in death.

T CELL DIVERSITY

The first seminal report on the diversification of memory T cells was by Sallusto and Lanzavecchia (15), showing that memory T cells can be subdivided by distinct expression pattern of adhesion molecules and chemokine receptors allowing different migratory pathways. Naïve T (T_N) cells and central memory T (T_{CM}) cells (both expressing high-level of lymphoid homing markers CD62L and CCR7) continuously recirculate *via* the bloodstream to lymphoid organs. In addition, T_{CM} cells persist by an IL-7 and/or IL15-dependent homeostatic proliferation, without the antigen persistence, produce high IL-2 levels and display high self-renewal/proliferation potential upon antigen re-encounter (16–18). By contrast, the various functional subsets of effector memory T (T_{EM}) cells lose the high proliferation potential and the lymphoid homing markers, acquire diverse patterns of inflamed tissue homing markers (see classification of T cell subsets in **Figure 1**) and display prompt effector functions, according to the type of peripheral tissue and cytokine milieu, in which they differentiate and migrate (**Figure 1**) (19). Recently, the surface expression of the chemokine receptor CX3CR1 has been used to better classify effector and memory T cells (20, 21). CX3CR1 identifies a subset termed peripheral memory T cells (T_{PM}) that migrate from blood to tissue to lymph nodes, show higher self-renewal capacity and proliferation than the conventional T_{CM} population, display the ability to perform cytotoxic function, and survey non-lymphoid tissues. In parallel, a subset of effector CX3CR1^{high} T cells appears primarily restricted to the intravascular space and spleen and represent a major source of T_{EM} cells. Furthermore, a pool of tissue-resident memory CD8$^+$ T (T_{RM}) cells has been more recently identified (22). T_{RM} cells persist long term in non-lymphoid tissues, express a transcriptional signature shared with both T_{CM} and T_{ME} cells that can be conditioned by individual tissues in which they survive, and control possible foreign "invasions" by recruiting other immune cells and triggering inflammatory processes.

Recent technological advances tracing CD8$^+$ T cells at single-cell level in mouse *in vivo* support the "one cell, multiple fates" hypothesis, according to which a single naïve T cell (with a single specificity) generates multiple phenotypically and functionally distinct effector and memory T cells with the same TCR (23) (**Figure 1**). However, we cannot completely exclude the "one cell, one fate" hypothesis, dictating that single T cell clones with various degrees of affinity for a given peptide select unique fates for each single clone: for instance, a clone will become Th1, another Th2, still another Th17, etc. (23). Consistently, by combining antigenic stimulation and TCR deep sequencing technologies, it has been elegantly proposed that CD4$^+$ T cell responses can develop according to both the hypotheses in humans. Indeed, single naïve or memory CD4$^+$ T cells primed by various pathogens (*Candida albicans*, *Mycobacterium tuberculosis*, *tetanus toxoid*) *in vitro* can undergo multiple fates, that is Th1, Th2, and Th17 cells with different migratory capacity, comprising both clones polarizing toward a single fate, and clones whose progeny acquire multiple fates (24) (**Figure 1**). The stochastic combination of several events (e.g., TCR affinity and costimulatory signals, the cytokine milieu, the type and dose of antigens, the duration of antigen exposure) may condition the different (single or multiple) fates in the context of the same polyclonal immune responses. Altogether, these multiple epigenetics-driven fates provide a high level of plasticity to the single memory T cells, which can thus employ different and prompt alternative strategies to fight and eliminate each type of pathogens and to maintain long-term memory.

Because the generation of the different memory T cell subsets after infection (or in response to vaccination) is principally addressed both to eliminate the "invader" (recovery) and to recall rapid secondary responses in the case of reinfection (memory), a main question at the center of immunology research is: how is the T cell diversification regulated and capable to provide immunological memory in condition of chronic (long-lasting) self- or non-self-antigen stimulation, as it happens in the course of chronic infections, tumors, and autoimmune diseases?

Addressing these questions is of pivotal importance to understand the basic role of adaptive T cell immunity and memory and their implications in infection resolution, effective vaccination, chronic infection, cancer, or autoimmunity, in order to develop new therapeutic strategies (tuning of immune responses by biologicals, adaptive immunotherapy, vaccination) in the different clinical conditions.

T CELL DIVERSITY IN ACUTE INFECTIONS OR VACCINATION

The resolution of most acute infections or the vaccination against the related pathogens (e.g., smallpox, mumps, rubella, chickenpox, measles, diphtheria, polio, meningococci, hepatitis A virus [HAV], HBV) correlate with protective adaptive effector responses (i.e., neutralizing antibodies and effector CD4$^+$ and CD8$^+$ T cells) and development of long-term memory (**Figures 2A, B**). In particular, high affinity TCRs and the coreceptors (CD4 or CD8) on naïve T cells, following receiving sustained antigenic signals 1 by pAPCs, deliver the signaling cascades through the phosphorylation of multiple consecutive molecules (e.g., ITAM, ZAP70, LCK, LAT, PLCγ, IP3,…), ultimately leading to the nucleus translocation of various transcription factors (TFs) (e.g., NFκB, NAFT family) that, through their own conserved DNA binding domains, favor the expression of a wide series of genes associated to T cell activation and memory (25–28). The costimulatory molecules on naïve T cells (engaged by the respective ligands expressed on APCs [signal 2]) amplify the activation signal cascade, through the phosphorylation of additional messengers (e.g., PIK3, ERK, RAS…) essential for T cell priming, without which signal 1 alone could cause T cell anergy. The effective TCR signal strength must be transient and not persistent, to avoid a prolonged expression of genes associated with the "T cell exhaustion" (e.g., *Pdcd1* or *CTLA4* encoding the inhibitory receptors PD-1 and CTLA-4, respectively), and to guarantee thus the full T cell effector responses and the generation of long-term memory. The short duration of the TCR signaling has been proposed to induce a transient DNA demethylation of the *Pdcd1* locus (encoding PD-1), followed by *Pdcd1* re-methylation that coincides with efficient effector functions addressed to fight the "invaders" (29). In the late phase of activation (i.e., in the absence of antigen-stimulation due to the pathogen clearance), T cells upregulate a wide repertoire of inhibitory signals (i.e., immune check-points [ICs], such as CTLA-4, PD-1, TIM-3, LAG-3, TIGIT, VISTA), which, following contact with the respective ligands expressed by both lymphoid and non-lymphoid cells, deliver an inhibitory cascade leading to the dephosphorylation of the molecules associated with the TCR, co-receptor, and co-stimulatory signaling (30). This intrinsic immunoregulatory mechanism was likely selected during evolution to terminate the immune responses that would be useless if not harmful, when a given infection cleared. Under these conditions (that is, the combination of termination of antigen exposure and IC expression), effector T cells drastically decrease and die upon performing their (protective) effector functions, whereas the sister memory cells selected by specificity and function persist without the presence of antigen, and promptly respond on demand, by generating new waves of effector immune responses in the case of reinfection (**Figure 2B**). Therefore, the stop signals contributing to the "crash" of effector responses, can also contribute to develop immunological memory (**Figures 2A, B**).

The generation and distribution of each of these memory T cell subsets obey highly diverse epigenetic, transcriptional and proteome pathways (2, 19, 23, 31–33). The studies on genome-wide transcriptional and epigenetic changes (by using the assay for transposase-accessible chromatin with sequencing (34) during infection or vaccination showed that DNA methylation,

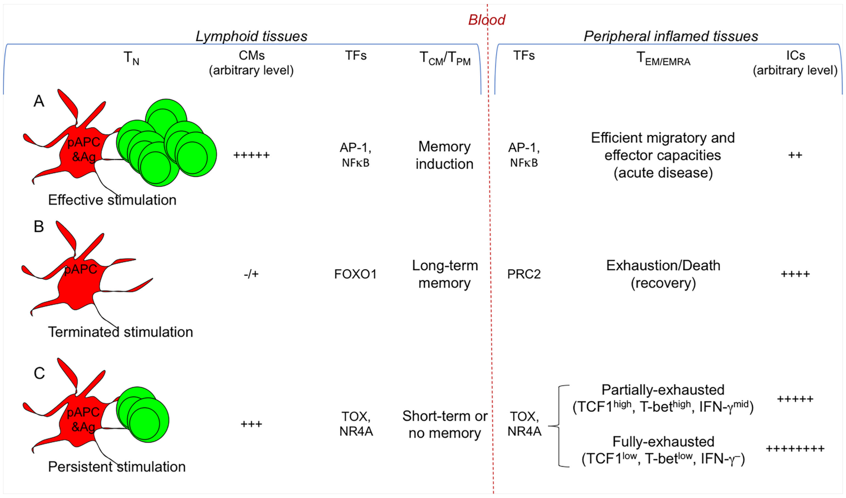

FIGURE 2 | Signals conditioning T cell diversification. Different strengths of T cell stimulation result in different fates. The most relevant TFs involved are indicated. **(A)** Efficient and transient antigenic and co-stimulatory molecule (CM) signals by pAPCs condition strong T cell proliferation and differentiation into memory T cells (T$_{CM}$/T$_{PM}$) and the various types of T$_{EM/EMRA}$ cell subsets (Th/c1, Th/c2, Th/c17,…), selected according to the cytokine milieu in which the response takes place (see **Figure 1**). TFs (e.g., AP-1, NFκB) activate memory (e.g., *IL7R*, *BCL2*) and effector genes (e.g., *IFNG*, *GZMB*). **(B)** Under these conditions, the T cell response generally results with the eradication of a given pathogen and recovery: the combination of termination of antigen exposure and upregulation of ICs on T$_{EM/EMRA}$ cells will lead to their drastic decrease and death, whereas memory cells will persist without the presence of antigen, and will provide long-term memory. TFs such as FOXO1 maintain long-term memory, whereas PRC2 contributes in silencing effector genes. **(C)** In the presence of persistent antigen-stimulation (e.g., chronic infections or tumors), the continuous viral or tumor mutations will induce the generation of continuous waves of T cells, which, because chronically exposed to antigen-stimulation, will upregulate a wide repertoire of ICs, and will undergo chronic T cell exhaustion resulting in the lack of (long-term) immunological memory. TFs (e.g., TOX, NR4A) favor the transcription of exhaustion genes (e.g., encoding PD-1, TIM-3, CTLA-4), overwhelming the work of those (e.g., AP-1, NFκB) activating effector genes (e.g., *IFNG*, *GZMB*) or memory genes (e.g., *IL7R*, *BCL2*). In the early phase of the persistent antigen-stimulation, T$_{EM/EMRA}$ cells will become partially-exhausted (TCF1^{high}, T-bet^{hgh}, IFN-γ^{mid}), then they will degenerate in fully-exhausted cells (TCF1^{low}, T-bet^{low}, IFN-γ$^-$) and will further upregulate ICs. Partially-exhausted T cells can be rescued by ICB.

histone modifications, and transcriptional signatures diversifies T cell effector and memory differentiation. These analyses in mouse models revealed that long-lived memory T cells have a naïve-like transcriptome but an effector-like open chromatin map (i.e., demethylation of *IFNG* and *GZMB* genes and an open chromatin near their promoters), suggesting a mechanism by which memory T cells are equipped to rapidly perform effector functions (35). *Vice versa*, open chromatin regions were found in the *IL7R* and *BCL2* genes in both naïve and memory cells, but not in effector cells, suggesting that memory cells conserve important molecular features of naïve cells, associated to survival and self-renewal (**Figure 2A**). In addition, various studies demonstrated that active transcriptional maintenance by FOXO1 is required to sustain memory T cell longevity and self-renewal, whereas the epigenetic factor PRC2 contributes in silencing genes associated with terminally-effector T cells, following infection resolution (36–39) (**Figure 2B**).

An unresolved question regards the generation of long- or short-term memory, after different types of infection or vaccination. The majority of the current vaccines are administrated subcutaneously and cause long-term memory against the pathogens towards which they are directed (e.g., smallpox, mumps, rubella, chickenpox, measles, diphtheria, polio, meningococci, HAV, HBV). By contrast, the immunological memory resulting upon SARS-CoV-2, various common cold or influenza virus infections or the related vaccinations is generally short-term, likely because a much higher production of specific immune responses at the level of the upper respiratory tracts of the lung would be needed to generate long-lasting protection in these infections (40). In particular, vaccines administrated through the mucosal airways (the gateway to viruses such as SARS-CoVs, common colds or influenza) should likely generate more efficient immune responses in these sites than the current vaccines administrated subcutaneously, and favor long-term memory. These hypotheses could be confirmed by using single-cell sequencing technology, allowing to analyze the complexed module, namely, the transcriptional pathways, the level of transcription factors, and the chromatin accessibility in various immune cell types after the different infection recoveries or vaccination types.

T CELL DIVERSITY IN CHRONIC INFECTION AND CANCER

The sustained antigenic stimulation provided by persisting infection or cancer breaks the fine molecular balance conditioning the protective effector responses and the generation of long-term memory by various interacting mechanisms, namely, viral or tumor immune escape, T cell exhaustion, and suppression by regulatory T cells (Tregs).

Immune Escape and T Cell Diversity in Chronic Infection and Cancer

A principal mechanism of immune escape evading both T and B cell recognition and affecting T cell diversity is caused by viral or tumoral mutations, resulting in the establishment of a state of chronic low-level immunopathology that, despite unable to clear the persisting virus or tumor, delays ultimately the "catastrophe" (i.e., failure of chronically-infected organs or rapid spread of metastatic tumors) as much as possible. The mechanisms establishing chronic low-level immunopathology are likely selected, during the evolutionary process, to allow a long-term survival of the host (i.e., compromise between the host and the persisting viruses or tumors), by avoiding excessive damage of normal tissues, on the one hand, and excessive virus or tumor spread in the body, on the other hand (41).

Persisting viruses, such as HCV (a single strand RNA virus causing chronic hepatitis in 60–80% of infected individuals, depending on the geographical areas), HIV-1 (a lentivirus belonging to the *Retroviridae* family, infecting human immune cells and causing AIDS in the majority of infected individuals without treatment), and to a lesser extent HBV (a double strand DNA virus causing chronic hepatitis in less than 3% of infected individuals), provide different mutation rates that can have equally different impact on BCR or TCR diversity. The lack of proofreading activity by HIV-1 reverse transcriptase or by HCV-RNA-dependent RNA polymerase makes replication of HIV-1 or HCV (in contrast to HBV) extremely error-prone: these errors have been estimated in a range of 1 mutation in 1,000 to 100,000 nucleotides per replication cycle for RNA viruses (e.g., HCV or HIV-1), and approximately 1 mutation in 100,000,000 nucleotides per replication cycle for DNA viruses (e.g., HBV) (42, 43). These differences in the mutational fitness can contribute to the capacity of HCV or HIV-1 to escape from the huge B or T cell repertoire specific to the "wild-type" viral epitopes and to establish chronic infection much more frequently than HBV, and, as a consequence, to the efficient development of immunological memory in the latter, as compared with the former. By contrast, the capacity of the coronaviruses, including SARS-CoV-2, to proofread and clear mismatched nucleotides during replication (44), leads to hypothesize that these viruses cannot persist and establish chronic infection because of the low mutation rate, although the evident epidemiological role of these mutations. The lack of long-term immunological memory in these infections is likely due to the rapid subversion of mucosal immunity (innate and then adaptive) at the level of the gate entry (i.e., upper respiratory tracts).

As well as persisting viruses, "hot" tumors, such as melanoma or non-small cell lung cancer (NSCLC) that, in contrast to "cold" tumors, are characterized by significant DNA instability, principally due to the lack of mismatching repair mechanisms, show a very high mutational burden generating a huge repertoire of mutated (passenger) neoantigens, and a high number of tumor-infiltrating T cells (TILs) (45, 46). T cells specific to these mutated neoantigens, which are not purged by central tolerance, can migrate in the periphery, massively infiltrate hot tumors and be of particular relevance to tumor control (47, 48). Therefore, regardless of the origin of mutated (viral or tumor) antigens, the immune system is equipped to chase the continuous viral or tumor mutations through the generation of equally continuous new waves of mutated antigen-specific T cell clones (49). However, the generation of the huge repertoire of mutations can escape from B and T cells and contribute to the tumor mutational fitness and to the difficulty in developing effective immunological memory.

T Cell Exhaustion and Memory in Chronic Infection and Cancer

In the course of chronic infections or tumors, T cells will be unable to eliminate the persisting (hyper-mutational) virus or tumor, upregulate a wide repertoire of ICs, and, in the long run, will undergo the combination of a T cell dysfunctional state defined "T cell exhaustion", and the lack of long-term memory, resulting ultimately in irreversible chronic infection or tumor progression (41) (**Figure 2C**).

The molecular bases of T cell exhaustion and absence of long-term memory include a multitude of simultaneous and progressive transcriptional and epigenetic events. First, the long duration of TCR signaling by persistent antigens has been demonstrated to lead to a complete demethylation of the *Pdcd1* regulatory region that remains persistently unmethylated, and impedes thus the re-stabilization of efficient effector functions, as in the case of short duration of TCR signaling, shown in resolving infections (29, 50). Then, various types of histone modifications lead to a state, in which the chromatin is stably open and accessible to a multitude of TFs (e.g., TOX, NR4A) favoring the transcription of exhaustion genes (e.g., encoding PD-1, TIM-3, CTLA-4), and overwhelming the work of those (e.g., AP-1, NFκB,…) activating effector (e.g., *IFNG*, *GZMB*) or memory (e.g., *IL7R*, *BCL2*) genes (35, 51, 52) (**Figure 2C**).

Depending on the time these processes start, they may or may not be restored. In the early phases of persistent stimulation, exhausted T cells (PD-1$^+$CTLA-4$^+$TIM-3$^+$…) can be rescued principally if they express a further TF, the TCF1 encoded by the *TCF7* gene: TCF1^{high} cells express the master TF for IFN-γ production T-bet, at a level enough for producing moderated levels of IFN-γ (partially-exhausted T cells), although not at the levels observed in resolving infections, and may hence contribute to maintain the state of chronic low-level inflammation (53–57). The TCF1^{high} T cells can be efficiently rescued and acquire a stronger effector profile and anti-tumor activity by the treatment with IC inhibitors (e.g., anti-PD-1, anti-PDL-1, anti-CTLA-4 mAbs), or the combination of the latter with vaccine therapy containing mutated tumor neo-antigens (58). By contrast, in the late exhaustion phase, T cells become TCF1^{low}, acquire a fully-exhaustion phenotype (PD-1^{high}CTLA-4^{high}TIM-3^{high}), and, as a consequence, cannot be rescued by IC blockade (ICB) or vaccination therapies, likely because the TFs favoring expression of ICs have stably blocked the chromatin accessibility to the TFs favoring effector and memory gene expression (53). Therefore, ICB (better if associated with possible therapeutic vaccines) can provide extraordinary beneficial effects in early hot tumors rather than in very late tumors or chronic infections, where the majority of TILs will have become fully-exhausted.

A consistent proportion of tumor neoantigens can also be non-mutated neoantigens, when they derive from various forms of protein modifications occurring at post-transcriptional level in tumor cells, such as protein splicing, dysregulated phosphorylation or glycosylation, proteasome generation of spliced peptides, peptide citrullination, impaired peptide processing in TAP-deficient tumor cells, or proteasomal degradation of defective ribosomal products (59–65). These non-mutated neoantigens may provide rational targets for cancer immunotherapy, because they should not be expressed or expressed at concentrations that are not enough to delete specific T cells in the thymus. In addition, also chemotherapy- or radiotherapy-based apoptosis of tumor cells, and also providing various danger signals (e.g., ATP, UTP, calreticulin, HMGB1) that activate DCs and can strengthen T cell priming and memory (immunogenic cell death) (66), enable tumor cells to unveil non-mutated neoantigens, in the form of caspase-cleaved antigenic fragments (67). A wide variety of them has been recently identified by using stable isotope labeling by amino acids in cell culture-based mass spectrometry in human NSCLC cells, namely, caspase-cleaved fragments from olfactory receptor 5H2, Ras and EF-hand domain-containing protein, proactivator polypeptide, protein LYRIC, zinc transporter SLC39A7, ADP/ATP translocase 2, chatepsin D, and ruvB-like 2 (67). These caspase-cleaved fragments were upregulated only in apoptotic tumor cells, targeted to the processing machinery and cross-presented in form of peptides by APCs much more efficiently than their entire protein counterparts, supporting their definition of tumor non-mutated neoantigens (67). The immunogenicity of these non-mutated neoantigens is proved by the evidence that CD8$^+$ T cells specific to the related epitopes were significantly represented in NSCLC patients following chemotherapy treatment, increased in their frequency upon ICB therapy, and correlated with overall survival, suggesting their contribution in the tumor control and possibly in the immunological memory improvement (67).

Tregs and T Cell Memory in Chronic Infection and Cancer

Under conditions of long-lasting tumors or chronic infections, which are characterized by impaired effector and memory responses principally due to the irreversible T cell exhaustion, other immunosuppressive mechanisms amplified and are intertwined. First of all, the intervention of various subsets of Tregs, namely, CD4$^+$ Tregs expressing the master transcription factor FOXP3 (68, 69), can be either committed in the thymus (thymus-derived Tregs) or induced in the periphery [as reviewed in (70)], or the suppressor CD8$^+$ T cell subset representing, historically, the most ancient population with suppression function described (71–74). Regardless of the cell lineage, Tregs can provide various homeostatic effects that can result in being beneficial or detrimental, depending on the setting in which they govern the homeostasis. Tissue-resident CD4$^+$ or CD8$^+$ Tregs perform tissue-protective activities, by promoting tissue repair, systemic metabolism, and immunosuppression, particularly by the production of TGF-β or IL-10 (75, 76). These activities are beneficial in resolving acute inflammatory diseases by promoting tissue health, but become detrimental in chronic inflammatory diseases, because they contribute to organ failure *via* the persisting tissue repair mechanisms, resulting in tissue subversion (e.g., fibrosis and cirrhosis) and tumor development. In addition, the beneficial effects by Tregs, for which they have evolutionarily selected, are based on their primary function to prevent the differentiation of autoreactive T_N cells into harmful effector cells (avoiding thus autoimmunity) in the periphery (peripheral tolerance), and to stop or limit the excessive immunopathology by self- or non-self-reactive T effector cells through a wide range of immunosuppressive mechanisms (77, 78). Again, these immunoregulatory effects can result in being detrimental in the course of chronic infections or tumors, because FOXP3$^+$ Tregs acquire strong suppression capacity in these contexts, through various signals (e.g., by interaction between OX40L expressed on tumor-associated macrophages and OX40 delivering survival signals in Tregs) favoring demethylation of the Treg-specific demethylated region that acts as a transcriptional stabilizer of *FOXP3* gene and consequent suppression function [as reviewed in (70, 79)]. In addition, Tregs in stable tumors or chronic infections receive signals from the tumor microenvironment that provide supplemental energetic routes involving lipid metabolism, conferring a preferential proliferative advantage to Tregs (80). Interestingly, the excessive Treg improvement can be limited by Treg intrinsic mechanisms that try to govern the excess suppression, in order to contribute to slow down the progression of chronic infections or tumors. The first report describing counter-suppression of FOXP3$^+$ Tregs showed that the interaction between PD-1 and PD-L1, both expressed on well-stabilized activated FOXP3$^+$ Tregs, provided a negative signal into these Tregs by PD-1 limiting STAT-5 phosphorylation and Treg expansion and suppression (81). Conversely, other studies demonstrated that PD-1 and also TIM-3, contribute to the conversion of naïve CD4$^+$ T cells into induced FOXP3$^+$ Tregs through various molecular pathways, namely, the capacity of PD-1 signaling to inhibit the sparaginyl endopeptidase enzyme normally cleaving FOXP3 in induced Tregs [reviewed in (82)]. Therefore, PD-1 may act as a double-edged sword with the effect dependent on the phase of Treg activation: it contributes to induce Tregs from conventional naïve CD4$^+$ T cells, on the one hand, and to downregulate stable Treg expansion and functions, on the other. The counter-suppression effect by PD-1 on stable activated Tregs could in turn be countered by ICB treatment, improving Treg proliferation and suppression (81). This data suggests to use ICB carefully both to avoid the detrimental effects by rescued Tregs resulting in "hyperprogression" of tumors (or chronic infections) by excessive suppression of protective effector T cells [reviewed in (83)], and to employ ICB selectively in tumors (and likely chronic infections) expressing PD-1 on CD8$^+$ TILs rather than on Tregs (84).

Collectively, the various mechanisms that cause effective Treg-mediated suppression contribute to get worse the T cell dysfunctional state and to impede the long-term memory development, resulting ultimately in irreversible chronic infections or tumor progression.

May T Cell Memory be Restored in Chronic Infection or Cancer?

An open question is: can exhausted T cells upon elimination of chronic antigenic stimulation or that have been restored by ICB in terms of effector functions, differentiate into long-term memory cells? Chronically-infected HCV patients following virological cure by direct antiviral agents allowing complete HCV clearance, and also mouse models of chronic viral infection, showed that upon eliminating the virus, TCF-1$^+$ exhausted T cells downregulate ICs and partially acquire phenotypic and transcriptional features of memory-like cells (85–87). Importantly, T cells that were exposed to HCV antigens for less time were functionally and transcriptionally more similar to memory T cells from spontaneously resolved HCV infection (87, 88). These data confirm that exhausted T cells may or not may be (at least partially) restored providing differentiation of memory-like cells, depending on the time in which the process initiated and on the frequency of TCF1$^+$ exhausted T cells (53–57). However, functionally, exhausted T cells, which have been rescued by the elimination of chronic antigenic stimulation, maintain critical transcriptional regulators in the exhaustion state, and their recall capacity remained limited and not durable over time as compared to true memory T cells from competent mice (85). Chromatin-accessibility profiling revealed a failure to recover memory epigenetic circuits and maintenance of a largely exhausted open chromatin landscape, constraining the establishment of long-term immunological memory (85). We cannot exclude that a longer time of antigen-free recovery can reinvigorate previously exhausted CD8$^+$ T cells that can persist and respond to reinfection (89). More in depth molecular analyses, particularly at epigenetic level, need to discriminate these possibilities in order to delineate new therapeutic interventions addressed to develop immunological memory in chronic infections and tumors.

The triple combination of immunogenic cell death by chemotherapy, vaccination with the resulting non-mutated neoantigens (i.e., generated following chemotherapy-induced apoptosis of tumor cells), and ICB treatment switching off the inhibitory T cell signals, may result in being beneficial in the immunotherapy of "cold" tumors, such as small cell lung cancer, MSS-colorectal cancer or MSS-hepatocellular carcinoma, characterized by DNA stability, effective mismatching repair mechanisms, low generation of mutated neoantigens, and very low number of TILs, in order to convert them into hot tumors (**Figure 3**). This combination may also provide beneficial effects in those hot tumors, in which TILs specific to mutated neoantigens became fully exhausted, in order to generate new tumor-specific immune responses and memory. Definitely, this combinatorial module may represent a tremendous resource for a new tumor immunotherapy approach providing the essential signals (1, 2, and 3) required for optimal T cell memory development (**Figure 3**).

Finally, systems to dampen Treg-mediated suppression of immune responses have been considered as further therapeutic approaches to verify their effect in improving immunological memory, for instance through targeting CD25, CTLA-4, or CCR4 on Tregs in order to deplete intratumoral Tregs (90–92).

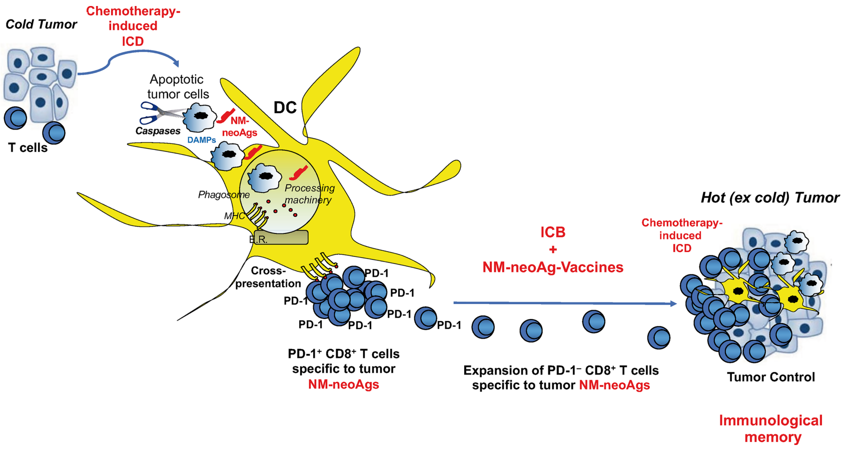

FIGURE 3 | Combination of immunogenic cell death, non-mutated neoantigen-based vaccination, and ICB in tumor immunotherapy. Immunogenic cell death (ICD) by chemotherapy unveils both danger signals (activating DCs) and non-mutated neoantigens (NM-neoAgs) in apoptotic tumor cells that are efficiently phagocytosed by DCs. NM-neoAgs derive by caspase cleavage of a variety of tumor antigens, are efficiently processed and (cross-)presented by DCs in form of peptides on MHC molecules (67) to T cells. CD8$^+$ T cells proliferate and further expand in response to ICB treatment (anti-PD-1 therapy), providing improvement of effector function and conversion of PD-1$^+$ T cells into PD-1$^-$ T cells. Effector CD8$^+$ T$_{EM}$ cells can migrate into the tumor microenvironment and be further boosted by NM-neoAgs derived from chemotherapy-induced apoptotic tumor cells cross-presented by tissue DCs: CD8$^+$ T$_{EM/EMRA}$ cells provide tumor control through the by-stander effect of strong inflammatory cytokines and the recruitment of other T cells and innate immune cells (macrophages, neutrophils, natural killer cells,…). This scenario is supported by the evidence showing that NM-neoAg-specific CD8$^+$ T cells are significantly represented in NSCLC patients previously submitted to chemotherapy, increase in their frequency upon ICB therapy, and correlated with overall survival (67). The addition of therapeutic NM-neoAg-based vaccines may improve T cell memory and tumor immunity, as well as convert cold into hot tumors.

More recently, data on the metabolic profile of activated Tregs proposed that metabolic drugs targeting specific molecules of lipid turnover may preferentially modulate Tregs compared to other T cells (80).

T CELL MEMORY AND TREGS IN AUTOIMMUNITY

A further important question is: how do most autoimmune diseases persist for several years in patients, despite the fact that immune responses are not conditioned by persisting (non-self) "invaders", but presumably by a breakdown of peripheral immunological tolerance (e.g., anergy, exhaustion, Treg suppression) causing the unleash and activation of diverse autoaggressive B and T cells against self-antigens? Might the same immunoregulatory mechanisms ultimately maintaining the long-lasting relationship between persisting "invaders" (chronic infections or tumors) and the host, fine-tune the autoimmune responses, thus allowing that the final failure/destruction of the self-organs or tissues by the autoaggressive responses is delayed for many years?

Chronic TCR signaling is common in chronic infection, cancer, and autoimmunity, but the persisting antigens providing TCR signaling are generally different in the three contexts: (non-self) infectious antigens in chronic infection, (non-self) neoantigens in cancer, and self-antigens in autoimmunity. A main paradigm at the center of immunology is that, in the periphery, non-self-antigens (infectious or neoantigens) are recognized by high affinity TCRs (which are positively selected in the thymus and migrate in the periphery), whereas the self-antigens by low-affinity TCRs (high affinity T cells for the "self" having been purged in the thymus). An alternative, but not mutually exclusive route leading to autoimmunity is based on the evidence that not necessarily the antigenic targets of the so-called autoimmune diseases are self-antigens, but they can also be represented by neo(ex-self)-antigens generally generated by post-translational modifications of self-antigens in the periphery. Prototypical examples are neo(ex-self)-antigens in type 1 diabetes (T1D) (i.e., tissue transglutaminase-dependent deamidation or alternative-reading-frame-encoding of pro-insulin peptides), or in rheumatoid arthritis (i.e., citrullination or deamination of vimentin, lamin B1, non-muscle myosin, actin and other cytoskeleton or nuclear self-antigens) (93–98). In this perspective, these neo(ex-self)-antigens are recognized by non-self-specific T cells expressing high affinity TCRs, which are positively selected in the thymus and migrate in the periphery, because neo (ex-self)-antigens would not be expressed or expressed at concentrations that are not enough to delete them in the thymus. As a consequence, chronic stimulation with non-self-antigens (infectious or tumoral) or neo(ex-self)-antigens (modified self-antigens) should cause T cell exhaustion more efficiently than chronic stimulation with native self-antigens, with divergent impact in the development of the immunological memory. Consistent with this hypothesis, recent data in both experimental and human T1D showed that self- or non-self-reactive T cells shared common phenotypic, transcriptional and epigenetic program features of exhaustion, those autoreactive displayed a wider level of heterogenicity, depending on the TCR affinity for self-antigens (99, 100). Therefore, we could envisage that chronic tissue damage in autoimmunity may be established by alternate waves of self-reactive (the minority that have been able to escape central tolerance in the thymus) or neo(ex-self)-reactive T cells with moderate/high affinity TCRs, and self-reactive T cells with low affinity TCRs that are not purged in the thymus. In particular, recent data demonstrated that self-reactive or neo(ex-self)-reactive T cells with high affinity TCRs are more harmful and can evade peripheral Treg-mediated tolerance (e.g., by counter-suppressing Tregs) (98), but they should be more susceptible to exhaustion than those with low affinity TCRs, due to the stronger stimulation by persistent self- or neo(ex-self)-antigens. By contrast, self-reactive T cells with low affinity TCRs are significantly less harmful than the former, and are efficiently controlled by Tregs, contributing hence to maintain a state of chronic low-level inflammation (98). Thus, the persistence of self-antigens or neo(ex-self)-antigens conditions, in the long run, promote exhaustion of specific T cells with high affinity TCRs, and Treg-mediated suppression of those with low affinity TCRs. The alternate fluctuation by self-reactive or neo(ex-self)-antigens T cells with high and low affinity TCRs may in part explain the clinical outcome of autoimmune diseases characterized by a chronic alternation of acute and quiescent phases that finally undergo tissue destruction after a long time. This scenario could account for results showing that, unlike in chronic infections or tumors, $CD8^+$ T cell exhaustion is associated with a good outcome and a low risk of relapse in autoimmune diseases, proposing that manipulation of exhaustion may represent a novel therapeutic strategy to suppress autoreactivity by using agonists of ICs (e.g., CTLA-4, PD-1, TIM-3, LAG-3), or antagonists of activating receptors (e.g., CD28, OX40, GITR, CD137) (99, 100).

Regarding the role of Tregs, if the aim is to inhibit them in chronic infections or tumors, *vice versa* the therapeutic goal is the induction or activation of Tregs in autoimmune diseases by various approaches, namely, the transfer of autologous *in vitro*-expanded Tregs to suppress autoimmune responses (101), or induction of Tregs directly *in vivo* by administration of immunocomplexes of IL-2 and specific anti-IL2 antibody selectively promoting the expansion of Tregs (expressing the high-affinity trimeric IL-2R that includes IL-2Rα) without expanding activated effector T cells (102, 103).

CONCLUDING REMARKS

Immunological memory is a major and unique resource of the adaptive immunity allowing to remember for a long time the antigens that the individuals encounter, and to promptly respond on demand in the case of antigen re-encounter. The molecular mechanisms governing immunological memory in the different B or T cell subsets at the transcriptional and epigenetics level, are revealing fundamental pathways. The generation of new selective compounds capable to influence the immunological memory (improvement or suppression) may become extremely useful in the therapy of the different pathological contexts in the next years. The major goal in chronic infection or cancer is to restore protective immune responses that have been made dysfunctional by excessive exhaustion and Treg-suppression, in order to help eliminate persistent pathogens or tumors providing chronic stimulation, and to develop long-term immunological memory controlling possible re-emergences of the primary infections or tumors. By contrast, the major goal in autoimmunity is exactly the opposite, namely to restore the tolerance of the persisting self-antigens through the use of agonists of T cell ICs, antagonists of T cell activating receptors, or by reinvigorating Tregs, so as to convert the picture of autoimmune aggression into that of exhaustion and suppression of autoreactive B or T cells, and to keep the autoimmunological memory under tone.

AUTHOR CONTRIBUTION

VB ideated and wrote this review.

FUNDING

This work was supported by the following grants: Associazione Italiana per la Ricerca sul Cancro (AIRC) (progetti “Investigator Grant” [IG]-2014 id. 15199 and IG-2017 id. 19939 to VB); The Accelerator Award 2018 (Project 620 Id. 22794 to VB); Fondazione Italiana Sclerosi Multipla (FISM) onlus (cod. 2015/R/04 and 2019/R-Single/053 to VB); Ministero della Salute (Ricerca finalizzata [RF-2010-2310438 and RF 2010-2318269] to VB); Ministero dell’Istruzione, dell’Università e della Ricerca (MIUR) (PRIN 2010–2011 prot. 2010LC747T_004 to VB); Fondo per gli investimenti di ricerca di base (FIRB)-2011/13 (no. RBAP10TPXK to VB); Istituto Pasteur Italia—Fondazione Cenci Bolognetti (grant 2014–2016); International Network Institut Pasteur, Paris—”Programmes Transversaux De Recherche” (PTR n. 20-16).

REFERENCES

1. Ahmed R, Bevan MJ, Reiner SL, Fearon DT. The Precursors of Memory: Models and Controversies. *Nat Rev Immunol* (2009) 9(9):662–8. doi: 10.1038/nri2619
2. Farber DL, Netea MG, Radbruch A, Rajewsky K, Zinkernagel RM. Immunological Memory: Lessons From the Past and a Look to the Future. *Nat Rev Immunol* (2016) 16(2):124–8. doi: 10.1038/nri.2016.13
3. Williams MA, Bevan MJ. Effector and Memory CTL Differentiation. *Annu Rev Immunol* (2007) 25(1):171–92. doi: 10.1146/annurev.immunol.25.022106.141548
4. Jenkins MK, Moon JJ. The Role of Naive T Cell Precursor Frequency and Recruitment in Dictating Immune Response Magnitude. *J Immunol* (2012) 188(9):4135–40. doi: 10.4049/jimmunol.1102661
5. Sun JC, Bevan MJ. Defective CD8 T Cell Memory Following Acute Infection Without CD4 T Cell Help. *Science* (2003) 300(5617):339–42. doi: 10.1126/science.1083317
6. Ridge JP, Di Rosa F, Matzinger P. A Conditioned Dendritic Cell can be a Temporal Bridge Between a CD4+ T-Helper and a T-Killer Cell. *Nature* (1998) 393(6684):474–8. doi: 10.1038/30989
7. Janssen EM, Lemmens EE, Wolfe T, Christen U, von Herrath MG, Schoenberger SP. CD4+ T Cells Are Required for Secondary Expansion

and Memory in CD8+ T Lymphocytes. *Nature* (2003) 421(6925):852–6. doi: 10.1038/nature01441

8. Swain SL, McKinstry KK, Strutt TM. Expanding Roles for CD4+ T Cells in Immunity to Viruses. *Nat Rev Immunol* (2012) 12(2):136–48. doi: 10.1038/nri3152
9. Rahemtulla A, Fung-Leung WP, Schilham MW, Kündig TM, Sambhara SR, Narendran A, et al. Normal Development and Function of CD8+ Cells But Markedly Decreased Helper Cell Activity in Mice Lacking CD4. *Nature* (1991) 353(6340):180–4. doi: 10.1038/353180a0
10. Buller RML, Holmes KL, Hügin A, Frederickson TN, Morse HC. Induction of Cytotoxic T-Cell Responses *In Vivo* in the Absence of CD4 Helper Cells. *Nature* (1987) 328(6125):77–9. doi: 10.1038/328077a0
11. Charles A, Janeway J, Medzhitov R. Innate Immune Recognition. *Annu Rev Immunol* (2002) 20(1):197–216. doi: 10.1146/annurev.immunol.20.083001.084359
12. Iwasaki A, Medzhitov R. Toll-Like Receptor Control of the Adaptive Immune Responses. *Nat Immunol* (2004) 5(10):987–95. doi: 10.1038/ni1112
13. e Sousa CR. Dendritic Cells as Sensors of Infection. *Immunity* (2001) 14 (5):495–8. doi: 10.1016/S1074-7613(01)00136-4
14. Pulendran B,S, Arunachalam P, O'Hagan DT. Emerging Concepts in the Science of Vaccine Adjuvants. *Nat Rev Drug Discov* (2021) 20(6):454–75. doi: 10.1038/s41573-021-00163-y
15. Sallusto F, Lenig D, Förster R, Lipp M, Lanzavecchia A. Two Subsets of Memory T Lymphocytes With Distinct Homing Potentials and Effector Functions. *Nature* (1999) 402(6763):34–8. doi: 10.1038/35005534
16. Lau LL, Jamieson BD, Somasundaram T, Ahmed R. Cytotoxic T-Cell Memory Without Antigen. *Nature* (1994) 369(6482):648–52. doi: 10.1038/369648a0
17. Hou S, Hyland L, Ryan KW, Portner A, Doherty PC. Virus-Specific CD8+ T-Cell Memory Determined by Clonal Burst Size. *Nature* (1994) 369 (6482):652–4. doi: 10.1038/369652a0
18. Swain SL, Hu H, Huston G. Class II-Independent Generation of CD4 Memory T Cells From Effectors. *Science* (1999) 286(5443):1381–3. doi: 10.1126/science.286.5443.1381
19. Sallusto F, Geginat J, Lanzavecchia A. Central Memory and Effector Memory T Cell Subsets: Function, Generation, and Maintenance. *Annu Rev Immunol* (2004) 22(1):745–63. doi: 10.1146/annurev.immunol.22.012703.104702
20. Böttcher JP, Beyer M, Meissner F, Abdullah Z, Sander J, Höchst B, et al. Functional Classification of Memory CD8+ T Cells by CX3CR1 Expression. *Nat Commun* (2015) 6(1):8306. doi: 10.1038/ncomms9306
21. Gerlach C, Moseman EA, Loughhead SM, Alvarez D, Zwijnenburg AJ, Waanders L, et al. The Chemokine Receptor CX3CR1 Defines Three Antigen-Experienced CD8#Xa0;T Cell Subsets With Distinct Roles in Immune Surveillance and Homeostasis. *Immunity* (2016) 45(6):1270–84. doi: 10.1016/j.immuni.2016.10.018
22. Kok L, Masopust D, Schumacher TN. The Precursors of CD8+ Tissue Resident Memory T Cells: From Lymphoid Organs to Infected Tissues. *Nat Rev Immunol* (2021) 3:1–11. doi: 10.1038/s41577-021-00590-3
23. Buchholz VR, Schumacher TNM, Busch DH. T Cell Fate at the Single-Cell Level. *Annu Rev Immunol* (2016) 34(1):65–92. doi: 10.1146/annurev-immunol-032414-112014
24. Becattini S, Latorre D, Mele F, Foglierini M, Gregorio CD, Cassotta A, et al. Functional Heterogeneity of Human Memory CD4+ T Cell Clones Primed by Pathogens or Vaccines. *Science* (2015) 347(6220):400–6. doi: 10.1126/science.1260668
25. Germain RN, Stefanová I. THE DYNAMICS OF T CELL RECEPTOR SIGNALING: Complex Orchestration and the Key Roles of Tempo and Cooperation. *Annu Rev Immunol* (1999) 17(1):467–522. doi: 10.1146/annurev.immunol.17.1.467
26. Gaud G, Lesourne R, Love PE. Regulatory Mechanisms in T Cell Receptor Signalling. *Nat Rev Immunol* (2018) 18(8):485–97. doi: 10.1038/s41577-018-0020-8
27. Courtney AH, Lo W-L, Weiss A. TCR Signaling: Mechanisms of Initiation and Propagation. *Trends Biochem Sci* (2018) 43(2):108–23. doi: 10.1016/j.tibs.2017.11.008
28. Mørch AM, Bálint Š, Santos AM, Davis SJ, Dustin ML. Coreceptors and TCR Signaling – The Strong and the Weak of it. *Front Cell Dev Biol* (2020) 8:597627. doi: 10.3389/fcell.2020.597627
29. Youngblood B, Oestreich Kenneth J, Ha S-J, Duraiswamy J, Akondy Rama S, West Erin E, et al. Chronic Virus Infection Enforces Demethylation of the Locus That Encodes PD-1 in Antigen-Specific CD8+ T Cells. *Immunity* (2011) 35(3):400–12. doi: 10.1016/j.immuni.2011.06.015
30. He X, Xu C. Immune Checkpoint Signaling and Cancer Immunotherapy. *Cell Res* (2020) 30(8):660–9. doi: 10.1038/s41422-020-0343-4
31. Youngblood B, Hale JS, Kissick HT, Ahn E, Xu X, Wieland A, et al. Effector CD8 T Cells Dedifferentiate Into Long-Lived Memory Cells. *Nature* (2017) 552(7685):404–9. doi: 10.1038/nature25144
32. Hudson WH, Gensheimer J, Hashimoto M, Wieland A, Valanparambil RM, Li P, et al. Proliferating Transitory T Cells With an Effector-Like Transcriptional Signature Emerge From PD-1+ Stem-Like CD8+ T Cells During Chronic Infection. *Immunity* (2019) 51(6):1043–58.e1044. doi: 10.1016/j.immuni.2019.11.002
33. Pace L, Goudot C, Zueva E, Gueguen P, Burgdorf N, Waterfall JJ, et al. The Epigenetic Control of Stemness in CD8+ T Cell Fate Commitment. *Science* (2018) 359(6372):177–86. doi: 10.1126/science.aah6499
34. Buenrostro JD, Giresi PG, Zaba LC, Chang HY, Greenleaf WJ. Transposition of Native Chromatin for Fast and Sensitive Epigenomic Profiling of Open Chromatin, DNA-Binding Proteins and Nucleosome Position. *Nat Methods* (2013) 10(12):1213–8. doi: 10.1038/nmeth.2688
35. Akondy RS, Fitch M, Edupuganti S, Yang S, Kissick HT, Li KW, et al. Origin and Differentiation of Human Memory CD8 T Cells After Vaccination. *Nature* (2017) 552(7685):362–7. doi: 10.1038/nature24633
36. Delpoux A, Michelini RH, Verma S, Lai C-Y, Omilusik KD, Utzschneider DT, et al. Continuous Activity of Foxo1 Is Required to Prevent Anergy and Maintain the Memory State of CD8+ T Cells. *J Exp Med* (2017) 215(2):575–94. doi: 10.1084/jem.20170697
37. Utzschneider DT, Delpoux A, Wieland D, Huang X, Lai C-Y, Hofmann M, et al. Active Maintenance of T Cell Memory in Acute and Chronic Viral Infection Depends on Continuous Expression of FOXO1. *Cell Rep* (2018) 22 (13):3454–67. doi: 10.1016/j.celrep.2018.03.020
38. Gray SM, Amezquita RA, Guan T, Kleinstein SH, Kaech SM. Polycomb Repressive Complex 2-Mediated Chromatin Repression Guides Effector CD8+ T Cell Terminal Differentiation and Loss of Multipotency. *Immunity* (2017) 46(4):596–608. doi: 10.1016/j.immuni.2017.03.012
39. Kakaradov B, Arsenio J, Widjaja CE, He Z, Aigner S, Metz PJ, et al. Early Transcriptional and Epigenetic Regulation of CD8+ T Cell Differentiation Revealed by Single-Cell RNA Sequencing. *Nat Immunol* (2017) 18(4):422–32. doi: 10.1038/ni.3688
40. Hayward SL, Scharer CD, Cartwright EK, Takamura S, Li Z-RT, Boss JM, et al. Environmental Cues Regulate Epigenetic Reprogramming of Airway-Resident Memory CD8+ T Cells. *Nat Immunol* (2020) 21(3):309–20. doi: 10.1038/s41590-019-0584-x
41. Timperi E, Barnaba V. Viral Hepatitides, Inflammation and Tumour Microenvironment. In: A Birbrair, editor. *Tumor Microenvironment: State of the Science*. Cham: Springer International Publishing (2020). p. 25–43. doi: 10.1007/978-3-030-44518-8_3
42. Cuevas JM, Geller R, Garijo R, López-Aldeguer J, Sanjuán R. Extremely High Mutation Rate of HIV-1 *In Vivo*. *PloS Biol* (2015) 13(9):e1002251. doi: 10.1371/journal.pbio.1002251
43. Rehermann B, Nascimbeni M. Immunology of Hepatitis B Virus and Hepatitis C Virus Infection. *Nat Rev Immunol* (2005) 5(3):215–29. doi: 10.1038/nri1573
44. Robson F, Khan KS, Le TK, Paris C, Demirbag S, Barfuss P, et al. Coronavirus RNA Proofreading: Molecular Basis and Therapeutic Targeting. *Mol Cell* (2020) 79(5):710–27. doi: 10.1016/j.molcel.2020.07.027
45. Rosenthal R, Cadieux EL, Salgado R, Bakir MA, Moore DA, Hiley CT, et al. Neoantigen-Directed Immune Escape in Lung Cancer Evolution. *Nature* (2019) 567(7749):479–85. doi: 10.1038/s41586-019-1032-7
46. Schumacher TN, Schreiber RD. Neoantigens in Cancer Immunotherapy. *Science* (2015) 348(6230):69–74. doi: 10.1126/science.aaa4971
47. Gubin MM, Zhang X, Schuster H, Caron E, Ward JP, Noguchi T, et al. Checkpoint Blockade Cancer Immunotherapy Targets Tumour-Specific Mutant Antigens. *Nature* (2014) 515(7528):577–81. doi: 10.1038/nature13988
48. Rizvi NA, Hellmann MD, Snyder A, Kvistborg P, Makarov V, Havel JJ, et al. Cancer Immunology. Mutational Landscape Determines Sensitivity to PD-1

Blockade in non-Small Cell Lung Cancer. *Sci (New York NY)* (2015) 348 (6230):124–8. doi: 10.1126/science.aaa1348

49. Lakatos E, Williams MJ, Schenck RO, Cross WCH, Househam J, Zapata L, et al. Evolutionary Dynamics of Neoantigens in Growing Tumors. *Nat Genet* (2020) 52(10):1057–66. doi: 10.1038/s41588-020-0687-1
50. Pauken KE, Sammons MA, Odorizzi PM, Manne S, Godec J, Khan O, et al. Epigenetic Stability of Exhausted T Cells Limits Durability of Reinvigoration by PD-1 Blockade. *Science* (2016) 354(6316):1160–5. doi: 10.1126/science.aaf2807
51. Alfei F, Kanev K, Hofmann M, Wu M, Ghoneim HE, Roelli P, et al. TOX Reinforces the Phenotype and Longevity of Exhausted T Cells in Chronic Viral Infection. *Nature* (2019) 571(7764):265–9. doi: 10.1038/s41586-019-1326-9
52. Liu X, Wang Y, Lu H, Li J, Yan X, Xiao M, et al. Genome-Wide Analysis Identifies NR4A1 as a Key Mediator of T Cell Dysfunction. *Nature* (2019) 567(7749):525–9. doi: 10.1038/s41586-019-0979-8
53. Blank CU, Haining WN, Held W, Hogan PG, Kallies A, Lugli E, et al. Defining 'T Cell Exhaustion'. *Nat Rev Immunol* (2019) 19(11):665–74. doi: 10.1038/s41577-019-0221-9
54. Schinzari V, Timperi E, Pecora G, Palmucci F, Gallerano D, Grimaldi A, et al. Wnt3a/β-Catenin Signaling Conditions Differentiation of Partially Exhausted T-Effector Cells in Human Cancers. *Cancer Immunol Res* (2018) 6(8):941–52. doi: 10.1158/2326-6066.Cir-17-0712
55. Pacella I, Cammarata I, Focaccetti C, Miacci S, Gulino A, Tripodo C, et al. Wnt3a Neutralization Enhances T-Cell Responses Through Indirect Mechanisms and Restrains Tumor Growth. *Cancer Immunol Res* (2018) 6 (8):953–64. doi: 10.1158/2326-6066.Cir-17-0713
56. Chu T, Zehn D. Charting the Roadmap of T Cell Exhaustion. *Immunity* (2020) 52(5):724–6. doi: 10.1016/j.immuni.2020.04.019
57. Beltra J-C, Manne S, Abdel-Hakeem MS, Kurachi M, Giles JR, Chen Z, et al. Developmental Relationships of Four Exhausted CD8+ T Cell Subsets Reveals Underlying Transcriptional and Epigenetic Landscape Control Mechanisms. *Immunity* (2020) 52(5):825–41.e828. doi: 10.1016/j.immuni.2020.04.014
58. Schumacher TN, Scheper W, Kvistborg P. Cancer Neoantigens. *Annu Rev Immunol* (2019) 37(1):173–200. doi: 10.1146/annurev-immunol-042617-053402
59. Hanada K-i, Yewdell JW, Yang JC. Immune Recognition of a Human Renal Cancer Antigen Through Post-Translational Protein Splicing. *Nature* (2004) 427(6971):252–6. doi: 10.1038/nature02240
60. Cobbold M, Peña HDL, Norris A, Polefrone JM, Qian J, English AM, et al. MHC Class I–Associated Phosphopeptides Are the Targets of Memory-Like Immunity in Leukemia. *Sci Trans Med* (2013) 5(203):203ra125–203ra125. doi: 10.1126/scitranslmed.3006061
61. Oliveira-Ferrer L, Legler K, Milde-Langosch K. Role of Protein Glycosylation in Cancer Metastasis. *Semin Cancer Biol* (2017) 44:141–52. doi: 10.1016/j.semcancer.2017.03.002
62. Liepe J, Marino F, Sidney J, Jeko A, Bunting DE, Sette A, et al. A Large Fraction of HLA Class I Ligands are Proteasome-Generated Spliced Peptides. *Science* (2016) 354(6310):354–8. doi: 10.1126/science.aaf4384
63. Brentville VA, Metheringham RL, Gunn B, Symonds P, Daniels I, Gijon M, et al. Citrullinated Vimentin Presented on MHC-II in Tumor Cells Is a Target for CD4+ T-Cell–Mediated Antitumor Immunity. *Cancer Res* (2016) 76(3):548–60. doi: 10.1158/0008-5472.Can-15-1085
64. Marijt KA, Blijleven L, Verdegaal EME, Kester MG, Kowalewski DJ, Rammensee H-G, et al. Identification of Non-Mutated Neoantigens Presented by TAP-Deficient Tumors. *J Exp Med* (2018) 215(9):2325–37. doi: 10.1084/jem.20180577
65. Yewdell JW, Nicchitta CV. The DRiP Hypothesis Decennial: Support, Controversy, Refinement and Extension. *Trends Immunol* (2006) 27 (8):368–73. doi: 10.1016/j.it.2006.06.008
66. Kroemer G, Galluzzi L, Kepp O, Zitvogel L. Immunogenic Cell Death in Cancer Therapy. *Annu Rev Immunol* (2013) 31(1):51–72. doi: 10.1146/annurev-immunol-032712-100008
67. Grimaldi A, Cammarata I, Martire C, Focaccetti C, Piconese S, Buccilli M, et al. Combination of Chemotherapy and PD-1 Blockade Induces T Cell Responses to Tumor Non-Mutated Neoantigens. *Commun Biol* (2020) 3 (1):85. doi: 10.1038/s42003-020-0811-x
68. Hori S, Nomura T, Sakaguchi S. Control of Regulatory T Cell Development by the Transcription Factor Foxp3. *Science* (2003) 299(5609):1057–61. doi: 10.1126/science.1079490
69. Fontenot JD, Gavin MA, Rudensky AY. Foxp3 Programs the Development and Function of CD4+CD25+ Regulatory T Cells. *Nat Immunol* (2003) 4 (4):330–6. doi: 10.1038/ni904
70. Hamann A. Regulatory T Cells Stay on Course. *Immunity* (2012) 36(2):161–3. doi: 10.1016/j.immuni.2012.02.004
71. Gershon RK, Cohen P, Hencin R, Liebhaber SA. Suppressor T Cells. *J Immunol* (1972) 108(3):586–90.
72. Chess L, Jiang H. Resurrecting CD8+ Suppressor T Cells. *Nat Immunol* (2004) 5(5):469–71. doi: 10.1038/ni0504-469
73. Shevach EM. The Resurrection of T Cell-Mediated Suppression. *J Immunol* (2011) 186(7):3805–7. doi: 10.4049/jimmunol.1100364
74. Barnaba V, Schinzari V. Induction, Control, and Plasticity of Treg Cells: The Immune Regulatory Network Revised? *Eur J Immunol* (2013) 43(2):318–22. doi: 10.1002/eji.201243265
75. Panduro M, Benoist C, Mathis D. Tissue Tregs. *Annu Rev Immunol* (2016) 34(1):609–33. doi: 10.1146/annurev-immunol-032712-095948
76. Accapezzato D, Francavilla V, Paroli M, Casciaro M, Chircu LV, Cividini A, et al. Hepatic Expansion of a Virus-Specific Regulatory CD8+ T Cell Population in Chronic Hepatitis C Virus Infection. *J Clin Invest* (2004) 113(7):963–72. doi: 10.1172/JCI20515
77. Rudensky AY, Campbell DJ. *In Vivo* Sites and Cellular Mechanisms of T Reg Cell–Mediated Suppression. *J Exp Med* (2006) 203(3):489–92. doi: 10.1084/jem.20060214
78. Liu Z, Gerner MY, Van Panhuys N, Levine AG, Rudensky AY, Germain RN. Immune Homeostasis Enforced by Co-Localized Effector and Regulatory T Cells. *Nature* (2015) 528(7581):225–30. doi: 10.1038/nature16169
79. Piconese S, Timperi E, Pacella I, Schinzari V, Tripodo C, Rossi M, et al. Human OX40 Tunes the Function of Regulatory T Cells in Tumor and Nontumor Areas of Hepatitis C Virus–Infected Liver Tissue. *Hepatology* (2014) 60(5):1494–507. doi: 10.1002/hep.27188
80. Pacella I, Procaccini C, Focaccetti C, Miacci S, Timperi E, Faicchia D, et al. Fatty Acid Metabolism Complements Glycolysis in the Selective Regulatory T Cell Expansion During Tumor Growth. *Proc Natl Acad Sci* (2018) 115(28): E6546–55. doi: 10.1073/pnas.1720113115
81. Franceschini D, Paroli M, Francavilla V, Videtta M, Morrone S, Labbadia G, et al. PD-L1 Negatively Regulates CD4+CD25+Foxp3+ Tregs by Limiting STAT-5 Phosphorylation in Patients Chronically Infected With HCV. *J Clin Invest* (2009) 119(3):551–64. doi: 10.1172/JCI36604
82. Piconese S, Cammarata I, Barnaba V. Viral Hepatitis, Inflammation, and Cancer: A Lesson for Autoimmunity. *J Autoimmun* (2018) 95:58–68. doi: 10.1016/j.jaut.2018.10.021
83. Champiat S, Ferrara R, Massard C, Besse B, Marabelle A, Soria J-C, et al. Hyperprogressive Disease: Recognizing a Novel Pattern to Improve Patient Management. *Nat Rev Clin Oncol* (2018) 15(12):748–62. doi: 10.1038/s41571-018-0111-2
84. Kumagai S, Togashi Y, Kamada T, Sugiyama E, Nishinakamura H, Takeuchi Y, et al. The PD-1 Expression Balance Between Effector and Regulatory T Cells Predicts the Clinical Efficacy of PD-1 Blockade Therapies. *Nat Immunol* (2020) 21(11):1346–58. doi: 10.1038/s41590-020-0769-3
85. Abdel-Hakeem MS, Manne S, Beltra J-C, Stelekati E, Chen Z, Nzingha K, et al. Epigenetic Scarring of Exhausted T Cells Hinders Memory Differentiation Upon Eliminating Chronic Antigenic Stimulation. *Nat Immunol* (2021) 22(8):1008–19. doi: 10.1038/s41590-021-00975-5
86. Hensel N, Gu Z, Wieland D, Jechow K, Kemming J, Llewellyn-Lacey S, et al. Memory-Like HCV-Specific CD8+ T Cells Retain a Molecular Scar After Cure of Chronic HCV Infection. *Nat Immunol* (2021) 22(2):229–39. doi: 10.1038/s41590-020-00817-w
87. Tonnerre P, Wolski D, Subudhi S, Aljabban J, Hoogeveen RC, Damasio M, et al. Differentiation of Exhausted CD8+ T Cells After Termination of Chronic Antigen Stimulation Stops Short of Achieving Functional T Cell Memory. *Nat Immunol* (2021) 22(8):1030–41. doi: 10.1038/s41590-021-00982-6
88. Aregay A, Owusu Sekyere S, Deterding K, Port K, Dietz J, Berkowski C, et al. Elimination of Hepatitis C Virus has Limited Impact on the Functional and

Mitochondrial Impairment of HCV-Specific CD8+ T Cell Responses. *J Hepatol* (2019) 71(5):889–99. doi: 10.1016/j.jhep.2019.06.025

89. Wieland D, Kemming J, Schuch A, Emmerich F, Knolle P, Neumann-Haefelin C, et al. TCF1+ Hepatitis C Virus-Specific CD8+ T Cells Are Maintained After Cessation of Chronic Antigen Stimulation. *Nat Commun* (2017) 8(1):15050. doi: 10.1038/ncomms15050
90. Dannull J, Su Z, Rizzieri D, Yang BK, Coleman D, Yancey D, et al. Enhancement of Vaccine-Mediated Antitumor Immunity in Cancer Patients After Depletion of Regulatory T Cells. *J Clin Invest* (2005) 115 (12):3623–33. doi: 10.1172/JCI25947
91. Arce Vargas F, Furness AJS, Litchfield K, Joshi K, Rosenthal R, Ghorani E, et al. Fc Effector Function Contributes to the Activity of Human Anti-CTLA-4 Antibodies. *Cancer Cell* (2018) 33(4):649–63.e644. doi: 10.1016/j.ccell.2018.02.010
92. Romano E, Kusio-Kobialka M, Foukas PG, Baumgaertner P, Meyer C, Ballabeni P, et al. Ipilimumab-Dependent Cell-Mediated Cytotoxicity of Regulatory T Cells Ex Vivo by Nonclassical Monocytes in Melanoma Patients. *Proc Natl Acad Sci* (2015) 112(19):6140–5. doi: 10.1073/pnas.1417320112
93. Roep BO, Kracht MJL, van Lummel M, Zaldumbide A. A Roadmap of the Generation of Neoantigens as Targets of the Immune System in Type 1 Diabetes. *Curr Opin Immunol* (2016) 43:67–73. doi: 10.1016/j.coi.2016.09.007
94. Kracht MJL, van Lummel M, Nikolic T, Joosten AM, Laban S, van der Slik AR, et al. Autoimmunity Against a Defective Ribosomal Insulin Gene Product in Type 1 Diabetes. *Nat Med* (2017) 23(4):501–7. doi: 10.1038/nm.4289
95. Propato A, Cutrona G, Francavilla V, Ulivi M, Schiaffella E, Landt O, et al. Apoptotic Cells Overexpress Vinculin and Induce Vinculin-Specific Cytotoxic T-Cell Cross-Priming. *Nat Med* (2001) 7(7):807–13. doi: 10.1038/89930
96. Rawson PM, Molette C, Videtta M, Altieri L, Franceschini D, Donato T, et al. Cross-Presentation of Caspase-Cleaved Apoptotic Self Antigens in HIV Infection. *Nat Med* (2007) 13(12):1431–9. doi: 10.1038/nm1679
97. Citro A, Scrivo R, Martini H, Martire C, De Marzio P, Vestri AR, et al. CD8+ T Cells Specific to Apoptosis-Associated Antigens Predict the Response to Tumor Necrosis Factor Inhibitor Therapy in Rheumatoid Arthritis. *PloS One* (2015) 10(6):e0128607. doi: 10.1371/journal.pone.0128607
98. Cammarata I, Martire C, Citro A, Raimondo D, Fruci D, Melaiu O, et al. Counter-Regulation of Regulatory T Cells by Autoreactive CD8+ T Cells in Rheumatoid Arthritis. *J Autoimmun* (2019) 99:81–97. doi: 10.1016/j.jaut.2019.02.001
99. Collier JL, Weiss SA, Pauken KE, Sen DR, Sharpe AH. Not-So-Opposite Ends of the Spectrum: CD8+ T Cell Dysfunction Across Chronic Infection, Cancer and Autoimmunity. *Nat Immunol* (2021) 22(7):809–19. doi: 10.1038/s41590-021-00949-7
100. McKinney EF, Lee JC, Jayne DRW, Lyons PA, Smith KGC. T-Cell Exhaustion, Co-Stimulation and Clinical Outcome in Autoimmunity and Infection. *Nature* (2015) 523(7562):612–6. doi: 10.1038/nature14468
101. Bluestone JA, Buckner JH, Fitch M, Gitelman SE, Gupta S, Hellerstein MK, et al. Type 1 Diabetes Immunotherapy Using Polyclonal Regulatory T Cells. *Sci Trans Med* (2015) 7(315):315ra189. doi: 10.1126/scitranslmed.aad4134
102. Boyman O, Kovar M, Rubinstein MP, Surh CD, Sprent J. Selective Stimulation of T Cell Subsets With Antibody-Cytokine Immune Complexes. *Science* (2006) 311(5769):1924–7. doi: 10.1126/science.1122927
103. Trotta E, Bessette PH, Silveria SL, Ely LK, Jude KM, Le DT, et al. A Human Anti-IL-2 Antibody That Potentiates Regulatory T Cells by a Structure-Based Mechanism. *Nat Med* (2018) 24(7):1005–14. doi: 10.1038/s41591-018-0070-2

Conflict of Interest: The author declares that the research was conducted in the absence of any commercial or financial relationships that could be construed as a potential conflict of interest.

frontiers
in Immunology

ORIGINAL RESEARCH
published: 24 March 2022
doi: 10.3389/fimmu.2022.851868

Public T-Cell Receptors (TCRs) Revisited by Analysis of the Magnitude of Identical and Highly-Similar TCRs in Virus-Specific T-Cell Repertoires of Healthy Individuals

Wesley Huisman[1,2]*, *Lois Hageman*[1], *Didier A. T. Leboux*[1], *Alexandra Khmelevskaya*[3], *Grigory A. Efimov*[3], *Marthe C. J. Roex*[1], *Derk Amsen*[2], *J. H. Frederik Falkenburg*[1] *and Inge Jedema*[1]

[1] Department of Hematology, Leiden University Medical Center, Leiden, Netherlands, [2] Department of Hematopoiesis, Sanquin Research and Landsteiner Laboratory for Blood Cell Research, Amsterdam, Netherlands, [3] Laboratory of Transplantation Immunology, National Research Center for Hematology, Moscow, Russia

OPEN ACCESS

Edited by:
Uri Hershberg,
University of Haifa, Israel

Reviewed by:
Irun R. Cohen,
Weizmann Institute of Science, Israel
Niels A. W. Lemmermann,
Johannes Gutenberg University Mainz, Germany

***Correspondence:**
Wesley Huisman
w.huisman@lumc.nl

Specialty section:
This article was submitted to Immunological Memory, a section of the journal Frontiers in Immunology

Received: *10 January 2022*
Accepted: *04 March 2022*
Published: *24 March 2022*

Citation:
Huisman W, Hageman L, Leboux DAT, Khmelevskaya A, Efimov GA, Roex MCJ, Amsen D, Falkenburg JHF and Jedema I (2022) Public T-Cell Receptors (TCRs) Revisited by Analysis of the Magnitude of Identical and Highly-Similar TCRs in Virus-Specific T-Cell Repertoires of Healthy Individuals. Front. Immunol. 13:851868. doi: 10.3389/fimmu.2022.851868

Since multiple different T-cell receptor (TCR) sequences can bind to the same peptide-MHC combination and the number of TCR-sequences that can theoretically be generated even exceeds the number of T cells in a human body, the likelihood that many public identical (PUB-I) TCR-sequences frequently contribute to immune responses has been estimated to be low. Here, we quantitatively analyzed the TCR-repertoires of 190 purified virus-specific memory T-cell populations, directed against 21 epitopes of Cytomegalovirus, Epstein-Barr virus and Adenovirus isolated from 29 healthy individuals, and determined the magnitude, defined as prevalence within the population and frequencies within individuals, of PUB-I TCR and of TCR-sequences that are highly-similar (PUB-HS) to these PUB-I TCR-sequences. We found that almost one third of all TCR nucleotide-sequences represented PUB-I TCR amino-acid (AA) sequences and found an additional 12% of PUB-HS TCRs differing by maximally 3 AAs. We illustrate that these PUB-I and PUB-HS TCRs were structurally related and contained shared core-sequences in their TCR-sequences. We found a prevalence of PUB-I and PUB-HS TCRs of up to 50% among individuals and showed frequencies of virus-specific PUB-I and PUB-HS TCRs making up more than 10% of each virus-specific T-cell population. These findings were confirmed by using an independent TCR-database of virus-specific TCRs. We therefore conclude that the magnitude of the contribution of PUB-I and PUB-HS TCRs to these virus-specific T-cell responses is high. Because the T cells from these virus-specific memory TCR-repertoires were the result of successful control of the virus in these healthy individuals, these PUB-HS TCRs and PUB-I TCRs may be attractive candidates for immunotherapy in immunocompromised patients that lack virus-specific T cells to control viral reactivation.

Keywords: virus-specific T cell responses, TCR - T cell receptor, public T cell receptors, computational analysis, CDR3 amino acid motifs, memory T cells (Tmem), V-D-J recombination, TCR repertoire analysis

INTRODUCTION

Human virus-specific CD8^{pos} T cells express heterodimeric alpha (α)/beta(β) TCRs that can specifically recognize viral peptides presented by HLA-class-I molecules (1). The TCRα- and the TCRβ-chain repertoires are highly variable due to the genetic recombination process involved in their generation. For the TCRβ-chains, recombination of 1 of 48 functional T-cell Receptor Beta Variable (TRBV), 1 of 2 functional T-cell receptor Beta Diversity (TRBD) and 1 of 12 functional T-cell Receptor Beta Joining (TRBJ) gene segments leads to a V-D-J reading frame (2). The TCRα-chains are generated by a similar recombination process with the exception of a diversity gene, resulting in a V-J reading frame (3). Insertion of template-independent nucleotides between the recombined segments (junctional region) results in a significant further increase in variability (4). The sequence around these junctions encodes for the Complementary Determining Region 3 (CDR3), a loop that reaches out and interacts with a peptide embedded in an HLA molecule, together with the loops of the CDR1 and CDR2 regions, which are fixed within the germline variable gene sequence (5, 6). It has been calculated that these gene rearrangements could potentially generate a repertoire of 10^{15}-10^{20} unique TCRs that may interact with all possible peptide-HLA complexes (7).

Pathogenic viruses like Cytomegalovirus (CMV), Epstein-Barr virus (EBV) and Adenovirus (AdV) can infect humans for life by staying latently present in target cells after a primary infection. In healthy individuals these latent viruses are controlled by the virus-specific T cells. As a result, reactivations of these latent viruses are observed frequently, but do not result in severe virus-associated disorders like malignancies and/or organ failure. However, in the absence of a competent immune system, these latent viruses remain uncontrolled and are associated with high-morbidity and mortality in immune-compromised patients, including patients after stem cells or organ tranplantation (8, 9). To control these viruses, antigen-experienced (central-memory and effector-memory) virus-specific T cells have to develop from the naïve T-cell repertoire. Due to the high diversity of the naïve T-cell repertoire (10), T-cell responses against the many potential viral epitopes presented in multiple HLA alleles may be composed of a large variety of different TCRs. Indeed, when naïve umbilical cord blood-derived T cells were stimulated *in vitro* to generate *de novo* responses against proteins from CMV or Human Immunodeficiency Virus (HIV), this resulted in responding virus-specific T-cell populations with a highly diverse repertoire of TCRs, recognizing many different CMV (11) or HIV-derived peptides (12). However, from *ex vivo* analyses in adults it became clear that *in vivo* the virus-specific memory T-cell populations are shaped during control and clearance of the infection and target only a limited number of viral-peptides, as was shown for T-cell populations specific for viruses like CMV (13), EBV (14), AdV (15), Influenza A (16) and also more recently SARS-Cov-2 (17, 18). Nevertheless, the multiple viral-peptides that are targeted in the various HLA alleles make it theoretically unlikely that individuals would frequently share exactly the same virus-specific TCR, unless T cells expressing certain TCRs would favor control of infections and would therefore dominate the responses. Since latent viruses like CMV, EBV and AdV are not fully eradicated, reactivations are frequent and trigger the expansion of antigen-experienced virus-specific memory T cells. This unique biology might contribute to the favor and skewing of specific TCRs expressed by T cells that dominate the response and control the virus.

Evidence for selection of certain virus-specific TCR-expressing T cells in controlling viruses has come from several reports identifying identical TCR amino-acid (AA) sequences in dominant virus-specific memory T-cell populations in different individuals, designated as public TCR-sequences [from here on referred to as public-identical (PUB-I) TCR-sequences]. Most studies investigated the presence of PUB-I TCR-sequences in TCRβ-chains, since this is the most diverse TCR chain and the CDR3β sequence of CD8 T cells is positioned to interact with the antigenic peptide presented by HLA-class-I molecules. However, dominant virus-specific memory T-cell populations with PUB-I TCRα chains have also been described previously (19). Such PUB-I TCR sequences are most overtly observed in antigen-experienced memory virus-specific T cells due to the *in vivo* antigen-driven proliferation, but are also present within the naïve T-cell compartment, although at low frequency (20). PUB-I TCRβ sequences have been found in T-cell populations specific for latent viruses like CMV-specific T-cell responses (21–23), EBV-specific T-cell responses (24, 25), but also for non-latent viruses like Influenza-specific T-cell responses (16), respiratory syncytial virus-specific T-cell responses (26) and SARS-Cov-2-specific T-cell responses (17, 27). In addition, some of these virus-specific T-cell populations also contained TCR AA-sequences that were highly-similar to the identical shared TCR AA-sequence [from here on referred to as highly-similar to PUB-I (PUB-HS) TCR-sequences]. However, the magnitude, defined as prevalence within the population and frequencies within virus-specific T-cell repertoires, of PUB-I and PUB-HS TCR-sequences is not known. A high probability to be generated during V-D-J recombination may play a role (28), but since virus-specific memory T-cell repertoires in the circulation are shaped based on antigen encounter and subsequent proliferation, the PUB-I and PUB-HS TCR-sequences most likely reflect highly functional T cells capable of antigen-driven proliferation.

We hypothesize that frequent induction of antigen-driven proliferation of virus-specific T cells targeting frequently reactivating latent viruses will increase the prevalence and frequencies of PUB-I and PUB-HS TCR-sequences within the repertoire of antigen-experienced virus-specific T-cells. Molecular analysis of these TCRs will add in the analysis of the development, presence and quality of memory T-cell responses, and tracking of virus-specific T-cell responses. Furthermore, Identification of dominant TCRs with shared core-sequences may be utilized for the design of future immunotherapy purposes including TCR-gene transfer. Therefore, the aim of our study was to quantitively analyze the magnitude of PUB-I and PUB-HS TCRβ-sequences within the antigen-experienced virus-specific

TCR-repertoires of CMV, EBV and AdV-specific CD8^{Pos} memory T cells. We confirmed that healthy individuals generate many different virus-specific TCRs, illustrated by the >3000 TCR nucleotide-sequences that were found *ex vivo* in virus-specific memory T-cell populations. However, a significant part of the virus-specific TCR-repertoires contained PUB-I and PUB-HS TCR nucleotide-sequences. The AAs of these PUB-HS TCRs varied on specific positions in the CDR3β-region, while maintaining a conserved core-AA-sequence that was also present in the respective PUB-I TCR. We identified conserved TCR core-AA-sequences for each specificity that could be used for diagnostic purposes looking at anti-viral immune responses. Additionally, PUB-I or PUB-HS TCRs with the highest frequencies in healthy individuals may be utilized to develop off-the-shelf immunotherapeutics (using TCR-gene transfer) to effectively control CMV, EBV or AdV-infections or reactivations in immunocompromised patients.

METHODS

Collection of Donor Material

After informed consent according to the Declaration of Helsinki, healthy individuals (homozygously) expressing HLA-A*01:01 and HLA-B*08:01 or HLA-A*02:01 and HLA-B*07:02 were selected from the Sanquin database and the biobank of the department of Hematology, Leiden University Medical Center (LUMC). Peripheral blood mononuclear cells (PBMCs) were isolated by standard Ficoll-Isopaque separation and used directly or thawed after cryopreservation in the vapor phase of liquid nitrogen. Donor characteristics (HLA typing, CMV and EBV serostatus) are provided in **Table 1**. For isolation of donor-derived virus-specific T cells using fluorescence-activated cell sorting (FACS, gating strategy see **Supplementary Figure 1**) with pMHC-tetramers (**Table 2**) and expansion of donor-derived virus-specific T cells, see **Supplementary Material** and *Methods*.

TCRβ-Library Preparation

TCRβ-sequences were identified using ARTISAN PCR adapted for TCR PCR (29, 30). Total mRNA was extracted from 190 pMHC-tetramer^{pos} purified (**Supplementary Figure 2A**) virus-specific T-cell populations (31) using magnetic beads (Dynabead mRNA DIRECT kit; Invitrogen, Thermo Fisher Scientific). Ten μl (~1μg) of mRNA per sample was mixed with TCRβ constant region-specific primers (1μM final concentration) and SmartSeq2modified template-switching oligonucleotide (SS2m_TSO; 1μM final concentration) and denatured for 3 minutes at 72°C. After cooling, cDNA was synthesized for 90 minutes at 42°C with 170 U SMARTscribe reverse transcriptase (Takara, Clontech) in a total volume of 20μl containing 1.7U/μl RNasin (Promega), 1.7mM DTT (Invitrogen, Thermo Fisher Scientific), 0.8mM each of high-purity RNAse-free dNTPs (Invitrogen, Thermo Fisher Scientific) and 4μl of 5x first-strand buffer. During cDNA synthesis, a non-templated 3'polycytosine terminus was added (**Supplementary Figure 2B**), which created a template for extension of the cDNA with the TSO (32). PCR (2min at 98°C followed by 40 cycles of [1s at 98°C, 15s at 67°C, 15s at 72°C], 2 min at 72°C) of 5μl of cDNA was then performed using Phusion Flash (Thermo Fisher Scientific) with anchor-specific primer (SS2m_For; 1μM final concentration) and each (1μM final concentration) of the nested primers specific for the constant regions of TCRβ constant 1 and TCRβ constant 2. Both forward and reverse PCR primers contained overhanging sequences suitable for barcoding. Amplicons were purified and underwent a second PCR (2min at 98°C followed by 10 cycles of [1s at 98°C, 15s at 65°C, 30s at 72°C], 2 min at 72°C) using forward and reverse primers (1μM final concentration) with overhanging sequences containing identifiers (sequences of 6 base-pairs) and adapter sequences appropriate for Illumina HiSeq platforms (or PacBio; Pacific Biosciences). Unique identifiers were used for each T-cell population targeting one epitope. Forward or reverse identifiers were shared between T-cell populations targeting different epitopes. For all primer sequences see **Supplementary Table 1**. For identifier sequences see **Supplementary Table 2**. Amplicons with identifiers were purified, quantified and pooled into one library for paired-end sequencing of 150bp on an Illumina HiSeq4000. Deep sequencing was performed at GenomeScan (Leiden, The Netherlands). Raw data were de-multiplexed and aligned to the matching TRBV, TRBD, TRBJ and constant (TRBC) genes. CDR3β-sequences were built using MIXCR software using a bi-directional approach (5'-3' and 3'-5' read) (**Supplementary Figure 2C**) (33). CDR3β-sequences with a stop-codon were removed from the library. Bi-directional readings using MIXCR could result in out-of-frame CDR3β AA-sequences due to the even number of nucleotides. These sequences (n=392) were manually aligned with the germline TRBV and TRBJ-sequence. CDR3β-sequences were further processed using custom scripts in R to compare specificities and sharing of CDR3β-sequences.

Computational Unbiased Repertoire Analysis

The following R-packages were used in R-software to generate a nodal plot of CDR3β AA-sequences with the levenshtein distance as parameter for similarity: "igraph" to create network objects, obtain the degree of a node and its betweenness (34), "data.table" to organize CDR3β-sequences; "stringdist" to calculate Levenshtein distances (35), "Biostrings" for fast manipulation of large biological sequences or sets of sequences (36), "dplyr" to arrange and filter data (37), "tibble" for providing opinionated data frames, "ggplot2" for generating figures (38) and "RColorBrewer" to create graphics (39). A levenshtein distance of 0.25 was added to visualize multiple identical sequences. Nodes with identical sequences (levenshtein distance of 0.25) were manually replaced by pie-charts using Adobe Illustrator CC 2018.

Sequence Logo Plots

To identify which positions of PUB-I and PUB-HS CDR3β AA-sequences were conserved and which were variable, all CDR3β AA-sequences with the most frequent CDR3 length were included and the AAs were stacked for each position in the sequence. The overall height of the stacks indicates the sequence

TABLE 1 | HLA typing and CMV/EBV-serostatus of healthy donors.

#	Age	CMV	EBV	HLA-A		HLA-B		HLA-C		HLA-DR		HLA-DQ		HLA-DP	
1	62	Pos	Pos	01:01	30:01	08:01	13:02	07:01	06:02	03:01	07:01	02:01	02:02	04:01	09:01
2	48	Pos	Pos	01:01		08:01		07:01		03:01	01:02	02:01	05:01	01:01	04:01
3	53	Pos	Pos	01:01		08:01		07:01		03:01	15:01	02:01	06:02	N.D	
4	44	Pos	Pos	01:01		08:01		07:01		03:01		02:01		04:01	
5	65	Pos	pos	01:01	30:01	08:01	13:02	07:01	06:02	04:07	15:01	03:01	06:02	04:01	
6	26	Pos	Pos	01:01		08:01		07:01		03:XX		02:XX		N.D	
7	42	Pos	pos	01:01	30:01	08:01	13:02	07:01	06:02	03:01	04:01	02:01	03:01	04:01	
8	41	Pos	pos	02:01	24:02	08:01	35:01	07:01	11:01	02:02	03:01	02:02	03:01	02:01	13:01
9	27	Neg	Pos	01:01		08:01		07:01		03:01		02:01		04:01	
10	48	Neg	Pos	01:01		08:01		07:01		03:01		02:01		04:01	05:01
11	35	Neg	Pos	01:01		08:01		07:01		03:01		02:01		01:01	09:01
12	49	Neg	Pos	01:01		08:01		07:01		03:01		02:01		04:01	05:01
13	50	Neg	Pos	01:01		08:01		07:01		03:01		02:01		04:01	04:02/01
14	57	Pos	Pos	01:01	68:01	08:01	35:01	04:01	07:01	01:01	03:01	02	05:01	04:01	04:02
15	32	Neg	Pos	01:01		08:01		07:0		03:XX		02:XX		N.D	
16	25	Neg	pos	01:01	24:02	08:01	35:01	04:01	07:01	03:01	08:01	02:01	04:02	04:01	
17	38	Neg	Pos	01:01		08:01		07:01		03:XX		02:XX		N.D	
18	N.K.	Pos	Pos	02:01		07:02	44:02	07:02	05:01	15:01	04:01	06:02	03:01	04:XX	02:01
19	64	Pos	Pos	02:01		07:02		07:02		15:01		06:02		04:01	
20	33	Pos	Pos	02:01	03:01	07:02		07:02		15:01		06:02		04:01	03:01
21	53	Pos	Pos	02:01		07:02		07:02		15:01		06:02		04:01	05:01
22	62	Pos	Pos	02:01		07:02		07:02		15:01		06:02		02:01	04:01
23	43	Pos	Pos	02:01		07:02		07:02		15:01		06:02		04:01	
24	50	Pos	Pos	02:01	03:01	07:02	44:02	07:02	05:01	15:01	01:01	06:02	05:01	04:01	14:01
25	50	Pos	Pos	02:01		07:02		07:02		07:01	15:01	03:03	06:02	04:01	13:01
26	63	Pos	Pos	02:01		07:02		07:02		15:XX		06:XX		N.D	
27	29	Neg	Pos	02:01		07:02		07:02		15:01		06:02		04:01	
28	26	Neg	Pos	02:01		07:02		07:02		15:01		06:02		04:01	13:01
29	52	Neg	Pos	02:01		07:02		07:02		15:XX		06:XX		N.D	

*Virus-specific T cells restricted to HLA-A*01:01/HLA-B*08:01 or HLA-A*02:01/HLA-B*07:02 were isolated from donors #1-17 and donors #18-29, respectively. CMV and EBV serostatus and age are indicated for each donor. HLA typing was determined either by serology, where the second digits could not be determined (XX), or with high resolution HLA typing unless indicated by N.D. Blanks indicate homozygosity for the given allele. For one of the unrelated stem cell donors the age was not known (N.K.).*

conservation at that position, while the height of symbols within the stacks indicates the relative frequency of each AA at that position. AAs have colors according to their chemical properties; polar AAs (G, S, T, Y, C, Q, N) show as green, basic (K, R, H) blue, acidic (D, E) red, and hydrophobic (A, V, L, I, P, W, F, M) AAs as black (40).

Generation of Independent TCR-Database From Virus-Specific T-Cell Products Generated for a Clinical Trial

As an independent TCR-database containing TCR-sequences from virus-specific T cells, we used the information obtained from the virus-specific T-cell products generated in the context of the phase I/II safety and feasibility study T Control (EudraCT-number 2014-003171-39) using the MHC-I-Streptamer isolation technology (Juno Therapeutics, Munich, Germany) (20, 41). Sequencing was performed as described above for all virus-specific T-cell populations per donor, resulting in unique identifiers for all virus-specific T-cell populations in the TCRβ-library.

Data Deposition

TCR-Sequencing data is deposited to the Sequence Read Archive (SRA); submission: SUB10993301 (access to bioproject: https://www.ncbi.nlm.nih.gov/bioproject/PRJNA803981).

RESULTS

Generation and Validation of a Library of TCR-Sequences Derived From FACsorted Virus-Specific T-Cell Populations

To examine the composition of the virus-specific TCR-repertoires in different individuals, the CDR3β-regions of purified expanded pMHC-tetramer-binding virus-specific T-cell populations were sequenced (**Supplementary Figure 2**). We analyzed the TCR-repertoires of CMV, EBV and AdV-specific T cells, restricted to four prevalent HLA alleles (HLA-A*01:01, HLA-A*02:01, HLA-B*07:02 and HLA-B*08:01) and specific for 21 different peptides (**Table 2**). Purified CMV, EBV and AdV-specific T-cell populations targeting CMV (n=8), EBV (n=10) or AdV (n=3)-derived peptides were isolated from 17 HLA-A*01:01/B*08:01^{pos} individuals and 12 HLA-A*02:01/B*07:02^{pos} individuals (**Tables 1**, **2**). In total, 190 virus-specific T-cell populations, each targeting a single viral epitope, were successfully isolated and showed high purity (>97% pMHC-tetramer positive). The mean precursor frequencies of the different T-cell specificities in the starting PBMC materials are shown in **Supplementary Figure 3**. Sequencing of the CDR3β-regions of these virus-specific T-cell populations resulted in 3346 CDR3β nucleotide-sequences that occurred at frequencies of more than 0.1%. 135 of these nucleotide-sequences were

TABLE 2 | Number of isolated virus-specific T-cell populations.

Virus	Antigen	HLA	Peptide	# of isolated T-cell populations/# of attempted isolations (%)		
				Per specificity	**Per virus**	**Per HLA**
CMV	pp50	HLA-A*01:01	VTEHDTLLY	7/8 (88%)	**CMV:**	**HLA-A*01:01:**
	pp65	HLA-A*01:01	YSEHPTFTSQY	6/8 (75%)	53/70	29/39
	pp65	HLA-A*02:01	NLVPMVATV	8/9 (89%)	*(76%)*	*(74%)*
	IE-1	HLA-A*02:01	VLEETSVML	5/9 (56%)		
	pp65	HLA-B*07:02	TPRVTGGGAM	8/9 (89%)		
	pp65	HLA-B*07:02	RPHERNGFTVL	8/9 (89%)		**HLA-A*02:01:**
	IE-1	HLA-B*08:01	ELRRKMMYM	5/9 (56%)		70/90
	IE-1	HLA-B*08:01	QIKVRVDMV	6/9 (67%)		*(78%)*
EBV	LMP2	HLA-A*01:01	ESEERPPTPY	4/6 (67%)	**EBV:**	
	LMP2	HLA-A*02:01	FLYALALLL	11/12 (92%)	111/129	
	LMP2	HLA-A*02:01	CLGGLLTMV	10/12 (83%)	(86%)	
	EBNA3C	HLA-A*02:01	LLDFVRFMGV	7/12 (58%)		**HLA-B*07:02**:
	BMLF1	HLA-A*02:01	GLCTLVAML	10/12 (83%)		33/42
	BRLF1	HLA-A*02:01	YVLDHLIVV	11/12 (92%)		*(79%)*
	EBNA3A	HLA-B*07:02	RPPIFIRRL	11/12 (92%)		
	BZLF1	HLA-B*08:01	RAKFKQLL	17/17 (100%)		
	EBNA3A	HLA-B*08:01	FLRGRAYGL	13/17 (76%)		**HLA-B*08:01:**
	EBNA3A	HLA-B*08:01	QAKWRLQTL	17/17 (100%)		58/69
AdV	HEXON	HLA-A*01:01	TDLGQNLLY	12/17 (71%)	**AdV:**	*(84%)*
	E1A	HLA-A*02:01	LLDQLIEEV	8/12 (67%)	26/41	
	HEXON	HLA-B*07:02	KPYSGTAYNAL	6/12 (50%)	(63%)	

*Seventeen donors were used to isolate HLA-A*01:01/B*08:01-restricted virus-specific T cells and 12 donors were used to isolate HLA-A*02:01/B*07:02-restricted virus-specific T cells. CMV, Cytomegalovirus; EBV, Epstein-Barr virus; AdV, Adenovirus.*

present at high frequencies (>5%) within one specificity, but were also found at low frequencies (around 0.1%) in another specificity, indicating contamination due to FACSorting impurities. These low frequency nucleotide-sequences were discarded from further analysis. 41 nucleotide-sequences were present at low frequencies in two unrelated specificities and could not be correctly annotated and these 41 duplicates (n=82) were also discarded from the analysis. Therefore, a total of 3129 nucleotide-sequences could be annotated. In total, 2224 (71%) of these nucleotide-sequences represented unique CDR3β AA-sequences that were found in only one individual and 905 nucleotide-sequences (29%) resulted in 131 different PUB-I CDR3β AA-sequences that were found in two or more unrelated individuals (Flowchart; **Figure 1**).

To investigate the relationship between the numbers of CDR3β nucleotide-sequences and the translated number of CDR3β AA-sequences, we compared the nucleotide-sequences of the 131 PUB-I CDR3β AA-sequences found in different individuals. Different nucleotide-sequences can result in the same CDR3β AA-sequence, a phenomenon known as convergent recombination. We found that PUB-I CDR3β AA-sequences present at high (representative example**; Figure 2A**) or low frequencies (range 0.1-1%) (representative example; **Figure 2B**) could be encoded by different CDR3β nucleotide-sequences in the junctional regions of the CDR3β-regions in TCRs of T cells isolated from different individuals (**Figures 2C, D** and **Supplementary Figure 4**). Because the majority of nucleotide-sequences encoding the same CDR3β AA-sequences were different between individuals, these data exclude contamination as an explanation for the finding of PUB-I CDR3β AA-sequences.

PUB-I and PUB-HS CMV-, EBV- and AdV-Specific CDR3β AA-Sequences Are Abundant in Virus-Specific T-Cell Populations

We then investigated the distribution of the 131 PUB-I CDR3β AA-sequences within the 21 different specificities and the prevalence among individuals for each of the PUB-I CDR3β AA-sequences per viral-epitope. T cells with PUB-I CDR3β AA-sequences were found for 19 out of the 21 specificities (**Supplementary Table 3**). PUB-I CDR3β AA-sequences were not observed in AdV-IE1$^{\text{LLD}}$ and EBV-LMP2$^{\text{ESE}}$-specific T-cell populations. Some T-cell populations (e.g. EBV-LMP2$^{\text{FLY}}$) contained many different PUB-I CDR3β AA-sequences (n=24) that were all highly-similar. For this reason, we investigated the distribution of PUB-I CDR3β AA-sequences with unique TRBV and TRBJ-gene usage. This resulted in 29 different PUB-I CDR3β AA-sequences, distributed over 19 specificities (**Figure 3A**; grey bars). Six specificities contained two or three different (expressing different TRBV and/or TRBJ-genes) PUB-I CDR3β AA-sequences that were highly prevalent among individuals. To investigate how often these PUB-I CDR3β AA-sequences could be found in our cohort of healthy donors, we quantified the prevalence of each of these 29 PUB-I CDR3β AA-sequence (**Figure 3A**; grey bars). Because we classified a PUB-I CDR3β AA-sequence as being present in at least 2 individuals, the prevalence among donors could not be less than 2 out of 17 (12%; 17 is maximum number of T-cell populations for 1 specificity). Only 4 out of 29 PUB-I CDR3β AA-sequences were found in only 2 individuals (**Figure 3A**; grey bars). Overall, these 29 PUB-I CDR3β AA-sequences had a prevalence of 33% among healthy individuals (median; range

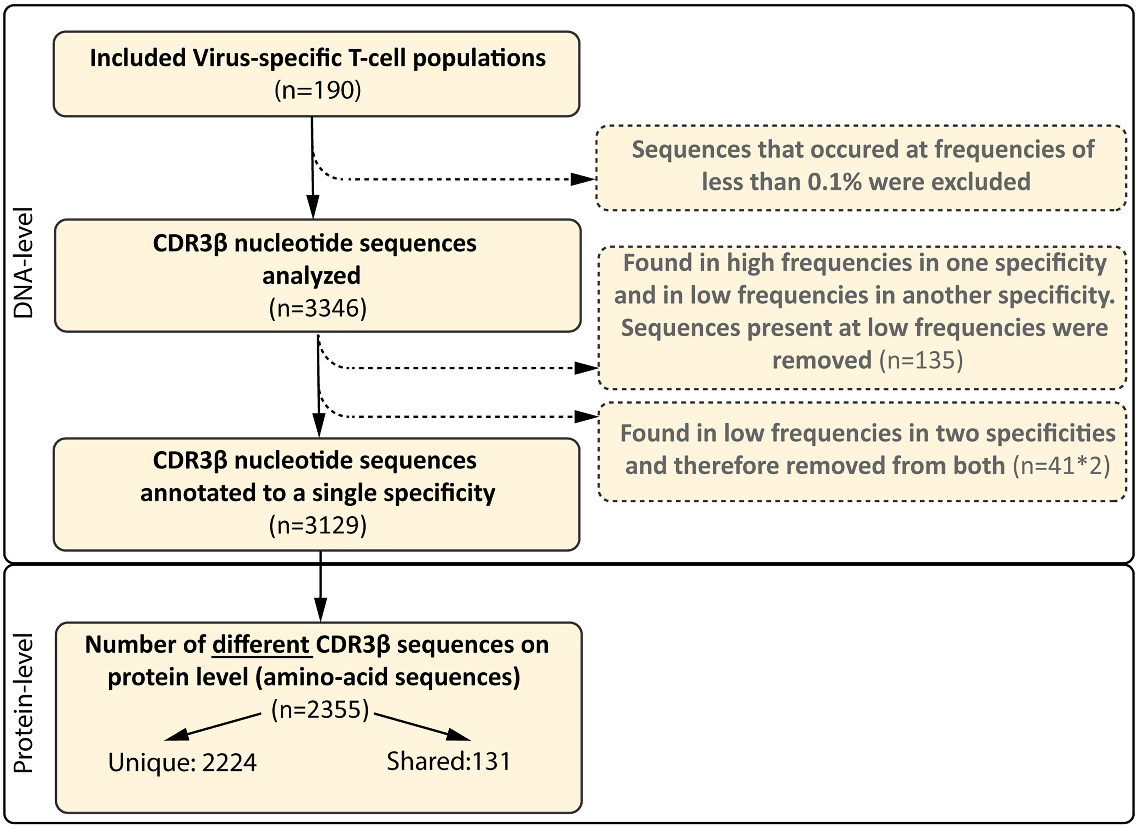

FIGURE 1 | Flowchart of included and excluded CDR3β nucleotide and AA-sequences. In total, 190 different virus-specific T-cell populations were FACsorted using pMHC-tetramers, followed by a short-term *in vitro* stimulation. The CDR3β nucleotide-sequences were determined using next-gen Illumina sequencing. CDR3β nucleotide-sequences that occurred at a frequency of less than 0.1% in each sample were excluded. CDR3β nucleotide-sequences that were identical and present in two different specificities, but present at high frequencies in one specificity, were only removed from the specificity that contained the sequences at very low frequencies (0.1-0.5%; n=135). CDR3β nucleotide-sequences that were identical and present in two different specificities at low frequency were considered contamination and removed from the library (82 sequences, 41 different-sequences). The numbers of different CDR3β AA-sequences that were encoded by the CDR3β nucleotide-sequence are shown at protein level. We then assessed how many CDR3β-AA-sequences were found in multiple individuals (shared) and how many were only found in a single individual (unique).

12%-82%). Importantly, most PUB-I CDR3β AA-sequences were found in at least 25% of individuals and 5 were even present in more than half the donors.

We and others hypothesized that the binding/docking of TCRs to HLA-peptide complexes might allow for small changes/flexibility in the CDR3 AA-sequences without significantly changing the conformation or interaction (42). Therefore, we investigated if there were CDR3β AA-sequences present in our data set that were highly-similar (PUB-HS) to PUB-I CDR3β AA-sequences and differed by 1, 2 or 3 AAs. The 2224 unique TCR nucleotide-sequences identified in our previous analysis may contain PUB-HS CDR3β AA-sequences that are in fact part of the same public response as the respective PUB-I TCRs. In total, 379 PUB-HS CDR3β nucleotide-sequences were present that also resulted in 379 PUB-HS CDR3β AA-sequences that differed by 1, 2 or 3 AAs from one of the 131 PUB-I CDR3β AA-sequences. This shows that 41% of the total virus-specific TCR-repertoire contained PUB-I and PUB-HS CDR3β nucleotide-sequences. We investigated if these PUB-HS CDR3β AA-sequences were also present in individuals that did not contain the respective PUB-I CDR3β AA-sequences. PUB-HS CDR3β AA-sequences were present for 21 out of 29 PUB-I CDR3β AA-sequences (**Figure 3A**; shaded orange bars). When we include the PUB-HS CDR3β AA-sequences and quantified the 29 PUB-I and PUB-HS CDR3β AA-sequences, these had a median prevalence of 50% among healthy individuals (range 23%-100%). The AdV-IE1^{LLD} and EBV-LMP2^{ESE}-specific T-cell populations, where PUB-I CDR3β AA-sequences were not found, did contain PUB-HS CDR3β AA-sequences in multiple individuals at high frequencies (43) (**Supplementary Figure 5**). The frequencies of PUB-I combined with PUB-HS CDR3β AA-sequences were relatively high within each virus-specific T-cell population of each individual (**Figure 3B**). The frequencies of all PUB-I and PUB-HS CDR3β AA-sequences ranged from 0.1%-99.4% within the 19 different virus-specific T-cell populations with a median of 13.1%. When combined, all but one PUB-I plus PUB-HS CDR3β

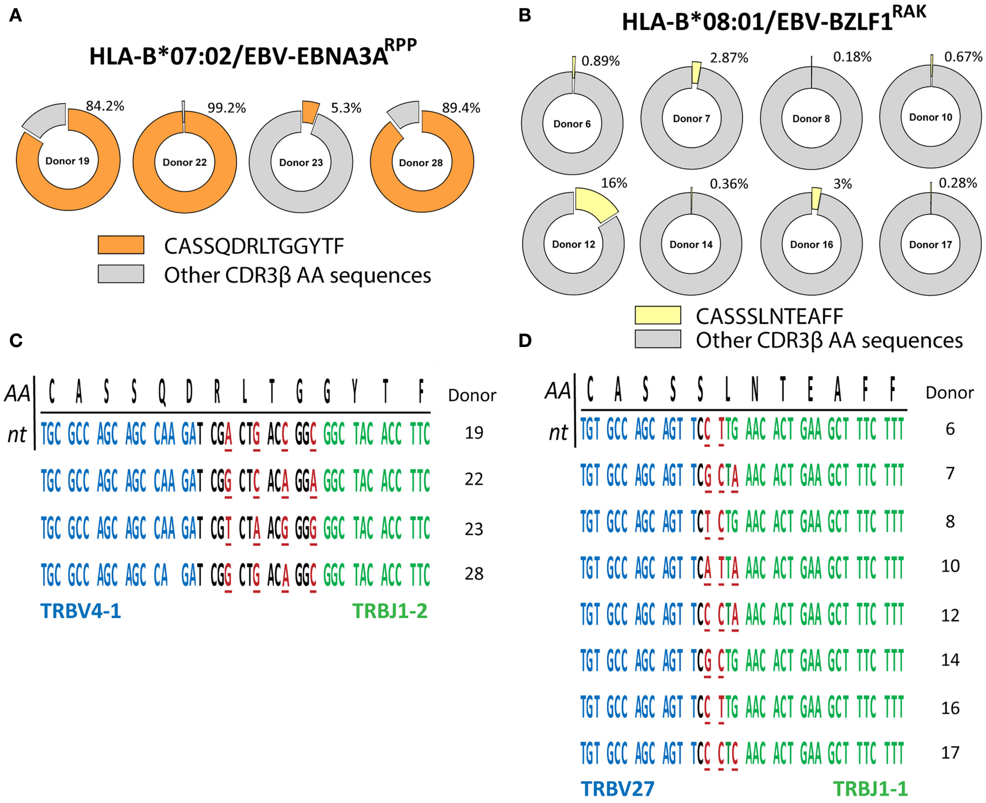

FIGURE 2 | PUB-I CDR3β-sequences can be found in different individuals with small nucleotide-differences as a result of convergent recombination. The library of virus-specific CDR3β AA-sequences contained 131 sequences that were found in multiple different individuals (≥2). The nucleotide-sequences of these CDR3β AA-sequences were analyzed to investigate differences and similarities. **(A, B)** Shown are two representative examples of the frequencies of the PUB-I CDR3β AA-sequences CASQDRLTGGYTF and CASSSLNTEAFF, that were specific for HLA-B*07:02-restricted EBV-EBNA3A^{RPP} and HLA-B*08:01-restricted EBV-BZLF1^{RAK}, respectively. **(C, D)** Shown are the nucleotide-sequences of the CDR3β AA-sequences CASSQDRLTGGYTF and CASSSLNTEAFF that were shared by different individuals. Underlined nucleotides represent differences between the different individuals. Nucleotides in red represent differences to the consensus sequence. Nucleotide-sequences in blue and green represent perfect alignment with the germline sequences of the TRBV-gene and TRBJ-gene, respectively. AA, amino-acids; nt, nucleotides.

AA-sequences were found in at least 25% of individuals and 3 were even found in over 75% of individuals. These data show that for many PUB-I CDR3β AA-sequences we found sequences that were similar (1, 2 or 3 AA-differences), making up more than 40% of the total virus-specific TCR-repertoire and together these sequences were found in the majority of individuals at high frequencies.

Identical and Highly-Similar CDR3β AA-Sequences Contain Conserved Regions in the Junctional Region

To investigate how the PUB-HS CDR3β AA-sequences related to the PUB-I CDR3β AA-sequences, we analyzed if the PUB-HS (1, 2 or 3 AA-differences) CDR3β AA-sequences showed variations at random positions or at specific positions compared to the PUB-I CDR3β AA-sequences. We hypothesized that if the binding/docking of PUB-HS TCRs was not significantly different, conserved regions and regions that allow for some variation could be identified in the CDR3β AA-sequences. As Illustrated in **Figure 4A** for the EBV-LMP2^{FLY}-specific PUB-I CDR3β AA-sequence CASSYQGGNYGYTF, two motifs were identified with AA-differences predominantly located at positions 5 and 9/10 of the CDR3β-region. The AAs [QGG] at positions 6-8 were conserved for both motifs. In total, the two motifs consisted of 86 PUB-HS CDR3β AA-sequences with 1 or 2 AA-differences. The majority (n=71) had the same CDR3 length of 14 AAs as the PUB-I CDR3β AA-sequence, implying that variations were caused by AA-substitutions. The remaining 15 PUB-HS CDR3β AA-sequences had a CDR3 length of 15 AAs, due to AA-inserts, compared to the PUB-I CDR3β AA-sequence (**Figure 4B**). Similar rules were found for the other 20 PUB-I CDR3β AA-sequences. Also here, some AA-positions were highly conserved, whereas others were variable. However, the precise locations of the variable AAs differed between specificities (Representative examples; **Figure 4C**). Interestingly, the corresponding CDR3-alpha sequences of a few highly-frequent PUB-I and PUB-HS CDR3β-sequences were also identical or highly-similar between different individuals (**Supplementary Table 4**).

As a control, we assessed if these conserved motifs were predictive for the specificity when searching in our database of

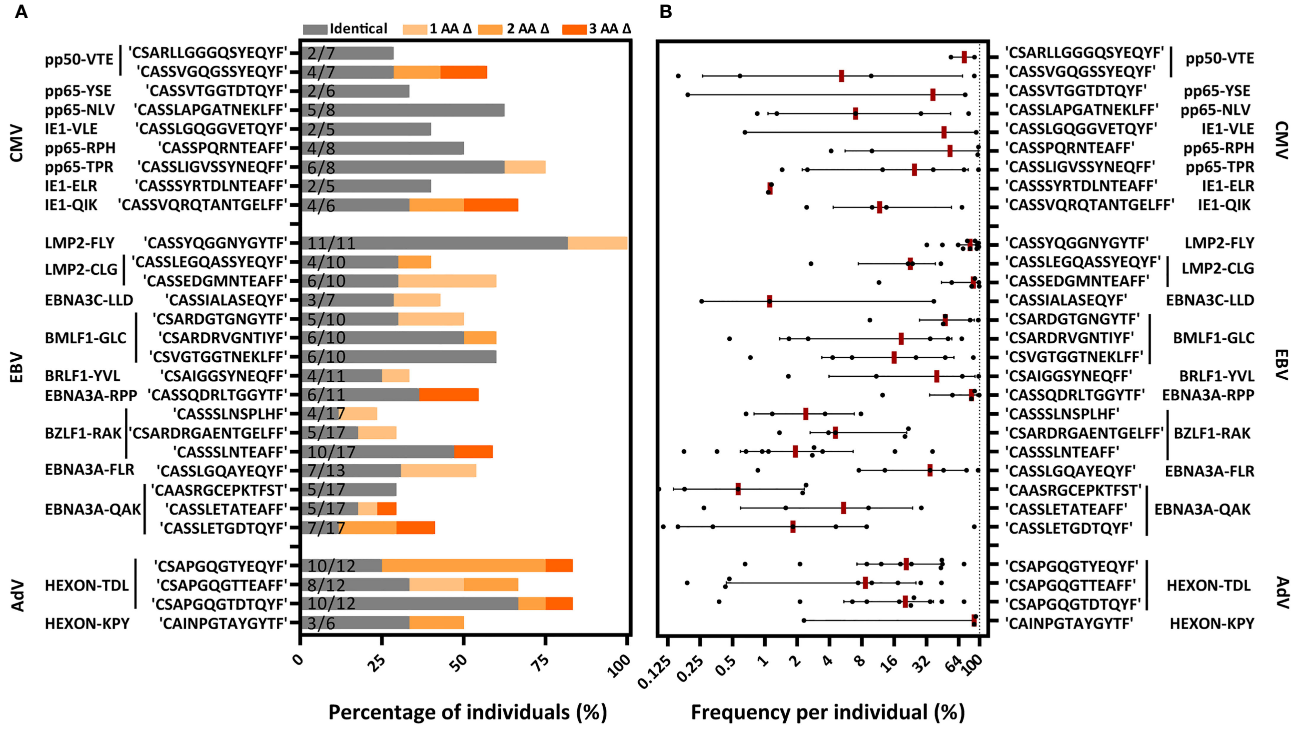

FIGURE 3 | PUB-I and PUB-HS CMV, EBV and AdV-specific CDR3β AA-sequences are common in different individuals and of high frequencies within the T-cell specificities. **(A)** Nine-teen different specificities contained PUB-I CDR3β-sequences, shared by at least 2 individuals. Six specificities contained 2 or 3 different (with different TRBV and/or TRBJ-genes) CDR3β AA-sequences that were found frequently in different individuals. The total numbers of different T-cell populations (different donors) that contained the PUB-I or PUB-HS CDR3β AA-sequences are indicated at the inner-side of the y-axis. The occurrence, shown as percentage among healthy individuals, is shown per CDR3β AA-sequence. PUB-I sequences are shown in grey. Individuals containing PUB-HS sequences with 1, 2 or 3 AA-differences (shown in light-dark orange) compared to the PUB-I sequence were stacked on top of the individuals where the PUB-I sequence was already identified. **(B)** Shown is the sum of frequencies of the PUB-I and PUB-HS (1, 2 and 3 AA-differences) CDR3β AA-sequences per individual. Each dot is one individual, and the red-lines represent the medians with interquartile ranges. AA, amino-acids; nt, nucleotides; Δ, difference(s).

2355 unique CDR3β AA-sequences. The requirement was that each motif should not be present in another specificity. We observed that some specificities contained motifs of only 3 or 4 AAs that were exclusive for that specificity and were not observed in any other specificity (**Table 3**). Altogether, these data show that the variations in the CDR3β AA-sequences were not random, but occurred at specific positions that resulted in conserved regions that were predictive for the specificities.

Computational Analysis Reveals Conserved Regions in CDR3β AA-Sequences Despite Using Different TRBJ-Genes

We hypothesized that if the conserved junctional region is a crucial part of the peptide-HLA binding, virus-specific TCR-repertoires could also contain CDR3β AA-sequences with the same conserved region, while allowing different TRBJ-gene usage, as long as the 3-dimensional conformation would allow this. Since the TRBJ-regions often differ by more than 3 AAs, we were not able to include these as PUB-HS CDR3β AA-sequences. Such PUB-HS CDR3β AA-sequences that use different TRBJ-genes might even further increase the prevalence of PUB-I and PUB-HS CDR3β AA-sequences in the virus-specific TCR-repertoire. To investigate this, we performed a computational analysis using the levenshtein-distances (AA-differences) between all different CDR3β AA-sequences. For four different specificities (EBV-LMP2^{FLY}, EBV-EBNA3A^{RPP}, AdV-E1A^{LLD}, and AdV-HEXON^{TDL}) we observed clustering of CDR3β AA-sequences that expressed the same TRBV-genes while using different TRBJ-genes. For example (**Figure 5A**), the HLA-A*02:01-restricted EBV-LMP2^{FLY}-specific CD8^{pos} T-cell repertoire contained 2 clusters within the cluster of TRBV6-5-expressing T cells (TRBV6-5/TRBJ1-2 and TRBV6-5/TRBJ2-1). The majority of CDR3β AA-sequences within the TRBJ1-2 cluster had a length of 14 AAs, while CDR3β AA-sequences from the TRBJ2-1 cluster had a length of 13 AAs (**Figure 5B**). Analysis of the junctional regions of the TRBV6-5/TRBJ1-2 and TRBV6-5/TRBJ2-1-encoded CDR3β AA-sequences revealed strong conservation of AAs [QGG] on positions 6-8, despite different TRBJ-usage and CDR3 lengths (**Figure 5C**). Similarly, the HLA-A*01:01-restricted AdV-HEXON^{TDL}-specific CD8^{pos} T-cell repertoire contained two large clusters of CDR3β AA-sequences, using TRBV20-1 or TRBV5-1 (**Figure 5D**), all with a CDR3 length of 13 AAs. The first cluster (TRBV20-1) contained

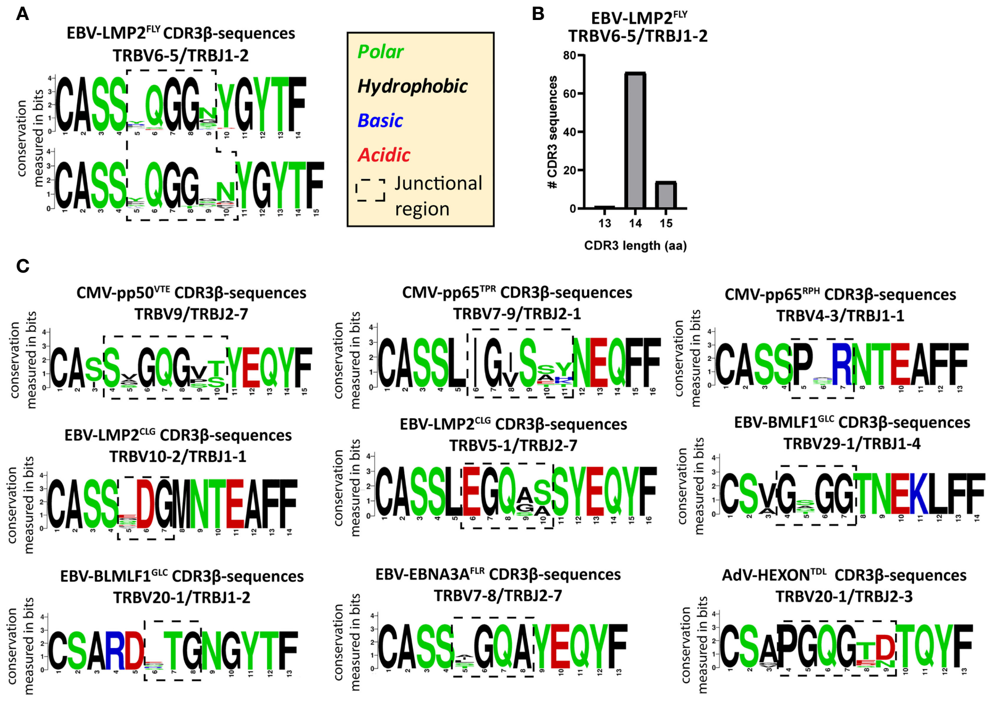

FIGURE 4 | PUB-HS CDR3β AA-sequences show conserved regions and regions with high variability. The levenshtein distance was calculated (i.e. substitution, deletions or insertions of AAs) between CDR3β AA-sequences that express the same TRBV/TRBJ-genes as the PUB-I CDR3β AA-sequence. PUB-HS CDR3β AA-sequences were included with 1, 2 and 3 AA-differences compared to the PUB-I CDR3β AA-sequence. Sequence logos generated using WebLogo (http://weblogo.berkeley.edu/logo.cgi) show the relative frequency of each AA at each given position. The junctional regions (AAs that do not align with the germline TRBV or TRBJ-gene) are shown within the dotted-line box. **(A)** The CDR3β AA-sequences specific for HLA-A*02:01-restricted EBV-LMP2^{FLY} with a CDR3 length of 14 and 15 AAs were stacked and show conserved and variable regions in the CDR3β-region. **(B)** Shown are the CDR3 length distributions of CDR3β AA-sequences specific for EBV-LMP2^{FLY}-expressing TRBV6-5/TRBJ1-2. **(C)** Shown are representative examples of PUB-HS (1, 2 or 3 AA differences) and PUB-I CDR3β AA-sequences that were stacked per specificity and TRBV/TRBJ-usage.

sub-clusters of CDR3β AA-sequences using TRBJ1-1, TRBJ2-3 or TRBJ2-7 and the second cluster (TRBV5-1) contained CDR3β AA-sequences using TRBJ2-1 or TRBJ2-7. AdV-HEXON^{TDL}-specific CDR3β AA-sequences expressing TRBV20-1 revealed strong conservation of AAs [PGQG] on positions 4-7, which fell outside the region encoded by TRBJ (**Figure 5E**). Additionally, AdV-HEXON^{TDL}-specific CDR3β AA-sequences expressing TRBV5-1 revealed strong conservation of AAs [N:D] on positions 4 and 7, despite different TRBJ-usage. These examples illustrate that virus-specific TCR-repertoires can have conserved CDR3β-regions, while using different TRBJ-genes, allowing substantial variability at specific positions encoded by the TRBJ-region. This will further increase the prevalence of PUB-I and PUB-HS CDR3β AA-sequences in the total virus-specific TCR-repertoire.

Individuals With Heterozygous HLA Backgrounds Contain the Same Shared Identical and Highly-Similar CDR3β AA-Sequences

To determine whether the magnitude of PUB-I and PUB-HS CDR3β AA-sequences was particular for our cohort of individuals with a homozygous HLA background, we investigated if the same phenomenon was also present in individuals with a heterogeneous HLA background. We performed the same analyses on virus-specific CD8^{pos} T-cell populations targeting 11 different viral epitopes that were generated and used in the context of a clinical study (20). A total of 1157 CDR3β nucleotide-sequences could be correctly annotated. In total, 695 (61%) nucleotide-sequences resulted in unique CDR3β AA-sequences, that were only found in one individual, and 462 nucleotide-sequences (39%) resulted in 89 different PUB-I CDR3β AA-sequences. From the 695 unique CDR3β AA-sequences, 134 PUB-HS CDR3β nucleotide-sequences were present that differed by 1, 2 or 3 AAs from one of the 89 PUB-I CDR3β AA-sequences. This shows again that also in this cohort a large part (51%) of the total virus-specific TCR-repertoire contained PUB-I and PUB-HS CDR3β nucleotide-sequences. Because the targeted viral epitopes were not fully identical in both cohorts, we could investigate the prevalence of 20 out of 29 PUB-I CDR3β AA-sequences in this cohort. In total, 17 out of 20 CDR3β AA-sequences that were previously identified, could also be identified in this independent cohort. When we included the PUB-HS CDR3β AA-sequences and quantified the 17 PUB-I and PUB-HS CDR3β AA-sequences, these sequences had a similar high prevalence of a

TABLE 3 | Conserved motifs that predict the specificity.

Specificity	TRBV	Shared TCR	TRBJ	Motif
CMV-pp50^{VTE}	9	CAS**S**V**GQG**SSYEQYF	2-7	**S**$\underline{x}$**GQG**
CMV-pp65^{YSE}	9	CASS**VTGGT**DTQYF	2-3	**VTGGT**
CMV-pp65^{NLV}	7-6	CASS**LAPG**ATNEKLFF	1-4	**LAPG**
CMV-IE1^{VLE}	9	CASSL**GQGGV**ETQYF	2-5	**GQGGV**
CMV-pp65^{TPR}	7-9	CAS**SLIG**V**S**SYNEQFF	2-1	**SLIG**$\underline{x}$**S**
CMV-pp65^{RPH}	4-3	CASS**P**Q**RNT**EAFF	1-1	**P**$\underline{x}$**RNT**
CMV-IE1^{QIK}	9	CASS**V**Q**R**QT**ANT**GELFF	2-2	**V**$\underline{x}$**R**$\underline{xx}$**ANT**
CMV-IE1^{ELR}	27	CASSSYR**TDLN**TEAFF	1-1	**TDLN**
EBV-LMP2^{FLY}	6-5	CAS**S**Y**QGG**NYGYTF	1-2	**S**$\underline{x}$**QGG**
EBV-LMP2^{CLG}	10-2	CASSE**DGMN**TEAFF	1-1	**DGMN**
	5-1	CASSL**EGQ**AS**S**YEQYF	2-7	**EGQ**$\underline{xx}$**S**
EBV-EBNA3C^{LLD}	19	CASS**IAL**ASEQYF	2-7	**IAL**
EBV-BMLF1^{GLC}	20-1	CSA**RDR**V**G**NTIYF	1-3	**RDR**(V/T)**G**
	29-1	CSV**G**T**GGTN**EKLFF	1-4	**G**$\underline{x}$**GGTN**
EBV-BRLF1^{YVL}	20-1	CS**AIGGS**YNEQFF	2-1	**AIGGS**
EBV-EBNA3A^{RPP}	4-1	CASSQD**RLTG**GYTF	1-2	**RLTG**
EBV-BZLF1^{RAK}	27	CA**SSSLN**TEAFF	2-1	**SSSLN**
	20-1	CSA**RDR**GA**EN**TGELFF	2-2	**RDR**$\underline{xx}$**EN**
EBV-EBNA3A^{FLR}	7-8	CAS**S**L**GQA**YEQYF	2-7	**S**$\underline{x}$**GQA**
EBV-EBNA3A^{QAK}	5-1	CASS**LET**GGYGYTF	1-2	**LET**(A/G)
AdV-HEXON^{TDL}	20-1	CSA**PGQ**GTDTQYF	2-3	(A/V)**PGQ**
AdV-E1A^{LLD}	20-1	CS**AR**P**GLA**DEQFF	2-1	**AR**$\underline{x}$**GLA**
AdV-HEXON^{KPY}	10-3	CA**INP**GTAYGYTF	1-2	**INP**

We investigated which regions of PUB-I or PUB-HS CDR3β AA-sequences were predictive for the specificity. We searched for each motif in our library of 2355 CDR3β AA-sequences to determine what part of the junctional regions were unique for each specificity, without being present in any other specificity. Underscores with an x represent any of the 20 AAs. Some motifs contain two possible AAs that can be part of the motif which are shown between brackets. The minimum motifs are also shown in bold font in the original CDR3β AA-sequences.

median of 89% among healthy individuals (range 26-100%). (**Figure 6A**). These CDR3β AA-sequences were also present at high frequencies within each virus-specific T-cell population (**Figure 6B**). These data show that the same PUB-I or PUB-HS CDR3β AA-sequences are also present in virus-specific T cells isolated from an independent cohort of individuals with a heterogeneous HLA background with a similar prevalence among donors and frequency within donors.

DISCUSSION

In this study, we quantitatively analyzed the magnitude, defined as prevalence within the population and frequencies within individuals, of public-identical (PUB-I) together with public-highly-similar (PUB-HS) TCRs in TCR-repertoires of CMV, EBV and AdV-specific CD8^{pos} T-cell populations. In total, 2224 (71%) TCR-CDR3β nucleotide-sequences resulted in unique CDR3β AA-sequences, and 905 nucleotide-sequences (29%) resulted in 131 different PUB-I CDR3β AA-sequences that were found in two or more unrelated individuals. These PUB-I CDR3β AA-sequences were distributed over 19 out of 21 virus-specificities and contained 29 different PUB-I CDR3β AA-sequences that were often found in multiple individuals at high frequencies. The virus-specific T-cell populations additionally contained 12% PUB-HS CDR3β AA-sequences, which differed by 1, 2 or 3 AAs compared to the respective PUB-I CDR3β AA-sequences. PUB-HS CDR3β AA-sequences could be found in virus-specific T-cell populations of individuals who did not contain the PUB-I CDR3β AA-sequence as well as of individuals who already contained the PUB-I CDR3β AA-sequence. Analysis of the PUB-I and PUB-HS CDR3β AA-sequences revealed strong conservation of specific AA motifs in the junctional region together with variability of AAs at specific positions at the TRBV/TRBD- and/or TRBD/TRBJ-border regions. Positions with high variability were often adjacent to or even interspersed with the conserved motif. The conserved motifs that we identified were unique for each specificity, and could not be identified in any other specificity in our database. This makes it very likely that these motifs are important for binding of the TCRs to the peptide-HLA complexes. Combined, 41% of the total virus-specific TCR-repertoire consisted of PUB-I and PUB-HS CDR3β nucleotide-sequences. These findings were based on virus-specific T-cell populations derived from two homogeneous donor cohorts that homozygously expressed HLA-A*01:01/HLA-B*08:01 or HLA-A*02:01/HLA-B*07:02. However, we found similar high percentages (51%) of PUB-I and PUB-HS CDR3β nucleotide-sequences within virus-specific T-cell populations from healthy donors with heterogeneous HLA-backgrounds that were generated for a recent clinical study (20). These dominant PUB-I and PUB-HS TCRs probably are a reflection of the viral-antigen-specific T-cell responses that most optimally encountered the peptide-HLA complexes on the infected target cells and could be utilized for the design of future immunotherapy purposes including TCR-gene transfer strategies.

Various explanations have been suggested to underlie the development of public TCRs in T-cell responses targeting the same antigenic epitope (44). One was a high probability that these PUB-I sequences can be generated during V-D-J recombination (28, 45). Furthermore, various nucleotide-sequences can result in the same TCR AA-sequences that

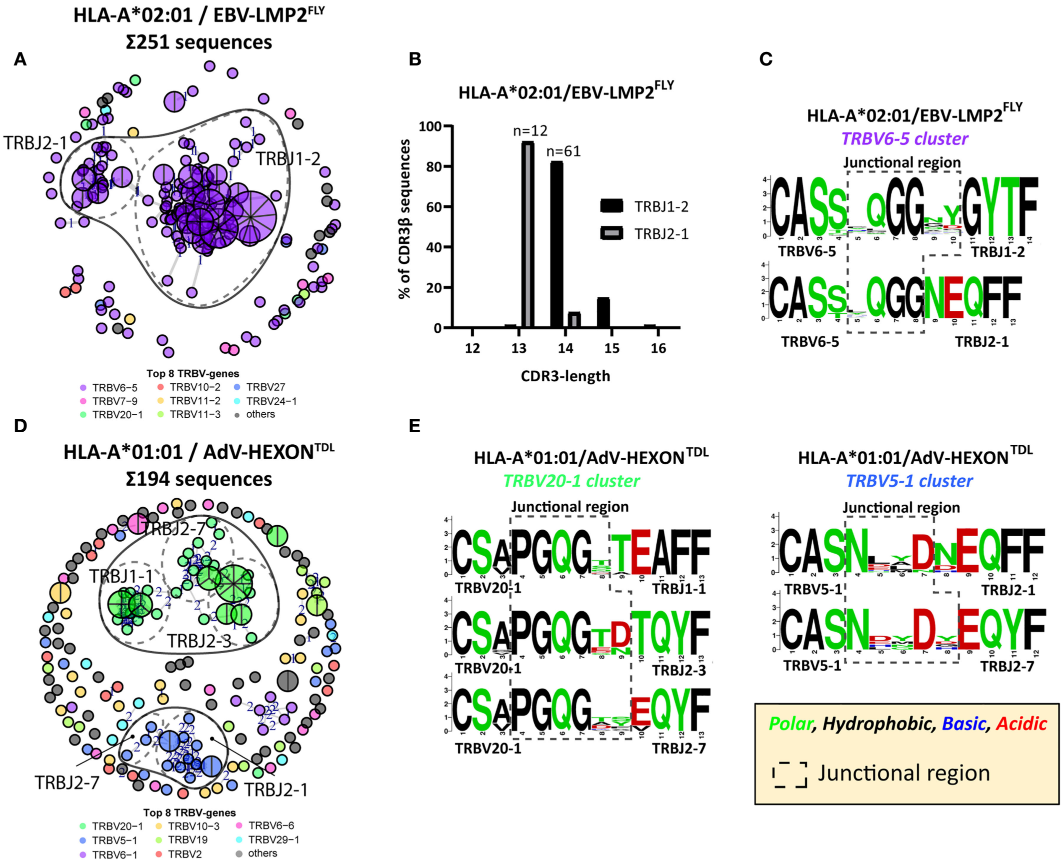

FIGURE 5 | Computation analysis reveals clustering of PUB-HS CDR3β AA-sequences that contained conserved regions in the CDR3β-region. Computational analysis was performed using the levenshtein distance (differences in AAs) between CDR3β AA-sequences of one specificity. CDR3β AA-sequences were plotted and colored according to the top 8 most frequent TRBV-genes and were clustered and linked by a line if they were similar, with a number (levenshtein distance of 1, 2 or 3) representing the differences in AAs. PUB-I CDR3β AA-sequences were plotted as a pie-chart, whereby the size and number of slices indicate in how many individuals this CDR3β AA-sequence was present. Sequence logos generated using WebLogo (http://weblogo.berkeley.edu/logo.cgi) show the relative frequency of each AA at each given position. The junctional region (AAs that do not align with the germline TRBV or TRBJ-gene) are shown within the box with the dotted-line **(A)** Shown is a representative example of a virus-specific CD8^{pos} T-cell population, specific for EBV-LMP2^{FLY} with overlapping clusters of sequences that express different TRBJ-genes, while expressing the same TRBV-gene. **(B)** The lengths of the CDR3β-regions of the two clusters of EBV-LMP2^{FLY}-specific CDR3β-sequences are shown. Varying lengths of the CDR3β-region within a cluster would suggest deletions or insertions, whereby the same length would indicate AA substitutions. **(C)** Shown are the sequence motifs of the two EBV-LMP2^{FLY}-specific clusters. **(D)** Shown is a second representative example of a virus-specific CD8^{pos} T-cell population, specific for AdV-HEXON^{TDL}, with overlapping clusters of sequences that express different TRBJ-genes, while expressing the same TRBV-gene. **(E)** Shown are the sequence motifs of the TRBV20-1 and TRBV5-1-expressing EBV-HEXON^{TDL}-specific clusters.

further increase the probability (46). Selection *in vivo* by optimal antigen-specific proliferation may result in a dominant antigen-specific memory T-cell population (47). These determinants may also lead to TCRs that are highly-similar to the PUB-I sequence, although they were often not included in the analyses of such public T-cell responses. It has been shown that conserved AAs in the CDR3 loop provide a structural framework that is required for the maintenance of the three dimensional TCR-structure (48). A similar structural framework between the PUB-I and PUB-HS sequences can thus lead to a conserved engagement with the peptide/HLA complex (49). Our rationale is that the PUB-I and PUB-HS sequences are part of the same public T-cell response when the same peptide-HLA complex is targeted, the same variable gene is expressed to have identical CDR1 and CDR2 regions and contains the same conserved AAs in the CDR3 loop. With this set of rules, we were able to quantitatively analyze the public T-cell responses and showed that T cells expressing PUB-I TCRs together with T cells that express PUB-HS TCRs made up at least 41% of the total TCR-repertoire. To assess the role of the alpha chains in PUB-I and PUB-HS TCRs, we identified the CDR3α sequence usage of a selection of virus-specific T-cell populations that contained shared TCRβ sequences and the corresponding CDR3α sequences all showed to be identical or highly similar between individuals. However, the high percentages of shared TCR-sequences contradict the findings observed by Madi et al. (50), where they performed immunization in mice with foreign ovalbumin (OVA)-derived peptide that resulted in dominant private TCR-repertoires and

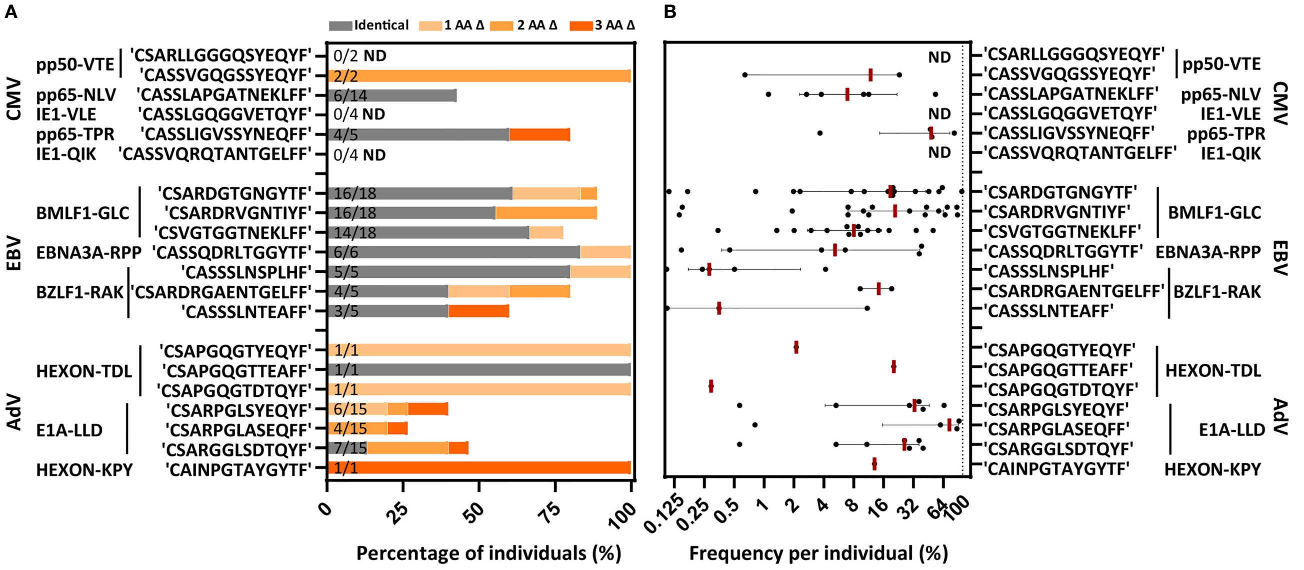

FIGURE 6 | Individuals with a different HLA background from an independent database contain the same PUB-I and PUB-HS CDR3β AA-sequences. Virus-specific T-cell populations targeting 11 different viral-antigens, derived from an independent database, could be evaluated for the occurrence of PUB-I pr PUB-HS CDR3β AA-sequences. **(A)** Nine out of the 11 specificities contained the same PUB-I or PUB-HS CDR3β AA-sequences as in our database. The occurrence, shown as percentages among healthy donors, is shown per CDR3β AA-sequence. PUB-I sequences are shown in grey. PUB-HS CDR3β AA-sequences from other individuals with 1, 2 or 3 AA differences, were stacked on top of the already identified public-identical sequences. The total numbers of different T-cell populations (different donors) that contained the PUB-I or PUB-HS CDR3β-sequences are indicated at the inner-side of the y-axis. **(B)** Shown are the sum of frequencies of the PUB-I or PUB-HS CDR3β AA-sequences per donor. Each dot is one donor shown and the red-lines represent the medians with interquartile ranges. AA, amino-acid; Δ, difference(s); ND, Not detected.

less public TCRs (51). Since virus-specific memory T-cell repertoires in the circulation are shaped based on antigen encounter and subsequent proliferation, the PUB-I and PUB-HS TCR-sequences most likely reflect highly functional T cells capable antigen-driven proliferation. For latent viruses such as CMV, EBV and AdV, virus-specific T cells frequently encounter antigen during episodes of viral reactivation. The presence of PUB-I and PUB-HS TCR-sequences for these virus-specific T cells could be rather high due to this frequent antigen encounter. However, multiple reports also observed shared CDR3β sequences in T-cell populations specific for non-latent viruses such as Influenza, RSV, and SARS-CoV-2 (16, 17, 26), suggesting that this phenomenon is not unique for latent viruses, although the unexpected high magnitude of PUB-I and PUB-HS TCR-sequences that we observed can be unique for latent viruses.

These percentages of PUB-I and PUB-HS TCRs within these virus specific T-cell responses may still be an underestimation since the prerequisite of the identification of a PUB-HS TCR was similarity to a PUB-I TCR that was present in at least 2 individuals. Highly similar TCRs with only mutual similarities without identity in at least 2 individuals were not included as PUB-HS TCRs. Therefore, some of the unique TCRs within the virus-specific T-cell repertoire may also be part of a public T-cell response. This was indeed illustrated by the growing percentages of PUB-I and PUB-HS sequences when including more sampled sequences (51). Although it was suggested that HLA polymorphisms might be a confounding factor that affect the sharing of TCRs (50, 52), we showed that our validation cohort with different HLA-backgrounds revealed frequencies of the PUB-I and PUB-HS TCRs with at least a similar magnitude. Our approach involved a short *ex vivo* expansion of the isolated virus-specific T cells that might have created a bias towards the expansion of the presently identified PUB-I and PUB-HS TCRs, indicating that the actual numbers of PUB-I and PUB-HS in unmanipulated peripheral blood may have even been higher.

In conclusion, our findings demonstrate that a large part of the virus-specific TCR-repertoire contains PUB-I and PUB-HS TCRs at high frequencies in multiple different individuals. Because virus-specific memory T-cell repertoires in the circulation are shaped based on antigen encounter and subsequent proliferation, the PUB-I and PUB-HS TCR-sequences most likely reflect highly functional T cells capable of antigen-driven proliferation. Since it is plausible that the highly-similar TCRs with conserved motifs similarly dock to the peptide-HLA complex as the identical shared TCR-sequences, these PUB-I and PUB-HS sequences can be considered part of the same public T-cell response. Such public TCRs may then be utilized for diagnostic purposes or therapeutic benefit in TCR-gene transfer-based immunotherapy strategies to effectively control viral-reactivation in immuno-compromised patients.

DATA AVAILABILITY STATEMENT

The original contributions presented in the study are publicly available. This data can be found here: https://www.ncbi.nlm.nih.gov/bioproject/PRJNA803981.

AUTHOR CONTRIBUTIONS

WH, DL, LH, and MR performed experiments. AK and GE designed the R-script for computational analyses. WH analyzed results and made the figures. WH, JF, DA, and IJ designed the research and wrote the paper. All authors contributed to the article and approved the submitted version.

FUNDING

This work was supported by Sanquin Research and Landsteiner Laboratory for Blood Cell research [PPO 15-37/Lnumber 2101]. This study was in part also supported by research funding from Stichting den Brinker (The Netherlands, Zeist) that made a donation to the Leukemia fund from the Bontius Foundation (Leiden University Medical Center).

SUPPLEMENTARY MATERIAL

The Supplementary Material for this article can be found online at: https://www.frontiersin.org/articles/10.3389/fimmu.2022.851868/full#supplementary-material

REFERENCES

1. Chien YH, Gascoigne NR, Kavaler J, Lee NE, Davis MM. Somatic Recombination in a Murine T-Cell Receptor Gene. *Nature* (1984) 309 (5966):322–6. doi: 10.1038/309322a0
2. Lefranc MP. Nomenclature of the Human T Cell Receptor Genes. *Curr Protoc Immunol* (2001) Appendix 1:Appendix 1O. doi: 10.1002/0471142735.ima01os40
3. Padovan E, Casorati G, Dellabona P, Meyer S, Brockhaus M, Lanzavecchia A. Expression of Two T Cell Receptor Alpha Chains: Dual Receptor T Cells. *Science* (1993) 262(5132):422–4. doi: 10.1126/science.8211163
4. Davis MM, Bjorkman PJ. T-Cell Antigen Receptor Genes and T-Cell Recognition. *Nature* (1988) 334(6181):395–402. doi: 10.1038/334395a0
5. Borg NA, Ely LK, Beddoe T, Macdonald WA, Reid HH, Clements CS, et al. The CDR3 Regions of an Immunodominant T Cell Receptor Dictate the 'Energetic Landscape' of Peptide-MHC Recognition. *Nat Immunol* (2005) 6 (2):171–80. doi: 10.1038/ni1155
6. Garboczi DN, Ghosh P, Utz U, Fan QR, Biddison WE, Wiley DC. Structure of the Complex Between Human T-Cell Receptor, Viral Peptide and HLA-A2. *Nature* (1996) 384(6605):134–41. doi: 10.1038/384134a0
7. Robins HS, Campregher PV, Srivastava SK, Wacher A, Turtle CJ, Kahsai O, et al. Comprehensive Assessment of T-Cell Receptor Beta-Chain Diversity in Alphabeta T Cells. *Blood* (2009) 114(19):4099–107. doi: 10.1182/blood-2009-04-217604
8. Hebart H, Einsele H. Clinical Aspects of CMV Infection After Stem Cell Transplantation. *Hum Immunol* (2004) 65(5):432–6. doi: 10.1016/j.humimm.2004.02.022
9. Englund J, Feuchtinger T, Ljungman P. Viral Infections in Immunocompromised Patients. *Biol Blood Marrow Transplant* (2011) 17(1 Suppl):S2–5. doi: 10.1016/j.bbmt.2010.11.008
10. Hanley PJ, Cruz CR, Shpall EJ, Bollard CM. Improving Clinical Outcomes Using Adoptively Transferred Immune Cells From Umbilical Cord Blood. *Cytotherapy* (2010) 12(6):713–20. doi: 10.3109/14653249.2010.517518
11. Hanley PJ, Cruz CR, Savoldo B, Leen AM, Stanojevic M, Khalil M, et al. Functionally Active Virus-Specific T Cells That Target CMV, Adenovirus, and EBV can be Expanded From Naive T-Cell Populations in Cord Blood and Will Target a Range of Viral Epitopes. *Blood* (2009) 114(9):1958–67. doi: 10.1182/blood-2009-03-213256
12. Patel S, Chorvinsky E, Albihani S, Cruz CR, Jones RB, Shpall EJ, et al. HIV-Specific T Cells Generated From Naive T Cells Suppress HIV *In Vitro* and Recognize Wide Epitope Breadths. *Mol Ther* (2018) 26(6):1435–46. doi: 10.1016/j.ymthe.2018.04.009
13. Provenzano M, Mocellin S, Bettinotti M, Preuss J, Monsurro V, Marincola FM, et al. Identification of Immune Dominant Cytomegalovirus Epitopes Using Quantitative Real-Time Polymerase Chain Reactions to Measure Interferon-Gamma Production by Peptide-Stimulated Peripheral Blood Mononuclear Cells. *J Immunother* (2002) 25(4):342–51. doi: 10.1097/00002371-200207000-00006
14. Long HM, Meckiff BJ, Taylor GS. The T-Cell Response to Epstein-Barr Virus-New Tricks From an Old Dog. *Front Immunol* (2019) 10:2193. doi: 10.3389/fimmu.2019.02193
15. Schone D, Hrycak CP, Windmann S, Lapuente D, Dittmer U, Tenbusch M, et al. Immunodominance of Adenovirus-Derived CD8(+) T Cell Epitopes Interferes With the Induction of Transgene-Specific Immunity in Adenovirus-Based Immunization. *J Virol* (2017) 91(20):e01184-17. doi: 10.1128/JVI.01184-17
16. Sant S, Grzelak L, Wang Z, Pizzolla A, Koutsakos M, Crowe J, et al. Single-Cell Approach to Influenza-Specific CD8(+) T Cell Receptor Repertoires Across Different Age Groups, Tissues, and Following Influenza Virus Infection. *Front Immunol* (2018) 9:1453. doi: 10.3389/fimmu.2018.01453
17. Schultheiß C, Paschold L, Simnica D, Mohme M, Willscher E, von Wenserski L, et al. Next-Generation Sequencing of T and B Cell Receptor Repertoires From COVID-19 Patients Showed Signatures Associated With Severity of Disease. *Immunity* (2020) 53(2):442–55.e4. doi: 10.1016/j.immuni.2020.06.024
18. Shomuradova AS, Vagida MS, Sheetikov SA, Zornikova KV, Kiryukhin D, Titov A, et al. SARS-CoV-2 Epitopes Are Recognized by a Public and Diverse Repertoire of Human T Cell Receptors. *Immunity* (2020) 53(6):1245–57.e5. doi: 10.1016/j.immuni.2020.11.004
19. Kamga L, Gil A, Song I, Brody R, Ghersi D, Aslan N, et al. CDR3alpha Drives Selection of the Immunodominant Epstein Barr Virus (EBV) BRLF1-Specific CD8 T Cell Receptor Repertoire in Primary Infection. *PloS Pathog* (2019) 15 (11):e1008122. doi: 10.1371/journal.ppat.1008122
20. Roex MCJ, van Balen P, Germeroth L, Hageman L, van Egmond E, Veld SAJ, et al. Generation and Infusion of Multi-Antigen-Specific T Cells to Prevent Complications Early After T-Cell Depleted Allogeneic Stem Cell Transplantation-A Phase I/II Study. *Leukemia* (2020) 34(3):831–44. doi: 10.1038/s41375-019-0600-z
21. Moss PA, Moots RJ, Rosenberg WM, Rowland-Jones SJ, Bodmer HC, McMichael AJ, et al. Extensive Conservation of Alpha and Beta Chains of the Human T-Cell Antigen Receptor Recognizing HLA-A2 and Influenza A Matrix Peptide. *Proc Natl Acad Sci USA* (1991) 88(20):8987–90. doi: 10.1073/pnas.88.20.8987
22. Venturi V, Chin HY, Price DA, Douek DC, Davenport MP. The Role of Production Frequency in the Sharing of Simian Immunodeficiency Virus-Specific CD8+ TCRs Between Macaques. *J Immunol* (2008) 181(4):2597–609. doi: 10.4049/jimmunol.181.4.2597
23. Huth A, Liang X, Krebs S, Blum H, Moosmann A. Antigen-Specific TCR Signatures of Cytomegalovirus Infection. *J Immunol* (2019) 202(3):979–90. doi: 10.4049/jimmunol.1801401
24. Burrows SR, Khanna R, Burrows JM, Moss DJ. An Alloresponse in Humans is Dominated by Cytotoxic T Lymphocytes (CTL) Cross-Reactive With a Single Epstein-Barr Virus CTL Epitope: Implications for Graft-Versus-Host Disease. *J Exp Med* (1994) 179(4):1155–61. doi: 10.1084/jem.179.4.1155
25. Nguyen TH, Bird NL, Grant EJ, Miles JJ, Thomas PG, Kotsimbos TC, et al. Maintenance of the EBV-Specific CD8(+) TCRalphabeta Repertoire in Immunosuppressed Lung Transplant Recipients. *Immunol Cell Biol* (2017) 95(1):77–86. doi: 10.1038/icb.2016.71
26. Billam P, Bonaparte KL, Liu J, Ruckwardt TJ, Chen M, Ryder AB, et al. T Cell Receptor Clonotype Influences Epitope Hierarchy in the CD8+ T Cell Response to Respiratory Syncytial Virus Infection. *J Biol Chem* (2011) 286 (6):4829–41. doi: 10.1074/jbc.M110.191437

27. Shomuradova AS, Vagida MS, Sheetikov SA, Zornikova KV, Kiryukhin D, Titov A, et al. SARS-CoV-2 Epitopes are Recognized by a Public and Diverse Repertoire of Human T-Cell Receptors. *Immunity* (2020) 53(6):1245–57.e5.
28. Venturi V, Price DA, Douek DC, Davenport MP. The Molecular Basis for Public T-Cell Responses? *Nat Rev Immunol* (2008) 8(3):231–8. doi: 10.1038/nri2260
29. Koning MT, Nteleah V, Veelken H, Navarrete MA. Template-Switching Anchored Polymerase Chain Reaction Reliably Amplifies Functional Lambda Light Chain Transcripts of Malignant Lymphoma. *Leuk Lymphoma* (2014) 55(5):1212–4. doi: 10.3109/10428194.2013.828353
30. van Bergen CA, van Luxemburg-Heijs SA, de Wreede LC, Eefting M, von dem Borne PA, van Balen P, et al. Selective Graft-Versus-Leukemia Depends on Magnitude and Diversity of the Alloreactive T Cell Response. *J Clin Invest* (2017) 127(2):517–29. doi: 10.1172/JCI86175
31. Huisman W, Leboux DAT, van der Maarel LE, Hageman L, Amsen D, Falkenburg JHF, et al. Magnitude of Off-Target Allo-HLA Reactivity by Third-Party Donor-Derived Virus-Specific T Cells Is Dictated by HLA-Restriction. *Front Immunol* (2021) 12:630440. doi: 10.3389/fimmu.2021.630440
32. Zhu YY, Machleder EM, Chenchik A, Li R, Siebert PD. Reverse Transcriptase Template Switching: A SMART Approach for Full-Length cDNA Library Construction. *Biotechniques* (2001) 30(4):892–7. doi: 10.2144/01304pf02
33. Bolotin DA, Poslavsky S, Mitrophanov I, Shugay M, Mamedov IZ, Putintseva EV, et al. MiXCR: Software for Comprehensive Adaptive Immunity Profiling. *Nat Methods* (2015) 12(5):380–1. doi: 10.1038/nmeth.3364
34. Csardi G, Nepusz T. The Igraph Software Package for Complex Network Research. *InterJournal* (2005). Complex Systems:1695.
35. Loo MPJ. The Stringdist Package for Approximate String Matching. *R J* (2014) 6:111–22. doi: 10.32614/RJ-2014-011
36. Pagès H, Aboyoun P, Gentleman R, DebRoy S. *Biostrings: Efficient Manipulation of Biological Strings*. R Package Version 2.52.0 (2019).
37. Wickham H, François R, Henry L, Müller K. *dplyr: A Grammar of Data Manipulation*. R Package Version 0.7.6. (2018).
38. Villanueva RAM, Chen ZJ. Ggplot2: Elegant Graphics for Data Analysis (2nd Ed.). *Measurement: Interdiscip Res Perspect* (2019) 17(3):160–7. doi: 10.1080/15366367.2019.1565254
39. Neuwirth E, Neuwirth ME. *RColorBrewer: ColorBrewer Palettes*. R Package Version 1.1-2 (2014).
40. Lewin B. *Genes V. 5th ed*. Oxford, England: Oxford University Press (1994).
41. Roex MCJ, Hageman L, Heemskerk MT, Veld SAJ, van Liempt E, Kester MGD, et al. The Simultaneous Isolation of Multiple High and Low Frequent T-Cell Populations From Donor Peripheral Blood Mononuclear Cells Using the Major Histocompatibility Complex I-Streptamer Isolation Technology. *Cytotherapy* (2018) 20(4):543–55. doi: 10.1016/j.jcyt.2018.01.008
42. Marrack P, Scott-Browne JP, Dai S, Gapin L, Kappler JW. Evolutionarily Conserved Amino Acids That Control TCR-MHC Interaction. *Annu Rev Immunol* (2008) 26:171–203. doi: 10.1146/annurev.immunol.26.021607.090421
43. Huisman W, Gille I, van der Maarel LE, Hageman L, Morton LT, de Jong RCM, et al. Identification of Functional HLA-A*01 :01-Restricted EBV-LMP2-Specific T-Cell Receptors. *J Infect Dis* (2020). doi: 10.1093/infdis/jiaa512
44. Li H, Ye C, Ji G, Han J. Determinants of Public T Cell Responses. *Cell Res* (2012) 22(1):33–42. doi: 10.1038/cr.2012.1
45. Robins HS, Srivastava SK, Campregher PV, Turtle CJ, Andriesen J, Riddell SR, et al. Overlap and Effective Size of the Human CD8+ T Cell Receptor Repertoire. *Sci Transl Med* (2010) 2(47):47ra64. doi: 10.1126/scitranslmed.3001442
46. Quigley MF, Greenaway HY, Venturi V, Lindsay R, Quinn KM, Seder RA, et al. Convergent Recombination Shapes the Clonotypic Landscape of the Naive T-Cell Repertoire. *Proc Natl Acad Sci U S A* (2010) 107(45):19414–9. doi: 10.1073/pnas.1010586107
47. Price DA, Brenchley JM, Ruff LE, Betts MR, Hill BJ, Roederer M, et al. Avidity for Antigen Shapes Clonal Dominance in CD8+ T Cell Populations Specific for Persistent DNA Viruses. *J Exp Med* (2005) 202(10):1349–61. doi: 10.1084/jem.20051357
48. Bourcier KD, Lim D-G, Ding Y-H, Smith KJ, Wucherpfennig K, Hafler DA. Conserved CDR3 Regions in T-Cell Receptor (TCR) Cd8+T Cells That Recognize the Tax11-19/HLA-A*0201 Complex in a Subject Infected With Human T-Cell Leukemia Virus Type 1: Relationship of T-Cell Fine Specificity and Major Histocompatibility Complex/Peptide/TCR Crystal Structure. *J Virol* (2001) 75(20):9836–43. doi: 10.1128/JVI.75.20.9836-9843.2001
49. Szeto C, Lobos CA, Nguyen AT, Gras S. TCR Recognition of Peptide-MHC-I: Rule Makers and Breakers. *Int J Mol Sci* (2020) 22(1):68. doi: 10.3390/ijms22010068
50. Madi A, Poran A, Shifrut E, Reich-Zeliger S, Greenstein E, Zaretsky I, et al. T Cell Receptor Repertoires of Mice and Humans Are Clustered in Similarity Networks Around Conserved Public CDR3 Sequences. *Elife* (2017) 6.
51. Madi A, Shifrut E, Reich-Zeliger S, Gal H, Best K, Ndifon W, et al. T-Cell Receptor Repertoires Share a Restricted Set of Public and Abundant CDR3 Sequences That Are Associated With Self-Related Immunity. *Genome Res* (2014) 24(10):1603–12. doi: 10.1101/gr.170753.113
52. Murugan A, Mora T, Walczak AM, Callan CGJr. Statistical Inference of the Generation Probability of T-Cell Receptors From Sequence Repertoires. *Proc Natl Acad Sci USA* (2012) 109(40):16161–6. doi: 10.1073/pnas.1212755109

Conflict of Interest: The authors declare that the research was conducted in the absence of any commercial or financial relationships that could be construed as a potential conflict of interest.

frontiers
in Immunology

ORIGINAL RESEARCH
published: 28 March 2022
doi: 10.3389/fimmu.2022.842870

The Host Peritoneal Cavity Harbors Prominent Memory Th2 and Early Recall Responses to an Intestinal Nematode

Ivet A. Yordanova[1]*, Karsten Jürchott[2], Svenja Steinfelder[3], Katrin Vogt[4], Ulrike Krüger[5], Anja A. Kühl[6], Birgit Sawitzki[4] and Susanne Hartmann[1]*

[1] Institute of Immunology, Center for Infection Medicine, Freie Universität Berlin, Berlin, Germany, [2] Berlin Institute of Health Center for Regenerative Therapies (BCRT), Charité Universitätsmedizin Berlin, Berlin, Germany, [3] Max-Delbrück Center for Molecular Medicine, Berlin, Germany, [4] Institute of Medical Immunology, Charité Universitätsmedizin Berlin, Berlin, Germany, [5] Core Unite Genomics, Berlin Institute of Health (BIH), Berlin, Germany, [6] Charité Universitätsmedizin Berlin, Corporate Member of Freie Universität Berlin und Humboldt-Universität zu Berlin, iPATH.Berlin, Core Unit for Immunopathology for Experimental Models, Berlin, Germany

Edited by:
Francesca Di Rosa,
Italian National Research Council, Italy

Reviewed by:
Dragana Jankovic,
National Institute of Allergy and Infectious Diseases (NIH), United States
Lucy Helen Jackson-Jones,
Lancaster University, United Kingdom
Simon Babayan,
University of Glasgow, United Kingdom

***Correspondence:**
Ivet A. Yordanova
ivet.yordanova@fu-berlin.de
Susanne Hartmann
susanne.hartmann@fu-berlin.de

Specialty section:
This article was submitted to Immunological Memory, a section of the journal Frontiers in Immunology

Received: 24 December 2021
Accepted: 04 March 2022
Published: 28 March 2022

Citation:
Yordanova IA, Jürchott K, Steinfelder S, Vogt K, Krüger U, Kühl AA, Sawitzki B and Hartmann S (2022) The Host Peritoneal Cavity Harbors Prominent Memory Th2 and Early Recall Responses to an Intestinal Nematode. Front. Immunol. 13:842870. doi: 10.3389/fimmu.2022.842870

Intestinal parasitic nematodes affect a quarter of the world's population, typically eliciting prominent effector Th2-driven host immune responses. As not all infected hosts develop protection against reinfection, our current understanding of nematode-induced memory Th2 responses remains limited. Here, we investigated the activation of memory Th2 cells and the mechanisms driving early recall responses to the enteric nematode *Heligmosomoides polygyrus* in mice. We show that nematode-cured mice harbor memory Th2 cells in lymphoid and non-lymphoid organs with distinct transcriptional profiles, expressing recirculation markers like CCR7 and CD62-L in the mesenteric lymph nodes (mLN), and costimulatory markers like Ox40, as well as tissue homing and activation markers like CCR2, CD69 and CD40L in the gut and peritoneal cavity (PEC). While memory Th2 cells persist systemically in both lymphoid and non-lymphoid tissues following cure of infection, peritoneal memory Th2 cells in particular displayed an initial prominent expansion and strong parasite-specific Th2 responses during early recall responses to a challenge nematode infection. This effect was paralleled by a significant influx of dendritic cells (DC) and eosinophils, both also appearing exclusively in the peritoneal cavity of reinfected mice. In addition, we show that within the peritoneal membrane lined by peritoneal mesothelial cells (PeM), the gene expression levels of cell adhesion markers VCAM-1 and ICAM-1 decrease significantly in response to a secondary infection. Overall, our findings indicate that the host peritoneal cavity in particular harbors prominent memory Th2 cells and appears to respond directly to *H. polygyrus* by an early recall response *via* differential regulation of cell adhesion markers, marking the peritoneal cavity an important site for host immune responses to an enteric pathogen.

Keywords: memory Th2 cell, intestinal nematode, peritoneal cavity, dendritic cells, eosinophils, Ox40, recall response

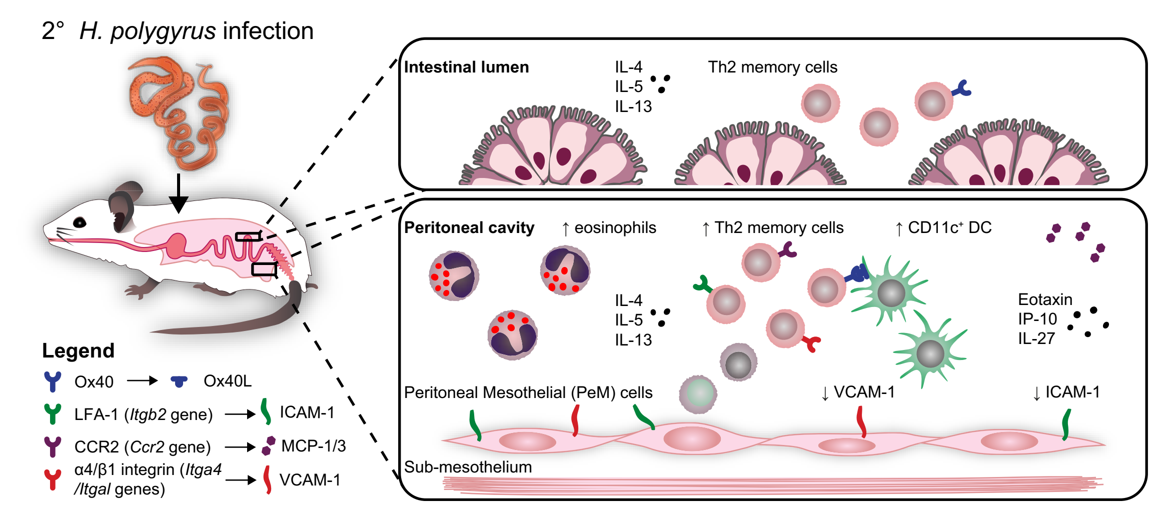

GRAPHICAL ABSTRACT | Freie Universität Berlin owns the copyright to the graphical abstract.

INTRODUCTION

Following antigen exposure during a primary infection, the host immune system typically initiates molecular and cellular processes of immunological memory, reliant on functional long-lived CD4$^+$ or CD8$^+$ memory T cells (1, 2). These memory T cells normally seed lymphoid and non-lymphoid tissues as either tissue-resident memory (T_{RM}), recirculating effector memory (T_{EM}) or central memory T cells (T_{CM}). While T_{CM} cells with a typical CD4$^+$CD44$^+$CD62-L$^+$ phenotype primarily recirculate between blood and secondary lymphoid organs, CD4$^+$CD44$^+$CD62-L$^-$ T_{EM} migrate between blood and non-lymphoid tissues. In contrast, CD4$^+$CD44$^+$CD62-L$^-$ T_{RM} express various tissue homing and retention markers like CD49d, CD69 or CD103 and take up residence in mucosal barrier tissues (3, 4). Upon pathogen re-exposure, T_{RM} cells are thus able to coordinate a faster, localized recall immune response to re-infection.

Humans typically develop only limited protective immunity against re-infection with parasitic nematodes, evidenced by commonly occurring re-infections in endemic areas (5, 6). Nevertheless, some evidence exists of the development of effective, albeit partial protective immunity against nematodes with age (7, 8). In both humans and animals, the signature effector responses to a primary nematode infection rely on Gata3$^+$ effector Th2 cells, IgE and IgG antibody production, alternatively-activated macrophages (AAM) and suppressive Foxp3$^+$ regulatory T cells (Treg) (9–12). We have shown that mice infected with the strictly intestinal nematode *Heligmosomoides polygyrus* harbor prominent tissue-resident memory Th2 cells in various locations, including the small intestinal lamina propria (siLP) and the peritoneal cavity (PEC) 8 weeks post-cure of infection (4). These cells secrete high levels of IL-4, IL-5 and IL-13 cytokines upon *in vitro* restimulation, while upon adoptive transfer they reduce female worm fecundity, indicative of a protective role (4). Functional memory Th2 cells also accumulate in the lung following infection with the tissue-migratory nematode *Nippostrongylus brasiliensis* in mice, conferring protection to re-infection in an IL-4- and eosinophil-dependent manner (13, 14). *H. polygyrus*-induced activated T cells in the lung are also associated with cross-protection to a *N. brasiliensis* challenge infection (15), highlighting the systemic distribution and cross-protective potential of memory T cells against unrelated nematodes (16).

In light of our previous findings on the presence of highly functional peritoneal memory Th2 cells in *H. polygyrus*-cured mice, the local mechanisms driving immune cell recruitment and activation in the peritoneal cavity during an otherwise strictly intestinal infection remain unclear. Thus, here we focused on characterizing the transcriptional profiles of nematode-induced peritoneal memory Th2 cells, their activation during early recall responses to *H. polygyrus* and local mechanisms in the peritoneal compartment potentially influencing immune cell recruitment and activation following cure and reinfection.

RESULTS

Nematode-Cured Mice Harbor Long-Lived, Phenotypically Distinct CD4$^+$ T Cells in Lymphoid and Non-Lymphoid Organs

Building on our previous work, here we assessed the persistence of memory Th2 cells in lymphoid and non-lymphoid organs up to 3 months (12 weeks) following the cure of a primary nematode infection (**Figure 1A**). We could show that *H. polygyrus*-cured mice harbor overall stable frequencies (**Figures 1B**, **S1A**) and absolute numbers (data not shown) of memory Th2 cells up to 3 months post-cure in the PEC and siLP at 8 and 12 weeks post-cure, and a trend for mildly elevated frequencies of memory Th2 cells in the mLN and lungs of mice by 12 weeks post-cure,

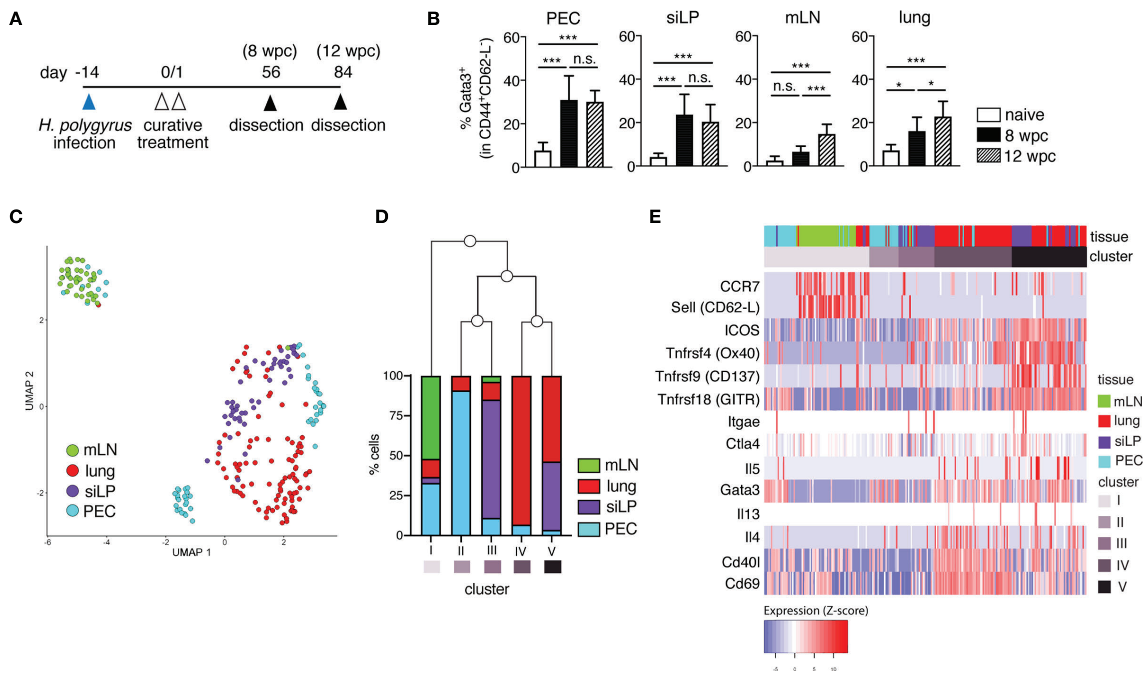

FIGURE 1 | Memory T cells persist long-term and display distinct transcriptional profiles in lymphoid versus non-lymphoid tissues following primary nematode infection. **(A)** Experimental set-up. Mice were infected *via* oral inoculation with 225 infective L3 *H. polygyrus* larvae and were cured of infection 14 days later *via* oral administration of 2 mg/mouse pyrantel pamoate anthelminthic on two consecutive days. The mice were then allowed to rest and were sacrificed 8- and 12-weeks post-cure. **(B)** Frequencies of memory Th2 cells in peritoneal cavity (PEC), small intestinal lamina propria (siLP), mesenteric lymph nodes (mLN) and lung of naïve and cured mice. **(C)** UMAP of single-cell RNA-seq data of sorted CD4$^+$ T cells from PEC, siLP, mLN and lungs of mice sacrificed at 8 weeks post-cure. **(D)** Bar graph illustrating the five different clusters defined by hierarchical clustering of hyper-variable expressed genes in the single cell transcriptomes and the frequencies of cells from each tissue contributing to each cluster. **(E)** Heatmap representation of selected marker genes. The order of the columns derived from the hierarchical clustering of the hyper-variable expressed genes and the order of the rows was predefined by the authors. Different colours correspond to the scaled expression (Z-score) of each gene in each cell. The data in **(B)** are pooled from two independent experiments with n = 3-5 mice per group. Statistical analysis in **(B)** was done using one-way ANOVA combined with Tukey's multiple comparison test. * $p < 0.05$, *** $p < 0.001$, n.s., not significant. For sorting of CD4$^+$ T cells for RNA-seq analysis, two mice were infected and cured as described in **(A)**. 8 weeks post-cure the mice were killed for single cell sorting.

possibly as a contribution of recirculating populations of memory Th2 cells at these tissue sites.

To characterize the transcriptional profiles of nematode-induced memory T cells, next we performed single cell transcriptomics on sorted CD4$^+$CD45.2$^-$ T cells from two *H. polygyrus*-cured mice at 8 weeks post-cure (**Figures 1C–E** and **S1B**, **S2**; **Tables S1–3**). CD4$^+$ T cells sorted from PEC, siLP, mLN and lung at a purity of > 90% and displayed distinct clustering primarily based on their tissue origin (**Figures 1C, D** and **S1B**). Expectedly, mLN-sorted cells (cluster I) clustered more distinctly from CD4$^+$ T cells sorted from non-lymphoid organs (cluster II-V), while clusters comprising high proportions of cells sorted from the same organ (e.g. clusters IV and V) related more closely to each other. Interestingly, for clusters II and III comprising predominantly PEC and siLP-sorted cells, respectively, we observed a shared transcriptional profile of peritoneal-resident and gut-resident CD4$^+$ T cells (**Figure 1D**). We also found upregulated expression of several genes like *Ccr7* (CCR7) and *Sell* (CD62-L) in mLN cells, markers typically associated with recirculating T$_{CM}$ cells (**Figure 1E**; **Table S1**). In contrast, Th2-associated genes like *Gata3, Il4, Il5, Il13*, costimulatory markers *Icos*, *Tnfrsf4* (Ox40), *Tnfrsf9* (CD137) and *Tnfrsf18* (GITR), as well as genes like *Cd69* and *CD40l* encoding tissue-homing and activation markers were differentially expressed in PEC, siLP and lung, consistent with the expected tissue-resident phenotype of memory cells in these tissues (**Figure 1E** and **Table S1**).

To better evaluate the heterogeneous transcriptional profile of peritoneal T cells in nematode-cured mice, we further analyzed the three smaller sub-clusters of peritoneal sorted CD4$^+$ T cells (**Figures 1C–E, S1B, S2**). Here, marker genes of cluster 1 (PEC1) showed prominent over-representation in gene ontology (GO) terms like *cell migration*, *cell-cell adhesion*, *interleukin-4 secretion* and *CD4-positive alpha-beta T cell differentiation*, but no *cellular response to interleukin-7*, in line with the expected transcriptional profile of quiescent memory T cells. In contrast, over-representation of genes in cluster 3 (PEC3) can be found in GO terms like *positive regulation of T cell mediated cytotoxicity*, *positive regulation of T-cell tolerance induction* and *regulation of T-cell anergy*, rather indicative of a cluster of peritoneal regulatory T cells (Treg) (**Figure S2**). Thus, a diverse pool of memory Th2 cells could be identified in the peritoneal cavity 8 weeks after cure of infection.

Overall, our RNAseq analysis in *H. polygyrus*-cured mice revealed that, at 8 weeks following cure of a primary nematode infection, mice harbor both a circulating pool of central memory-type CD4^{+} cells in secondary lymph organs like the mLN, and CD4^{+} T cells with a tissue-resident, antigen-experienced Th2 phenotype. Moreover, distinct sub-clustering of PEC cells further highlights the presence of both memory Th2 and Treg-like populations, highlighting the accumulation of diverse CD4^{+} populations in the peritoneal cavity of nematode-cured mice.

Re-Infected Mice Display a Strong Th2 Recall Response to *H. polygyrus*

To better characterize the early memory Th2 recall responses to a secondary nematode infection, we infected and cured C57BL/6 mice of *H. polygyrus* (cured). 8 weeks post-cure, 8-12 of the cured mice were challenged with a secondary *H. polygyrus* infection and were analyzed 3 days post-challenge (reinfected, **Figure 2A**). One major novel finding here was the significant expansion of Gata3^{+}CD44^{+}CD62-L^{-}Foxp3^{-} memory Th2 cells observed in the peritoneal compartment only, but not in the siLP, mLN or lungs of reinfected mice (**Figure 2B**). Furthermore, the expanding population of peritoneal memory Th2 cells was strongly cytokine competent, evidenced by the significantly elevated numbers of IL-4, IL-5 and IL-13-producing memory Th2 cells detected in the PEC (**Figures 2C, D**). In contrast, a significant expansion of cytokine^{+} memory Th2 cells was not observed in the siLP, mLN or lung of reinfected mice 3 days post-challenge infection (**Figures 2B, D** and **S3B–D**). Interestingly, the marked increase in peritoneal IL-5^{+} Th2 cell numbers in the *H. polygyrus*-reinfected group was further paralleled by a significant influx of eosinophils into the peritoneal cavity, but not in other tissue sites, indicative of memory Th2-driven peritoneal eosinophilia (**Figure S4**). This finding was further

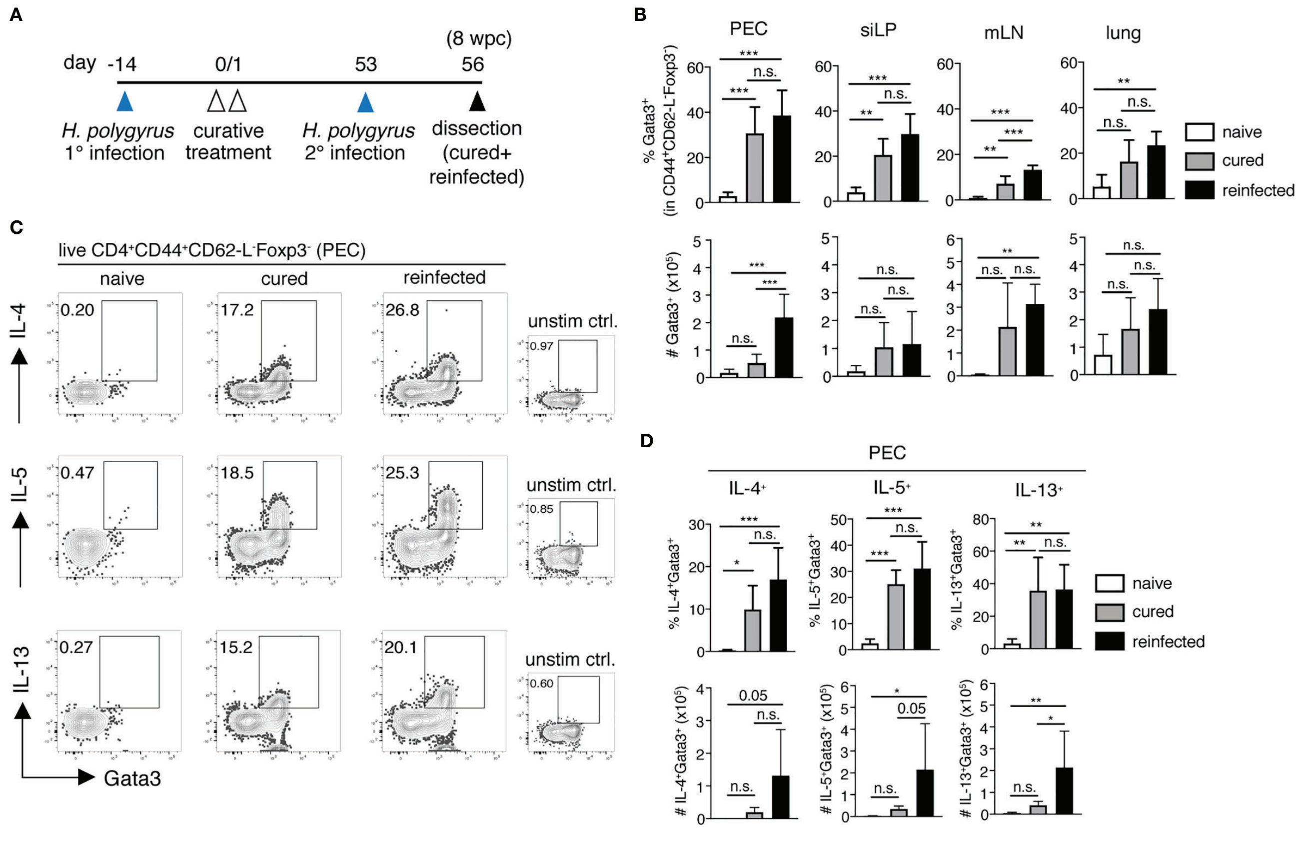

FIGURE 2 | The peritoneum harbours significant memory Th2 cell expansion and cytokine release following *H. polygyrus* challenge infection. **(A)** Experimental set-up. Briefly, mice were infected *via* oral inoculation with 225 infective L3 *H. polygyrus* larvae and were cured of infection 14 days later *via* oral administration of 2mg/mouse pyrantel pamoate anti-helminthic on two consecutive days. All the cured mice were then allowed to rest. 8 weeks post-cure (day 53), a number of cured mice received a challenge *H. polygyrus* infection (reinfected group) and were sacrificed 3 days post-challenge (day 56) alongside un-challenged cured mice (cured group) and naïve controls for further analysis. **(B)** Frequencies (top panel) and absolute cell numbers (bottom panel) of Gata3^{+}CD4^{+}CD44^{+}CD62-L^{-}Foxp3^{-} memory Th2 cells in the peritoneal cavity (PEC), small intestinal lamina propria (siLP), mesenteric lymph nodes (mLN) and lungs of naïve, cured and reinfected mice. **(C)** Representative FACS plots showing cytokine^{+} PEC-resident memory Th2 cells following *in vitro* PMA/Ionomycin stimulation and corresponding unstimulated controls. **(D)** Frequencies (top panel) and absolute cell numbers (bottom panel) of IL-4^{+}, IL-5^{+} and IL-13^{+} memory Th2 cells in the PEC of naïve, cured and reinfected mice. The data are pooled from two independent experiments with n = 3-5 mice per group. Statistical analysis was done using one-way ANOVA combined with Tukey's multiple comparison test. * $p < 0.05$, ** $p < 0.01$, *** $p < 0.001$. n.s., not significant.

emphasized by a lack of notable eosinophil infiltration into the peritoneal cavity of mice at 3 days post-primary infection (data not shown) and therefore confirms peritoneal eosinophilia as a particular feature of host recall responses to a secondary nematode infection. Thus, our results reveal the presence of a prominent Th2 recall response, localized specifically in the peritoneal cavity early following secondary *H. polygyrus* infection.

The Peritoneal Cavity Harbors Activated Parasite-Specific Ox40$^+$ Memory Th2 Cells

Among the several upregulated costimulatory markers highlighted by the scRNA-seq analysis of non-lymphoid organs, including the PEC, was Ox40 (CD134) (**Figure 1E** and **Table S1**). Ox40 is an early inducible costimulatory molecule, normally promoting the survival and function of memory Th2 cells. Mice deficient for its only known ligand Ox40L (Ox40L$^{-/-}$ mice) show impaired adult worm expulsion, lower IL-4 production and parasite-specific IgE responses following a secondary *H. polygyrus* infection, highlighting Ox40-Ox40L interactions as key for host immunity to a challenge nematode infection (17). Here, we profiled the *ex vivo* Ox40 expression on memory Th2 cells, comparing our cured and reinfected groups as a measure of the early induction and reactivation of host T cell responses. We found that *H. polygyrus* induces a prominent expansion of Ox40$^+$ memory Th2 cell numbers specifically in the PEC, but not in other organs, as early as 3 days post-challenge infection (**Figure 3A**). Furthermore, peritoneal Ox40$^+$ memory Th2 cells expressed significantly higher levels of the activation marker CD69 compared with Ox40$^-$ memory Th2 cells, in line with the early inducible nature of Ox40 upon T-cell engagement with antigen-presenting cells (APCs) (**Figure 3B**).

Next, we asked whether this early memory Th2 cell reactivation in the peritoneal cavity constitutes a parasite-specific recall response. For this, we restimulated whole PEC and mLN cells from naïve and cured mice *in vitro* with anti-CD3/CD28 antibodies or with *H. polygyrus* excretory-secretory products (HES, 10µg/mL) for 72h (3 days), matching the *ex vivo* end-point of secondary infection in the reinfected group (**Figures 3C–F** and **S5**). While HES failed to induce a detectable parasite-specific Ox40 expression in naïve mice, we observed a significant increase in Ox40 expression on PEC, but not mLN cells from cured mice (**Figures 3E** and **S5A**). This was paralleled by increased levels of HES-specific IL-5 release in restimulated samples from the PEC of cured mice (**Figure 3F**). In contrast, no significant parasite-specific IL-5 was detected in restimulated mLN cells (**Figure S5B**). These findings therefore clearly indicate that the murine peritoneal compartment specifically conditions an early parasite-specific memory Th2 recall response against an intestinal parasitic nematode.

Early Peritoneal Recall Responses to *H. polygyrus* Involve Ox40/Ox40L Interactions

To establish whether a corresponding increase in Ox40L expression on peritoneal APCs occurs during early recall responses to *H. polygyrus*, next we assessed the expression of Ox40L on CD11c$^+$MHC-II$^+$ dendritic cells (DCs) in the PEC, siLP, mLN and lungs of naïve, cured and reinfected mice (**Figures 3G, H**). DCs are a known source of Ox40L and provide key signaling for the priming and induction of both primary and memory Th2 cell responses (17, 18). Here, analysis of total CD11c$^+$MHC-II$^+$ DC numbers revealed a significant influx of DCs in the peritoneal compartment and to a lesser extent into the mLN of *H. polygyrus*-reinfected mice (**Figure 3G**). More importantly, however, a significant increase in Ox40L expression was only detectable on peritoneal DCs following secondary nematode infection (**Figure 3H**). A correlation analysis also revealed that the upregulated Ox40L expression on peritoneal DCs strongly correlates with the increased Ox40 expression on peritoneal memory Th2 cells (**Figure 3I**). Overall, these results therefore suggest that the murine peritoneal cavity is an early site of Ox40-Ox40L interactions between DCs and resident memory Th2 cells as early as 3 days post-challenge infection with *H. polygyrus*.

The Peritoneum Downregulates VCAM-1 and ICAM-1 Expression in Response to *H. polygyrus*

Considering the notable peritoneal localization of early host recall responses to secondary *H. polygyrus* infection shown here, next we aimed to decipher what mechanisms potentially drive this influx of immune cells into the peritoneal cavity of nematode-reinfected mice. The peritoneal membrane is typically lined by a layer of squamous peritoneal mesothelial (PeM) cells, expressing various cell adhesion and migration markers (19–21). Returning to our scRNAseq analysis, we found that compared with sorted gut CD4$^+$ T cells, peritoneal T cells show elevated gene expression levels of cell adhesion-associated markers like *Itgb2* (encodes lymphocyte function associated antigen-1 (LFA-1), which binds induced cell adhesion marker 1 (ICAM-1)), *Ccr2* (encodes chemokine receptor 2 (CCR2), which binds monocyte chemoattractant proteins 1 and 3 (MCP-1/3)), *Itga4* and *Itgal* (encode the integrin α4β1 (CD49d/CD29), which binds vascular cell adhesion marker 1 (VCAM-1)) (**Figure 4A**).

Assessing the gene expression of *Vcam1* and *Icam1* on PeM cells *via* immunofluorescence microscopy and qPCR, we found that while in naive and cured mice there are stable gene expression levels of both *Vcam1* and *Icam1*, reinfected mice display significantly lower expression of both genes (**Figures 4B, C**). In contrast, a similar downregulation of *Vcam1* or *Icam1* gene expression was not observed in mice killed at 3 days post-primary infection (data not shown). Next, to see whether these changes in *Vcam1* and *Icam1* expression potentially correlate with later shifts in host Th2 recall responses towards the site of infection in the gut, we also assessed the numbers of Th2 cells in both the PEC and the gut-draining mLN of mice at 14 days post-challenge infection (**Figure 4D**). Here, by day 14 post-challenge we found that while total numbers of Gata3$^+$ Th2 cells in the PEC were no longer increasing, there was a contrasting significant increase in Th2 cell numbers in the mLN (**Figure 4D**). In summary, these findings indicate that while the host peritoneum maintains stable levels of cell adhesion marker expression of VCAM-1 and ICAM-1 under

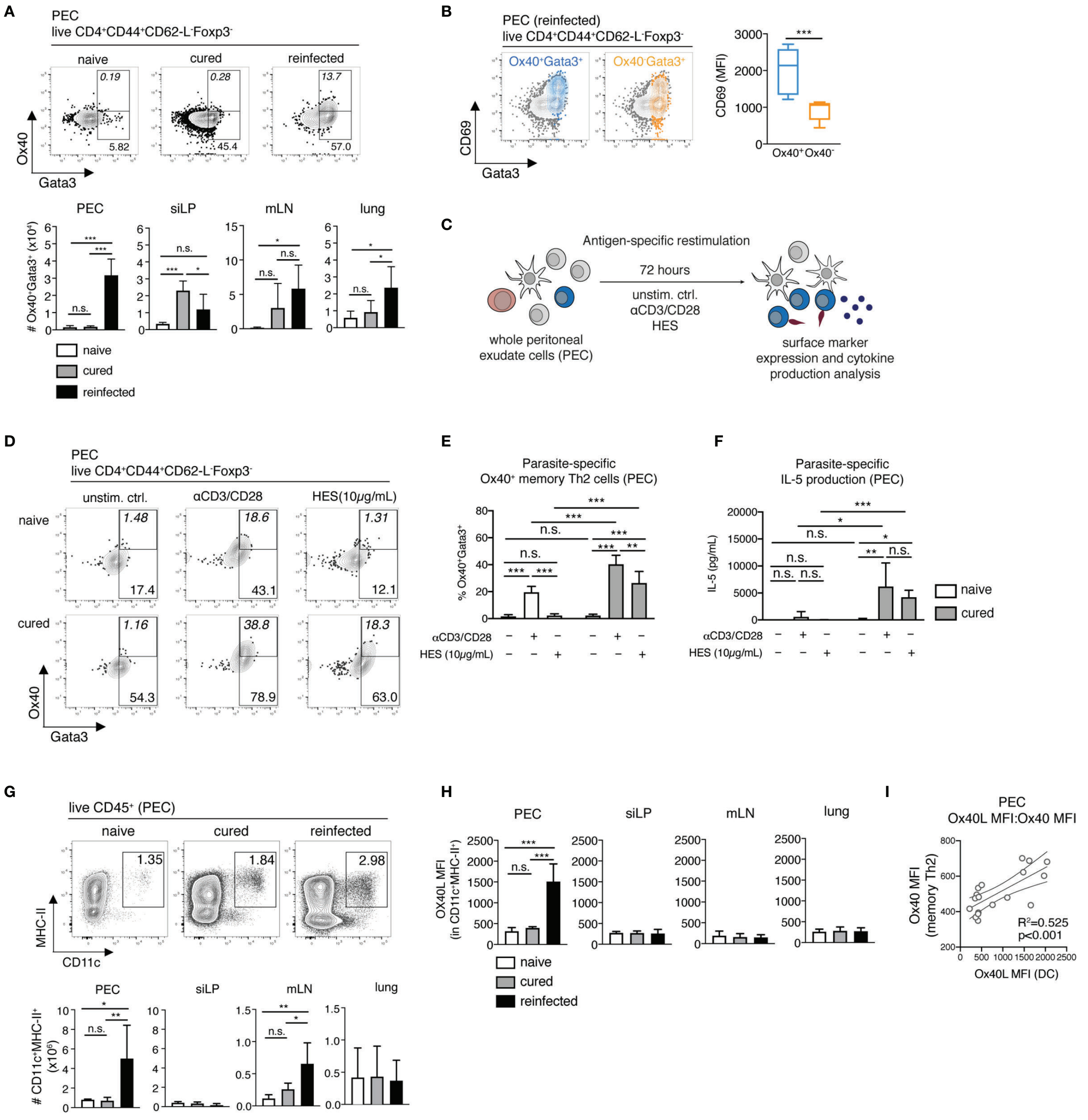

FIGURE 3 | Parasite-specific Ox40$^+$ memory Th2 cells and Ox40L$^+$ DCs accumulate in the peritoneum during early recall responses to *H. polygyrus*. **(A)** Exemplary contour plots of Ox40 and Gata3 expression and absolute cell numbers of Ox40$^+$Gata3$^+$ memory Th2 cells in the PEC, siLP, mLN and lung of naïve, cured and reinfected mice. **(B)** Exemplary overlay plots and mean fluorescence intensity of CD69 expression by Ox40$^+$Gata3$^+$ (blue) and Ox40$^-$Gata3$^+$ (yellow) memory Th2 cells in the PEC of reinfected mice. **(C)** Schematic representation of the antigen-specific *in vitro* restimulation of whole PEC and mLN cells. **(D)** Exemplary plots of Ox40 and Gata3 expression by CD4$^+$CD44$^+$CD62-L$^-$Foxp3$^-$ memory Th2 cells following a 72-hour *in vitro* restimulation with αCD3/CD28 monoclonal antibodies and *H. polygyrus* excretory/secretory antigen (HES) of whole PEC cells from naïve and cured mice. **(E)** Frequencies of Ox40$^+$Gata3$^+$ memory Th2 cells following antigen-specific *in vitro* restimulation. **(F)** IL-5 cytokine levels in cell culture supernatants following the *in vitro* restimulation of whole PEC cells. **(G)** Exemplary FACS plots and absolute cell numbers of peritoneal CD11c$^+$MHC-II$^+$CD45$^+$ dendritic cells (DC) in a naïve, cured and reinfected mouse. **(H)** Mean fluorescence intensities (MFI) of Ox40L on DCs in PEC, siLP, mLN and lung of naïve, cured and reinfected mice. **(I)** Correlation analysis of Ox40L expression on PEC-resident DCs and Ox40 expression on PEC-resident memory Th2 cells. Statistical analysis in **(A-C)** was done using one-way ANOVA combined with Tukey's multiple comparison test. Statistical analysis in **(I)** was performed using Pearson's r test. * $p < 0.05$, ** $p < 0.01$, *** $p < 0.001$, n.s., not significant.

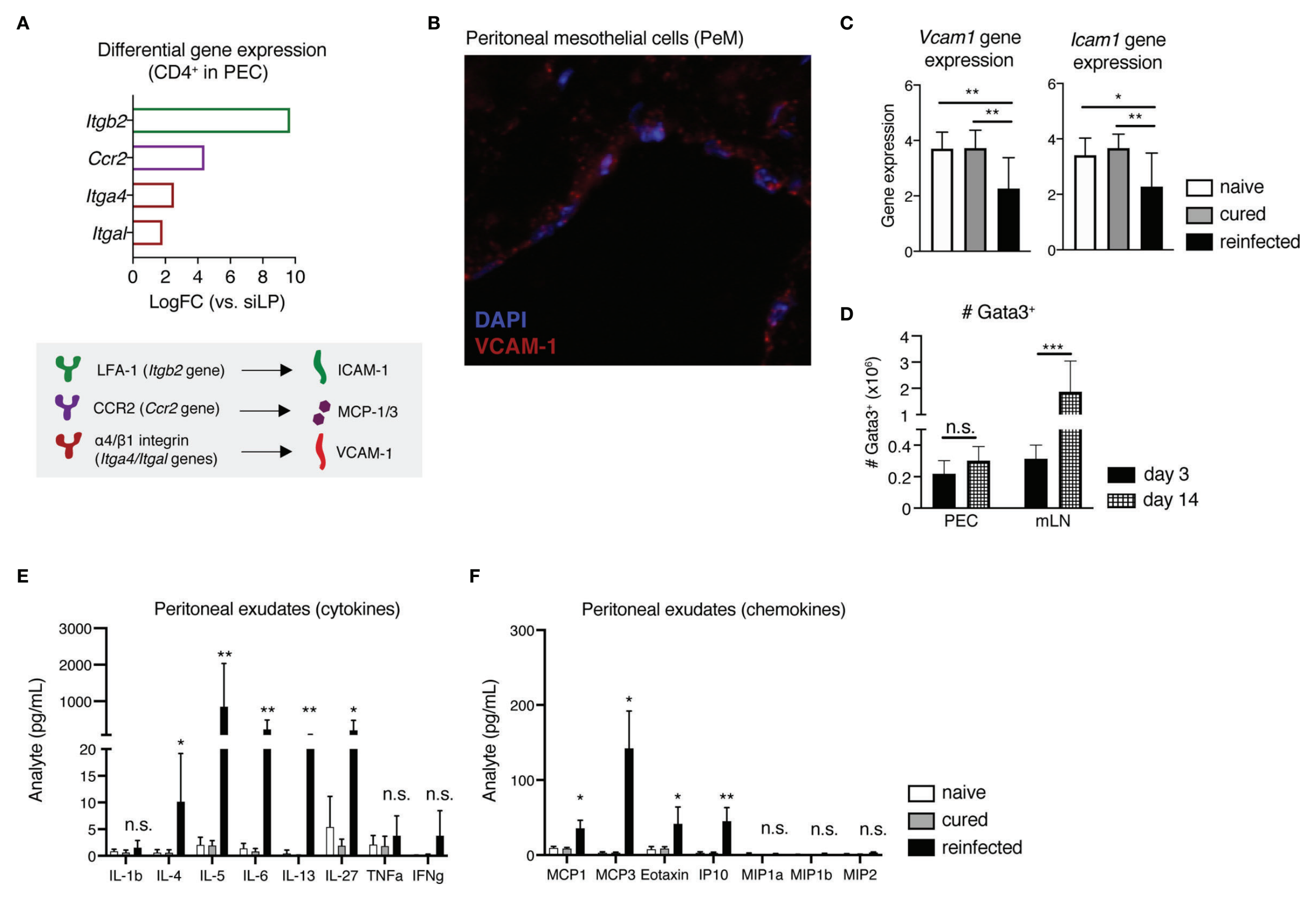

FIGURE 4 | Peritoneal mesothelial cells (PeM) express several cell adhesion markers consistent with the influx of immune cells during early recall responses to *H. polygyrus* into the peritoneum. **(A)** Differential gene expression levels of *Itgb2, Ccr2, Itga4* and *Itgal* in sorted CD4$^+$ T cells from the PEC in comparison with siLP-sorted cells, as quantified *via* scRNAseq (top) and a graphical legend of cell adhesion marker-ligand binding pairs (bottom). **(B)** Immunofluorescence staining of a peritoneal membrane snip from a naïve C57BL/6 mouse. DAPI nuclear staining is shown in blue and VCAM-1 staining in red. **(C)** Relative gene expression of *Vcam1* and *Icam1* in peritoneal membrane snips from naïve, cured and reinfected mice, against GAPDH as a housekeeping gene. **(D)** Absolute cell numbers of Gata3$^+$CD4$^+$CD44$^+$CD62-L$^-$Foxp3$^-$ Th2 cells in the PEC and mLN of *H. polygyrus*-reinfected mice at 3 and 14 days post-challenge infection. Quantification of secreted **(E)** cytokines and **(F)** chemokines in peritoneal exudates from naïve, cured and reinfected mice. The data are pooled from two to three independent experiments with n = 2-4 mice per group. Statistical analysis was done using one-way ANOVA combined with Tukey's multiple comparison test. * $p < 0.05$, ** $p < 0.01$, *** $p < 0.001$. n.s., not significant.

homeostasis and following cure of a primary infection, a *H. polygyrus* challenge induces a significant downregulation of gene expression levels of both markers, likely enabling immune cell influx out of the peritoneal compartment. In addition, the peritoneal cavity appears to prime and support only early host recall responses to a strictly intestinal pathogen, as by day 14 post-challenge we start observing stronger host Th2 responses in the gut-draining lymph nodes instead.

Considering the high gene expression levels of cell adhesion and chemokine receptors LFA-1, α4β1 and CCR2 found on peritoneal compared with intestinal CD4$^+$ T cells (**Figure 4A**), we also quantified the amounts of secreted cytokines and chemokines in peritoneal exudates of naïve, cured and reinfected mice using a magnetic bead multiplex assay (**Figure 4E**). We detected expectedly elevated levels of Th2 cytokines like IL-4, IL-5, IL-6 and IL-13, in line with the marked reactivation and expansion of peritoneal memory Th2 cells shown earlier. One novel finding here was the markedly elevated levels of the APC-secreted immunomodulatory cytokine IL-27 in the peritoneal cavity of reinfected mice, fitting well with the observed influx of peritoneal DCs following *H. polygyrus* challenge (**Figure 4E**). Considering the known immunomodulatory functions of both IL-27 and nematode-derived molecules, we also checked whether HES/IL-27-mediated signaling potentially contributes to the observed downregulation of *Vcam1* and *Icam1* in the peritoneum of reinfected mice. For this, we performed an *in vitro* restimulation of whole peritoneal membrane snips with either the pro-inflammatory cytokine IFNγ, known to increase ICAM-1 and VCAM-1 expression on human pleural mesothelial cells (22), or with HES either in the presence or absence of IL-27. Here, while IFNγ restimulation induced an increase in gene expression of *Icam1*, but not *Vcam1*, HES and IL-27 did not significantly modulate neither *Vcam1* nor *Icam1* expression on murine PeM cells *in vitro*, indicating that alternative signaling mechanisms in the peritoneum regulate cell adhesion marker expression in response to a nematode infection (**Figure S6**). Finally, we found that reinfected mice displayed significantly elevated levels of several chemokines. including MCP-1/3 and the eosinophil-attracting chemokine Eotaxin (CCL11) (**Figure 4F**), fitting with the differential gene expression of CCR2 on peritoneal T cells and the marked peritoneal eosinophilia, respectively (**Figure 4F**).

In summary, we could show that within the murine peritoneal cavity, the peritoneal membrane lined by PeM cells expresses stable levels of cell adhesion markers VCAM-1 and ICAM-1 under steady state and following cure of a primary infection, and significantly downregulates the gene expression of both markers in response to a challenge nematode infection. In line with this finding, within our scRNA-seq data we also observe high differential gene expression of the binding molecules for both VCAM-1 ($\alpha4\beta1$) and ICAM-1 (LFA-1) on peritoneal CD4$^+$ T cells, therefore indicating that the notable recruitment and retention of memory Th2 cells in the peritoneal cavity of mice cured of a primary *H. polygyrus* infection is potentially cell adhesion marker-driven. Finally, we highlight the presence of significantly elevated levels of several APC-derived and signature Th2 cytokines, as well as chemokines associated with monocyte recruitment and activation in peritoneal exudates of reinfected mice, further highlighting the murine peritoneal compartment as a site of diverse immune cell recruitment, retention and reactivation in response to an otherwise strictly enteric pathogen.

DISCUSSION

The formation, distribution and rapid recall abilities of memory T cells are crucial elements of immunological memory responses. Here, we focused on characterizing the early Th2 recall responses to a challenge infection with the small intestinal nematode *H. polygyrus* in mice. We could show that along with the siLP and the lung, the peritoneal cavity harbors a pool of CD4$^+$ T cells with a typical tissue-resident memory transcriptional profile, including upregulated expression of costimulatory markers like Ox40 and tissue retention markers like CD69 (23, 24). As an early inducible marker, Ox40 normally promotes the survival and function of memory Th2 cells *via* positive regulation of anti-apoptotic proteins like Bcl-2 and Bcl-xl (25–27). Several studies have shown that Ox40/Ox40L signaling is critical for memory Th2 cell functionality during allergic airway inflammation in mice (27–29). For nematode infections, Ox40L$^{-/-}$ mice have been shown to exhibit impaired adult worm expulsion, and weaker IL-4 and IgE responses to secondary *H. polygyrus* infection, confirming Ox40/Ox40L interactions as important for efficient host recall responses to intestinal parasitic nematodes (17). Here, we highlight for the first time the host peritoneal cavity as a key site of parasite-specific upregulation of Ox40 expression on memory Th2 cells, paralleled by an influx of peritoneal Ox40L$^+$ DCs as early as 3 days following a secondary infection with an otherwise strictly enteric nematode. Moreover, even though nematode infections are typically associated with eosinophil infiltration at the site of infection, we now demonstrate that a secondary *H. polygyrus* infection also induces a significant early eosinophil accumulation at distal sites such as the peritoneal cavity. This therefore further highlights a novel importance of the peritoneal compartment for priming and harboring early recall responses to infections with gut-restricted pathogens.

Under homeostasis, during infection or inflammation the cellular composition of the peritoneal cavity is typically regulated *via* the bidirectional migration of immune cells, a process reliant on chemokine receptors and cell adhesion markers (30–33). In our previous study, we found that the majority of memory Th2 cells from the peritoneal cavity of nematode-cured mice express the $\alpha4$ integrin subunit (CD49d), while less than 10% of intestinal memory Th2 cells were CD49d$^+$ (4). Importantly, *via* interactions with their complementary receptors $\alpha4\beta1$ and LFA-1, the cell adhesion markers VCAM-1 and ICAM-1 have been shown to mediate mononuclear leukocyte infiltration, increase T cell and APC avidity and thus to modulate T cell activation and differentiation (34, 35). In line with previous findings (20) and expanding on our own work (4), here we can now show that the murine peritoneal membrane, lined by PeM cells, is a source of both VCAM-1 and ICAM-1 under homeostasis and following cure of a primary *H. polygyrus* infection, thus explaining the prominent recruitment and retention of tissue-resident CD49d$^+$ memory Th2 cells in the peritoneal compartment, rather than the gut of nematode-cured mice.

Several studies have previously shown that human pleural mesothelial cells upregulate their ICAM-1 expression and serve as chemokine sources in response to bacterial infection, thus directly participating in the recruitment of monocytes and CD4$^+$ T cells (22, 36, 37). In contrast, blocking ICAM-1 leads to lower CD4$^+$ T cell activation *in vitro* (22) and to a significant reduction in monocyte transmigration in response to chemotactic stimuli (36). In light of this data, an additional new finding in our current study is that the murine peritoneum can directly respond to a challenge intestinal nematode infection by rather decreasing its gene expression levels of *Vcam1* and *Icam1* early during recall responses to *H. polygyrus*, likely enabling the immune cell efflux out of the peritoneal cavity. Furthermore, considering the initial expansion of peritoneal Th2 cells during early recall responses at 3 days post-challenge in the PEC only, and the contrasting later expansion of Gata3$^+$ cells in the gut-draining lymph nodes by 14 days post-challenge infection, our findings therefore suggest that the host peritoneal compartment participates in and supports specifically early recall responses to the enteric parasite *H. polygyrus*. Considering the gut-restricted colonization of *H. polygyrus*, efficient control of this pathogen ultimately relies on strong host Th2 responses in the siLP and mLN, rather than in peripheral sites like the peritoneal cavity. The efflux of immune cell subsets like B cells out of the peritoneum requires the downregulation of integrin molecules, correlating with a corresponding increasing appearance of B cells in lymph nodes

(33). Even though here we don't show evidence of lower integrin expression on peritoneal-resident Th2 cells following *H. polygyrus* reinfection, we rather present evidence of significantly downregulated *Vcam1* and *Icam1* gene expression levels in the peritoneum of nematode-reinfected mice at 3 days post-challenge, coupled with increasing numbers of Th2 cells in the mLN by 14 days post-secondary infection. Our findings therefore support one potential new mechanism of immune cell recirculation *via* the peritoneum, where nematode-induced LFA-1 and CD49d-expressing CD4$^+$ T cells take up residence in the host peritoneal cavity, attracted by the stable expression levels of ICAM-1 and VCAM-1 following the cure of a primary *H. polygyrus* infection. Upon nematode reinfection, the peritoneal membrane starts downregulating its cell adhesion marker expression to allow for immune cell efflux out of the peritoneum and towards the site of infection in the gut, complementing the already initiated *de novo* induction of Th2 effector cells expected in the mLN of reinfected mice.

Despite the upregulated levels of secreted chemokines like MCP-1/3 and Eotaxin in peritoneal exudates, we did not observe a corresponding elevated gene expression of either marker in the peritoneal membrane of reinfected mice 3 days post-challenge (data not shown). This therefore indicates that other immune cell subsets such as peritoneal macrophages, rather than PeM cells, serve as important chemokine sources, potentially complementing APC-driven immune cell reactivation.

Several studies in recent years have highlighted the APC-derived IL-27 as an immunomodulatory cytokine, capable of regulating Th1 cell differentiation (38), chemokine production in human bronchial epithelial cells (39), as well as mediating intestinal epithelial barrier function (40). IL-27 also appears to inhibit activation-induced cell death (AICD) of CD4$^+$ T cells, sustaining their expansion upon activation (41). Similarly, IL-27 is reported to enhance eosinophil survival, migration and activation (42). The high concentrations of IL-27 in the peritoneal exudates are therefore in line with the strong expansion and parasite-specific reactivation of peritoneal Th2 cells, as well as with the prominent peritoneal eosinophil influx in *H. polygyrus*-reinfected mice and points to a role for IL-27 in T cell and granulocyte attraction and activation in the host peritoneal cavity during early recall responses to infection. Finally, *H. polygyrus* itself is also a potent immunomodulator and can regulate host immune responses *via* the release of a diverse cocktail of parasite-derived molecules (43–45). In the current study, we observed a significant increase of both DCs and secreted IL-27 levels in the peritoneal cavity of reinfected mice, but neither *H. polygyrus*-released products (HES), nor IL-27 induced a decrease in the cell adhesion markers VCAM-1 and ICAM-1 *in vitro*, possibly as a result of a lack of IL-27 receptor expression on murine PeM cell.

In summary, our study places a novel focus on the involvement of the host peritoneal cavity in driving the recruitment and reactivation of memory Th2 cells, DCs and eosinophils during early recall responses to a gut-restricted parasitic nematode. We could show that the peritoneal compartment of nematode-reinfected mice harbors notable numbers of parasite-specific, functional memory Th2 cells, as well as a significant influx of both DCs and eosinophils. Furthermore, we show for the first time that the murine peritoneum, typically lined by PeM cells, responds to an intestinal nematode infection by decreasing its gene expression of the cell adhesion markers VCAM-1 and ICAM-1 as early as 3 days post-challenge infection, despite otherwise stable expression of both markers following cure of a primary infection. We therefore highlight the host peritoneal compartment as an important player in the development of early Th2 recall immune responses to challenge infections with an enteric pathogen.

MATERIALS AND METHODS

Mice and Nematode Infection

Wild-type female C57BL/6 mice (age 8-10 weeks) were purchased from Janvier Labs (Saint-Berthevin, France). All animals were maintained under specific pathogen-free (SPF) conditions and were fed standard chow *ad libidum*. *H. polygyrus* was maintained by serial passage in C57BL/6 mice (H0099/13). Mice were infected with 225 third-stage infective (L3) *H. polygyrus* larvae *via* oral gavage in 200µL drinking water. For cure of infection, mice were treated on two consecutive days during the acute stage of infection (day 14-15) with 2mg pyrantel pamoate (Sigma, St. Louis, MO, USA) in 200µL drinking water *via* oral gavage. On indicated days, mice were sedated *via* isofluorane inhalation, followed by cervical dislocation. The efficacy of curative treatment with pyrantel pamoate was confirmed at dissection by the lack of adult worms in the small intestine of cured mice. All animal experiments were performed in accordance with the National Animal Protection Guidelines and approved by the German Animal Ethics Committee for the Protection of Animals (LAGeSo, G0176/20).

Preparation of Single Cell Suspensions

The isolation of PEC, siLP and mLN was performed as previously described (4). For the isolation of lung cells, the chest cavity was opened *via* incision and the whole lung was perfused with 20mL ice-cold PBS *via* puncture to the heart using a 27G needle and syringe. Each lung was then removed and manually minced into small pieces. The minced tissue was then transferred to a 50mL falcon tube containing 10mL digestion medium (150µg/mL collagenase D and DNase I in PBS). The samples were incubated for 1 hour at 37°C under continuous shaking at 250rpm. Following the digestion step, the lung tissue was passed through a 70µm cell strainer into a fresh 50mL falcon tube. After erythrocyte lysis, the lung samples were washed and resuspended in cRPMI. All cell suspensions were counted using a CASY automated cell counter (Roche-Innovatis, Reutlingen, Germany).

CD4$^+$ T Cell Sorting and Library Preparation

Cell suspensions from PEC, siLP, mLN and lung were obtained and counted as described above from two *H. polygyrus*-cured C57BL/6 mice at 8 weeks post-cure. Immediately prior to dissection, each mouse was injected intravenously with anti-mouse CD45.2-A700 (clone 104) to allow for the exclusion of any blood-derived cells in circulation. Each sample was stained with anti-mouse CD4-PerCP (clone RM4-5) and was sorted for live single $CD4^{+}CD45.2^{-}$ T cells on a FACS Aria cell sorter (BD Biosciences, Heidelberg, Germany).

Capture and processing of single $CD4^{+}$ T cells was performed using the Fluidigm C1 autoprep system. Sorted $CD4^{+}$ T cells (50 cells/µl) were mixed with (ratio 6/4) C1 Cell Suspension Reagent (Fluidigm) and subsequently loaded onto a 5-10-µm-diameter C1 Integrated Fluidic Circuit (IFC; Fluidigm From the nine chips used, we captured 517 single cells (59.8%). ERCC (External RNA Controls Consortium) spike-in RNAs (Ambion, Life Technologies) were added to the lysis mix. Reverse transcription and cDNA preamplification were performed using the SMARTer Ultra Low RNA kit (Clontech). Sequencing libraries were prepared using Nextera XT DNA Sample Preparation kit with 96 indices (Illumina), according to the protocol supplied by Fluidigm. Size distribution in final libraries was analyzed by Bioanalyzer High Sensitivity DNA assay (Agilent) and library concentrations were quantified by Qubit High Sensitivity DNA assay (ThermoFisher). A total of 384 libraries were pooled equimolar and sequenced on an Illumina HiSeq 1500 system in rapid mode v1 by a paired-end dual-indexing run with 2x 125 cycle reads. Subsequently, the generation and trimming of fastq files was performed followed by alignment of the reads to mm10 mouse genome version.

Quality control of the raw fastq files was done with FastQC (https://www.bioinformatics.babraham.ac.uk/projects/fastqc/). Trimming of the raw reads was done with Trimmomatic v0.36, with the following filters and settings in this order: Nextera adaptors, ILLUMINACLIP:${ADAPTER}:2:30:10 (adapter trimming), LEADING:3 (5' Trimming phred<3), TRAILING:3 (3' Trimming phred<3), SLIDINGWINDOW:3:20 (mean phred score in sliding window size 3 had to be at least 20), MINLEN:36 (discard reads shorter than 36bp) (46).

RNA Sequencing and Data Analysis

Single cell RNA-Seq data were analyzed using R and the indicated R-packages. At first, counts per gene were calculated from the bam files by adding all counts mapped to the region of a corresponding gene (Rsamtools) (47). Quality control of the count data was performed with the R-package scater (48, 49). Cells with low library size, low numbers of features or a high number of mitochondrial sequences were filtered out using the quickPerCellQC function. Features (genes) without any count in all remaining cells were removed from the dataset and count data were normalized and log2-transformed after adding a pseudocount to each value. Variances in the expression profile of each gene were modelled based on a fitted mean-variance trend (scran - modelGeneVar) (50), decomposing it into technical and biological components. Hypervariable expressed genes were identified by applying a threshold of 4 for the variances of the biological component. 500 genes with the highest biological variances were selected for dimension reduction using the UMAP algorithm (scater) (48). In order to further stratify the dataset to genes driving systemic substructures and to remove noise, pairwise correlations between all genes were calculated (scran - correlatePairs) (50). P-values were adjusted for multiple testing by calculating the false discovery rates and significant genes were selected by a fdr below 0.05. These genes were used in a hierarchical clustering with euclidean distances and ward.D2 linkage (R - inbuilt dist and hclust function) (49). Five clusters were defined by the cutTreeDynamic function (dynamicTreeCut) (51). The dendrogram information (order of the columns), as well as the cluster definitions were used in the heatmap representation of pre-selected genes (heatmap3) (52).

Differential expression of genes between PEC and other tissues were determined by fitting negative binomial generalized linear models combined with likelihood ratio tests (edgeR - glmFIT and glmLRT) (53). Ranks were determined for each comparison and the whole set was ordered according to the minimal rank of each gene.

Marker genes for the three PEC clusters were determined by combined pairwise comparisons (t-Tests) using the findMarkers function of the scran package. Significant genes were selected by a combined p-value below 0.05. Functional annotation and overrepresentation analysis of these gene sets was done by DAVID using the R package "RDAVIDWebService" (54). Comparison of functional aspects between the three PEC clusters was done using the R-package "clusterProfiler" (55). Results for the biological branch of the gene ontology system were further processed. GO terms with overrepresentation in all PEC clusters were removed to focus for the differences. Each term was mapped (if possible) to the significant most specific (child) term. 15 top-ranking terms from this processed set for each PEC cluster were then compared in a dotplot.

Flow Cytometry

The antibodies used for the detection of surface and intracellular markers are described in **Table S4**. Dead cells were excluded using eFluor780 or eF560 fixable viability dye (Thermo Fisher, Waltham, USA). For intracellular staining of cytokines and transcription factors, cells were fixed and permeabilized using the Fixation/Permeabilization kit and Permeabilization buffer from ThermoFisher/eBioscience. Samples were analyzed on a Canto II flow cytometer and on an Aria cell sorter (BD Biosciences, Heidelberg, Germany). The data was analyzed using FlowJo software Version 10 (Tree star Inc., Ashland, OR, USA). The data for naïve, cured (8wpc and 12wpc) and reinfected mice presented in this study are pooled from two independent experiments with 3-5 mice per group in each experiment.

Cell Culture and *In Vitro* Re-Stimulation

For the analysis of parasite-specific Ox40 expression and IL-5 secretion, $5x10^{5}$ whole PEC or mLN cells were plated out per well in a round-bottom 96-well cell culture plate in a final volume of 200µL RPMI medium, containing 10% FCS, 100U/mL penicillin and 100µg/mL streptomycin (all from PAA, Pasching, Austria). The cells were stimulated with either anti-CD3/CD28 antibodies (1µg/mL) or *H. polygyrus* excretory-secretory (HES) antigen (10µg/mL). The cells were then incubated for 72 hours at 37°C and 5% CO_2. After 72 hours, the cell pellets were collected and stained for flow cytometric analysis, as described above, while the culture supernatants were collected and used for quantifying IL-5 secretion *via* ELISA, as described below. The data presented for this assay are pooled from two independent experiments with 2-4 mice per group in each experiment.

Quantification of Parasite-Specific IL-5 Production *In Vitro*

Parasite-specific IL-5 production of restimulated PEC and mLN cells was measured *via* sandwich ELISA using the Mouse IL-5 Uncoated ELISA kit as per the manufacturer's instructions (Invitrogen). Absorbance was measured on a Biotek Synergy H1 Hybrid Reader at a 450nm wavelength.

Eosinophil Peroxidase Quantification in Serum

Eosinophil peroxidase (EPO) levels in blood serum were quantified using the Mouse Eosinophil Peroxidase (EPX) ELISA Kit as per the manufacturer's instructions (DLdevelop, Jiangsu, PRC). Serum samples were diluted 1:5 in Diluent Buffer and were added to the plate with serially diluted standards. Absorbance was measured on a Biotek Synergy H1 Hybrid Reader at a 450nm wavelength. The data presented for this assay are pooled from two independent experiments with 3-5 mice per group in each experiment.

Immunohistochemistry

Sections were cut from formalin-fixed and paraffin-embedded tissues, dewaxed and subjected to a heat-induced epitope-retrieval step. For immunofluorescence, endogenous peroxidase was blocked (Dako REAL Peroxidase-Blocking Solution, Agilent, Santa Clara, CA, U.S.) and sections were incubated with anti-VCAM-1 (clone EPR5047, Abcam, Cambridge, U.K.). For detection, the EnVision+ Single Reagent (HRP. Rabbit, Agilent) and the Opal 570 reagent (Akoya Biosciences, MA, U.S.) were used. Nuclei were stained with DAPI (Sigma-Aldrich Chemie GmbH, Munich, Germany) and slides were cover-slipped in Fluoromount G (Southern Biotech, Birmingham, AL, U.S.). Stained sections were analyzed in a blinded manner using an AxioImager Z1 microscope (Carl Zeiss Microscopy Deutschland GmbH, Oberkochen, Germany). The immunohistochemistry data shown here are representative of two independent experiments with 2-4 mice per group in each experiment.

Quantitative Real-Time PCR (qPCR)

At necropsy, 1cm^2 tissue snips of peritoneal membrane were excised, flash-frozen in liquid nitrogen and were stored at -80°C. RNA was isolated using the Monarch Total RNA Miniprep kit (New England BioLabs, MA, USA) according to the manufacturer's instructions. 2µg of RNA was then reverse-transcribed to cDNA using the High-Capacity RNA-to-cDNA kit (Applied Biosystems, Foster City, CA, USA). Relative gene expression was determined *via* quantitative real-time PCR (qPCR) using 10 ng of cDNA and FastStart Universal SYBR Green Master Mix (Roche). Primer pairs are described in **Table S5**. Efficiencies for each primer pair were determined by generating a standard curve. mRNA expression was normalized to the housekeeping gene glyceraldehyde 3-phosphate dehydrogenase (GAPDH) and was calculated by the Roche Light Cycler 480 software. The qPCR data are pooled from three independent experiments with 2-4 mice per group in each experiment.

Magnetic Bead Immunoassay and Peritoneal Analyte Quantification

At necropsy, 1mL of PBS buffer was carefully injected and retracted from the cavity of naïve, cured and reinfected mice using a 20G needle and syringe. These peritoneal exudate samples were then centrifuged, the supernatants were collected and stored at -20°C for performing a multiplex sandwich ELISA-based Luminex immunoassay using the Mouse Cytokine & Chemokine 26-plex ProcartaPlex kit as per the manufacturer's instructions. The results were read using a Luminex MagPix machine. The data presented for this assay are pooled from two independent experiments with 3-4 mice per group in each experiment.

In Vitro PeM cell restimulation

For the *in vitro* restimulation of murine PeM cells, snips from naïve C57BL/6 mice were carefully excised and were plated out in 200µL cRPMI medium in 96-well plates (one snip per well). Snips from each mouse were then either left unstimulated as a negative control or were incubated with IFNγ (10ng/mL), HES (10µg/mL) or HES and IL-27 (10µg/mL + 50ng/mL, respectively) for 24h at 37°C, 5% CO_2. After the 24h incubation, the snips were then snap frozen and stored at -80°C for later RNA extraction, reverse transcription and qPCR analysis of *Vcam1* and *Icam1* gene expression levels as described above. The data presented for this assay are pooled from two independent experiments with 2-4 mice per group in each experiment.

Statistical Analysis

Statistical analysis of FACS data was performed using GraphPad Prism software version 9.0.1 (La Jolla, CA, USA). Results are displayed as mean ± SD and significance is displayed as *p<0.05, **p<0.01, ***p<0.001. Results were tested for normal distribution using the Shapiro-Wilk normality tests, followed by ANOVA or Kruskal-Wallis combined with Tukey's or Dunn's multiple comparison testing.

DATA AVAILABILITY STATEMENT

The RNAseq data presented in the study are deposited in the GEO database (NCBI) repository, accession number GSE198203.

ETHICS STATEMENT

The animal study was reviewed and approved by LAGeSO, G0176/20.

AUTHOR CONTRIBUTIONS

IAY, SS, BS, and SH planned and designed the study. IAY, SS, and AAK performed experiments, data analysis and interpretation.

KV and UK performed the library preparation and single-cell RNA sequencing. KJ performed the bioinformatics analysis. KJ and BS interpreted the scRNA-seq data. AAK performed and interpreted the immunohistochemistry analysis. IAY wrote the manuscript. IAY, KJ, SS, KV, UK, AAK, BS, and SH edited the manuscript. BS and SH supervised the study and provided critical review of the manuscript. All authors contributed to the article and approved the submitted version.

FUNDING

This study was supported by a German Research Foundation (DFG) grant HA 2542/8-1 awarded to SH.

ACKNOWLEDGMENTS

The authors would like to thank Yvonne Weber, Marion Müller, Bettina Sonnenburg, Christiane Palissa and Beate Anders for providing excellent technical support, as well as to Marten Jäger at the BIH Core Unite Genomics for his help with the generation, trimming and alignment of the fastq files. Gratitudes are also extended to Joel Hornby for his support with graphical design.

SUPPLEMENTARY MATERIAL

The Supplementary Material for this article can be found online at: https://www.frontiersin.org/articles/10.3389/fimmu.2022.842870/full#supplementary-material

REFERENCES

1. Pradeu T, Du P,L. Immunological Memory: What's in a Name? *Immunol Rev* (2018) 283:7–20. doi: 10.1111/imr.12652
2. Jameson SC, Masopust D. Understanding Subset Diversity in T Cell Memory. *Immunity* (2018) 48:214–26. doi: 10.1016/j.immuni.2018.02.010
3. Nguyen QP, Deng TZ, Witherden DA, Goldrath AW. Origins of CD4 + Circulating and Tissue-Resident Memory T-Cells. *Immunology* (2019) 157:3–12. doi: 10.1111/imm.13059
4. Steinfelder S, Rausch S, Michael D, Kühl AA, Hartmann S. Intestinal Helminth Infection Induces Highly Functional Resident Memory Cd4+T Cells in Mice. *Eur J Immunol* (2017) 47:353–63. doi: 10.1002/eji.201646575
5. King EM, Kim HT, Dang NT, Michael E, Drake L, Needham C, et al. Immuno-Epidemiology of Ascaris Lumbricoides Infection in a High Transmission Community: Antibody Responses and Their Impact on Current and Future Infection Intensity. *Parasite Immunol* (2005) 27:89–96. doi: 10.1111/j.1365-3024.2005.00753.x
6. Jia TW, Melville S, Utzinger J, King CH, Zhou XN. Soil-Transmitted Helminth Reinfection After Drug Treatment: A Systematic Review and Meta-Analysis. *PloS Negl Trop Dis* (2012) 6(5):e1621. doi: 10.1371/journal.pntd.0001621
7. Butterworth AE, Fulford AJ, Dunne DW, Ouma JH, Sturrock RF. Longitudinal Studies on Human Schistosomiasis. *Philos Trans R Soc Lond B Biol Sci* (1988) 321(1207):495–511. doi: 10.1098/rstb.1988.0105
8. Faulkner H, Turner J, Kamgno J, Pion SD, Boussinesq M, Bradley J. Age- and Infection Intensity-Dependent Cytokine and Antibody Production in Human Trichuriasis: The Importance of Ige. *J Infect Dis* (2002) 185:665–72. doi: 10.1086/339005
9. Rausch S, Huehn J, Kirchoff D, Rzepecka J, Schnoeller C, Pillai S, et al. Functional Analysis of Effector and Regulatory T Cells in a Parasitic Nematode Infection. *Infect Immun* (2008) 76:1908–19. doi: 10.1128/IAI.01233-07
10. Rausch S, Hoehn J, Loddenkemper C, Hepworth M, Klotz C, Sparwasser T, et al. Establishment of Nematode Infection Despite Increased Th2 Responses and Immunopathology After Selective Depletion of Foxp3+ Cells. *Eur J Immunol* (2009) 39:3066–77. doi: 10.1002/eji.200939644
11. Blankenhaus B, Klemm U, Eschbach ML, Sparwasser T, Hoehn J, Kühl AA, et al. Strongyloides Ratti Infection Induces Expansion of Foxp3+ Regulatory T Cells That Interfere With Immune Response and Parasite Clearance in Balb/C Mice. *J Immunol* (2011) 186:4295–305. doi: 10.4049/jimmunol.1001920
12. Maizels RM, McSorley HJ. Regulation of the Host Immune System by Helminth Parasites. *J Allergy Clin Immunol* (2016) 138:666–75. doi: 10.1016/j.jaci.2016.07.007
13. Harvie M, Camberis M, Tang SC, Delahunt B, Paul W, Le Gros G. The Lung is an Important Site for Priming CD4 T-Cell-Mediated Protective Immunity Against Gastrointestinal Helminth Parasites. *Infect Immun* (2010) 78:3753–62. doi: 10.1128/IAI.00502-09
14. Obata-Ninomiya K, Ishiwata K, Nakano H, Endo Y, Ichikawa T, Onodera A, et al. Cxcr6+St2+ Memory T Helper 2 Cells Induced the Expression of Major Basic Protein in Eosinophils to Reduce the Fecundity of Helminth. *Proc Natl Acad Sci* (2018) 115:E9849–58. doi: 10.1073/pnas.1714731115
15. Filbey KJ, Camberis M, Chandler J, Turner R, Kettle AJ, Eichenberger RM. Intestinal Helminth Infection Promotes IL-5- and CD4 + T Cell-Dependent Immunity in the Lung Against Migrating Parasites. *Mucosal Immunol* (2019) 12:352–62. doi: 10.1038/s41385-018-0102-8
16. Mohrs K, Harris DP, Lund FE, Mohrs M. Systemic Dissemination and Persistence of Th2 and Type 2 Cells in Response to Infection With a Strictly Enteric Nematode Parasite. *J Immunol* (2005) 175:5306–13. doi: 10.4049/jimmunol.175.8.5306
17. Ekkens MJ, Liu Z, Whitmire J, Xiao S, Foster A, Pesce J, et al. The Role of Ox40 Ligand Interactions in the Development of the Th2 Response to the Gastrointestinal Nematode Parasite Heligmosomoides Polygyrus. *J Immunol* (2003) 170:384–93. doi: 10.4049/jimmunol.170.1.384
18. Jenkins SJ, Perona-Wright G, Worsley AGF, Ishii N, MacDonald AS. Dendritic Cell Expression of OX40 Ligand Acts as a Costimulatory, Not Polarizing, Signal for Optimal Th2 Priming and Memory Induction *In Vivo*. *J Immunol* (2007) 179:3515–23. doi: 10.4049/jimmunol.179.6.3515
19. Shimotsuma M, Kawata M, Hagiwara A, Takahashi T. Milky Spots in the Human Greater Omentum. Macroscopic and Histological Identification. *Acta Anat* (1989) 136:211–6. doi: 10.1159/000146888
20. Suassuna JHR, Neves FCD, Hartley RB, Ogg CS, Cameron JS. &Immunohistochemical Studies of the Peritoneal Membrane and Infiltrating Cells in Normal Subjects and in Patients on CAPD. *Kidney Int* (1994) 46:443–54. doi: 10.1038/ki.1994.292
21. Jonjic BN, Peri G, Bernasconi S, Sciacca FL, Colotta F, Pelicci P, et al. Expression of Adhesion Molecules and Chemotactic Cytokines in Cultured Human Mesothelial Cells. *J Exp Med* (1992) 176:1165–74. doi: 10.1084/jem.176.4.1165
22. Yuan ML, Tong ZH, Guang X, Zhang JC, Wang XJ, Ma WL, et al. Regulation of Cd4+ T Cells by Pleural Mesothelial Cells *via* Adhesion Molecule-Dependent Mechanisms in Tuberculous Pleurisy. *PloS One* (2013) 8:1–10. doi: 10.1371/journal.pone.0074624
23. Carbone FR. Tissue-Resident Memory T Cells and Fixed Immune Surveillance in Nonlymphoid Organs. *J Immunol* (2015) 195:17–22. doi: 10.4049/jimmunol.1500515
24. Schenkel JM, Masopust D. Tissue-Resident Memory T Cells. *Immunity* (2014) 41:886–97. doi: 10.1016/j.immuni.2014.12.007
25. Gramaglia I, Weinberg AD, Lemon M, Croft M. Ox-40 Ligand: A Potent Costimulatory Molecule for Sustaining Primary CD4 T Cell Responses. *J Immunol* (1998) 161:6510–7.
26. Rogers PR, Song J, Gramaglia I, Killeen N, Croft M. OX40 Promotes Bcl-Xl and Bcl-2 Expression and Is Essential for Long-Term Survival of CD4 T Cells. *Immunity* (2001) 15:445–55. doi: 10.1016/s1074-7613(01)00191-1
27. Salek-Ardakani S, Song J, Halteman BS, Jember AGH, Akiba H, Yagita H, et al. Ox40 (Cd134) Controls Memory T Helper 2 Cells That Drive Lung Inflammation. *J Exp Med* (2003) 198:315–24. doi: 10.1084/jem.20021937
28. Jember AGH, Zuberi R, Liu FT, Croft M. Development of Allergic Inflammation in a Murine Model of Asthma Is Dependent on the

Costimulatory Receptor Ox40. *J Exp Med* (2001) 193:387–92. doi: 10.1084/jem.193.3.387

29. Gracias DT, Sethi GS, Mehta AK, Miki H, Gupta RK, Yagita H, et al. Combination Blockade of Ox40l and Cd30l Inhibits Allergen-Driven Memory Th2 Reactivity and Lung Inflammation. *J Allergy Clin Immunol* (2021) 147(6):1–14. doi: 10.1016/j.jaci.2020.10.037
30. Ohnmacht C, Pullner A, Rooijen Nv, Voehringer D. Analysis of Eosinophil Turnover *In Vivo* Reveals Their Active Recruitment to and Prolonged Survival in the Peritoneal Cavity. *J Immunol* (2017) 179:4766–74. doi: 10.4049/jimmunol.179.7.4766
31. Ruiz-Campillo MT, Hernandez VM, Escamilla A, Stevenson M, Perez J, Martinez-Moreno A, et al. Immune Signatures of Pathogenesis in the Peritoneal Compartment During Early Infection of Sheep With Fasciola Hepatica. *Sci Rep* (2017) 7:1–14. doi: 10.1038/s41598-017-03094-0
32. Höpken UE, Winter S, Achtman AH, Krüger K, Lipp M. CCR7 Regulates Lymphocyte Egress and Recirculation Through Body Cavities. *J Leukoc Biol* (2010) 87:671–82. doi: 10.1189/jlb.0709505
33. Berberich S, Dähne S, Schippers A, Peters T, Müller W, Kremmer E, et al. Differential Molecular and Anatomical Basis for B Cell Migration Into the Peritoneal Cavity and Omental Milky Spots. *J Immunol* (2008) 180:2196–203. doi: 10.4049/jimmunol.180.4.2196
34. Leitner J, Grabmeier-Pfistershammer K, Steinberger P. Receptors and Ligands Implicated in Human T Cell Costimulatory Processes. *Immunol Lett* (2010) 128:89–97. doi: 10.1016/j.imlet.2009.11.009
35. Schmidt EP, Kuebler WM, Lee WL, Downey GP. Adhesion Molecules: Master Controllers of the Circulatory System. *Compr Physiol* (2016) 6:945–73. doi: 10.1002/cphy.c150020
36. Nasreen N, Mohammed KA, Ward MJ, Antony VB. Mycobacterium-Induced Transmesothelial Migration of Monocytes Into Pleural Space: Role of Intercellular Adhesion Molecule-1 in Tuberculous Pleurisy. *J Infect Dis* (1999) 180:1616–23. doi: 10.1086/315057
37. Ye ZJ, Zhou Q, Yuan ML, Du RH, Yang WB, Xiong XZ, et al. Differentiation and Recruitment of Il-22-Producing Helper T Cells Stimulated by Pleural Mesothelial Cells in Tuberculous Pleurisy. *Am J Respir Crit Care Med* (2012) 185:660–9. doi: 10.1164/rccm.201107-1198OC
38. Lucas S, Ghilardi N, Li J, Sauvage FJDe. IL-27 Regulates IL-12 Responsiveness of Naïve CD4+ T Cells Through Stat1-Dependent and -Independent Mechanisms. *Proc Natl Acad Sci USA* (2003) 100:15047–52. doi: 10.1073/pnas.2536517100
39. Pereira ABM, de Oliveira JR, Teixeira MM, da Silva PR, Junior VR, Rogerio ADeP. IL-27 Regulates IL-4-Induced Chemokine Production in Human Bronchial Epithelial Cells. *Immunobiology* (2021) 226:152029. doi: 10.1016/j.imbio.2020.152029
40. Diegelmann J, Olszak T, Göke B, Blumberg RS, Brand S. A Novel Role for Interleukin-27 (IL-27) as Mediator of Intestinal Epithelial Barrier Protection Mediated *via* Differential Signal Transducer and Activator of Transcription (STAT) Protein Signaling and Induction of Antibacterial and Anti-Inflammatory Protein Signaling and Induction of Antibacterial and Anti-Inflammatory Proteins. *J Biol Chem* (2012) 287:286–98. doi: 10.1074/jbc.M111.294355
41. Kim G, Shinnakasu R, Saris CJM, Cheroutre H, Kronenberg M. A Novel Role for IL-27 in Mediating the Survival of Activated Mouse CD4 T Lymphocytes. *J Immunol* (2013) . 190:1510–8. doi: 10.4049/jimmunol.1201017
42. Hu S, Wong CK, Lam CWK. Activation of Eosinophils by IL-12 Family Cytokine IL-27: Implications of the Pleiotropic Roles of IL-27 in Allergic Responses. *Immunobiol* (2011) . 216:54–65. doi: 10.1016/j.imbio.2010.03.004
43. Grainger JR, Smith KA, Hewitson JP, McSorley HJ, Harcus Y, Filbey KJ, et al. Helminth Secretions Induce *De Novo* T Cell Foxp3 Expression and Regulatory Function Through the Tgf-B Pathway. *JEM* (2010) 207(11):2331–41. doi: 10.1084/jem.20101074
44. Coakley G, McCaskill JL, Borger JG, Simbari F, Robertson E, Millar M, et al. Extracellular Vesicles From a Helminth Parasite Suppress Macrophage Activation and Constitute an Effective Vaccine for Protective Immunity. *Cell Rep* (2017) 19:1545–57. doi: 10.1016/j.celrep.2017.05.001
45. Johnston CJC, Smyth DJ, Kodali RB, White MPJ, Harcus Y, Filbey KJ, et al. A Structurally Distinct Tgf-B Mimic From an Intestinal Helminth Parasite Potently Induces Regulatory T Cells. *Nat Commun* (2017) 8:1741. doi: 10.1038/s41467-017-01886-6
46. Bolger AM, Lohse M, Usadel B. Trimmomatic: A Flexible Trimmer for Illumina Sequence Data. *Bioinformatics* (2014). 30(15):2114–20 doi: 10.1093/bioinformatics/btu170
47. Morgan M, Obenchain V, Hayden N. *Rsamtools: Binary Alignment (BAM), FASTA, Variant Call (BCF), and Tabix File Import. R Package Version 2.4.0* (2020). Available at: http://bioconductor.org/packages/Rsamtools.
48. McCarthy DJ, Campbell KR, Lun ATL, Willis QF. Scater: Pre-Processing, Quality Control, Normalisation and Visualisation of Single-Cell RNA-Seq Data in R. *Bioinformatics* (2017) 33(8):1179–86. doi: 10.1101/069633
49. R Core Team. *R: A Language and Environment for Statistical Computing*. Vienna, Austria: R Foundation for Statistical Computing (2020). Available at: https://www.R-project.org/.
50. Lun ATL, McCarthy DJ, Marioni JC. A Step-By-Step Workflow for Low-Level Analysis of Single-Cell RNA-Seq Data With Bioconductor. *F1000Research* (2016) 5:2122. doi: 10.12688/f1000research.9501.2
51. Langfelder P, Zhang B, Horvath S. *Dynamictreecut: Methods for Detection of Clusters in Hierarchical Clustering Dendrograms. R Package Version 1* (2016). Available at: https://CRAN.R-project.org/package=dynamicTreeCut.
52. Zhao S, Yin L, Guo Y, Sheng Q, Shyr Y. *Heatmap3: An Improved Heatmap Package. R Package Version 1. 1.9* (2021). Available at: https://CRAN.R-project.org/package=heatmap3.
53. Robinson MD, McCarthy DJ, Smyth GK. Edger: A Bioconductor Package for Differential Expression Analysis of Digital Gene Expression Data. *Bioinformatics* (2010) 26:139–40. doi: 10.1093/bioinformatics/btp616
54. Fresno C, Fernández EA. Rdavidwebservice: A Versatile R Interface for DAVID. *Bioinformatics* (2013) 29(21):2810–1. doi: 10.1093/bioinformatics/btt487
55. Wu TWu T, Hu E, Xu S, Chen M, Guo P, Dai Z, et al, et al. Clusterprofiler 4.0: A Universal Enrichment Tool for Interpreting Omics Data. *Innovation* (2021) 2(3):100141.55. doi: 10.1016/j.xinn.2021.100141

Conflict of Interest: The authors declare that the research was conducted in the absence of any commercial or financial relationships that could be construed as a potential conflict of interest.

frontiers | Frontiers in Immunology

ORIGINAL RESEARCH
published: 30 May 2022
doi: 10.3389/fimmu.2022.870542

Redefining the Foreign Antigen and Self-Driven Memory CD4$^+$ T-Cell Compartments *via* Transcriptomic, Phenotypic, and Functional Analyses

Takeshi Kawabe[1,2*†], Thomas Ciucci[3,4†], Kwang Soon Kim[5], Shunichi Tayama[1], Akihisa Kawajiri[1], Takumi Suzuki[1], Riou Tanaka[1], Naoto Ishii[1], Dragana Jankovic[2], Jinfang Zhu[6], Jonathan Sprent[7,8], Rémy Bosselut[3] and Alan Sher[2*]

[1] Department of Microbiology and Immunology, Tohoku University Graduate School of Medicine, Sendai, Japan, [2] Immunobiology Section, Laboratory of Parasitic Diseases, National Institute of Allergy and Infectious Diseases, National Institutes of Health, Bethesda, MD, United States, [3] Laboratory of Immune Cell Biology, Center for Cancer Research, National Cancer Institute, National Institutes of Health, Bethesda, MD, United States, [4] David H. Smith Center for Vaccine Biology and Immunology, Department of Microbiology and Immunology, University of Rochester, Rochester, NY, United States, [5] Department of Integrative Biosciences and Biotechnology, Pohang University of Science and Technology, Pohang, South Korea, [6] Molecular and Cellular Immunoregulation Section, Laboratory of Immune System Biology, National Institute of Allergy and Infectious Diseases, National Institutes of Health, Bethesda, MD, United States, [7] Immunology Division, Garvan Institute of Medical Research, Darlinghurst, NSW, Australia, [8] St. Vincent's Clinical School, University of New South Wales, Sydney, NSW, Australia

Edited by:
Francesca Di Rosa,
Italian National Research Council, Italy

Reviewed by:
Jose Borghans,
Utrecht University, Netherlands
Wolfgang Kastenmüller,
Julius Maximilian University of Würzburg, Germany

***Correspondence:**
Takeshi Kawabe
kawabet@med.tohoku.ac.jp
Alan Sher
asher@niaid.nih.gov

†These authors have contributed equally to this work

Specialty section:
This article was submitted to Immunological Memory, a section of the journal Frontiers in Immunology

Received: *07 February 2022*
Accepted: *29 April 2022*
Published: *30 May 2022*

Citation:
Kawabe T, Ciucci T, Kim KS, Tayama S, Kawajiri A, Suzuki T, Tanaka R, Ishii N, Jankovic D, Zhu J, Sprent J, Bosselut R and Sher A (2022) Redefining the Foreign Antigen and Self-Driven Memory CD4$^+$ T-Cell Compartments via Transcriptomic, Phenotypic, and Functional Analyses. Front. Immunol. 13:870542. doi: 10.3389/fimmu.2022.870542

Under steady-state conditions, conventional CD4$^+$ T lymphocytes are classically divided into naïve (CD44^{lo} CD62L^{hi}) and memory (CD44^{hi} CD62L^{lo}) cell compartments. While the latter population is presumed to comprise a mixture of distinct subpopulations of explicit foreign antigen (Ag)-specific "authentic" memory and foreign Ag-independent memory-phenotype (MP) cells, phenotypic markers differentially expressed in these two cell types have yet to be identified. Moreover, while MP cells themselves have been previously described as heterogeneous, it is unknown whether they consist of distinct subsets defined by marker expression. In this study, we demonstrate using combined single-cell RNA sequencing and flow cytometric approaches that self-driven MP CD4$^+$ T lymphocytes are divided into CD127^{hi} Sca1^{lo}, CD127^{hi} Sca1^{hi}, CD127^{lo} Sca1^{hi}, and CD127^{lo} Sca1^{lo} subpopulations that are Bcl2^{lo}, while foreign Ag-specific memory cells are CD127^{hi} Sca1^{hi} Bcl2^{hi}. We further show that among the four MP subsets, CD127^{hi} Sca1^{hi} lymphocytes represent the most mature and cell division-experienced subpopulation derived from peripheral naïve precursors. Finally, we provide evidence arguing that this MP subpopulation exerts the highest responsiveness to Th1-differentiating cytokines and can induce colitis. Together, our findings define MP CD4$^+$ T lymphocytes as a unique, self-driven population consisting of distinct subsets that differ from conventional foreign Ag-specific memory cells in marker expression and establish functional relevance for the mature subset of CD127^{hi} Sca1^{hi} MP cells.

Keywords: CD4$^+$ T lymphocytes, memory, homeostasis, innate immunity, phenotypic analysis

INTRODUCTION

Conventional CD4$^+$ T lymphocytes are classically divided into two main compartments in the steady state: naïve (CD44^{lo} CD62L^{hi}) and memory (CD44^{hi} CD62L^{lo}) cells. The latter cell population is thought to comprise a mixture of "authentic" memory cells derived from naïve T lymphocytes responding to explicit stimulation with foreign antigens (Ags), together with cells of a similar phenotype that are formed from naïve precursors independently of foreign Ag recognition (1–3). While the function of these foreign Ag-independent "memory-phenotype (MP)" T cells is not fully understood, we have recently shown that they are able to exert innate immune function. Thus, MP CD4$^+$ T cells can contribute to host defense against *Toxoplasma* infection by producing IFN-γ in response to IL-12 in the absence of Ag recognition (4, 5). Based on these findings, we proposed that together with their CD8$^+$ counterparts [referred to as virtual memory (T_{VM}) cells], CD4$^+$ MP T cells are participants in the lymphocyte-mediated innate immunity known to be provided by natural killer (NK) and innate lymphoid cells as well as unconventional T lymphocytes such as NKT and mucosal-associated invariant T cells (6–10).

Because of the abovementioned phenotypic similarities between CD4$^+$ MP and foreign Ag-specific memory cells, MP T lymphocytes were initially presumed to represent memory cells specific for foreign Ags derived from commensal microflora and/or food (1–3). Moreover, while previous studies attempted to define signals that are essential for the maintenance and survival of MP cells (11–13), most of the findings on the properties of these cells have proven to be equally applicable to foreign Ag-specific memory cells (12, 14, 15). Hence, the question of whether MP cells do indeed represent a phenotypically distinct cell population has remained unclear.

Nonetheless, there is accumulating evidence suggesting that MP and foreign Ag-specific memory cells arise from different developmental pathways. Traditionally, the generation of CD4$^+$ MP cells was studied using lymphopenic animals such as irradiated or gene-manipulated mice (16–20). When naïve T lymphocytes are transferred to such animals, a few clones can generate robust proliferative responses as a result of homeostatic proliferation and acquire a memory phenotype even in the absence of explicit foreign Ag recognition. More recently, we showed that this homeostatic expansion can be driven in physiologic, lymphoreplete conditions as well (4). Thus, when transferred to lymphosufficient hosts, some naïve cells proliferate to generate a CD44^{hi} CD62L^{lo} phenotype in an Ag-recognition- and CD28-dependent fashion. Because these MP cells are equally present in unimmunized specific pathogen-free (SPF) and germ-free (GF) mice (4), self Ags are thought to be the major stimulus for their steady-state development as opposed to foreign Ags that induce conventional memory T lymphocytes. Moreover, once generated, MP cells further differentiate into an innate T-bet$^+$ subset in the presence of IL-12 tonically produced by type 1 dendritic cells (5). Because this cytokine production occurs in the absence of foreign agonist-derived stimuli, T-bet$^+$ MP differentiation is considered to be a self-dependent process, unlike conventional Th1 development where foreign agonist-induced IL-12 plays a critical role (21).

In addition to being expanded by different agonists, MP and foreign Ag-specific memory T cells are known to be maintained differently once generated. Thus, in a lymphopenic environment, MP cells display two different types of homeostatic proliferation referred to as slow and fast cell division, while foreign Ag-specific memory T lymphocytes exhibit a homogeneous mild rate of proliferation (12). This suggests the involvement of distinct mechanisms for MP maintenance. Under more physiologic, lymphosufficient conditions, foreign Ag-specific memory T lymphocytes are known to be quiescent (15, 22). By contrast, more than 30% of MP cells are in the cell cycle at any given time point during homeostasis (22), and during a 4-week period, ~60% have divided at least once (23). These observations suggest that MP T lymphocytes in the steady state are maintained as two different (rapidly expanding and more quiescent) subpopulations in contrast to foreign Ag-specific memory cells that divide infrequently, again supporting the concept that MP cells are qualitatively distinct.

In the present study, we have employed transcriptomic and phenotypic analyses to address the unresolved issue of whether MP and foreign Ag-specific memory CD4$^+$ T lymphocytes are distinguishable from each other. Our data identify CD127, Sca1, and Bcl2 as key markers differentially expressed in these two cell populations and demonstrate the use of these markers in defining a previously unappreciated functional heterogeneity within the MP population.

RESULTS

Memory-Phenotype CD4$^+$ T Lymphocytes Consist of Four Subpopulations Based on CD127 and Sca1 Expression, While Foreign Antigen-Specific Memory Cells Are All CD127^{hi} Sca1^{hi}

In the case of CD8$^+$ T lymphocytes, the population of CD44^{hi} CD62L^{lo} but not CD44^{hi} CD62L^{hi} cells expands in response to immunization with foreign Ags (24). Indeed, the former cell compartment is large in feral mice while small in animals housed under SPF conditions (25). As a first step in comparing MP CD4$^+$ T lymphocytes with foreign Ag-driven memory cells, we wished to determine if a similar foreign Ag-driven expansion of the CD44^{hi} CD62L^{lo} population occurs in CD4$^+$ T cells as well. To do so, we infected SPF C57BL/6 mice with lymphocytic choriomeningitis virus (LCMV) Armstrong and waited for 6 weeks to generate foreign Ag-specific memory cells defined by tetramer staining. The CD44^{hi} CD62L^{lo} but not CD44^{hi} CD62L^{hi} CD4$^+$ T-cell fraction was found to be significantly larger in infected versus uninfected control animals, while the naïve (CD44^{lo} CD62L^{hi}) cell compartment if anything was decreased in size (**Figure 1A**). As expected, viral Ag GP66-specific as well as NP309-specific memory CD4$^+$ T cells were detected exclusively in the infected CD44^{hi} CD62L^{lo} cell population (**Figures 1B,**

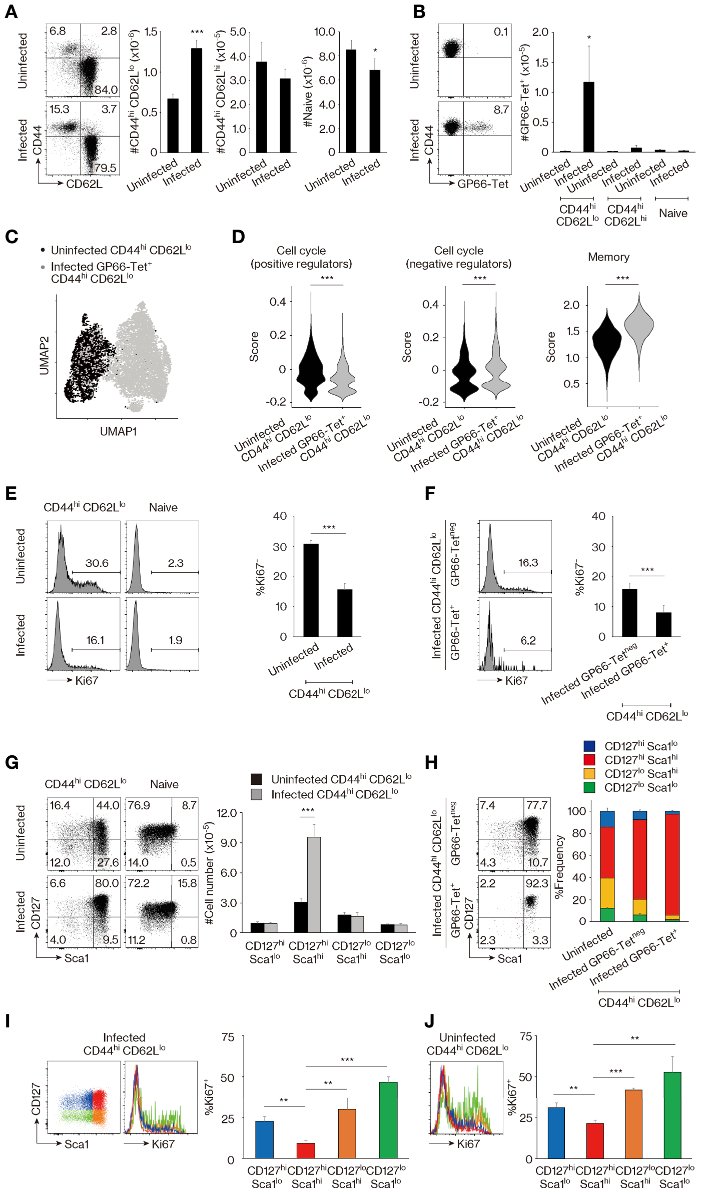

FIGURE 1 | CD44^{hi} CD62L^{lo} CD4^{+} T lymphocytes represent a mixture of memory-phenotype (MP) and foreign antigen (Ag)-specific memory cells. **(A, B)** CD44^{hi} CD62L^{lo} CD4^{+} T-cell population size is larger in lymphocytic choriomeningitis virus (LCMV)-infected versus uninfected mice because of the presence of foreign Ag-specific memory cells. **(A)** The representative dot plots show CD44 and CD62L expression in Foxp3^{neg} CD4^{+} T lymphocytes from uninfected and infected animals, while the bar graphs indicate the number (mean ± SD) of CD44^{hi} CD62L^{lo}, CD44^{hi} CD62L^{hi}, and CD44^{lo} CD62L^{hi} (naïve) cells in the same T-cell population (n = 5 mice). **(B)** Dot plots displaying GP66-tetramer binding in CD44^{hi} CD62L^{lo} CD4^{+} T lymphocytes from each group as well as a bar graph indicating the number (mean ± SD) of GP66-tetramer^{+} cells in the indicated cell populations are shown (n = 5 mice). Data are representative of 3 independent experiments performed. **(C, D)** Comparison of MP versus foreign Ag-specific memory T lymphocytes by single-cell RNA sequencing (scRNAseq) analysis. **(C)** The plot displays single cells determined by the Uniform Manifold Approximation and Projection (UMAP) algorithm. Each dot represents a cell. **(D)** The violin plots show relative expression of genes from the indicated signatures across populations. The gene list for each signature is provided in *Materials and Methods* and **Table S1**. **(E, F)** Ki67 expression is high and low in MP and foreign Ag-specific memory cells, respectively. The histograms display Ki67 expression in the indicated cell populations, while the bar graphs indicate the frequency (mean ± SD) of Ki67^{+} cells among each population (n = 3 mice). Data are representative of 3 independent experiments performed. **(G, H)** MP cells consist of CD127^{hi} Sca1^{lo}, CD127^{hi} Sca1^{hi}, CD127^{lo} Sca1^{hi}, and CD127^{lo} Sca1^{lo} subpopulations, while foreign Ag-specific memory cells are all CD127^{hi} Sca1^{hi}. Representative dot plots display CD127 and Sca1 expression in the indicated cell populations, while the bar graphs show **(G)** the number (mean ± SD) and **(H)** the frequency (mean ± SD) of each cell subpopulation (n = 5 mice). Data are representative of 2 independent experiments. **(I, J)** Ki67 levels are the lowest in the CD127^{hi} Sca1^{hi} cell subpopulation in both infected and uninfected mice. Bar graphs depicting the frequency (mean ± SD) of Ki67^{+} cells among the indicated cell subsets from **(I)** infected and **(J)** uninfected animals are shown (n = 3 mice). Representative histograms displaying Ki67 expression are also included. Data are representative of 2 independent experiments. Statistically significant differences are indicated as *$p < 0.05$, **$p < 0.01$, ***$p < 0.001$.

Figure S1A). These findings suggested that the CD44^{hi} CD62L^{lo} CD4^{+} T-cell population seen in infected animals represents a mixture of preexisting MP cells and LCMV-driven foreign Ag-specific memory cells.

To search for markers that are differently expressed in MP and foreign Ag-specific memory T lymphocytes, we compared the CD44^{hi} CD62L^{lo} cell population preexisting in the SPF environment with GP66-specific memory cells in infected mice by means of single-cell RNA sequencing (scRNAseq). Uniform Manifold Approximation and Projection (UMAP) analysis revealed that these two populations are transcriptomically distinct (**Figure 1C**), and subsequent scoring analysis indicated that expression of genes encoding positive regulators in the cell cycle (26) was higher in MP versus foreign Ag-specific memory cells, while the opposite was true for negative regulators (**Figure 1D**). Consistent with this finding, the uninfected CD44^{hi} CD62L^{lo} cell population displayed significantly higher Ki67 expression than did its counterpart in infected mice (**Figure 1E**), and closer analysis of the latter cell population revealed that GP66-specific memory cells are almost all Ki67^{neg} (**Figure 1F**). The above observations are in agreement with previous findings demonstrating that MP cells are rapidly proliferating while foreign Ag-specific memory cells are quiescent (22) and confirm the scRNAseq data shown in **Figure 1C**. Our data also support the hypothesis that the CD44^{hi} CD62L^{lo} CD4^{+} T-cell population is flexible in size, with CD44^{hi} CD62L^{lo} cells from infected mice, and especially their tetramer^{neg} subpopulation, representing a mixture of MP and foreign Ag-specific memory T lymphocytes since their Ki67^{+} fraction was intermediate in magnitude between those observed in uninfected CD44^{hi} CD62L^{lo} and infected foreign Ag-specific memory cells (as defined by GP66-tetramer staining) (**Figures 1E, F**).

Through further scoring analysis of the above scRNAseq data, we found that the expression of genes associated with memory T-cell formation (27) was significantly lower in the MP compared to the foreign Ag-specific memory compartment (**Figure 1D**). Because CD127 (IL-7 receptor α chain) and Sca1 (also referred to as Ly6a) are known to be expressed on foreign Ag-specific memory T lymphocytes (12, 28–30), we next compared their expression on CD4^{+} T cells in uninfected versus infected animals. MP (and minor population of CD44^{hi} CD62L^{hi}) cells in uninfected mice were found to consist of CD127^{hi} Sca1^{lo}, CD127^{hi} Sca1^{hi}, CD127^{lo} Sca1^{hi}, and CD127^{lo} Sca1^{lo} subsets, while naïve cells were largely CD127^{hi} Sca1^{lo} (**Figures 1G**, **S2A**). In CD44^{hi} CD62L^{lo} cells, the CD127^{hi} Sca1^{hi} but no other subpopulations increased in size in infected CD4^{+} T lymphocytes (**Figure 1G**). These results suggested that in comparison with heterogeneous MP cells, foreign Ag-specific memory cells are CD127^{hi} Sca1^{hi}. Consistent with this hypothesis, GP66- as well as NP309-tetramer^{+} memory cells were essentially all CD127^{hi} Sca1^{hi}, while the tetramer^{neg} cells that presumably represent a mixture of MP and foreign Ag-specific memory populations as described above contained a frequency of CD127^{hi} Sca1^{hi} cells intermediate between that in uninfected MP and tetramer^{+} memory cells (**Figures 1H**, **S1B**). Furthermore, in CD44^{hi} CD62L^{lo} CD4^{+} T lymphocytes, the CD127^{hi} Sca1^{hi} subset had the lowest Ki67 expression in both infected and uninfected mice (**Figures 1I, J**). Together, these data demonstrate that MP cells preexisting in an SPF environment are subdivided into four different populations based on CD127 and Sca1 expression, while foreign Ag-specific memory T lymphocytes are all CD127^{hi} Sca1^{hi}, with both populations constituting the CD44^{hi} CD62L^{lo} CD4^{+} T-cell compartment at homeostasis.

Self-Driven Memory-Phenotype T Lymphocytes Are Distinguishable From Foreign Antigen-Specific Memory Cells Based on Bcl2 Expression

Because foreign Ag-driven memory cells are CD127^{hi} Sca1^{hi} and this phenotype is partially shared by MP cells (**Figures 1G, H**), we sought to determine whether or not MP lymphocytes with the same phenotype represent a subpopulation of foreign Ag-specific memory cells. For this purpose, we re-analyzed the scRNAseq data obtained in **Figure 1C** and found that expression of anti-apoptotic genes (31) was significantly lower in MP versus foreign Ag-specific memory cells (**Figure 2A**). Given that *Bcl2* plays a critical role as an anti-apoptotic factor in T lymphocytes (32), we measured its protein expression levels in these two populations. While CD127^{hi} Sca1^{hi} MP cells were largely Bcl2^{lo}, ~90% of CD127^{hi} Sca1^{hi} GP66- and NP309-tetramer^{+} memory T lymphocytes were Bcl2^{hi} (**Figures 2B**, **S1C**). Thus, CD127^{hi} Sca1^{hi} MP cells appear to represent a unique population that is distinct from foreign Ag-specific memory T lymphocytes in terms of Bcl2 expression. In addition, we observed a small fraction (~10%) of Bcl2^{hi} cells in CD127^{hi} Sca1^{hi} MP CD4^{+} T cells, and this fraction was more enriched in CD44^{hi} CD62L^{hi} cells (**Figures 2B**, **S2B**). The significance of this finding will be discussed later.

To further investigate whether the development of the CD127^{hi} Sca1^{hi} MP subset is foreign Ag-dependent or Ag-independent, we examined MP cells from SPF, GF, and antigen-free (AF) mice, the latter being deprived of both food and commensal Ags (33). MP as well as CD44^{hi} CD62L^{hi} and naïve CD4^{+} T cells were essentially intact in SPF, GF, and AF mice (**Figure 2C**). Surprisingly, CD127^{hi} Sca1^{hi} MP cells were largely unchanged in the three animal groups (**Figure 2D**). In addition, Ki67 expression was not significantly increased in GF or AF mice, and Bcl2 levels were not decreased and instead were elevated in the former animals (**Figures 2E, F**). This was also the case in the minor CD44^{hi} CD62L^{hi} CD4^{+} T-cell population (**Figure S2C, D**). Thus, CD127^{hi} Sca1^{hi} Bcl2^{lo} MP cells can be generated in the absence of foreign Ags, presumably in response to self Ags.

Among the Four Memory-Phenotype Subsets, CD127^{hi} Sca1^{hi} Cells Represent the Most Mature Subpopulation Generated From Peripheral Naïve Precursors

The above results identify CD127, Sca1, and Bcl2 as markers that are differently expressed in foreign Ag-specific memory versus

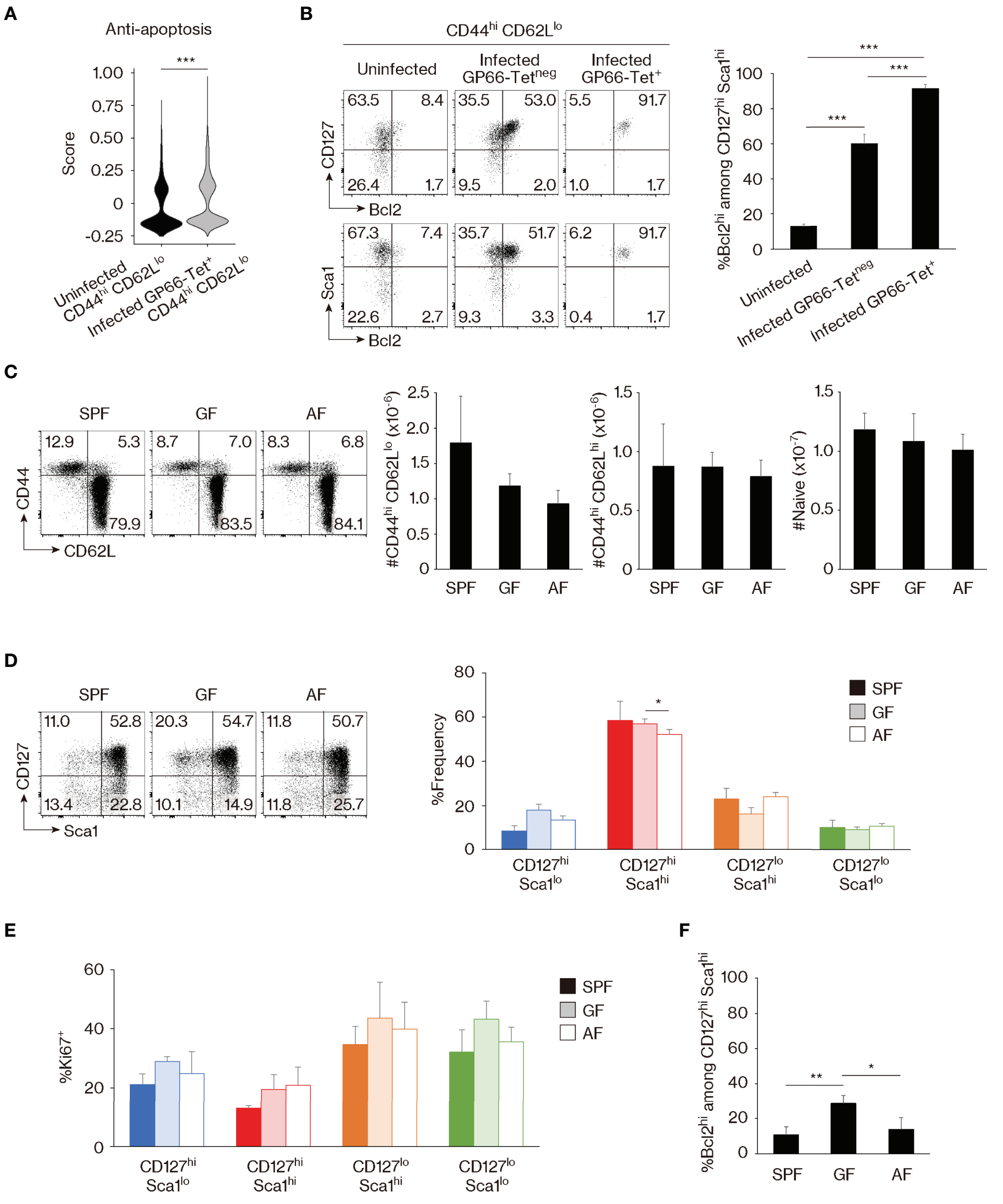

FIGURE 2 | Bcl2 marks foreign antigen (Ag)-specific memory versus self-driven memory-phenotype (MP) cells. **(A)** Comparison of gene expression between MP versus foreign Ag-specific memory cells. The violin plot shows relative expression of anti-apoptotic genes across populations. The anti-apoptotic gene list is provided in *Materials and Methods* and **Table S1**. **(B)** Foreign Ag-specific memory cells are Bcl2^{hi}. The representative dot plots display expression levels of CD127, Sca1, and Bcl2 in the indicated CD44^{hi} CD62L^{lo} cell populations, while the bar graph shows the frequency (mean ± SD) of Bcl2^{hi} cells among the indicated CD127^{hi} Sca1^{hi} subpopulations (n = 3–4 mice). Data are representative of 2 independent experiments. **(C, D)** Commensal or food Ags do not significantly contribute to generation of CD127^{hi} Sca1^{hi} MP cells in specific pathogen-free (SPF) environment. Dot plots depicting expression of **(C)** CD44 and CD62L in CD4^{+} T lymphocytes as well as **(D)** CD127 and Sca1 in MP cells from the indicated animals together with bar graphs indicating **(C)** the number (mean ± SD) of CD44^{hi} CD62L^{lo} (MP), CD44^{hi} CD62L^{hi}, and CD44^{lo} CD62L^{hi} (naïve) CD4^{+} T cells as well as **(D)** the frequency (mean ± SD) of MP subpopulations among total MP cells from each group are displayed (n = 3–4 mice). Data are representative of 2 independent experiments performed. **(E, F)** Expression levels of Ki67 and Bcl2 in MP cells are largely unaltered in the absence of commensal and/or food Ags. **(E)** The bar graph shows the frequency (mean ± SD) of Ki67^{+} cells among the indicated MP subpopulations (n = 3–4 mice). **(F)** A bar graph indicating the frequency (mean ± SD) of Bcl2^{hi} cells among CD127^{hi} Sca1^{hi} MP cells from the indicated groups (n = 3–4 mice). Data are representative of 2 independent experiments. Statistically significant differences are indicated as *$p < 0.05$, **$p < 0.01$, and ***$p < 0.001$.

MP cells and indicate that MP CD4^{+} T lymphocytes comprise 4 distinct subsets: CD127^{hi} Sca1^{lo}, CD127^{hi} Sca1^{hi}, CD127^{lo} Sca1^{hi}, and CD127^{lo} Sca1^{lo}. Because CD127^{hi} Sca1^{hi} MP cells are present in almost equal numbers in SPF, GF, and AF mice, self Ags are thought to be the major stimuli for the generation of CD127^{hi} Sca1^{hi} as well as the other MP subsets in an SPF environment. To address how the four MP subpopulations defined by these phenotypic markers are generated and maintained, we measured CD127 and Sca1 levels in MP cells from mice of different ages. As expected, MP cells were rare in 1-week-old animals, and most of these cells were CD127^{hi} Sca1^{lo} (**Figures 3A, B**). Thereafter, the proportion of CD127^{hi} Sca1^{hi} lymphocytes increased progressively with age, in parallel with the total MP pool size.

In the case of CD8$^+$ MP cells, a subpopulation referred to as innate memory cells are directly generated in the thymus (34). To ask whether CD127^{hi} Sca1^{hi} CD4$^+$ MP cells arise in the thymus, we prevented lymphocyte egress from the thymus by injecting mice with FTY720 for 2 weeks. As expected, numbers of both CD4$^+$ and CD8$^+$ single-positive thymocytes accumulated in the thymus (**Figure S3A**), and in parallel, naïve CD4$^+$ T cells decreased in number in secondary lymphoid tissues (**Figures S3B, C**). By contrast, peripheral MP CD4$^+$ T lymphocytes as well as their four subfractions were largely unaffected by the treatment (**Figures S3B–D**), suggesting that MP cells are self-maintained in the periphery once generated. Consistent with this conclusion,

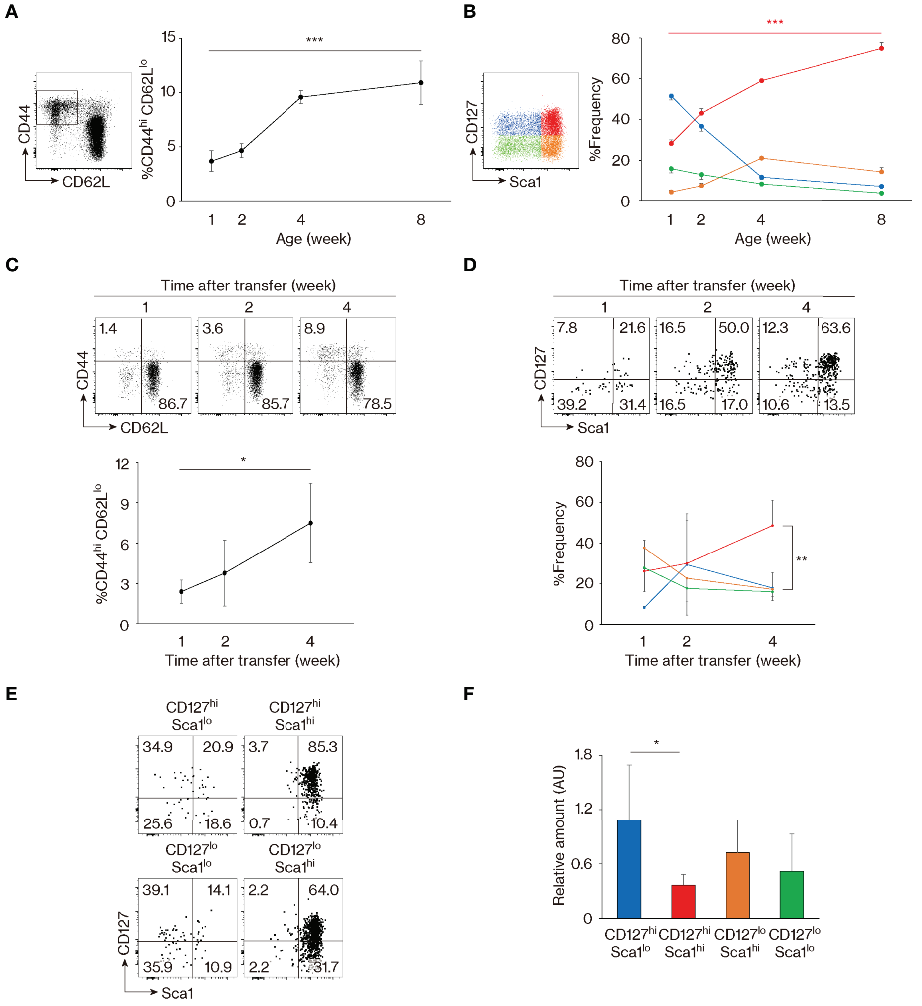

FIGURE 3 | Memory-phenotype (MP) T lymphocytes are composed of four subsets representing different stages of maturation. **(A, B)** CD127^{hi} Sca1^{hi} MP cells develop with age. The graphs indicate the fractions (mean ± SD) of **(A)** CD44^{hi} CD62L^{lo} among CD4$^+$ T cells and **(B)** each subpopulation among MP cells (n = 3–5 mice). Representative dot plots displaying expression of **(A)** CD44 and CD62L in CD4$^+$ T lymphocytes and **(B)** CD127 and Sca1 in MP CD4$^+$ T cells are also included. Data shown are pooled from 2 independent experiments performed. **(C, D)** CD127^{hi} Sca1^{hi} MP cells are generated from naïve precursors. Naïve CD4$^+$ T lymphocytes sorted from CD45.2 mice were transferred to CD45.1 wild-type (WT) recipients and analyzed several weeks later. Dot plots show **(C)** CD44 and CD62L expression in the donor cell population and **(D)** CD127 and Sca1 levels in the newly generated MP donor cells, while the graphs indicate the frequency (mean ± SD) of **(C)** MP cells in the donor cell population and **(D)** the indicated subpopulations among MP donor cells (n = 3–4 mice). Data are representative of 2 independent experiments. **(E)** All four MP subsets eventually differentiate into CD127^{hi} Sca1^{hi} cells. Four MP subpopulations sorted from CD45.2 mice were transferred to CD45.1 WT recipients and analyzed for their CD127 and Sca1 expression 2 weeks later. Dot plots in the indicated donor MP subpopulations are shown. Data are representative of 4–5 recipient mice from 3 independent experiments performed. **(F)** CD127^{hi} Sca1^{hi} MP T lymphocytes have the lowest amount of TRECs. A bar graph indicating the amount (mean ± SD) of TRECs relative to *Gapdh* that was calculated by the ΔCt method in each MP subpopulation is depicted (n = 5 mice). Data are representative of 2 independent experiments performed. Statistically significant differences are indicated as *$p < 0.05$, **$p < 0.01$, and ***$p < 0.001$.

the four MP subpopulations were not altered by adult thymectomy (**Figure S3E**). Based on these results, it is unlikely that peripheral CD127^{hi} Sca1^{hi} and other MP subpopulations are actively replaced by emigrants generated in the thymus.

To test the possibility that CD127^{hi} Sca1^{hi} MP cells are generated from peripheral naïve precursors, we transferred sorted naïve CD4^{+} T lymphocytes into wild-type (WT) recipients and analyzed the donor cells 1 to 4 weeks later. MP cells developed slowly with time (**Figure 3C**), with the CD127^{hi} Sca1^{hi} subset dominating by 4 weeks after transfer (**Figure 3D**). Thus, the four MP subsets including the CD127^{hi} Sca1^{hi} fraction appear to be generated from naïve T lymphocytes in the periphery.

To further examine the dynamics of MP cell maintenance following their development, we sorted for CD127^{hi} Sca1^{lo}, CD127^{hi} Sca1^{hi}, CD127^{lo} Sca1^{hi}, and CD127^{lo} Sca1^{lo} MP subpopulations and transferred them individually to WT recipients. When the donor cell population was analyzed 2 weeks later, Sca1^{lo} cells were found to increase their Sca1 expression, while Sca1^{hi} cells remained Sca1^{hi} (**Figure 3E**). In addition, some CD127^{hi} cells converted to CD127^{lo} and vice versa (**Figure 3E**). Overall, these data argue that while naïve cells are CD127^{hi} Sca1^{lo}, as they differentiate into MP cells, they eventually acquire a CD127^{hi} Sca1^{hi} phenotype, either directly from CD127^{hi} Sca1^{lo} precursors or *via* CD127^{lo} intermediates. Consistent with this notion, when the levels of T-cell receptor (TCR) excision circles (TRECs) were measured in the four MP subpopulations sorted from intact mice, levels were the highest and lowest in CD127^{hi} Sca1^{lo} and CD127^{hi} Sca1^{hi} cell populations, respectively, with CD127^{lo} cells expressing TRECs at an intermediate level (**Figure 3F**). Together, these data identify CD127^{hi} Sca1^{hi} MP cells as the most mature of the four subsets, their generation reflecting extensive cell division of their precursors.

Memory-Phenotype Subpopulations Are Maintained Through T-Cell Receptor and CD28 Signaling

We previously reported that, as a whole population, MP cells become less dependent on TCR signaling once generated (4). This notion was based on the observation that treatment of SPF mice with either anti-I-Aβ monoclonal antibody (mAb) or cyclosporin A significantly inhibits the generation of MP cells from naïve precursors but has only a negligible effect on their steady-state proliferation. While these data established a lesser dependence of MP cell maintenance on Ag recognition, it was still unclear whether this function is completely independent of TCR signaling.

To address this issue, we analyzed the strength of TCR signaling that MP subpopulations receive at baseline. Initial experiments revealed that the four MP subsets express equivalent levels of TCRβ and CD3 as well as CD5 (**Figures 4A, B**), a marker that reflects TCR affinity to self Ags (35). Nevertheless, in Nur77-GFP reporter mice where the sum of TCR signal strength that T cells receive is reflected by reporter expression (36), CD127^{lo} Sca1^{hi} and CD127^{lo} Sca1^{lo} MP subpopulations showed significantly higher levels of GFP as well as CD69 than did their CD127^{hi} counterparts (**Figures 4C, D**). Given that CD127^{hi} and CD127^{lo} subsets are interchangeable in the steady state (**Figure 3E**), it is possible that the former MP subpopulation downregulates CD127 immediately after TCR ligation.

To test this hypothesis *in vivo*, we utilized CD4-CreERT2 TCRα^{flox} mice in which we previously established that ~50% of MP cells lose their TCR expression as a consequence of tamoxifen (TMX) treatment (5). Thus, by examining the four MP subfractions in TCRβ^{+} and TCRβ^{neg} MP subpopulations 10 days after TMX treatment, we could compare their steady-state proliferation in the presence or absence of normal levels of tonic TCR signaling in the same mouse. Using these animals, we found that Ki67 expression was significantly reduced by TCR ablation in all four MP subpopulations (**Figure 4E**). Moreover, the CD127^{hi} fraction increased while the CD127^{lo} decreased in size when TCR levels were reduced (**Figure 4F**). These results show that the four MP subpopulations proliferate in the presence of tonic TCR signaling, presumably delivered by self Ag recognition, and further suggest the existence of TCR-dependent interchangeability between CD127^{hi} and CD127^{lo} MP cells in a dynamic steady state.

In addition to TCR engagement, CD28 ligation plays an essential role in MP cell maintenance (4). To assess the function of the same signaling pathway in the four MP subpopulations, we treated mice with CTLA4-Ig for 10 days. In a similar manner to that induced by TCR signal blockade, Ki67 expression was reduced in the CTLA4-Ig-treated group, and CD127^{hi} cells increased while their CD127^{lo} counterparts decreased in the same animals (**Figures 4G, H**). Thus, optimal proliferation and dynamic equilibrium of MP cell subpopulations require tonic CD28 engagement in addition to TCR signaling.

CD127^{hi} Sca1^{hi} Memory-Phenotype Cells Have a Th1 Cytokine Signature

The above observation that CD127, Sca1, and Bcl2 are differently expressed in MP and foreign Ag-driven memory CD4^{+} T cells revealed an unexpected phenotypic heterogeneity within the former lymphocyte population (**Figures 1–4**). This finding prompted us to ask whether these four MP cell subpopulations possess different functions. The experiments performed above defined MP subpopulations based on markers (CD127 and Sca1) that are well known to characterize foreign Ag-driven memory cells, but left open the possibility that other molecules might better characterize functional MP subsets. To address this question, we analyzed the MP cell population in the scRNAseq dataset generated in **Figure 1C** by unsupervised clustering, to define its components based on the full transcriptome rather than on predefined markers. This analysis divided the MP cell population into four clusters (I–IV) (**Figures 5A, B**). Comparing the expression of *Il7r* and *Ly6a* among these four clusters showed a clear demarcation into *Il7r*^{hi} *Ly6a*^{lo}, *Il7r*^{hi} *Ly6a*^{hi}, *Il7r*^{lo} *Ly6a*^{hi}, and *Il7r*^{lo} *Ly6a*^{lo} gene expression patterns for clusters (I), (II), (III), and (IV), respectively; importantly, these correspond respectively to the CD127^{hi} Sca1^{lo}, CD127^{hi} Sca1^{hi}, CD127^{lo}

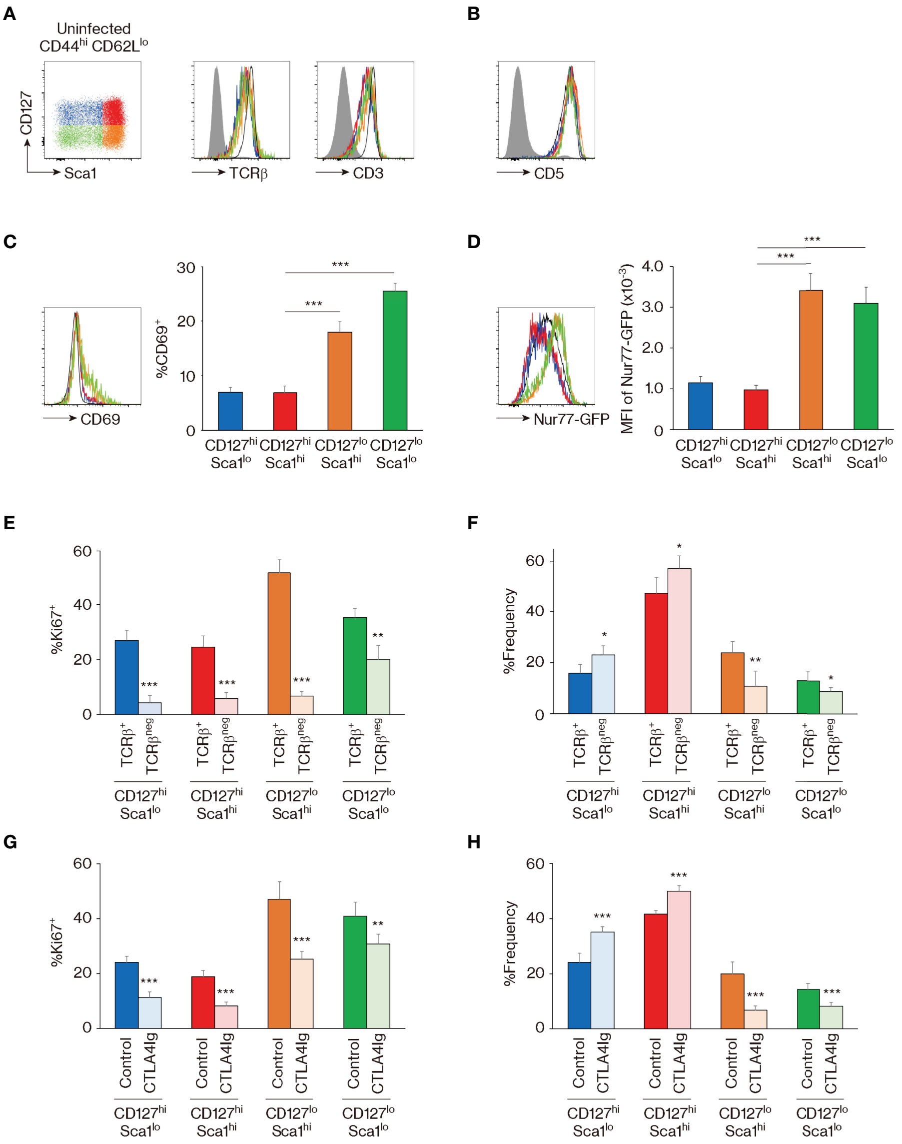

FIGURE 4 | The four memory-phenotype (MP) subpopulations are maintained *via* T-cell receptor (TCR) and CD28 signaling. **(A–D)** CD127^{lo} MP subsets represent cell populations that have recently received TCR signaling. Representative histograms display **(A)** TCRβ, CD3, **(B)** CD5, **(C)** CD69, and **(D)** GFP expression in the indicated MP subpopulations from Nur77-GFP reporter mice, while the bar graphs indicate **(C)** the frequency (mean ± SD) of CD69$^+$ and **(D)** the mean fluorescence intensity (MFI) (mean ± SD) of GFP among the MP subpopulations (n = 5 mice). Filled histograms show negative control staining, whereas black and open histograms display naïve CD4$^+$ T cells. **(E, F)** TCR signaling is essential for proliferation and dynamic equilibrium of MP subpopulations. CD4-CreERT2 TCRα^{flox} mice received tamoxifen (TMX) and were analyzed 10 days later. Bar graphs indicating the frequency (mean ± SD) of **(E)** Ki67$^+$ cells among both TCRβ$^+$ and TCRβ^{neg} fractions from each MP subset and **(F)** the indicated subpopulations among the TCRβ$^+$ or TCRβ^{neg} MP cells are depicted (n = 5 mice). **(G, H)** CD28 signals are critical for optimal maintenance of MP subpopulations. Mice received CTLA4-Ig and were analyzed 10 days later. The bar graphs show the frequency (mean ± SD) of **(G)** Ki67$^+$ cells among the indicated MP subpopulations from each group and **(H)** the indicated subsets among total MP T lymphocytes (n = 5 mice). Data are representative of 2 independent experiments. Statistically significant differences are indicated as $^*p < 0.05$, $^{**}p < 0.01$, and $^{***}p < 0.001$.

Sca1^{hi}, and CD127^{lo} Sca1^{lo} MP subpopulations defined in **Figure 1G**. The results of this analysis thus provide independent support to the conclusion that CD127 and Sca1 expression define four transcriptomically distinct MP subpopulations. Further clustering and scoring analyses revealed that the cluster (II), that is *Il7r*^{hi} *Ly6a*^{hi} and thus equivalent to the CD127^{hi} Sca1^{hi} MP subpopulation, has the highest Th1-associated gene signature (27) (**Figures 5B, C**), suggesting that this subset displays Th1-related function.

We have previously shown that MP CD4$^+$ T lymphocytes can respond to IL-12 and produce IFN-γ *in vivo* (4). Consistent with this finding, when whole splenocytes were cultured in the presence of IL-12, IL-18, IL-2, or a combination of these cytokines *in vitro*, CD4$^+$ MP cells produced IFN-γ in response

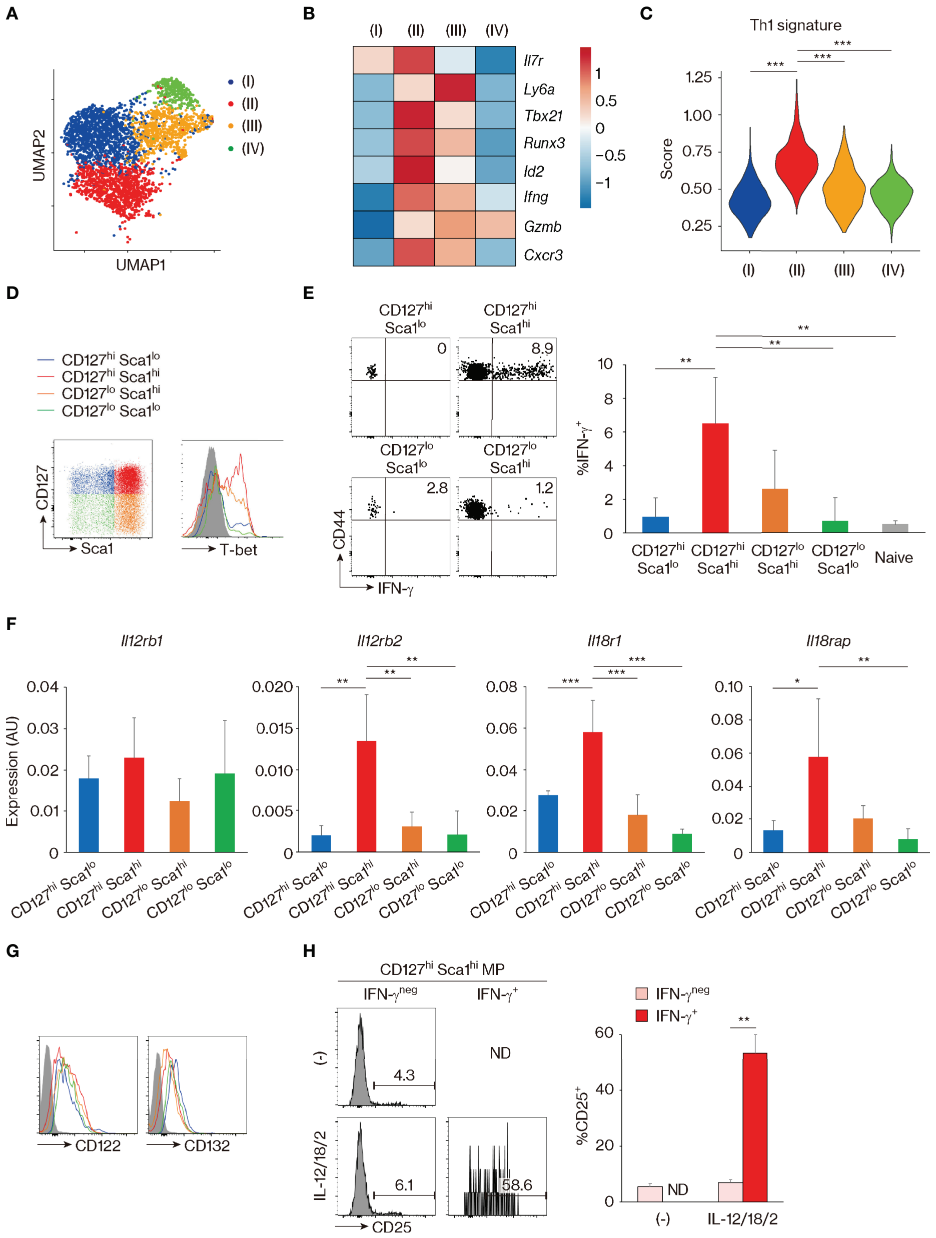

FIGURE 5 | CD127^{hi} Sca1^{hi} memory-phenotype (MP) T lymphocytes can exert innate Th1-like activity *in vitro*. **(A–C)** Clustering analysis of MP T lymphocyte population. Single-cell RNA sequencing (scRNAseq) data of MP cells in Figure 1C were analyzed by unsupervised clustering. **(A)** The plot displays single cells determined by the Uniform Manifold Approximation and Projection (UMAP) algorithm. Each dot represents a cell, and colors highlight unsupervised cell clusters. Clusters representing less than 5% of the total MP population were excluded. **(B)** A heatmap showing row-standardized expression of selected genes among MP clusters. **(C)** A violin plot depicting relative expression of Th1-associated genes in the indicated MP clusters. **(D)** CD127^{hi} Sca1^{hi} MP cells express the highest levels of T-bet. A representative histogram showing T-bet levels in each MP subset from 3 mice is depicted. **(E)** CD127^{hi} Sca1^{hi} MP subpopulation can produce IFN-γ in response to Th1-differentiating cytokines in the absence of antigen (Ag) recognition. Sorted MP as well as naïve CD4^{+} T cell subpopulations were stimulated with IL-12, IL-18, and IL-2 for 24 h. The dot plots show IFN-γ production by the indicated cells, while the bar graph depicts the IFN-γ^{+} fraction (mean ± SD) among the MP and naïve subpopulations (n = 4 mice). Data shown are representative of 2 independent experiments performed. **(F)** The CD127^{hi} Sca1^{hi} MP subset expresses high amounts of *Il12rb2*, *Il18r1*, and *Il18rap*. Bar graphs showing relative expression levels of the indicated genes in each MP subpopulation are depicted (n = 4 mice). Data are representative of 2 independent experiments. **(G, H)** CD127^{hi} Sca1^{hi} MP cells express functional IL-2 receptors under the presence of Th1-differentiating cytokines. Representative histograms in **(G)** display CD122 and CD132 expression in each MP subset from 4 mice in steady state, while those in **(H)** show CD25 expression in IFN-γ^{neg} and IFN-γ^{+} fractions of sorted CD127^{hi} Sca1^{hi} MP cells that were cultured in the presence or absence of IL-12, IL-18, and IL-2 for 24 h. A bar graph indicating the frequency (mean ± SD) of CD25^{+} cells among each group is also depicted (n = 3 mice). Data are representative of 2 independent experiments performed. Statistically significant differences are indicated as $*p < 0.05$, $**p < 0.01$, and $***p < 0.001$. ND, not detected.

to IL-12 (**Figure S4A**). The latter response increased with the addition of IL-18 and IL-2 and peaked at 24–48 h after cytokine stimulation (**Figures S4A, B**). With this *in vitro* system, we asked which of the MP subpopulation(s) can generate the above-described Th1-like response. To do so, we first checked the expression of T-bet, which we previously reported to play an essential role in the determination of Th1-like MP cell activity (4, 5). As shown in **Figure 5D**, CD127^{hi} Sca1^{hi} cells expressed the highest levels of T-bet, confirming the result of clustering analysis in **Figure 5B**. Consistent with this observation, when each MP subpopulation as well as naïve cells was sort-purified and cultured individually in the presence of IL-12, IL-18, and IL-2, CD127^{hi} Sca1^{hi} MP cells produced high amounts of IFN-γ (**Figure 5E**). Furthermore, the same MP subpopulation expressed high levels of *Il12rb2*, *Il18r1*, and *Il18rap* in the steady state (**Figure 5F**). In terms of IL-2 receptor expression, CD122 and CD132 were expressed on all four MP subsets (**Figure 5G**). However, CD25 (IL-2 receptor α chain) was only induced when CD127^{hi} Sca1^{hi} MP cells were stimulated by Th1 cytokines (**Figure 5H**), consistent with previous reports showing that IL-12 upregulates CD25 on Th1 cells (37, 38). Together, these results identify CD127^{hi} Sca1^{hi} MP T lymphocytes as a resting population with selective Th1 effector potential.

Finally, we sought to validate the above functional observations *in vivo*. Naïve CD4$^+$ T lymphocytes are known to induce severe colitis when transferred to *Rag2* knockout (KO) mice (39, 40). Using this approach, we tested the capacity of MP cell subpopulations to induce colitis by individually transferring CD127^{hi} Sca1^{lo}, CD127^{hi} Sca1^{hi}, CD127^{lo} Sca1^{hi}, and CD127^{lo} Sca1^{lo} Foxp3$^-$ MP CD4$^+$ T cell subsets from Foxp3-reporter mice to *Rag2* KO recipients. CD127^{hi} Sca1^{hi} cells were found to induce mild body weight loss and clinical as well as histological colitis (**Figures 6A–C**). Consistent with this observation, the total number of recovered donor cells was the highest in the CD127^{hi} Sca1^{hi} recipient group (**Figure 6D**). Thus, among the four MP subpopulations, the CD127^{hi} Sca1^{hi} subset induces the most severe colitis when transferred to *Rag2* KO mice. We further asked whether colitis driven by the CD127^{hi} Sca1^{hi} MP subpopulation is dependent on IL-12 and/or IL-23. To do so, we blocked IL-12 p40 using mAb specific for the cytokine after donor cell transfer. As shown in **Figures 6E–G**, body weight loss, clinical symptoms, and histological colitis were almost completely abrogated as a result of mAb treatment. Consistent with this, the total number of donor cells and their IFN-γ$^+$ fraction were dramatically reduced in the same mAb-treated animals (**Figures 6H, I**). These data suggest that in *Rag2* KO mice, CD127^{hi} Sca1^{hi} MP cells can generate inflammatory responses, thus supporting their functional relevance.

DISCUSSION

CD4$^+$ T lymphocytes with a memory phenotype present in normal, unimmunized animals have been known for more than 30 years and have been presumed to comprise a mixture of explicit foreign Ag-specific “authentic” memory and foreign Ag-independent MP cells (1–3). A number of previous studies have addressed the features of these two CD4$^+$ T-cell populations. Thus, we and other groups showed that nearly all conventional foreign Ag-specific memory cells are resting cells with a slow turnover and are largely major histocompatibility complex (MHC)-independent while heavily dependent on the cytokines IL-7 and/or IL-15. In contrast, naturally arising MP cells comprise a mixture of fast-proliferating, MHC-dependent cells together with slowly proliferating, IL-7-dependent cells (12, 22, 23). However, a definitive comparison of these subsets was not possible because of the lack of phenotypic markers.

Our present study addressed this long-standing problem by searching for phenotypic differences between MP and foreign Ag-specific memory CD4$^+$ T cells. As shown here, we have identified CD127, Sca1, and Bcl2 as key markers that are differently expressed in these two lymphocyte populations. Thus, our data demonstrate that foreign Ag-specific memory T lymphocytes comprise a homogeneous population of CD127^{hi} Sca1^{hi} Bcl2^{hi} cells, while MP cells are a heterogeneous mixture of CD127$^{lo\sim hi}$ Sca1$^{lo\sim hi}$ that are mostly Bcl2^{lo} (summarized in **Figure S5**). While in the case of CD8$^+$ T lymphocytes T_{VM} and foreign Ag-specific memory cells have been previously reported to be distinguishable from each other based on their levels of integrins α4, α1, and β1 as well as NKG2D (41, 42), our findings are the first to demonstrate differential marker expression between CD4$^+$ MP and foreign Ag-specific memory cells and strongly support the notion that these two cell types are qualitatively distinct. Furthermore, employing these markers, we have identified distinct types of subsets within the MP population, with inflammatory activity predominantly associated with the CD127^{hi} Sca1^{hi} phenotype.

The mechanisms responsible for the generation and maintenance of foreign Ag-specific memory CD4$^+$ T lymphocytes are well defined (2). Thus, in conventional adaptive immune responses against pathogens, naïve T lymphocytes that are specific for challenge Ags robustly proliferate to give rise to effector cells that contribute to host defense. After pathogen clearance, most effector cells die, leaving a small residual population of foreign Ag-specific memory cells that protects the host from secondary infection with the same pathogen. For memory cells to exert such long-term host-protective function, they need to survive long term in the absence of stimulation by cognate foreign Ags. IL-7 serves a major role in this function (12, 14, 15). This cytokine triggers T cells through its receptor to promote their survival by inducing Bcl2 upregulation and basal turnover in memory cells. In this context, our finding that foreign Ag-specific memory cells express high levels of CD127 and Bcl2 is not surprising.

In contrast, the mechanisms responsible for MP cell maintenance have been less clearly understood (1–3). In the past, this process has been investigated primarily by transferring MP cells to congenic, usually lymphopenic, recipient mice and analyzing the donor cells 1~2 weeks later. Previous reports established that under such situations, MP CD4$^+$ T lymphocytes exhibit two different types of cell division (i.e., slow and fast homeostatic proliferation) as compared to foreign Ag-specific memory cells that exhibit mild and homogeneous cell expansion, and that slow proliferation requires IL-7 while rapid

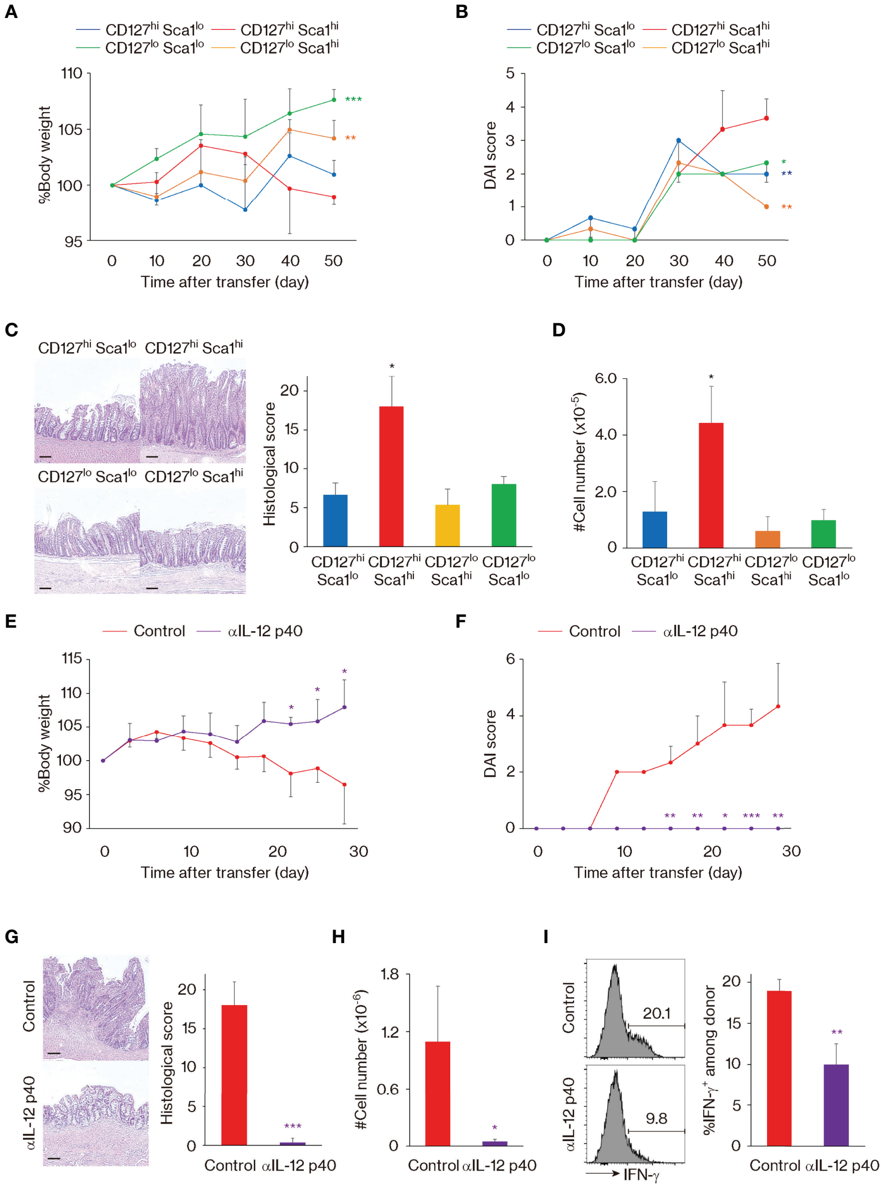

FIGURE 6 | The CD127^{hi} Sca1^{hi} memory-phenotype (MP) cell subset can induce colitis in *Rag2* knockout (KO) mice. **(A–D)** Among the four MP subsets, CD127^{hi} Sca1^{hi} cells can induce the most severe colitis. Sorted MP subpopulations were individually transferred to *Rag2* KO recipient mice. Graphs indicate **(A)** relative body weight (mean ± SD) and **(B)** disease activity index (DAI) score (mean ± SD) in each group at different time points as well as **(C)** histological score (mean ± SD) and **(D)** the number (mean ± SD) of donor cells in the colon on day 50 (n = 3 mice). Representative images showing histology of the colon from each group are also included in panel **(C)**. **(E–I)** Blockade of IL-12 p40 ameliorates MP-induced colitis. Sorted CD127^{hi} Sca1^{hi} MP cells were transferred to *Rag2* KO mice that were then treated with anti-IL-12 p40 mAb or control IgG. Graphs show **(E)** relative body weight (mean ± SD) and **(F)** DAI score (mean ± SD) in each group at different time points as well as **(G)** histological score (mean ± SD), **(H)** the number (mean ± SD) of donor cells, and **(I)** their IFN-γ$^+$ fraction (mean ± SD) in the colon on day 28 (n = 3 mice). Histological images of the colon from each group on day 28 are displayed in **(G)**. Data shown are representative of 2 independent experiments. Scale bars in histological images show 100 μm. Statistically significant differences are indicated as *$p < 0.05$, **$p < 0.01$, and ***$p < 0.001$.

cell division is more dependent on TCR and costimulatory signaling (11–13). Here we provide new evidence suggesting that IL-7-dependent slow expansion can occur homeostatically in physiologic, non-transferred conditions since we observed that some MP cells express functional IL-7 receptors as evidenced by the joint presence of CD127 and CD132 (**Figures 1G**, **5G**) and that such CD127^{hi} subsets display lower levels of Ki67 than their CD127^{lo} counterparts (**Figure 1J**). In addition, under these normal lymphoreplete conditions, TCR-dependent fast cell division was the most conspicuous for CD127^{lo} MP cells and was marked by a Ki67$^+$ phenotype (**Figure 1J**) together with evidence of strong TCR and CD28 signaling (**Figure 4**).

In lymphosufficient conditions, we previously suggested that rapid proliferation of MP CD4$^+$ T lymphocytes is balanced by comparable cell death (4), a situation distinct from that observed with quiescent foreign Ag-specific memory cells (15, 22). Our present data are consistent with this difference since Bcl2, which is critical for T lymphocyte longevity (32), was significantly lower in MP as compared to foreign Ag-specific memory cells (**Figure 2B**). This low Bcl2 expression in MP cells was maintained after LCMV infection, a situation that is particularly apparent in the CD127^{lo} or Sca1^{lo} subsets within the CD44^{hi} CD62L^{lo} population in infected mice (**Figure 2B**). Together with our observation that the CD127^{lo} or Sca1^{lo} subsets (i.e., CD127^{hi} Sca1^{lo}, CD127^{lo} Sca1^{hi}, and CD127^{lo} Sca1^{lo} cells) were largely unchanged after LCMV infection (**Figure 1G**), these data argue that the Bcl2^{lo} as well as CD127$^{lo\sim hi}$ and Sca1$^{lo\sim hi}$ phenotype is a unique feature of MP T lymphocytes regardless of whether animals have been pathogen exposed. The above findings are also consistent with our hypothesis based on previous studies with *Toxoplasma* infection that during the early stages following pathogen challenge, the short-lived Bcl2^{lo} MP cell population contributes to transient host protection until this function is replaced through the development of Bcl2^{hi} foreign Ag-specific memory cells (4, 5).

In addition to the large low Bcl2 expression in MP cells, we observed that ~10% of CD127^{hi} Sca1^{hi} MP cells are Bcl2^{hi} (**Figures 2B**, **S1C**). In this regard, a previous study pointed out that MP cells contain a minor fraction of cells that closely resemble Ag-specific memory cells, although whether the Ags driving the MP cells are foreign or self was unclear (12). In the present study, the minor CD127^{hi} Sca1^{hi} Bcl2^{hi} MP cells were not reduced in GF or AF mice and even increased in the former animals (**Figure 2F**), arguing that these cells can arise through contact with self Ags, although the explanation for why the same fraction was elevated in GF mice remains unclear. Interestingly, the Bcl2^{hi} MP cell compartment was enriched in CD44^{hi} CD62L^{hi} CD4$^+$ T cells (**Figure S2**), i.e., the counterpart of the "central memory" cells that form the bulk of CD44^{hi} MP CD8$^+$ T lymphocytes (41, 43). These CD62L^{hi} cells may be viewed as fully differentiated MP cells, for both CD4$^+$ and CD8$^+$ T cells.

For CD4$^+$ MP cells, the relative paucity of CD44^{hi} CD62L^{hi} cells correlates with low expression of CD122 on CD4$^+$ versus CD8$^+$ T cells, thereby making mature CD4$^+$ MP cells poorly reactive to IL-15 and therefore largely dependent on IL-7 for their survival (12). Since levels of IL-7 are low in lymphoreplete animals (44), one can envision that survival of MP CD4$^+$ T cells is heavily dependent on contact with self Ag/MHC complexes, with only a few of the responding cells able to slowly differentiate into an MHC-independent resting state. This small fraction of Bcl2^{hi} cells may reflect the self-driven counterparts of foreign Ag-specific memory CD4$^+$ T cells. In the case of the latter population, their rapid switch to a fully differentiated state after initial induction may simply reflect that, unlike MP cells, foreign Ag-specific memory cells rapidly lose contact with stimulatory Ags when the pathogen concerned is eliminated, forcing the surviving cells to become MHC-independent.

The factors controlling the generation and maintenance of MP cells through contact with available ligands including self Ags are still poorly understood (1–3). For CD4$^+$ MP cells, it is striking that the component of fast-proliferating cells in lymphoreplete hosts is far more conspicuous than for CD8$^+$ cells (12, 16) and, as mentioned above, is accompanied by prominent signs of TCR activation on the responding CD4$^+$ T cells (**Figures 4C, D**). The reason for this difference is unclear but it could reflect higher intrinsic TCR affinity for self ligands by CD4$^+$ than CD8$^+$ T cells. Thus, CD5 expression is substantially higher on naïve CD4$^+$ than CD8$^+$ T cells (45). Furthermore, this higher affinity to self Ags in CD4$^+$ T lymphocytes may account for their capacity to regulate T-cell homeostasis. Indeed, a previous report showed that CD4$^+$ T cells that react to subthreshold, endogenous peptide ligands compete with other T-cell clones with similar TCR specificities, thus preventing their outgrowth (46). However, why some naïve T lymphocytes spontaneously initiate responses to self Ags and then differentiate into resting cells remains unclear.

Despite their still undefined origin, MP CD4$^+$ T cells can exert host protective effector function in response to IL-12 (4, 5). Our finding that these cells vary in their expression of CD127, Sca1, and Bcl2 allowed us to examine which subsets of CD4$^+$ MP cells possess this cytokine reactivity. We observed that the capacity to respond to IL-12 and exert Th1-dependent inflammation *in vitro* is controlled largely by the mature CD127^{hi} Sca1^{hi} subset (**Figure 5**). We further identified that the same subset induces the most severe colitis when transferred to *Rag2* KO mice (**Figure 6**), demonstrating its potential role in inflammation *in vivo*. Because in the present study we employed an artificial transfer model where MP subsets are individually transferred to host mice deficient in B and T lymphocytes including regulatory T cells (Tregs), further investigation using more physiological settings is needed to confirm this proposed function.

The above evidence that CD127^{hi} Sca1^{hi} MP cells can exhibit inflammatogenic properties *in vitro* and *in vivo* supports our previous hypothesis that MP cells may have the ability to drive and/or exacerbate inflammation because of their self-specificity and tonic T-bet expression (4, 5). Given that MP cells can also contribute to Th1 cytokine-dependent host resistance to infection (4, 5), the inflammatory CD127^{hi} Sca1^{hi} subset can be regarded as a double-edged sword. This raises the interesting question of how their potentially immunopathologic function is inhibited in healthy animals. One possibility is that the activity of MP T lymphocytes is normally dampened by Tregs. In support of this notion, acute depletion of Tregs is known to induce systemic inflammation even in the absence of foreign Ags (47, 48). In addition, pathological autoreactivity might be repressed by other cell-intrinsic mechanisms. Indeed in CD8$^+$ T cells, TCR signaling is known to be inhibited by upregulation of CD5 and CD45 and by downregulation of CD8 (49–51). Whether this is also the case in CD4$^+$ MP lymphocytes remains to be investigated.

The findings reported here define MP CD4$^+$ T lymphocytes as a unique but heterogeneous population that differs from conventional foreign Ag-specific memory cells in marker expression and establishes functional relevance for the mature subset of CD127^{hi} Sca1^{hi} MP cells. With defined markers now available, it will be of interest to search for further phenotypic and functional differences between the two cell types in future studies. Similarly, it will be important to determine if similar phenotypic differences between self-driven MP and foreign Ag-specific memory cells occur in humans. The existence of an MP-like population in humans is suggested by the observation of CD4$^+$ T lymphocytes with an activated phenotype in cord blood and fetal tissues where an encounter with foreign Ags is likely to be very limited or non-existent (52, 53). Should such a population exists, one would predict it to display a low-level expression of CD127 and Bcl2. If an MP subpopulation can be demonstrated in humans, the subset could serve as a potential therapeutic target, either by boosting its activity to limit infection or by inhibiting its function to treat autoimmune and other inflammatory conditions.

MATERIALS AND METHODS

Mice

C57BL/6 CD45.2$^+$ WT mice were purchased from Taconic Biosciences (Rensselaer, NY, USA) or Japan SLC (Hamamatsu, Japan). *Rag2* KO and CD45.1$^+$ WT mice were obtained from the National Institute of Allergy and Infectious Diseases (NIAID) contract facility at Taconic Biosciences or breeding stock maintained at Tohoku University Graduate School of Medicine. Nur77-GFP and Foxp3-RFP reporter mice were obtained from Jackson Laboratory (Bar Harbor, ME, USA). CD4-CreERT2 TCRα^{flox} mice are previously described (5). All mice were maintained in SPF animal facilities in the NIAID, National Cancer Institute (NCI), National Institutes of Health (NIH), or Tohoku University Graduate School of Medicine except for GF and AF mice, which were bred and maintained in the animal facility of Pohang University of Science and Technology as previously described (33). All mice were used at the age of 8–16 weeks except in the case of **Figures 3A, B**, where mice of indicated ages were utilized. The care and handling of the animals used in our studies were in accordance with the animal study protocols approved by the NIAID or NCI Animal Care and Use Committee, by the Institutional Committee for the Use and Care of Laboratory Animals of Tohoku University, or by the Institutional Animal Care and Use Committees of the Pohang University of Science and Technology.

Thymectomy

Thymectomy was performed on 8~12-week-old mice under aseptic conditions. Sham thymectomy was conducted with the same procedure except that thymic lobes were left intact. At the end of the experiments, the thymic deficiency was confirmed by careful macroscopic inspection.

Lymphocytic Choriomeningitis Virus Infection

LCMV Armstrong was propagated in baby hamster kidney-21 fibroblast cells [American Type Culture Collection (ATCC)]. Viral titers were determined by plaque assay using Vero African-green-monkey kidney cells (ATCC). Viral stocks were frozen at −80°C until use. For infection, mice were intraperitoneally injected with 2×10^5 plaque-forming unit/mouse of the virus as previously described (22).

In Vivo Chemical and mAb Treatment

To activate CreERT2 recombinases, mice received an intraperitoneal injection of TMX (20 mg/mouse) dissolved in corn oil (both Sigma-Aldrich, St. Louis, MO, USA) as previously described (5). To block IL-12 p40 or CD80/86 signals, anti-IL-12B p40 (C17.8), CTLA4-Ig, or control IgG (300 μg/20 g body weight; all from Bio X Cell, West Lebanon, NH, USA) were administered every 3 days as reported (4, 5). To inhibit lymphocyte egress from the thymus and lymph nodes, FTY720 (20 μg/20 g body weight; Cayman Chemicals, Ann Arbor, MI, USA) dissolved in phosphate-buffered saline (PBS) or control PBS was given to mice every day (20).

Cell Sorting and Adoptive Transfer

Total CD4$^+$ T lymphocytes were obtained from pooled splenocytes and lymph node cells of donor mice using a CD4$^+$ T Cell Isolation Kit or CD4 Microbeads (Miltenyi Biotec, Bergisch Gladbach, Germany). Naïve CD4$^+$ T cells were then purified by sorting for CD4$^+$ CD25^{neg} CD44^{lo} CD62L^{hi} cells using a fluorescence-activated cell sorting (FACS) Aria II (BD Biosciences, San Jose, CA, USA). To obtain MP cell subsets, CD127^{hi} Sca1^{lo}, CD127^{hi} Sca1^{hi}, CD127^{lo} Sca1^{hi}, and CD127^{lo} Sca1^{lo} subpopulations among CD4$^+$ CD25^{neg} CD44^{hi} CD62L^{lo} cells from WT mice or CD4$^+$ Foxp3^{neg} CD44^{hi} CD62L^{lo} cells from Foxp3-RFP reporter mice were sorted. Purity was >96%. For adoptive transfer experiments, depending on the experiments, 2×10^5 to 1×10^6 donor cells were intravenously injected into recipient animals.

Assessment of Severity of Colitis

After MP subpopulations were transferred to *Rag2* KO mice, the animals were monitored for body weight. The disease activity index (DAI) score was assessed based on clinical symptoms as previously described (54). The histological score of the proximal portion of the colon was measured as previously reported (55).

Flow Cytometric Analysis

Single-cell suspensions were prepared from spleens and red blood cells lysed in ACK buffer. In some experiments, splenic cells were further enriched for CD4$^+$ T lymphocytes using a CD4$^+$ T Cell Isolation Kit or CD4 Microbeads (Miltenyi Biotec). To obtain colonic cells, lamina propria mononuclear cells were isolated as previously described (54). Cells were suspended in staining buffer (PBS supplemented with 2% fetal bovine serum (FBS)) and incubated with CD16/32 mAb (2.4G2; Harlan Bioproducts, Indianapolis, IN, USA) for 10 min on ice. Cells were then incubated with the following mAbs or their combination for 20 min on ice: CD4 (RM4-5), CD8 (53-6.7), CD44 (IM7), CD62L (MEL-14), anti-NK1.1 (PK136), anti-TCRβ (H57-597) (Thermo Fisher Scientific, Waltham, MA, USA), CD3 (17A2), CD5 (53-7.3), CD25 (PC61), CD45.1 (A20), CD45.2 (104), CD69 (H1.2F3), CD122 (TM-β1), CD127 (A7R34), CD132 (TUGm2) (BioLegend, San Diego, CA, USA), and Sca1 (D7) (BD Biosciences). Tetramer staining used CD1d (PBS-57), I-Aβ-GP66, and I-Aβ-NP309 tetramers, obtained from the NIH Tetramer Core Facility (Emory University, Atlanta, GA, USA). To detect intracellular products, cells were fixed and permeabilized using Foxp3/Transcription Factor Staining Buffer Set for 30 min on ice after surface staining and then stained with mAbs against Bcl2 (10C4), Foxp3 (FJK-16s), Ki67 (SolA15) (Thermo Fisher Scientific), and/or IFN-γ (XMG1.2) (BioLegend) for 20 min on ice. For T-bet detection, fixed cells were stained with anti-T-bet (O4-46; BD Biosciences) mAb for 2 h at room temperature. Flow cytometry was performed using either Canto II, LSR II, Fortessa, or Symphony cytometers, and the data were analyzed with FlowJo software (BD Biosciences). Gating strategies are previously described (4, 5) and briefly summarized in **Figure S6**.

Single-Cell RNA Sequencing Analysis

MP and foreign Ag-specific memory CD4$^+$ T lymphocytes were obtained by sorting for TCRβ$^+$ CD4$^+$ CD25^{neg} CD44^{hi} CD62L^{lo} CD1d-tetramer^{neg} cells from uninfected mice and TCRβ$^+$ CD4$^+$ CD25^{neg} CD44^{hi} CD62L^{lo} GP66-tetramer$^+$ cells from LCMV-infected mice, respectively. Sorted cells were then loaded onto the 10× Chromium platform using the Chromium Single Cell 3′ Library & Gel Bead Kit V2 according to the manufacturer's instructions (56). Libraries were sequenced on the Illumina NextSeq using paired-end 26 × 98 bp, and sequencing files were processed to extract count matrices using the Cell Ranger Single Cell Software Suite (v2.2.0). Further analyses were performed in R using the Seurat package (3.0) (57). Scoring analyses for memory and Th1 signatures were performed as previously described (27). For cell cycle and anti-apoptotic signatures, genes were determined based on previous studies (26, 31) (**Table S1**). The obtained dataset is deposited on the Gene Expression Omnibus (GEO) (GEO number: GSE145999; token: kdspeciofrwhdod).

Real-Time qPCR

For detection of *Il12rb1*, *Il12rb2*, *Il18r1*, and *Il18rap* mRNA, total RNA was extracted from sorted cells using the RNeasy Mini Kit (Qiagen, Hilden, Germany) and reverse-transcribed with SuperScript III Reverse Transcriptase (Thermo Fisher Scientific). For detection of TRECs, total DNA was isolated from sorted cells using the DNeasy Blood & Tissue Kit (Qiagen). Real-time PCR was performed using the THUNDERBIRD SYBR qPCR Mix (Toyobo, Osaka, Japan). qPCR analysis was carried out using a 7500 real-time PCR system (Thermo Fisher Scientific). Relative gene expression was calculated by the ΔCt method and normalized to the amount of *Gapdh*. The following primer sets were used: *Il12rb1*, 5′-CCCCAGCGCTTTAGCTTT-3′ and 5′-GCCAATGTATCCGAGACTGC-3′ (58); *Il12rb2*, 5′-AATTCTTCTTCACTTCCGCATACG-3′ and 5′-GCTCCCAGAAGCATTTAGAAAGT-3′ (59); *Il18r1*, 5′-GCTCAGACCCTAATGTGCAAG-3′ and 5′-TGCAGTTTGCCTTCAGAAATC-3′; *Il18rap*, 5′-TGCAATGAAGCGGCATCTGT-3′ and 5′-CCGGTGATTCTGTTCAGGCT-3′ (60); TRECs, 5′-CATTGCCTTTGAACCAAGCTG-3′ and 5′-TTATGCACAGGGTGCAGGTG-3′ (61); and *Gapdh*, 5′-CCAGGTTGTCTCCTGCGACTT-3′ and 5′-CCTGTTGCTGTAGCCGTATTCA-3′ (4).

In Vitro Cell Culture and Cytokine Detection

In **Figures 5**, **S4**, total splenocytes or FACS-sorted MP subsets were stimulated with IL-12p70 (10 ng/ml; PeproTech, Cranbury, NJ, USA), IL-18 (10 ng/ml; MBL, Nagoya, Japan), and/or IL-2 (10 ng/ml; Ajinomoto, Tokyo, Japan) in Roswell Park Memorial Institute (RPMI) complete media for the indicated period at 37°C. At the last 6 h of incubation, Brefeldin A (1 μg/ml; BioLegend) was added. In **Figure 6I**, total cell suspensions were incubated in RPMI complete media supplemented with phorbol myristate acetate (PMA) (20 ng/ml) and ionomycin (1 μg/ml; both from Sigma-Aldrich) for 5 h at 37°C in the presence of Brefeldin A. Cells were then harvested and subjected to intracellular staining as described above.

Statistical Analysis

A Student's t-test was employed to establish statistical significance. p-Values <0.05 were considered significant.

DATA AVAILABILITY STATEMENT

The datasets presented in this study can be found in online repositories. The names of the repository/repositories and accession number(s) can be found below: https://www.ncbi.nlm.nih.gov/geo/, GSE145999.

ETHICS STATEMENT

The animal study was reviewed and approved by the NIAID/NCI Animal Care and Use Committee, the Institutional Committee for the Use and Care of Laboratory Animals of Tohoku University, or the the Institutional Animal Care and Use Committees of the Pohang University of Science and Technology.

AUTHOR CONTRIBUTIONS

TK and AS designed the research. TK, TC, KK, ST, AK, TS, and RT performed the experiments. NI, DJ, JZ, JS, and RB provided collaborative support. TK, JS, and AS wrote the manuscript. All authors listed have made a substantial, direct, and intellectual contribution to the work and approved it for publication.

FUNDING

This work was supported in part by the Intramural Research Programs of the NIAID and the NCI, Center for Cancer Research, NIH. TK also received support from the Japan Society for the Promotion of Science, Astellas Foundation for Research on Metabolic Disorders, Daiichi Sankyo Foundation of Life Science, Kobayashi Foundation, Mochida Memorial Foundation for Medical and Pharmaceutical Research, Life Science Foundation of Japan, Ohyama Health Foundation, Senshin Medical Research Foundation, Takeda Science Foundation, The Cell Science Research Foundation, The Chemo-Sero-Therapeutic Research

Institute, The Mitsubishi Foundation, The Sumitomo Foundation, The Uehara Memorial Foundation, and The Waksman Foundation of Japan. In addition, TK received funding from Bristol-Myers Squibb. The funder was not involved in the study design, collection, analysis, interpretation of data, the writing of this article or the decision to submit it for publication.

ACKNOWLEDGMENTS

We are grateful to the late William E. Paul for his initial conceptualization of this study area. We also thank V. Bundoc (NIAID, NIH), A. Asao, H. Kuji, and M. Ishii (Tohoku University Graduate School of Medicine) for technical assistance; C. Eigsti, T. Hawley, and D. Stephany (NIAID, NIH) for cell sorting; and NIH Tetramer Core Facility for the tetramers.

SUPPLEMENTARY MATERIAL

The Supplementary Material for this article can be found online at: https://www.frontiersin.org/articles/10.3389/fimmu.2022.870542/full#supplementary-material

REFERENCES

1. Sprent J, Surh CD. Normal T Cell Homeostasis: The Conversion of Naive Cells Into Memory-Phenotype Cells. *Nat Immunol* (2011) 12(6):478–84. doi: 10.1038/ni.2018
2. Kawabe T, Yi J, Sprent J. Homeostasis of Naive and Memory T Lymphocytes. *Cold Spring Harb Perspect Biol* (2021) 13(9):a037879. doi: 10.1101/cshperspect.a037879
3. Kawabe T, Sher A. Memory-Phenotype Cd4 + T Cells: A Naturally Arising T Lymphocyte Population Possessing Innate Immune Function. *Int Immunol* (2022) 34(4):189–96. doi: 10.1093/intimm/dxab108
4. Kawabe T, Jankovic D, Kawabe S, Huang Y, Lee PH, Yamane H, et al. Memory-Phenotype Cd4(+) T Cells Spontaneously Generated Under Steady-State Conditions Exert Innate Th1-Like Effector Function. *Sci Immunol* (2017) 2(12):eaam9304. doi: 10.1126/sciimmunol.aam9304
5. Kawabe T, Yi J, Kawajiri A, Hilligan K, Fang D, Ishii N, et al. Requirements for the Differentiation of Innate T-Bet(High) Memory-Phenotype Cd4(+) T Lymphocytes Under Steady State. *Nat Commun* (2020) 11(1):3366. doi: 10.1038/s41467-020-17136-1
6. Artis D, Spits H. The Biology of Innate Lymphoid Cells. *Nature* (2015) 517 (7534):293–301. doi: 10.1038/nature14189
7. White JT, Cross EW, Kedl RM. Antigen-Inexperienced Memory CD8(+) T Cells: Where They Come From and Why We Need Them. *Nat Rev Immunol* (2017) 17(6):391–400. doi: 10.1038/nri.2017.34
8. Kawabe T, Zhu J, Sher A. Foreign Antigen-Independent Memory-Phenotype CD4(+) T Cells: A New Player in Innate Immunity? *Nat Rev Immunol* (2018) 18(3):1. doi: 10.1038/nri.2018.12
9. Bendelac A, Savage PB, Teyton L. The Biology of Nkt Cells. *Annu Rev Immunol* (2007) 25:297–336. doi: 10.1146/annurev.immunol.25.022106.141711
10. Godfrey DI, Koay HF, McCluskey J, Gherardin NA. The Biology and Functional Importance of Mait Cells. *Nat Immunol* (2019) 20(9):1110–28. doi: 10.1038/s41590-019-0444-8
11. Tan JT, Ernst B, Kieper WC, LeRoy E, Sprent J, Surh CD. Interleukin (IL)-15 and IL-7 Jointly Regulate Homeostatic Proliferation of Memory Phenotype Cd8+ Cells But Are Not Required for Memory Phenotype Cd4+ Cells. *J Exp Med* (2002) 195(12):1523–32. doi: 10.1084/jem.20020066
12. Purton JF, Tan JT, Rubinstein MP, Kim DM, Sprent J, Surh CD. Antiviral CD4+ Memory T Cells Are Il-15 Dependent. *J Exp Med* (2007) 204(4):951–61. doi: 10.1084/jem.20061805
13. Yamaki S, Ine S, Kawabe T, Okuyama Y, Suzuki N, Soroosh P, et al. Ox40 and Il-7 Play Synergistic Roles in the Homeostatic Proliferation of Effector Memory Cd4(+) T Cells. *Eur J Immunol* (2014) 44(10):3015–25. doi: 10.1002/eji.201444701
14. Kondrack RM, Harbertson J, Tan JT, McBreen ME, Surh CD, Bradley LM. Interleukin 7 Regulates the Survival and Generation of Memory CD4 Cells. *J Exp Med* (2003) 198(12):1797–806. doi: 10.1084/jem.20030735
15. Lenz DC, Kurz SK, Lemmens E, Schoenberger SP, Sprent J, Oldstone MB, et al. Il-7 Regulates Basal Homeostatic Proliferation of Antiviral Cd4+T Cell Memory. *Proc Natl Acad Sci USA* (2004) 101(25):9357–62. doi: 10.1073/pnas.0400640101
16. Ernst B, Lee DS, Chang JM, Sprent J, Surh CD. The Peptide Ligands Mediating Positive Selection in the Thymus Control T Cell Survival and Homeostatic Proliferation in the Periphery. *Immunity* (1999) 11(2):173–81. doi: 10.1016/s1074-7613(00)80092-8
17. Viret C, Wong FS, Janeway CAJr. Designing and Maintaining the Mature Tcr Repertoire: The Continuum of Self-Peptide:Self-Mhc Complex Recognition. *Immunity* (1999) 10(5):559–68. doi: 10.1016/s1074-7613(00)80055-2
18. Kieper WC, Troy A, Burghardt JT, Ramsey C, Lee JY, Jiang HQ, et al. Recent Immune Status Determines the Source of Antigens That Drive Homeostatic T Cell Expansion. *J Immunol* (2005) 174(6):3158–63. doi: 10.4049/jimmunol.174.6.3158
19. Min B, Yamane H, Hu-Li J, Paul WE. Spontaneous and Homeostatic Proliferation of Cd4 T Cells Are Regulated by Different Mechanisms. *J Immunol* (2005) 174(10):6039–44. doi: 10.4049/jimmunol.174.10.6039
20. Kawabe T, Sun SL, Fujita T, Yamaki S, Asao A, Takahashi T, et al. Homeostatic Proliferation of Naive CD4+ T Cells in Mesenteric Lymph Nodes Generates Gut-Tropic Th17 Cells. *J Immunol* (2013) 190(11):5788–98. doi: 10.4049/jimmunol.1203111
21. Schulz O, Edwards AD, Schito M, Aliberti J, Manickasingham S, Sher A, et al. Cd40 Triggering of Heterodimeric IL-12 P70 Production by Dendritic Cells *in Vivo* Requires a Microbial Priming Signal. *Immunity* (2000) 13(4):453–62. doi: 10.1016/s1074-7613(00)00045-5
22. Younes SA, Punkosdy G, Caucheteux S, Chen T, Grossman Z, Paul WE. Memory Phenotype CD4 T Cells Undergoing Rapid, Nonburst-Like, Cytokine-Driven Proliferation Can Be Distinguished From Antigen-Experienced Memory Cells. *PloS Biol* (2011) 9(10):e1001171. doi: 10.1371/journal.pbio.1001171
23. Tough DF, Sprent J. Turnover of Naive- and Memory-Phenotype T Cells. *J Exp Med* (1994) 179(4):1127–35. doi: 10.1084/jem.179.4.1127
24. Vezys V, Yates A, Casey KA, Lanier G, Ahmed R, Antia R, et al. Memory Cd8 T-Cell Compartment Grows in Size With Immunological Experience. *Nature* (2009) 457(7226):196–9. doi: 10.1038/nature07486
25. Beura LK, Hamilton SE, Bi K, Schenkel JM, Odumade OA, Casey KA, et al. Normalizing the Environment Recapitulates Adult Human Immune Traits in Laboratory Mice. *Nature* (2016) 532(7600):512–6. doi: 10.1038/nature17655
26. Otto T, Sicinski P. Cell Cycle Proteins as Promising Targets in Cancer Therapy. *Nat Rev Cancer* (2017) 17(2):93–115. doi: 10.1038/nrc.2016.138
27. Ciucci T, Vacchio MS, Gao Y, Tomassoni Ardori F, Candia J, Mehta M, et al. The Emergence and Functional Fitness of Memory CD4(+) T Cells Require the Transcription Factor Thpok. *Immunity* (2019) 50(1):91–105.e4. doi: 10.1016/j.immuni.2018.12.019
28. Kaech SM, Hemby S, Kersh E, Ahmed R. Molecular and Functional Profiling of Memory CD8 T Cell Differentiation. *Cell* (2002) 111(6):837–51. doi: 10.1016/s0092-8674(02)01139-x
29. Zhang Y, Joe G, Hexner E, Zhu J, Emerson SG. Host-Reactive CD8+ Memory Stem Cells in Graft-Versus-Host Disease. *Nat Med* (2005) 11(12):1299–305. doi: 10.1038/nm1326
30. DeLong JH, Hall AO, Konradt C, Coppock GM, Park J, Harms Pritchard G, et al. Cytokine- and Tcr-Mediated Regulation of T Cell Expression of Ly6c and Sca-1. *J Immunol* (2018) 200(5):1761–70. doi: 10.4049/jimmunol.1701154
31. Jourdan M, Reme T, Goldschmidt H, Fiol G, Pantesco V, De Vos J, et al. Gene Expression of Anti- and Pro-Apoptotic Proteins in Malignant and Normal Plasma Cells. *Br J Haematol* (2009) 145(1):45–58. doi: 10.1111/j.1365-2141.2008.07562.x

32. Akashi K, Kondo M, von Freeden-Jeffry U, Murray R, Weissman IL. Bcl-2 Rescues T Lymphopoiesis in Interleukin-7 Receptor-Deficient Mice. *Cell* (1997) 89(7):1033–41. doi: 10.1016/s0092-8674(00)80291-3
33. Kim KS, Hong SW, Han D, Yi J, Jung J, Yang BG, et al. Dietary Antigens Limit Mucosal Immunity by Inducing Regulatory T Cells in the Small Intestine. *Science* (2016) 351(6275):858–63. doi: 10.1126/science.aac5560
34. Weinreich MA, Odumade OA, Jameson SC, Hogquist KA. T Cells Expressing the Transcription Factor Plzf Regulate the Development of Memory-Like CD8 + T Cells. *Nat Immunol* (2010) 11(8):709–16. doi: 10.1038/ni.1898
35. Mandl JN, Monteiro JP, Vrisekoop N, Germain RN. T Cell-Positive Selection Uses Self-Ligand Binding Strength to Optimize Repertoire Recognition of Foreign Antigens. *Immunity* (2013) 38(2):263–74. doi: 10.1016/j.immuni.2012.09.011
36. Moran AE, Holzapfel KL, Xing Y, Cunningham NR, Maltzman JS, Punt J, et al. T Cell Receptor Signal Strength in Treg and Inkt Cell Development Demonstrated by a Novel Fluorescent Reporter Mouse. *J Exp Med* (2011) 208 (6):1279–89. doi: 10.1084/jem.20110308
37. Yanagida T, Kato T, Igarashi O, Inoue T, Nariuchi H. Second Signal Activity of Il-12 on the Proliferation and IL-2r Expression of T Helper Cell-1 Clone. *J Immunol* (1994) 152(10):4919–28.
38. Nguyen T, Wang R, Russell JH. IL-12 Enhances IL-2 Function by Inducing CD25 Expression Through a P38 Mitogen-Activated Protein Kinase Pathway. *Eur J Immunol* (2000) 30(5):1445–52. doi: 10.1002/(SICI)1521-4141(200005) 30:5<1445::AID-IMMU1445>3.0.CO;2-M
39. Sher A, Kelsall BL. The Colon as a Major Site of Immunoregulation by CD4 (+) T Cell Subsets in the Steady State. *J Immunol* (2019) 203(7):1683–4. doi: 10.4049/jimmunol.1900960
40. Powrie F, Leach MW, Mauze S, Caddle LB, Coffman RL. Phenotypically Distinct Subsets of CD4+ T Cells Induce or Protect From Chronic Intestinal Inflammation in C. B-17 Scid Mice. *Int Immunol* (1993) 5(11):1461–71. doi: 10.1093/intimm/5.11.1461
41. Haluszczak C, Akue AD, Hamilton SE, Johnson LD, Pujanauski L, Teodorovic L, et al. The Antigen-Specific CD8+ T Cell Repertoire in Unimmunized Mice Includes Memory Phenotype Cells Bearing Markers of Homeostatic Expansion. *J Exp Med* (2009) 206(2):435–48. doi: 10.1084/jem.20081829
42. Grau M, Valsesia S, Mafille J, Djebali S, Tomkowiak M, Mathieu AL, et al. Antigen-Induced But Not Innate Memory CD8 T Cells Express Nkg2d and Are Recruited to the Lung Parenchyma Upon Viral Infection. *J Immunol* (2018) 200(10):3635–46. doi: 10.4049/jimmunol.1701698
43. Lee JY, Hamilton SE, Akue AD, Hogquist KA, Jameson SC. Virtual Memory CD8 T Cells Display Unique Functional Properties. *Proc Natl Acad Sci USA* (2013) 110(33):13498–503. doi: 10.1073/pnas.1307572110
44. Martin CE, Spasova DS, Frimpong-Boateng K, Kim HO, Lee M, Kim KS, et al. Interleukin-7 Availability Is Maintained by a Hematopoietic Cytokine Sink Comprising Innate Lymphoid Cells and T Cells. *Immunity* (2017) 47(1):171–82.e4. doi: 10.1016/j.immuni.2017.07.005
45. Matson CA, Choi S, Livak F, Zhao B, Mitra A, Love PE, et al. CD5 Dynamically Calibrates Basal Nf-Kappab Signaling in T Cells During Thymic Development and Peripheral Activation. *Proc Natl Acad Sci USA* (2020) 117(25):14342–53. doi: 10.1073/pnas.1922525117
46. Singh NJ, Bando JK, Schwartz RH. Subsets of Nonclonal Neighboring Cd4+ T Cells Specifically Regulate the Frequency of Individual Antigen-Reactive T Cells. *Immunity* (2012) 37(4):735–46. doi: 10.1016/j.immuni.2012.08.008
47. Kim JM, Rasmussen JP, Rudensky AY. Regulatory T Cells Prevent Catastrophic Autoimmunity Throughout the Lifespan of Mice. *Nat Immunol* (2007) 8(2):191–7. doi: 10.1038/ni1428
48. Yi J, Jung J, Hong SW, Lee JY, Han D, Kim KS, et al. Unregulated Antigen-Presenting Cell Activation by T Cells Breaks Self Tolerance. *Proc Natl Acad Sci USA* (2019) 116(3):1007–16. doi: 10.1073/pnas.1818624116
49. Tarakhovsky A, Kanner SB, Hombach J, Ledbetter JA, Muller W, Killeen N, et al. A Role for CD5 in Tcr-Mediated Signal Transduction and Thymocyte Selection. *Science* (1995) 269(5223):535–7. doi: 10.1126/science.7542801
50. Takada K, Jameson SC. Self-Class I Mhc Molecules Support Survival of Naive CD8 T Cells, But Depress Their Functional Sensitivity Through Regulation of CD8 Expression Levels. *J Exp Med* (2009) 206(10):2253–69. doi: 10.1084/jem.20082553
51. Cho JH, Kim HO, Ju YJ, Kye YC, Lee GW, Lee SW, et al. CD45-Mediated Control of TCR Tuning in Naive and Memory CD8(+) T Cells. *Nat Commun* (2016) 7:13373. doi: 10.1038/ncomms13373
52. Byrne JA, Stankovic AK, Cooper MD. A Novel Subpopulation of Primed T Cells in the Human Fetus. *J Immunol* (1994) 152(6):3098–106.
53. Szabolcs P, Park KD, Reese M, Marti L, Broadwater G, Kurtzberg J. Coexistent Naive Phenotype and Higher Cycling Rate of Cord Blood T Cells as Compared to Adult Peripheral Blood. *Exp Hematol* (2003) 31(8):708–14. doi: 10.1016/s0301-472x(03)00160-7
54. Teratani T, Mikami Y, Nakamoto N, Suzuki T, Harada Y, Okabayashi K, et al. The Liver-Brain-Gut Neural Arc Maintains the Treg Cell Niche in the Gut. *Nature* (2020) 585(7826):591–6. doi: 10.1038/s41586-020-2425-3
55. Koelink PJ, Wildenberg ME, Stitt LW, Feagan BG, Koldijk M, van 't Wout AB, et al. Development of Reliable, Valid and Responsive Scoring Systems for Endoscopy and Histology in Animal Models for Inflammatory Bowel Disease. *J Crohns Colitis* (2018) 12(7):794–803. doi: 10.1093/ecco-jcc/jjy035
56. Zheng GX, Terry JM, Belgrader P, Ryvkin P, Bent ZW, Wilson R, et al. Massively Parallel Digital Transcriptional Profiling of Single Cells. *Nat Commun* (2017) 8:14049. doi: 10.1038/ncomms14049
57. Stuart T, Butler A, Hoffman P, Hafemeister C, Papalexi E, Mauck WM 3rd, et al. Comprehensive Integration of Single-Cell Data. *Cell* (2019) 177(7):1888–902.e21. doi: 10.1016/j.cell.2019.05.031
58. Barik S, Cattin-Roy AN, Miller MM, Ukah TK, Zaghouani H. IL-4 and IL-13 Guide Early Thymic Progenitors to Mature Toward Dendritic Cells. *J Immunol* (2018) 201(10):2947–58. doi: 10.4049/jimmunol.1701186
59. Niedbala W, Wei XQ, Campbell C, Thomson D, Komai-Koma M, Liew FY. Nitric Oxide Preferentially Induces Type 1 T Cell Differentiation by Selectively Up-Regulating Il-12 Receptor Beta 2 Expression *Via* Cgmp. *Proc Natl Acad Sci USA* (2002) 99(25):16186–91. doi: 10.1073/pnas.252464599
60. Patra V, Wagner K, Arulampalam V, Wolf P. Skin Microbiome Modulates the Effect of Ultraviolet Radiation on Cellular Response and Immune Function. *iScience* (2019) 15:211–22. doi: 10.1016/j.isci.2019.04.026
61. Sempowski GD, Gooding ME, Liao HX, Le PT, Haynes BF. T Cell Receptor Excision Circle Assessment of Thymopoiesis in Aging Mice. *Mol Immunol* (2002) 38(11):841–8. doi: 10.1016/s0161-5890(01)00122-5

Conflict of Interest: The authors declare that the research was conducted in the absence of any commercial or financial relationships that could be construed as a potential conflict of interest.

frontiers | Frontiers in Immunology

TYPE Original Research
PUBLISHED 19 July 2022
DOI 10.3389/fimmu.2022.843128

OPEN ACCESS

EDITED BY
Filippo Castiglione,
National Research Council (CNR), Italy

REVIEWED BY
Elia Onofri,
Roma Tre University, Italy
Patrizia Brigidi,
University of Bologna, Italy

*CORRESPONDENCE
George M. Spyrou
georges@cing.ac.cy

SPECIALTY SECTION
This article was submitted to Immunological Memory, a section of the journal Frontiers in Immunology

RECEIVED 24 December 2021
ACCEPTED 28 June 2022
PUBLISHED 19 July 2022

CITATION
Onisiforou A and Spyrou GM (2022) Immunomodulatory effects of microbiota-derived metabolites at the crossroad of neurodegenerative diseases and viral infection: network-based bioinformatics insights. *Front. Immunol.* 13:843128. doi: 10.3389/fimmu.2022.843128

Immunomodulatory effects of microbiota-derived metabolites at the crossroad of neurodegenerative diseases and viral infection: network-based bioinformatics insights

Anna Onisiforou and George M. Spyrou*

Bioinformatics Department, Cyprus Institute of Neurology & Genetics, Nicosia, Cyprus

Bidirectional cross-talk between commensal microbiota and the immune system is essential for the regulation of immune responses and the formation of immunological memory. Perturbations of microbiome-immune system interactions can lead to dysregulated immune responses against invading pathogens and/or to the loss of self-tolerance, leading to systemic inflammation and genesis of several immune-mediated pathologies, including neurodegeneration. In this paper, we first investigated the contribution of the immunomodulatory effects of microbiota (bacteria and fungi) in shaping immune responses and influencing the formation of immunological memory cells using a network-based bioinformatics approach. In addition, we investigated the possible role of microbiota-host-immune system interactions and of microbiota-virus interactions in a group of neurodegenerative diseases (NDs): Amyotrophic Lateral Sclerosis (ALS), Multiple Sclerosis (MS), Parkinson's disease (PD) and Alzheimer's disease (AD). Our analysis highlighted various aspects of the innate and adaptive immune response systems that can be modulated by microbiota, including the activation and maturation of microglia which are implicated in the development of NDs. It also led to the identification of specific microbiota components which might be able to influence immune system processes (ISPs) involved in the pathogenesis of NDs. In addition, it indicated that the impact of microbiota-derived metabolites in influencing disease-associated ISPs, is higher in MS disease, than in AD, PD and ALS suggesting a more important role of microbiota mediated-immune effects in MS.

KEYWORDS

microbiota, neurodegenerative diseases, immune system, viruses, microbiota-virus-disease interactions

1 Introduction

Gut microbiota play an essential role in maintaining homeostasis in the human host, with more than 100 trillion microorganisms (including bacteria, viruses, fungi and archaea) colonizing our gastrointestinal (GI) tract (1, 2). These microbes do not just habitat our GI tract but rather help to regulate various host physiological functions, including metabolic, endocrine and immune functions (3). Gut microbiota have key role in human metabolism as they encode enzymes that are not found in the human genome which are important for the degradation of exogenous and endogenous substrates, resulting in the production of a range of metabolic products (4–6).These microbiota-derived metabolites are key orchestrators of the bidirectional cross-talk that exists between host and microbiota. This molecular dialogue is essential for the regulation of immune responses and the formation of immunological memory, which are important for maintaining body homeostasis and human health.

Symbiosis between commensal microbiota and the immune system is a fine-tuned dynamic process. On the one hand, the immune system plays an important role in maintaining health homeostasis by reacting and eliciting innate immune responses against invading pathogenic organisms such as viral infections, and at the same time maintaining tolerance to beneficial microbiota (7, 8). On the other hand, commensal gut microbiota can regulate and shape immune responses such as influencing various steps of the hematopoiesis process, influence the intestine immune cell population, affecting myeloid cells and lymphoid cell functions and differentiation, thus affecting responses to viral infections (9). In addition, commensal microbiota can also influence the formation of both innate and adaptive memory *via* the production of microbiota-derived bioactive molecules, such as short-chain fatty acids (SCFAs) and neurotransmitters (NTs) (10, 11). However, although several mechanisms have been identified on how commensal microbiota can influence the immune system, the exact mechanisms on how they can affect the formation of innate and adaptive immune memories is still an emerging area of investigation (10).

Perturbations of the microbiome-immune system cross-talk due to microbiome-host dysbiosis can lead to the dysregulation of immune responses against invading pathogens and/or the loss of self-tolerance, leading to systemic inflammation and the genesis of several immune-mediated diseases. Perturbations of microbiome-host symbiosis, resulting in dysbiosis, can be caused by both environmental and genetic factors. However it is believed that the environmental-mediated perturbations outweigh host genetic polymorphism-mediated perturbations in shaping microbiome-host interactions (12).Important environmental factors that can contribute to microbiome-host dysbiosis is diet, antibiotic use, lifestyle (stress) and infection with pathogenic organisms, such as viral infections (13, 14).

Gut microbiota dysbiosis has been associated with the development and/or progression of several NDs, including ALS, AD, MS and PD *via* perturbations of the microbiota-brain-gut axis (15). Microbiota are involved in the production of several metabolic products, such as NTs and SCFAs, which are important for gut-brain communication, brain homeostasis, neurogenesis and neuroinflammation (3, 16–21). Several pathological mechanisms have been suggested by which microbiota can contribute to the development and/or progression of NDs, for example they can increase blood brain barrier (BBB) permeability, augment neuroinflammation and affect the production of several NTs produced by gut microbiota, such as dopamine which is dysregulated in PD (17, 18). However, although gut microbiota dysbiosis is associated with the development of NDs, it remains unknown how ND-associated microbiota profiles contribute to neuroinflammation and lead to the development of specific disease phenotypes.

Interestingly, evidences also suggests that commensal microbiota can suppress or promote certain viral infections *via* microbiota- mediated direct or indirect mechanisms (13, 22). The development of several NDs is associated with numerous viral infections (23–25), hence this bidirectional interaction between viruses and commensal microbiota could possibly contribute to the onset or progression of a ND. According to the “multiple hit” hypothesis the development of NDs requires the combinatorial action of multiple ND-associated risk factors (26). However, it still remains undetermined how the combinatorial effect of multiple risk factors contributes to disease development. Therefore, as both microbiota and viral infections are environmental factors associated with NDs, it is important to investigate how microbiota-virus interactions might contribute to ND development.

Network-based approaches have been extensively utilized to provide insight into microbe-host interactions, through the analysis of various single-omics data including proteomics, transcriptomics and metabolomics (27–30).Various network-based methodologies have been employed to analyze microbe-host interaction networks, with the most common methods being topological analysis, such as modules and community detection, as well as functional analysis (31, 32). In addition, some studies have used multi-omics approaches to investigate pathogen-host interactions (33). However, only a few studies used multi-omics network approaches to investigate microbiome data (27). Moreover, several studies have used network approaches to investigate microbe-microbe interactions, with the majority investigating bacteria-to-bacteria interactions, whereas only a few studies have investigated viral or fungal interactions (27, 34). Although several studies have used network approaches to investigate the role of viruses in the triggering of diseases, there is a lack of studies that focus specifically in the development of NDs (35). In our previous work, we have developed our own integrative network-based bioinformatics methodology which was utilized to identify viral-mediated pathogenic mechanisms by which viruses associated as risk factors for MS could lead to its development, through virus-host protein-protein interactions (PPIs) (36).

In this paper, we extend upon the methodology developed in our previous work (36) and use an integrative multi-omics network-based bioinformatics approach to investigate the immunomodulatory effects of both microbiota (bacteria and fungi) and viruses in general and ND specific states. To our knowledge, this is the first study that uses network-based approaches to investigate how microbiota-virus interactions might contribute to NDs development. We first, investigate the contribution of the immunomodulatory effects of microbiota (bacteria and fungi) in shaping immune responses and influencing the formation of immunological memory cells *via* the production of their metabolic products. We aim to also identify microbiota components which, through their immunomodulatory effects, might be able to influence ISPs involved in the pathogenesis of NDs. In addition, as a case study, we explore how microbiota-Epstein-Barr Virus (EBV)-immune system interactions might facilitate the development and/progression of several NDs.

2 Methods

Our pipeline approach consists of the following steps: (A) Collection from well-known Data Sources, (B) Network Reconstruction and Enrichment Analysis, (C) Similarity-Based Analysis, (D)Network Topology Analysis, and (F) Network Re-Wiring Analysis. Figure 1 illustrates the main components of our methodology.

2.1 Data sources

(i) Collection of microbiota data

To investigate the effects of microbiota-derived metabolic products on ISPs we first mined the Human Metabolome Database (HMDB) (version 4.0) (37) to collect microbiota derived-metabolites found in the feces, blood and cerebrospinal

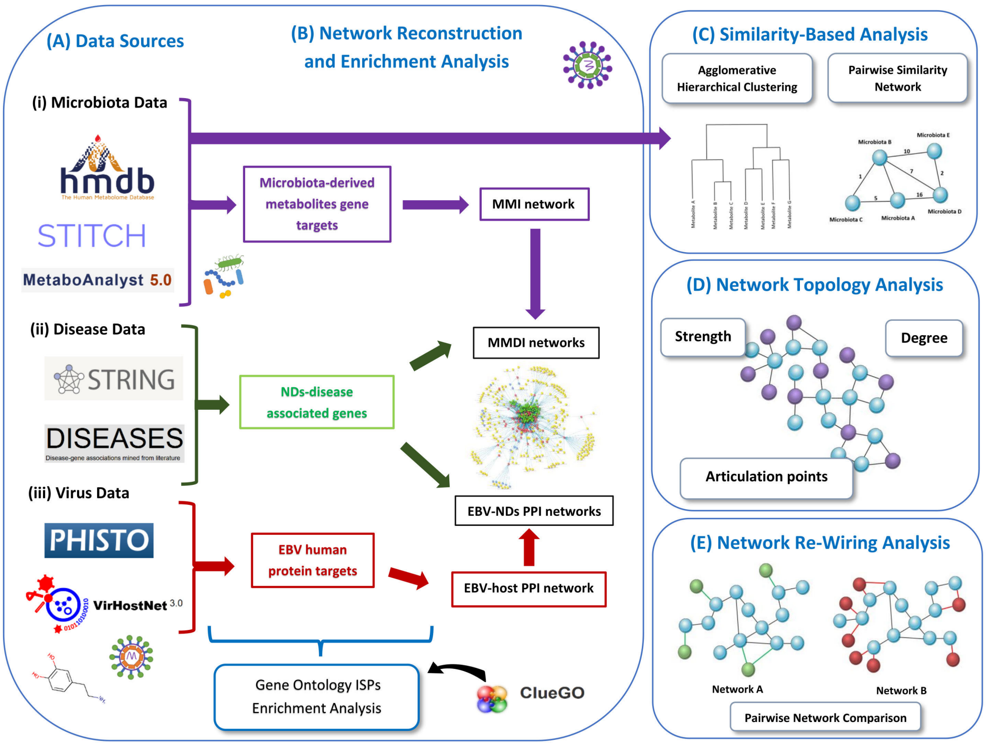

FIGURE 1
Schematic representation of our methodology used in this paper. We present the various data sources that we used to collect the data **(A)**. Then we represent the data used for enrichment analysis and how the networks are reconstructed, including the MMI network, MMDI networks, EBV-ND PPI networks and EBV-host PPI network **(B)**. Then we also present the two similarity-based analysis methods used to analyze the data, the agglomerative hierarchical clustering analysis and the pairwise similarity network analysis **(C)**. We also indicate the three network topology metrics (degree, strength and articulation points) **(D)**, that were used to analyze the pairwise similarity network (microbiota-to-microbiota association network). Finally, we present the re-wiring analysis that was used to perform pairwise network comparison between the MMDI networks **(E)**.

fluid (CSF) of human samples. We used an in-house developed R script to parse the feces, serum and CSF xml datasets (datasets downloaded in xml format) from the HMDB with the aim to identify and extract only the metabolites that had biological disposition in bacteria and/or fungi (release date:2020-09-10). Specifically, for each of the metabolite's data contained within each of the three xml datasets, our script examined whether the metabolite in their biological disposition section was containing the terms "Fungi" or "Bacteria". If these terms were present in the metabolite data, the algorithm classified the corresponding metabolites as associated to fungi and/or bacteria and it also extracted the names of these fungi or bacteria, if they were available Overall, from the feces, serum and CSF xml datasets, after removing duplicates, we identified 188 metabolites that were indicated to be produced by bacteria and fungi. From these 188 metabolites, 157 were indicated to be produced only by bacteria and 11 to be produced only by fungi, whereas 20 of them were indicated to be produced by both bacteria and fungi. Based on the data extracted after parsing the xml datasets from HMDB, we were able to collect the names of microbiota that produce most of the 188 identified microbiota-derived metabolites, which included either species or strains or genera names. More specifically, we extracted 397 names (genera/species/strains) of bacteria or fungi which were associated with 138 out of the 188 identified microbiota-derived metabolites. However, although the other 50 of the microbiota-derived metabolites were indicated to have biological disposition in bacteria or fungi, no specific names were provided by the HMDB database. From these 50 microbiota-derived metabolites, 49 were indicated to be produced by bacteria and 1 by fungi. Therefore, in total we extracted 671 microbiota names-to-metabolite associations, including the 50 microbiota-derived metabolites without associated names, which were indicated under the general annotation of bacteria or fungi associated.

Through the above-mentioned parsing of HMDB, we generated metabolite-to-gene associations by collecting the associated genes for each metabolite. For the same set of the 188 metabolites, we also collected metabolite-to-gene associations using the *MetaboAnalyst* tool (version 5.0) (38), that provides metabolite-to-gene associations which are extracted from STITCH ('search tool for interactions of chemicals') database (39). Then we combined the metabolite-to-gene associations obtained from HMDB and STITCH databases, and we removed duplicate entries. These resulted in 5931 metabolite-to-gene associations between 130 out of the 188 microbiota-derived metabolites and 2085 human genes, whereas no metabolite-to-gene association data were available for the rest 58 microbiota-derived metabolites.

(ii) Collection of NDs disease-associated data

Using the same approach as in our previous work (36), we obtained disease-associated gene data for each of the four NDs (ALS, AD, PD and MS) using the S*TRING: disease* query of the StringApp in Cytoscape, which is a network visualization and analysis tool (40). The *STRING: disease* app allows to easily import disease-associated data which are extracted from the DISEASES database (41) into Cytoscape, which automatically creates a PPI disease network. We obtained the top 200 highly disease-associated genes, which had the highest disease association score, for each of the four NDs. The confidence cut-off score of interactions between the human proteins was set at 0.8 for all four ND disease-associated networks. The confidence cut-off score determines the quality of the evidence on whether the interaction between the proteins is likely to be true, with confidence values ranging from 0 (low) to 1.0 (high) (42).

(iii) Collection of viruses-host PPI data

Virus-host PPI data for EBV were obtained from PHISTO (43) and VirHostNet 3.0 (44) databases, which provide experimentally validated pathogen-host PPIs. Then we combined the virus-host PPIs data that we obtained from these two databases and removed duplicated entries, resulting into 7069 EBV-human host PPIs. The data contains 153 EBV proteins from four EBV viral strains (GD1, B95-8, AG876, HHV4 type 2) that target 1247 human proteins. Based on its genome, EBV has been found to have a coding potential of around 80 viral proteins, however not all proteins have yet been identified. The generated EBV-human host PPIs dataset contains 48, 59, 45 and 1 viral proteins from the EBV strains GD1 (taxid id:10376), B95-8 (taxid id: 10377), AG876 (taxid id: 82830) and HHV-4 type 2 (taxid id: 12509), respectively.

2.2 Network reconstruction and enrichment analysis

For the purpose of this investigation, using the data collected above we reconstructed and visualized the following three types of networks:

(i) Microbiota - metabolites - GO ISP terms network

To model the immunomodulatory effects of microbiota-derived metabolites produced by bacteria and fungi, we constructed a microbiota - metabolites -Gene Ontology Immune System Processes (GO ISPs) network, called MMI network, using *visNetwork* package in R (45). The constructed network contains three types of nodes, (a) microbiota (bacteria and fungi), (b) metabolites and (c) GO ISPs terms. It also contains three types of edge interactions between the nodes: (a) microbiota-to-metabolite, (b) metabolite-to-GO ISP and (c) GO ISPs-to-GO ISPs. To identify the GO ISPs that are modulated by microbiota-derived metabolites, we performed enrichment analysis on the 2085 human genes that are targeted by the 130 microbiota-derived metabolites. Enrichment analysis was performed using the ClueGO app (46) in Cytoscape using the GO ISPs database and keeping only significantly enriched terms with adjusted *P* -value ≤0.05 (corrected with Benjamini-Hochberg). Then the enriched GO ISPs terms were merged with the microbiota-to-metabolite associations obtained from the HMDB database, in order to construct the MMI network. Table 1 indicates the characteristics of the MMI network, which is composed of 472 nodes and 3770 edges.

(ii) Microbiota-metabolites-ND associated genes- GO ISPs networks

To identify disease-associated genes that can be modulated by microbiota components in each of the four NDs (ALS, MS, AD and PD), we merged the microbiota-metabolites-genes interactions, collected in Section 2.1 (i), with each of the 200 disease-associated genes of these diseases. For each of the four NDs we then constructed a microbiota-metabolites-ND associated genes- GO ISPs (MMDI) network. More specifically, to create the four MMDI networks we first performed enrichment analysis on the 200 disease-associated genes for each of the four NDs, using the same parameters as in the enrichment analysis performed in part (i). Then we merged the microbiota-metabolites-genes interactions with the ND-associated genes and the ND siginificantly enriched GO ISP terms, allowing to construct the four MMDI networks. Then for each of the four MMDI networks we only retained microbiota components and metabolites that interact with the ND-associated genes. This allowed to identify microbiota components which produce metabolites that target genes associated with these diseases and therefore can modulate ND-associated GO ISPs. The characteristics of each of the four MMDI networks are described in Table 2.

(iii) EBV-ND PPI Networks

To investigate the possible contribution of microbiota - virus interactions in the development of NDs, we used the case of EBV, which has been associated with the development of three out of the four selected NDs, namely AD, MS and PD (47–49). The development of ALS was not strongly associated with EBV and hence was excluded from this part of the analysis. First, we created an EBV-host PPI network in Cytoscape using the virus-host PPI data collected in Section 2.1 (iii), resulting in a network of 1400 nodes and 7069 edges. We then performed enrichment analysis on the 1247 human protein targets of EBV proteins in the EBV-host PPI network, using the same parameters as before, with the aim to identify GO ISPs that can be modulated by EBV.

In order to identify the immunomodulatory effects of EBV in the three remaining NDs, we merged the EBV-host PPI network with each of the 200 disease-associated proteins (from the corresponding genes), resulting in the construction of three integrated EBV-ND PPI networks. Then we performed enrichment analysis on the human protein targets of EBV and their first neighbors, extracted from each of the three integrated EBV-ND PPI networks. The human proteins used to perform enrichment analysis were 1392, 1389 and 1381 for AD, PD and MS respectively.

TABLE 1 Characteristics of the MMI network.

	Number of nodes/edges
Nodes	
Microbiota nodes	259
Metabolite nodes	93
GO ISPs nodes	120
Total	**472**
Edges	
Microbiota-to-Metabolite	437
Metabolite-to-GO ISPs	3005
GO ISPs-to-GO ISPs	328
Total	**3770**

2.3 Similarity-based analysis

(i) Microbiota and microbiota-derived metabolites based on GO ISPs interactions

Using the MMI network, we extracted three network projections that involve the direct relationships between (A) metabolites and GO ISPs, (B) microbiota and GO ISPs and (C) microbiota and metabolites, illustrated in Figure 2. From the MMI network we isolated the edge interactions between metabolites and GO ISPs, and the edge interactions between microbiota and metabolites, to generate the two projections respectivelly, namely the (A) metabolites and GO ISPs and the (C) microbiota and metabolites. In addition, in order to extract the projection (B) microbiota-to-GO ISPs, we had to first identify for each microbiota in the MMI network all the connected metabolites and also identify the GO ISPs that interact with these metabolites. For the last two network projections, (B) and (C), we only retained microbiota with known genera/species/strain name, thus removing microbiota with unknown name. Then, we performed similarity-based analysis to identify clusters of (A)microbiota-derived metabolites, shown in Figure 2A, and (B) microbiotas (genera/species/strains), shown in Figure 2B, that have similar or dissimilar immunomodulatory effects, based on the GO ISPs that they can modulate. By using the two projections that involve the direct relationships between (A) metabolites and GO ISPs and (B) microbiota and GO ISPs we created two binary matrices. The microbiota to GO ISPs matrix included 256 microbiota and 120 GO ISPs, whereas the microbiota-derived metabolites to GO ISPs included 73 metabolites and 120 GO ISPs. Then by using the *vegan* package in R (50) we measured the similarity between

TABLE 2 Characteristics of the MMDI networks of MS, PD, ALS and AD.

	Number of nodes/edges			
Nodes	**MS**	**PD**	**ALS**	**AD**
Microbiota nodes	94	108	84	104
Metabolite nodes	27	30	26	29
Gene nodes	50	30	22	32
GO ISP nodes	295	63	28	95
Total	**466**	**231**	**160**	**260**
Edges				
Microbiota-to-Metabolites	119	147	107	133
Metabolites-to-Genes	179	136	97	141
Genes-to-GO ISPs	1680	283	117	515
Genes-to-Genes	313	88	83	148
GO ISPs-to-GO ISPs	3104	251	41	609
Total	**5395**	**905**	**445**	**1546**

metabolites and microbiota based on GO ISP terms effects using the Jaccard similarity index. Then, by using the *factoextra* package in R (51) we performed agglomerative hierarchical clustering on the two projection similarity results, using the average method. Agglomerative hierarchical clustering is an unsupervised clustering method that allows to group objects into clusters based on their similarity. It works very well for small datasets and allows to easily extract information from the analyzed data. There are several methods that can be used to compute the distance between the clusters in hierarchical clustering, such as "average", "single" or "median" methods. In analyzing these datasets, we used the "average" method because it had the highest correlation coefficient value between the cophenetic distance (distance in the vertical axis of the tree) and the original distance metric used for the clustering. This was a marker of validity of the clustering method that we used. The similarity-based analysis that was performed on the metabolites and GO ISPs projection, Figure 2A, and the microbiota to GO ISPs projection, Figure 2B, were used to identify metabolites and microbiota, respectively, which had similar or dissimilar immunomodulatory effects.

(ii) Synergestic relatioships between microbiota components in modulating ISPs

Microbiota components that produce the same metabolites influence the same ISPs and thus have the same effects on those processes. Thus, we used the direct relationships of microbiota components and their metabolic products, Figure 2C, to investigate the possible presence of synergestic actions between microbiota components in modulating ISPs. To identify the microbiota components that can affect the same GO ISPs we created a microbiota-to-microbiota associations network, based on pairwise similarity using List2Net (https://c-big.shinyapps.io/list2net/), a shiny application created by our group, that transforms lists of data to networks based on pairwise commonalities. Therefore, within the network, a microbiota component is connected with an edge with another microbiota component based on the common metabolites they produce. The weight of each edge is the sum of the common metabolites between each two connected microbiota components. The application also provides network metrics of various topological analysis measures, including degree and strength centralities. The degree centrality indicates the number of connections between two microbiota components and it was used to identify the microbiota components that have the highest number of associations with other microbiota components. The strength centrality, indicates the sum of the weights of all the links each node has and it was used to identify the Top 10 microbiota components with the highest potential to exert synergistic ISP effects. In addition, List2Net also provides other network metrics, such as identifying articulation points within the network whose removal will disconnect the largest connected microbial module within the network into several smaller modules. The articulation points metric was used to identify microbiota components within the network whose presence was important for ensuring network connectivity.

(iii) EBV and microbiotas common ISP effects in general and ND specific states

We used a Venn diagram, to compare the 53 EBV significantly enriched GO ISP terms obtained from the EBV-host PPI network with the 120 GO ISP terms associated with microbiota from the MMI network. The comparison revealed 24 common GO ISPs that can be modulated by EBV and microbiota components. The number of the microbiota components that co-modulate with EBV these 24 GO ISPs was found to be 241. Similarity-based analysis was performed between the 241 microbiotas and EBV based on their similarity to modulate the 24 common GO ISPs, by using the same methodology as in part (i). The similarity-based analysis

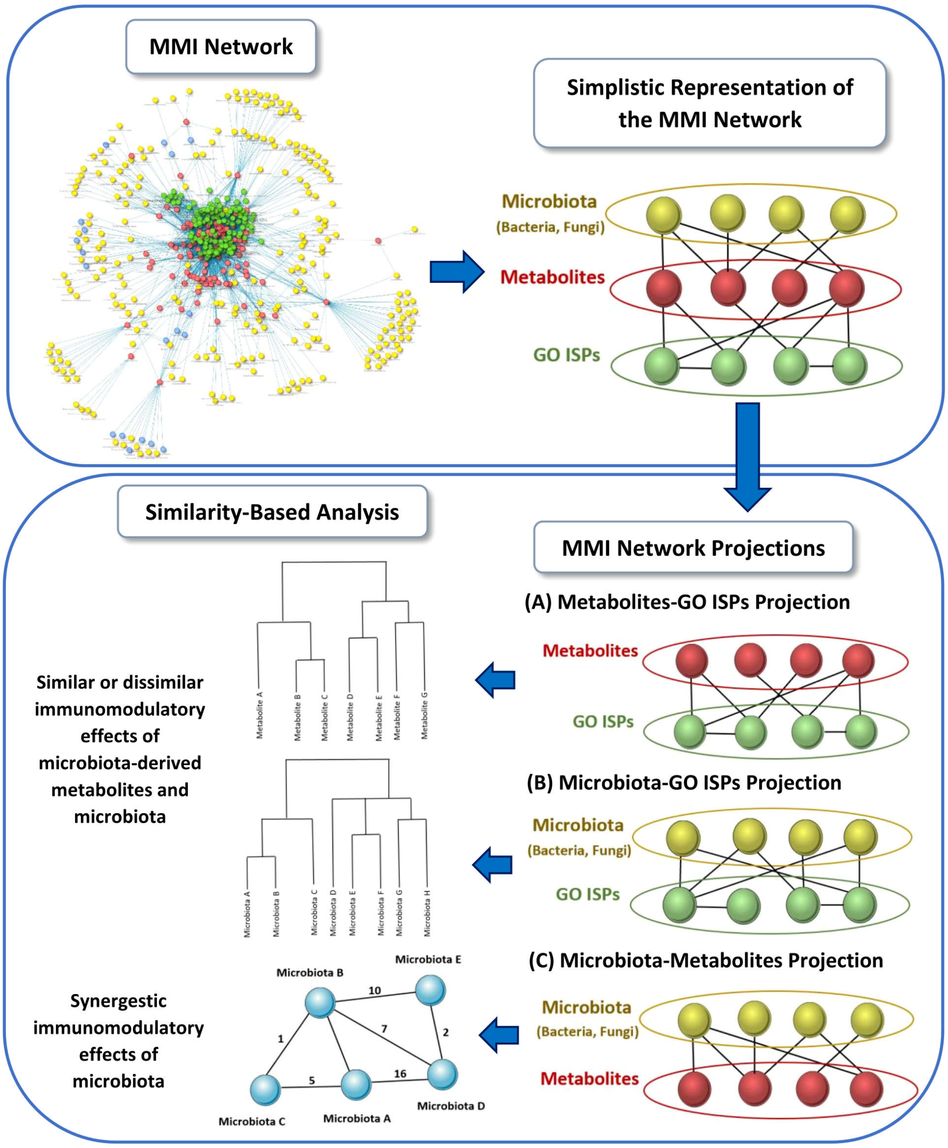

FIGURE 2
Schematic representation of the three network projections extracted from the MMI network, that involves the direct relationships between: **(A)** metabolites and GO ISPs, **(B)** microbiota and GO ISPs and **(C)** microbiota and metabolites. For each projection the illustration indicates the main methodology used and the output obtained from each projection.

was used to arrange the 241 microbiotas based on how similar or dissimilar immunomodulatory effects they had in respect to these 24 common GO ISPs with EBV.

In addition, we compared the EBV significantly enriched GO ISPs per disease (AD, MS and PD) with the GO ISPs that have been identified to be modulated by microbiota components in the corresponding MMDI networks identified in Section 2.2 parts (ii) and (iii). This allowed to identify ND-associated GO ISPs that can be modulated by both microbiota components and EBV.

2.4 Network re-wiring of the immunomodulatory effects of microbiota in ND states

Microbiota-host interactions are not static, but rather a dynamic process that changes in different conditions, such as in disease states. Network re-wiring allows to capture how the connectivity of molecular interactions changes under different disease states. Therefore, to investigate the role of microbiota-host interactions in influencing ISPs in the four NDs, we used the *DyNet* app in Cytoscape which allows to visualize and analyze dynamic changes in molecular interactions in multi-states (52, 53). The *DyNet* app performs pairwise network comparison, where two networks are compared based on their similarity of their nodes and edges. Therefore, it allows to identify nodes and edges which are present in both networks and are indicated in white color, Figure 7. It also indicates nodes/edges that are only present within one of two networks, indicated in the one network as red and in the other as green, Figure 7. Network-rewiring analysis allows to identify differences and commonalities of the interaction of microbiota with the GO ISPs associated with the four ND states.

3 Results

3.1 Comparison between bacterial- versus fungi-derived metabolites

Based on the data collected from the HMDB, we were able to identify 188 metabolites in the feces, serum and CSF human samples that can be produced by bacteria and fungi. From these metabolites, 157 can be produced only by bacteria, 11 can be produced only by fungi, whereas 20 can be produced by both bacteria and fungi. Comparison between the bacterial-derived metabolites found in the different human samples, Figure 3A, indicates that from the 152 metabolites that were found in the feces samples, 125 can also be found in the serum samples and 48 of these metabolites are also in the CSF samples. This possibly suggests that 125 metabolites from the gut can pass into the bloodstream (systemic circulation) and then 48 of these metabolites can also reach the brain. In addition, comparison between the fungi-derived metabolites found in the different human samples, Figure 3B, indicates that 21 of the metabolites found in the gut (feces samples) can enter into the bloodstream and then 12 of these metabolites can also possibly reach the brain.

However, we also observe that some bacterial-derived metabolites, Figure 3A, are not found in the feces samples. More specifically, 17 metabolites are only found in the serum, 6 both in the serum and CSF and 2 only in the CSF. Also, similarly few fungi-derived metabolites, Figure 3B, are not found in the feces samples. Specifically, 2 metabolites are only found in the serum and 2 metabolites are found in both the serum and CSF. This is probably because these microbiota-derived metabolites are not produced by microbiota located in the gut, but are rather produced by other commensal microbiota in other tissues.

3.2 GO ISPs associated with the gene targets of the microbiota-derived metabolites

The GO ISPs enrichment analysis results of the 2085 human genes that are targeted by the 130 microbiota-derived metabolites revealed 120 statistically significant GO ISPs, which are associated with 542 out of the 2085 of the human genes used for enrichment analysis, Table 3. These 542 human genes are targeted by 93 microbiota-derived metabolites, of which 81 are known to be produced only by bacteria and 12 are produced by both bacteria and fungi.

The GO ISPs results, shown in Table 3, indicated that 20.49% of the GO ISP terms belong to the group of positive regulation of leukocyte migration and 7.38% belong to the group of myeloid leukocyte differentiation. This indicates that microbiota can regulate and shape myeloid and lymphoid cells function and differentiation, which is also supported by existing literature (9). For example, microbiota-derived metabolites were shown to be able to stimulate the migration of neutrophiles at the site of inflammation or injury (54–56).

In addition, 14.75% of the enriched terms belong to the group of complement activation, classical pathway that involves processes that lead to the negative or positive regulation of the complement system *via* activation through the classical pathway. The results of our analysis is consistent with existing evidence indicating that pathogenic bacteria and commensal microbiota can hijack regulatory proteins of the complement system (57) and its activation (58). The complement system plays an important role in innate immune system defenses against pathogens and it also complements antibody responses against pathogens by the adaptive immune system (59). It also plays a critical role in commensal microbiota-immune system symbiosis and health homeostasis (60, 61). Improper complement system recognition of commensal microbiota as pathogenic will result in excessive immune responses and lead to the emergence of immune-mediated diseases (60, 61). Therefore, the ability of microbiotas to modulate the classical complement pathway indicates that they can affect both innate and adaptive immune responses against opportunistic pathogens and improper activation of this system can contribute to disease emergence.

The enrichment analysis results also indicated that 11.48% of the enriched GO ISPs terms belong to the group of antigen receptor-mediated signaling pathway, that involves the molecular signals that are initiated by the cross-linking of an antigen receptor on B or T cells. This pathway is essential for the activation of B-cells and their differentiation into either short-lived plasma cells that produce and secrete antibodies or memory B cells (62). In addition, this pathway is also essential for the activation of T cells and their differentiation into effector T cells that have different functions: cytotoxic T cells, helper T cells, regulatory T cells and memory T cells (63). Therefore, the results of our analysis indicate that microbiota have the ability to modulate through metabolite -gene interactions the signaling pathways that are involved in the activation and differentiation of B and T cells and thus the formation of immunological memory.

Moreover, 10.66% of the enriched terms belong to the group of humoral immune response mediated by circulating

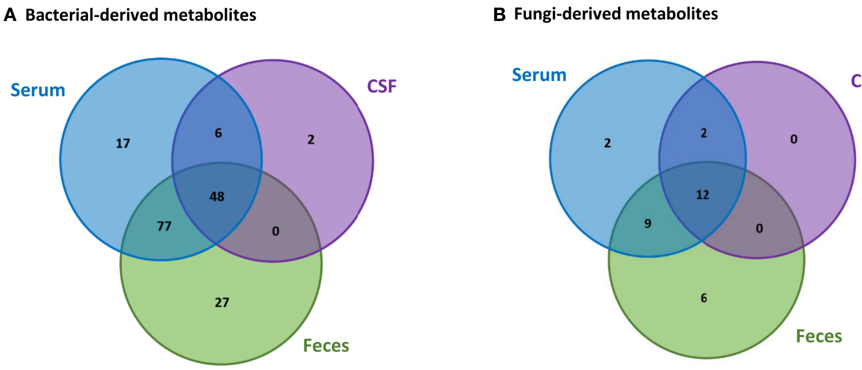

FIGURE 3
Comparison of the **(A)** bacterial-derived and **(B)** fungi-derived metabolites found in the feces, serum and CSF human samples, obtained from the HMDB database.

immunoglobulin, which involves immune responses mediated by antibodies produced by plasma B cells. Interestingly, 1.64% of the terms belong to the group of antimicrobial humoral immune response mediated by antimicrobial peptides, which suggests that microbiota can also specifically modulate antibody immune responses against microbes. In addition, 3.28% of terms belong to the group of neutrophil-mediated killing of symbiont cell that involves the direct killing by a neutrophil of symbiotic microbiota. Therefore, microbiota can upregulate or downregulate humoral immune responses against invading pathogens and also modulate ISPs that are involved in host-symbionts interactions. This is supported by evidence that indicates that gut commensal microbiota can affect antibody production, particularly immunoglobulin A (IgA), and the production of autoantibodies (64, 65).

TABLE 3 GO ISPs enrichment analysis results of the 2085 human gene targets of the 130 microbiota-derived metabolites indicating the % of terms that belong into each functional group.

Functional groups of GO ISPs terms	Percentage of Terms per group
positive regulation of leukocyte migration	20.49
complement activation, classical pathway	14.75
antigen receptor-mediated signaling pathway	11.48
humoral immune response mediated by circulating immunoglobulin	10.66
myeloid leukocyte differentiation	7.38
neutrophil mediated immunity	6.56
positive regulation of B cell activation	4.92
neutrophil-mediated killing of symbiont cell	3.28
cellular response to interferon-gamma	2.46
negative regulation of inflammatory responses to antigenic stimulus	2.46
negative regulation of cellular extravasation	2.46
hematopoietic stem cell differentiation	2.46
complement receptor mediated signalling pathway	1.64
antimicrobial humoral immune response mediated by antimicrobial peptide	1.64
defense response to Gram-negative bacterium	1.64
microglial cell activation	1.64
eosinophil migration	1.64
antigen processing and presentation of exogenous peptide antigen	0.82
myeloid dendritic cell chemotaxis	0.82
megakaryocyte differentiation	0.82

Furthermore, 1.64% of the terms belong to the group of microglia cell activation, which are considered as the resident macrophages of the CNS and play an important role in inflammation and infection within the brain (66). Therefore, the results of our analysis indicate that microbiota can also affect the regulation of innate immune responses in the CNS. This is supported by experimental evidence indicating that microbiota can affect the maturation and activation of microglia cells through the production of SFCAs and NTs (67, 68).

3.3 Similarity-based analysis results on the immunomodulatory effects of microbiota and their metabolites

The agglomerative hierarchical clustering of the 93 microbiota-derived metabolites that interact with the 542 genes that are associated with the 120 GO ISPs, indicated the presence of 14 clusters of metabolites based on similarity of GO ISP effects, shown in Figure 4. The clustering analysis results showed that several NTs, such as acetylcholine, gamma-aminobutyric acid, serotonin, norepinephrine, epinephrine, histamine and dopamine belong to the same cluster and descent from the same branch indicating that they exert similar immunomodulatory effects. Interestingly, acetaldehyde metabolite which is a byproduct of alcohol and the metabolite ethanol also belong to the same cluster and descent from the same branch as these NTs. Also, the hormone metalonin and the gasotransmitter hydrogen sulfide belong the the same cluster. In addition, the SCFAs butyric acid,proprionic acid, and salicylic acid which is the major metabolite of aspirin are also in the same cluster. This indicates that these microbiota-derived metabolites can exert similar immunomodulatory effects.

Whereas, contrary to formic acid and proprionic acid, acetic acid which is also an SCFA, belongs in a distant cluster, inidicating dissimilar immunomodulatory effects between acetic acid and these two SCFAs. Disimilar effects can also be seen between L-lactic acid and its harmful enantiomer D-lactic acid, where the former is in the same cluster as 4-hydroxcinammic acid and the neurotransmitter phenylethylamine. Whereas, D-lactic acid is in a distant cluster and exert similar effects with the metabolites hydrocinammic acid, which is a carboxylic acid, and tyrosol, which is a phenolic antioxidant compound that can be found in natural sources, such as wine an virgin olive oil.

Moroevoer, the clustering results indicated that several metabolites can exert exactly the same immunomodulatory effects, such as the SCFA formic acid which exerts exactly the same ISP effects as flutaric acid. Exactly the same immunomodulatory effects can also be observed between the metabolites phenol, glycolic acid and ascorbic acid, also known as vitamin C.

Furthermore, the agglomerative hierarchical clustering results of the 256 microbiotas based on GO ISP terms similarity indicated the presence of 14 clusters. The results of the agglomerative hierarchical clustering can be found in Figure 1 of Supplementary File 1. The analysis results indicated that several microbiotas can affect exactly the same ISPs *via* their metabolic products. This suggests that groups of microbiota can influnce the same ISPs, however it does not necessarily mean that their effect on these processes is the same as they might Interact with different genes. Therefore, the composition of the metabolites they produce and their respective gene targets will determine the outcome of the interaction between a microbiota and an ISP, resulting in its activation or inhibition.

3.4 Synergistic combinatorial effects of microbiota components on ISPs

To identify modules of microbiota that produce the same metabolites and thus affect the same ISPs, we created a microbiota-to-microbiota associations network (256 nodes, 2654 edges) based on pairwise similarity of the 72 metabolites the 256 microbiotas (genera/species/strain) produce. Visualization of the network indicated that the majority of microbiota components produce at least one metabolite that is also produced by another microbiota component, forming a large connected microbial module. This suggests that several pairwise groups of microbiota components can modulate ISPs *via* similar mechanisms through their metabolic products, resulting in synergistic immune mediated effects. In addition, based on the constructed network, only 6 microbiota components produce unique metabolites. The network is also composed by two small connected microbial modules. The first one contains only methane producing bacteria, known as methanogens, thus these microbiota components modulate the immune system in the same way. The second microbial module contains two *Lactobacillus* species, the *Lactobacillus plantarum* and *Lactobacillus paracasei*, where they share 1 metabolite that is not shared by other microbiota components.

In addition, network analysis of the microbiota-to-microbiota associations network, revealed 9 microbiota components that can act as articulation points within the network, namely: *Clostridium beijerinckii* species, *Pseudomonas putida* species, *Micrococcus* genus, *Klebsiella* genus, *Pseudomonas fluorescens* species, *Escherichia coli* species, *Lactobacillus* genus, *Corynebacterium glutamicum* species and *Alcaligenes* genus. Articulation points are nodes within the network, whose removal will disconnect the largest connected microbial module into several smaller modules, thus these microbiota components are essential for ensuring network connectivity. Some of the identified articulation points are known opportunistic pathogenic organisms, such as *Escherichia coli* species, *Klebsiella* genus, *Alcaligenes* genus and *Pseudomonas putida* species. Whereas, other articulation points, such as *Lactobacillus* genus, are known beneficial gut microbiota, which are also found in probiotic supplements. *Pseudomonas fluorescens* species, which act as an articulation point, reside in low levels in various body sites and are considered non-pathogenic. However, they can cause acute opportunistic infection in rare occasions, and interestingly they have been associated with the development of Chron's disease (69, 70). In addition, *Clostridium beijerinckii* is also a non-pathogenic clostridia species, unlike other known clostridia species, like *Clostridium difficile* and *Clostridium botulinum* that are known human disease-causing pathogens (71).

Network analysis also allowed to identify the microbiota components which have the highest degree of pairwise similarity of metabolites which are also produced by other microbiota components, with the Top 10 high degree indicated in Figure 5A. Interestingly, almost all of the Top 10 high degree microbiota components are either known human pathogenic or opportunistic pathogens, with the exception of *Ruminococcus* genus which are not considered to be opportunistic pathogens. However, several members of the *Ruminococcus* genus are commensal gut microflora and alternations in their abundance has been found in several NDs, including MS (72, 73), PD (74–76), AD (77) and ALS

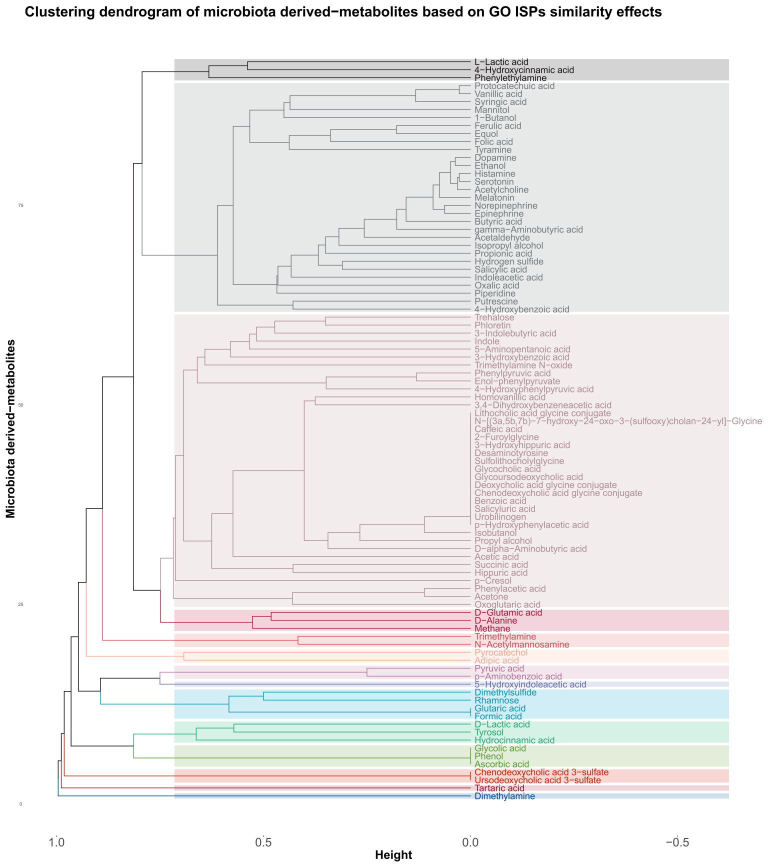

FIGURE 4

Clustering dendrogram of the 93 metabolites that target the 542 genes that were found to be associated with the 120 GO ISPs, based on their interaction similarity with GO ISPs.

(78), but also other diseases such as Chron's disease (79–81). *Escherichia coli* genus which has the highest degree of pairwise similarity of metabolites which are also produced by other 129 microbiota is also a commensal gut microbiota, but it can become pathogenic when it infects other tissues. Moreover, several of the other high degree microbiota components are also commensal microbiota that can become pathogenic when their abundance increases or they migrate to other tissues, such as the genera *Staphylococcus*, *Streptococcus*, *Alcaligenes* and *Enterococcus*. Therefore, the network analysis results indicate that human pathogenic bacteria have a high degree of pairwise similarity with other microbiota components, which not only allows them to influence multiple ISPs, but also allows them to exert synergistic immunomodulatory effects. In addition, Figure 5B, indicates the Top 10 microbiota components which have the highest node strength, which is the sum of weights of the links connected to the node, hence node strength indicates the microbiota components with the highest potential of synergistic immunomodulatory effects.

3.5 Possible microbiome-host-immune system interactions in NDs

Perturbations in microbiome-immune system interactions have been associated with the development of NDs (82, 83). Therefore, to investigate the possible role of the immunomodulatory effects of microbiota-metabolic products in NDs we first identified for each of the four NDs (AD, PD, MS and ALS) the number of disease-associated genes that can be also targeted by microbiota components *via* their metabolic products, which are termed intersections nodes. More specifically, we identified 68, 91, 72 and 93 intersection nodes in MS, AD, ALS and PD, respectively. Table 4, indicates the number of genes out of the top 200-disease associated genes included in the analysis for each ND, which can act as intersection nodes, including also the number of microbiota components and their metabolic products that interact with these intersection nodes. The results indicate that AD and PD have the highest number of disease-associated genes that are targeted by microbiota-derived metabolites, as they have 91 and

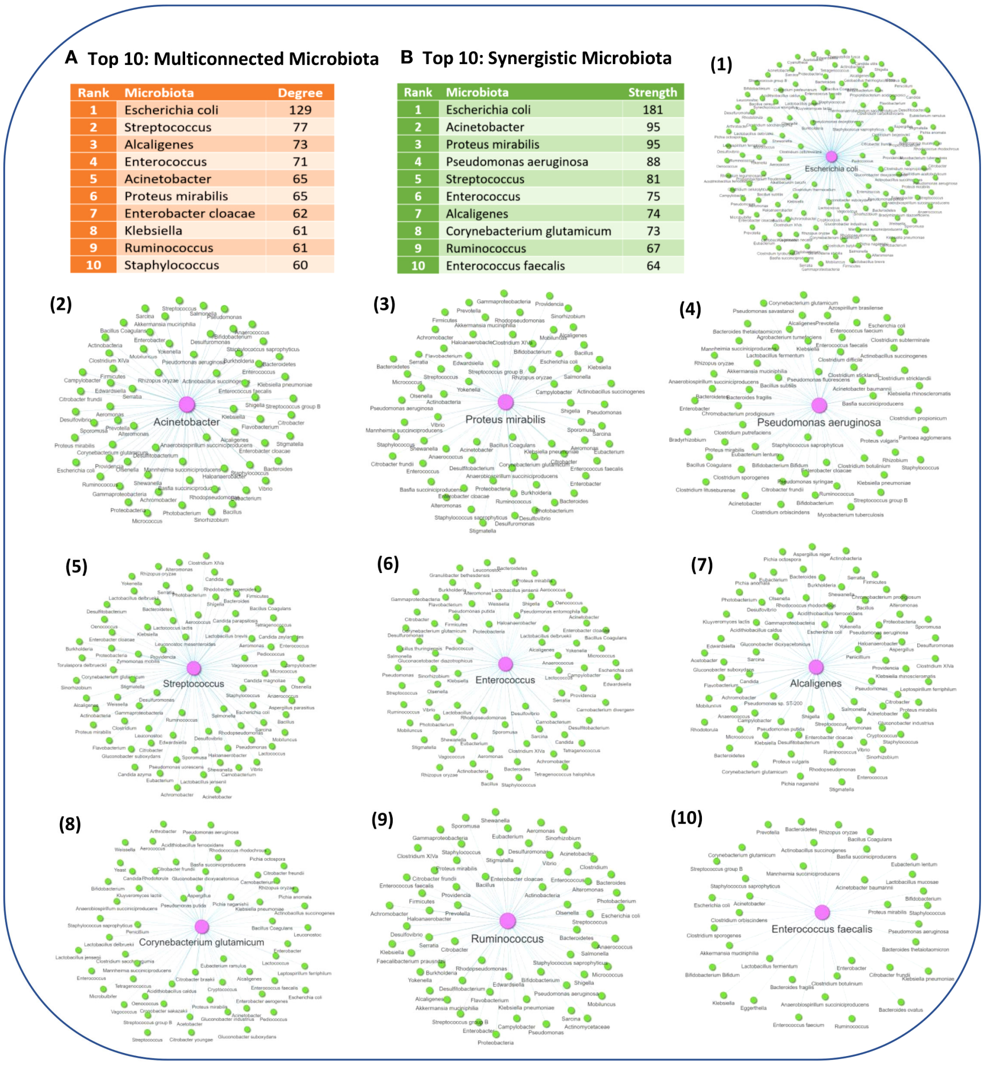

A Top 10: Multiconnected Microbiota

Rank	Microbiota	Degree
1	Escherichia coli	129
2	Streptococcus	77
3	Alcaligenes	73
4	Enterococcus	71
5	Acinetobacter	65
6	Proteus mirabilis	65
7	Enterobacter cloacae	62
8	Klebsiella	61
9	Ruminococcus	61
10	Staphylococcus	60

B Top 10: Synergistic Microbiota

Rank	Microbiota	Strength
1	Escherichia coli	181
2	Acinetobacter	95
3	Proteus mirabilis	95
4	Pseudomonas aeruginosa	88
5	Streptococcus	81
6	Enterococcus	75
7	Alcaligenes	74
8	Corynebacterium glutamicum	73
9	Ruminococcus	67
10	Enterococcus faecalis	64

FIGURE 5
(A) The Top 10 microbiota components with the highest degree of pairwise similarity of metabolites that are also produced by another microbiota component. **(B)** The Top 10 microbiota components with the highest strength topology, thus having the highest potential to exert synergistic effects. Figure also illustrates the associated microbiota pairs of each of the Top 10 synergistic microbiota components as a microbiota-to-microbiota association network.

93 intersection nodes, respectively. In addition, the number of microbiota components that can interact with these intersection nodes is also higher in AD and PD compared to MS.

Moreover, through the reconstruction and visualization of the MMDI networks for the four NDs, we were able to identify specific disease-associated genes associated with ISPs that are also interactors and modulated by microbiota *via* metabolite-to-gene interactions. Table 5 indicates for each of the four MMDI networks the number of intersection nodes that are associated with ISPs and the number of microbiota nodes and their metabolic products that interact with the ISP- associated intersection nodes. These results indicate that although MS has the least number of disease-associated genes that are targeted by microbiota-derived metabolites, the majority of these genes are associated with GO ISP enriched terms. On the contrary, in AD and PD which have the highest number of disease-associated genes that are targeted by microbiota-derived metabolites, only approximately one-third of these intersection nodes are also associated with GO ISPs. In addition, in ALS less than one-third of intersection genes are associated with GO ISP enriched terms. However, the results also indicated that these GO ISP- associated intersection nodes in each of the four NDs can influence either all or the majority of the GO ISP terms associated with these diseases. More specifically, the GO ISP-associated intersection nodes participate in 295 out of the 303, 63 out of the 63, 28 out of the 30 and 95 out of the 97 ISPs, in MS, PD, ALS and AD, respectively. This suggest that the GO ISPs-associated intersection nodes which are targeted by microbiota have pleiotropy in ISP effects, which possible allows microbiota to affect multiple disease related ISPs.

Comparison between the microbiota components and microbiota-derived metabolites that have been identified to influence the ISP-associated intersection nodes for the four NDs, indicated that there are 65 common microbiotas and 21 common metabolites between all four NDs. In addition, comparison between the GO ISPs that can be modulated by microbiota in the four ND states indicated that they share 19 common GO ISPs, that can be modulated by microbiota components, shown in Figure 6.

3.6 Network re-wiring of the immunomodulatory effects of microbiota in NDs

The immune system at equilibrium has a certain set of interactions and nodes, whereas at disequilibrium new nodes and interactions will emerge due to the activation of ISPs associated with the inflammatory trigger or the disease state. This dynamic change of immune system molecular interactions gives rise to specific disease immune phenotypic profiles. This "re-wiring" in the network of molecular interactions due the presence of a disease state could be also reflected in the re-wiring in the networks of microbiota-host interactions. Therefore, it is expected that the effect of the same microbiotas might be different in different diseases due to the different immune profiles and different perturbations that will emerge from microbiota-host interactions. This is because immune system re-wiring due to a disease condition will lead to the emergence of new interactions and nodes which would also change the immunomodulatory effects of microbiota-host interactions.

To investigate the level of re-wiring of the immunomodulatory effects of microbiota *via* metabolite-gene interactions under the four NDs we used the *DyNet* app in Cytoscape, where we performed pairwise network comparison which allowed to identify nodes and edges that differ between two networks. Figure 7, illustrates the pairwise comparison between all the pairs of MMDI networks. The pairwise comparison between the four MMDI networks, indicated that MS compared to the other three NDs (ALS, PD and AD) has a higher level of network re-wiring due to the presence of several nodes and edges that are not present in the other three networks. In addition, the pairwise comparison indicated that ALS has the least level of network re-wiring compared to the other three NDs (AD, PD and MS). Moreover, the comparison indicated that the level of re-wiring between AD and PD is not high, as they share several common nodes and edges, and have relatively few different nodes and edges.

3.7 Possible contribution of microbiota - EBV interactions in the development of NDs

Both microbiota and viruses have the ability to influence ISPs, with microbiota exerting their immunomodulatory effects *via* their metabolic products and viruses through their viral proteins. In addition, both viruses and microbiota have been associated with the development of NDs, hence microbiota-virus interactions might contribute to the development of NDs as well. Viruses, through PPIs can manipulate host ISPs and lead to their dysregulation, which might contribute to the development or progression of NDs. Therefore, we explored whether microbiota components that have immunomodulatory effects can modulate similar ISPs as viruses associated with NDs. To explore these similarities, we used the case of EBV which is associated with the development of three NDs (AD, PD and MS) and because EBV is a well-studied virus that has lots of available PPI data.

We first performed enrichment analysis on the 1247 human protein targets of EBV proteins to investigate the effects of EBV in general, which revealed 53 significantly enriched GO ISP terms. Then we compared the EBV significantly enriched GO ISP terms with the 120 GO ISP terms associated with microbiota from the MMI network, which revealed 24 common GO ISPs that can be modulated by both EBV and the 241 microbiotas. Subsequently by using the microbiota-to-GO ISPs projection of the MMI network we extracted and identified the microbiota components which can influence these 24 GO ISPs which are also modulated by EBV. Then we performed similarity-based analysis between the 241 microbiotas and EBV to group them into clusters based on their ability to modulate these 24 common GO ISPs. The clustering results indicated the presence of 24 clusters of microbiotas. The clustering results (see Figure 2 of Supplementary File 1) indicated that 9 out of the 241 microbiotas belong to the same cluster with EBV and thus, like EBV, they can modulate all of the 24 GO ISPs, Figure 8.

TABLE 4 Characteristics of the interaction of microbiota and their metabolites with NDs-associated genes.

	PD	MS	ALS	AD
Microbiota nodes that produce metabolites that interact with the intersection nodes	157	107	141	158
Metabolites nodes that target the intersection gene nodes	57	33	50	54
Intersection gene nodes	93	68	72	61

TABLE 5 Characteristics of the immunomodulatory effects of microbiota and their metabolites in the MMDI networks.

	PD	MS	ALS	AD
Microbiota with immunomodulatory effects	108	94	84	104
Microbiota-derived metabolites that interact with GO ISPs	30	27	26	29
Intersection nodes that are associated with GO ISPs	30	50	22	32
GO ISPs associated with each disease	63	295	28	95

More specifically these microbiota components are: *Roseburia* genus, *Lactobacillus* genus, *Hansenula polymorpha* species, *Faecalibacterium prausnitzii* species, *Eubacterium* genus, *Coprococcus comes* species, *Coprococcus eutactus* species, *Anaerostipes* genus and *Baccillus* genus. *Lactobacillus* are considered as "friendly" bacteria that live symbiotically within the human host exchibiting health promoting effects and protect against pathogenic organisms (84). In addition, the *Lactobacillus* and *Bacillus* genera are found in probiotic supplements, with *Lactobacillus* being the most common genus used for probiotics (85, 86).

However, as already mentioned, pathogen-host interactions in disease states differ from healthy state due to the emergence of new interactions and processes that arise based on the pathological mechanisms activated as a result of the disease. Therefore, in order to investigate the possible microbiota-EBV interactions in modulating GO ISPs associated with NDs, we first created three integrated EBV-ND PPI networks, where the EBV-host PPI network was merged with the disease-associated proteins of each of the three NDs (AD, PD and MS). Then, to identify GO ISPs that can be modulated by EBV in each of the three NDs, we performed enrichment analysis on the human protein targets of EBV proteins and their first neighbors in each of the integrated EBV-ND PPI networks. The enrichment analysis of EBV PPI in NDs, indicated that the number of significantly enriched GO ISPs that can be modulated by EBV in MS disease states are 235, in PD state are 87 and in AD state are 99.

Then we compared the EBV GO ISP enriched results in the three NDs, with the GO ISPs that can be modulated by microbiota components in the three ND states, which allowed to identify for each ND state the GO ISPs that can be modulated by both microbiota components and EBV. The comparison between the immunomodulatory effects of EBV and microbiota in MS disease, indicated that 169 MS-associated GO ISPs can be modulated by both microbiota components and EBV. Similarly, comparison of the immunomodulatory effects of EBV in PD and AD diseases with the immunomodulatory effects of microbiota on the GO ISPs associated with these disease states, indicated 18 and 36 common ISPs that can be modulated by both microbiota components and EBV, respectively. These results indicate that in MS there is a higher number of disease-associated ISPs that can be modulated by both microbiota and EBV infection, than in PD and AD. Therefore, it is possible that microbiota-EBV interactions, in terms of their immunomodulatory effects, might play a more significant role in MS pathogenesis rather than PD and AD.

4 Discussion

In this study we performed a network-based bioinformatics approach with the aim to first investigate the immunomodulatory

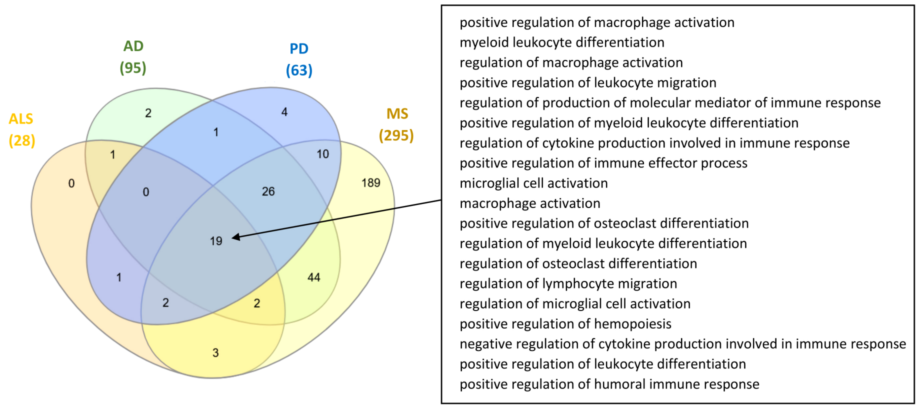

FIGURE 6
Comparison of the GO ISPs that can be modulated by microbiota components in the four ND states AD, MS, ALS and PD, highlighting the 19 common GO ISPs.

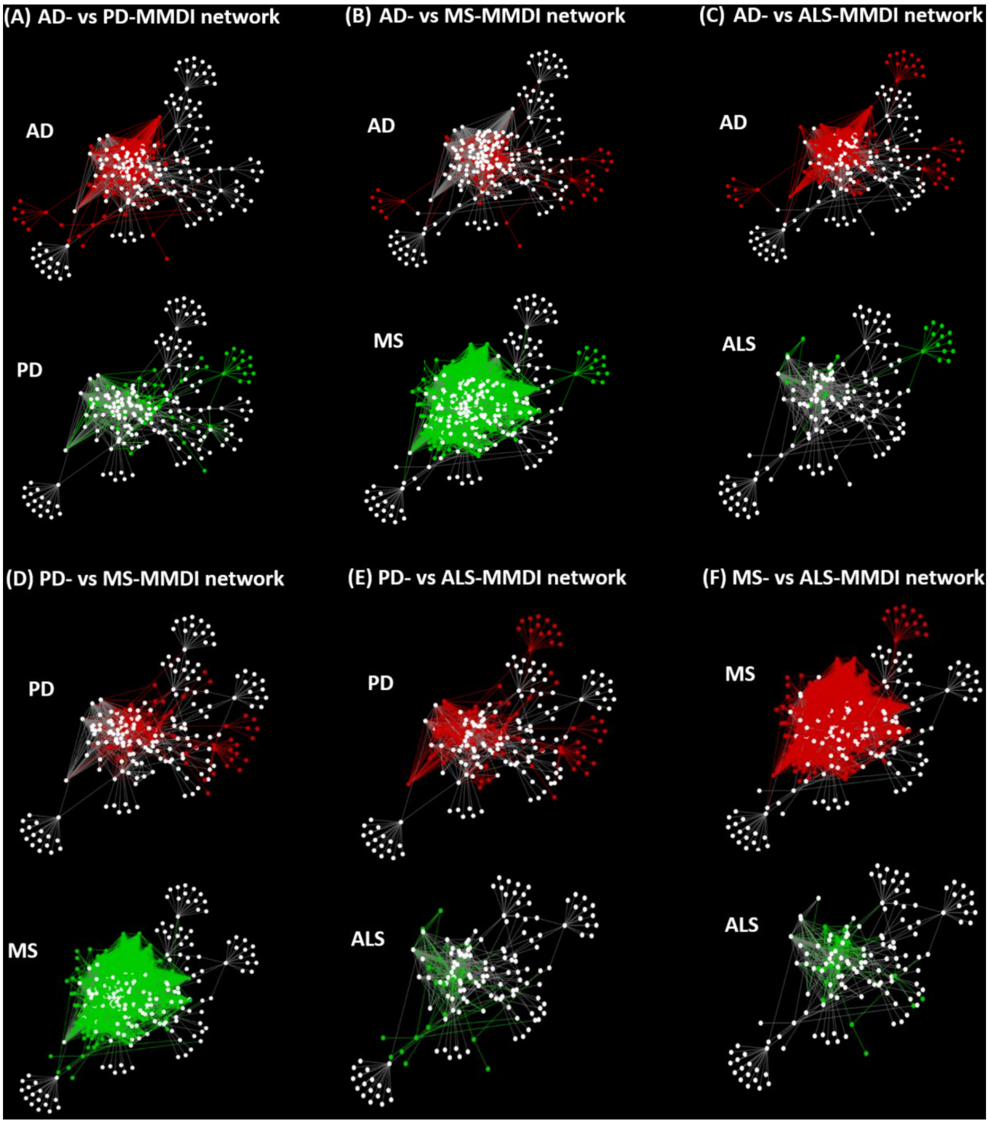

FIGURE 7
Pairwise network comparisons between the MMDI networks, with red nodes/edges indicating nodes only present in one network and green nodes/edges indicating nodes that are only present in the other network, whereas white nodes indicate common nodes between the two networks.

effects of microbiota (bacteria and fungi) through their metabolic products. We also explored how various microbiota components, through their immunomodulatory effects, might be able to influence ISPs associated with NDs, and thus possibly contribute to their development and/or progression. In addition, we explored the immunomodulatory effects of EBV, which is associated with the development of the three NDs, MS, AD and PD, both in general and ND specific states. Moreover, we examine how microbiota-virus interactions might contribute to the modulation of ISPs associated with pathogenic mechanisms involved in NDs. Our network-based methodology is summarized in Figure 1.

Statistically significant enrichment analysis revealed 120 GO ISP terms that can be modulated by 93 microbiota-derived metabolites through their interaction with 542 human gene targets. The GO ISPs results, Table 3, indicated that 20.49% of the GO ISP terms belong to the group of positive regulation of leukocyte migration. During tissue damage or infection migration of circulating blood leukocyte cells are an important component in the elimination of the inflammatory triggers and tissue repair process (87). Leukocyte migration is also essential for the resolution of inflammatory processes and uncontrolled migration of leukocytes cells is observed in inflammation and NDs. Therefore, microbiotas through their metabolic products can influence immune responses during inflammatory triggers.

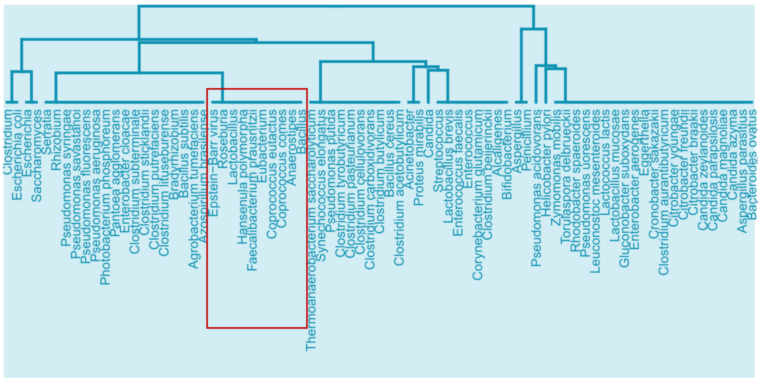

FIGURE 8

Cluster from the similarity results of EBV with the 241 microbiota that can affect the 24 ISPs that can be modulated by both microbiota components and EBV, highlighting the branch that EBV belongs to and the microbiota components that can also affect all 24 of the common GO ISPs.

In addition, 7.38% of the enriched terms belong to the group of myeloid leukocyte differentiation. Myeloid cells are important in mounting effective inflammatory responses during viral infections (88). Therefore, microbiota by affecting myelopoiesis can possibly affect innate immune responses and the formation of immunological memory against viral infections.

Moreover, 14.75% of the GO ISP terms belong to the group of complement activation, classical pathway, which plays an important role in innate immune system defenses against pathogens and also complements antibody responses against pathogens by the adaptive immune system. The complement system also plays a critical role in commensal microbiota-immune system symbiosis and health homeostasis. Improper complement system recognition of commensal microbiota as pathogenic would lead to excessive immune responses and hence to the emergence of immune-mediated diseases (60, 61). Therefore, microbiota, by interfering with the complement system, not only have the ability to affect both innate and adaptive immune responses against pathogens, but also regulate host responses against symbionts.

The enrichment analysis results also indicated that microbiota can affect the formation of memory B and T cells by modulating the signaling pathways that are involved in the differentiation of B and T cells, as 11.48% of the GO ISPs terms belong to the group of antigen receptor-mediated signaling pathway. In addition, the enrichment results indicated that microbiota can affect humoral immune response mediated by circulating immunoglobulin. This suggests that microbiota can affect antibody production. This is supported by evidence that indicates that gut commensal microbiota can affect the production of IgA, and the production of autoantibodies (64, 65). Evidence also indicates that SFCAs, which are produced by gut microbiota from dietary intake, can influence antibody production. Reduced intake of dietary fiber leads to the production of low levels of SFCAs, and this was shown to result in defective pathogen-specific antibody responses (89). Autoantibodies are a common feature of autoimmune diseases, but also of NDs, like MS, therefore improper diet in combination with altered microbiota composition might lead to the loss of self-tolerance and impaired immune responses to pathogenic organisms.

Furthermore, 1.64% of the terms belong to the group of microglia cell activation. Gut microbiota can affect the maturation and activation of microglia cells *via* the production of SCFAs (67) and microbiota-derived NTs (68). These microbiota-mediated effects on microglia were shown to also affect innate immune responses in the CNS against viral infections, mediated by the production of SCFAs (67). Microglia dysfunction has been implicated in the pathogenesis of several NDs, including MS, AD, PD and ALS, as they contribute to neuroinflammation (90). Altered microbiota composition has also been associated with the development of NDs, therefore microbiome-microglia interactions might influence NDs pathogenesis (68). Viruses which are also associated with the development of NDs and can also interfere with microglia functions (91). Therefore, since alternation in microbiota can influence microglia immune responses against viral infection, microbiota-virus-microglia interactions could also influence the pathogenesis of NDs.

The next step of our methodology involved the reconstruction and visualization of the MMI network that contained microbiota - metabolites - GO ISP terms interactions. From the MMI network, we extracted three network projections that involve the direct relationships between (a) metabolites and GO ISPs, (b) microbiota and GO ISPs and (c) microbiota and metabolites, illustrated in Figure 2. Projections (a) and (b) were used to identify clusters of microbiota-derived metabolites and clusters of microbiotas genera/species/strains that have similar or dissimilar immunomodulatory effects, based on the GO ISPs that they can affect. The similarity analysis results of the microbiota-derived products indicated that the majority of the microbiota-derived NTs belong to the same cluster, therefore they exert similar immunomodulatory effects. NTs can influence both innate and adaptive immune responses, with leukocyte cells expressing receptors for several NTs including glutamate, dopamine, serotonin and acetylcholine (92, 93). A bidirectional cross-talk exists between the brain and the peripheral immune system as leukocyte can also synthesize and released NTs and they can also produce cytokines that participate in the neuroimmunomodulatory circuitry (93). Therefore, NTs produced by microbiota can indirectly modulate neuroinflammation and they can also possibly affect neural regulation of innate immunity, including microglia activation (68). Interestingly, evidence indicates that microglia have also the capacity to be ‘primed’ based on their history of inflammatory stimuli and develop innate immune memory (94). Depending on the initial stimuli, repeated exposure to secondary inflammatory stimuli may enhance their responses or lead to loss of responsiveness (94). This suggests that a form of classical conditioning learning might exist in the pairing of microglia with the initial stimuli that influences responses during re-exposure. In a mouse model of AD, it was shown that application of a peripheral stimuli caused innate immune memory training of microglia cells in the brain which exacerbated β amyloidosis, whereas innate immune tolerance alleviated this effect (95). Therefore, it is possible that microbiome-derived NTs and SFCAs, which can modulate microglia maturation and activation, might also affect the priming of microglia towards inflammatory stimuli and thus the development of innate immune memory by microglia, which might contribute to NDs development.

In addition, the clustering results also indicated that groups of microbiota can influnce the same ISPs. However it does not necessarily mean that by targeting the same ISP the outcome of their effect would be the same as they might interact with different genes in these ISPs, thus leading to either inhibition or activation of the ISPs. Therefore, in order to identify microbiota that have the same outcome on an ISP and thus possible synergistic effets, we extracted from the MMI network the direct relationships between microbiota and metabolites, Figure 2C. Then by using the microbiota to metabolites relationships we created a microbiota-to-microbiota associations network based on pairwise similiarity to identify pairs of microbiota components that can produce the same metabolites. Topological analysis of the microbiota-to-microbiota associations network indicated the Top 10 microbiota components that had the highest degree of pairwise similarity with metabolites produced by other microbiota components. Almost all of the Top 10 microbiota components were human pathogenic or opportunistic pathogens, with the exception of *Ruminococcus* genus. This suggests that pathogenic bacteria by producing several metabolites that can be also produced by other microbiota components are able to influence multiple ISPs effects. This also allows them the potential to exert synergistic immunomodulatory effects with other microbiota components, which possibly provides them with increased survival and pathogenicity. The potential of synergistic actions between microbiota components through their metabolic products can possibly affect the immune responses towards the emergence of a specific immune system phenotype. This can occur when there is either an increase or a decrease in the abundance of microbiota components that produce the same metabolite. However, the outcome of the immunomodulatory effects influenced by commensal microbiota composition is not only determined by the combinatorial action of their synergistic relationships, but also by their antagonistic relationships. The metabolites produced by one microbiota component can have an opposite effect on the host’s ISPs compared to the effect of the metabolic products produced by another microbiota component, thus leading to the emergence of antagonist relationships.

The reconstruction and visualization of microbiota-host-interactions in NDs (AD, ALS, PD and MS), allowed to identify mechanisms by which microbiota components *via* their metabolic products might influence pathologies associated with NDs, Table 4. More specifically, it allowed to identify intersection nodes, which are nodes that are ND-associated genes but they are also genes that are targeted by microbiota components *via* their metabolic products. In addition, it allowed to identify intersection nodes which are associated with GO ISPs in these four ND states, Table 5. The results indicated that although MS has the least number of disease-associated genes that are targeted by microbiota-derived metabolites, the majority of these genes are associated with almost all of the GO ISPs associated with MS disease. On the contrary, in AD and PD where microbiota had the highest number of disease-associated genes that are targeted by microbiota-derived metabolites, only approximately one-third of these intersection nodes are also associated with disease-associated GO ISPs. This possibly suggests that the influence of microbiota on GO ISPs-associated with MS disease is higher than in AD and PD, thus microbiota might have a more significant role in MS disease inflammation. However, this does not mean that microbiota do not play a role in the pathogenesis of AD and PD. At least, the impact of microbiota in these diseases seems not to be mediated by their immunomodulatory effects but it can be possibly mediated by the dysregulation of other host processes. Moreover, comparison between the microbiota components and microbiota-derived metabolites that influence ND- associated ISPs in the four ND states indicated that there are 65 common microbiotas and 21 common metabolites between all four NDs, as well as 19 common GO ISPs, indicated in Figure 6.

However, although these four NDs share common microbiota and metabolites it does not mean that the immunomodulatory effects of these microbiotas are the same in these diseases as network dynamics change, due to the emergence of new interactions and nodes that stem from the disease pathology. This "re-wiring" between molecular interactions due to the presence of a disease state is also expected to change microbiota-host interactions. We investigated network re-wiring of the immunomodulatory effects of microbiota between the four NDs (AD, ALS, PD and MS) by performing pairwise network comparison which allowed to identify nodes and edges that differ between two network pairs of NDs, Figure 7. The pairwise comparison between the four MMDI networks, indicated that MS compared to the other three NDs (ALS, PD and AD) has a higher level of network re-wiring due to the presence of several nodes that are not present in the other three networks. In addition, the network re-wiring analysis indicated that ALS has the least level of network re-wiring compared to the other three NDs (AD, PD and MS). Moreover, the comparison indicated that the level of difference between AD and PD is not high, as they share several common nodes and edges having only relatively few different nodes and edges.

Finally, to investigate the possible contribution of microbiota-virus interactions in the development of NDs, we explored whether microbiota that have immunomodulatory effects can modulate similar ISPs as EBV which is associated with the development of three NDs: AD, PD and MS. To investigate the possible presence of microbiota-EBV interactions in modulating GO ISPs associated with NDs, we first constructed three integrated EBV-ND PPI networks, where the EBV-host PPI network was enriched with the disease-associated proteins of each of the three NDs (MS, PD and AD). The enrichment analysis of EBV PPI interactions in NDs, indicated 235, 87 and 99 significantly enriched GO ISPs that can be modulated by EBV in MS, PD and AD states, respectively. Comparison of the EBV GO ISPs results in the three NDs, with the ISPs that can be modulated by microbiota components in the three NDs states, allowed to identify for each ND the ISPs that can be modulated by both microbiota components and EBV. The comparison results indicated that 160 GO ISPs associated with MS disease can be modulated by both microbiota components and EBV, whereas only 18 and 36 GO ISP can be modulated in PD and AD, respectively. This possibly indicates that microbiota-virus immunomodulatory-related interactions, might play a more significant role in MS disease pathogenesis rather than in the pathogenesis of PD and AD.

5 Conclusion

In this paper, we provided a bioinformatics insight approach that tries to capture the effects of microbiota, bacteria and fungi, in shaping immune responses and influencing the formation of immunological memory cells through their metabolic products, under ND states and under ND states with EBV viral infection. We recognize that our study might have certain limitations mainly based on the completeness and the possible biases of the databases used, however despite these limitations our approach allowed us to formulate the following conclusions.

The enrichment analysis of microbiota-host interactions allowed to highlight various aspects of the innate and adaptive immune response systems that can be modulated by microbiota, which includes responses during inflammatory triggers. The results also indicated that microbiota can influence the activation and maturation of microglia which are implicated in the development of NDs.

The reconstruction of the microbiota-to-microbiota associations network based on pairwise similiarity of pairs of microbiota components that can produce the same metabolites allowed to possibly identify a potential of synergestic immunomodulatory actions between microbiota components. The pairwise similarity also indicated that known pathogenic bacteria, such as the *Escherichia coli* and *Klebsiella* genera, that can produce several metabolites that are also produced by other microbiota components, allowing them to influence multiple ISPs and thus possibly contributing to their pathogenicity.

Investigation of possible microbiota-host-immune system interactions in NDs allowed for the isolation of specific microbiota components and metabolic products that interact with disease-associated genes that participate in ISPs. The results also suggest that the impact of microbiota-derived metabolites in influencing ISPs is higher in MS, than AD, PD and ALS.

Finally, investigation of the possible contribution of microbiota- virus interactions in the development of NDs, allowed to identify ISPs that can be modulated by both microbiota components and EBV. The result of the analysis also suggests that the combinatorial action of the immunomodulatory effects of microbiota-EBV interactions might play a more significant role in MS disease pathogenesis rather than in the pathogenesis of PD and AD.

Data availability statement

Publicly available datasets were analyzed in this study. This data can be found here: HMDB https://hmdb.ca/downloads, PHISTO https://phisto.org/, VirHostNet https://virhostnet.prabi.fr/, DISEASES https://diseases.jensenlab.org/Search.The in-house developed HMDB parsing R script can be provided upon request to the authors.

Author contributions

AO and GS have contributed to the conceptualization, methodology, review and editing of the manuscript. AO collected and analyzed the data, and wrote the original draft manuscript, under the supervision of GS. All authors have contributed to the article and have read and agreed to the published version of the article.

Funding

This study received support from the Cyprus Institute of Neurology & Genetics and funded by Telethon.

Acknowledgments

We thank Sotiroula Afxenti for developing the parsing R script used to parse the xml datasets from the HMDB.

Conflict of interest

The authors declare that the research was conducted in the absence of any commercial or financial relationships that could be construed as a potential conflict of interest.

Publisher's note

Supplementary material

The Supplementary Material for this article can be found online at: https://www.frontiersin.org/articles/10.3389/fimmu.2022.843128/full#supplementary-material

References

1. Gill SR, Pop M, DeBoy RT, Eckburg PB, Turnbaugh PJ, Samuel BS, et al. Metagenomic analysis of the human distal gut microbiome. *Science (80-)* (2006) 312(5778):1355–9. doi: 10.1126/science.1124234

2. Thursby E, Juge N. Introduction to the human gut microbiota. *Biochem J* (2017) 474(11):1823–36. doi: 10.1042/BCJ20160510

3. Dalile B, Van Oudenhove L, Vervliet B, Verbeke K. The role of short-chain fatty acids in microbiota–Gut–Brain communication. *Nat Rev Gastroenterol Hepatol* (2019) 16(8):461–78. doi: 10.1038/s41575-019-0157-3

4. Flint HJ, Scott KP, Duncan SH, Louis P, Forano E. Microbial degradation of complex carbohydrates in the gut. *Gut Microbes* (2012) 3(4):289–306. doi: 10.4161/gmic.19897

5. Rowland I, Gibson G, Heinken A, Scott K, Swann J, Thiele I, et al. Gut microbiota functions: Metabolism of nutrients and other food components. *Eur J Nutr* (2018) 57(1):1–24. doi: 10.1007/s00394-017-1445-8

6. Agus A, Clément K, Sokol H. Gut microbiota-derived metabolites as central regulators in metabolic disorders. *Gut* (2021) 70(6):1174–82. doi: 10.1136/gutjnl-2020-323071

7. Thaiss CA, Zmora N, Levy M, Elinav E. The microbiome and innate immunity. *Nature* (2016) 535:65–74. doi: 10.1038/nature18847

8. Slack E, Hapfelmeier S, Stecher B, Velykoredko Y, Stoel M, Lawson MAE, et al. Innate and adaptive immunity cooperate flexibly to maintain host-microbiota mutualism. *Science (80-)* (2009) 325(5940):617–20. doi: 10.1126/science.1172747

9. Gorjifard S, Goldszmid RS. Microbiota–myeloid cell crosstalk beyond the gut. *J Leukoc Biol* (2016) 100(5):865–79. doi: 10.1189/jlb.3ri0516-222r

10. McCoy KD, Burkhard R, Geuking MB. The microbiome and immune memory formation. *Immunol Cell Biol* (2019) 97(7):625–35. doi: 10.1111/imcb.12273

11. Negi S, Das DK, Pahari S, Nadeem S, Agrewala JN. Potential role of gut microbiota in induction and regulation of innate immune memory. *Front Immunol* (2019) 10:2441. doi: 10.3389/fimmu.2019.02441

12. Rothschild D, Weissbrod O, Barkan E, Kurilshikov A, Korem T, Zeevi D, et al. Environment dominates over host genetics in shaping human gut microbiota. *Nature* (2018) 555:210–15. doi: 10.1038/nature25973

13. Li N, Ma WT, Pang M, Fan QL, Hua JL. The commensal microbiota and viral infection: A comprehensive review. *Front Immunol* (2019) 10:1551. doi: 10.3389/fimmu.2019.01551

14. Vojdani A. A potential link between environmental triggers and autoimmunity. *Autoimmune Dis* (2014) 2014:437231. doi: 10.1155/2014/437231

15. Sinagra E, Utzeri E, Morreale GC, Fabbri C, Pace F, Anderloni A. Microbiota-Gut-Brain axis and its affect inflammatory bowel disease: Pathophysiological concepts and insights for clinicians. *World J Clin Cases* (2020) 8(6):1013–25. doi: 10.12998/wjcc.v8.i6.1013

16. Jenkins TA, Nguyen JCD, Polglaze KE, Bertrand PP. Influence of tryptophan and serotonin on mood and cognition with a possible role of the gut-brain axis. *Nutrients* (2016) 8(1):56. doi: 10.3390/nu8010056

17. Cryan JF, Dinan TG. Mind-altering microorganisms: The impact of the gut microbiota on brain and behaviour. *Nat Rev Neurosci* (2012) 18(6):552–8. doi: 10.1038/nrn3346

18. Roy Sarkar S, Banerjee S. Gut microbiota in neurodegenerative disorders. *J Neuroimmunol* (2019) 328:98–104. doi: 10.1016/j.jneuroim.2019.01.004

19. Ma N, Guo P, Zhang J, He T, Kim SW, Zhang G, et al. Nutrients mediate intestinal bacteria-mucosal immune crosstalk. *Front Immunol* (2018) 9:5. doi: 10.3389/fimmu.2018.00005

20. Wang S, Harvey L, Martin R, van der Beek EM, Knol J, Cryan JF, et al. Targeting the gut microbiota to influence brain development and function in early life. *Neurosci Biobehav Rev* (2018) 95:191–201. doi: 10.1016/j.neubiorev.2018.09.002

21. Ribeiro MF, Santos AA, Afonso MB, Rodrigues PM, Sá Santos S, Castro RE, et al. Diet-dependent gut microbiota impacts on adult neurogenesis through mitochondrial stress modulation. *Brain Commun* (2020) 2(2):fcaa165. doi: 10.1093/braincomms/fcaa165

22. Robinson CM, Pfeiffer JK. Viruses and the microbiota. *Annu Rev Virol* (2014) 1:55–69. doi: 10.1146/annurev-virology-031413-085550

23. Kristensson K. Potential role of viruses in neurodegeneration. *Mol Chem Neuropathol* (1992) 16(1–2):45–58. doi: 10.1007/BF03159960

24. Zhou L, Miranda-Saksena M, Saksena NK. Viruses and neurodegeneration. *Virol J* (2013) 10:172. doi: 10.1186/1743-422X-10-172

25. De Chiara G, Marcocci ME, Sgarbanti R, Civitelli L, Ripoli C, Piacentini R, et al. Infectious agents and neurodegeneration. *Mol Neurobiol* (2012) 46(3):614–38. doi: 10.1007/s12035-012-8320-7

26. Patrick KL, Bell SL, Weindel CG, Watson RO. Exploring the "Multiple-hit hypothesis" of neurodegenerative disease: Bacterial infection comes up to bat. *Front Cell Infect Microbiol* (2019) 9:138. doi: 10.3389/fcimb.2019.00138

27. Jiang D, Armour CR, Hu C, Mei M, Tian C, Sharpton TJ, et al. Microbiome multi-omics network analysis: Statistical considerations, limitations, and opportunities. *Front Genet* (2019) 10:995. doi: 10.3389/fgene.2019.00995

28. Durmuş Tekir SD, Ülgen KÖ. Systems biology of pathogen-host interaction: Networks of protein-protein interaction within pathogens and pathogen-human interactions in the post-genomic era. *Biotechnol J* (2013) 8(1):85–96. doi: 10.1002/biot.201200110

29. Levy R, Carr R, Kreimer A, Freilich S, Borenstein E. NetCooperate: A network-based tool for inferring host-microbe and microbe-microbe cooperation. *BMC Bioinf* (2015) 16(1):164. doi: 10.1186/s12859-015-0588-y

30. Durmus S, Çakir T, Özgür A, Guthke R. A review on computational systems biology of pathogen-host interactions. *Front Microbiol* (2015) 6:235. doi: 10.3389/fmicb.2015.00235

31. Pan A, Lahiri C, Rajendiran A, Shanmugham B. Computational analysis of protein interaction networks for infectious diseases. *Brief Bioinform* (2016) 17 (3):517–26. doi: 10.1093/bib/bbv059

32. Friedel CC. Computational analysis of virus-host interactions. In: SM Bailer and D Liebe, editors. *Viurs-host interactions: Methods and protocols.* Humana Press. p. 115–30.

33. Khan MM, Ernst O, Manes NP, Oyler BL, Fraser IDC, Goodlett DR, et al. Multi-omics strategies uncover host-pathogen interactions. *ACS Infect Dis* (2019). 5(4):493–505 doi: 10.1021/acsinfecdis.9b00080

34. Matchado MS, Lauber M, Reitmeier S, Kacprowski T, Baumbach J, Haller D, et al. Network analysis methods for studying microbial communities: A mini review. *Comput Struct Biotechnol J* (2021) 19:2687–98. doi: 10.1016/j.csbj.2021.05.001

35. Costa Sa AC, Madsen H, Brown JR. Shared molecular signatures across neurodegenerative diseases and herpes virus infections highlights potential mechanisms for maladaptive innate immune responses. *Sci Rep* (2019) 9(1):8795. doi: 10.1038/s41598-019-45129-8

36. Onisiforou A, Spyrou GM. Identification of viral-mediated pathogenic mechanisms in neurodegenerative diseases using network-based approaches. *Brief Bioinform* (2021) 22(6):bbab141. doi: 10.1093/bib/bbab141

37. Wishart DS, Feunang YD, Marcu A, Guo AC, Liang K, Vázquez-Fresno R, et al. HMDB 4.0: The human metabolome database for 2018. *Nucleic Acids Res* (2018) 46(D1):D608–17. doi: 10.1093/nar/gkx1089

38. Chong J, Soufan O, Li C, Caraus I, Li S, Bourque G, et al. MetaboAnalyst 4.0: Towards more transparent and integrative metabolomics analysis. *Nucleic Acids Res* (2018) 46(W1):W486–94. doi: 10.1093/nar/gky310

39. Szklarczyk D, Santos A, Von Mering C, Jensen LJ, Bork P, Kuhn M. STITCH 5: Augmenting protein-chemical interaction networks with tissue and affinity data. *Nucleic Acids Res* (2016) 44(D1):D380–4. doi: 10.1093/nar/gkv1277

40. Doncheva N, Morris J, Gorodkin J, Jensen L. Cytoscape stringapp: Network analysis and visualization of proteomics data. *Cytoscape StringApp Netw Anal Vis Proteomics Data* (2018) 18(2):623–32. doi: 10.1101/438192

41. Pletscher-Frankild S, Pallejà A, Tsafou K, Binder JX, Jensen LJ. DISEASES: Text mining and data integration of disease-gene associations. *Methods* (2015) 74:83–9. doi: 10.1016/j.ymeth.2014.11.020

42. Szklarczyk D, Gable AL, Lyon D, Junge A, Wyder S, Huerta-Cepas J, et al. STRING V11: Protein-protein association networks with increased coverage, supporting functional discovery in genome-wide experimental datasets. *Nucleic Acids Res* (2019) 47(D1):D607–13. doi: 10.1093/nar/gky1131

43. Durmuş Tekir S, Çakir T, Ardiç E, Sayilirbaş AS, Konuk G, Konuk M, et al. PHISTO: Pathogen-host interaction search tool. *Bioinformatics* (2013) 29 (10):1357–8. doi: 10.1093/bioinformatics/btt137

44. Guirimand T, Delmotte S, Navratil V. VirHostNet 2.0: Surfing on the web of Virus/Host molecular interactions data. *Nucleic Acids Res* (2015) 43(Database issue):D583–7. doi: 10.1093/nar/gku1121

45. Almende BV, Thieurmel B. Visnetwork: Network visualization using "Vis.Js" library. *CRAN* (2016).

46. Bindea G, Mlecnik B, Hackl H, Charoentong P, Tosolini M, Kirilovsky A, et al. ClueGO: A cytoscape plug-in to decipher functionally grouped gene ontology and pathway annotation networks. *Bioinformatics* (2009) 25(8):1091–3. doi: 10.1093/bioinformatics/btp101

47. Serafini B, Rosicarelli B, Franciotta D, Magliozzi R, Reynolds R, Cinque P, et al. Dysregulated Epstein-Barr virus infection in the multiple sclerosis brain. *J Exp Med* (2007) 204(12):2899–912. doi: 10.1084/jem.20071030

48. Le B, Wang X, Xiang Y, Shen LL, Wang QH, Liu YH, et al. The association between infectious burden and parkinson's disease: Acase-control study. *Park Relat Disord* (2015) 21(8):877–81. doi: 10.1016/j.parkreldis.2015.05.015

49. Carbone I, Lazzarotto T, Ianni M, Porcellini E, Forti P, Masliah E, et al. Herpes virus in alzheimer's disease: Relation to progression of the disease. *Neurobiol Aging* (2014) 35(1):122–9. doi: 10.1016/j.neurobiolaging.2013.06.024

50. Oksanen J, Blanchet FG, Friendly M, Kindt R, Legendre P, Mcglinn D, et al. Package "Vegan". a community ecology package. *Community Ecol Packag* (2019).

51. Kassambara A, Mundt F. Factoextra: Extract and visualize the results of multivariate data analyses. *Package Version 1.0.7. R Packag version* (2020).

52. Goenawan IH, Bryan K, Lynn DJ. DyNet: Visualization and analysis of dynamic molecular interaction networks. *Bioinformatics* (2016) 32(17):2713–5. doi: 10.1093/bioinformatics/btw187

53. Salamon J, Goenawan IH, Lynn DJ. Analysis and visualization of dynamic networks using the DyNet app for cytoscape. *Curr Protoc Bioinforma* (2018) 63(1): e55. doi: 10.1002/cpbi.55

54. Kanther M, Tomkovich S, Xiaolun S, Grosser MR, Koo J, Flynn EJ, et al. Commensal microbiota stimulate systemic neutrophil migration through induction of serum amyloid a. *Cell Microbiol* (2014) 16(7):1053–67. doi: 10.1111/cmi.12257

55. Zhang D, Frenette PS. Cross talk between neutrophils and the microbiota. *Blood* (2019) 133(29):2168–77. doi: 10.1182/blood-2018-11-844555

56. Vinolo MAR, Rodrigues HG, Hatanaka E, Hebeda CB, Farsky SHP, Curi R. Short-chain fatty acids stimulate the migration of neutrophils to inflammatory sites. *Clin Sci* (2009) 117(9):331–8. doi: 10.1042/CS20080642

57. Hovingh ES, van den Broek B, Jongerius I. Hijacking complement regulatory proteins for bacterial immune evasion. *Front Microbiol* (2016) 7:2004. doi: 10.3389/fmicb.2016.02004

58. Dunn AB, Dunlop AL, Hogue CJ, Miller A, Corwin EJ. The microbiome and complement activation: A mechanistic model for preterm birth. *Biol Res Nurs* (2017) 19(3):295–307. doi: 10.1177/1099800416687648

59. Janeway CA, Travers P, Walport M. The complement system and innate immunity - immunobiology - NCBI bookshelf. *Immunobiol Immune Syst Heal Dis* (2001).

60. Chehoud C, Rafail S, Tyldsley AS, Seykora JT, Lambris JD, Grice EA. Complement modulates the cutaneous microbiome and inflammatory milieu. *Proc Natl Acad Sci U.S.A.* (2013) 110(37):15061–6. doi: 10.1073/pnas.1307855110

61. Lambring CB, Siraj S, Patel K, Sankpal UT, Mathew S, Basha R. Impact of the microbiome on the immune system. *Crit Rev Immunol* (2019) 39(5):313–28. doi: 10.1615/CritRevImmunol.2019033233

62. Liu W, Sohn HW, Tolar P, Pierce SK. It's all about change: The antigen-driven initiation of b-cell receptor signaling. *Cold Spring Harb Perspect Biol* (2010) 2(7):a002295. doi: 10.1101/cshperspect.a002295

63. Hwang JR, Byeon Y, Kim D, Park SG. Recent insights of T cell receptor-mediated signaling pathways for T cell activation and development. *Exp Mol Med* (2020) 52(5):750–61. doi: 10.1038/s12276-020-0435-8

64. Petta I, Fraussen J, Somers V, Kleinewietfeld M. Interrelation of diet, gut microbiome, and autoantibody production. *Front Immunol* (2018) 9:439. doi: 10.3389/fimmu.2018.00439

65. Kim M, Kim CH. Regulation of humoral immunity by gut microbial products. *Gut Microbes* (2017) (4):392–9. doi: 10.1080/19490976.2017.1299311

66. Wake H, Moorhouse AJ, Nabekura J. Functions of microglia in the central nervous system-beyond the immune response. *Neuron Glia Biol* (2012) 7(1):47–53. doi: 10.1017/S1740925X12000063

67. Erny D, De Angelis ALH, Jaitin D, Wieghofer P, Staszewski O, David E, et al. Host microbiota constantly control maturation and function of microglia in the CNS. *Nat Neurosci* (2015) 18(7):965–77. doi: 10.1038/nn.4030

68. Abdel–Haq R, Schlachetzki JCM, Glass CK, Mazmanian SK. Microbiome–microglia connections *via* the gut–brain axis. *J Exp Med* (2019) 216(1):41–59. doi: 10.1084/jem.20180794

69. Wei B, Huang T, Dalwadi H, Sutton CL, Bruckner D, Braun J. Pseudomonas fluorescens encodes the crohn's disease-associated I2 sequence and T-cell superantigen. *Infect Immun* (2002) 70(12):6567–75. doi: 10.1128/IAI.70.12.6567-6575.2002

70. Scales BS, Dickson RP, Lipuma JJ, Huffnagle GB. Microbiology, genomics, and clinical significance of the pseudomonas fluorescens species complex, an unappreciated colonizer of humans. *Clin Microbiol Rev* (2014) 27(4):927–48. doi: 10.1128/CMR.00044-14

71. Patakova P, Branska B, Sedlar K, Vasylkivska M, Jureckova K, Kolek J, et al. Acidogenesis, solventogenesis, metabolic stress response and life cycle changes in clostridium beijerinckii NRRL b-598 at the transcriptomic level. *Sci Rep* (2019) 9 (1):1371. doi: 10.1038/s41598-018-37679-0

72. Cantarel BL, Waubant E, Chehoud C, Kuczynski J, Desantis TZ, Warrington J, et al. Gut microbiota in MS: Possible influence of immunomodulators HHS public access. *J Investig Med* (2015) 63(5):729–34. doi: 10.1097/JIM.0000000000000192

73. Reynders T, Devolder L, Valles-Colomer M, Van Remoortel A, Joossens M, De Keyser J, et al. Gut microbiome variation is associated to multiple sclerosis phenotypic subtypes. *Ann Clin Transl Neurol* (2020) 7(4):406–19. doi: 10.1002/acn3.51004

74. Ren T, Gao Y, Qiu Y, Jiang S, Zhang Q, Zhang J, et al. Gut microbiota altered in mild cognitive impairment compared with normal cognition in sporadic parkinson's disease. *Front Neurol* (2020) 11:137. doi: 10.3389/fneur.2020.00137

75. Petrov VA, Saltykova IV, Zhukova IA, Alifirova VM, Zhukova NG, Dorofeeva YB, et al. Analysis of gut microbiota in patients with parkinson's disease. *Bull Exp Biol Med* (2017) 162(6):734–37. doi: 10.1007/s10517-017-3700-7

76. Li W, Wu X, Hu X, Wang T, Liang S, Duan Y, et al. Structural changes of gut microbiota in parkinson's disease and its correlation with clinical features. *Sci China Life Sci* (2017) 60(11):1223–33. doi: 10.1007/s11427-016-9001-4

77. Liu P, Wu L, Peng G, Han Y, Tang R, Ge J, et al. Altered microbiomes distinguish alzheimer's disease from amnestic mild cognitive impairment and health in a Chinese cohort. *Brain Behav Immun* (2019) 80:633–43. doi: 10.1016/j.bbi.2019.05.008

78. Rowin J, Xia Y, Jung B, Sun J. Gut inflammation and dysbiosis in human motor neuron disease. *Physiol Rep* (2017) 5(18):e13443. doi: 10.14814/phy2.13443

79. Joossens M, Huys G, Cnockaert M, De Preter V, Verbeke K, Rutgeerts P, et al. Dysbiosis of the faecal microbiota in patients with crohn's disease and their unaffected relatives. *Gut* (2011) 60(5):631–7. doi: 10.1136/gut.2010.223263

80. Kang S, Denman SE, Morrison M, Yu Z, Dore J, Leclerc M, et al. Dysbiosis of fecal microbiota in crohn's disease patients as revealed by a custom phylogenetic microarray. *Inflammation Bowel Dis* (2010) 16(12):2034–42. doi: 10.1002/ibd.21319

81. Pérez-Brocal V, García-López R, Nos P, Beltrán B, Moret I, Moya A. Metagenomic analysis of crohn's disease patients identifies changes in the virome and microbiome related to disease status and therapy, and detects potential interactions and biomarkers. *Inflammation Bowel Dis* (2015) 21 (11):2515–32. doi: 10.1097/MIB.0000000000000549

82. Zheng D, Liwinski T, Elinav E. Interaction between microbiota and immunity in health and disease. *Cell Res* (2020) 30(6):492–506. doi: 10.1038/s41422-020-0332-7

83. Main BS, Minter MR. Microbial immuno-communication in neurodegenerative diseases. *Front Neurosci* (2017) 11:151. doi: 10.3389/fnins.2017.00151

84. Vlasova AN, Kandasamy S, Chattha KS, Rajashekara G, Saif LJ. Comparison of probiotic lactobacilli and bifidobacteria effects, immune responses and rotavirus vaccines and infection in different host species. *Vet Immunol Immunopathol* (2016) 172:72–84. doi: 10.1016/j.vetimm.2016.01.003

85. Lee NK, Kim WS, Paik HD. Bacillus strains as human probiotics: Characterization, safety, microbiome, and probiotic carrier. *Food Sci Biotechnol* (2019) 28(5):1297–1305. doi: 10.1007/s10068-019-00691-9

86. Ciorba MA. A gastroenterologist's guide to probiotics. *Clin Gastroenterol Hepatol* (2012) 10(9):960–8. doi: 10.1016/j.cgh.2012.03.024

87. Nourshargh S, Alon R. Leukocyte migration into inflamed tissues. *Immunity* (2014) 41(5):694–707. doi: 10.1016/j.immuni.2014.10.008

88. Stegelmeier AA, van Vloten JP, Mould RC, Klafuric EM, Minott JA, Wootton SK, et al. Myeloid cells during viral infections and inflammation. *Viruses* (2019) 11(2):168. doi: 10.3390/v11020168

89. Kim M, Qie Y, Park J, Kim CH. Gut microbial metabolites fuel host antibody responses. *Cell Host Microbe* (2016) 20(2):202–14. doi: 10.1016/j.chom.2016.07.001

90. Wojtera M, Sikorska B, Sobow T, Liberski PP. Microglial cells in neurodegenerative disorders. *Folia Neuropathol* (2005) 43(4):311–21.

91. Filgueira L, Larionov A, Lannes N. The influence of virus infection on microglia and accelerated brain aging. *Cells* (2021) 10(7):1836. doi: 10.3390/cells10071836

92. Franco R, Pacheco R, Lluis C, Ahern GP, O'Connell PJ. The emergence of neurotransmitters as immune modulators. *Trends Immunol* (2007) 28(9):400–7. doi: 10.1016/j.it.2007.07.005

93. Hodo TW, de Aquino MTP, Shimamoto A, Shanker A. Critical neurotransmitters in the neuroimmune network. *Front Immunol* (2020) 11:1869. doi: 10.3389/fimmu.2020.01869

94. Neher JJ, Cunningham C. Priming microglia for innate immune memory in the brain. *Trends Immunol* (2019) 40(4):358–74. doi: 10.1016/j.it.2019.02.001

95. Wendeln AC, Degenhardt K, Kaurani L, Gertig M, Ulas T, Jain G, et al. Innate immune memory in the brain shapes neurological disease hallmarks. *Nature* (2018) 556(7701):332–38. doi: 10.1038/s41586-018-0023-4

frontiers | Frontiers in Immunology

TYPE Original Research
PUBLISHED 08 August 2022
DOI 10.3389/fimmu.2022.947242

EDITED BY
Francesca Di Rosa,
Italian National Research Council,
Italy

REVIEWED BY
Kim Klonowski,
University of Georgia, United States
Filippo Castiglione,
National Research Council (CNR),
Italy

*CORRESPONDENCE
Arpit C. Swain
swainarpit@gmail.com

SPECIALTY SECTION
This article was submitted to
Immunological Memory,
a section of the journal
Frontiers in Immunology

RECEIVED 18 May 2022
ACCEPTED 07 July 2022
PUBLISHED 08 August 2022

CITATION
Swain AC, Borghans JAM and de Boer RJ (2022) Effect of cellular aging on memory T-cell homeostasis. *Front. Immunol.* 13:947242.
doi: 10.3389/fimmu.2022.947242

Effect of cellular aging on memory T-cell homeostasis

Arpit C. Swain[1,2]*, José A.M. Borghans[2] and Rob J. de Boer[1]

[1]Theoretical Biology, Utrecht University, Utrecht, Netherlands, [2]Center for Translational Immunology, University Medical Center Utrecht, Utrecht, Netherlands

The fact that T-cell numbers remain relatively stable throughout life, and that T-cell proliferation rates increase during lymphopenia, has led to the consensus that T-cell numbers are regulated in a density-dependent manner. Competition for resources among memory T cells has been proposed to underlie this 'homeostatic' regulation. We first review how two classic models of resource competition affect the T-cell receptor (TCR) diversity of the memory T-cell pool. First, 'global' competition for cytokines leads to a skewed repertoire that tends to be dominated by the very first immune response. Second, additional 'cognate' competition for specific antigens results in a very diverse and stable memory T-cell pool, allowing every antigen to be remembered, which we therefore define as the 'gold-standard'. Because there is limited evidence that memory T cells of the same specificity compete more strongly with each other than with memory T cells of different specificities, i.e., for 'cognate' competition, we investigate whether cellular aging could account for a similar level of TCR diversity. We define cellular aging as a declining cellular fitness due to reduced proliferation. We find that the gradual erosion of previous T-cell memories due to cellular aging allows for better establishment of novel memories and for a much higher level of TCR diversity compared to global competition. A small continual source (either from stem-cell-like memory T-cells or from naive T-cells due to repeated antigen exposure) improves the diversity of the memory T-cell pool, but remarkably, only in the cellular aging model. We further show that the presence of a source keeps the inflation of chronic memory responses in check by maintaining the immune memories to non-chronic antigens. We conclude that cellular aging along with a small source provides a novel and immunologically realistic mechanism to achieve and maintain the 'gold-standard' level of TCR diversity in the memory T-cell pool.

KEYWORDS

homeostatic regulation, T cell, mathematical modelling, competitive exclusion, Memory attrition, cellular aging

Introduction

It is well-accepted among immunologists that homeostatic mechanisms are crucial in regulating immune cell numbers. T-cell homeostasis is the phenomenon by which the T-cell population maintains its relatively stable numbers, despite considerable perturbations, such as a decline in thymic output with age and repeated exposure to antigenic challenges (1). The maintenance of CD8$^+$ memory T cells generated during acute immune responses is largely cytokine-dependent, although some studies suggest that it also requires interaction with major histocompatibility complex (MHC) molecules, albeit without cognate antigen (1–7). In a lymphopenic host, increased homeostatic (density-dependent) T-cell proliferation drives the expansion of memory T cells (6, 8). Homeostasis need not be perfect, as in both mice and humans, depleted T-cell pools do not always recover to normal levels (9, 10). Notably, after autologous stem-cell transplantation, even patients with reconstituted T-cell pools experienced significantly increased T-cell proliferation and loss rates when compared to healthy age-matched controls (11). These studies highlight our incomplete understanding of the homeostatic process. A better understanding of T-cell homeostasis is central to understanding the long-term maintenance of immunological memory.

CD8$^+$ memory T cells compete for the same cytokines. Interestingly, the maintenance of chronic immune responses to persisting pathogens is not only dependent on their interaction with cognate antigen (12), but also on the same cytokine(s) that the memories from acute responses depend on (5, 12–16). Due to the dependence of all memory T cells on the same resource(s), every new immune response disrupts the homeostatic balance. Responses with superior proliferative capacity (e.g., due to a higher affinity for a resource) outcompete other responses dependent on the same resource (17–20). This competition among memory T cells from different immune responses leads to moderate to severe attrition of existing memory T cells, and has been noted multiple times using both repeated vaccinations with heterologous viruses, as well as in prime-boost immunization strategies in mouse experiments (21–25). Early studies have postulated this attrition to be an effect of limited 'space' by showing that the total memory T-cell pool remained constant in size after consecutive infections (21, 22). Interestingly, a few recent studies report an increase in the total memory T-cell pool upon successive infections (24, 25), suggesting weaker attrition of existing memories, leading to a more diverse memory T-cell repertoire.

The mechanisms governing the maintenance of T-cell memory remain unclear. Mathematical modelling studies have assumed that memory T cells undergo global and cognate competition, concepts that correspond to well-studied ideas of inter-species and intra-species competition for resources in ecology. In mouse models, competition for cytokines, antigens, and 'space' in antigenic or survival niches, have been held responsible for the attrition of existing memory T cells (2, 15, 21, 22, 26–29). Competition for cytokines or physical niches leads to a non-cognate, i.e., 'global', form of competition between memory T cells (2, 26). Conversely, antigen-dependent competition, is confined to all cells that recognize the same cognate antigen (we refer to this as 'cognate' competition) (20, 27, 28, 30, 31). Low-level reactivation by cognate antigens has been suggested to have a positive effect on memory T-cell maintenance and homeostasis (22, 29, 32, 33). Several mathematical modelling studies have discussed the implications of global and cognate competition (20, 28–31, 34, 35). It was shown that global competition leads to competitive exclusion of all but the T-cell clone with the highest affinity for the resources the cells are competing for (20, 35). Global competition can be further regulated by cognate competition, even in the presence of persistent antigenic stimulation, due to competition among memory T cells sharing the same specificity (20, 28, 31, 34). Other modelling studies showed that fratricide among memory T cells crowding around the same antigen-presenting cells (APCs) can give rise to cognate competition among them, due to Fas-FasL mediated apoptosis, which provides a mechanism through which memory T-cell pools can be regulated (29, 30). Therefore, succinctly put, most current literature exploring the mechanisms underlying memory T-cell homeostasis fits in either the global or the cognate competition framework.

In this article, we propose cellular aging as an alternative mechanism that may play a role in T-cell homeostasis. That cells age is irrefutable (36–38). For instance, cellular aging has implications in cancer (37–41), and vaccination of the elderly is affected by the poor responsiveness of their aged T cells (40–47). Yet, due consideration has not been given to the aging of cells in models of memory T-cell homeostasis. Traditionally, models of T-cell homeostasis assume that cells can perform an infinite number of cell divisions, and are bounded only by the resources available at the time (29). However, a cell's inherent division and loss rates change over time due to age, differentiation stage and division history (48–53). We, therefore, investigate the role that cellular aging may play in homeostasis and the long-term maintenance of T-cell memory.

We start with a review of the existing global and cognate competition models of T-cell homeostasis, and later move on to explore the additional effect of cellular aging on the maintenance of memory T cells. Throughout the article, we use previously described attributes of the memory T-cell pool (e.g., attrition of existing memories and expanding population size) as guides to ascertain the suitability of these three different models in generating realistic memory T-cell pools. We demonstrate that, contrary to our intuition, cellular aging helps maintain memory T-cell diversity for extended periods of time. Further, we observe that a small source, from either stem-cell-like memory T cells or from naive T cells, together with cellular aging is sufficient to maintain a diverse memory T-cell repertoire that is robust to the presence of dominant competitors (e.g., chronic immune responses to persistent pathogens). We also discuss the potential disadvantages of longevity of memory T cells, and the effect of cellular aging on the phenotypic composition of the memory T-cell pool.

Models of memory T-cell maintenance

Three different mathematical models for the maintenance of memory T cells were defined. To keep the models simple, we considered three elements: (a) a source into the memory T-cell population (if any), (b) the most fundamental processes of any population of cells, i.e., cell division and cell death, and (c) the resources that have been demonstrated to be essential for the maintenance of memory T cells, i.e., cytokines such as IL-15, and antigens (for chronic responses). We consider both acute and chronic immune responses, where all memory T cells depend on the same homeostatic cytokine(s).

Global competition model

The cytokines, C (concentration, in mol/L), have a steady source, σ (in mol/L/day), from the stromal cells located across the body of a host (54, 55). Although there are other, transient sources of cytokines during inflammation, stromal cells are the major contributors during homeostatic circumstances (16, 54, 56). These cytokines are either utilized by memory T cells in a fixed amount, ϵ , during each cell division, or are degraded at a rate δ /day (Equation 1a). The dependence of all memory T cells on the same growth resource (cytokines), C , gives rise to global competition among the cells. The sizes of the memory T-cell populations, M_i , in a host having experienced n different antigen-specific immune responses are given by (Equation 1b, Figure 1A):

$$\frac{dC}{dt} = \sigma - \delta C - \epsilon \frac{C}{h+C} \sum_i p_i M_i \tag{1a}$$

$$\frac{dM_i}{dt} = s_i + p_i M_i \frac{C}{h+C} - d_i M_i \tag{1b}$$

where i=1,…,n (here n is the number of unique antigens encountered sequentially), and h is the cytokine concentration at which the homeostatic (i.e., density-dependent) proliferation rate is half-maximal estimate taken from (58). Cells of immune response M_i have a death rate d_i, and a maximal

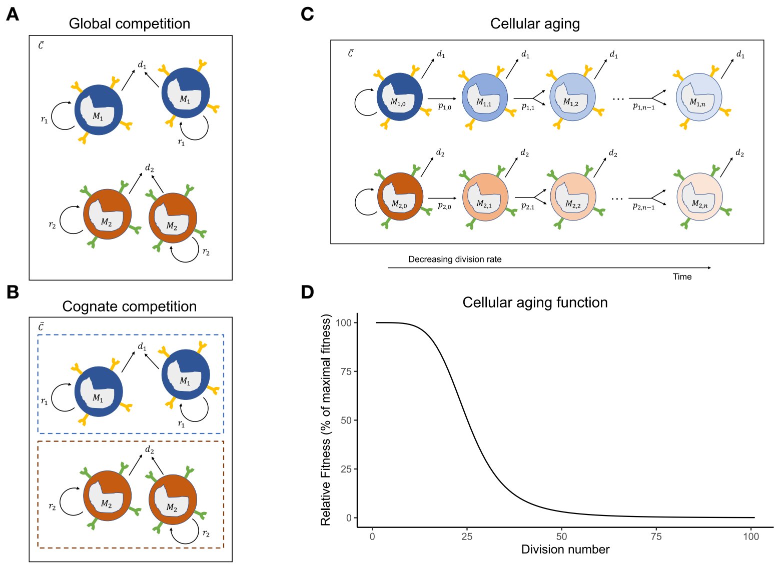

FIGURE 1
Mechanisms of homeostatic maintenance of memory T-cells. The cartoons of the **(A)** global competition, **(B)** cognate competition, and **(C)** cellular aging models showing the memory T-cell pool with two immune responses, M_1 and M_2 . The different immune responses can have different division rates, p_i, and death rates, d_i, and share the same cytokines, C . On top of the competition for shared global resources (cytokines) **(A)**, the cells of an immune response either compete with cells of the same specificity, leading to cognate competition **(B)** or lose their potential to divide with each cell division because of cellular aging **(C)**. The cellular aging function shows the drop in the relative fitness of a T-cell population as it divides **(D)**.

homeostatic proliferation rate p_i (also referred to as the fitness). The source term, s_i, defines the daily influx of memory T cells, which could be either from infrequent divisions of stem-cell-like memory T cells in the bone marrow, or from antigen-driven expansion of naive T cells (only for chronic responses) (59, 60). T cells downregulate their T-cell receptors after interactions with cytokines and are thus 'non-greedy' consumers of cytokines (61). Therefore, cytokine consumption was modelled to be proportional to proliferation of the memory T-cell population (Equation 1). The effective homeostatic division rate of memory T cells was set by a saturation function of the global cytokine concentration. An inverse dependence of the death rate on the cytokine concentration would give similar qualitative results (simulations not shown).

We assume that the timescales for production and degradation of cytokines are much faster than the timescales for division and death of memory T cells. Therefore, we consider the cytokines to be in quasi-steady state (Equation 2):

$$C = \frac{-\left(h + \gamma \sum_i p_i M_i - 1\right) + \sqrt{\left(h + \gamma \sum_i p_i M_i - 1\right)^2 + 4h}}{2} \tag{2}$$

The cytokine concentration was normalized to its maximal concentration (i.e., we set $\frac{\sigma}{\delta} = 1$), and $\gamma = \frac{\epsilon}{\delta}$ was set to 10^{-6} so that the size of the memory T-cell pool was in the order of 10^7.

Cognate competition model

Global competition due to sharing of growth resources leads to competition between different immune responses. Cognate competition defines the competition among the memory T cells generated during the same immune response, i.e., cells sharing the same antigen specificity (but not necessarily the same T-cell receptor). For 'acute' immune responses to pathogens that are eliminated, cognate competition has been proposed to follow from limited 'space' in specific survival niches in the bone marrow (57), or from limited availability of cross-reactive antigens (27, 28, 30). Allowing for both global and cognate competition (Figure 1B), the memory T-cell pools resulting from n different immune responses can be given by:

$$\frac{dC}{dt} = \sigma - \delta C - \epsilon \frac{C}{h + C} \sum_i \frac{p_i M_i}{1 + \beta_i M_i} \tag{3a}$$

$$\frac{dM_i}{dt} = s_i + \frac{p_i M_i}{1 + \beta_i M_i} \frac{C}{h + C} - d_i M_i \tag{3b}$$

for i= 1, 2, …, 100 antigens, and where all memory T cells specific for antigen i are considered to have a similar affinity for that antigen.

This extends the global competition model (Equation 1) with a cognate competition parameter, β_i , defining the size of the M_i population at which its division rate halves (which happens when M_i=1/β_i). All other parameters remain the same, i.e., we have in fact added an intra-specific competition term to the global competition model. As h was estimated before (58), the parameter β_i was used to tune the relative strength of the global and cognate competition. Note that global competition weakens as h→0 and that cognate competition declines as β_i→0. Again, due to the very different turnover timescales of cytokines and memory T cells, the cytokines were assumed to be in quasi-steady state:

$$C = \frac{-\left(h + \gamma \sum_i \frac{p_i M_i}{1 + \beta_i M_i} - 1\right) + \sqrt{\left(h + \gamma \sum_i \frac{p_i M_i}{1 + \beta_i M_i} - 1\right)^2 + 4h}}{2} \tag{4}$$

Cellular aging model

The properties of a cell may change with cell division. It is well-known that telomere shortening during division stunts a cell's ability to divide forever (62–64). However, in the global and cognate competition models, the cells have a constant fitness (p_i) and, by not aging, can expand indefinitely. To account for cellular ageing, we rewrote the global competition model (Equation 1) into a division-indexed model, where we used j=1,…,m, for the number of divisions a cell has completed (i.e., j is the 'generation' number of a cell, and m is the maximal number of divisions it can go through, which is commonly referred to as the 'Hayflick limit'). In our simulations, m=100 was chosen to be large enough so that in practice a cell never reaches its Hayflick limit. The model for the number of cells specific to antigen i in the j th division, $M_{i,j}$ (see Figure 1C), is given by:

$$\frac{dM_{i,j}}{dt} = s_{i,j} + 2p_{i,j-1} M_{i,j-1} \frac{C}{h + C} - d_i M_{i,j} - p_{i,j} M_{i,j} \frac{C}{h + C} \tag{5a}$$

$$p_{i,j} = \frac{p_{i,1}}{1 + (j/k)^5} \tag{5b}$$

where $p_{i,j}$ is the maximal homeostatic division rate of cells specific for antigen i that have completed j divisions; k=25 marks the generation number where $p_{i,j}$=$p_{i,1}/2$; and $M_i = \sum_j M_{i,j}$ defines the total number of cells in the i th immune response. For the special case where the division rates remain independent of the division number, i.e., when $p_{i,j} = p_i$ (i.e., k→∞), this model is identical to the global competition model (it would only track the division histories of cells). Otherwise, division rates decline with the division number (Equation 5b, Figure 1D).

Since in the scenarios with a source, each memory T-cell population was assumed to be seeded every day with s_i cells, we described their division history with a Poisson distribution, i.e.,

$$s_{i,j} \;= s_i \frac{\mu^j e^{-\mu}}{j\,!} \tag{6}$$

Here, μ is the average generation number of a precursor population formed during the expansion phase. It is defined as μ=2$\lambda\tau$, where τ is the typical length of the expansion phase (in days), and λ=2/day is the rate of division during the expansion phase (65). Two variations of the age-distribution of the source were modelled: 'young' cells (μ=1, or τ=0.25 days, i.e., cells that became quiescent after having completed one division, on average, during the expansion phase) or 'old' cells (μ=20, or τ=5 days, i.e., cells that divided extensively throughout the expansion phase). For simplicity, the T-cell death rate was kept the same across division numbers. Qualitatively similar results were found when implementing an increase in the death rate with increasing division number (simulations not shown). However, as less differentiated cells possess a higher expansion potential (66, 67), we chose to decrease the division rate with the division number.

Chronic responses

To model chronic responses, we introduced extra terms specific to only chronic responses. As chronic responses are subject to additional proliferative signals due to their interaction with antigen (17), chronic immune responses have an additional maximal antigen-driven proliferation rate, ρ_i, and a cognate (antigen-driven)-competition parameter, g_i. The models allowing for chronic responses are, therefore, extensions of the models defined above. In case of chronic immune responses, the global and cognate competition models described by equations (1) and (3) are extended with a second proliferation term:

$$+\frac{\rho_i M_i}{1+g_i M_i} \tag{7a}$$

The cellular aging model requires two terms to achieve a similar extension:

$$+\frac{2\rho_{i,j-1} M_{i,j-1}}{1+g_i M_i} - \frac{\rho_{i,j} M_{i,j}}{1+g_i M_i} \tag{7b}$$

with

$$\rho_{i,j} = \frac{\rho_{i,1}}{1+(j/k)^5} \tag{7c}$$

The cognate competition parameter, g_i, defines the strength of the cognate competition among memory T cells specific for antigen i. Notice that the antigen-driven proliferation rate follows the same cellular aging function as the homeostatic (density-dependent) proliferation rate. The quasi-steady state expressions for the cytokines do not change as we assume that cell division due to stimulation by cognate antigen does not depend on the cytokine concentration.

Parameter choices

For a fair comparison across the models, we used the same parameter values throughout this manuscript. CD8$^+$ memory T cells were found to be maintained at steady state with an inter-mitotic interval of ~50 days in an adoptive transfer experiment of LMCV-specific CD8$^+$ memory T cells into naive mice after being CFSE labelled (3). Reports of in-vivo deuterium labelling of non-specific CD8$^+$ memory T cells supported this time scale by showing that the CD8$^+$ memory T-cell pool is renewed, on an average, every ~66 days (52). Therefore, the death rate of memory T cells, d_i, was set to 0.02/day, irrespective of the immune response. The maximal homeostatic proliferation rate, p_i, of 0.5/day and the coefficient for global competition, h, of 10^{-5} were estimated based on temporal data of murine memory CD8$^+$ T cells (58). As all cells in the models have the same expected life span of 50 days, and differ only in their maximum homeostatic proliferation rate, p_i, we also refer to this proliferation rate as the 'fitness' of the immune response. Disparate immune responses differ in their fitness values. In the simulations, the fitness values were drawn from a normal distribution with a mean of 0.5 and a standard deviation of 0.05. The effective proliferation rate decreases as the memory T-cell pool increases and will approach d_i=0.02 when the memory of a particular response is at steady state. The coefficient for cognate competition, β_i (in the cognate competition model) and g_i (for chronic responses), were set to be 10^{-6} and 5×10^{-5} for all i, respectively, so that the total mouse memory CD8$^+$ T-cell pool was realistically in the order of 10^7 cells.

Simpson's Diversity Index

Simpson's diversity index has many variations. Here, we used a variation that provides an intuitive interpretation of the diversity in the memory T-cell pool. The index, based upon the relative abundances, $f_i = {}^{M_i}\Big/\sum_i M_i$, of all immune responses, gives an indication of the effective number of immune responses in a population. The index is defined as

$$\frac{1}{\sum_{i=1}^{n} f_i^2} \tag{8}$$

A memory T-cell pool with an index of n denotes a pool with n evenly abundant immune responses whereas an index of 1 denotes a scenario with a single, dominant immune response in the pool of immune responses.

Results

Three models of homeostasis were formulated based on the different competition schemes: global competition (Figure 1A), cognate competition (Figure 1B) and cellular aging (Figure 1C, see the Models section). The global and cognate competition models are conventional models differing only in the absence or presence of intra-specific competition among memory T cells, respectively. The cellular aging model is a novel variant of the global competition model, which we propose as an alternative because there is limited evidence for cognate (intra-specific) competition among memory T cells. As this manuscript focuses on the long-term maintenance of the memory T-cell pool, we abstained from modelling the short expansion phase after an antigenic challenge. Instead, in all the simulations, we assumed that after the introduction of each antigen, the memory T-cell pool is expanded with a random number of cognate memory T cells (drawn from a normal distribution centred around 10^5 with a 10% standard deviation), to model the beginning of a new memory phase. The simulations below reflect $CD8^+$ T cells in a representative mouse (i.e., parameter values used are specific to mice).

To realize the effect of the three different mechanisms on the immune dynamics over a simulated mouse's lifetime, we recorded and compared model simulations over 1000 days (Figure 2). To this end, the host was successively exposed to 100 different antigens that gave rise to 100 acute immune responses with different fitness levels (see Models for details). The 100 antigens were introduced over 1000 days in 10-day time intervals from day 0 until day 990. The number of an immune response marks the time point at which (and the antigen by which) it was triggered. For example, immune response M_i was triggered by antigen i on day $10\times(i-1)$.

Under global competition, the memory T-cell pool is dominated by a single immune response

The cytokine IL-15 is thought to be necessary for the expansion and maintenance of all memory T cells, thereby leading to global competition between the cells (20), irrespective of their antigen specificity (Figure 1A; see Models). In such a setting, the immune memory to the first encountered antigen, M_1, in a new-born mouse, expanded to fill up the memory T-cell pool almost entirely, simply by the virtue of being the only immune response depending on the abundantly available growth factor (Figure 2A). The size of M_1 increased, unabated, until the death in the population balanced the reduced growth of the population due to the depleted cytokine availability (i.e., $p_1 \frac{C}{h+C} = d_1 = 0.02$). M_1 started to decline only when the mouse was exposed to enough antigens of comparable, or higher, fitness (M_2 , M_6 , M_{71}). Nevertheless, M_1 dominated the memory T-cell pool

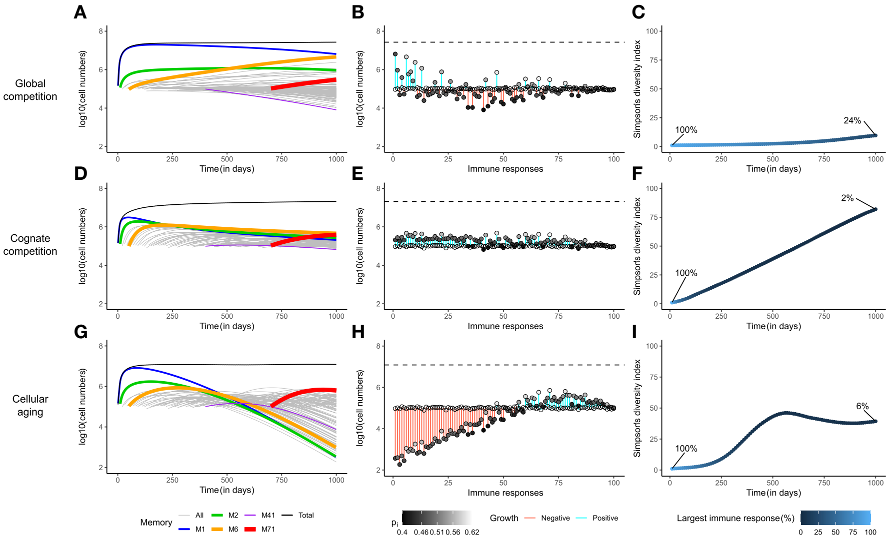

FIGURE 2
Cellular aging improves the diversity of the memory T-cell pool. Comparison of the three mechanisms for homeostatic maintenance of memory T cells showing the temporal dynamics (Panels **A**, **D**, **G**); the distribution of the sizes of all memory T-cell responses at day 1000, along with their expansion (blue) or contraction (red, indicated by the vertical bars) with respect to their initial value (indicated by the open circles) i.e., $M_i(1000)–M_i(10\times(i–1))$, as well as their maximal homeostatic proliferation rate (indicated by the shading of the filled circles) **(B, E, H)**; and the Simpson's diversity index of the T-cell repertoire over time **(C, F, I)**. The models were simulated for 1000 days. In panels **(A, D, G)**, the thickness of the coloured lines denotes the fitness of the immune response. The dashed lines in panels **(B, E, H)** depict the size of the total memory T-cell pool on day 1000. In these simulations, the memory T-cell pool consists of acute immune responses only.

almost throughout the entire lifetime of the mouse, because the rate of exclusion was very slow. At steady state, the actual division rate of the memory T cells with the highest fitness was close to their death rate d_i=0.02 . The division rate of memory cells with 10% lower fitness (corresponding to the standard deviation of our distribution) would then be 10% lower, leading to a net loss rate of just 0.002 per day. With a half-life of about a year, it would therefore take longer than the life-span of a mouse to lose a large population of specific memory T cells, even for T cells with a relatively low fitness.

The establishment of new memories became challenging when the memory T-cell pool was nearly saturated. Immune responses with low fitness (e.g., M_{41}) declined immediately upon introduction, due to the competitive pressure exerted by existing, fitter, immune responses (Figure 2A). Interestingly, even though existing immune responses went through attrition upon exposure to new antigens, the total memory T-cell pool showed modest growth over time (Figure 2A and Supplementary Figure 1A). This early signature of an increasing memory T-cell pool is in line with observations from previous studies on specific antigen-free laboratory mice (24, 25). In the very long run, global competition for cytokines dictated the survival of only the fittest immune response (Supplementary Figure 1B). Although such a scenario is disconcerting, competitive exclusion of less fit immune responses need not be achieved in a mouse's lifetime (Figure 2A), as long as cells are relatively long-lived (>50 days), and fitness differences are small.

The snapshot of the total memory T-cell pool on day 1000 revealed a clear positive dependence of the size of an immune response on its maximal homeostatic proliferation rate, p_i (Figure 2B). However, M_1 occupied the largest share (24%) of the memory T-cell pool even with a relatively low p_i, as it was the first immune response. Similarly, the fittest immune response, M_{71}, formed only a meagre 1% of the total memory T-cell pool, as it was triggered very late in the mouse's life (on day 700). Therefore, under global competition, the size of an immune response is determined not only by its maximal homeostatic proliferation rate but also by the time at which it was generated. The Simpson's diversity index (see Models) offers a measure of the diversity of a population by considering both the number and the disparity in the sizes of its constituents. The diversity in the memory T-cell pool barely increased over the course of the mouse's lifetime, evolving from a repertoire with a single immune response on day 0 to one with about 10 dominant responses, and 90 small responses, on day 1000, where the largest immune response made up as much as 24% of the total memory T-cell pool (Figure 2C). Therefore, global competition gives rise to a skewed memory T-cell pool in which the immunity of a host weakens over time due to the loss of less fit immune responses.

Cognate competition leads to an evenly distributed memory T-cell pool

Co-existence of multiple species is a well-known phenomenon in ecology. In a stable environment, co-existence can be achieved through intra-specific competition. Based on this idea, previous studies in immunology have suggested the presence of specific competition among the cells participating in the same immune response, because they bind similar (cross-reactive) antigens (2, 28, 29). In this section, we study a similar cognate competition model (despite a lack of experimental support), which employs competition among cells of an immune response on top of the global competition among all cells in the memory T-cell pool (Figure 1B; see Models).

The additional dependence on cognate resources introduced a strict limit on the size of an immune response. Despite considerable expansion, cognate competition prevented M_1 from taking over the memory T-cell pool, by limiting its size (Figure 2D and Supplementary Figure 1D). In contrast to what happened in the global competition model, the cytokine was now not depleted (not shown), as inflation of M_1 was avoided. So, upon exposure to new antigens, all new immune responses expanded initially, irrespective of their maximal homeostatic proliferation rate. These expansions came at the expense of the existing immune responses but contributed to the growth of the total memory T-cell pool (Supplementary Figure 1D). On day 1000, the memory T-cell pool was composed of many similarly-sized immune responses (Figure 2E), all of which (except M_{41}) eventually reached non-zero steady state sizes that were proportional to their fitness levels (Supplementary Figure 1D). The immune response with the lowest fitness, M_{41}, declined after a short bout of expansion, as its reduced homeostatic proliferation rate (due to global resource sharing) was lower than its death rate (Supplementary Figure 1D). The size distribution of the immune responses showed a much stronger dependence on the values of their maximal homeostatic proliferation rate (Figure 2E), and therefore the size of each immune response depended much less on the time at which the response was generated. In contrast to what was observed in the global competition model, the Simpson's diversity index of the total memory T-cell pool showed an impressive increase over time to a diverse immune repertoire, in which the largest immune response consisted of only 2% of the total memory T-cell pool (Figure 2F).

Notably, cognate competition among cells of an immune response gives rise to a highly diverse memory T-cell repertoire. Such a repertoire is beneficial, as it offers better protection to the host over its lifetime than the very skewed repertoire that was obtained with the global competition model. Therefore, we refer to the cognate competition model as the 'gold-standard' in the long-term homeostatic maintenance of almost all memories.

Immune memories are sustained for longer periods due to cellular aging

The cognate competition model gave rise to a diverse memory T-cell pool by limiting the size of the individual immune responses. Although competition in antigenic niches has been hypothesized (2, 28, 29, 68), experimental evidence for cognate competition in the memory T-cell pool is scarce. Instead, some experimental observations have shown that interactions with cognate resources (antigens) are not required for the survival of memory T cells (2, 8). Therefore, seeking for alternative mechanisms, we hypothesized that cellular aging of T cells may limit the growth of individual memory responses, and thereby generate a diverse memory T-cell repertoire. Here, we discuss the ramifications of cellular aging, in conjunction with global competition as the homeostatic mechanism, on the maintenance of the memory T-cell pool (Figure 1C; see Models).

The unabated expansion of the first immune response, M_1, was indeed prevented by cellular aging (Figure 2G). Continued antigen exposures resulted in the growth of the total memory T-cell pool, while existing immune responses underwent 1) moderate erosion due to new antigen exposures (Supplementary Figure 1E), and 2) major attrition due to cellular aging (Figure 2G). The limited consumption of cytokine by the existing immune responses allowed new immune responses to expand. However, on the long term all immune responses eventually declined (Figure 2G), as they were lost due to cellular aging (Supplementary Figure 1F). Interestingly, the maximal homeostatic proliferation rate hardly influenced the size distribution of the immune responses (Figure 2H). Rather, the sizes were largely determined by the time at which the responses were generated. The most recent responses made up the majority of the memory T-cell pool, as the older a response was, the more it was eroded. The diversity within the memory T-cell pool was much larger than in the global competition model but was only half of that achieved in the cognate competition model (Figure 2I). The largest immune response on day 1000 occupied a mere 6% of the memory T-cell pool, compared to the inflated 24% in the global competition model. Therefore, although the cellular aging model improves upon the global competition model, it cannot generate a memory T-cell pool as diverse as the 'gold-standard' memory T-cell pool that results from cognate competition.

A small source into an aging population helps to maintain a diverse memory T-cell pool

Multiple studies in the recent past have described subsets of memory T cells that have superior potential to generate other memory T-cell subsets (69). This self-sustaining population is sometimes referred to as the stem-cell-like memory T-cell population. Stem-cell-like memory T cells, generated during an acute response and residing in stromal niches in the bone marrow, could act as a slow but steady source into the circulating memory T-cell populations. We have seen that cellular aging can limit the expansion of the early memory populations, thereby reducing competition, but that the memory T-cell pool suffers in the long run, due to the eventual loss of all memories by cellular aging. The presence of a lowly-divided stem-cell-like source for each immune response would circumvent this issue. Importantly, this memory-maintaining source could also originate from circulating memory T cells due to repeated infections, from cross-reactions with other antigens, or from activation of new naive T cells (in case of persistent antigens).

Indeed, if each immune response had a small source (s_i=100 cells/day), none of the immune responses would be lost in the long-term (Figure 3). As the division history of the source might affect the memory T-cell repertoire, we evaluated two different scenarios: one, where the source population turned quiescent early in the expansion phase ('young' source, having completed 1 division on average), and the second, where the source population had divided as much as the circulating cells before becoming quiescent ('old' source, having completed an average of 20 divisions). A young source sustained the growth of early immune responses for longer periods of time compared to an older source (Figures 3A, D). Remarkably, the size distribution of the memory T-cell pool was completely different in both cases (Figures 3B, E). The presence of a young source resulted in a pool dominated (in size) by earlier immune responses, whereas a source from an older population favoured the prevalence of recently generated immune responses. This effect was due to a difference in the 'effective source'. Although both scenarios have the same source of 100 cells/day, the source from a younger population contributes more daughter cells because of their higher homeostatic proliferation rate. When the source population is old, it expands less and makes for a smaller effective source to the existing memories. Hence, with an old source the later immune responses expand more, due to weaker competition from existing immune responses, compared to the scenario with a young source. Even with such a stark difference in the immune profiles, the diversity within the memory T-cell pool was comparable in both scenarios, as none of the immune responses were lost (Figures 3C, F). The Simpson's diversity index revealed that the diversity achieved by adding a stem-cell-like source to the cellular aging model was comparable to the 'gold-standard' diversity achieved with the cognate competition model. Notably, the presence of a source in the global competition model failed to improve its diversity, demonstrating that adding a small source is not a trivial solution to maintaining the diversity of a population (figure not shown due to its similarity to Figures 2A–C). Therefore, we propose that a source into an aging population is a viable alternative to the cognate competition model.

The distribution of the division number in the memory T-cell pool of the global competition model in the absence of

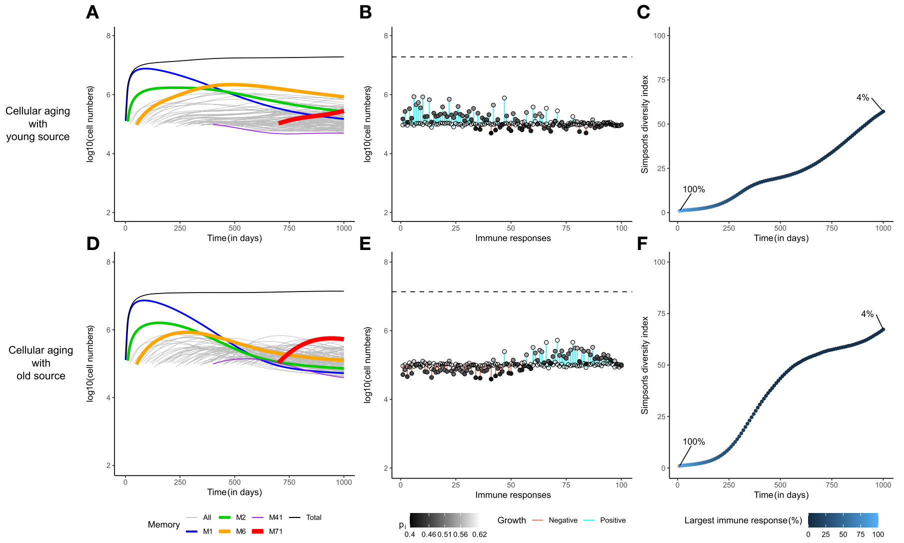

FIGURE 3
A small source helps to achieve the gold-standard diversity within the memory T-cell pool. The dynamics of the cellular aging model along with a source from either a young (upper row) or an old population (lower row). The memory T-cell pool was generated by acute immune responses only. Legends as in Figure 2.

cellular aging, i.e., when $p_{i,j}=p_i$, showed a large disparity in the average generation number of the immune responses, with early responses having divided 70 times on average, compared to an average of 25 divisions for recent responses (Figure 4A). The very first response (like all other responses) had gone through 25 divisions when seeded in the beginning of the memory phase, and subsequently accumulated 50 more divisions throughout the mouse's life (Figure 4B). Even though the cells of the first

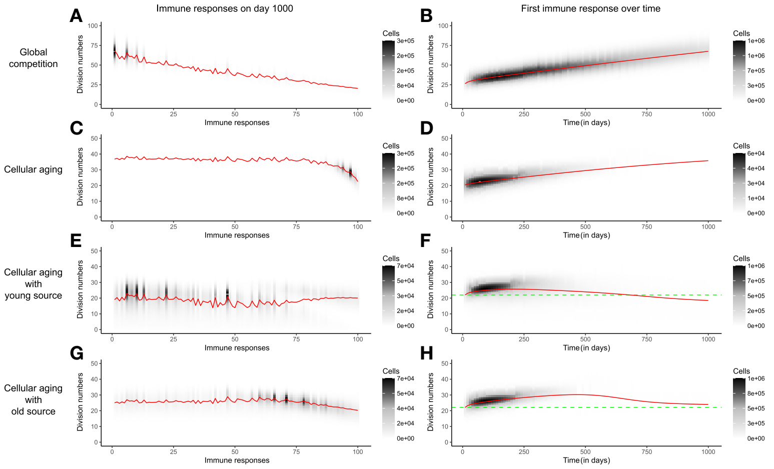

FIGURE 4
The distribution of division numbers in the memory T-cell pool is determined by the age of the source population. Comparison of the distribution of division numbers of all immune responses on day 1000 (Panels **A**, **C**, **E**, **G**), and the division history of the first immune response over time (Panels **B**, **D**, **F**, **H**), for different mechanisms. The red line plots the average generation number of an immune response. The grey and black shades show the number of cells at different division numbers. The green dotted line marks the starting division number of the first immune response. In these simulations the memory T-cell pool consists of acute immune responses only.

immune response accrued more divisions with time, the size of the first response declined over time due to global competition from successive immune responses (Figures 4B, 2A). The disparity found in the division distribution of the memory T-cell pool dropped considerably in the presence of cellular aging (Figure 4C). Cellular aging promoted the dominance of recent immune responses, even though they had divided less (Figures 4C, 2H). The number of divisions accrued by an immune response over a mouse's lifetime was also significantly lower due to cellular aging (Figure 4D). A continuous source reduced the disparity in the division distribution within the memory T-cell pool even more (Figures 4E, 4G). The average generation number of the first immune response on day 1000 was lower compared to that on day 0 when the source was from a younger population but was higher than that on day 0 in case of an older source (Figures 4F, 4H). Therefore, a small source counteracts the exhaustion of a population by cellular aging and the division history of the source determines the distribution of the division history within the memory T-cell pool.

A source into an aging T-cell population maintains immune memories in the long-term even in the presence of chronic responses

Our discussion until now has focused on a memory T-cell pool containing 100 memories to pathogens that were eliminated during the 'acute' immune response. However, chronic immune responses to pathogens (or antigens) that persist, may pose a big challenge in maintaining the diversity of the memory T-cell pool, due to their sometimes inflationary properties (12). We assessed whether our novel model, with a memory T-cell pool going through cellular aging in the presence of a source, could maintain T-cell diversity under the competitive pressure from chronic T-cell responses. We considered a host that generated 95 acute responses and 5 chronic responses, even though only 1% of all infections are estimated to lead to chronic responses (12). Chronic responses are maintained in part by homeostatic proliferation due to IL-15, and partly due to repeated stimulation by persistent antigen (see Models).

Chronic responses expanded to occupy a higher proportion of the memory T-cell pool than acute responses (Figure 5). The immune dynamics of the 95 acute responses were not severely affected by the addition of 5 chronic responses (compare Figures 3A, D with Figures 5A, D). Exposure to chronic antigens expanded the total memory T-cell pool, and the heightened competition reduced the sizes of the acute responses somewhat. The division histories and the prevalence patterns of the immune responses hardly changed (compare Figures 3B, E with Figures 5B, E, and Supplementary Figure 2). Like before, the division history showed that the memory T-cell pool became younger with time in the presence of a young source, which resulted in the prevalence of early immune responses. However, the diversity of the memory T-cell pool

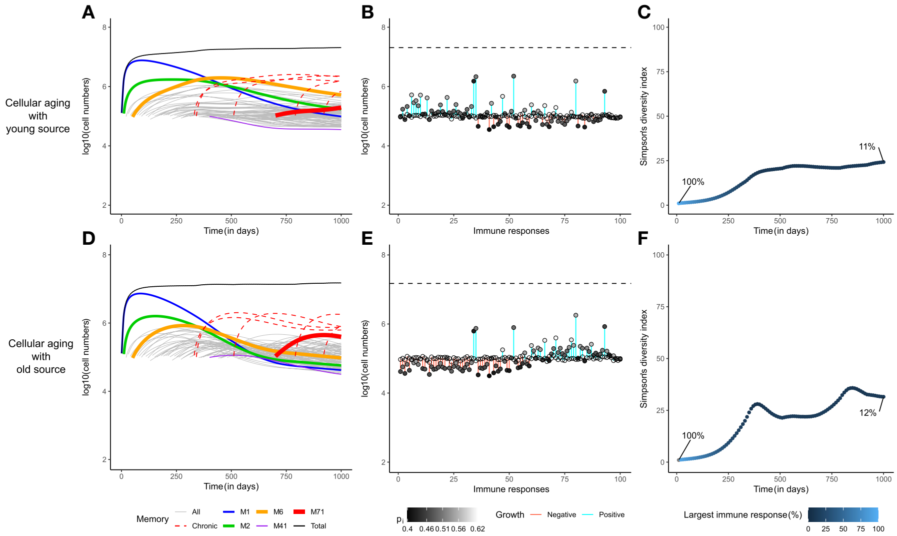

FIGURE 5
Chronic immune responses lower the long-term diversity of the memory T-cell pool. The dynamics of the cellular aging model along with a source from either a young source (upper row) or an old source (lower row). The memory T-cell pool consists of both acute and chronic immune responses shown as dashed red line. Legends as in Figure 2.

declined markedly in the presence of chronic responses as the largest immune response now made up only about 10% of the total memory T-cell pool (Figures 5C, F). The cellular aging model along with a source, thus, provides a robust mechanism for the long-term maintenance of memory T-cells, even though the diversity in the memory T-cell pool suffers from the presence of chronic responses.

Long-lived memory T cells lower the diversity of the memory T-cell pool

Circulating memory T cells have been shown to be relatively short-lived (70), while memory in itself is long-lived (71, 72). In an attempt to understand why memory T cells are relatively short-lived, we studied how the lifespan of memory T cells influences the diversity of memory T-cell repertoires. In our models, the attrition of existing memories was due to the relatively short lifespans of memory T cells. We examined whether memory T cells with longer lifespans would allow for higher diversity in the memory T-cell repertoires. To precisely underline the influence of memory T-cell lifespan (without the effect of a source) on the diversity of the memory T-cell repertoire, we only considered the three basic mechanisms: global competition, cognate competition, and cellular aging, without any source. The model characteristics were compared considering a scenario where memory T cells lived 10 times longer than their estimated lifespans, i.e., d_i=0.002/day (Supplementary Figure 3). The temporal dynamics corroborated the previous conclusions: M_1 filled up the memory T-cell pool under the influence of global competition, while this was strongly and moderately constrained in the cases of cognate competition and cellular aging, respectively (Supplementary Figure 3A, D, G). Notably, none of the cases showed the loss of any immune response (Supplementary Figure 3B, E, H). The degree of inflation of an immune response clearly correlated with how early the response was generated. More importantly, the levels of TCR diversity in the memory T-cell pool were a lot lower when compared to the corresponding cases with short-lived memory T cells (Supplementary Figure 3C, F, I). When memory T cells were long-lived, the diversity in the global competition and cellular aging models barely improved over time, whereas the index for the cognate competition model was half of that with short-lived memory T cells.

Although maintenance of all encountered immune responses may be advantageous, the inflation of early memories might pose significant challenges for the efficient protection of a host. The recall response to a recent antigen is expected to be delayed when the probability of finding cognate memory T cells decreases due to the presence of inflated early responses in the pool. A considerable delay in the recall response to a large infection may even be detrimental (25). Therefore, surprisingly, storing immunological memory in short-lived memory T cells may be more beneficial, as short-lived memory T cells allow for higher diversity in the memory T-cell pool.

Discussion

Here, we showed that cellular aging in the presence of a source population is a mechanism by which long-term maintenance of a diverse memory T-cell pool can be achieved. It preserves acute as well as chronic immune responses in the long-term and generates a diverse memory T-cell repertoire comparable to the gold-standard level of diversity generated with cognate competition. Whereas the occurrence of cognate competition is poorly supported by experimental evidence, the presence of both cellular aging and a source (from stem-cell-like memory T cells, re-activated memory T cells, cross-reactive memory T cells or newly activated naive T cells) are widely accepted. Therefore, we propose that a source into an aging population is an immunologically viable alternative to the cognate competition model.

The global competition model is prone to competitive exclusion of all but the fittest immune response. Using division and death rates of murine memory CD8$^+$ T cells, we showed that although competitive exclusion may not be seen in the lifetime of a mouse, global competition would lead to unrealistically skewed memory repertoires. Moreover, the slow exclusion of memory T-cell responses in our simulations was due to the small differences in the fitness values of the different immune responses. If the fitness values of the immune responses were to differ more than the 10% standard deviation considered in our simulations, the size disparity in the memory T-cell pool would be even higher.

The cellular aging model improves upon the global competition model by limiting the size of each self-renewing memory population, which reduces the competition among them. A source into an aging memory T-cell pool sustains the diversity of the memory T-cell repertoire in the long-term. A young source favours the frequency of early memory responses, while an old source causes recent responses to be more prevalent. The memory T-cell pool eventually turns younger due to the presence of a young source. This could present a potential explanation for the observation that reconstituted T-cell pools have higher proliferation rates after autologous stem-cell transplantation (11) as the highly-divided circulating memory T cells were replaced with lowly-divided memory T cells. Moreover, if the acquisition of different memory T-cell phenotypes were correlated with the division history of a cell (73), cellular aging would have exciting implications. For example, following the linear differentiation pathway (74), the absence of a source would predict the accumulation of effector memory T cells over time, whereas the presence of a source would suggest the accumulation of central memory T cells after multiple infections. Previous studies addressing repeated vaccinations (75) have shown diverging results. Some studies showed the enrichment of memory T cells with an effector memory phenotype (33, 76), whereas other studies showed the accumulation of central memory T cells after multiple rounds of heterologous, viral vaccinations (25). Similar effects of sustained, chronic responses on the phenotypes of both bystander and specific memory T cells have also been discussed (77, 78). Further, the declining fitness of immune responses in older hosts can explain their impaired response to vaccinations (79). In view of such observations, it is extremely interesting to study the mechanisms underlying the phenotypic distribution in memory T-cell pools, and thereby the erosion of protective immunity with age.

In absence of a source, an aging population will eventually be lost. The timescale of this extinction is much longer than the lifetime of a mouse. Interestingly, erosion of early memories could be beneficial for a host to maintain memory and mount responses against recently encountered pathogens, as the relative proportion of recently generated memory T cells would increase. In a changing natural environment, the probability of getting re-exposed to a pathogen is probably higher for recently encountered pathogens than for those encountered early in life. Therefore, maintenance of recent memories could be beneficial. Along similar lines, we also showed that long-lived memory T cells, or lack of regulation (due to competition or aging) early in life, would lead to a loss of diversity in the memory T-cell pool due to inflation of early memories. Virtual memory T cells are memory-phenotype cells that originate from naive T cells due to homeostatic proliferation in the absence of cognate antigen (80, 81). If virtual memory T cells would be highly inflated due to lack of competition early in life, and/or due to long lifespans, they would severely impair the efficacy of the memory T-cell repertoire against natural infections.

Many laboratory protocols, just like our simulations, use fixed time intervals between antigen introductions, a scheme that is, of course, rather artificial. In reality, a mouse's exposure to antigens is truly a random event. Statistically, random events follow a Poisson distribution, where the time between two consecutive events is exponentially distributed. Therefore, a mouse in its natural environment will be exposed to most unique antigens early on in its life and to relatively fewer novel antigens in its twilight years. For our models, simulations of this real world scenario led to considerably different results from the simulations presented here (Supplementary Figure 4). When emulating the real world scenario, the first immune response, M_1 , did not take over the memory T-cell pool in any of the models, due to competition with multiple other immune responses generated early in life. The snapshots of the memory T-cell pool on day 1000 showed a more marked attrition of immune responses, under the influence of global competition and cellular aging but not under cognate competition (Supplementary Figure 4). If anything, our simulations showed that random antigenic exposure accelerates the competitive dynamics and reduces the diversity of the memory T-cell repertoire.

Although our simulations were primarily based on murine parameters, the concerns and results discussed here are also applicable to humans. The expected lifespan of human circulating memory CD8$^+$ T cells is close to 200 days (50), which is 4 times longer than that in mice. However, the lifespan of a human is 30 times longer than that of a mouse. Thus, based upon our global competition model, one would expect early immune responses to be competitively excluded during a human's lifetime. Both cognate competition and cellular aging with a source would alleviate this problem, the latter providing a more immunologically sound mechanism. Unfortunately, we are not aware of any literature on the effects of cellular aging of memory T cells that could be used to test the prediction of our novel model. Single-cell sequencing studies have described the change in the memory T-cell repertoire with age (82). However, these studies have focused on the age of the host rather than the age of the cell, making a comparison of these results and our predictions speculative. Recent studies using the Cre-recombinase technology (48, 53) do provide an avenue that could be exploited to delineate the age of the cell from the age of its host. Such dedicated experiments would be required to test the predictions of the cellular aging model.

Barring a few studies (83), IL-7 is often implicated in the homeostatic maintenance of memory as well as naive T cells (4, 57, 61). The competition between naive and memory T-cell populations through IL-7 has not been taken into account in this study. As the production of new naive T cells declines with age (84, 85), reduced competition for IL-7 could alleviate some of the 'global' competitive pressure on the memory T-cell pool, leading to a larger memory pool size, but not to an alteration in the distribution of clone sizes (i.e., not to a different memory T-cell repertoire). Similarly, a temporal change in the source of homeostatic cytokines (IL-15, IL-7, etc.) e.g., due to aging, would affect the global competition among memory T cells and change the pool size but not the repertoire. IL-15 is produced by multiple tissues (e.g., bone marrow, heart, lung, kidney, thymic epithelium) and cell types (e.g., monocytes/ macrophages, blood-derived dendritic cells) (86) that are subject to alterations throughout a host's life. Since the lifespan of circulating memory T cells has a time scale of months in mice, the division rate is expected to average over such spatial heterogeneities. In our model, the source is considered to be either from naive T cells due to new or recurrent challenges, or from stem-cell-like memory T cells. As the exposure to antigens is random, the source from naive T cells could be stochastic. Further, newly generated stem-cell-like memory T cells in the bone marrow could either increase the source to an immune response (in case of a recurrent infection) (87, 88), or decrease the source (due to competition among memory T-cells for the limited number of stromal niches) (89, 90). Thus, the source need not be constant. It would be interesting to study such model variations in future studies and to quantify their effect on the long-term maintenance of the memory T-cell pool.

The cellular aging model, like existing models for the maintenance of memory T cells, presents a simplified view of the memory T-cell pool and its maintenance. However, unlike the current gold-standard based on cognate competition, cellular aging is well-supported. Therefore, this manuscript puts forth a realistic mechanism that might underlie the observed long-lived large diversity of the $CD8^+$ memory T-cell repertoire despite the relatively short lifespan of $CD8^+$ memory T cells.

Data availability statement

The original contributions presented in the study are included in the article/Supplementary Material. Further inquiries can be directed to the corresponding author.

Author contributions

AS performed mathematical modelling. AS, JB, RdB designed the study. AS, JB, RdB analyzed the data and wrote the manuscript. All authors contributed to the article and approved the submitted version.

Funding

This work was supported by an NWO grant (ALWOP.265) to RdB and an NWO Vici grant (R5732) to JB.

Conflict of interest

The authors declare that the research was conducted in the absence of any commercial or financial relationships that could be construed as a potential conflict of interest.

Publisher's note

Supplementary material

The Supplementary Material for this article can be found online at: https://www.frontiersin.org/articles/10.3389/fimmu.2022.947242/full#supplementary-material

SUPPLEMENTARY FIGURE 1
Global competition leads to the loss of all but the fittest immune response. Comparison of the three mechanisms (global competition, cognate competition, and cellular aging) for homeostatic maintenance of memory T cells focusing on the short-term (first 100 days in Panels **A**, **C**, **E**) and long-term (10,000 days in Panels **B**, **D**, **F**) temporal dynamics of a murine memory T-cell pool. The memory T-cell pool consists of acute immune responses only.

SUPPLEMENTARY FIGURE 2
Adding chronic responses hardly changed the division distributions. Comparison of the division distributions of all memory T-cell populations on day 1,000, and the division history of the first memory T-cell population over time. The red line plots the average generation number of an immune response. The grey and black shades show the number of cells at different division numbers. The green dotted line marks the starting division number of the first immune response. The memory T-cell pool consists of both acute and chronic immune responses.

SUPPLEMENTARY FIGURE 3
Memory T-cell pools with long-lived memory T cells are barely diverse. Comparison of three mechanisms (global competition, cognate competition, and cellular aging, without any source) for homeostatic maintenance of long-lived memory T cells. The expected lifespan of the memory T cells was set to 500 days (which is 10 times longer than their estimated lifespans (3)). The memory T-cell pool consists of acute immune responses only.

SUPPLEMENTARY FIGURE 4
Random antigen exposure aggravates the loss of immune memories due to intense competition. Comparison of three mechanisms (global competition, cognate competition, and cellular aging, without any source) for homeostatic maintenance of memory T cells when most novel pathogens appear early in life. The delay between antigen exposures was exponentially distributed, mimicking the random exposure to antigens in real life. The memory T-cell pool consists of acute immune responses only.

References

1. Surh CD, Sprent J. Homeostasis of naive and memory T cells. *Immunity* (2008) 29:848–62. doi: 10.1016/J.IMMUNI.2008.11.002

2. Freitas AA, Rocha B. Population biology of lymphocytes: the flight for survival. *Annu Rev Immunol* (2000) 18:83–111. doi: 10.1146/ANNUREV.IMMUNOL.18.1.83

3. Choo DK, Murali-Krishna K, Anita R, Ahmed R. Homeostatic turnover of virus-specific memory CD8 T cells occurs stochastically and is independent of CD4 T cell help. *J Immunol* (2010) 185:3436–44. doi: 10.4049/JIMMUNOL.1001421

4. Tan JT, Ernst B, Kieper WC, LeRoy E, Sprent J, Surh CD. Interleukin (IL)-15 and IL-7 jointly regulate homeostatic proliferation of memory phenotype CD8+

cells but are not required for memory phenotype CD4+ cells. *J Exp Med* (2002) 195:1523–32. doi: 10.1084/JEM.20020066

5. Hashimoto M, Im SJ, Araki K, Ahmed R. Cytokine-mediated regulation of CD8 T-cell responses during acute and chronic viral infection. *Cold Spring Harb Perspect Biol* (2019) 11:a028464. doi: 10.1101/CSHPERSPECT.A028464

6. Tanchot C, Lemonnier FA, Pérarnau B, Freitas AA, Rocha B. Differential requirements for survival and proliferation of CD8 naïve or memory T cells. *Science* (1997) 276:2057–62. doi: 10.1126/SCIENCE.276.5321.2057

7. Ku CC, Murakami M, Sakamoto A, Kappler J, Marrack P. Control of homeostasis of CD8+ memory T cells by opposing cytokines. *Science* (2000) 288:675–8. doi: 10.1126/SCIENCE.288.5466.675

8. Murali-Krishna K, Lau LL, Sambhara S, Lemonnier F, Altman J, Ahmed R. Persistence of memory CD8 T cells in MHC class I-deficient mice. *Science* (1999) 286:1377–81. doi: 10.1126/SCIENCE.286.5443.1377

9. Voehringer D, Liang H-E, Locksley RM. Homeostasis and effector function of lymphopenia-induced 'memory-like' T cells in constitutively T cell-depleted mice. *J Immunol* (2008) 180:4742. doi: 10.4049/JIMMUNOL.180.7.4742

10. Bouvy AP, Kho MML, Klepper M, Litjens NHR, Betjes MGH, Weimar W, et al. Kinetics of homeostatic proliferation and thymopoiesis after ratg induction therapy in kidney transplant patients. *Transplantation* (2013) 96:904–13. doi: 10.1097/TP.0B013E3182A203E4

11. Baliu-Piqué M, van Hoeven V, Drylewicz J, van der Wagen LE, Janssen A, Otto SA, et al. Cell-density independent increased lymphocyte production and loss rates post-autologous hsct. *Elife* (2021) 10:1–22. doi: 10.7554/ELIFE.59775

12. Virgin HW, Wherry EJ, Ahmed R. Redefining chronic viral infection. *Cell* (2009) 138:30–50. doi: 10.1016/J.CELL.2009.06.036

13. Baumann NS, Torti N, Welten SPM, Barnstorf I, Borsa M, Pallmer K, et al. Tissue maintenance of CMV-specific inflationary memory T cells by IL-15. *PloS Pathog* (2018) 14:e1006993. doi: 10.1371/JOURNAL.PPAT.1006993

14. Sandalova E, Laccabue D, Boni C, Tan AT, Fink K, Ooi EE, et al. Contribution of herpesvirus specific CD8 T cells to anti-viral T cell response in humans. *PloS Pathog* (2010) 6:e1001051. doi: 10.1371/JOURNAL.PPAT.1001051

15. Cupovic J, Ring SS, Onder L, Colston JM, Lütge M, Cheng HW, et al. Adenovirus vector vaccination reprograms pulmonary fibroblastic niches to support protective inflating memory CD8+ T cells. *Nat Immunol* (2021) 22 (8):1042–51. doi: 10.1038/s41590-021-00969-3

16. Block KE, Jameson SC. Inflating the role of stromal cells in CD8+ T cell memory. *Nat Immunol* (2021) 22:942–4. doi: 10.1038/s41590-021-00974-6

17. Yates A, Saini M, Mathiot A, Seddon B. Mathematical modeling reveals the biological program regulating lymphopenia-induced proliferation. *J Immunol* (2008) 180:1414–22. doi: 10.4049/JIMMUNOL.180.3.1414

18. Ku C-C, Kappler J, Marrack P. The growth of the very large CD8+ T cell clones in older mice is controlled by cytokines. *J Immunol* (2001) 166:2186–93. doi: 10.4049/JIMMUNOL.166.4.2186

19. Hogan T, Shuvaev A, Commenges D, Yates A, Callard R, Thiebaut R, et al. Clonally diverse T cell homeostasis is maintained by a common program of cell-cycle control. *J Immunol* (2013) 190:3985–93. doi: 10.4049/JIMMUNOL.1203213

20. De Boer RJ, Perelson AS. T Cell repertoires and competitive exclusion. *J Theor Biol* (1994) 169:375–90. doi: 10.1006/JTBI.1994.1160

21. Selin LK, Lin MY, Kraemer KA, Pardoll DM, Schneck JP, Varga SM, et al. Attrition of T cell memory: Selective loss of LCMV epitope–specific memory CD8 T cells following infections with heterologous viruses. *Immunity* (1999) 11:733–42. doi: 10.1016/S1074-7613(00)80147-8

22. Welsh RM, Selin LK. ATTRITION OF MEMORY CD8 T CELLS. *Nature* (2009) 459:E3. doi: 10.1038/NATURE08091

23. Schmidt NW, Harty JT. Cutting edge: Attrition of plasmodium -specific memory CD8 T cells results in decreased protection that is rescued by booster immunization. *J Immunol* (2011) 186(7):3836–40. doi: 10.4049/jimmunol.1003949

24. Vezys V, Yates A, Casey KA, Lanier G, Ahmed R, Antia R, et al. Memory CD8 T-cell compartment grows in size with immunological experience. *Nat* (2008) 457:196–9. doi: 10.1038/nature07486

25. Huster KM, Stemberger C, Gasteiger G, Kastenmüller W, Drexler I, Busch DH. Cutting edge: Memory CD8 T cell compartment grows in size with immunological experience but nevertheless can lose function. *J Immunol* (2009) 183:6898–902. doi: 10.4049/JIMMUNOL.0902454

26. Siracusa F, Alp ÖS, Maschmeyer P, McGrath M, Mashreghi MF, Hojyo S, et al. Maintenance of CD8+ memory T lymphocytes in the spleen but not in the bone marrow is dependent on proliferation. *Eur J Immunol* (2017) 47:1900. doi: 10.1002/EJI.201747063

27. Kedl RM, Rees WA, Hildeman DA, Schaefer B, Mitchell T, Kappler J, et al. T Cells compete for access to antigen-bearing antigen-presenting cells. *J Exp Med* (2000) 192:1105. doi: 10.1084/JEM.192.8.1105

28. Borghans JAM, Taams LS, Wauben MHM, De Boer RJ. Competition for antigenic sites during T cell proliferation: A mathematical interpretation of *in vitro* data. *Proc Natl Acad Sci* (1999) 96:10782–7. doi: 10.1073/PNAS.96.19.10782

29. Yates AJ, Chan CCT, Callard RE. 16 modelling T cell activation, proliferation, and homeostasis. *Stud Multidiscip* (2005) 3:281–308. doi: 10.1016/S1571-0831(06)80020-1

30. Callard RE, Stark J, Yates AJ. Fratricide: A mechanism for T memory-cell homeostasis. *Trends Immunol* (2003) 24:370–5. doi: 10.1016/S1471-4906(03)00164-9

31. De Boer RJ, Perelson AS. Antigen-stimulated CD4 T cell expansion can be limited by their grazing of peptide-MHC complexes. *J Immunol* (2013) 190:5454–8. doi: 10.4049/JIMMUNOL.1203569

32. Fraser KA, Schenkel JM, Jameson SC, Vezys V, Masopust D. Preexisting high frequencies of memory CD8+ T cells favors rapid memory differentiation and preservation of proliferative potential upon boosting. *Immunity* (2013) 39:171. doi: 10.1016/J.IMMUNI.2013.07.003

33. Masopust D, Ha S-J, Vezys V, Ahmed R. Stimulation history dictates memory CD8 T cell phenotype: Implications for prime-boost vaccination. *J Immunol* (2006) 177:831–9. doi: 10.4049/JIMMUNOL.177.2.831

34. Mayer A, Zhang Y, Perelson AS, Wingreen NS. Regulation of T cell expansion by antigen presentation dynamics. *Proc Natl Acad Sci USA* (2019) 116:5914–9. doi: 10.1073/PNAS.1812800116

35. Gaimann MU, Nguyen M, Desponds J, Mayer A. Early life imprints the hierarchy of T cell clone sizes. *Elife* (2020) 9:1–36. doi: 10.7554/ELIFE.61639

36. DiLoreto R, Murphy CT. The cell biology of aging. *Mol Biol Cell* (2015) 26:4524. doi: 10.1091/MBC.E14-06-1084

37. Mittelbrunn M, Kroemer G. Hallmarks of T cell aging. *Nat Immunol 2021 226* (2021) 22:687–98. doi: 10.1038/s41590-021-00927-z

38. Mays Hoopes LL. Aging, cell division | learn science at scitable. *Mays. Hoopes. L L Aging Cell Div Nat Educ* (2010) 3(9):55.

39. Thoma OM, Neurath MF, Waldner MJ. T Cell aging in patients with colorectal cancer-what do we know so far? *Cancers (Basel)* (2021) 13(24): 6227. doi: 10.3390/CANCERS13246227

40. Lamar DL, Wevand CL, Goronzy JJ. Age, T-cell Homeostasis, and T-cell Diversity in Humans. 167–92

41. Nikolich-Žugich J, Lang A.. Age-associated T-cell Clonal Expansion (TCE) in vivo – Implications for Pathogen Resistance. 219–33

42. Szabo P, Weksler ME, Nikolich-Zugich J, Potvin H, Nikolich-Zugich D, Dyall R, et al. Age-related dysregulation in CD8 T cell homeostasis: Kinetics of a diversity loss. *J Immunol* (2000) 165:2367–73. doi: 10.4049/JIMMUNOL.165.5.2367

43. Ferrando-Martínez S, Ruiz-Mateos E, Hernández A, Gutiérrez E, Rodríguez-Méndez MDM, Ordoñez A, et al. Age-related deregulation of naive T cell homeostasis in elderly humans. *Age (Dordr)* (2011) 33:197–207. doi: 10.1007/S11357-010-9170-8

44. Haynes L, Swain SL. Aged-related shifts in T cell homeostasis lead to intrinsic T cell defects. *Semin Immunol* (2012) 24:350–5. doi: 10.1016/J.SMIM.2012.04.001

45. Chou PJ, Effros RB. T Cell replicative senescence in human aging. *Curr Pharm Des* (2013) 19:1680–98. doi: 10.2174/138161213805219711

46. Goronzy JJ, Weyand CM. Mechanisms underlying T cell ageing. *Nat Rev Immunol* (2019) 19:573. doi: 10.1038/S41577-019-0180-1

47. Lanfermeijer J, Borghans JAM, van Baarle D. How age and infection history shape the antigen-specific CD8 + T-cell repertoire: Implications for vaccination strategies in older adults. *Aging Cell* (2020) 19(11):e13262. doi: 10.1111/ACEL.13262

48. Reynaldi A, Smith NL, Schlub TE, Tabilas C, Venturi V, Rudd BD, et al. Fate mapping reveals the age structure of the peripheral T cell compartment. *Proc Natl Acad Sci U.S.A.* (2019) 116:3974–81. doi: 10.1073/PNAS.1811634116/-/DCSUPPLEMENTAL

49. Rane S, Hogan T, Seddon B, Yates AJ. Age is not just a number: Naive T cells increase their ability to persist in the circulation over time. *PloS Biol* (2018) 16: e2003949. doi: 10.1371/JOURNAL.PBIO.2003949

50. Akondy RS, Fitch M, Edupuganti S, Yang S, Kissick HT, Li KW, et al. Origin and differentiation of human memory CD8 T cells after vaccination. *Nat* (2017) 552:362–7. doi: 10.1038/nature24633

51. Vibert J, Thomas-Vaslin V. Modelling T cell proliferation: Dynamics heterogeneity depending on cell differentiation, age, and genetic background. *PloS Comput Biol* (2017) 13:e1005417. doi: 10.1371/JOURNAL.PCBI.1005417

52. Baliu-Piqué M, Drylewicz J, Zheng X, Borkner L, Swain AC, Otto SA, et al. Turnover of murine cytomegalovirus–expanded CD8+ T cells is similar to that of memory phenotype T cells and independent of the magnitude of the response. *J Immunol* (2022) 208:799–806. doi: 10.4049/JIMMUNOL.2100883

53. Bresser K, Kok L, Swain AC, King LA, Jacobs L, Weber TS, et al. Replicative history marks transcriptional and functional disparity in the CD8+ T cell memory pool. *Nat Immunol* (2022) 23:791–801. doi: 10.1038/s41590-022-01171-9

54. Cui G, Hara T, Simmons S, Wagatsuma K, Abe A, Miyachi H, et al. Characterization of the IL-15 niche in primary and secondary lymphoid organs *in vivo*. *Proc Natl Acad Sci USA* (2014) 111:1915–20. doi: 10.1073/PNAS.1318281111/-/DCSUPPLEMENTAL

55. Krishnamurty AT, Turley SJ. Lymph node stromal cells: Cartographers of the immune system. *Nat Immunol* (2020) 21:369–80. doi: 10.1038/s41590-020-0635-3

56. Nitta T, Takayanagi H. Non-epithelial thymic stromal cells: Unsung heroes in thymus organogenesis and T cell development. *Front Immunol* (2021) 11:620894/BIBTEX. doi: 10.3389/FIMMU.2020.620894/BIBTEX

57. Sercan Alp Ö, Durlanik S, Schulz D, Mcgrath M, Grün JR, Bardua M, et al. Memory CD8+ T cells colocalize with IL-7+ stromal cells in bone marrow and rest in terms of proliferation and transcription. *Eur J Immunol* (2015) 45:975. doi: 10.1002/EJI.201445295

58. Mugwagwa T. Quantification of T cell dynamics in health and disease. *PhD Thesis.* (2010) 4:39–52.

59. Snyder CM, Cho KS, Bonnett EL, van Dommelen S, Shellam GR, Hill AB. Memory inflation during chronic viral infection is maintained by continuous production of short-lived, functional T cells. *Immunity* (2008) 29:650–9. doi: 10.1016/J.IMMUNI.2008.07.017

60. Utzschneider DT, Delpoux A, Wieland D, Huang X, Lai CY, Hofmann M, et al. Active maintenance of T cell memory in acute and chronic viral infection depends on continuous expression of FOXO1. *Cell Rep* (2018) 22:3454–67. doi: 10.1016/J.CELREP.2018.03.020

61. Gao J, Zhao L, Wan YY, Zhu B. Mechanism of action of IL-7 and its potential applications and limitations in cancer immunotherapy. *Int J Mol Sci* (2015) 16:10267–80. doi: 10.3390/IJMS160510267

62. Hayflick L, Moorhead PS. The serial cultivation of human diploid cell strains. *Exp Cell Res* (1961) 25:585–621. doi: 10.1016/0014-4827(61)90192-6

63. De Boer RJ NA. T Cell renewal rates, telomerase, and telomere length shortening. *J Immunol* (1998) 160(12):5832–7.

64. Goronzy JJ, Fujii H, Weyand CM. Telomeres, immune aging and autoimmunity. *Exp Gerontol.* (2006) 41:246–51. doi: 10.1016/j.exger.2005.12.002

65. De Boer RJ, Perelson AS. Quantifying T lymphocyte turnover. *J Theor Biol* (2013) 327:45–87. doi: 10.1016/J.JTBI.2012.12.025

66. Hinrichs CS, Borman ZA, Cassard L, Gattinoni L, Spolski R, Zhiya Y, et al. Adoptively transferred effector cells derived from naïve rather than central memory CD8+ T cells mediate superior antitumor immunity. *Proc Natl Acad Sci USA* (2009) 106:17469–74. doi: 10.1073/PNAS.0907448106/SUPPL_FILE/0907448106SI.PDF

67. Geginat J, Lanzavecchia A, Sallusto F. Proliferation and differentiation potential of human CD8+ memory T-cell subsets in response to antigen or homeostatic cytokines. *Blood* (2003) 101:4260–6. doi: 10.1182/BLOOD-2002-11-3577

68. Agenés F, Dangy JP, Kirberg J. T Cell receptor contact to restricting MHC molecules is a prerequisite for peripheral interclonal T cell competition. *J Exp Med* (2008) 205:2735–43. doi: 10.1084/JEM.20070467

69. Gattinoni L, Lugli E, Ji Y, Pos Z, Paulos CM, Quigley MF, et al. A human memory T-cell subset with stem cell-like properties. *Nat Med* (2011) 17:1290. doi: 10.1038/NM.2446

70. Baliu-Piqué M, Verheij MW, Drylewicz J, Ravesloot L, de Boer RJ, Koets A, et al. Short lifespans of memory T-cells in bone marrow, blood, and lymph nodes suggest that T-cell memory is maintained by continuous self-renewal of recirculating cells. *Front Immunol* (2018) 9:2054/BIBTEX. doi: 10.3389/FIMMU.2018.02054/BIBTEX

71. Emerson HPanum on Measles: Observations Made During the Epidemic of Measles on the Faroe Islands in the Year 1846 (A translation from the Danish). *Am J Public Health Nations Health.* (1940) 30(10):1245–6.

72. Cendón C, Du W, Durek P, Liu YC, Alexander T, Serene L, et al. Resident memory CD4+ T lymphocytes mobilize from bone marrow to contribute to a systemic secondary immune reaction. *Eur J Immunol* (2022) 0:1–16. doi: 10.1002/EJI.202149726

73. Henning AN, Roychoudhuri R, Restifo NP. Epigenetic control of CD8 + T cell differentiation. *Nat Rev Immunol* (2018) 18:340–56. doi: 10.1038/NRI.2017.146

74. Souquette A, Thomas PG. Past life and future effects-how heterologous infections alter immunity to influenza viruses. *Front Immunol* (2018) 9:1071. doi: 10.3389/FIMMU.2018.01071

75. Minervina AA, Pogorelyy MV, Kirk AM, Crawford JC, Allen EK, Chou C-H, et al. SARS-CoV-2 antigen exposure history shapes phenotypes and specificity of memory CD8+ T cells. *Nat Immunol* (2022) 23:781–90. doi: 10.1038/s41590-022-01184-4

76. Snell LM, MacLeod BL, Law JC, Osokine I, Elsaesser HJ, Hezaveh K, et al. CD8 + T cell priming in established chronic viral infection preferentially directs differentiation of memory-like cells for sustained immunity. *Immunity* (2018) 49:678–694.e5. doi: 10.1016/J.IMMUNI.2018.08.002

77. Barnstorf I, Borsa M, Baumann N, Pallmer K, Yermanos A, Joller N, et al. Chronic virus infection compromises memory bystander T cell function in an IL-6/STAT1-dependent manner. *J Exp Med* (2019) 216:571–86. doi: 10.1084/JEM.20181589

78. Wherry EJ, Blattman JN, Ahmed R. Low CD8 T-cell proliferative potential and high viral load limit the effectiveness of therapeutic vaccination. *J Virol* (2005) 79:8960. doi: 10.1128/JVI.79.14.8960-8968.2005

79. Sosinowski T, White JT, Cross EW, Haluszczak C, Marrack P, Gapin L, et al. CD8α+ dendritic cell trans presentation of IL-15 to naive CD8+ T cells produces antigen-inexperienced T cells in the periphery with memory phenotype and function. *J Immunol* (2013) 190:1936–47. doi: 10.4049/JIMMUNOL.1203149

80. Akue AD, Lee J-Y, Jameson SC. Derivation and maintenance of virtual memory CD8 T cells. *J Immunol* (2012) 188:2516. doi: 10.4049/JIMMUNOL.1102213

81. Mogilenko DA, Shchukina I, Artyomov MN. Immune ageing at single-cell resolution. *Nat Rev Immunol* (2021), 1–15. doi: 10.1038/s41577-021-00646-4

82. Xu A, Bhanumathy KK, Wu J, Ye Z, Freywald A, Leary SC, et al. IL-15 signaling promotes adoptive effector T-cell survival and memory formation in irradiation-induced lymphopenia. *Cell Biosci* (2016) 6:1–13. doi: 10.1186/S13578-016-0098-2/FIGURES/5

83. den Braber I, Mugwagwa T, Vrisekoop N, Westera L, Mögling R, Bregje de Boer A, et al. Maintenance of peripheral naive T cells is sustained by thymus output in mice but not humans. *Immunity* (2012) 36:288–97. doi: 10.1016/J.IMMUNI.2012.02.006

84. Tong QY, Zhang JC, Guo JL, Li Y, Yao LY, Wang X, et al. Human thymic involution and aging in humanized mice. *Front Immunol* (2020) 11:1399/BIBTEX. doi: 10.3389/FIMMU.2020.01399/BIBTEX

85. Fehniger TA, Caligiuri MA. Interleukin 15: biology and relevance to human disease. *Blood* (2001) 97:14–32. doi: 10.1182/BLOOD.V97.1.14

86. Radbruch A, McGrath MA, Siracusa F, Hoffmann U, Sercan-Alp Ö, Hutloff A, et al. Homeostasis and durability of T-cell memory-the resting and the restless T-cell memory. *Cold Spring Harb Perspect Biol* (2021) 13(7):a038083. doi: 10.1101/CSHPERSPECT.A038083

87. Siracusa F, McGrath MA, Maschmeyer P, Bardua M, Lehmann K, Heinz G, et al. Nonfollicular reactivation of bone marrow resident memory CD4 T cells in immune clusters of the bone marrow. *Proc Natl Acad Sci USA* (2018) 115:1334–9. doi: 10.1073/PNAS.1715618115/-/DCSUPPLEMENTAL

88. Di Rosa F. Maintenance of memory T cells in the bone marrow: survival or homeostatic proliferation? *Nat Rev Immunol* (2016) 16:271–1. doi: 10.1038/nri.2016.31

89. Chang HD, Radbruch A. Maintenance of quiescent immune memory in the bone marrow. *Eur J Immunol* (2021) 51:1592–601. doi: 10.1002/EJI.202049012

90. Schlub TE, Venturi V, Kedzierska K, Wellard C, Doherty PC, Turner SJ, et al. Division-linked differentiation can account for CD8+ T-cell phenotype *in vivo*. *Eur J Immunol* (2009) 39(1):67–77. doi: 10.1002/eji.200838554

frontiers | Frontiers in Immunology

TYPE Original Research
PUBLISHED 27 September 2022
DOI 10.3389/fimmu.2022.896310

EDITED BY
Francesca Di Rosa,
National Research Council (CNR), Italy

REVIEWED BY
Luigia Pace,
Italian Institute for Genomic Medicine
(IIGM), Italy
Annalisa Ciabattini,
University of Siena, Italy

*CORRESPONDENCE
Rebekka Duhen
rebekkaduhen@gmail.com

SPECIALTY SECTION
This article was submitted to Immunological Memory, a section of the journal Frontiers in Immunology

RECEIVED 14 March 2022
ACCEPTED 08 September 2022
PUBLISHED 27 September 2022

CITATION
Duhen R, Beymer M, Jensen SM, Abbina S, Abraham S, Jain N, Thomas A, Geall AJ, Hu H-M, Fox BA and Weinberg AD (2022) OX40 agonist stimulation increases and sustains humoral and cell-mediated responses to SARS-CoV-2 protein and saRNA vaccines. *Front. Immunol.* 13:896310. doi: 10.3389/fimmu.2022.896310

OX40 agonist stimulation increases and sustains humoral and cell-mediated responses to SARS-CoV-2 protein and saRNA vaccines

Rebekka Duhen[1]*, Michael Beymer[1], Shawn M. Jensen[1], Srinivas Abbina[2], Suraj Abraham[2], Nikita Jain[2], Anitha Thomas[2], Andrew J. Geall[2], Hong-Ming Hu[1], Bernard A. Fox[1] and Andrew D. Weinberg[1]

[1]Earle A. Chiles Research Institute, Providence Cancer Institute, Portland, OR, United States,
[2]Precision NanoSystems Inc, Vancouver, BC, Canada

To prevent SARS-CoV-2 infections and generate long-lasting immunity, vaccines need to generate strong viral-specific B and T cell responses. Previous results from our lab and others have shown that immunizations in the presence of an OX40 agonist antibody lead to higher antibody titers and increased numbers of long-lived antigen-specific CD4 and CD8 T cells. Using a similar strategy, we explored the effect of OX40 co-stimulation in a prime and boost vaccination scheme using an adjuvanted SARS-CoV-2 spike protein vaccine in C57BL/6 mice. Our results show that OX40 engagement during vaccination significantly increases long-lived antibody responses to the spike protein. In addition, after immunization spike protein-specific proliferation was greatly increased for both CD4 and CD8 T cells, with enhanced, spike-specific secretion of IFN-γ and IL-2. Booster (3rd injection) immunizations combined with an OX40 agonist (7 months post-prime) further increased vaccine-specific antibody and T cell responses. Initial experiments assessing a self-amplifying mRNA (saRNA) vaccine encoding the spike protein antigen show a robust antigen-specific CD8 T cell response. The saRNA spike-specific CD8 T cells express high levels of GrzmB, IFN-γ and TNF-α which was not observed with protein immunization and this response was further increased by the OX40 agonist. Similar to protein immunizations the OX40 agonist also increased vaccine-specific CD4 T cell responses. In summary, this study compares and contrasts the effects and benefits of both protein and saRNA vaccination and the extent to which an OX40 agonist enhances and sustains the immune response against the SARS-CoV-2 spike protein.

KEYWORDS

ANTI-OX40, co-stimulation, sa-RNA vaccine, T cell activation, SARS-CoV-2 vaccine, protein vaccine

Introduction

SARS-CoV-2 has been the leading cause of death in the years 2020 and 2021 in many parts of the world. The novel coronavirus-19 disease (COVID-19) has had a tremendous impact on society and daily life at present and will for years to come. To curb the spread of SARS-CoV-2, vaccines were proposed as a path to reduce viral spread, infections, and hospitalizations. Based on previous research, geared towards personalized cancer therapies, SARS-CoV-2 spike protein mRNA vaccines were quickly developed and then tested to combat COVID-19 (1–6). While other companies with differing approaches followed suit (7, 8), the ability to quickly produce a vast amount of a highly effective vaccine has made the mRNA approach the most promising and widely distributed vaccine in the world. The vaccines were initially shown to be up to 95% effective at protecting against viral infection with the original strain. Comparing the two mRNA vaccines, the Moderna vaccine (mRNA-1271) appeared to produce slightly higher antibody titers at the 6-months mark, compared to the Pfizer/BioNTech (BNT162b2) vaccine. This is not entirely surprising, given the higher dose of the Moderna vaccine (100 µg versus 30 µg, respectively). While the results of the mRNA approach seem quite promising, we still do not know the longevity of the immune responses induced by these vaccines. Data showed that B cell immunity induced by both mRNA vaccines waned over time (9) and models implied that this decrease is observed with most SARS-CoV-2 vaccines (10). Based on these findings, booster immunizations, 5 months following the primary dose, have now been approved in the USA for all adults as well as children from 5 years of age (11), and immunizations of 6 month-4 year old children were added recently, using either Pfizer or the Moderna vaccine. While mRNA vaccines have been reported to be safe, adenoviral vector vaccines were shown to cause thrombosis in a small minority of recipients (12). Furthermore, new SARS-CoV-2 variants (such as Delta and Omicron and its subvariants) are posing a constant challenge to the current vaccines; however, mRNA vaccines can quickly be adapted and modified to encode new mutated sequences.

To bind and enter cells SARS-CoV-2 uses a homotrimeric spike protein to interact with a cell surface receptor, the angiotensin converting enzyme 2 (ACE2), which triggers a cascade of events allowing membrane fusion and viral entry into cells (13). The spike protein domain crucial for this interaction is the receptor binding domain (RBD), which is present within the S1 subunit (14). B cell responses, *via* the production of neutralizing antibodies, are important to prevent the binding of SARS-CoV-2 to cells within the body. In support of this, Cavazzoni et al. showed that follicular helper T cells (Tfh) are essential for optimization of the germinal center response to SARS-CoV-2 protein vaccines and affinity maturation (15).

In addition to the humoral response, a potent antigen-specific T cell response is also important to induce long-lasting anti-viral immune memory (16). CD4 and CD8 T cells typically encounter foreign antigen presented by activated antigen presenting cells (APCs), expand, contract, and then persist as memory cells. These memory T cells can quickly respond if the host is re-infected with the pathogen. While several co-stimulatory molecules are involved and necessary to generate a strong memory T cell response, our lab and others have demonstrated that OX40 agonists not only enhance effector T cell activation, but also increase the number of memory T cells that persist long-term (17, 18). OX40, a member of the TNF receptor family (TNFRF), is upregulated on CD4 T cells (and to a lesser extent on CD8 T cells) after antigen recognition. Once expressed on the surface of T cells, engagement of OX40 with its ligand, OX40L, on activated APCs results in increased T cell expansion, effector function and survival (19). Engagement of OX40 *in vivo* by agonist antibodies or fusion proteins can lead to higher levels of T cell cytokines, aid in viral clearance, and augment anti-tumor T cell responses (20). Furthermore, OX40 stimulated T cells cooperate with ICOS expressed on the Tfh cells, to increase the humoral immune response. This leads to production of higher affinity antibodies and long-lived memory B cells, which help to sustain antibody production in future pathogen encounters (21). Hence, engaging OX40 during an ongoing immune response can increase both CD4 and CD8 T cells as well as antibody responses.

In this study, we examined whether an OX40 agonist could enhance immune responses to both protein and saRNA COVID-19 vaccine platforms. We hypothesized that this strategy would lead to stronger T cell responses as well as increased antibody titers that may help to neutralize spike protein binding to the ACE2 receptor. T cell responses and the persistence of spike-specific antibodies were examined after prime-boost vaccination. We found that injecting an OX40 agonist in both the prime and boost was the most effective way to maintain higher antibody titers over a long period of time and this approach also amplified vaccine-specific CD4 T cell responses. When compared to protein immunization the saRNA vaccine induced a much stronger spike-specific CD8 T cell response, which was enhanced by OX40 agonist administration. Similar to protein vaccination, the OX40 agonist also increased a vaccine-specific CD4 T cell response in saRNA vaccinated mice. Thus, our findings show that an OX40 agonist can enhance both, protein and saRNA COVID-19 vaccine approaches.

Results

An OX40 agonist enhances SARS-CoV-2 spike protein vaccination

Our laboratory has examined the effects of OX40 agonists enhancing T cell responses in both viral and cancer immunity for many years (22–25). We have generated a hexameric OX40L:Ig fusion protein (26), that has potent immune stimulatory effects in mice, non-human primates and humans (27). To examine the effect of OX40L:Ig to enhance protein vaccinations to SARS-CoV-2, we immunized mice with a prefusion stabilized trimeric spike protein (28). Mice were immunized with the spike protein and a TLR-4 agonist, monophosphoryl lipid A (MPLA), emulsified in Montanide ISA 51. In the boost, mice received the protein in PBS, without MPLA. Mice were treated with mouse IgG (mIgG) or OX40L:Ig in the prime vaccination, the boost vaccination or during both the prime and boost. The groups were boosted 28 days after the prime (Figures 1A, B). We first assessed the ability of the vaccine to activate T cells in the blood *via* ICOS/Ki67 upregulation on CD4 T cells, and GrzmB/Ki67 upregulation on CD8 T cells. CD4 and Treg cells were highly activated in the blood 5 days after the boost, with an average of 40.6% (± 15.9) Ki67+ICOShi CD4 T cells. CD8 T cells increased proliferation to a lesser extent and did not display a significant amount of GrzmB+Ki67+ cells (3.4% ± 2.6) (Supplementary Figures 1A, B). The activation of CD4 T cells was partially due to OX40 agonist alone in the absence of vaccine, as depicted in the OX40 agonist control group (14.0% ± 3.5). Thus, while upregulation of these activation markers on T cells could identify spike-specific T cells, we developed assays to enumerate the percentages of spike-specific T cells more accurately in the blood. Peripheral blood lymphocytes were isolated 6 weeks post-boost, and the cells were cultured with spike protein *in vitro*. After overnight incubation with the spike protein, CD40L and OX40 expression were analyzed on the surface of CD4 T cells, and PD-1 and 4-1BB on CD8 T cells (19, 29–31). CD40L and OX40 expression were detected on the surface of CD4 T cells from mice that had been injected with the OX40L:Ig fusion protein in both prime and boost, whereas the percentage of antigen-specific cells was significantly lower in animals receiving one injection of the OX40 agonist (in the prime or boost) and low in mice receiving vaccine alone (no OX40L:Ig) (Figure 1C top and D, left panel). In contrast to CD4 T cells we did not detect an increase in the percentage of 4-1BB+ CD8 T cells after ex vivo culture with the spike protein (Figure 1C bottom and D, right panel). In this short-term assay stimulation of CD4 T cells may be more efficient, as opposed to cross-presentation of peptides to CD8 T cells *via* MHC class I, which could take longer than 12-16 hrs to induce activation. Thus, we also analyzed the ability of the spike protein to induce T cell proliferation and cytokine secretion in 3-day cultures. While spike-specific CD4 T cells showed robust proliferation especially in mice receiving OX40L:Ig in the prime and boost, the CD8 T cells did proliferate, but not as vigorously (Figures 1E, F). When cytokines were assessed, the highest level of IFN-γ was observed in the supernatants of T cells isolated from mice treated with the OX40L:Ig protein in both the prime and the boost. IL-2 showed a similar pattern, albeit at much lower levels (Figure 1G). The Th2 specific cytokine, IL-4, was not detected in these cultures potentially due to the strong TLR agonist, MPLA, which tends to skew T cells towards a Th1 lineage phenotype (Supplementary Figure 1C).

TLR4 and OX40 stimulation and their effects in prime versus boost

We next addressed whether MPLA was more important for enhancing immune responses in combination with OX40L:Ig when delivered in the prime versus boost (see Figure 2A, B). Previous work from our group has shown that LPS, *via* TLR4 activation, can synergize with OX40 to enhance vaccines (17). MPLA, which also activates APCs *via* TLR4 uses TRIF signaling (instead of the MyD88 pathway) to release proinflammatory cytokines, is less toxic and skews T cells towards a Th1 phenotype (32, 33). Analyses of T cell activation in blood 5 days post-boost, showed that CD4 T cells were proliferating (Ki67+ICOS^{hi}) when MPLA was injected in the prime with the OX40 agonist delivered in the prime and boost (17.1% ± 12.3) (Supplementary Figures 2A, B). However, the OX40 agonist had a more substantial effect on proliferation/activation when MPLA was injected during the boost (35.8% ± 15.7 Ki67+ICOS^{hi} cells). In contrast, CD8 T cells were only minimally activated when examined for Ki67 and GrzmB expression (2.9% ± 2.2 and 5.9% ± 8.8) (Supplementary Figures 2A, B). Proliferation was generally greatest when MPLA was administered during the boost, for Tconv, Treg, CD8 T cells, as well as B cells (Supplementary Figure 2B). In parallel, we assessed the presence of Tfh cells in the animals, based on their role in fostering potent antibody responses. We tracked their frequencies at baseline, pre- and post-boost and found that, in line with recent studies (15, 34) CXCR5+ PD-1 positive Tfh cells are increased post vaccination, most prominently when OX40L:Ig was administered in both, prime and boost (Supplementary Figure 2C).

Mice were sacrificed 21 weeks post-boost and spleen and draining lymph nodes (drLN) were analyzed. We found increases in Tfh cells in both the drLN and spleen when OX40L:Ig was administered in prime and boost (Supplementary Figure 2D). To further analyze the spike-specific CD4 but also CD8 T cells responses we cultured the spleen and drLN cells not only with the spike protein but also overlapping 15-mers that cover the full-length protein with 2 peptide pools (S1 and S2). Peptides can bind better to MHCI (and MHCII) molecules and hence can be presented more efficiently to CD8 T cells. Supernatants from the splenocyte cultures incubated with these antigens were assessed for IFN-γ, IL-2 and IL-4 cytokine secretion. Antigen-specific IFN-γ production was significantly higher when the OX40 agonist was injected in both the prime and boost independent of whether MPLA was delivered in the prime or the boost (Figure 2C). Levels of IL-2 were also increased in the same groups, but IL-4 was very low to undetectable in all groups (Figure 2C and Supplementary Figure 2E).

We next assessed spike-specific T cell proliferation *via* CFSE dilution assay. This assay allowed us to determine proliferation in the absence of endogenous APCs that might harbor spike-

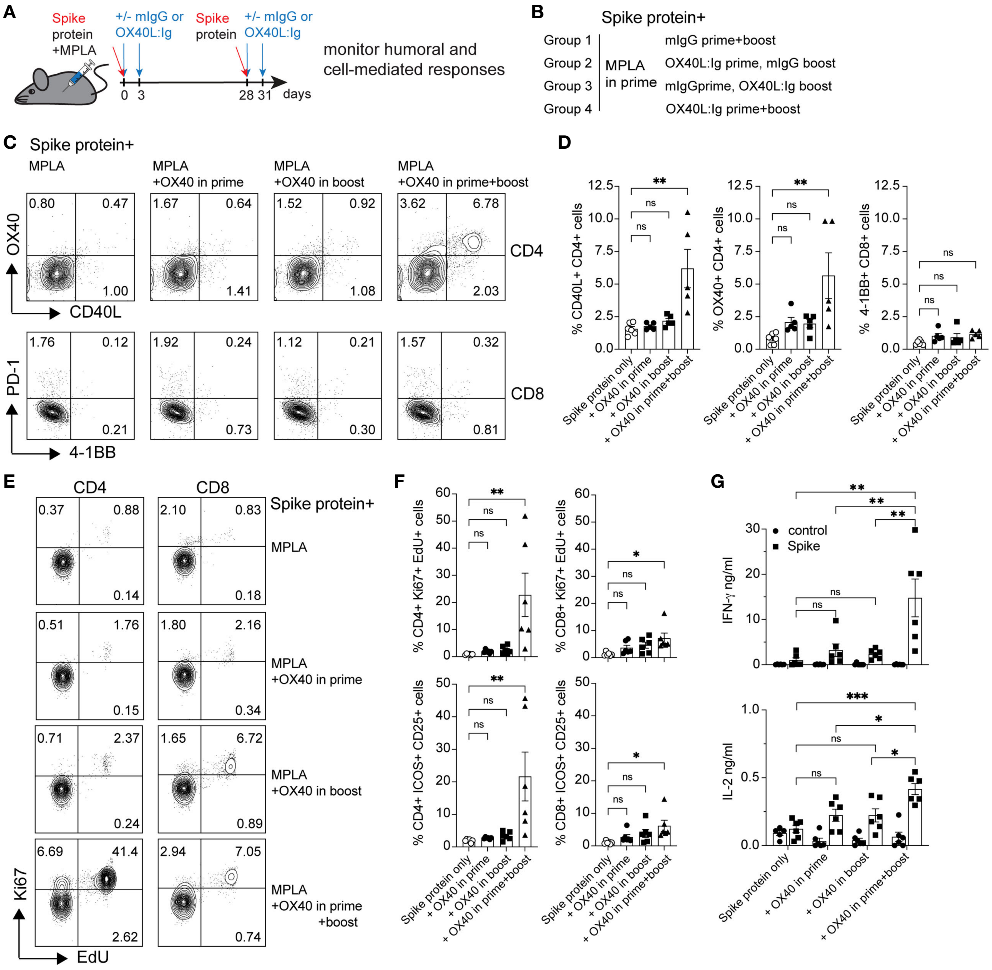

FIGURE 1

OX40 agonist enhances CD4 and CD8 antigen-specific T cell immunity to spike protein vaccination. Groups of mice were immunized with the SARS-CoV-2 spike protein emulsified in Montanide ISA 51 and MPLA (present in the prime), with mouse IgG (mIgG) or with OX40L:Ig injection in the prime, in the boost or both. Cells were isolated from the blood at 10 weeks post-immunization and cultured in the presence of recombinant spike protein. **(A)** Schematic representation of immunization with the spike protein and timing of the OX40L:Ig injections. **(B)** Description of the experimental group layout. **(C)** Expression of OX40 and CD40L on CD4 T cells (top) and PD-1 and 4-1BB on CD8 T cells (bottom) by flow cytometry after overnight incubation (16 hrs) with the spike protein. The dot plots shown are from representative mice in each group. Numbers in each quadrant indicate percent positive cells. **(D)** Summary of CD40L- and OX40-expressing CD4 T cells and 4-1BB-expressing CD8 T cells in all experimental groups. **(E)** Cells were cultured for 3 days in presence of antigen and EdU was added for 18 hrs to reveal replicating cells. Numbers in each quadrant indicate percent positive cells. **(F)** Ki67 expression and EdU incorporation (top panels) and ICOS/CD25 expression (bottom panels) were analyzed to assess T cell proliferation and activation in CD4 and CD8 T cells in all groups. **(G)** Supernatants of the 3-day cultures (blood) were assessed for the presence of IFN-γ and IL-2 in absence or presence of spike protein. N=6 animals per group, 1 of 2 experiments is shown. Each individual symbol in the bar graphs represents a single mouse. In **D**, **F** and **G**, bars indicate mean ± SEM. One-way ANOVA with Tukey's multiple-comparisons test. *P<0.05, **P<0.01, ***P<0.001, ns, not significant.

specific peptides. T cells were purified and pooled from each treatment group and cultured with irradiated splenocytes isolated from naïve mice, pulsed with the spike protein or peptides. CFSE dilution of CD4 T cells 4 days after antigen stimulation revealed that proliferation was amplified in mice injected with the OX40L:Ig protein. CD4 T cell proliferation was greatest when mice received the OX40 agonist in both the prime and boost. Mice receiving vaccine with two doses of OX40L:Ig displayed an 18-30-fold increase compared to vaccine/MPLA alone (Figures 2D, E). CD8 T cells proliferated more vigorously in the presence of peptide pools and proliferated the strongest when MPLA was administered in the prime with two doses of the OX40 agonist. The fold-increase of CFSE dilution in CD8 T cells (OX40L:Ig in prime and boost versus control mice) was lower (2 to 3-fold) than in CD4 T cells (Figure 2E).

In summary, MPLA increased T cell activation and proliferation in the blood when delivered after the boost and this effect was accentuated when combined with the OX40L:Ig

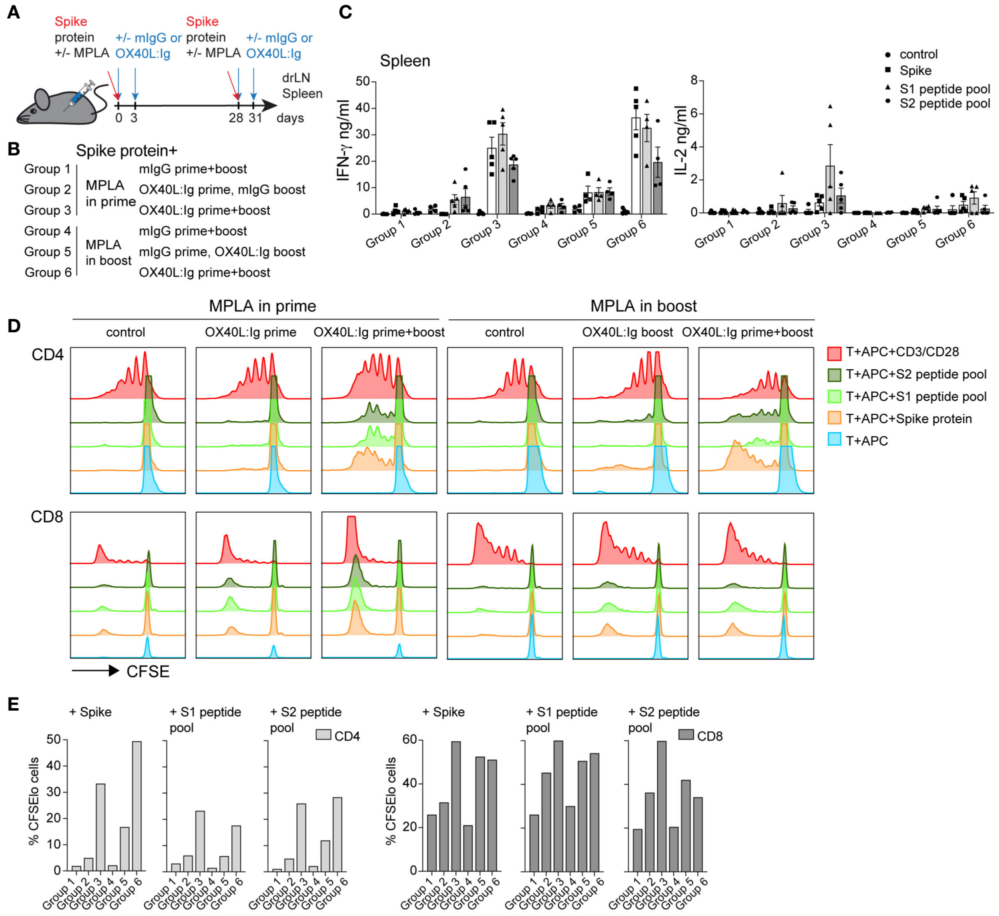

FIGURE 2

OX40 agonist enhances vaccine-specific T cell responses independent of whether a TLR4 agonist was administered in the prime or the boost. Groups of mice were immunized with the SARS-CoV-2 spike protein emulsified in Montanide ISA 51 with MPLA injected in the prime or boost. In groups 1-3, mIgG or OX40L:Ig were administered in the prime with MPLA or OX40L:Ig was given in both prime and boost. Groups 4-6 received MPLA in the boost with mIgG or OX40L:Ig or OX40L:Ig was given in both prime and boost. **(A)** Schematic representation of immunization with the spike protein, MPLA and timing of the OX40L:Ig injections. **(B)** Description of the experimental group layout. **(C)** Secretion of IFN-γ and IL-2 cytokines examined in the supernatant of splenocytes cultured for 3 days alone, in presence of spike protein, S1 or S2 spike peptide pools. Each data point represents an individual animal. Bars indicate mean ± SEM. **(D)** CFSE-labeled splenic T-cells, were cultured with irradiated APCs alone, pulsed with spike protein, or S1 and S2 spike peptide pools. CD3/CD28 stimulation was used as positive control for these experiments. Histograms show the cell division by dilution of CFSE as analyzed by flow cytometry after 4 days of culture, cells were gated on either CD4 or CD8 T cells. **(E)** Bar graphs showing the percentage of CFSE^{lo} CD4 and CD8 T cells in 4-day cultures after spike antigen stimulation. 1 of 2 experiments is shown in **(B–D)**.

protein. However, vaccine-specific CD4 and CD8 T cell responses were elevated when the OX40 agonist was injected in both the prime and boost, independent of whether MPLA was administered in the prime or the boost.

OX40 stimulation increases the longevity of vaccine-specific antibody responses

Vaccine-specific memory T and B cell responses are important to ensure long-term protection against the viral challenge. CD4 T cells help elicit and mature a potent B cell response which results in antibody production, affinity maturation and formation of long-lived plasma cells. The OX40L:Ig fusion protein greatly increased the vaccine-specific CD4 T cell response and induced Tfh cells (Figures 1, 2), hence we hypothesized that vaccine-specific antibodies would also be increased by OX40 stimulation. We tested this hypothesis by assessing antibodies after serial blood draws in the experiments described above, to monitor the magnitude and kinetics of vaccine-specific antibodies. Supplementary Figures 3A, B illustrate the presence of spike- and RBD-specific antibody titers in the serum, which persisted up to 15 weeks post-boost. Spike- and RBD-specific antibody titers were observed in all mice immunized with the spike protein and when the OX40 agonist was injected in both the prime and boost, antibody levels were higher and more sustained (Supplementary Figures 3A, B, bottom; C, right). Quantification of antigen-specific antibodies using $\log_{10}$EC50 values shows the strongest antibody responses were found 2 weeks post-boost and the titers remained elevated when the OX40 agonist was injected in both the prime and boost (Supplementary Figure 3C). We next explored antibody titers in spike protein vaccinated mice receiving MPLA in the prime versus boost w/wo an OX40 agonist (pre-boost, 2 weeks, and 21 weeks post-boost). In mice immunized with spike protein + MPLA (no OX40 agonist) total IgG levels were relatively low 2 weeks post-boost and returned to pre-boost levels by 25 weeks. Spike protein immunization in combination with MPLA + OX40 agonist in the prime or MPLA + OX40 agonist in the boost showed longer-lived antibody responses (Figure 3A). Interestingly, when MPLA was delivered in the prime or boost, with two injections of the OX40 agonist, the spike-specific antibody levels did not return to prime levels and remained elevated for 25 weeks (Figure 3A, right). Figure 3B displays the change in titers over time.

Since MPLA is known to skew the immune response towards a Th1 phenotype, we further dissected the antibody isotype composition in these treatment groups. We assessed whether IgG1 (mainly Th2 response) or IgG2a (mainly Th1 response) isotypes predominated in any of these conditions. Analyses of all 6 groups showed that spike-specific IgG1 antibody levels were similar under most conditions, with MPLA/OX40 agonist in prime/boost groups displaying highest long-lived antibody titers post-boost (Figure 3C). In accord with a previous report (35), MPLA as an adjuvant in the prime increased IgG2a spike-specific antibodies, whereas levels remained lower when MPLA was injected in the boost, w/wo OX40 agonist administration (Figure 3D). IgG2a titers were comparable when the OX40 agonist was administered in the prime and boost, independent of whether MPLA was injected in the prime or boost and the OX40 agonist increased the longevity of the IgG2a response (Figure 3D). To address whether the serum antibodies had the ability to interfere with the interaction between ACE2 and the spike protein, we assessed their neutralizing activity. In line with our results above, the most potent activity was observed when OX40L:Ig was given in prime and boost – with MPLA in the prime (Figure 3E).

In conclusion, we found that OX40 agonist injections strongly augmented the magnitude and persistence of the vaccine-specific antibodies in mice vaccinated with the spike protein.

OX40L:Ig injection when combined with a booster immunization amplifies vaccine-specific T cell responses

While spike-specific memory T cell responses were detected in most mice after prime-boost vaccination, we wanted to examine the effect of a booster vaccination in mice 7 months post-initial immunization. In the booster experiment, all mice were injected with the spike protein. The OX40 agonist was given to mice that had not previously received any OX40 stimulation and to mice that were previously injected with OX40L:Ig in both the prime and boost. The groups that received OX40L:Ig in either the prime or boost initially, received only mouse IgG in the re-boost. Figures 4A, B illustrate the layout of this experiment. Supplementary Figure 4A depicts early activation of Tconv, Treg and CD8 T cells 5 days post-booster immunization, and while OX40L:Ig fusion protein did increase activation, the vaccine alone also increased T cell activation. Interestingly, CD8 T cells proliferated more vigorously than after the initial prime/boost (Supplementary Figure 4B). We then assessed the antigen-specific T cell response in the spleen and drLNs of mice receiving the booster immunization. Mice were sacrificed 7 weeks after the booster and analyzed for spike protein-specific CD4 and CD8 T cells. In the short-term antigen-specific assays, both CD40L and OX40 were upregulated on CD4 T cells, in the drLN and spleen. Mice that received the OX40 agonist in both the prime/boost as well as in the booster immunization had the greatest vaccine-specific T cell response (Figures 4C, D). T cells isolated from animals receiving anti-OX40 in the boost and mIgG in the booster responded but to a lesser extent than the other groups (Figures 4C, D). The magnitude of the antigen-specific CD8 response was lower overall compared to CD4 T cells, but higher numbers of antigen-specific CD8 T cells were found in the spleen than in the drLN and OX40L:Ig accentuated this increase, as revealed by 4-1BB upregulation (Figure 4D, bottom right). T cell activation and proliferation were then assessed in cells cultured for three days in the presence or absence of the spike protein. CD4 T cells proliferated strongly in both drLN and spleen cultures, while CD8 T cell responses were lower in both tissues (Supplementary Figure 4C). We also examined cytokines that were produced by these T cells and found increased spike-specific IFN-γ in most conditions, compared to no antigen controls. Group C (no OX40L:Ig in the booster) had the lowest cytokine production, which was a consistent finding when compared to the other assays (Figure 4D). The greatest cytokine production was found in T cells isolated from mice receiving OX40 stimulation with the booster (groups B&D) (Figure 4E).

Thus, boosting mice increased the vaccine-specific T cell responses especially in mice that were injected with an OX40 agonist in the initial prime/boost and adding OX40 stimulation in the booster appears to further increase the vaccine-specific CD4 and CD8 T cell responses.

OX40 agonist stimulation increases spike-specific T cell responses to a self-amplifying mRNA vaccine

RNA vaccines have been approved for use in humans and have elicited both, vaccine-specific antibodies, and CD4 and CD8 T cell responses (16). Furthermore, in contrast to protein vaccines, mRNA vaccines have the potential for rapid, scalable

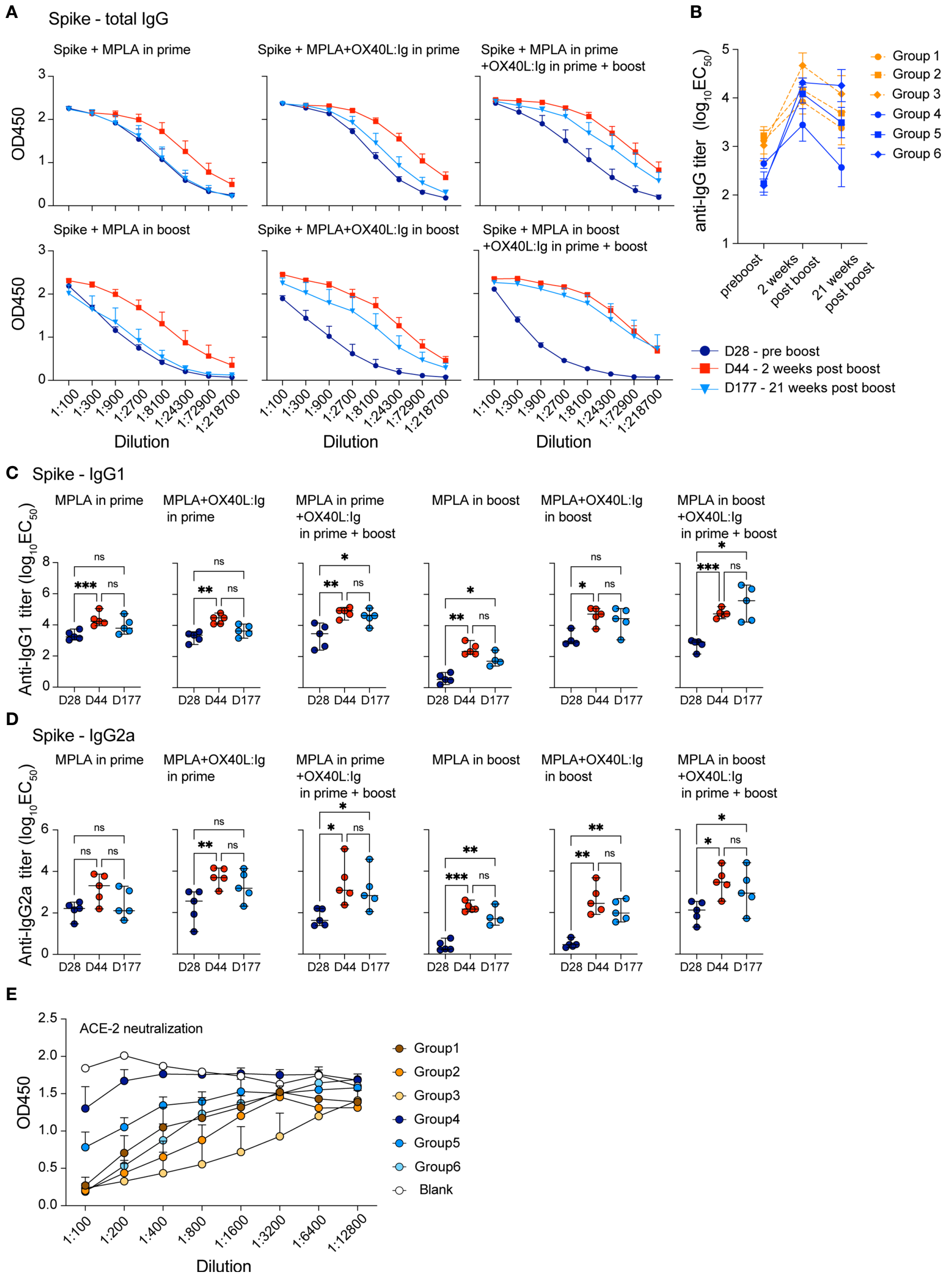

FIGURE 3
OX40 agonists increase the magnitude and longevity of spike vaccine-specific antibodies. Experimental scheme and groups are outlined in Figures 2A, B. Mice were bled on day 28, prior to the boost (indigo circles); day 44, 2 weeks post-boost (red squares); day 177, 21 weeks post-boost (blue triangles), and antibody titers to the spike protein were assessed. **(A)** shows total IgG titers against the spike protein. Values on the y-axis indicate absorbance measured at 450 nm. D=day **(B)** shows the $\log_{10}(EC_{50})$ titers of all groups at each timepoint pre boost, two weeks post boost and 21 weeks post boost **(C)** shows the $\log_{10}(EC_{50})$ titers of IgG1 isotype spike-specific antibodies and **(D)** shows the $\log_{10}(EC_{50})$ titers of IgG2a isotype spike-specific antibodies. C and D, one-way ANOVA with Tukey's multiple-comparisons test. $*P<0.05$, $**P<0.01$, $***P<0.001$, ns, not significant. **(E)** Data from the neutralization assay performed using the ACE2-Fc protein and supernatants from all groups 7 weeks post boost. All samples were diluted 1:100 and serially diluted 1:3 or 1:4 eight times in the assay and the serial dilutions are indicated by connecting lines.

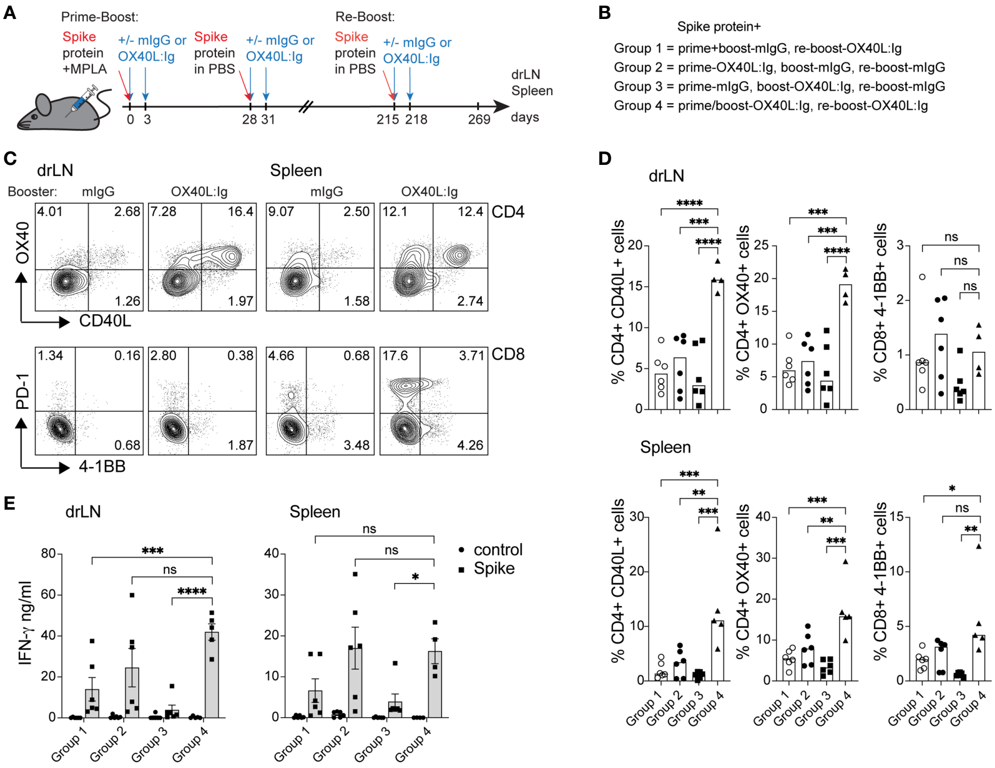

FIGURE 4

Booster immunization in combination with an OX40 agonist can increase T cell activation, antigen-specific CD4 T cells, and cytokine production. Mice initially immunized with the spike protein+MPLA in the prime received the OX40L:Ig in prime, boost or both. Animals were then boosted 30 weeks later. **(A)** Schematic representation of the booster immunization with spike protein w/wo OX40L:Ig injections. **(B)** Description of the experimental group layout. **(C, D)** Cells from drLN and spleen were isolated 7 weeks after the booster and examined for antigen-specific CD4 and CD8 T cells. **(C)** Flow cytometric analysis of the expression of CD40L and OX40 on CD4 T cells (top) and PD-1 and 4-1BB on CD8 T cells (bottom) after overnight incubation with the spike-protein (one representative mouse from each group is shown). Numbers in each quadrant indicate percent positive cells. **(D)** Bar graphs showing the summary of the percentages of CD40L+ CD4, OX40+ CD4 and 4-1BB+ CD8 T cells in the drLN and spleens of mice receiving booster immunizations ± OX40L:Ig. **(E)** Cytokine assessment for IFN-γ and IL-2 in the supernatant of 3-day cultures from drLN and spleen. N=5-6 animals per group, 1 of 2 experiments is shown. Each individual symbol in the bar graphs represents a single mouse. Bars indicate mean ± SEM. One-way ANOVA with Tukey's multiple-comparisons test. $^*P<0.05$, $^{**}P<0.01$, $^{***}P<0.001$, $^{****}P<0.0001$, ns, not significant.

manufacturing, owing to the high yields of *in vitro* transcription reactions (36). Hence, we wanted to test whether an OX40 agonist could also enhance immune responses to RNA vaccines. To test this hypothesis, we immunized mice with a self-amplifying mRNA, encoding an alphaviral replicase (to enable replication upon uptake in the cell cytoplasm) and the SARS-CoV-2 spike protein encapsulated in lipid nanoparticles (LNPs). SaRNA can provide high expression levels and simultaneously induce a strong innate immune response. Mice received two injections of 1 µg of saRNA (in prime and boost), 28 days apart, with or without the OX40L:Ig fusion protein. Proteins encoded by saRNA vaccines can take a few days to be produced and expression can be maintained for up to a month (37). Hence, the initial experiment assessed the optimal timing of OX40 agonist administration after saRNA vaccination (days 2/5, 4/7 and 7/10) (Figures 5A, B). Stimulation with the OX40L:Ig agonist, in absence of the saRNA vaccine, served as a negative control for these experiments. The activation status of T cells stimulated with the saRNA w/wo OX40 agonist was initially assessed 5 days after the boost. Mice that received OX40 stimulation at days 2/5 had the greatest level of CD4 T cell activation (41.27% ± 4.1, ICOS+Ki67+) and expression of these two makers declined in mice receiving the OX40 agonist at later timepoints (Figures 5C, D). The CD8 T cells expressed very high levels of GrzmB and Ki67 (26.42 ± 3.2, GrzmB+Ki67+) when the vaccine was combined with OX40 stimulation especially at days 2/5 after immunization (Figures 5C, D). Interestingly, this GrzmB+Ki67+ CD8+ cell phenotype was not observed when mice were immunized with protein (Supplementary Figures 1A, 2A). Since the activation data suggested that spike-specific CD8 T cell responses may be increased with the saRNA approach, we assessed the presence of spike-specific CD8 T cells after saRNA vaccination. A p:MHCI tetramer was used to quantify the vaccine-specific CD8 T cell response (an immunodominant

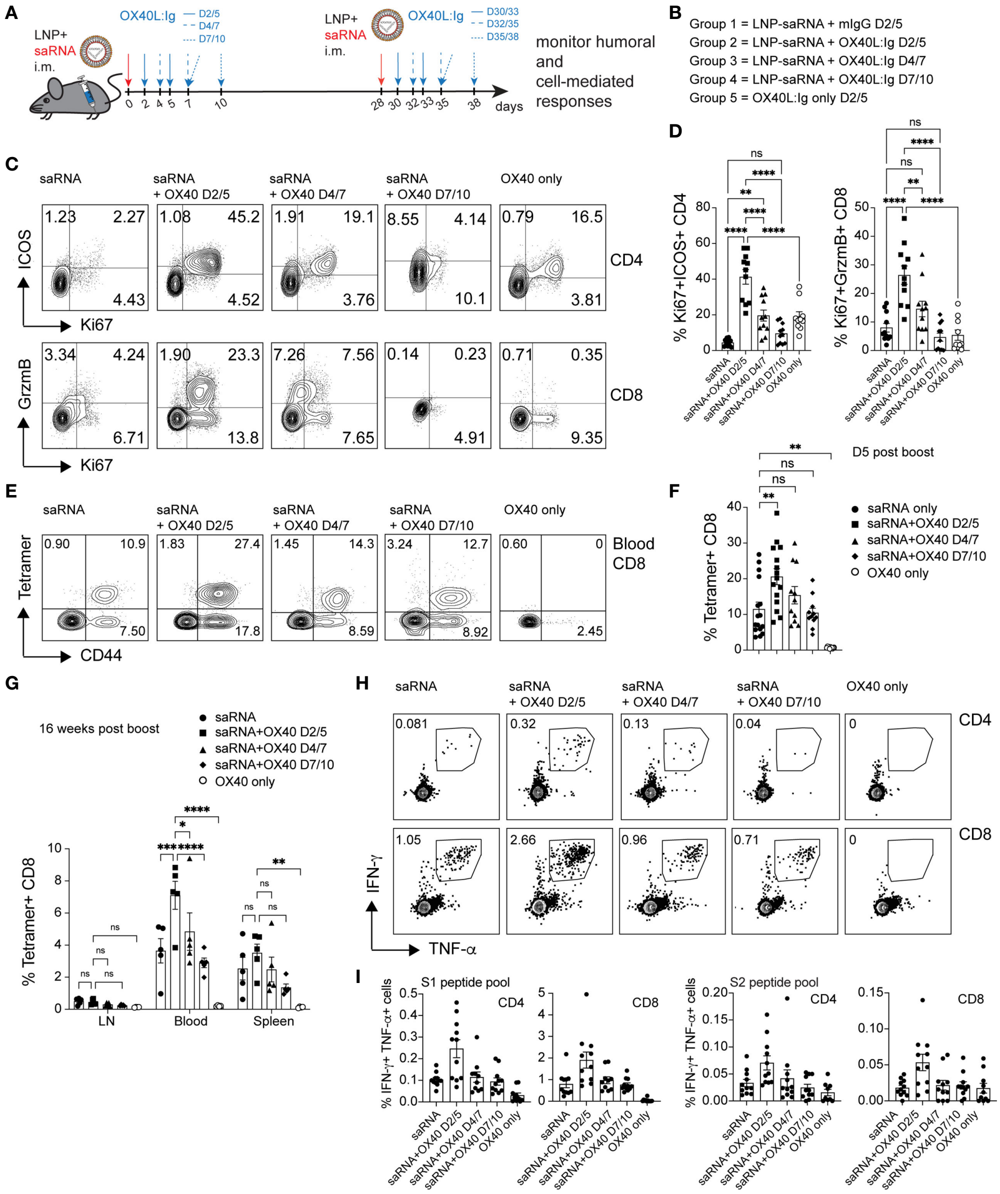

FIGURE 5

OX40 agonists enhance T cell responses in mice immunized with a self-amplifying RNA vaccine. Groups of mice were immunized i.m. with self-amplifying RNA (saRNA), encoding the spike-protein, encapsulated in lipid nanoparticles (LNPs). Mice received the vaccine alone or with OX40 stimulation on days 2/5, days 4/7 or days 7/10 post-vaccination. **(A)** Schematic representation of the timing of the administration of the saRNA vaccine w/wo OX40L:Ig. **(B)** Description of the experimental group layout. D=day **(C)** Flow cytometric assessment of the upregulation of ICOS/Ki67 on peripheral blood CD4 T cells and GrzmB/Ki67 on CD8 T cells five days after the 1st OX40L:Ig dose. The dot plots shown are from representative mice in each group. Numbers in each quadrant indicate percent positive cells. (D) Summary of the percentage activated Ki67+ICOS+ Tconv CD4 cells and Ki67+GrzmB+ CD8 T cells in blood. Bars indicate mean ± SEM. **(E)** Flow cytometric assessment of the frequency of tetramer+ CD44+ CD8 T cells 5 days post-boost (in each group). Each plot is from a representative animal per group. Numbers in the upper two quadrants represent the tetramer+ cells. **(F)** Summary of the data in **(E)**. **(G)** Summary of tetramer+ T cells in blood, LN and spleen, 16 weeks post-immunization (day118). **(H)** Mice were euthanized at day124. Frequency of IFN-γ+ and TNF-α+ CD4 and CD8 T cells among splenocytes after *in vitro* stimulation with the S1 peptide pool. One representative animal per group is shown. The outlined box indicates the IFN-γ+TNF-α+ double-positive cells. **(I)** Summary of the frequency of IFN-γ+TNF-α+ CD4 and CD8 T cells stimulated with either S1 or S2 peptide pools *in vitro*. Bar graphs show the mean frequencies ± SEM per group in D, F, G and **(I)** One-way ANOVA with Tukey's multiple-comparisons test. *P<0.05, **P<0.01, ***P<0.001, ****P<0.0001, ns, not significant. N=10-11 animals per group in **D, F, G**, and **(I)** 1 of 2 experiments is shown.

epitope of the spike protein in C57BL/6 mice) (38). Tetramer+ CD8 T cells were enumerated in peripheral blood 5 days after the boost OX40L:Ig injection. 11.5% (± 1.9) of peripheral blood CD8 T cells were tetramer+ in mice injected with saRNA vaccine alone. Mice injected with the OX40 agonist on days 2/5 showed an increase in tetramer$^+$ CD8 T cells (20.58% ± 2.2) compared to mice receiving vaccine alone. When the OX40 agonist was delivered at later time points the enhancement of vaccine-specific responses was lower (15.4% ± 2.4 and 10.44 ± 1.3 tetramer+ cells, respectively) (Figures 5E, F). The same analysis was repeated 16 weeks post-vaccination, when the mice were sacrificed, to monitor contraction of the CD8 T cell response in the LNs, spleen, and blood. Total memory CD8 T cells were lower in the lymph node (1.3%) and ranged on average between 9-13% in blood and spleen, with no significant differences between the groups (Figure 5G). As for tetramer$^+$ CD8 T cells (16 weeks post-vaccine), a similar trend to day 5 post-boost was observed. Mice injected with OX40 agonist at days 2/5 still contained the highest percentage of tetramer$^+$ CD8 T cells (2-fold above vaccine alone). However, compared to day 5 post-boost in the blood, the cells had contracted approximately 4-fold in each group (Figure 5G and Supplementary Figure 5A). Interestingly, when the frequency of spike-specific tetramer$^+$ CD8 T cells in mice immunized with the protein vaccine were evaluated in peripheral blood at the same time point (16 weeks post-boost) little to no tetramer$^+$ CD8 T cells were detected (Supplementary Figure 5B). Splenocytes followed a similar trend, but LNs contained much lower percentages of tetramer$^+$ CD8 T cells (Figure 5G and Supplementary Figure 5A). Production of IFN-γ and TNF-α was also assessed upon stimulation with spike peptide pools in the saRNA vaccinated mice. Both CD4 and CD8 T cells produced IFN-γ and TNF-α and the highest percentage of IFN-γ^+TNF-α^+ positive cells were found in the day 2/5 OX40 agonist treated group (Figure 5H). In general, the frequency of IFN-γ secreting cells was higher in CD8 T cells when compared to CD4 T cells (Figure 5I). Proliferation of CD4 and CD8 vaccine-specific T cells was also assessed by CFSE dilution. Mice injected with saRNA alone increased spike protein-induced CFSE dilution in CD4 and CD8 T cells compared to the negative control group (OX40 stimulation alone). When the OX40 agonist was delivered on days 2/5 and 4/7 there was an increase in the percentage of T cells that diluted CFSE when compared to mice receiving vaccine alone (Supplementary Figures 5C, D). Similar to the results from the protein vaccine experiment (CFSE dilution; Figures 2D, E), the OX40L:Ig induced the greatest fold-increase in spike-specific CD4 proliferation. It also increased CFSE dilution in CD8 T cells from mice vaccinated with saRNA, but to a lesser extent than in the CD4 cells. Interestingly, the magnitude of the CD4 response (maximum percentage of diluted cells) was a slightly higher in the protein versus saRNA vaccinated mice. Finally, the serum antibody levels in saRNA immunized groups were examined, prior to the boost and two- and 12-weeks post-boost. We found that, in contrast to the protein vaccine, spike-specific antibodies generated with the saRNA only and saRNA + OX40 stimulation at days 2/5 or 4/7 were predominantly of the IgG2a isotype, with lower IgG1 titers (Supplementary Figure 5E). OX40 agonist delivered late after vaccination at days 7/10 had almost no effect on either isotype and titers were low overall.

Taken together, the data suggests that the saRNA vaccine approach generates a strong Th1-type response with long lasting, potent spike-specific CD8 T cells and this response can be enhanced by OX40L:Ig administration shortly after immunization.

Discussion

The SARS-CoV-2 pandemic has been ongoing for two and a half years and in several countries individuals have received two vaccine doses, followed by one or two boosters. In order to reduce or eliminate the need for recurrent immunizations we tested whether an OX40 agonist would increase the immune response to a SARS-CoV-2 vaccine. This idea has been supported by previous publications showing that OX40 agonists can have strong immune adjuvant effects in the generating vaccine-specific T cells in mice, monkeys, and humans (22, 25, 39). OX40 agonists have been injected systemically to hundreds of cancer patients with low toxicity (22, 23), hence this is a strategy that could potentially be translated to human vaccines. Several studies suggest that co-stimulation *via* OX40 in a vaccine setting can not only increase CD4 T cell activation but can also boost CD8 T cell responses and increase secretion of vaccine-specific antibodies (24, 40, 41). The timing of OX40 agonist administration combined with vaccination has been explored, with findings showing that OX40 agonist injections delivered during the vaccine boost (14 days after a priming immunization) resulted in increased long-lived polyfunctional CD4 and CD8 T cells (39). However, another study showed that if the OX40 agonist was delivered after protein vaccination or viral challenge it could dampen immune responses (42).

In this study, we found that an OX40L:Ig fusion protein greatly increased vaccine-specific CD4 T cell responses and augmented spike-specific antibody secretion when injected with a protein vaccine. Interestingly, the saRNA vaccine was much more effective at generating spike-specific CD8 T cells, which was accentuated by the OX40L:Ig agonist.

Based on the differences observed in the publications discussed above, we examined the timing of OX40 agonist administration (OX40L:Ig in prime, boost or both) in combination with a spike protein vaccine. Panagioti et al. observed that if an OX40 agonist was injected during the booster phase of vaccination, it was more efficient to enhance T cell immunity than if it were administered during the priming phase (39). When we analyzed T cell activation 5 days after the boost, the OX40 agonist administered with the boost induced stronger proliferation in the CD4 T cell compartment than when given during the prime. However, contrary to the Panagioti manuscript, we detected the greatest increase of vaccine-specific T cell percentages when the OX40 agonist was injected in both the prime and the boost (Figures 1 and 2B). Differences between the two studies included the use of synthetic long peptides for vaccination by Panagioti et al, while we vaccinated with a whole protein; the time interval between prime and boost, which was 14 days, whereas in our study it was 28 days; and lastly we used the OX40L:Ig protein versus an OX40 agonist antibody (OX86) used in their study.

Successful SARS-CoV-2 vaccines should elicit long-lasting protection (via memory T and B cell responses), which will allow us to live with this virus in an endemic phase. In this study we explored how to increase the longevity of the vaccine-specific immune response by co-administration of an OX40 agonist with two different SARS-CoV-2 vaccines. We assessed the presence of spike-specific T cells and antibodies in mice several months after prime/boost immunizations w/wo the OX40L:Ig protein. Injecting the OX40 agonist in both the prime and the boost delivered the greatest numbers of functional spike-specific CD4 T cells as well as Tfh cells. Similarly, mice subjected to two rounds of OX40 agonist stimulation showed the greatest increase in spike- and RBD-specific antibody titers in their serum, and these levels were sustained for 6 months. This is an important observation because antibody responses elicited by the currently approved vaccines wane 3-6 months after the boost immunization (9). Thus, injecting the OX40 agonist in the prime and boost appears to increase the longevity of vaccine-specific immunity, which would potentially alleviate the need for repeated booster immunizations.

When vaccinated mice were re-challenged with a booster immunization 7 months later, they mounted an increased T cell response. OX40 engagement further increased the levels of activated and proliferating CD4 and CD8 T cells after the booster (Supplementary Figure 4). When analyzing the spike-specific immune responses in drLN and spleen several weeks after the booster it was clear that delivering the OX40L:Ig protein with all immunizations (prime/boost/booster) elicited the highest levels of spike-specific CD4 and CD8 T cells. These data suggest that an OX40 agonist added to a booster vaccine could enhance spike protein-specific immunity in individuals already immunized against the spike protein.

While mice injected with the spike protein vaccine combined with an OX40 agonist elicited a strong vaccine-specific antibody response (Figure 3), the CD8 T cell response was not very robust. Since RNA vaccines are known to elicit a potent CD8 T cell response, we determined whether an OX40 agonist could enhance CD8 responses when combined with a SARS-CoV-2 mRNA vaccine (16, 43, 44). mRNA vaccines have some advantages over protein vaccines, as they are easier and faster to produce as well as scalable for large immunization studies (36). In particular for this study we tested whether an OX40 agonist could enhance a self-amplifying RNA vaccine which contains an alphaviral replicase together with a gene of interest (spike protein) that is encapsulated in lipid nanoparticles (45). The saRNA vaccines require a much lower dose (0.1-1 µg/dose) compared to “traditional” mRNA vaccines (30-100 µg/dose), while at the same time leading to expression of higher protein levels (37). In our experiments, the saRNA-LNP vaccine was able to generate a strong vaccine-specific CD8 T cell response when compared to protein vaccination, and the antibody titers were biased towards a Th1-type response. Of importance for this study, the OX40 agonist was able to increase T cell activation and the magnitude of antigen-specific CD4 and CD8 T cell responses. In particular, the vaccine-specific CD8 T cell response elicited by the saRNA vaccine alone was strong (20% tetramer+ cells) at the peak of activation and the OX40-agonist increased it approximately 1.5 to 2-fold. The vaccine-specific CD4 T cell response to the saRNA vaccine was lower than with protein vaccination; however, the OX40-agonist did increase the CD4 T cell response to the saRNA vaccine as assessed by both proliferation and cytokine production (Figure 5).

It is clear from these studies that OX40 agonists can enhance vaccine-specific immune responses for both protein and RNA vaccines. In particular, both the magnitude and longevity of vaccine-specific responses were increased by the OX40L:Ig fusion protein especially when delivered both in the prime and the boost. A recent study combined an OX40 agonist antibody with a Sindbis alphavirus vector that expressed the spike protein and they found an enhancement of T cell activation, cytokine production and antibody titers (46). In most experiments however, mice were analyzed at only 7 days after the prime for metabolic and transcriptional changes, effects on T cell subsets, secretion of cytokines and cell surface markers. The authors assessed activation of total T cell populations with little distinction for vaccine-specific T cells, which differs from our study. Also, in this study we evaluated the longevity of the B and T cell responses, which was not emphasized in their study.

While both studies show that OX40 agonists can enhance COVID-19-specific vaccines, injecting a protein OX40 agonist is not practical for delivery for human vaccines. Engineering the OX40L:Ig fusion protein into viral vaccine vectors or adding the OX40L:Ig mRNA into the same lipid nanoparticles as RNA vaccines would be an economical and practical approach that will be pursued by our group in the future.

The data obtained with both protein and saRNA vaccines in these studies, suggest that a heterologous prime/boost approach may be beneficial to increase the lack of a CD8 response in the protein setting. Heterologous prime/boost vaccinations have been performed in humans for the spike protein (e.g. adenoviral vector vaccines + mRNA vaccines, or mRNA-Pfizer, followed by mRNA-Moderna) and this approach has officially been accepted by the government authorities. A heterologous and efficient prime-boost setting has been reported decades ago for HIV vaccines (47) and has since gained momentum for a wide range of pathogens. Heterologous vaccination can foster a broader array of immune responses (e.g. Th1 versus Th2), increase the effectiveness of existing vaccines and induce more immunogenic responses. It can lead to higher neutralizing antibody titers and more potent T cell responses compared to using the same vaccine in the prime-boost setting (48). While this suggests that heterologous prime/boost may lead to superior immune responses, careful analysis of combined approaches in the COVID-19 vaccine setting, is lacking. Our data suggest that there are differences in the potency of generating humoral and cell-mediated immune responses with the protein and RNA vaccine approaches. Of course, there are limitations - the assessment of the T cell and antibody responses in mice does not always correlate with level of protection in humans. Therefore, future experiments will combine both vaccine approaches, together with increased T cell costimulation. In summary, we observed differential immune stimulating effects when comparing protein versus saRNA SARS-Cov2 vaccines and it is clear that OX40 agonists can enhance immunity to both approaches.

Material and methods

Animals

C57BL/6 mice were purchased from the Jackson Laboratory. All animals were bred and maintained under specific pathogen-free conditions in the Providence Portland Medical Center (Portland, OR) animal facility and all experiments were performed in accordance with the guidelines of the Institutional Animal Care and Use Committee. Only females were used for the COVID vaccination studies. Control polyclonal mouse IgG was purchased from BioXCell. Anti-OX40L:Ig mAb was produced by MedImmune/AstraZeneca. Animals were randomly assigned to treatment cohorts. No outliers were excluded from the data presented.

Synthesis of self-amplifying mRNA encoding the SARS-CoV-2 spike protein

The codon-optimized gene, encoding the full-length spike protein of SARS-CoV-2 with a single dominant mutation was synthesized and cloned into Precision NanoSystem's proprietary custom self-amplifying mRNA cloning vector. The vector incorporates non-structural proteins encoding VEEV alphavirus replicases and a strong sub-genomic promoter with an engineered multiple cloning site. The cloned codon-optimized genes were synthetically constructed and amplified in Escherichia coli and purified using a Plasmid Maxi kit (QIAGEN). High quality saRNA was synthesized using a proprietary manufacturing process developed by PNI. Briefly, the plasmid DNA was linearized by restriction digest at the 3′ end of the saRNA sequence. Next, the linearized DNA templates were transcribed into RNA using the cell-free *in vitro* transcription and enzymatic capping method described by Geall A et al. (49).

Formulation of lipid nanoparticles encapsulating saRNA

A lipid mix was prepared at a concentration of 37.5 mM in ethanol using a proprietary ionizable lipid, 1,2-distearoyl-sn-glycero-3-phosphocholine, cholesterol and 1,2-dimyristoyl-rac-glycero-3-methoxypolyethylene glycol-2000. saRNA was diluted to a concentration of 252 µg/ml in RNA formulation buffer at pH 4. Lipid mix in ethanol and saRNA in aqueous buffer were mixed to form lipid nanoparticles using a NanoAssemblr® Ignite™ NxGen™ microfluidic mixer at a flow rate ratio of 3:1 (saRNA to lipids), total flow rate of 12 ml/min and start waste volumes of 0.35 ml and end waste volume of 0.05 ml. The LNP were then diluted 40× in PBS (Ca^{2+} and Mg^{2+} free) and further processed using Amicon® ultra 15 10kDa MWCO units (EMD Millipore) filtration technique at 2000 x g for 30 min at 4°C to remove ethanol. The final LNPs were mixed with a PNI proprietary cryobuffer (1:1 V/V) and stored at -80°C. The LNPs were thawed at RT before immunization of animals.

LNP characterization

After preparation of LNPs as described above, particle size (hydrodynamic diameter of the particles) was determined by Dynamic Light Scattering (DLS) using a ZetaSizer™ Nano ZS™ (Malvern Instruments, UK). He/Ne laser of 633 nm wavelength was used as the light source. Data were measured from the scattered intensity data conducted in backscattering detection mode (measurement angle = 173°). Measurements were an average of 10 runs of two cycles each per sample. Z -average size was reported as the particle size and is defined as the harmonic intensity averaged particle diameter. All solutions were analyzed using polystyrene cuvettes.

saRNA encapsulation efficiency

saRNA encapsulation efficiency (EE%) was measured by a modified Ribogreen™ assay (Quanti-iT RiboGreen™ RNA assay kit, Fisher).1x TE buffer, and a 2% Triton-X (*w*/*v*) in 1x TE buffer were prepared for diluting the LNPs to the required concentrations for the assay. A 20 ug/mL RNA stock solution was prepared using 1x TE. Solutions for standard curve were prepared in the range of 0.1 – 2 ug/mL in Triton-X TE buffer in a

96 well. LNP solutions were then diluted in the 96 well plate using 50 ul 1x TE or 2% Triton-X TE buffer and incubated for 10 min at 37 °C (total 100 uL). 100 µL of 1:100 diluted Ribogreen reagent in 1x TE was then added to the wells and gently agitated for 30 sec. saRNA concentrations were quantified by measuring fluorescence (λem = 525 nm, λex = 485nm) at room temperature using a BioTek^{TM} Synergy^{TM} H1 Hybrid Multi-Mode Monochromator^{TM} Fluorescence Microplate Reader. Encapsulation efficiency (EE) was calculated using the following equation:

EE= 100x {(Total RNA$_{\text{(RNA in Triton TE)}}$ - RNA outside LNP$_{\text{(Ribogreen in TE)}}$)/Total RNA$_{\text{(Ribogreen in Triton TE)}}$}

Immunization

Animals were immunized s.c. in the right flank/inguinal area of the animal with an emulsion of Montanide ISA 51 with 20 µg/ml of spike protein (Lake Pharma, Inc) with or without Monophosphoryl Lipid A (MPLA) (Avanti Polar Lipids, Inc) as adjuvant. Additionally, the animals received anti-OX40L:Ig injected i.p. on days 0 and 3 post immunization, or mIgG. Mice were boosted with 20 µg/ml of spike protein in PBS, with or without MPLA. saRNA-LNP preparation was obtained from PNI. Animals were immunized i.m. in the left or right footpad with 1 µg of saRNA in lipid nanoparticles, diluted in 50 µl of PBS. Animals also received two injections of anti-OX40L:Ig or mIgG, i.p., on differing days post immunization, 3 days apart.

Blood collection and lymphocyte isolation

Blood was isolated from the animals by bleeding from the saphenous or submandibular veins. Between 0.1 and 0.4 ml of blood were collected, depending on the downstream applications. When mononuclear cells were isolated and analyzed, blood was collected in heparin-coated tubes. For T cell activation assays, peripheral blood mononuclear cells were separated using Fico/Lite-LM (R&D Systems) mouse cell separation medium. The peripheral mononuclear cells were washed with complete RPMI 1640 (Gibco) containing 0.292 ng/ml glutamine, 100 U/ml streptomycin/penicillin, 0.1 µM nonessential amino acids, 1 mM sodium pyruvate, and 10 mM HEPES (Sigma-Aldrich) and used in further experiments. For assessing cell phenotypes in blood, the blood was incubated with the ammonium-chloride-potassium (ACK) buffer to lyse red blood cells, prior to staining. When serum was isolated, blood was directly harvested in serum separation tubes (Microtainer, BD). Serum was aliquoted and stored at -80°C and thawed prior to use in the ELISA.

Draining lymph nodes (drLN) and spleens were harvested and processed to obtain single-cell suspensions using the plunger of a syringe and a petri dish. Spleens were incubated with ACK lysing buffer (Lonza) for 3 min at room temperature to lyse the red blood cells. Cells were rinsed with PBS containing 1% FBS and 4 mM EDTA prior to staining or washed with complete RPMI prior to *in vitro* cell culture.

T cell activation assay

PBMC or cells from LN and spleen were plated at 1.5 – 2 x 10^5 cells per well in 96-well u-bottom plates. As positive control, cells were stimulated with 1 µg/ml anti CD3 (clone 145-2C11) and anti-CD28 (clone 37.51), both Biolegend, Inc. 2 µg/ml of spike protein (LakePharma, Inc) or a peptide mix (1 µg/ml) spanning the S1 and S2 regions of the spike protein, were used to assess the antigen-specific responses (JPT Peptide Technologies, GmbH). To reveal upregulation of CD40L in response to antigen, a blocking anti-mouse CD40 antibody (clone HM40-3) and an APC-conjugated CD40L antibody (clone MR1) were present in the culture for the duration of the assay (29–31). Cells were stained for surface and intranuclear markers after 16-20 hrs.

Proliferation assay

Mononuclear cells isolated from blood, LN or spleen, were incubated in absence of or with spike protein or spike peptide pools in 96 well plates. After 3 days, 5-ethynyl-2'-deoxyuridine (EdU) was added at 2 µM to the culture medium. Cells were labeled for 16 hrs. Plates were spun down and supernatants were collected for analysis by ELISA and cells were pelleted for staining. Cells were washed twice with PBS prior to labeling with a viability dye. Cells were then washed with 1% BSA in PBS and surface labeled. The pellet was then fixed with 4% PFA for 20 min in 100 µl. After an additional wash with 1% BSA/PBS, cells were washed with a saponin-containing wash buffer and incubated for 20 min in 100 µl. The cells were pelleted again and resuspended in 50 µl of Click-iT reaction cocktail (PBS with Cu_2SO_4, Alexa647-Azide and the reducing agent sodium ascorbate). After 30 min of incubation at RT in the dark, cells were washed with wash buffer and intracellular antibodies were added in 30 µl/well. Cells were washed in wash buffer and resuspended in 250 µl PBS/1%BSA prior to analysis on a flow cytometer.

Antibodies and flow cytometry

For flow cytometric analysis, cells were washed in PBS, then incubated on ice for 20 with a viability dye (zombie yellow; ThermoFisherScientific) to exclude dead cells. Cells were washed with FACS buffer containing PBS, 1% FCS and 0.01% NaN_3.

Surface antibodies used in the study were: TCRβ (clone H57-597), CD4 (clone RM4-5), CD8 (clone 53-6.7), CD44 (clone IM7), CD62L (clone MEL-14), ICOS (clone C398.4A), PD1 (clone J43), CD40L (clone MR1) CD25 (clone PC61.5), OX40 (clone OX-86), CD19 (clone eBio1D3), CXCR5 (clone 2G8)4. Intracellular proteins were detected with the following antibodies: Foxp3 (clone FJK-16s), Ki67 (clone SolA15), granzyme B (clone NGZB). For tetramer analysis, cells were stained separately with the PE-conjugated tetramer (VNFNFNGL, H-2Kb, NIH tetramer core) for 30 min at RT, followed by surface staining or intranuclear staining, as indicated above. All samples were analyzed on an AttuneNxt flow cytometer (ThermoFisherScientific), and data were analyzed with FlowJo software v10.8.1 (Tree Star).

Spike and RBD direct ELISA

Nunc Maxisorp 96 well u-bottom plates (Thermo Scientific™, high-binding) were coated with Sars-CoV-2 spike or RBD protein (1-2 µg/ml in 50 µl of PBS) and incubated at 4°C overnight. Plates were washed 6x using an automated plate washer with 0.05% Tween20 in PBS. Plates were blocked with 10% non-fat dry milk blocking buffer (BioRad, in PBS/Tween 0.05%) at 100 µl per well for 2 hours at 37°C. Plates were washed 6x times with PBS/Tween 0.05%. Serum was serially diluted 7-11 times in 50 µl of blocking buffer, across the plate. Binding was performed for 90 minutes on a plate shaker at 300rpm protected from light at room temperature. After 6 washes, a secondary HRP conjugated F(ab')$_2$ fragment goat anti-mouse IgG (H+L) antibody (Jackson ImmunoResearch Laboratories, Inc) was prepared at a 1/6000 dilution in blocking buffer. For IgG1-specific antibody detection, an HRP-conjugated goat anti-mouse IgG, Fcγ subclass 1-specific antibody was used (1:6000, Jackson ImmunoResearch Laboratories, Inc); for IgG2a-specific antibody detection, an HRP-conjugated goat anti-mouse IgG2a antibody was used (1:1000, ThermoFisherScientific). The antibody was incubated for 30 minutes on a plate shaker at 300 rpm at room temperate. Plates were washed 6x times and Sureblue™ TMB substrate (VWR) was added at 50 µl/well and allowed to develop for 3 to 5 minutes. The reaction was stopped with 25 µl of H_2SO_4. Plates were read at 450 nm absorbance. Three- or four-fold serial dilutions were analyzed and graphed in Prism. EC50 values were calculated using a non-linear regression analysis.

Cytokine ELISA

Nunc Maxisorp 96 well flat-bottom plates (Thermo Scientific, high-binding) were coated with the monoclonal antibody AN18 (IFN-γ) 1A12 (IL-2) or 11B11 (IL-4) all from Mabtech, at 1 µg/ml in PBS at 100 µl per well. The plates were incubated overnight at 4°C. Plates were washed twice with PBS. Plates were blocked for 1 hour with incubation buffer (PBS, 0.05% Tween 20, and 0.1% BSA) at room temperature. Plates were washed 6x on an automated plate washer with PBS/0.05% Tween 20. The recombinant mouse IFN-γ standard was serially diluted, in incubation buffer, starting at 5 µg/ml, and incubated in 100 µl/well for 2 hours at RT (IL-2 and IL-4 were added at 4 and 1 µg/ml, respectively). The secondary biotinylated antibody R4-6A2 (IFN-γ) 5H4 (IL-2) or BVD6-24G2 (IL-4) were added at 0.5 µg/mL in incubation buffer, after washing the plates, then incubated for 1 hour at RT. After 6 washes, Streptavidin-HRP (BD) was added at 1:250 in incubation buffer and incubated on the plate for 1 hour. For development, Sureblue™ TMB substrate (VWR) was added at 100 µl/well and developed for 5-10 minutes. The reaction was stopped with 25 µl of 0.2M H_2SO_4. Plates were read at 450 nm absorbance. Cytokine concentrations in the cell cultures were extrapolated from the standard curve and graphed in Prism.

T cell isolation and CFSE assay

Total T cells were freshly isolated from pooled splenocytes (pooled by treatment group) using the Easysep negative mouse T cell isolation kit (#19851, Stemcell Technologies). Isolation was performed according to the manufacturer's protocols. (Stemcell Technologies). After T cell isolation, cells were washed in PBS and labeled with 0.5 µM CFSE diluted in PBS. T cells were cocultured with splenocytes, isolated from C57BL/6 animals and irradiated at 5000 rad prior to pulsing with whole spike protein or S1 and S2 peptide pools. Anti-CD3 and anti-CD28 served as positive control. Cells were cultured in complete RPMI for 3 days, then harvested and stained, prior to analysis on a flow cytometer. CFSE low cells indicate the proportion of proliferating cells.

Statistical analysis

Statistical analysis was performed with GraphPad Prism v9 software (GraphPad). The p values were calculated with a Student paired t test (for comparison between two groups), or a one way ANOVA for multiple comparisons. A p value <0.05 was considered significant. Error bars denote ± SEM as indicated. The number of biological replicates (individual animals) for each experiment is indicated in the figure legends. The titer for each mouse was calculated as $\log_{10}$EC50.

Data availability statement

The original contributions presented in the study are included in the article/Supplementary Material. Further inquiries can be directed to the corresponding author.

Ethics statement

The animal study was reviewed and approved by the Institutional Animal Care and Use Committee, Earle A. Chiles Research Institute, Providence Cancer Institute.

Author contributions

AW, RD and H-MH initiated and AW and RD supervised the study. RD and AW designed the experiments. RD and MB performed the experiments. RD, MB and AW analyzed the data. SAbb, SAbr, NJ, AT and AG designed, generated and provided the saRNA-LNP. SJ and BF provided reagents and protocols for the antibody assays. RD and AW wrote the manuscript. All authors contributed to the article and approved the submitted version.

Funding

This work was supported by the Providence Portland Medical Foundation.

Acknowledgments

We thank the Earle A. Chiles Research Institute vivarium staff for assistance with injections and husbandry of animals on these studies. We thank Newsha Arezi and Helena Son for their support with formulation of lipid nanoparticles and Sitalakshmi Thampatty and Emily Soon for their support in design and synthesis of saRNAs. We also thank the National Institutes of Health Tetramer Facility for generating the H-2K(b) tetramer for use within the study presented in this manuscript. Marie-Eve Koziol at SEPPIC, Inc. provided the Montanide ISA 51.

Conflict of interest

AW is founder of AgonOx, which has an ownership interest in OX40 patents. Authors SAbb, SAbr, NJ, AT and AG are/were employed by Precision Nanosystems (PNI).

The remaining authors declare that the research was conducted in the absence of any commercial or financial relationships that could be construed as a potential conflict of interest.

Publisher's note

Supplementary material

The Supplementary Material for this article can be found online at: https://www.frontiersin.org/articles/10.3389/fimmu.2022.896310/full#supplementary-material

References

1. Anderson EJ, Rouphael NG, Widge AT, Jackson LA, Roberts PC, Makhene M, et al. Safety and immunogenicity of SARS-CoV-2 mRNA-1273 vaccine in older adults. *N Engl J Med* (2020) 383(25):2427–38. doi: 10.1056/NEJMoa2028436

2. Baden LR, El Sahly HM, Essink B, Kotloff K, Frey S, Novak R, et al. Efficacy and safety of the mRNA-1273 SARS-CoV-2 vaccine. *N Engl J Med* (2021) 384 (5):403–16. doi: 10.1056/NEJMoa2035389

3. Dagan N, Barda N, Kepten E, Miron O, Perchik S, Katz MA, et al. BNT162b2 mRNA covid-19 vaccine in a nationwide mass vaccination setting. *N Engl J Med* (2021) 384(15):1412–23. doi: 10.1056/NEJMoa2101765

4. Polack FP, Thomas SJ, Kitchin N, Absalon J, Gurtman A, Lockhart S, et al. Safety and efficacy of the BNT162b2 mRNA covid-19 vaccine. *N Engl J Med* (2020) 383(27):2603–15. doi: 10.1056/NEJMoa2034577

5. Thompson MG, Burgess JL, Naleway AL, Tyner HL, Yoon SK, Meece J, et al. Interim estimates of vaccine effectiveness of BNT162b2 and mRNA-1273 COVID-19 vaccines in preventing SARS-CoV-2 infection among health care personnel, first responders, and other essential and frontline workers - eight U.S. locations, December 2020-march 2021. *MMWR Morb Mortal Wkly Rep* (2021) 70 (13):495–500. doi: 10.15585/mmwr.mm7013e3

6. Frenck RWJr., Klein NP, Kitchin N, Gurtman A, Absalon J, Lockhart S, et al. Safety, immunogenicity, and efficacy of the BNT162b2 covid-19 vaccine in adolescents. *N Engl J Med* (2021) 385(3):239–50. doi: 10.1056/NEJMoa2107456

7. Sadoff J, Le Gars M, Shukarev G, Heerwegh D, Truyers C, de Groot AM, et al. Interim results of a phase 1-2a trial of Ad26.COV2.S covid-19 vaccine. *N Engl J Med* (2021) 384(19):1824–35. doi: 10.1056/NEJMoa2034201

8. Voysey M, Clemens SAC, Madhi SA, Weckx LY, Folegatti PM, Aley PK, et al. Safety and efficacy of the ChAdOx1 nCoV-19 vaccine (AZD1222) against SARS-CoV-2: an interim analysis of four randomised controlled trials in Brazil, south Africa, and the UK. *Lancet* (2021) 397(10269):99–111. doi: 10.1016/S0140-6736 (20)32661-1

9. Levin EG, Lustig Y, Cohen C, Fluss R, Indenbaum V, Amit S, et al. Waning immune humoral response to BNT162b2 covid-19 vaccine over 6 months. *N Engl J Med* (2021) 385(24):e84. doi: 10.1056/NEJMoa2114583

10. Khoury DS, Cromer D, Reynaldi A, Schlub TE, Wheatley AK, Juno JA, et al. Neutralizing antibody levels are highly predictive of immune protection from symptomatic SARS-CoV-2 infection. *Nat Med* (2021) 27(7):1205–11. doi: 10.1038/s41591-021-01377-8

11. Walter EB, Talaat KR, Sabharwal C, Gurtman A, Lockhart S, Paulsen GC, et al. Evaluation of the BNT162b2 covid-19 vaccine in children 5 to 11 years of age. *N Engl J Med* (2022) 386(1):35–46. doi: 10.1056/NEJMoa2116298

12. Baker AT, Boyd RJ, Sarkar D, Teijeira-Crespo A, Chan CK, Bates E, et al. ChAdOx1 interacts with CAR and PF4 with implications for thrombosis with thrombocytopenia syndrome. *Sci Adv* (2021) 7(49):eabl8213. doi: 10.1126/sciadv.abl8213

13. Li W, Moore MJ, Vasilieva N, Sui J, Wong SK, Berne MA, et al. Angiotensin-converting enzyme 2 is a functional receptor for the SARS coronavirus. *Nature* (2003) 426(6965):450–4. doi: 10.1038/nature02145

14. Babcock GJ, Esshaki DJ, Thomas WDJr., Ambrosino DM. Amino acids 270 to 510 of the severe acute respiratory syndrome coronavirus spike protein are required for interaction with receptor. *J Virol* (2004) 78(9):4552–60. doi: 10.1128/JVI.78.9.4552-4560.2004

15. Cavazzoni CB, Hanson BL, Podesta MA, Bechu ED, Clement RL, Zhang H, et al. Follicular T cells optimize the germinal center response to SARS-CoV-2 protein vaccination in mice. *Cell Rep* (2022) 38(8):110399. doi: 10.1016/j.celrep.2022.110399

16. Sahin U, Muik A, Vogler I, Derhovanessian E, Kranz LM, Vormehr M, et al. BNT162b2 vaccine induces neutralizing antibodies and poly-specific T cells in humans. *Nature* (2021) 595(7868):572–7. doi: 10.1038/s41586-021-03653-6

17. Maxwell JR, Weinberg A, Prell RA, Vella AT. Danger and OX40 receptor signaling synergize to enhance memory T cell survival by inhibiting peripheral deletion. *J Immunol* (2000) 164(1):107–12. doi: 10.4049/jimmunol.164.1.107

18. Rogers PR, Song J, Gramaglia I, Killeen N, Croft M. OX40 promotes bcl-xL and bcl-2 expression and is essential for long-term survival of CD4 T cells. *Immunity* (2001) 15(3):445–55. doi: 10.1016/S1074-7613(01)00191-1

19. Croft M. Control of immunity by the TNFR-related molecule OX40 (CD134). *Annu Rev Immunol* (2010) 28:57–78. doi: 10.1146/annurev-immunol-030409-101243

20. Fu Y, Lin Q, Zhang Z, Zhang L. Therapeutic strategies for the costimulatory molecule OX40 in T-cell-mediated immunity. *Acta Pharm Sin B* (2020) 10(3):414–33. doi: 10.1016/j.apsb.2019.08.010

21. Tahiliani V, Hutchinson TE, Abboud G, Croft M, Salek-Ardakani S. OX40 cooperates with ICOS to amplify follicular Th cell development and germinal center reactions during infection. *J Immunol* (2017) 198(1):218–28. doi: 10.4049/jimmunol.1601356

22. Curti BD, Kovacsovics-Bankowski M, Morris N, Walker E, Chisholm L, Floyd K, et al. OX40 is a potent immune-stimulating target in late-stage cancer patients. *Cancer Res* (2013) 73(24):7189–98. doi: 10.1158/0008-5472.CAN-12-4174

23. Duhen R, Ballesteros-Merino C, Frye AK, Tran E, Rajamanickam V, Chang SC, et al. Neoadjuvant anti-OX40 (MEDI6469) therapy in patients with head and neck squamous cell carcinoma activates and expands antigen-specific tumor-infiltrating T cells. *Nat Commun* (2021) 12(1):1047. doi: 10.1038/s41467-021-21383-1

24. Evans DE, Prell RA, Thalhofer CJ, Hurwitz AA, Weinberg AD. Engagement of OX40 enhances antigen-specific CD4(+) T cell mobilization/memory development and humoral immunity: comparison of alphaOX-40 with alphaCTLA-4. *J Immunol* (2001) 167(12):6804–11. doi: 10.4049/jimmunol.167.12.6804

25. Weinberg AD, Thalhofer C, Morris N, Walker JM, Seiss D, Wong S, et al. Anti-OX40 (CD134) administration to nonhuman primates: immunostimulatory effects and toxicokinetic study. *J Immunother* (2006) 29(6):575–85. doi: 10.1097/01.cji.0000211319.00031.fc

26. Morris NP, Peters C, Montler R, Hu HM, Curti BD, Urba WJ, et al. Development and characterization of recombinant human fc : OX40L fusion protein linked *via* a coiled-coil trimerization domain. *Mol Immunol* (2007) 44 (12):3112–21. doi: 10.1016/j.molimm.2007.02.004

27. Oberst MD, Auge C, Morris C, Kentner S, Mulgrew K, McGlinchey K, et al. Potent immune modulation by MEDI6383, an engineered human OX40 ligand IgG4P fc fusion protein. *Mol Cancer Ther* (2018) 17(5):1024–38. doi: 10.1158/1535-7163.MCT-17-0200

28. Hsieh CL, Goldsmith JA, Schaub JM, DiVenere AM, Kuo HC, Javanmardi K, et al. Structure-based design of prefusion-stabilized SARS-CoV-2 spikes. *Science* (2020) 369(6510):1501–5. doi: 10.1126/science.abd0826

29. Chattopadhyay PK, Yu J, Roederer M. A live-cell assay to detect antigen-specific CD4+ T cells with diverse cytokine profiles. *Nat Med* (2005) 11(10):1113–7. doi: 10.1038/nm1293

30. Frentsch M, Arbach O, Kirchhoff D, Moewes B, Worm M, Rothe M, et al. Direct access to CD4+ T cells specific for defined antigens according to CD154 expression. *Nat Med* (2005) 11(10):1118–24. doi: 10.1038/nm1292

31. Kirchhoff D, Frentsch M, Leclerk P, Bumann D, Rausch S, Hartmann S, et al. Identification and isolation of murine antigen-reactive T cells according to CD154 expression. *Eur J Immunol* (2007) 37(9):2370–7. doi: 10.1002/eji.200737322

32. Mata-Haro V, Cekic C, Martin M, Chilton PM, Casella CR, Mitchell TC. The vaccine adjuvant monophosphoryl lipid a as a TRIF-biased agonist of TLR4. *Science* (2007) 316(5831):1628–32. doi: 10.1126/science.1138963

33. Cekic C, Casella CR, Eaves CA, Matsuzawa A, Ichijo H, Mitchell TC. Selective activation of the p38 MAPK pathway by synthetic monophosphoryl lipid a. *J Biol Chem* (2009) 284(46):31982–91. doi: 10.1074/jbc.M109.046383

34. Baumjohann D, Fazilleau N. Antigen-dependent multistep differentiation of T follicular helper cells and its role in SARS-CoV-2 infection and vaccination. *Eur J Immunol* (2021) 51(6):1325–33. doi: 10.1002/eji.202049148

35. Netea MG, van der Meer JW, Sutmuller RP, Adema GJ, Kullberg BJ. From the Th1/Th2 paradigm towards a toll-like receptor/T-helper bias. *Antimicrob Agents Chemother* (2005) 49(10):3991–6. doi: 10.1128/AAC.49.10.3991-3996.2005

36. Pardi N, Hogan MJ, Porter FW, Weissman D. mRNA vaccines - a new era in vaccinology. *Nat Rev Drug Discovery* (2018) 17(4):261–79. doi: 10.1038/nrd.2017.243

37. Vogel AB, Lambert L, Kinnear E, Busse D, Erbar S, Reuter KC, et al. Self-amplifying RNA vaccines give equivalent protection against influenza to mRNA vaccines but at much lower doses. *Mol Ther* (2018) 26(2):446–55. doi: 10.1016/j.ymthe.2017.11.017

38. Poluektov Y, George M, Daftarian P, Delcommenne MC. Assessment of SARS-CoV-2 specific CD4(+) and CD8 (+) T cell responses using MHC class I and II tetramers. *Vaccine* (2021) 39(15):2110–6. doi: 10.1016/j.vaccine.2021.03.008

39. Panagioti E, Boon L, Arens R, van der Burg SH. Enforced OX40 stimulation empowers booster vaccines to induce effective CD4(+) and CD8(+) T cell responses against mouse cytomegalovirus infection. *Front Immunol* (2017) 8:144. doi: 10.3389/fimmu.2017.00144

40. Salek-Ardakani S, Moutaftsi M, Crotty S, Sette A, Croft M. OX40 drives protective vaccinia virus-specific CD8 T cells. *J Immunol* (2008) 181(11):7969–76. doi: 10.4049/jimmunol.181.11.7969

41. Salek-Ardakani S, Moutaftsi M, Sette A, Croft M. Targeting OX40 promotes lung-resident memory CD8 T cell populations that protect against respiratory poxvirus infection. *J Virol* (2011) 85(17):9051–9. doi: 10.1128/JVI.00619-11

42. Gamse JT, Freebern W, Haynes Ii R, Simutis F, Pazian M, Crona J, et al. Decreased immune response in monkeys administered a human T-effector cell agonist (OX40) antibody. *Toxicol Appl Pharmacol* (2020) 409:115285. doi: 10.1016/j.taap.2020.115285

43. Oberhardt V, Luxenburger H, Kemming J, Schulien I, Ciminski K, Giese S, et al. Rapid and stable mobilization of CD8(+) T cells by SARS-CoV-2 mRNA vaccine. *Nature* (2021) 597(7875):268–73. doi: 10.1038/s41586-021-03841-4

44. Schulien I, Kemming J, Oberhardt V, Wild K, Seidel LM, Killmer S, et al. Characterization of pre-existing and induced SARS-CoV-2-specific CD8(+) T cells. *Nat Med* (2021) 27(1):78–85. doi: 10.1038/s41591-020-01143-2

45. Perri S, Greer CE, Thudium K, Doe B, Legg H, Liu H, et al. An alphavirus replicon particle chimera derived from venezuelan equine encephalitis and sindbis viruses is a potent gene-based vaccine delivery vector. *J Virol* (2003) 77(19):10394–403. doi: 10.1128/JVI.77.19.10394-10403.2003

46. Scaglione A, Opp S, Hurtado A, Lin Z, Pampeno C, Noval MG, et al. Combination of a sindbis-SARS-CoV-2 spike vaccine and alphaOX40 antibody elicits protective immunity against SARS-CoV-2 induced disease and potentiates long-term SARS-CoV-2-Specific humoral and T-cell immunity. *Front Immunol* (2021) 12:719077. doi: 10.3389/fimmu.2021.719077

47. Hu SL, Klaniecki J, Dykers T, Sridhar P, Travis BM. Neutralizing antibodies against HIV-1 BRU and SF2 isolates generated in mice immunized with recombinant vaccinia virus expressing HIV-1 (BRU) envelope glycoproteins and boosted with homologous gp160. *AIDS Res Hum Retroviruses* (1991) 7(7):615–20. doi: 10.1089/aid.1991.7.615

48. Lu S. Heterologous prime-boost vaccination. *Curr Opin Immunol* (2009) 21 (3):346–51. doi: 10.1016/j.coi.2009.05.016

49. Geall AJ, Verma A, Otten GR, Shaw CA, Hekele A, Banerjee K, et al. Nonviral delivery of self-amplifying RNA vaccines. *Proc Natl Acad Sci U S A* (2012) 109(36):14604–9. doi: 10.1073/pnas.1209367109

frontiers | Frontiers in Immunology

TYPE Original Research
PUBLISHED 24 October 2022
DOI 10.3389/fimmu.2022.998262

EDITED BY
Tara Marlene Strutt,
University of Central Florida,
United States

REVIEWED BY
Sira Nanthapisal,
Thammasat University, Thailand
Yasutoshi Kido,
Osaka City University, Japan
Pranesh Padmanabhan,
University of Queensland, Australia

*CORRESPONDENCE
Enrico Mastrostefano
e.mastrostefano@iac.cnr.it
Antonella Prisco
antonella.prisco@igb.cnr.it

SPECIALTY SECTION
This article was submitted to
Immunological Memory,
a section of the journal
Frontiers in Immunology

RECEIVED 19 July 2022
ACCEPTED 22 September 2022
PUBLISHED 24 October 2022

CITATION
Stolfi P, Castiglione F, Mastrostefano E,
Di Biase I, Di Biase S, Palmieri G and
Prisco A (2022) In-silico evaluation of
adenoviral COVID-19 vaccination
protocols: Assessment of
immunological memory up to 6
months after the third dose.
Front. Immunol. 13:998262.
doi: 10.3389/fimmu.2022.998262

In-silico evaluation of adenoviral COVID-19 vaccination protocols: Assessment of immunological memory up to 6 months after the third dose

Paola Stolfi[1], Filippo Castiglione[1], Enrico Mastrostefano[1]*,
Immacolata Di Biase[2], Sebastiano Di Biase[2],
Gianna Palmieri[3] and Antonella Prisco[4]*

[1]Institute for Applied Computing, National Research Council of Italy, Rome, Italy, [2]MeriGen Res, Naples, Italy, [3]Institute of Biosciences and BioResources, National Research Council, Naples, Italy, [4]Institute of Genetics and Biophysics, National Research Council, Naples, Italy

Background: The immune response to adenoviral COVID-19 vaccines is affected by the interval between doses. The optimal interval is unknown.

Aim: We aim to explore in-silico the effect of the interval between vaccine administrations on immunogenicity and to analyze the contribution of pre-existing levels of antibodies, plasma cells, and memory B and T lymphocytes.

Methods: We used a stochastic agent-based immune simulation platform to simulate two-dose and three-dose vaccination protocols with an adenoviral vaccine. We identified the model's parameters fitting anti-Spike antibody levels from individuals immunized with the COVID-19 vaccine AstraZeneca (ChAdOx1-S, Vaxzevria). We used several statistical methods, such as principal component analysis and binary classification, to analyze the correlation between pre-existing levels of antibodies, plasma cells, and memory B and T cells to the magnitude of the antibody response following a booster dose.

Results and conclusions: We find that the magnitude of the antibody response to a booster depends on the number of pre-existing memory B cells, which, in turn, is highly correlated to the number of T helper cells and plasma cells, and the antibody titers. Pre-existing memory T cytotoxic cells and antibodies directly influence antigen availability hence limiting the magnitude of the immune response. The optimal immunogenicity of the third dose is achieved over a large time window, spanning from 6 to 16 months after the second dose. Interestingly, after any vaccine dose, individuals can be classified into two groups, *sustainers* and *decayers*, that differ in the kinetics of decline of their antibody titers due to differences in long-lived plasma cells. This suggests that the *decayers* may benefit from a tailored boosting schedule with a shorter interval to avoid the temporary loss of serological immunity.

KEYWORDS

immunological memory, adenoviral COVID-19 vaccine, booster, *in silico*, agent-based modeling (ABM), simulation, anti-vector immunity

1 Introduction

Most COVID-19 vaccines are given in a two-dose primary schedule, whereas additional booster doses may be required to maintain immunity. The time interval between vaccine administrations can greatly affect the logistics of the vaccination campaign and its efficacy (1–3). The effect of the dosing interval on COVID-19 vaccine efficacy has not been specifically tested in Randomized Clinical Trials (RCT), however, available data suggest that longer intervals between the first and second dose result in higher antibody titers (4). Since the investigation of vaccine dosing protocol in RCT is limited by feasibility issues, in-silico modeling can make an important contribution to the field, allowing the extensive exploration of different schedules and the identification of the immunological variables that correlate with the endpoints of interest (5, 6). In this study, we utilized stochastic agent-based modeling to study the effect of the dosing protocol on the immune response to an adenoviral vaccine. Agent-based models exhibit emergent properties and thus can also lead to the discovery of patterns in the complex behavior of the immune system.

Adenoviral vaccines are less expensive and easier to store and transport than mRNA vaccines. On the other hand, vectored vaccines are not expected to be ideal for repeated administration (7). Their efficacy can be reduced by at least two factors: i) a preexistent antibody response to the vector that interferes with transduction (anti-vector immunity) (8) and/or ii) a preexistent cytotoxic T cell response against either the vector or the insert that limits the persistence of transduced cells (9). The determination of the optimal time interval between doses of adenoviral vaccines is still an unresolved question, and not enough is known about tailored schedules for groups that might need additional doses, such as the elderly or immunocompromised individuals.

The COVID-19 vaccine AstraZeneca is based on a chimpanzee adenovirus, utilized to generate the vector ChAdOx1. A low prevalence of anti-vector neutralizing antibodies has been observed in humans (10). Nevertheless, among the participants of clinical trials, before vaccination, some had high titer (IC50 > 200) or low titer (IC50< 200) neutralizing antibodies against ChAdOx1 (11, 12). The first dose induced anti-vector neutralizing antibodies that persisted until the last assessed time point (84 days) but did not prevent boosting (12). Indeed, clinical trials have shown that repeated use of AstraZeneca is effective: the second dose induces a marked surge of antibody titers and increased protection (12–14). The vaccine has been approved as a two-dose vaccine, with an inter-dose interval of 4 to 12 weeks (15). A clinical study analyzed immune responses to the AstraZeneca vaccine over an extended interval between the first and second administration, and after a third dose. It was shown that a longer inter-dose interval leads to higher antibody titers and that a third dose greatly increases antibody titers (11). Interestingly, in aged individuals, one dose of either the mRNA-based Pfizer vaccine or the adenoviral-vectored AstraZeneca vaccine elicits similar antibody levels on day 35 (16), whereas the second homologous dose, given after an 8–12 week interval, results in higher antibody titers in those vaccinated with the mRNA vaccine (17). This observation is consistent with the idea that the immunogenicity of the first dose of Pfizer and AstraZeneca are comparable, whereas the immunogenicity of the second dose of the adenoviral vaccine is reduced, with the caveat that the different kinetics of the antibody responses to the first dose may limit the significance of the day 35 comparison (17). Individuals vaccinated with a first dose of AstraZenca show a robust immune response when the second dose is an mRNA vaccine (18). A comparison of homologous and heterologous dosing protocols showed that after one dose of AstraZeneca, a second heterologous dose elicits higher antibody titers (19–21). After two doses of AstraZeneca, a third homologous dose elicits lower anti-Spike antibody titers than a third heterologous dose of mRNA vaccine (22).

By comparing different vaccination protocols we aim to investigate the effect of the interval between adenoviral vaccine doses by means of a stochastic agent-based immune simulation platform. We adjusted the model parameters using anti-Spike antibody data from individuals immunized with the COVID-19 vaccine AstraZeneca, from two sets of data, namely i) the “Vaxab dataset”, a retrospective observational study on anti-RBD-Spike total antibodies in individuals vaccinated against COVID-19 in Naples, Italy, and ii) published serological data from the COV001 and COV002 trials (11).

In the following sections, we describe the clinical data used to identify the parameters of the computational model, the model itself, the statistical procedures used to set the parameters, the definition of the numerical experiments to be conducted in-silico, and, finally, the analysis of the results obtained and the conclusions drawn.

2 Material and methods

2.1 Dataset 1: The observational study Vaxab

Vaxab is an observational study of serological data in COVID-19 vaccinees. The study was approved by the Ethical Committee of the University of Naples Federico II, protocol 376/21. Inclusion criteria for participation were: i) having received a COVID-19 vaccine, ii) requesting a Roche Elecsys® Anti-SARS-CoV-2 S assay at the MeriGen laboratory (Naples, Italy), iii) answering a questionnaire, and iv) signing the informed consent. Most study participants measured their antibody levels just once. Each dataset entry includes the age and sex of the participant, vaccination date(s), vaccine brand for each dose, the SARS-CoV-2 infection history (self-reported), the date of the serological test, and the result of the Roche Elecsys® Anti-SARS-CoV-2 S assay, expressed in Binding Antibody Units (BAU). The Roche Elecsys®Anti-SARS-CoV-2S assay quantifies antibodies against the Receptor Binding Domain (RBD) of the S protein (the Spike) of SARS-CoV-2; the dynamic range can be scaled by automated sample dilution (23). The test was performed according to the manufacturer's instructions (Roche Diagnostics GmbH. Elecsys® Anti-SARS-Cov-2 s, Instructions for Use. 2021). The Vaxab study includes participants vaccinated with AstraZeneca, Pfizer, Moderna, and Johnson & Johnson vaccines. It contains 120 antibody measures from individuals immunized with one dose of AstraZeneca and who reported no previous SARS-CoV-2 infection. The age range of this subset of participants was 20-79 (median 53, IQR 38-61), with 62% females. The timing of blood tests was between 10 and 89 days after the first dose. Six individuals had no anti-Spike antibodies (baseline value of the test, 0.4 BAU), whereas two outliers (not visible in Figure 1) had anti-Spike BAU levels >10000. The data

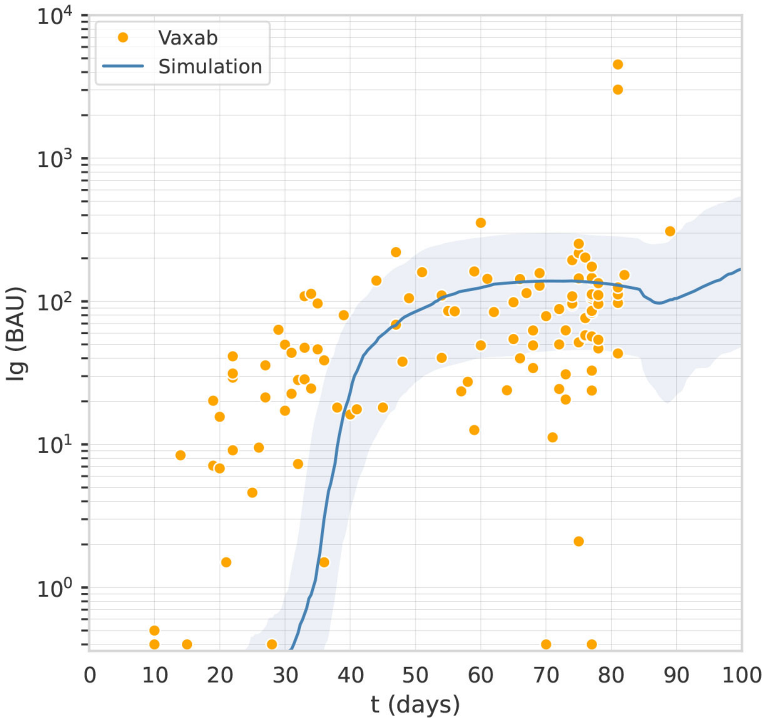

FIGURE 1
The computational model captures the antibody titer trajectory, characterized by a plateau. Overlay of a line graph representing in-silico Ig levels after the first dose (the line represents the median, the shading represents the IQR) with a dot plot representing RBD-Spike Ig BAU in individuals who have received one dose of AstraZeneca, in the Vaxab dataset.

points of the Vaxab study (one dose of AstraZeneca, no previous SARS-CoV-2 infection) are shown in Figure 1.

2.2 Dataset 2: The trials COV001 and COV002

Flaxman et al. (11) reported the immunogenicity of AstraZeneca with 3 different dosing intervals, namely 8–12, 15–25, and 44–45 weeks. Blood samples were taken on the day of vaccination and then at 14 and/or 28 days after vaccination. Antibody levels to SARS-CoV-2 Victoria/01/2020 spike were measured by standardized single dilution total IgG ELISA, and the median for each group was reported. On day 28 the median total IgG titer was 923 Elisa Units (EU) with Interquartile Range (IQR) [525–1764] for the 8–12 weeks interval, 1860 EU and IQR [917–4934] for the 15–25 weeks interval, and 3738 EU IQR [1824–6625] for the 44–45 weeks interval. Antibody levels 6 months after the second dose of vaccine were higher in the group with a 15–25 weeks interval between doses, median 1240 EU IQR [432–2002], compared with the group with 8–12 week interval, median 278 EU IQR [166–499]. Data points for this data set are shown in Figure 2.

2.3 Computational model

The computational model we used in this study has been previously employed to simulate the immune response to different antigens including SARS-CoV-2 virus (24). Most of the model parameters have already been fixed either by manual curation with literature information or by numerical estimation in general settings. For the current purpose, we modified this computational model to simulate the immune response to a non-replicative adenovirus carrying a transgene encoding the Spike protein of SARS-Cov-2, and then we adjusted the model's parameters using data from human vaccination with Astra Zeneca. The model represents both the innate immune response by macrophages, dendritic cells, and natural killer cells and the adaptive immune response by B lymphocytes, antibody-producing plasma cells, CD4 T helper, and CD8 T cytotoxic lymphocytes. It is a polyclonal model as it embodies

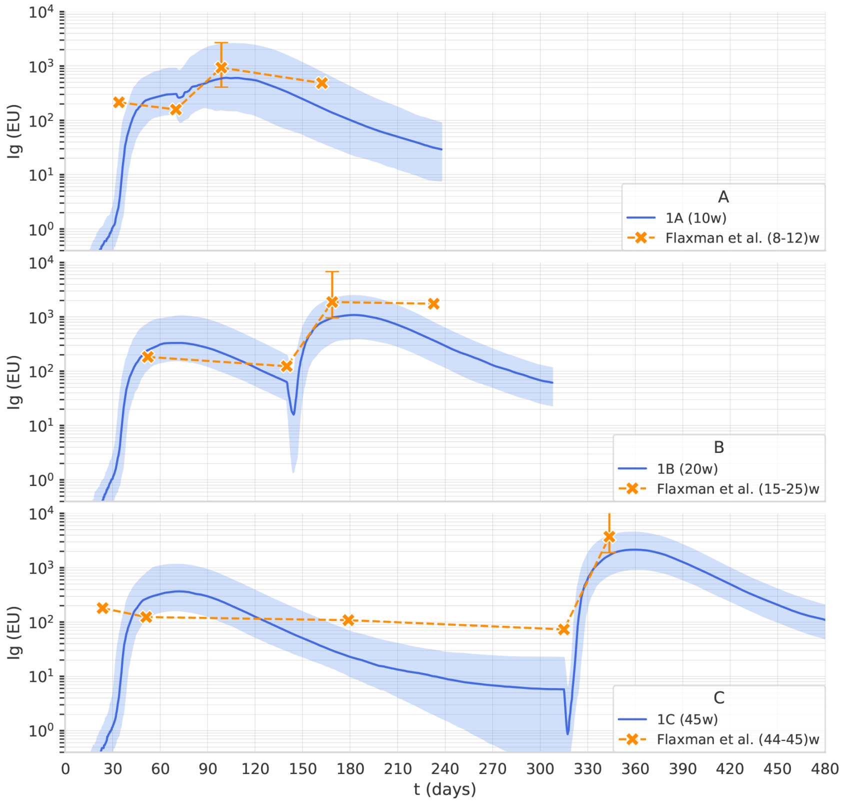

FIGURE 2
The computational model reproduces the effect of the dosing interval observed in clinical trials. Overlay of in-silico Ig levels in two-dose protocols 1A, 1B, and 1C (the line represents the median, the shading represents the IQR) with a dotplot representing median anti-Spike Elisa Units in clinical trial data from (11), corresponding to inter-dose periods of 8-12, 15-25 and 44-45 weeks for panel **(A–C)**, respectively.

the primary sequences of the binding sites of B-cell receptors (BCR) and T-cell receptors (TCR), as well as the peptides and epitopes of the infectious agent or vaccine. It represents a portion of i) the muscle, where the vaccine is injected, ii) primary lymphatic organs where lymphocytes are formed and mature, and iii) secondary lymphoid organs where antigens are presented to naïve B and T-cells. Further details are provided in the Supplementary Material.

To evaluate different vaccination protocols we have used the antibody level as a significant endpoint representative of the immunogenicity of the vaccine construct. Neutralizing antibody levels are known to correlate with immunity from symptomatic SARS-CoV-2 infection (25, 26).

2.4 Parameters identification

The parameters of the immune system simulator were identified fitting two datasets introduced in *Dataset 1: The observational study Vaxab* and *Dataset 2: The trials COV001 and COV002.* The first round of manual calibration, based on the Vaxab dataset, aimed at reproducing the trajectory of the antibody levels after the first vaccine dose. The Vaxab dataset shows that, after the first dose of AstraZeneca, anti-Spike antibody levels increase for 5-6 weeks and then remain stable until the 12th week, when the second dose is received. This antibody titer trajectory, characterized by a plateau, was captured by acting on parameters related to vaccine dosage, antigen release kinetics from the adenovirus-transfected cells, and the scaling factor that adjusts the model scale to the antibody concentrations expressed in BAU (Figure 1).

The second fine-tuning step, using data from the published clinical trials described in *Dataset 2: The trials COV001 and COV002*, aimed to capture the effect of dosing interval on antibody titers. We used the Approximate Bayesian Calculation (details provided in Supplementary Material) to estimate some parameters, namely the persistence of phagocytosed antigen before it is degraded in the cytosol of APCs, the plasma-long-lived/normal half-life, and the rate of spike production from infected muscle cells. As shown in Figure 2, the computational model reproduces the effect of the dosing interval observed in clinical trials. Note that the scaling factor used in Figure 2 is different from the one employed in Figure 1 as it relates to antibody titers obtained with a different assay and expressed in EU rather than in BAU.

2.5 In-Silico experiments

We used the model to perform in-silico experiments of vaccination with two doses (in what we call experiment 1) or three doses (experiment 2) of adenoviral COVID-19 vaccine. Each experiment included multiple treatment groups, differing in the time interval between doses (Table 1). In particular, experiment 1 includes three treatment groups, denoted 1A, 1B, and 1C, that differ in the interval between the first and second dose, which is 10 weeks in protocol 1A, 20 in protocol 1B, and 45 in protocol 1C. While experiment 2 includes nine treatment groups, denoted 2A-I that differ in the interval between the second and third dose, which is 4 months in protocol 2A, 6 in protocol 2B, 8 in protocol 2C, 10 in protocol 2D, 12 in protocol 2E, 14 in protocol 2F, 16 in protocol 2G, 20 in protocol 2H and 24 months in protocol 2I. In all treatment groups of experiment 2, the second dose is given 12 weeks after the first dose. Each treatment group included 200 individuals and the follow-up was 6 months after the last dose.

TABLE 1 *In-silico* vaccination experiments.

	Vaccination regimen	Treatment group (dosing protocol)	Interval between 1^{st} and 2^{nd} dose	Interval between 2^{nd} and 3^{rd} dose	Follow-up
Experiment 1	Two doses	1A	10 weeks	–	6 months after 2nd dose
		1B	20 weeks	–	
		1C	45 weeks	–	
Experiment 2	Three doses	2A	12 weeks	4 months	6 months after 3rd dose
		2B	12 weeks	6 months	
		2C	12 weeks	8 months	
		2D	12 weeks	10 months	
		2E	12 weeks	12 months	
		2F	12 weeks	14 months	
		2G	12 weeks	16 months	
		2H	12 weeks	20 months	
		2I	12 weeks	24 months	

2.6 Statistical analysis

The statistical analysis aimed at i) establishing whether the immune response is statistically different among the protocols detailed in *In-silico experiments*, ii) identifying the right timing for the third dose and iii) investigating whether the antibody response is linked to some immunological variable. To this end we focused our analysis on five components of the immune system, that play a critical role in vaccine efficacy, namely antibodies (*i.e.*, the sum of IgG1and IgG2), denoted by *Ab*, plasma cells, denoted by *Plb*, memory T helper cells, denoted by *Th*, memory T cytotoxic cells, denoted by *Tc*, and memory B cells, denoted by *B*.

The dynamics of these variables is shown in Figure 4.

To fulfill the tasks detailed above, we analyzed the variables of interest at crucial time points, namely the time before the second dose, denoted by t_1, the time when the variable reaches its peak after the second dose, denoted by t_m, and the latest time point of the simulation six months after the second dose, denoted by t_f (Figure 3.)

First, for each treatment group (Table 1), we report standard sample statistics such as median, IQR, minimum and maximum. Mann-Whitney test is used to asses significant differences in the variables of interest at $t_{1,}$ t_m and t_f among the different treatment group, task i), and, in particular, differences in

$Ab(t_m)$ is used to asses the optimal timingfor the third dose, task ii). Stepwise regression (explained in detail in Supplementary Material) is used to determine whether variables $Ab(t_1)$, $Plb(t_1)$, $Th(t_1)$, $Tc(t_1)$, and $B(t_1)$ can be used as explanatory variables for the increment of *Ab* induced by the second dose, that is $\Delta_{Ab}= (Ab(t_m)\ -Ab(t_1))$, task iii). Then, correlations and cross-correlations at $t_{1,}$ t_m and t_f (Figure 3) between the variables of interest are investigated in terms of Pearson's correlation coefficient. Finally, given the results of correlations analysis, Principal Component Analysis and Principal Component Regression (explained in detail in Supplementary Material) are employed to better investigate the link between the antibody response and the other immunological variables.

Moreover, to test whether in-silico experiments show patterns that can be traced to immunological behavior of interest, we performed unsupervised clustering on $Ab(t_1)$ Specifically, we applied a machine learning method, k-means clustering, which partitions N observations into K groups such that the within-cluster variance is minimal, see (27) for details.

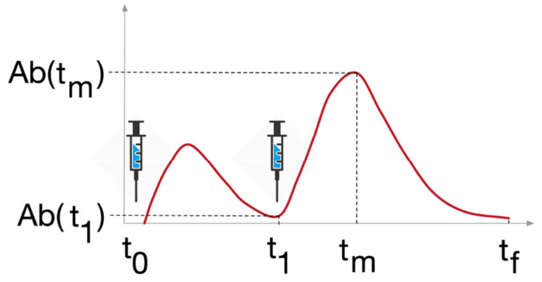

FIGURE 3
Study design. Variables Ab, Plb, Th, Tc and B were analyzed at 3 timepoints, t_1 is the timepoint before the last dose of vaccine, t_m is the timepoint when the variable reaches its maximum after the last dose, and t_f is the last timepoint of the simulation, 6 months after the last dose.

3 Results

3.1 The interval between doses affects immunological memory

In Figure 4, we report the dynamics of *Ab*, *Plb*, *Th*, *Tc* and *B* in the treatment groups 1A, 1B, and 1C. The second dose of the vaccine induces a peak of plasma cells, higher than the peak induced by the first dose. Plasma cell peaks are mirrored by antibody peaks. *Th* and *B* after the second dose reach a higher level, and their increase persists for the following 6 months of simulation. When we compare 1A, 1B, and 1C, we see that as the interval between the two doses becomes longer, the humoral response (*i.e.*, *Ab*, *Pbl*, *B*) and the T helper response (*Th*) to the second dose improve. This advantage of the longer protocols is still evident 6 months after the second dose (Supplementary Material Figure S3). Interestingly, the trajectory of *Tc* is markedly different from all other trajectories. The first dose has the major effect on *Tc* expansion, not the second (Figure 4). This finding agrees with studies reporting the absence of a significant boost of the cellular response after the second ChAdOx1 nCoV-19 dose (13).

3.2 The antibody response to the second dose correlates with the number of pre-existing memory B cells and is mitigated by pre-existing cytotoxic T cells and antibodies

Protocols with longer inter-dose intervals induce higher *Ab*, *Plb*, *Th*, and *B* (Figure 4). To shed light on the immunological mechanisms underlying this phenomenon, we set out to analyze how the immune status at t_1 (*i.e.*, before vaccination) affects the subsequent antibody increment Δ_{Ab}, that is the difference between the peak value $Ab(t_m)$ and the pre-existing antibody level $Ab(t_1)$. A stepwise regression analysis indicates that, within each protocol 1A, 1B and 1C, pre-existing memory B cells $B(t_1)$ is the only variable which significantly influence ΔAb. $B(t_1)$ is not significantly different between protocols 1A, 1B, and 1C (Figure 5), therefore, the differences in the magnitude of the

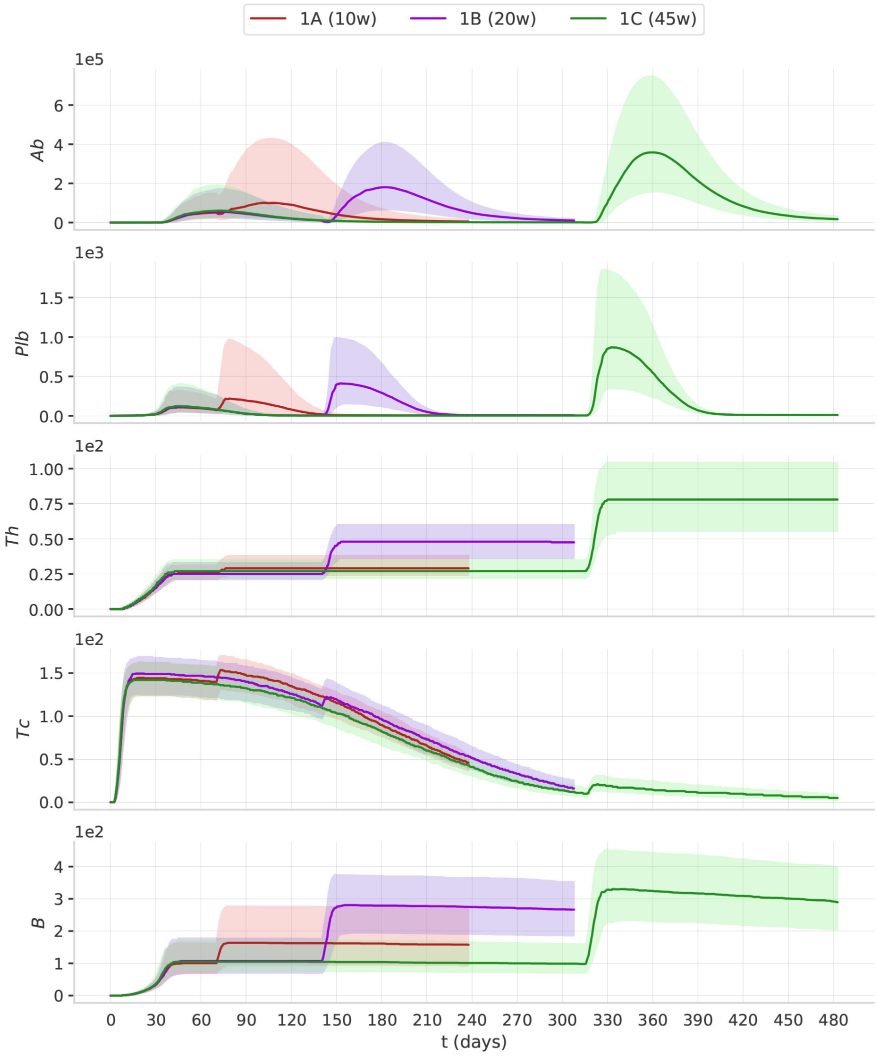

FIGURE 4
The timing of the second dose affects the dynamics of the immune response. The plots represent the median (solid lines) and IQR (shaded area) of *Ab, Plb, Th, Tc, B.* Protocols with longer intervals between the first and second dose achieve higher antibody responses.

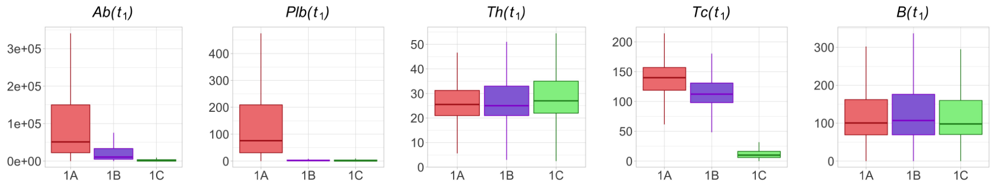

FIGURE 5
Th and B are not significantly different in protocols 1A, 1B and 1C at time t_1, whereas Ab, Plb and Tc are lower in the longer protocols. The box plots show the median, IQR, and range of Ab, Plb, Th, Tc and B in treatment groups 1A, 1B and 1C at time t_1.

antibody response to the second dose between the shorter and longer protocols cannot be imputed to memory B cells. Instead, both $Ab(t_1)$ and $Tc(t_1)$ are significantly lower in the longer protocols (Figure 5). This supports the hypothesis that either $Ab(t_1)$ or $Tc(t_1)$, or both, may have an inhibitory effect on the antibody response to the second dose.

However, by exploring the correlations and cross-correlations among variables *Ab*, *Plb*, *Th*, *Tc* and *B*, it was found that at t_1, in all three protocols, antibodies, plasma cells, memory B cells and memory T helper cells were positively correlated with each other, whereas memory T cytotoxic cells were not significantly correlated with the other variables (Figure 6). Note that significant correlations among variables may influence the results of the stepwise regression.

To better understand how the interplay between the variables of interest in t_1 contributes to the enhanced antibody response to the second dose after longer intervals, we performed a Principal Component Regression between $Ab(t_1)$, $Plb(t_1)$, $Th(t_1)$, $Tc(t_1)$, $B(t_1)$ and the peak value of the antibody response to the second dose, $Ab(t_m)$. We obtain five principal components, PC1-5, that explain 45% of the variance of $Ab(t_m)$. Of these, PC1 and PC2 are the two most important components, and together explain 38.54% of the variance of $Ab(t_m)$. Figure 7 shows a scatterplot of PC1 vs PC2. Each dot represent one simulation, *i.e.*, one virtual individual. Protocols 1A, 1B and 1C form separate clusters. At t_1, 1A, 1B and 1C are similar in PC1, and are separated by PC2, suggesting that PC1 explains differences in $Ab(t_m)$ among individuals who received the same dosing protocol, whereas PC2 is more relevant to understand the difference between the 1A, 1B and 1C, *i.e.*, the effect of the timing of the second dose on $Ab(t_m)$. Interestingly, the 1C group separates into two distinct clusters that are different in PC1. The

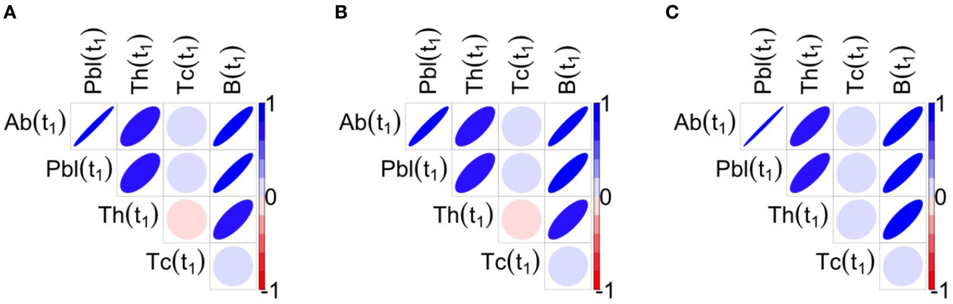

FIGURE 6
Correlations between the variables of interest at t_1 for the three protocols 1A, 1B, 1C are shown respectively in panels **(A–C)**. Blue ellipses mean positive correlations while red ellipses mean negative correlations, as reported in the color bar. The shape of ellipse helps in the understanding: the more stretched the ellipse the higher the value of the correlation in absolute value. At t_1, antibodies, plasma cells, memory B cells and memory T helper cells are positively correlated among them, whereas Tc is not significantly correlated with the Other variables.

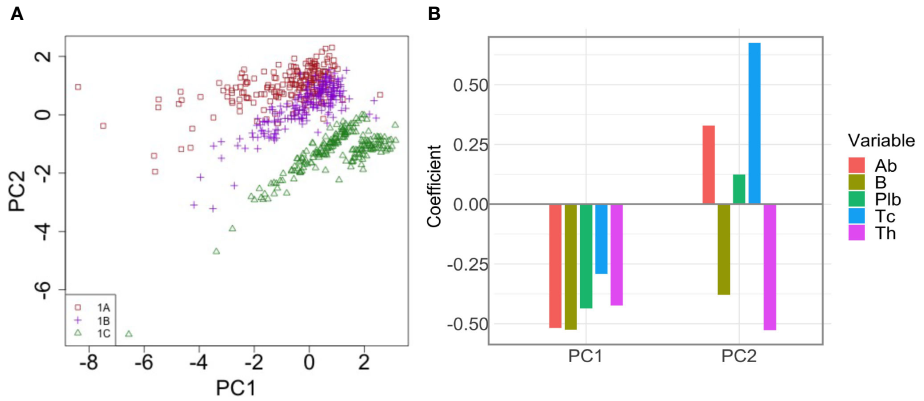

FIGURE 7
Principal Component Analysis of the correlation between pre-existing immunological memory at t_1 and the peak value of the antibody response to the second dose. **(A)** The dot plot shows PC1 and PC2 in individuals in treatment groups 1A, 1B and 1C. PC2 separates the different dosing protocols. **(B)** Loadings of PC1 and PC2. In PC2, Tc has the highest loading.

most important variables (highest coefficient or loading) within PC1 are $B(t_1)$ (loading -0.525), and $Ab(t_1)$ (loading -0.519) (Figure 7). So PC1 mainly represents pre-existing antibody levels and B cell memory, which are positively correlated to Ab(t_m), irrespective of the timing of the second dose. The highest loadings within PC2 are $Tc(t_1)$ (0.675) and $Th(t_1)$ (-0.527) (Figure 7), therefore PC2 mainly represents T cells. Notably, memory T cytotoxic cells and memory T helper cells exert opposite effects (*i.e.*, opposite sign of the loading coefficients). Overall, the PCA suggests that pre-existing memory T cytotoxic cells are the major correlates of the reduced immunogenicity that is observed when the second dose is given at earlier time points. In PC2, the pre-existing antibodies also display the same sign of the coefficient as memory T cytotoxic cells, yet with a lower absolute value.

3.3 The Tc response to the second dose of vaccine is limited by the number of antigen presenting cells

The increase of *Tc* after the second dose is much smaller than the increase of *Tc* after the first dose (Figure 4). In order to proliferate, *Tc* need to recognize their cognate epitopes complexed with MHC class I on the vaccine-transduced muscle cells. Hence, to understand what may cause the poor response of *Tc* to the second dose, we analyzed antigen presentation on MHC class I, in muscle cells, after each dose. To estimate the total amount of antigen presentation on MHC class I that occurs after the first and second dose of vaccine, we calculated the Area Under the Curve (AUC) of the model variable "class-I-presenting" (AUC $= \int_{t_1}^{t_f} m(t)dt$ where $m(t)$ is the number of antigen presenting cells, which indicates the cumulative number of muscle cells that present vaccine antigen peptides on MHC class I, in the time interval $[t_1,t_f]$). The AUC of the first dose was calculated from t_0 to t_1, while the AUC of the second dose was calculated from t_1 to t_f. Table 2 reports the median and interquartile range of AUC, in protocols 1A, 1B and 1C. Antigen presentation on MHC class I on muscle cells after the second dose of vaccine is lower than after the first dose, which explains why *Tc* are poorly stimulated by the second dose (see Table 2).

3.4 The optimal antibody response to the third dose is achieved over a large time window

To predict the optimal timing for the third dose, we analyzed the results of experiment 2. The simulations predict that the optimal antibody response to the third, booster dose, is achieved over a large time window, spanning from 6 to 16 months after the second dose (Figure 8). Over this time window, the peak

TABLE 2 Antigen presentation on MHC class I in muscle cells.

	AUC MHC class-I-presenting	
	First dose (t_0 to t_1)	**Second dose (t_1 to t_f)**
1A	7904 (6314.50-9971)	114.5 (82.75-154.50)
1B	8002 (6604.25-10117)	272.5 (177.24-366.25)
1C	7569 (6125.50-9451)	540.5 (309.75-871)

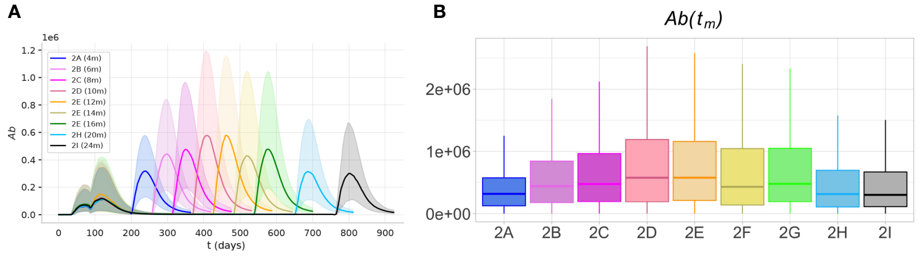

FIGURE 8
The optimal immunogenicity of antibody response to the third dose is achieved over a large time window. The protocols with intervals between the second and third dose between 6 and 16 months achieve peak antibody responses significantly higher ($p < 0.05$)) than shorter or longer protocols. **(A)** The plots represent the dynamics of the median (solid lines) and the IQR (shaded area) of variable *Ab*, in experiments 2A-I. **(B)** The box plots show the median, IQR, and range of the antibody peak after the third dose, *Ab*(t_m).

antibody levels are significantly higher ($p < 0.05$, Mann-Whitney test) than those achieved with earlier or later boosters.

Presumably, in the first months after the second dose, the high levels of antibodies and cytotoxic T cells inhibit the response to the third dose. On the other hand, much later after the second dose, when the memory Th and B cells and long-lived plasma cells decline, the antibody response to the third dose is reduced.

3.5 At late timepoints individual responses form two clusters with different antibody dynamics, sustainers and decayers

Interestingly, the principal component analysis revealed two separate clusters in the experiment 1C at t_1. The level of $Ab(t_1)$ allows separation of the two clusters (Figure 9A). The cluster with the lower level of antibodies has memory B cells (Figure 9B), but no plasma cells (Figure 9C). The number of memory B cells and memory T helper cells at t_1 is significantly different between cluster 1 and cluster 2 ($p < 10^{-7}$).

We analyzed the antibody dynamics in the two clusters (Figure 9D). Once the peak of antibodies generated by the first dose of vaccine has declined, individuals from cluster 1 (antibody *sustainers*) reach a plateau in their antibody levels that reflects the production by long-lived plasma cells. In contrast, individuals in cluster 2 (antibody *decayers*), have no long-lived plasma cells, therefore the decline of their antibody levels continues. These two patterns in the antibody trajectories result in the bimodal distribution of antibody levels in the population, at late timepoints after the last dose (Figure 9A).

We observed *decayers* both after one dose of vaccine (Figure 9), and after two doses (Figure 10). The frequency of *decayers* however was lower after two doses (36.5% after 2 doses vs 20% after 3 doses). This suggests that as multiple doses of vaccine are administered, the number of individuals that will lose their serological immunity over time is reduced.

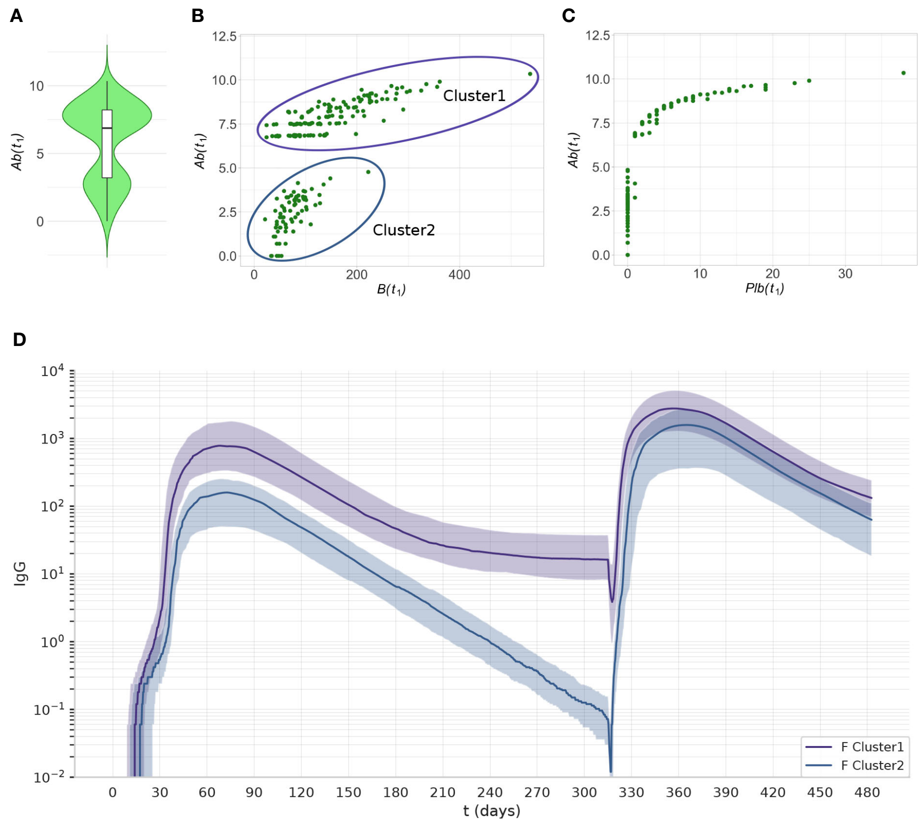

FIGURE 9
The two clusters identified by PCA can be separated by their level of $Ab(t_1)$ Data from experiment 1C are reported. **(A)** The violin plot of $Ab(t_1)$ reveals two clusters with different levels of Ab. **(B)** The scatterplot shows that the individuals with low antibody levels have, in most cases, no plasma cells. **(C)** the scatterplot shows that the individuals with low levels of antibody have memory B cells. **(D)** The antibody dynamics of the two clusters is different, cluster 1 represents antibody *sustainers*, and cluster 2 represents antibody *decayers*. The plots represent the median (lines) and IQR (shaded area) of variable *Ab* in cluster 1 and cluster 2.

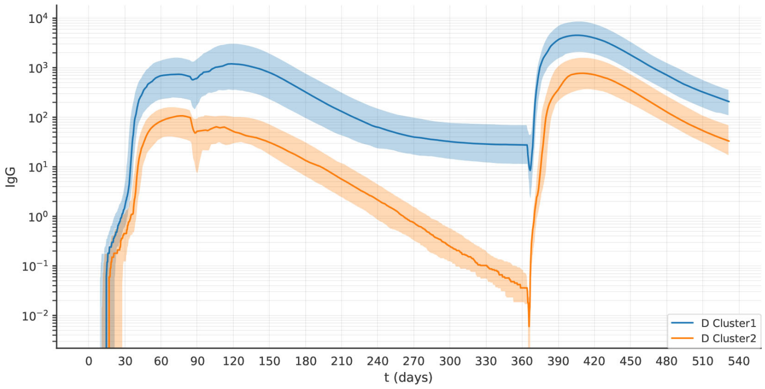

FIGURE 10
After two doses of vaccine, the virtual individuals can still be separated into clusters 1 and 2, representing antibody *sustainers* and *decayers*. The plots represent the median (lines) and IQR (shaded area) of variable Ab in clusters 1 and 2 in experiment 2D.

In experiment 1C, we identified the *decayers* looking at t_1, namely 45 weeks after the first dose. We asked if, by machine learning clustering on antibody titers, *decayers* could be reliably identified at earlier time points. Therefore, to identify the optimal time to detect *decayers*, we performed k-means clustering at different weeks from the first dose and we compared the performance in terms of accuracy (*i.e.*,$(TP+TN)/N$ where TP=true positive, TN=true negative, N=total population).

It turned out that from 28 weeks after the first dose, clustering on antibody titers allows the identification of antibody *decayers* with accuracy above 90% (Table 3).

4 Discussion and conclusions

In the context of the COVID-19 pandemic, vaccination policies had to take into account vaccine supply constraints and disease burden. In some cases, due to vaccine supply shortage, the second dose was delayed to allow for a higher initial coverage with one dose. On the other hand, in some countries, in situations of high dose availability, a third dose of COVID-19 vaccine has been offered to the general population as early as 4 months after the second dose, to try and mitigate large infection waves driven by virus variants. The time delay between vaccine doses can affect the durability of the antibody response, as well as the probability of an enhanced response to a subsequent encounter with the same antigen (28–30).

We explored, in-silico, the optimal timing for the third dose of an adenoviral vaccine. We adjusted the model parameters using two sets of anti-Spike antibody measures obtained with two different assays. While different antibody assays can show different kinetics (31) because some assays are tuned for high-avidity antibodies (32), the antibody assays employed in the two datasets give a similar kinetics after the first dose of AstraZeneca, i.e., no major variation in the antibody titer between 4 and 12 weeks. For this reason, in Figures 1, 2 we could simply use two different scaling factors to adjust the scale of the model output to the antibody concentrations obtained with the two different assays.

Simulations predict that the optimal immunogenicity of the third dose is achieved over a large time window, spanning from 6 to 16 months after the second dose. We analyzed the contribution of pre-existing antibodies, plasma cells, memory B cells, memory CD8 T cells, and memory CD4 T cells on immunogenicity, in vaccination schedules with different intervals between the first and second dose, namely 10, 20, and 45weeks. We observe a strong positive correlation between antibodies, plasma cells, memory B cells, and memory CD4 T cells after the first dose of vaccine. It is important to underline that these strong correlations complicate the identification of the causal correlates of the effect of the timing

TABLE 3 Accuracy of the identification of decayers.

	Weeks						
	20	**24**	**28**	**32**	**36**	**40**	**45**
Accuracy	0.805	0.840	0.925	0.975	0.985	0.990	1

of the second dose on immunogenicity. On the other hand, these correlations imply that the antibody titer, an element that can be very easily measured, is a biomarker of the numbers of memory B cells, plasma cells, and CD4 T cells.

In-silico, we allowed the antibodies induced by the first dose of vaccine to inhibit the entry of the adenoviral vaccine into cells, to reproduce the effect of antibodies directed against the adenoviral capsid. In clinical trials, anti-vector neutralizing antibodies have been detected after the first dose of adenoviral vaccine, but no correlation was observed between pre-existing anti-vector neutralizing antibodies and the response to the second dose. Also in our in-silico analysis, the mere analysis of the correlation between the pre-existing antibody titer within one experiment and the subsequent response does not reveal a negative correlation. The potential inhibitory effect of antibodies is revealed by the comparison between simulations in which antibodies were or were not allowed to neutralize the adenoviral entry in muscle cells (Supplementary Material Figure S2). Interestingly, longer intervals resulted in higher immunogenicity in both scenarios, therefore irrespective of the action of neutralizing anti-vector antibodies. In this context, we should emphasize that cytotoxic T cells against the Spike, a desired outcome of immunization, can contribute to reduced immunogenicity of subsequent doses.

The scenario that emerged from our in-silico analysis is that memory B cells and memory CD8 T cells have opposite effects on the antibody response to the boost. Increased antibody response to late booster doses appears to be due to the combined effect of the decline in antibody levels and in the number of memory CD8 T cells, which results in a higher amount of Spike antigens being produced.

In the simulations, the number of memory B cells is similar at 12, 20 and 45 weeks after the first dose of the vaccine. This prediction is in line with the long persistence observed after Sars-CoV-2 infection (33, 34), and in mouse studies of B cell memory (35).

Garg et al. previously analyzed the effect of prime-boost interval on the antibody response to vaccination in a stochastic simulation model of the germinal center reaction, and concluded that increased B cell selection stringency in the germinal center can explain improved COVID-19 vaccine efficacy with delayed boost (36). Affinity maturation is implemented in our model; however, we did not measure the effect of dose interval on affinity due to computational constraints. On the other hand, our model considers the impact of pre-existing antibodies, plasma cells, memory T helper cells and memory T cytotoxic on the magnitude of the response to the boost, and we show a major contribution of cytotoxic T cells and antibodies.

An interesting observation coming from the principal component analysis is that the individuals who underwent a longer inter dosage vaccination schedule separated into two distinct clusters. The two clusters contain, respectively, individuals that generated or did not generate long-lived plasma cells. The dynamics of the antibody titers is markedly different between the two groups: one group reaches a plateau of antibody levels (*sustainers*), while the other group is destined to sero-revert (*decayers*). In this in-silico system, these qualitative differences stem from stochastic inter-individual differences in the immune repertoire and the efficacy of priming. We speculate that, in real life, aged and immunocompromised people may be prone to the decayer pattern and may benefit from receiving their booster after a shorter interval. Indeed, after two doses of adenoviral vaccine, waning of vaccine effectiveness against symptomatic COVID-19 is greater in older adults and in those in a clinical risk group (37). Machine learning clustering on antibody titers allows the identification of the *decayers* with 0.925 accuracy as early as 28 weeks after the first dose.

Our observation of two subsets of vaccinated individuals with different antibody dynamics over time resembles the observation of two subsets of COVID-19 convalescents, antibody *sustainers*, that exhibited the same or increasing antibody levels over time, and antibody *decayers* that lost antibody levels over the same time frame (38). A tetramer-based analysis of T follicular helper cells suggested a connection between Spike-specific CD4+ T cell responses and anti-Spike antibody durability (39). In addition, more memory B cell cross-reactivity with endemic coronaviruses was identified as a marker for more sustained antibody responses after infection (40). Our in-silico experiments replicate these correlations, as also in the simulation antibody *sustainers* have more memory T helper and memory B cells than antibody *decayers*. Our analysis suggests that a stronger response of T helper and B cells has a higher probability of resulting in the development of long-lived plasma cells.

Following asymptomatic or pauci-symptomatic SARS-CoV-2 infection, higher peak anti-Spike responses have been associated with longer time to sero-reversion (41). Our in-silico experiments replicate this correlation, as also in the simulations antibody *decayers* have a lower anti-Spike peak than antibody *sustainers*.

Neutralizing antibodies against the SARS-CoV-2 Spike are known to correlate with immunity from symptomatic infection, therefore unraveling the long-term kinetics of antibodies after SARS-CoV-2 infection or COVID-19 vaccination, and the factors influencing it, is essential to optimize vaccine boosting strategies (25, 26). Our analysis suggests that while the time window for the optimal immunogenicity of the third dose of an adenoviral vaccine is ample (6-16 months), however, some individuals, namely the antibody *decayers*, may benefit from receiving the third dose at the beginning of the optimal time window, to avoid loss of serological protection.

Data availability statement

The raw data supporting the conclusions of this article will be made available by the authors, without undue reservation.

Ethics statement

The studies involving human participants were reviewed and approved by Ethical Committee of the University of Naples Federico II, protocol 376/21. The patients/participants provided their written informed consent to participate in this study.

Author contributions

FC and AP contributed to the conception and design of the study. IDB and GP collected informed consents from study participants. IDB, SDB, GP, and AP organized the database. FC and EM performed the in-silico experiments. PS performed the statistical analysis. AP wrote the first draft of the manuscript. AP, PS, FC, and EM contributed to data interpretation. FC, PS, and EM wrote sections of the manuscript. All authors contributed to manuscript revision, read, and approved the submitted version.

Funding

FC and PS wish to thank the Italian Ministry of Education, University and Research, for partial support under the frame of JPI AMR (project MAGIcIAN, N. 0000873).

Acknowledgments

The investigators express their gratitude for the contribution of the Vaxab participants. AP acknowledges Mariarosaria Aletta for bibliographic assistance.

Conflict of interest

Authors IDB and SDB were employed by company MeriGen Res.

The remaining authors declare that the research was conducted in the absence of any commercial or financial relationships that could be construed as a potential conflict of interest.

Publisher's note

Supplementary material

The Supplementary Material for this article can be found online at: https://www.frontiersin.org/articles/10.3389/fimmu.2022.998262/full#supplementary-material

References

1. Blumental S, Debré P. Challenges and issues of anti-SARS-CoV-2 vaccines. *Front Med* (2021) 8:664179. doi: 10.3389/fmed.2021.664179

2. Wouters OJ, Shadlen KC, Salcher-Konrad M, Pollard AJ, Larson HJ, Teerawattananon Y, et al. Challenges in ensuring global access to covid-19 vaccines: Production, affordability, allocation, and deployment. *Lancet* (2021) 397:1023–34. doi: 10.1016/S0140-6736(21)00306-8

3. Liu Y, Pearson CA, Sandmann FG, Barnard RC, Kim JH, Flasche S, et al. Dosing interval strategies for two-dose covid-19 vaccination in 13 middle-income countries of europe: Health impact modelling and benefit-risk analysis. *Lancet Reg Health-Eur* (2022) 17:100381. doi: 10.1016/j.lanepe.2022.100381

4. Rodrigues CM, Plotkin SA. The influence of interval between doses on response to vaccines. *Vaccine* (2021) 39:7123. doi: 10.1016/j.vaccine.2021.10.050

5. Castiglione F, Celada F. *Immune system modelling and simulation.* (Boca Raton, FL, USA: CRC Press) (2015).

6. Bonabeau E. Agent-based modeling: Methods and techniques for simulating human systems. *Proc Natl Acad Sci* (2002) 99:7280–7. doi: 10.1073/pnas.082080899

7. Ahi YS, Bangari DS, Mittal SK. Adenoviral vector immunity: Its implications and circumvention strategies. *Curr Gene Ther* (2011) 11:307–20. doi: 10.2174/156652311796150372

8. Boehncke WH, Brembilla NC. Immunogenicity of biologic therapies: Causes and consequences. *Expert Rev Clin Immunol* (2018) 14:513–23. doi: 10.1080/1744666X.2018.1468753

9. Mendonça SA, Lorincz R, Boucher P, Curiel DT. Adenoviral vector vaccine platforms in the sars-cov-2 pandemic. *NPJ Vaccines* (2021) 6:1–14. doi: 10.1038/s41541-021-00356-x

10. Dicks MD, Spencer AJ, Edwards NJ, Wadell G, Bojang K, Gilbert SC, et al. A novel chimpanzee adenovirus vector with low human seroprevalence: Improved systems for vector derivation and comparative immunogenicity. *PloS One* (2012) 7:e40385. doi: 10.1371/journal.pone.0040385

11. Flaxman A, Marchevsky NG, Jenkin D, Aboagye J, Aley PK, Angus B, et al. Reactogenicity and immunogenicity after a late second dose or a third dose of chadox1 ncov-19 in the uk: a substudy of two randomised controlled trials (cov001 and cov002). *Lancet* (2021) 398:981–90. doi: 10.1016/S0140-6736(21)01699-8

12. Barrett JR, Belij-Rammerstorfer S, Dold C, Ewer KJ, Folegatti PM, Gilbride C, et al. Phase 1/2 trial of sars-cov-2 vaccine chadox1 ncov-19 with a booster dose induces multifunctional antibody responses. *Nat Med* (2021) 27:279–88. doi: 10.1038/s41591-020-01179-4

13. Folegatti PM, Ewer KJ, Aley PK, Angus B, Becker S, Belij-Rammerstorfer S, et al. Safety and immunogenicity of the chadox1 ncov-19 vaccine against sars-cov-2: A preliminary report of a phase 1/2, single-blind, randomised controlled trial. *Lancet* (2020) 396:467–78. doi: 10.1016/S0140-6736(20)31604-4

14. Voysey M, Clemens SAC, Madhi SA, Weckx LY, Folegatti PM, Aley PK, et al. Single-dose administration and the influence of the timing of the booster dose on immunogenicity and efficacy of chadox1 ncov-19 (azd1222) vaccine: A pooled analysis of four randomised trials. *Lancet* (2021) 397:881–91. doi: 10.1016/S0140-6736(21)00432-3

15. European Medicines Agency. *COVID-19 vaccine AstraZeneca product information as approved by the CHMP on 29 January 2021, pending endorsement by the European commission.* (2021). Available at: https://www.ema.europa.eu/en/documents/product-information/vaxzevria-previously-covid-19-vaccine-astrazeneca-epar-product-information_en.pdf.

16. Parry H, Bruton R, Tut G, Ali M, Stephens C, Greenwood D, et al. Immunogenicity of single vaccination with bnt162b2 or chadox1 ncov-19 at 5–6 weeks post vaccine in participants aged 80 years or older: An exploratory analysis. *Lancet Healthy Longevity* (2021) 2:e554–60. doi: 10.1016/S2666-7568(21)00169-0

17. Parry H, Bruton R, Stephens C, Brown K, Amirthalingam G, Otter A, et al. Differential immunogenicity of bnt162b2 or chadox1 vaccines after extended-interval homologous dual vaccination in older people. *Immun Ageing* (2021) 18:1–8. doi: 10.1186/s12979-021-00246-9

18. Borobia AM, Carcas AJ, Pérez-Olmeda M, Castaño L, Bertran MJ, García-Pérez J, et al. Immunogenicity and reactogenicity of bnt162b2 booster in chadox1-s-primed participants (combivacs): A multicentre, open-label, randomised, controlled, phase 2 trial. *Lancet* (2021) 398:121–30. doi: 10.1016/S0140-6736(21)01420-3

19. Barros-Martins J, Hammerschmidt SI, Cossmann A, Odak I, Stankov MV, Morillas Ramos G, et al. Immune responses against sars-cov-2 variants after heterologous and homologous chadox1 ncov-19/bnt162b2 vaccination. *Nat Med* (2021) 27:1525–9. doi: 10.1038/s41591-021-01449-9

20. Schmidt T, Klemis V, Schub D, Mihm J, Hielscher F, Marx S, et al. Immunogenicity and reactogenicity of heterologous chadox1 ncov-19/mrna vaccination. *Nat Med* (2021) 27:1530–5. doi: 10.1038/s41591-021-01464-w

21. Pozzetto B, Legros V, Djebali S, Barateau V, Guibert N, Villard M, et al. Immunogenicity and efficacy of heterologous chadox1–bnt162b2 vaccination. *Nature* (2021) 600:701–6. doi: 10.1038/s41586-021-04120-y

22. Munro AP, Janani L, Cornelius V, Aley PK, Babbage G, Baxter D, et al. Safety and immunogenicity of seven covid-19 vaccines as a third dose (booster) following two doses of chadox1 ncov-19 or bnt162b2 in the uk (cov-boost): a blinded, multicentre, randomised, controlled, phase 2 trial. *Lancet* (2021) 398:2258–76. doi: 10.1016/S0140-6736(21)02717-3

23. Jochum S, Kirste I, Hortsch S, Grunert VP, Legault H, Eichenlaub U, et al. Clinical utility of elecsys anti-sars-cov-2 s assay in covid-19 vaccination: An exploratory analysis of the mrna-1273 phase 1 trial. *Front Immunol* (2021) 12. doi: 10.1101/2021.10.04.21264521

24. Castiglione F, Deb D, Srivastava AP, Liò P, Liso A. From infection to immunity: Understanding the response to sars-cov2 through in-silico modeling. *Front Immunol* (2021) 12:3433. doi: 10.3389/fimmu.2021.646972

25. Khoury DS, Cromer D, Reynaldi A, Schlub TE, Wheatley AK, Juno JA, et al. Neutralizing antibody levels are highly predictive of immune protection from symptomatic sars-cov-2 infection. *Nat Med* (2021) 2:1205–11. doi: 10.1038/s41591-021-01377-8

26. Padmanabhan P, Desikan R, Dixit NM. Modeling how antibody responses may determine the efficacy of covid-19 vaccines. *Nat Comput Sci* (2022) 2:123–31. doi: 10.1038/s43588-022-00198-0

27. Hastie T, Tibshirani R, Friedman JH, Friedman JH. *The elements of statistical learning: data mining, inference, and prediction. vol. 2.* (New York, NY, USA:Springer) (2009).

28. Castiglione F, Mantile F, De Berardinis P, Prisco A. How the interval between prime and boost injection affects the immune response in a computational model of the immune system. *Comput Math Methods Med* (2012) 2012:1–9. doi: 10.1155/2012/842329

29. Mantile F, Capasso A, De Berardinis P, Prisco A. Identification of a consolidation phase in immunological memory. *Front Immunol* (2019) 10:508. doi: 10.3389/fimmu.2019.00508

30. Mantile F, Capasso A, De Berardinis P, Prisco A. Analysis of the consolidation phase of immunological memory within the igg response to a b cell epitope displayed on a filamentous bacteriophage. *Microorganisms* (2020) 8:564. doi: 10.3390/microorganisms8040564

31. Matsuura T, Fukushima W, Nakagama Y, Kido Y, Kase T, Kondo K, et al. Kinetics of anti-sars-cov-2 antibody titer in healthy adults up to 6 months after bnt162b2 vaccination measured by two immunoassays: a prospective cohort study in japan. *Vaccine* (2022) 40:5631–40. doi: 10.1016/j.vaccine.2022.08.018

32. Nakagama Y, Nitahara Y, Kaku N, Tshibangu-Kabamba E. Kido y. a dual-antigen sars-cov-2 serological assay reflects antibody avidity. *J Clin Microbiol* (2022) 60:e02262–21. doi: 10.1128/JCM.02262-21

33. Sakharkar M, Rappazzo CG, Wieland-Alter WF, Hsieh CL, Wrapp D, Esterman ES, et al. Prolonged evolution of the human b cell response to sars-cov-2 infection. *Sci Immunol* (2021) 6:eabg6916. doi: 10.1126/sciimmunol.abg6916

34. Dan JM, Mateus J, Kato Y, Hastie KM, Yu ED, Faliti CE, et al. Immunological memory to sars-cov-2 assessed for up to 8 months after infection. *Science* (2021) 371:eabf4063. doi: 10.1126/science.abf4063

35. Jones DD, Wilmore JR, Allman D. Cellular dynamics of memory b cell populations: Igm+ and igg+ memory b cells persist indefinitely as quiescent cells. *J Immunol* (2015) 195:4753–9. doi: 10.4049/jimmunol.1501365

36. Garg AK, Mittal S, Padmanabhan P, Desikan R, Dixit NM. Increased b cell selection stringency in germinal centers can explain improved covid-19 vaccine efficacies with low dose prime or delayed boost. *Front Immunol* (2021) 12. doi: 10.3389/fimmu.2021.776933

37. Andrews N, Tessier E, Stowe J, Gower C, Kirsebom F, Simmons R, et al. Duration of protection against mild and severe disease by covid-19 vaccines. *New Engl J Med* (2022) 386:340–50. doi: 10.1056/nejmoa2115481

38. Chen Y, Zuiani A, Fischinger S, Mullur J, Atyeo C, Travers M, et al. Quick covid-19 healers sustain anti-sars-cov-2 antibody production. *Cell* (2020) 183:1496–507. doi: 10.1016/j.cell.2020.10.051

39. Nelson RW, Chen Y, Venezia OL, Majerus RM, Shin DSMGH COVID-19 Collection & Processing Team,, et al. Sars-cov-2 epitope-specific cd4+ memory t cell responses across covid-19 disease severity and antibody durability. *Sci Immunol* (2022) 7:eabl9464. doi: 10.1126/sciimmunol.abl9464

40. Chen Y, Tong P, Whiteman N, Moghaddam AS, Zarghami M, Zuiani A, et al. Immune recall improves antibody durability and breadth to sars-cov-2 variants. *Sci Immunol* (2022):eabp8328. doi: 10.1126/sciimmunol.abp8328

41. Manisty C, Treibel TA, Jensen M, Semper A, Joy G, Gupta RK, et al. Time series analysis and mechanistic modelling of heterogeneity and sero-reversion in antibody responses to mild sars-cov-2 infection. *EBioMedicine* (2021) 65:103259. doi: 10.1016/j.ebiom.2021.103259

frontiers in Immunology

TECHNOLOGY AND CODE
published: 26 October 2022
doi: 10.3389/fimmu.2022.822834

IgTreeZ, A Toolkit for Immunoglobulin Gene Lineage Tree-Based Analysis, Reveals CDR3s Are Crucial for Selection Analysis

Hadas Neuman[1*], **Jessica Arrouasse**[1], **Meirav Kedmi**[1,2,3], **Andrea Cerutti**[4,5], **Giuliana Magri**[4] **and Ramit Mehr**[1*]

[1] The Mina and Everard Goodman Faculty of Life Sciences, Bar Ilan University, Ramat Gan, Israel, [2] Division of Hematology and Bone Marrow Transplantation, Chaim Sheba Medical Center, Ramat Gan, Israel, [3] Sackler School of Medicine, Tel-Aviv University, Tel Aviv, Israel, [4] Translational Clinical Research Program, Institut Hospital del Mar d'Investigacions Mèdiques (IMIM), Barcelona, Spain, [5] Catalan Institute for Research and Advanced Studies (ICREA), Barcelona, Spain

Edited by:
Uri Hershberg,
University of Haifa, Israel

Reviewed by:
Susana Magadan,
University of Vigo, Spain
Hong Zan,
The University of Texas Health Science Center at San Antonio, United States

***Correspondence:**
Ramit Mehr
ramit.mehr@biu.ac.il
Hadas Neuman
hadas.doron@gmail.com

Specialty section:
This article was submitted to Immunological Memory, a section of the journal Frontiers in Immunology

Received: *26 November 2021*
Accepted: *08 February 2022*
Published: *26 October 2022*

Citation:
Neuman H, Arrouasse J, Kedmi M, Cerutti A, Magri G and Mehr R (2022) IgTreeZ, A Toolkit for Immunoglobulin Gene Lineage Tree-Based Analysis, Reveals CDR3s Are Crucial for Selection Analysis. Front. Immunol. 13:822834. doi: 10.3389/fimmu.2022.822834

Somatic hypermutation (SHM) is an important diversification mechanism that plays a part in the creation of immune memory. Immunoglobulin (Ig) variable region gene lineage trees were used over the last four decades to model SHM and the selection mechanisms operating on B cell clones. We hereby present IgTreeZ (Immunoglobulin Tree analyZer), a python-based tool that analyses many aspects of Ig gene lineage trees and their repertoires. Using simulations, we show that IgTreeZ can be reliably used for mutation and selection analyses. We used IgTreeZ on empirical data, found evidence for different mutation patterns in different B cell subpopulations, and gained insights into antigen-driven selection in corona virus disease 19 (COVID-19) patients. Most importantly, we show that including the CDR3 regions in selection analyses – which is only possible if these analyses are lineage tree-based – is crucial for obtaining correct results. Overall, we present a comprehensive lineage tree analysis tool that can reveal new biological insights into B cell repertoire dynamics.

Keywords: antibody, B cell receptor (BCR), B cell repertoire, immunoglobulin, lineage tree, somatic hypermutation (SHM)

INTRODUCTION

SHM can take place in germinal centers (GC) as well as in extrafollicular (EF) sites (1) and introduces base-pair changes into rearranged Ig variable region genes. B cells that gain mutations that improve their receptors' affinity to the antigen are selected to expand, and eventually generate plasma cells and memory B cells with an improved receptor affinity (2). The resulting high-affinity memory B cells and long-lived plasma cells allow faster and more efficient secondary immune responses. Therefore, SHM is an important mechanism in the generation of broad and effective immune responses.

The above-described affinity maturation can be modeled using Ig gene lineage trees. A lineage tree (sometimes also called pedigree or dendrogram) is a rooted tree, similar to a phylogenetic tree, in which nodes correspond to B cell receptor chain variable region gene sequences. The shapes of lineage trees hold information on the dynamics of the GC response that generated the trees (3). Properties such as the degree of branching can point to the strength of selection and initial affinity to the antigen. Insights on transitions between populations, such as class switch recombination (CSR), cell differentiation and migration, can be deduced from the relationships between tree nodes. Finally and most importantly, tree-based mutation analysis is more accurate than analysis based on comparing each sequence to the putative germline sequence (**Figure 1**) (4, 5).

Over the last three decades, lineage trees were used to elucidate many features of the B cell repertoire dynamics. Meng et al. created an atlas of the B cell distribution and found that the repertoire is divided into two major networks of large clones, one in the blood, bone marrow, spleen and lung, and another in the gastrointestinal track (6). Tipton et al. found in 2015 that activated naïve B cells are the precursors for antibody-secreting cells in Systemic Lupus Erythematosus (7). Tabibian-Keissar and colleagues found evidence for B-cell trafficking between gut-lymph node in ulcerative colitis (8) and Hoehn et al. used phylogenetic model to characterize the effects of aging on B cell repertoire development and B cell responses to influenza vaccination (5). Overall, the analysis of lineage tree properties sheds light on affinity maturation and the diversification of Ig genes in health and in various pathological conditions. However, these analyses were done using different, separate tools, each of which reveals different aspects of lineage trees.

Diffuse large B-cell lymphoma (DLBCL) is the most common form of lymphoma and accounts for 25–35% of all non-Hodgkin lymphomas. About 30–50% of patients treated with the standard-of-care therapy are either refractory to treatment or have relapsed disease after the complete response (9). Detecting an early stage of a relapsed disease may have a positive impact on the therapy outcome. There is a wide interest in applying machine learning on biological fields and more precisely on Adaptive Immune Receptor Repertoire (AIRR) data sequencing, from an adaptation of the natural language processing (NLP) technique for B cell receptor (BCR) sequencing data (10) to disease classification based on BCR repertoires (11). Here, we demonstrate that we can apply machine learning classification models to the IgTreeZ (mutation analysis) output, and use it to distinguish between lineage trees from DLBCL patients and those from healthy controls.

This study presents a comprehensive python-based tool for the analysis of many aspects of Ig gene lineage trees. The program was developed on LINUX and most of its features are compatible with Windows as well (including the population and topology analyses, filtering and drawing). The next versions will be fully compatible with all operating systems. IgTreeZ allows the analysis of population transitions, tree topology, and mutations at the repertoire level. The program also includes utility scripts for filtering trees by population and size, and for graphical and statistical comparisons of the results of analyzing more than one repertoire. Finally, we used simulated and empirical data to demonstrate the usefulness of this tool and the potential of lineage tree-based Ig gene repertoire analysis, and applied a successful classification model on IgTreeZ's mutation counts of DLBCL patients and healthy controls.

METHODS

Mutation Analyses

An Ig gene lineage tree represents the diversification of a B-cell clone. Hence, a mutation count based on tree topology is more accurate than counting the mutations on each sequence separately (4, 5). Currently in IgTreeZ, prior to mutation count, the nodes are linked to the corresponding sequences. Sequences can be given as a Fasta file or as AIRR/Change-O database, or as an AIRR JSON rearrangement scheme, which includes the trees and sequences. Once given, each of the sequences is linked to the corresponding node by name. Hypothetical nodes, created by the tree inference program, sometimes lack representation in the input files. In the case of an internal node with no corresponding sequence, if the edge between the node and its parent indicates a zero distance – the node is linked to its parent's sequence; if not, a consensus sequence is generated, with a priority to gaps and Ns (that is, if the number of Ns is equal to the number As in a certain position, the program prefers the N, or a gap, over the A), to avoid mutation over-count.

Once all nodes on the tree are linked to their sequences, the program traverses all tree nodes, counts all the observed

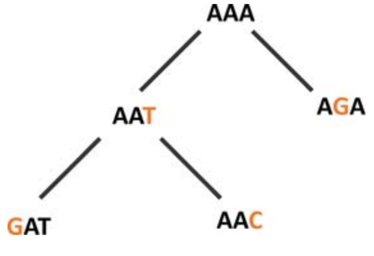

Mutation count method	#
By representative sequence	1 or 2
By consensus (AAT)	1
By tree	4

FIGURE 1 | Mutations are best described, and more precisely counted, using lineage trees. In the example one-codon "clone", a mutation count that is based on a representative sequence results in one or two mutations. Using a consensus sequence, which is AAT for this clone, results in 1 mutation. Only a tree-based mutations count results in the exact number of mutations, which in this case is 4.

mutations, and characterizes each mutation by its location (CDR/FWR), based on IMGT region definitions (12). Since each tree is handled separately, mutations in the CDR3 can also be identified as CDR mutations; the program compares CDR3 nucleotides to the clone's consensus CDR3, and thus counts only mutations generated by SHM and not the diversity generated by N/P nucleotide. The program also characterizes each mutation by its nucleotide source, mutation type (transition/transversion) and amino-acid change (replacement/silent). If it is a replacement mutation, the program characterizes also the amino-acid type – charge, hydropathy, volume, chemical, hydrogen donor or acceptor atoms and polarity, based on the IMGT physicochemical amino acid classes (13, 14). The resulting data are saved as a CSV file with mutation counts for each tree, and graphs can be included in the output using the 'plot' argument.

Selection Analyses

Selection analysis is based on IgTreeZ' mutation analysis, which calculates the number of silent and replacement mutations in the CDRs and FWRs for all sequences each tree. The resulting counts are sent, together with the corresponding germline sequence and the length of the CDR3 of each tree, to ShazaM (15, 16). Using ShazaM, we calculate the expected mutation frequency, estimate the selection strength for each tree, and compare the selection scores of multiple repertoires. We include the CDR3 by modifying the region definition parameter according to each tree's CDR3 length and calculating the expected mutation frequency for each germline separately. All these steps were performed by our R script 'shazam_selection_on_igtreez_output.r', which is included in IgTreeZ.

Tree Topology Analysis (MTree)

This analysis quantifies the shape properties of Ig gene lineage trees. This was first suggested by Shannon and Mehr (17), who postulated that lineage tree shapes can be used to reveal the dynamics of hypermutation and antigen-driven selection in GCs. Later, seven variables were found to have a significant correlation with several B cell response parameters (3). Recently, we wrote a python version of MTree©, which calculates these seven variables for each tree in parallel and saves them in CSV files. The MTree results of different repertoires are compared using a second tool, which creates a box plot for each variable, and a scatter plot of each pair of variables. IgTreeZ now includes this analysis as part of its functions.

Tree Drawing

The tree drawing function of IgTreeZ aims to visually illustrate lineage tree shapes. We base our drawing on the graph description language DOT, as implemented in the Graphviz program (18). The input Newick-format trees are first translated to the DOT language. The translated DOT files can then be saved as image files (in several formats) or colored for quick impression. The coloring is based on the cell population names associated with tree nodes, with multi-population nodes colored with multiple colors. The font size and line width can also be adjusted using program parameters. Examples are given in the *Results* section.

Tree Filtering

Some comparative analyses require choosing only trees with certain characteristics, such as trees belonging to specific cell populations or tissues. To address this need, we developed a script to filter trees based on tree size (number of nodes or leaves), population composition or other features. Filtering by features such as population composition is done using one of three logical gates: AND, which selects trees composed of nodes associated with all the given populations; OR, which select trees composed of nodes associated with at least one of the given populations; and NOT, which selects trees that lack nodes associated with any of the given populations. The selected tree names are saved in a CSV file, and these trees can be automatically copied to a new directory using a parameter.

Simulation

To test our mutation counts in a CDR/FWR region connotation, we used Yermanos et al.'s AbSim simulation (19). We simulated 100 lineages under each condition, using the 'data' SHM method, which focuses mutation events during SHM to the CDR regions (defined based on IMGT), and has an increased probability for transition mutations relative to transversions. We used different probabilities for SHM nucleotide changes, different probabilities for a given sequence to undergo SHM, and different baseline probabilities for each nucleotide to be mutated. We annotated the output sequences using IgBlast version 1.14.0 (20) on IMGT/GENE-DB (21) reference sequences from March 26, 2020, and built parsimony trees using AlakazaM version 1.0.1 (16). Overall, more than 2800 trees were simulated and analyzed.

Empirical Data Processing

Healthy Ileum Data

We used Ig sequencing data from sorted B cell subsets from histologically normal human ileum tissue samples of two adult individuals (**Table 1**), which were barcoded with unique molecular identifiers, amplified, sequenced and analyzed using our lab's pipeline (Tejedor Vaquero S et al. manuscript in preparation). Briefly, the sequences were preprocessed using pRESTO version 0.5.8 (22), annotated online using IMGT/HighV-QUEST version 3.4.15 (23) with the IMGT/GENE-DB

TABLE 1 | Cerutti Lab dataset – patient information.

Patient number	Gender	Age	B cell subsets
3	Female	35	Naïve, Memory, GC, Plasma cells
4	Female	63	Naïve, Memory, GC, Plasma cells

(21) reference sequences from January 17, 2019, and processed and assigned for clones using Change-O version 0.4.1 (16). Lineage tree construction was performed using IgTree© (24).

COVID-19 Data

We used data obtained from Montague et al. (25), who sequenced and analyzed B cells from blood samples of COVID patients in various severity levels at several time points from the appearance of clinical symptoms. We downloaded sequences of 20 samples (including replicates) from three patients with different disease severity from different time points, and from three healthy controls (**Table 2**). All sequences were downloaded from iReceptor (26). We annotated the sequences using IgBlast version 1.14.0 (20) on IMGT/GENE-DB (21) reference sequences from March 26, 2020. We filtered the functional sequences and assigned them into clones, based on trimming thresholds, using Change-O (16); and built parsimony trees using AlakazaM version 1.0.1 (16). Trees were not constructed for clones with more than 3000 sequences, for the sake of rapid analysis.

Data for Machine Learning Models

We used data from three datasets. Data of one healthy donor were obtained from (27) and downloaded from iReceptor (26), and another healthy donor's data were obtained from (28) directly. Six peripheral blood and bone marrow samples of four DLBCL patients were sequenced by Kedmi et al. (**Table 3**). All the DLBCL samples were taken from relapsed patients before treatment. Data were analyzed and lineage trees generated as described in section 2.7.2.

Machine Learning Classification Model Application to IgTreeZ Mutation Count

Tree-Based Mutation Analysis and Dataset Preprocessing

Mutations on the DLBCL and healthy control lineage trees were analyzed using IgTreeZ. We defined the resulting mutation counts as the features for the machine-learning models, together with one additional feature that represents the number of mutations per sequence (**Supplementary Table 1**). A binary column named 'status' with the value of 1 for patients and 0 for controls was added. The control and patient data frames were concatenated. All "Nan" values were replaced with 0 (since Nan values mean no mutations were found).

Data Resampling

We chose to resample the training set because our data were imbalanced (**Table 3**), and over-sampling of the DLBCL data caused overfitting. We tried a combination of over-and under-sampling (over-sampling the patient data, and under-sampling the healthy control data) using methods such as SMOTETomek, which combines SMOTE and Tomek links. However, this also caused overfitting, together with low prediction scores. Using a specific pipeline to choose the required sample size also caused overfitting together with low predictions scores. We concluded that any over-sampling causes overfitting. Therefore, we chose to under-sample the control data using OneSidedSelection (since a random under-sampling also returned low prediction scores), and only under-sampled the training set and not the test set, to make the test as reliable as possible.

Machine Learning Models

Six machine learning models were built (using the scikit-learn package in python) to predict whether a tree-based mutation count originated from a healthy person or a DLBCL patient. The feature values (except the first two columns – sample name and tree ID) were defined as the input, and the status as the output. We chose to scale our data using Normalizer, after trying 8 different scaling methods and finding that Normalizer returns the best results. This can be due to the Normalizer scaling method using rows while other scalers use columns. Since each row in our data represents a separate tree, using Normalizer made the most sense. Data were split into training (75%) and testing (25%) set. To optimize the hyperparameters of all the models, we used GridSearchCV, a method for hyperparameter tuning in which we define a grid of possible parameter values (**Supplementary Table 2**), and GridSearch searches for the optimal set of hyperparameter combinations, using the k-fold cross-validation (CV) approach (cv = 5). In other words, this method trains the model using different combinations of the above-mentioned features and gives the best combinations based on the optimal k-fold CV score obtained.

TABLE 2 | COVID-19 donor data.

Severity	Subject ID	Sex	Age	Collection time (days from symptom onset)
Healthy	H1	F	28	
Healthy	H2	F	30	
Healthy	H3	M	45	
Mild	2	F	37	2
Mild				15
Mild				34
Moderate	8	M	37	14
Moderate				32
Severe				34
Severe	18	F	62	8
Severe				30

TABLE 3 | Healthy control and DLBCL patient datasets.

Group	Sample name	Patient	Tissue	Study	# Trees
Healthy Controls	H1	H1	PB	(27)	18,068
	H2	H2	PB	(28)	9,190
	Overall healthy control trees				27,258
DLBCL	D1	P1	PB	Kedmi et al.	1,651
	D2	P2	PB		1,309
	D3	P3	PB		35
	D4	P4	BM		738
	D5	P1	BM		2,419
	D6	P2	BM		4,834
	Overall DLCBL trees				10,915

RESULTS

Tree-Based Selection Analysis Reflects Mutation Distributions and Shows Inclusion of CDR3s Is Crucial

A lineage tree-based mutation analysis is obviously more accurate than an analysis based on comparing each sequence to the germline (4, 5). On trees, the ancestor sequence for each mutation is better defined; moreover, successive mutations on the same nucleotide, including reversion mutations, can be identified (**Figure 1**). In addition to a more accurate mutation identification and counts on the V and J segments, a tree-based analysis makes it possible to account for mutation in the CDR3 region, which is better defined for a clone (where the putative "germline" CDR3 sequence is clone's consensus CDR3 sequence, and the tree tracks mutations on the CDR3 as well as the V and J segments) than for a single sequence (where the putative "germline" CDR3 sequence is identical to that of the sequence, and hence no mutations can be identified there). Since selection analysis is based on mutation counts, this analysis can also benefit from the more precise lineage tree-based mutation counts.

To test these functions of IgTreeZ, we used Yermanos et al.'s AbSim simulation, which is a time-resolved antibody repertoire simulation that enables the modeling of several immunologically relevant parameters (19). We tested both our tree-based mutation count, especially in the CDR/FWR regions, and its influence on the selection analysis. We modified three simulation parameters and found that the SHM nucleotide change rate has the most impact on mutation profiles. We simulated 100 lineages for each of 13 different probabilities for SHM nucleotide change. By analyzing the resulting 1300 trees we found that, as expected, more mutations are counted, in both the CDRs and FWRs, with higher SHM nucleotide change rate (**Figure 2A**). However, when we used these counts to estimate the selection strengths using ShazaM (15, 16), we found opposite trends – the selection for replacement mutations is weaker as the SHM nucleotide change rate is higher in the CDR. The FWR presents stable selection against replacement mutations (**Figure 2B**). To understand the reason for these opposite trends in the CDRs, we tested the mutation distribution in each region and found that, indeed, the mutation counts in the CDR3 region become relatively greater than those of other regions as the SHM nucleotide change rate is decreased (**Figure 2C**). These results emphasize the importance of the inclusion of the CDR3 in the selection analysis, and thus the potential of lineage tree-based selection analysis, which enables the inclusion of the CDR3 region.

Different Mutation and Selection Patterns in B-Cell Sub-Populations in Human Gut

In order to test our program on empirical data, we analyzed lineage trees from sorted B cells from two histologically normal ileal tissue samples (**Table 1**) processed using our lab's pipeline (Tejedor Vaquero S et al. manuscript in preparation). We used IgTreeZ to record the mutation distributions in these trees and found several consistent patterns, as follows. The relative fractions of CDR3 mutations were highest in GC cells (18 and 23% in Donor 3 and 4 respectively, **Figures 3A, B** and **Tables 4**, **5**). The relative fractions of FWR3 mutations were highest in naïve cells, but not those of the FWR1 and FWR2 regions. Correspondingly, the overall CDR region mutation relative fractions were lowest in naïve cells. Plasma cells of both donors exhibited the highest relative fractions of mutations in FWR1 regions (13 and 12% in donor 3 and 4, respectively), and the lowest relative fractions in FWR3 regions (36 and 39% in donor 3 and 4, respectively).

Using the ShazaM R package (15, 16) to perform selection analysis on the IgTreeZ mutation counts revealed consistent results in both donors, in which GC cell lineage trees exhibited the strongest selection for replacement mutations in the CDRs, and plasma cell lineage trees show the strongest selection against replacement mutations in the FWRs (**Figures 3C–F**). This may suggest that gut plasma cells are selected for their receptors' stability, rather than affinity. Memory B cell lineage trees exhibited a slightly weaker selection for replacement mutations than GC cell lineage trees in the CDRs, and naïve cell lineage trees seem to undergo the weakest selection in CDRs and strong selection for replacement mutations in FWRs. These findings illustrate the different mutation and selection courses of each B cell sub-population in human gut, and, again, the potential of lineage tree-based mutation and selection analyses.

Lineage Tree-Based Transition, Mutation and Selection Analyses of Data From COVID-19 Patients Elucidates the Immune Response to SARS-COV-2

To further demonstrate the potential of IgTreeZ, we analyzed B cell sequences from three COVID-19 patients that differed in

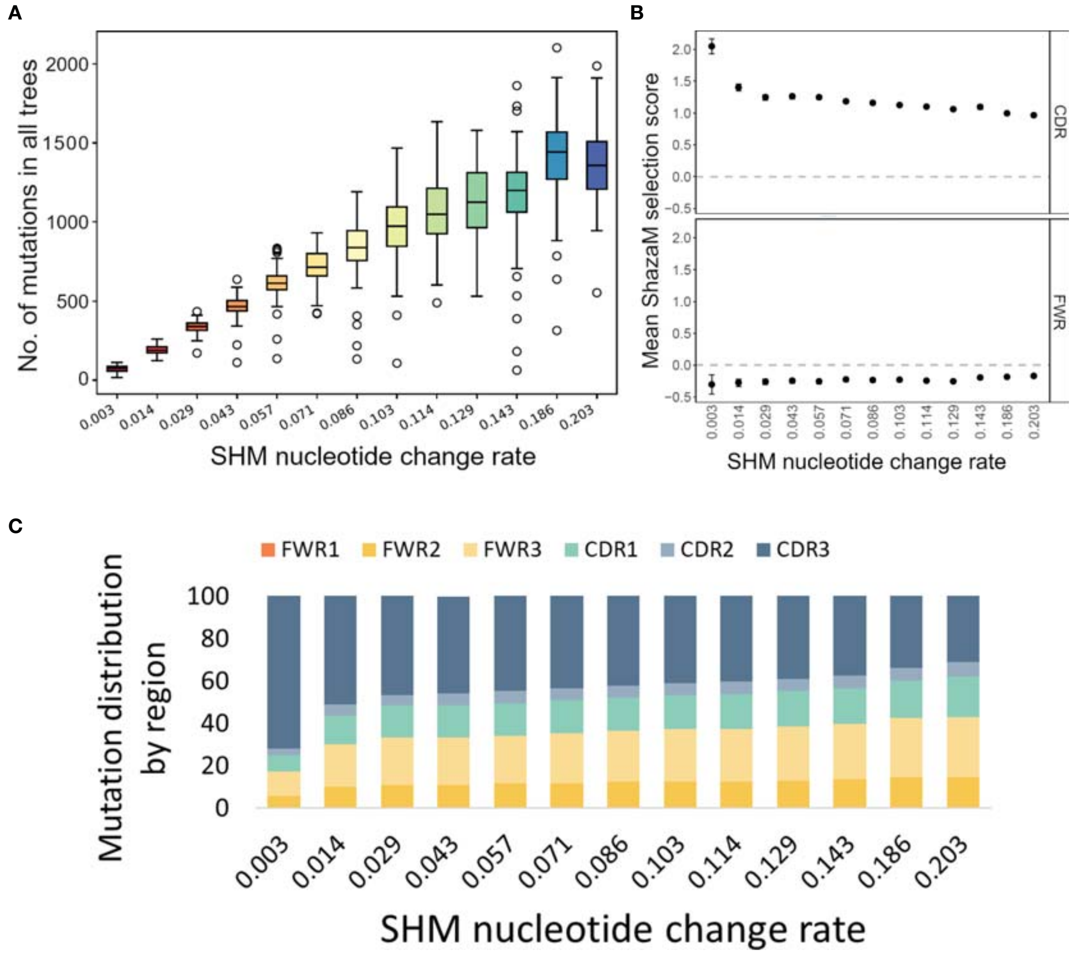

FIGURE 2 | Mutation and selection analyses of simulated trees. **(A)** Mutation counts per whole sequence based on simulated trees under different probabilities for SHM nucleotide change. The plot was created using the compare-reps script based on IgTreeZ-mutations result. **(B)** The means and confidence intervals of the selection scores for tree-based mutation count as calculated and plotted using ShazaM (15, 16). **(C)** The distribution of mutations in the different regions, as counted by IgTreeZ' program poptree-mutations. All trees and sequences were simulated using AbSim (19). CDR, complementarity determining region. FWR, framework region.

disease severity, obtained by Montague et al. at two or three time points from clinical symptom onset for each patient (**Figure 4A**), and of three healthy donors (**Table 2**) (25). We annotated the sequences, labeled the sequences by time point, and constructed lineage trees using AlakazaM (16). Next, we used IgTreeZ to filter trees based on their time point composition, to analyze the transitions between time points, and to perform tree-based mutation and selection analyses.

Counting the number of mutations involved in transitions between time points (defined as transition distance) reveals that transitions between day ~15 to day ~30 and between day ~8 to day ~30 included the highest mutation counts (**Figures 4B–D**). This indicates an extensive GC response that took place at these times. Of note, impossible transitions (such as from day 30 to day 8) were also found, as tree construction algorithm are geared towards choosing the minimal tree out of the infinite number of possible trees, and the minimal tree is not always the best representation of the actual response; the same mutation could, in reality, occur simultaneously in parallel branches of the clone. However, the transition distances associated with impossible transitions were low (median of 2 mutations in the patients with severe and moderate disease, and 3-7 mutations in the patient with mild disease). This implies that the impossible transitions were probably the results of incorrect inference of the relationships of very similar sequences, as a result of the requirements of tree generating algorithms. It is not recommended to constrain such algorithms, because this will result in trees that are more grossly incorrect.

IgTreeZ' mutation analysis function includes mutation profiling, in which mutations are characterized by their source and destination nucleotides, their location (FWR or CDR), and their type (transition or transversion, silent or replacement mutation). In addition, replacement mutations are characterized by source and destination amino acid charge,

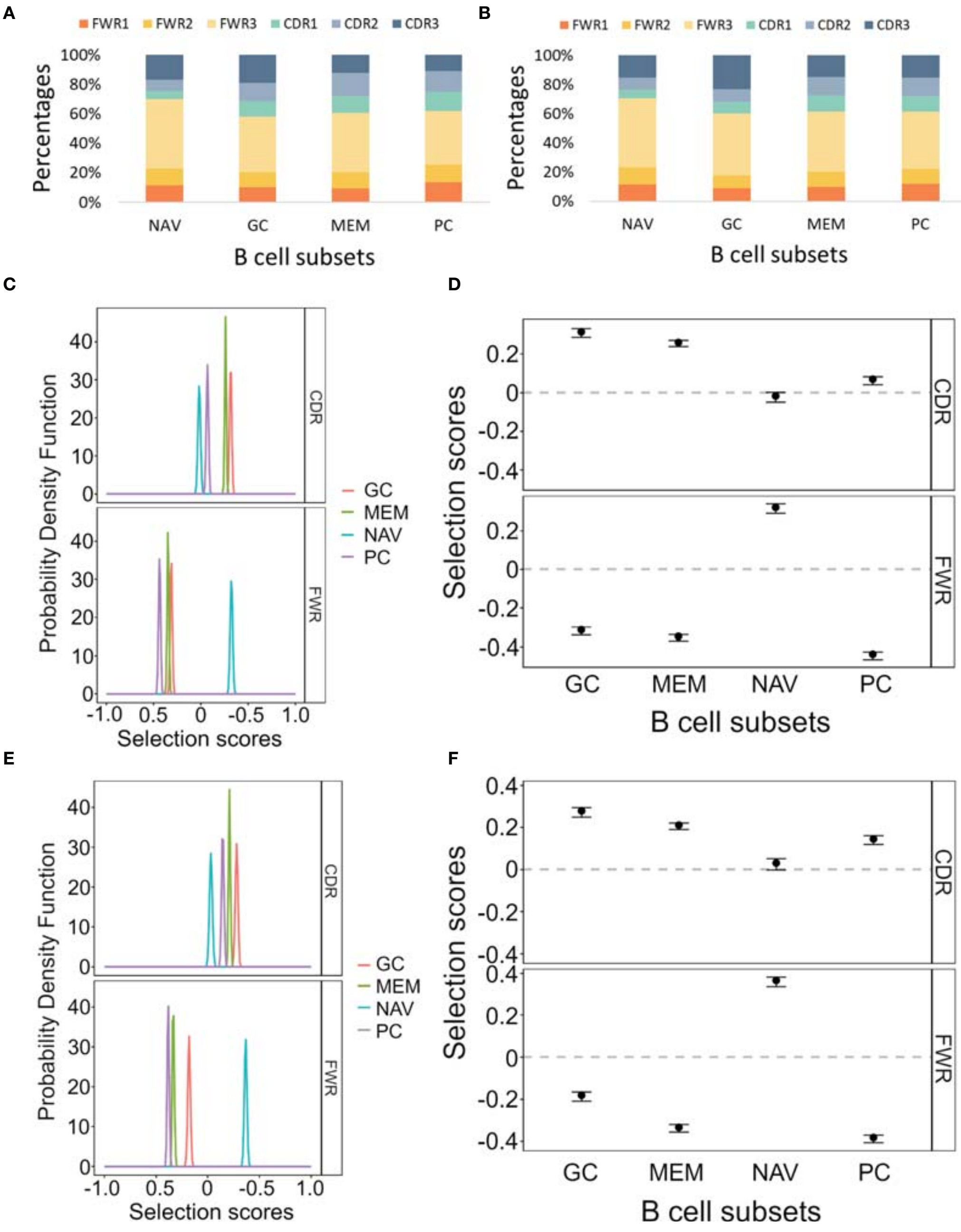

FIGURE 3 | Mutation and selection analyses of IgV gene sequences from different ileal B cell and plasma cell subsets. **(A, B)** The mutation distributions as counted by the IgTreeZ program function "mutations" for Donor 3 and Donor 4, respectively. **(C, E)** The probability density function of the selection scores for the lineage tree-based mutation counts of the different cell subsets for Donor 3 and Donor 4, respectively. **(D, F)** Means and confidence intervals of the selection scores for the same mutation counts for Donor 3 and Donor 4, respectively. Panels **(A–D)** were calculated and plotted using ShazaM (15, 16). MEM, memory; PC, plasma cell; NAV, naïve; CDR, complementarity determining region; FWR, framework region.

TABLE 4 | Donor 3 mutation distribution.

Region	Naïve (%)	GC (%)	Memory (%)	Plasma (%)
FWR1	11.6	10.2	9.3	13.4
FWR2	11.4	10	10.9	12
FWR3	46.7	37.9	40.5	36.2
CDR1	5.6	10.4	11.5	13.1
CDR2	7.7	12.6	15.4	14.1
CDR3	17	18.9	12.4	11.1

TABLE 5 | Donor 4 mutation distribution.

Region	Naïve (%)	GC (%)	Memory (%)	Plasma (%)
FWR1	11.3	9	9.8	12
FWR2	12	8.5	10.7	10.2
FWR3	47	42.6	41.6	39.1
CDR1	5.8	7.7	11.1	11
CDR2	8.4	9	12.6	12.6
CDR3	15.5	23.2	15.2	15.2

hydropathy, volume, chemical, hydrogen donor or acceptor atoms and polarity. We analyzed the data from COVID-19 patients and healthy donors using this function, and compared the results by subject and time point. The relative fractions of mutations involving a positive amino acid out of all the source mutations was the lowest in COVID-19 patients at time points 8-15 days. Moreover, the relative fractions of mutations involving a positive amino acid out of all the destination mutations in COVID-19 at these time points was among the highest (**Figure 4E**). This suggests a tendency of the affinity maturation in COVID-19 patients to avoid mutating positively charged amino acids, and to favor mutation that create such amino acids.

Next, we used ShazaM to evaluate selection strengths in the same lineage tree repertoires. The three patients' lineage trees showed the strongest selection against replacement mutations in FWRs around 30 days from clinical symptom onset (**Figures 4F–H**). This indicates dominance of affinity-matured, structurally stable antibodies. On the other hand, the selection for replacement mutations in CDRs showed dynamic changes in the mild and moderate disease patients, but not in the severe disease patient. This may reflect the absence of an effective antibody selection process in the latter patient. On day 2, the mild disease patient showed the weakest selection for both the CDRs and the FWRs. This may indicate the generation of a large number of low affinity, pre-GC BCRs. Finally, to focus our analysis on clones that may have been involved in the immune response to SARS-COV-2, we filtered clones that were sampled at all three time points. Such clones had higher selection for replacement mutations in the CDRs (**Figures 4I, J**). Moreover, the patient with the severe COVID-19 disease showed the lowest selection for replacement mutations among the three patients.

Machine Learning Models Using IgTreeZ Output Can Distinguish Lymphoma From Normal Lineage Trees

IgTreeZ mutations analysis returns an extensive data table. This data can be used for machine learning. To demonstrate the potential of this application, we built six machine learning models to predict whether a tree-based mutation count originated from a healthy person or a DLBCL patient. Preceding model construction, we performed an exploratory data analysis (**Supplementary Figures S1**, **S2**) and a dimensionality reduction. We used PCA with two and three dimensions, and T-SNE, and found that all of them separated the data very well (**Supplementary Figure S3**). Therefore, we used the full dataset for the different models. Among the six models tested, the Support-Vector Machine (SVM) returned the best results.

SVM Model

We built an SVM model and tested a parameter space to obtain the optimal parameter values. We chose to define the following parameter options: kernel (the kernel type to be used in the algorithm) - ['poly', 'rbf', 'sigmoid'] and C (the regularization parameter) - [50, 10, 1.0, 0.1, 0.01]). We defined gamma, the kernel coefficient, to be 'scale'. We found the optimal parameter values to be kernel=rbf and C=10. Using these parameter values, the training and test sets show similar and high results – the macro avg scores are 0.97085 for the training and 0.95784 for the test sets, respectively (**Tables 6**, **7**, respectively). The confusion matrices are also consistent, and the true prediction rate of the control trees was 0.99 for the training set and 0.98 for the test set, while the true prediction rate of the DLBCL trees was 0.95 and 0.92 for the training and test sets, respectively (**Figures 5A, B**, respectively). The ROC was 1 and 0.99 for the training and test sets, respectively, and overall exhibits a very high learning rate (**Figure 5C**).

KNN, Decision Trees, Random Forest, AdaBoost and LDA Models

We chose to define parameter options for KNN, decision trees, Random Forest, AdaBoost and LDA models as shown in **Supplementary Table 2**. LDA results exhibit a small increase from the training set to the test set. However, since we analyzed a relatively small dataset, this increase is negligible. Since Random Forest and AdaBoost returns information on feature importance, we re-trained a simple, non-cross validation model, with the optimized parameters we found earlier. We found that the two most important features for Random Forest are 'sequences' and 'nodes' and for AdaBoost these are 'sequences' and 'mutations_per_sequence' (**Supplementary Tables 3**, **4** for Random Forest and AdaBoost, respectively), and tested their distributions (**Supplementary Figure S4**). From the 'mutations_per_sequence' distribution, it is apparent that DLBCL trees tend to have fewer mutations per sequence, with a narrower distribution than the control trees. On the other hand, we can see that the DLBCL trees have more diverse sequence and node numbers, and tend to have more sequences than the control trees. The two features seem to be two sides of the same coin – the DLBCL clones are larger, but this is mostly due to branching, as they contain fewer unique mutations in each sequence.

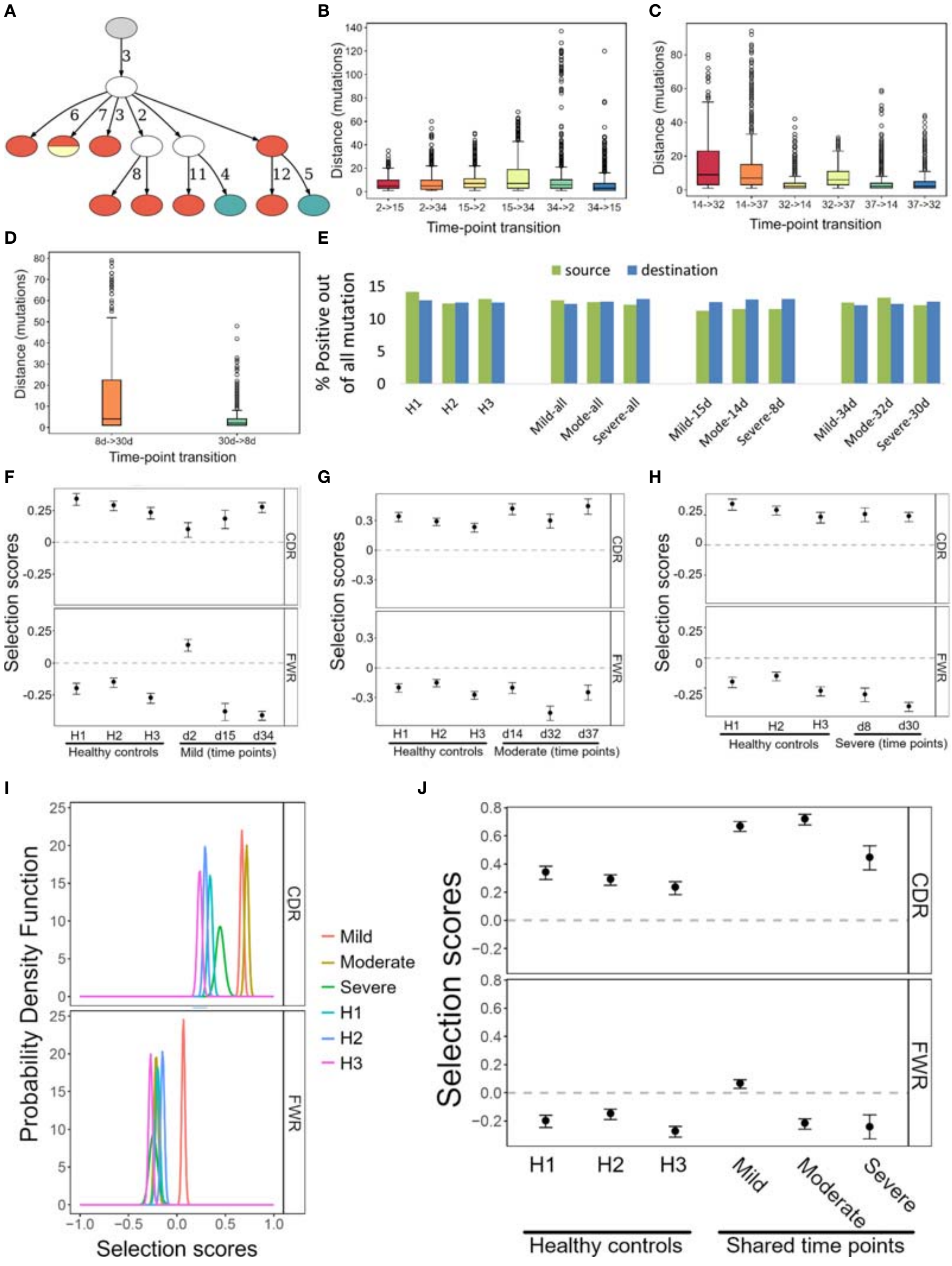

FIGURE 4 | Transition, mutation and selection analyses of human B cells of COVID-19 patients and healthy donors. **(A)** An example lineage tree from the patient with mild disease. Filled nodes represent sampled sequences, nodes with more than one color represent multiple sequences from different time points, and the numbers on edges correspond to numbers of mutations between nodes. The graph was created using the function IgTreeZ-draw. **(B–D)** The numbers of mutations involved in transitions for the mild, moderate, and severe disease patients. The plots were created using IgTreeZ-poptree. **(E)** The partial fractions of the mutations that involved positive amino acids out of all mutations. Source/Destination – the mutation source/destination that involved a positive amino acid. **(F–H)** The mean and confidence interval of the selection scores for the tree-based mutation counts of the mild, moderate, and severe disease patients. **(I)** The probability density function of the selection scores for clones that were shared between time points of the mild, moderate, and severe disease patients and of healthy donors. **(J)** The mean and confidence interval of the selection scores for the tree-based mutation counts of the same data as I. Panels **(D–F, I, J)** were calculated and plotted using ShazaM (15, 16).

TABLE 6 | Classification report of the training set.

	Precision	Recall	f1-score	support
0	0.95235	0.99111	0.97134	8407
1	0.99079	0.95074	0.97036	8263
accuracy			0.97086	16470
Macro avg	0.97157	0.97092	0.97085	16470
Weighted avg	0.97164	0.97086	0.97085	16470

DISCUSSION

In this work, we present IgTreeZ, a comprehensive tool for lineage tree analysis, and demonstrate the value of this tool. Several studies emphasized the importance of lineage tree-based mutation and selection analysis. Zuckerman et al. predicted an alteration in the SHM mechanism in myasthenia gravis thymic ectopic GCs that was later verified by gene expression analysis (4). Yaari and colleagues used lineage trees to show that the FWR and CDR are designed under different selection patterns and that long-term selection is dependent on the heavy chain variable gene family (29). Lineage tree-based mutation counts can reveal multiple mutation patterns that are under-counted using clone consensus sequences and over-counted using a direct sequence-based approach (**Figure 1**). Moreover, CDR3s include the junction between the V gene segment and the J gene segment, and part of the D segment in heavy chains. These segments include the nucleotide deletion and insertions, that can increase the CDR3 sequence diversity beyond the pre-encoded V-D-J germline sequences. All of this makes the CDR3 the most variable region in Ig genes, and it is most often critical for antigen binding. However, its variable nature makes it hard to analyze and thus it is often excluded from the selection analysis (16). Here we propose a method that also accounts for the mutations in the CDR3, and show that CDR3 mutations have a significant impact on the results of selection analysis (**Figure 2**).

We used IgTreeZ to show that tree-based mutation analysis reveals different mutation profiles of gut B cell sub-populations. We found that naïve trees are not subject to positive nor negative selection in the CDRs, and that naïve trees' FWRs seem to be subject to selection for replacement mutation. The latter finding is surprising, as naïve B cells are defined as cells that have not yet been exposed to an antigen, and did not undergo affinity maturation, hence their IgV genes are not expected to contain any mutations. Indeed, 60-70% of the naïve cell sequences contained no mutations, and those that did had only very few mutations per sequence (Tejedor Vaquero S et al. manuscript in preparation). There are several possible explanations for the observation of SHM in cells that were identified as naïve B cells. First, cannot completely exclude PCR errors, however these should have been eliminated by the use of unique molecular identifiers; the relatively high percentage of naïve B cell sequences with mutations also argues against this possibility. The latter consideration, and the low SHM frequency in these sequences, also argue against many of these cells having been contaminating IGM memory cells. Recent studies show that "naïve B cells" (typically IgD^{high}IgM^{+}CD10^{-} CD27^{-}CD38^{low}) are more heterogeneous than expected and may include a fraction recently activated by antigen. So our naïve cells with IgV gene mutations may represent, at least in part, recently activated naïve cells which have just been instructed to become GC B cells and begun to express activation-induced cytidine deaminase (AID). An exciting possibility is that these are similar to the "activated naïve" B cells observed in systemic lupus erythematosus (7, 30) and COVID-19 (31). Whatever the explanation, the selection for replacement mutations in the FWRs is inconsistent with selection for receptor stability. Perhaps the Ig undergoes many mutations in the FWRs during early activation, with selection not yet operative, so that these results only reflect mutations and not selection. The differentiation pathways of this fraction of naïve B cells are still being elucidated; they may or may not enter the GC at a later time point, and may even participate in a wholly extrafollicular activation pathway.

We also analyzed COVID-19 patient repertoires and found indications for extensive SHM between the second and fourth week after onset of clinical symptoms and evidence for the generation of affinity maturated, structurally stable antibodies by day ~32 post-infection in the patients with mild and moderate responses. A tree-based mutation analysis of the lineage trees of all COVID-19 patients revealed a tendency of SHM to avoid mutating away from positive amino acids, but a high tendency to create them. Recently, Khan and colleagues found that an acidic tandem repeat in the Nsp3 subdomain of the HCoV-HKU1 polyprotein was the predominant target of antibody responses in adult donors (32). This may explain the positive tendency we recognized. In a review from 2021 (33), the authors note that high neutralizing antibody titers are associated with potentially

TABLE 7 | Classification report of the test set.

	Precision	Recall	f1-score	support
0	0.96985	0.98304	0.97640	6838
1	0.95589	0.92325	0.93929	2723
accuracy			0.96601	9561
Macro avg	0.96287	0.95314	0.95784	9561
Weighted avg	0.96587	0.96601	0.96583	9561

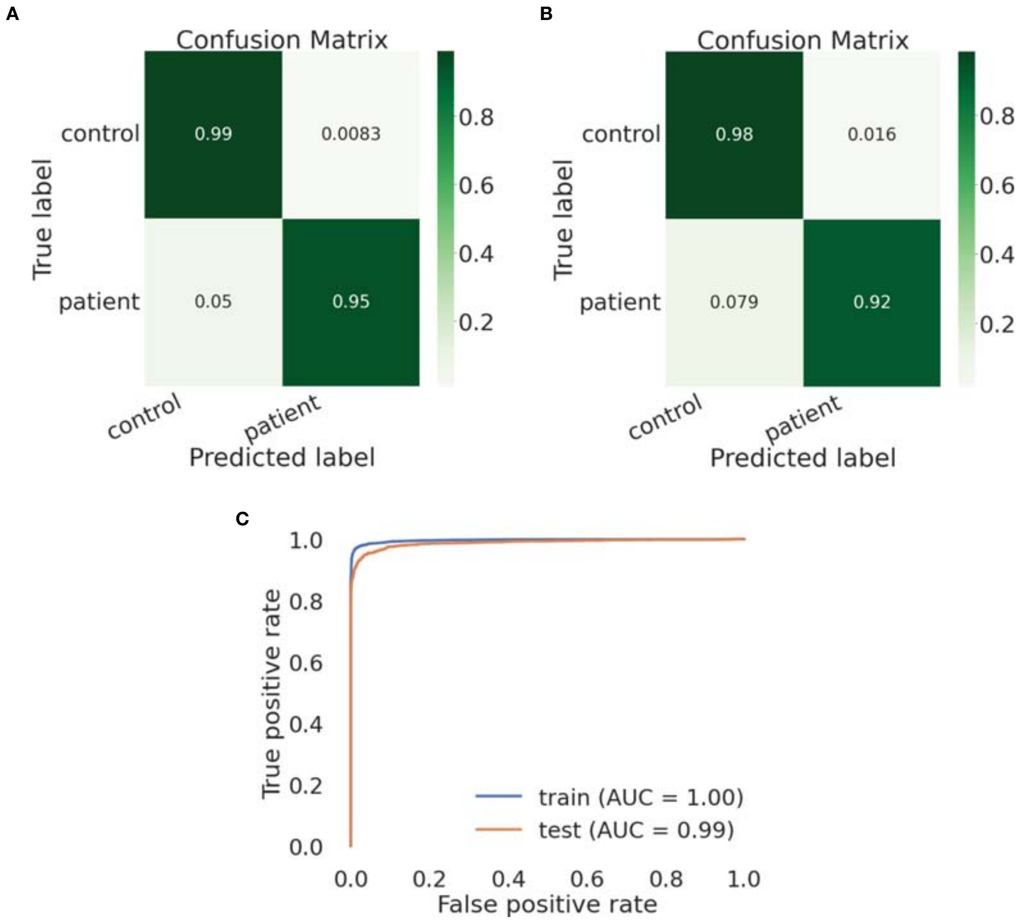

FIGURE 5 | An SVM model can distinguish lymphoma from healthy control lineage trees using IgTreeZ output. **(A, B)** Confusion matrices for the training and test set, respectively. **(C)** Roc curves for both sets. Confusion matrices and ROC curves were created using Python's scikit-learn package.

extrafollicular B cell responses, and suggest that the development of neutralizing antibodies against SARS-CoV-2 can be accomplished by many B cells with little or no affinity maturation required. This is consistent with our finding that the mild disease patient shows the lowest selection pressure on the second day from the appearance of clinical symptoms.

COVID-19 patient clones that were sampled at all three time points had higher selection for replacement mutations in the CDRs (**Figures 4I, J**). Although clones shared between all three time points tend to be larger and include more mutations, the overall mutation counts had less impact on the selection than mutation location [**Figure 4B**, and as shown by (15)]. For this reason, this higher selection for replacement mutations may be part of the effort exerted by the immune system to generate efficient antibodies against the virus, an effort which may have been less effective in the patient who suffered from a severe disease.

Finally, we have shown that the output from IgTreeZ can be used in machine learning models, for example to distinguish between lymphoma and normal lineage trees. Mutation-based machine learning was recently shown to predict a sequence's cell type (34). An accurate tree-based mutation profiling can be useful for machine learning based classification as well.

IgTreeZ is designed for repertoires. The program can process a large number of trees using parallel processing, and by default uses the maximal number of processors available, but this can be adjusted using a parameter. Using 4 CPU cores, the mutation analysis, the most complex of IgTreeZ functions, takes less than 30 minutes for 90,000 trees containing 2,000,000 sequences. Utilizing 64 CPU cores decreases the running time of the same tree set to 12 minutes. To overcome the operating system's maximum argument number limit, IgTreeZ can receive its input trees as a directory name, and process the whole directory's content. A tree with more than 5000 nodes is analyzed in less than two minutes, even on an 8G RAM. These features theoretically allow IgTreeZ to process any number of trees, even large ones.

In summary, B cell lineage tree analysis may shed light on many of aspects of B cell affinity maturation in GCs in particular, and on B cell response population dynamics in general. Our new tool, IgTreeZ, performs various types of lineage tree-based analysis in a simple command line mode, making all these analyses easily accessible to non-bioinformaticians. An important conclusion from our analysis is that CDR3 regions, which are often excluded from selection analyses, must be included for the results to be correct; while CDR3 inclusion is only possible if these analyses are lineage tree-based.

DATA AVAILABILITY STATEMENT

The program IgTreeZ can be found in GitHub - https://github.com/neumanh/IgTreeZ. The DLBCL data can be found in the NCBI Sequence Read Archive under accession number PRJNA796500 - https://www.ncbi.nlm.nih.gov/bioproject/PRJNA796500. The COVID-19 data were downloaded from iReceptor (Montague et al., 2021) - https://gateway.ireceptor.org/samples?query_id=55507. The healthy ileum data can be found in the NCBI Sequence Read Archive under accession number PRJNA596067, and will be released upon publication of Tejedor Vaquero S et al. (in preparation at the time of this manuscript's publication) - https://dataview.ncbi.nlm.nih.gov/object/PRJNA596067?reviewer=fh0r7gajkn50dcpiarrdss18d9.

ETHICS STATEMENT

The use of ileum tissue samples was approved by the Ethical Committee for Clinical Investigation of the Institut Hospital del Mar d' Investigacions Mèdiques (CEIC-IMIM 20114/5892/I) and by the Mount Sinai Institutional Review Board (HS#14-00174). The DLBCL study was approved by the Sheba Medical Center and Israeli Ministry of Health review boards. The patients/participants provided their written informed consent to participate in this study.

AUTHOR CONTRIBUTIONS

HN wrote the IgTreeZ program and all other scripts described here unless otherwise noted, performed the research and wrote the manuscript. JA and HN wrote the ML scripts, performed the ML analysis, and wrote the manuscript. MK, GM, and AC contributed experimental data and wrote the manuscript. RM designed and supervised the research and wrote the manuscript. All authors contributed to the article and approved the submitted version.

FUNDING

HN was supported by a Bar-Ilan University President's Scholarship. AC is supported by the Spanish Ministry of Economy and Competitiveness (MINECO) grant RTI2018-093894-B-100. GM is supported by Spanish Institute of Health Carlos III (Miguel Servet grant 2020-2024).

ACKNOWLEDGMENTS

The Mehr lab members are grateful to Guy Bitansky for assistance with the establishment of our lab's analysis pipeline. The machine learning studies were performed as a project for a course taught by Sol Efroni and Tom Snir. We thank Dr. Johannes Trück for providing the healthy control data.

SUPPLEMENTARY MATERIAL

The Supplementary Material for this article can be found online at: https://www.frontiersin.org/articles/10.3389/fimmu.2022.822834/full#supplementary-material

REFERENCES

1. Elsner RA, Shlomchik MJ. Germinal Center and Extrafollicular B Cell Responses in Vaccination, Immunity, and Autoimmunity. *Immunity* (2020) 53:1136–50. doi: 10.1016/j.immuni.2020.11.006
2. De Silva NS, Klein U. Dynamics of B Cells in Germinal Centres. *Nat Rev Immunol* (2015) 15:137–48. doi: 10.1038/nri3804
3. Shahaf G, Barak M, Zuckerman NS, Swerdlin N, Gorfine M, Mehr R. Antigen-Driven Selection in Germinal Centers as Reflected by the Shape Characteristics of Immunoglobulin Gene Lineage Trees: A Large-Scale Simulation Study. *J Theor Biol* (2008) 255:210–22. doi: 10.1016/j.jtbi.2008.08.005
4. Zuckerman NS, McCann KJ, Ottensmeier CH, Barak M, Shahaf G, Edelman H, et al. Ig Gene Diversification and Selection in Follicular Lymphoma, Diffuse Large B Cell lymphomZa and Primary Central Nervous System Lymphoma Revealed by Lineage Tree and Mutation Analyses. *Int Immunol* (2010) 22:875–87. doi: 10.1093/intimm/dxq441
5. Hoehn KB, Vander Heiden JA, Zhou JQ, Lunter G, Pybus OG, Kleinstein SH. Repertoire-Wide Phylogenetic Models of B Cell Molecular Evolution Reveal Evolutionary Signatures of Aging and Vaccination. *Proc Natl Acad Sci USA* (2019) 116:22664–72. doi: 10.1073/pnas.1906020116
6. Meng W, Zhang B, Schwartz GW, Rosenfeld AM, Ren D, Thome JJC, et al. An Atlas of B-Cell Clonal Distribution in the Human Body. *Nat Biotechnol* (2017) 35:879–86. doi: 10.1038/nbt.3942
7. Tipton CM, Fucile CF, Darce J, Chida A, Ichikawa T, Gregoretti I, et al. Diversity, Cellular Origin and Autoreactivity of Antibody-Secreting Cell Population Expansions in Acute Systemic Lupus Erythematosus. *Nat Immunol* (2015) 16:755–65. doi: 10.1038/ni.3175
8. Tabibian-Keissar H, Zuckerman NS, Barak M, Dunn-Walters DK, Steiman-Shimony A, Chowers Y, et al. B-Cell Clonal Diversification and Gut-Lymph Node Trafficking in Ulcerative Colitis Revealed Using Lineage Tree Analysis. *Eur J Immunol* (2008) 38:2600–9. doi: 10.1002/eji.200838333
9. Miao Y, Medeiros LJ, Li Y, Li J, Young KH. Genetic Alterations and Their Clinical Implications in DLBCL. *Nat Rev Clin* (2019) 16:634–52. doi: 10.1038/s41571-019-0225-1
10. Ostrovsky-berman M, Frankel B, Polak P, Yaari G. Immune2vec: Embedding B / T Cell Receptor Sequences in N Using Natural Language Processing. *Front Immunol* (2021) 12:1–13. doi: 10.3389/fimmu.2021.680687
11. Shemesh O, Polak P, Lundin KEA, Sollid LM, Yaari G. Machine Learning Analysis of Naïve B-Cell Receptor Repertoires Stratifies Celiac Disease Patients and Controls. *Front Immunol* (2021) 12:627813. doi: 10.3389/fimmu.2021.627813

12. Lefranc M-P. Antibody Informatics: IMGT, the International ImMunoGeneTics Information System. *Microbiol Spectr* (2014) 2:1–14. doi: 10.1128/microbiolspec.AID-0001-2012
13. Kyte J, Doolittle RF. A Simple Method for Displaying the Hydropathic Character of a Protein. *J Mol Biol* (1982) 157:105–32. doi: 10.1016/0022-2836(82)90515-0
14. Pommié C, Levadoux S, Sabatier R, Lefranc G, Lefranc MP. IMGT Standardized Criteria for Statistical Analysis of Immunoglobulin V-Region Amino Acid Properties. *J Mol Recognit* (2004) 17:17–32. doi: 10.1002/jmr.647
15. Yaari G, Uduman M, Kleinstein SH. Quantifying Selection in High-Throughput Immunoglobulin Sequencing Data Sets. *Nucleic Acids Res* (2012) 40:10–2. doi: 10.1093/nar/gks457
16. Gupta NT, Vander Heiden JA, Uduman M, Gadala-Maria D, Yaari G, Kleinstein SH. Change-O: A Toolkit for Analyzing Large-Scale B Cell Immunoglobulin Repertoire Sequencing Data. *Bioinformatics* (2015) 31:3356–8. doi: 10.1093/bioinformatics/btv359
17. Shannon M, Mehr R. Reconciling Repertoire Shift With Affinity Maturation: The Role of Deleterious Mutations. *J Immunol* (1999) 162:3950–6.
18. Ellson J, Gansner ER, Koutsofios E, North SC, Woodhull G. Graphviz and Dynagraph — Static and Dynamic Graph Drawing Tools. *Immunity* (2004) 53:127–48. doi: 10.1007/978-3-642-18638-7_6
19. Yermanos A, Greiff V, Krautler NJ, Menzel U, Dounas A, Miho E, et al. Comparison of Methods for Phylogenetic B-Cell Lineage Inference Using Time-Resolved Antibody Repertoire Simulations (AbSim). *Bioinformatics* (2017) 33:3938–46. doi: 10.1093/bioinformatics/btx533
20. Ye J, Ma N, Madden TL, Ostell JM. IgBLAST: An Immunoglobulin Variable Domain Sequence Analysis Tool. *Nucleic Acids Res* (2013) 41:34–40. doi: 10.1093/nar/gkt382
21. Giudicelli V, Chaume D, Lefranc M-P. IMGT / GENE-DB : A Comprehensive Database for Human and Mouse Immunoglobulin and T Cell Receptor Genes. *Nucleic Acids Res* (2005) 33:256–61. doi: 10.1093/nar/gki010
22. Vander Heiden JA, Yaari G, Uduman M, Stern JNH, O'connor KC, Hafler DA, et al. PRESTO: A Toolkit for Processing High-Throughput Sequencing Raw Reads of Lymphocyte Receptor Repertoires. *Bioinformatics* (2014) 30:1930–2. doi: 10.1093/bioinformatics/btu138
23. Brochet X, Lefranc MP, Giudicelli V. IMGT/V-QUEST: The Highly Customized and Integrated System for IG and TR Standardized V-J and V-D-J Sequence Analysis. *Nucleic Acids Res* (2008) 36:503–8. doi: 10.1093/nar/gkn316
24. Barak M, Zuckerman NS, Edelman H, Unger R, Mehr R. IgTree©: Creating Immunoglobulin Variable Region Gene Lineage Trees. *J Immunol Methods* (2008) 338:67–74. doi: 10.1016/j.jim.2008.06.006
25. Montague Z, Lv H, Otwinowski J, DeWitt WS, Isacchini G, Yip GK, et al. Dynamics of B Cell Repertoires and Emergence of Cross-Reactive Responses in Patients With Different Severities of COVID-19. *Cell Rep* (2021) 35:109173. doi: 10.1016/j.celrep.2021.109173
26. Corrie BD, Marthandan N, Zimonja B, Jaglale J, Zhou Y, Barr E, et al. Ireceptor: A Platform for Querying and Analyzing Antibody/B-Cell and T-Cell Receptor Repertoire Data Across Federated Repositories. *Immunol Rev* (2018) 284:24–41. doi: 10.1111/imr.12666
27. Kuri-Cervantes L, Pampena MB, Meng W, Rosenfeld AM, Ittner CAG, Weisman AR, et al. Comprehensive Mapping of Immune Perturbations Associated With Severe COVID-19. *Sci Immunol* (2020) 5. doi: 10.1126/sciimmunol.abd7114
28. Ghraichy M, Galson JD, Kovaltsuk A, von Niederhäusern V, Pachlopnik Schmid J, Recher M, et al. Maturation of the Human Immunoglobulin Heavy Chain Repertoire With Age. *Front Immunol* (2020) 11:1734. doi: 10.3389/fimmu.2020.01734
29. Yaari G, Benichou JIC, Vander Heiden JA, Kleinstein SH, Louzoun Y. The Mutation Patterns in B-Cell Immunoglobulin Receptors Reflect the Influence of Selection Acting at Multiple Time-Scales. *Philos Trans R Soc B Biol Sci* (2015) 370. doi: 10.1098/rstb.2014.0242
30. Jenks SA, Cashman KS, Zumaquero E, Marigorta UM, Patel AV, Wang X, et al. Distinct Effector B Cells Induced by Unregulated Toll-Like Receptor 7 Contribute to Pathogenic Responses in Systemic Lupus Erythematosus. *Immunity* (2018) 49:725–39.e6. doi: 10.1016/j.immuni.2018.08.015
31. de Campos-Mata L, Tejedor Vaquero S, Tachó-Piñot R, Piñero J, Grasset EK, Arrieta Aldea I, et al. SARS-CoV-2 Sculpts the Immune System to Induce Sustained Virus-Specific Naïve-Like and Memory B-Cell Responses. *Clin Transl Immunol* (2021) 10:1–21. doi: 10.1002/cti2.1339
32. Khan T, Rahman M, Al Ali F, Huang SSY, Ata M, Zhang Q, et al. Distinct Antibody Repertoires Against Endemic Human Coronaviruses in Children and Adults. *JCI Insight* (2021) 6:1–34. doi: 10.1172/jci.insight.144499
33. Sette A, Crotty S. Adaptive Immunity to SARS-CoV-2 and COVID-19. *Cell* (2021) 184:861–80. doi: 10.1016/j.cell.2021.01.007
34. Ghraichy M, von Niederhäusern V, Kovaltsuk A, Galson JD, Deane CM, Trück J. Different B Cell Subpopulations Show Distinct Patterns in Their IgH Repertoire Metrics. *Elife* (2021) 10:e73111. doi: 10.7554/eLife.73111

Conflict of Interest: The authors declare that the research was conducted in the absence of any commercial or financial relationships that could be construed as a potential conflict of interest.

frontiers | Frontiers in Immunology

TYPE Original Research
PUBLISHED 14 February 2023
DOI 10.3389/fimmu.2023.1043631

EDITED BY
Vandana Kalia,
School of Medicine, University of Washington, United States

REVIEWED BY
Erin West,
National Heart, Lung, and Blood Institute (NIH), United States
Veena S. Patil,
National Institute of Immunology, India

*CORRESPONDENCE
Ambra Natalini
ambra.natalini@crick.ac.uk
Francesca Di Rosa
francesca.dirosa@cnr.it

†PRESENT ADDRESS
Ambra Natalini,
Immunosurveillance Laboratory, The Francis Crick Institute, London, United Kingdom
Sonia Simonetti,
Medical Oncology Department, Campus Bio-Medico University, Rome, Italy
Miguel Muñoz-Ruiz,
Department of Immunology, Ophthalmology and ENT, Complutense University School of Medicine and 12 de Octubre Health Research Institute (imas12), Madrid, Spain

SPECIALTY SECTION
This article was submitted to Immunological Memory, a section of the journal Frontiers in Immunology

RECEIVED 13 September 2022
ACCEPTED 09 January 2023
PUBLISHED 14 February 2023

CITATION
Natalini A, Simonetti S, Favaretto G, Lucantonio L, Peruzzi G, Muñoz-Ruiz M, Kelly G, Contino AM, Sbrocchi R, Battella S, Capone S, Folgori A, Nicosia A, Santoni A, Hayday AC and Di Rosa F (2023) Improved memory CD8 T cell response to delayed vaccine boost is associated with a distinct molecular signature.
Front. Immunol. 14:1043631.
doi: 10.3389/fimmu.2023.1043631

Improved memory CD8 T cell response to delayed vaccine boost is associated with a distinct molecular signature

Ambra Natalini[1*†], Sonia Simonetti[1†], Gabriele Favaretto[1], Lorenzo Lucantonio[1,2], Giovanna Peruzzi[3], Miguel Muñoz-Ruiz[4†], Gavin Kelly[5], Alessandra M. Contino[6], Roberta Sbrocchi[6], Simone Battella[6], Stefania Capone[6], Antonella Folgori[6], Alfredo Nicosia[7,8], Angela Santoni[9], Adrian C. Hayday[4,10,11] and Francesca Di Rosa[1*]

[1]Institute of Molecular Biology and Pathology, National Research Council of Italy (CNR), Rome, Italy, [2]Department of Molecular Medicine, University of Rome “Sapienza”, Rome, Italy, [3]Center for Life Nano- & Neuro-Science, Fondazione Istituto Italiano di Tecnologia (IIT), Rome, Italy, [4]Immunosurveillance Laboratory, The Francis Crick Institute, London, United Kingdom, [5]Bioinformatic and Biostatistics Science and Technology Platform, The Francis Crick Institute, London, United Kingdom, [6]ReiThera S.R.L., Rome, Italy, [7]CEINGE, Naples, Italy, [8]Department of Molecular Medicine and Medical Biotechnology, University of Naples Federico II, Naples, Italy, [9]IRCCS Neuromed, Isernia, Italy, [10]Peter Gorer Department of Immunobiology, King’s College London, London, United Kingdom, [11]National Institute for Health Research (NIHR), Biomedical Research Center (BRC), Guy’s and St Thomas’ NHS Foundation Trust and King’s College London, London, United Kingdom

Effective secondary response to antigen is a hallmark of immunological memory. However, the extent of memory CD8 T cell response to secondary boost varies at different times after a primary response. Considering the central role of memory CD8 T cells in long-lived protection against viral infections and tumors, a better understanding of the molecular mechanisms underlying the changing responsiveness of these cells to antigenic challenge would be beneficial. We examined here primed CD8 T cell response to boost in a BALB/c mouse model of intramuscular vaccination by priming with HIV-1 gag-encoding Chimpanzee adenovector, and boosting with HIV-1 gag-encoding Modified Vaccinia virus Ankara. We found that boost was more effective at day(d)100 than at d30 post-prime, as evaluated at d45 post-boost by multi-lymphoid organ assessment of gag-specific CD8 T cell frequency, CD62L-expression (as a guide to memory status) and *in vivo* killing. RNA-sequencing of splenic gag-primed CD8 T cells at d100 revealed a quiescent, but highly responsive signature, that trended toward a central memory (CD62L$^+$) phenotype. Interestingly, gag-specific CD8 T cell frequency selectively diminished in the blood at d100, relative to the spleen, lymph nodes and bone marrow. These results open the possibility to modify prime/boost intervals to achieve an improved memory CD8 T cell secondary response.

KEYWORDS

CD8 T cells, memory, prime-boost interval, transcriptomic profile, vaccination

Introduction

CD8 T cells are one of the pillars of adaptive immunity. Naïve CD8 T cells are primed in lymph nodes (LNs) and the spleen by mature dendritic cells (DCs), which present short antigen (Ag)-derived peptides in the groove of Major Histocompatibility Complex (MHC) class I (MHC-I) molecules, together with sufficient costimulatory signals and in the context of CD4 T cell help. Thereupon, Ag-responding CD8 T cells proliferate and differentiate as effectors and memory cells. In contrast to naïve T cells that mostly recirculate in blood, spleen and LNs, effector and memory T cells have enhanced capacity to migrate to the bone marrow (BM) and extra-lymphoid tissues (1). Upon recognition of Ag-MHC-I presented by target cells, effector CD8 T cells display cytotoxic activity and/or cytokine production, thus critically contributing to the clearance of Ag-expressing cells. Afterwards most effector CD8 T cells die, while a few memory CD8 T cells remain durable, ready to provide an enhanced secondary response in case of subsequent encounter with the same Ag (2).

Although memory CD8 T cells are critical for durable protection against viral infections and tumors (3), some questions of their biology are still unsolved, hampering the possibility to manipulate CD8 T cell responses, for example in vaccine design. Generating CD8 T cell-eliciting vaccines proved challenging for many years. The obstacles have now been reduced by some effective platforms, including those based on adenoviral vectors (4–6) and on mRNA (7). Nevertheless, there is no clear protocol for how best to induce long-lasting immunity in a predictable manner in respect to vaccine dose and route of administration. Similarly, even though it has been suggested that delaying vaccine boost can be beneficial for improved CD8 T cell response, at least to adenoviral vector-based vaccines, there is no current agreement on the criteria for setting the appropriate time intervals between repeated injections (8–10). Solving these issues can be extremely beneficial for immunological understanding and for public health policy, as emphasized by the current COVID-19 pandemic (11–13).

We previously showed that the Chimpanzee adenovector ChAd-gag induced a strong clonal expansion of CD8 T cells against the model antigen Human Immunodeficiency Virus-1 (HIV-1) gag in BALB/c mice (14). Indeed, after intramuscular (i.m.) injection with ChAd-gag, gag-specific CD8 T cells in S-G_2/M phases of cell cycle were found not only in LNs and spleen, but also in peripheral blood. Results were similar after boosting with Modified Vaccinia virus Ankara (MVA)-gag (14). Using this ChAd-gag/MVA-gag model (14, 15), we have now addressed here the impact of the prime/boost time interval on gag-specific CD8 T cell immunity. Our hypothesis was that establishment and regulation of quiescence in primed CD8 T cells after clonal expansion would be closely related to the cells' responsiveness to boosting. To test this hypothesis, we evaluated in parallel the post-proliferative tail of the primary response in spleen, LNs, BM and blood, and the kinetics of responsiveness to boost. We identified the time-shift from low to high responsiveness, and characterized the molecular profile of highly responsive splenic memory CD8 T cells.

Methods

Adenoviral and MVA vectors

Replication defective, ΔE1 ΔE2 ΔE3 ChAd3 vector encoding HIV-1 gag protein under HCMV promoter (ChAd-gag) and MVA encoding the HIV-1 gag protein under the control of vaccinia p7.5 promoter (MVA-gag) were generated as described and used in all experiments (14–17).

Vaccination

Six-week-old female BALB/c mice were purchased from Envigo (S. Pietro al Natisone, Udine, Italy), housed at Plaisant animal facility (Castel Romano, Rome, Italy), and used for experiments at 7-9 weeks of age. Mice were divided into groups of at least 35 mice each (untreated and vaccinated). All mice of the vaccinated group were primed at day (d) 0 with ChAd-gag, and either analyzed at the indicated times post-prime, i.e. d30 (range 27-35), d60 (range 60-67), or d100 (range 95-109), or boosted. For prime/boost experiments, primed mice were divided in different sets, each boosted at a single time after prime, i.e. at either d30 or d100 (ranges as above). Viral vectors were administered intramuscularly (i.m.) in the quadriceps at a dose of 10^7 viral particles (vp) for ChAd-gag and 10^6 plaque-forming units (pfu) for MVA-gag, in a volume of 50 µl per side (100 µl total) (14). All experimental procedures were approved by the local animal ethics council and performed in accordance with national and international laws and policies (UE Directive 2010/63/UE; Italian Legislative Decree 26/2014; authorization n. 1065/2015-PR).

Organs

Spleen, LNs, BM and blood were analyzed either at the indicated days after prime or at d45 (range 41-46) after boost. At each time, organs were collected from 3 vaccinated and 3 untreated mice, and cells from the 3 mice of each group were pooled. Spleen, LNs (iliac and inguinal), and blood were processed as described (14, 18). Femurs and tibias were cleared of muscle tissues, and cut at the extremities. The open bone was placed in a cut pipette tip, placed in a microfuge tube, thereby keeping the bone away from the bottom of the tube and allowing the BM to be centrifuged out of the bone at 800xg for 1 minute. The bone was discarded and the pellet resuspended, thus obtaining a single cell suspension of BM cells (19). All cell suspensions were prepared in RPMI medium with 2 mM L-Glutamine, 100 U/ml Penicillin, 100 µg/ml streptomycin, 50 µM β-Mercaptoethanol + 10% volume/volume (v/v) Fetal Bovine Serum (FBS), and filtered with pre-separation filters (70 µm) (Miltenyi Biotech, Bergisch Gladbach, Germany).

Cell membrane and Ki-67/DNA staining

Cells were incubated with purified anti-mouse CD16/CD32 clone 2.4G2 (Fc block; BD Biosciences, San Jose, CA, USA), and stained as described with H-2k(d) AMQMLKETI (gag$_{197\text{-}205}$) allophycocyanin (APC)-labeled Tetramer (Tetr-gag, NIH Tetramer Core Facility, Atlanta, GA, USA) and phycoerythrin (PE)-labeled Pentamer (Pent-gag, Proimmune, Oxford, UK), fluorochrome conjugated monoclonal Antibodies (mAbs) against surface (CD3, CD8, CD127, CD62L) and intracellular (Ki-67) molecules, and Hoechst 33342 (Thermo Fisher Scientific, Waltham, MA, USA) (14). The following mAbs were used: anti-CD3ε peridinin chlorophyll protein (PerCP)-Cy5.5 (clone 145-2C11, BD Biosciences), anti-CD8α BUV805 (clone 53-6.7, BD Biosciences), anti-CD127 biotin (clone A7R34, eBioscience, Thermo Fisher Scientific) plus Streptavidin PE-Cy7 (BD Biosciences), or anti-CD62L PE-Cy7 (clone MEL-14, Biolegend, San Diego, CA, USA), and anti-Ki-67 mAb conjugated with Fluorescein isothiocyanate (FITC) or Alexafluor 700 (clone SolA-15; eBioscience, Thermo Fisher Scientific). Dead cells were excluded with eBioscience Fixable Viability Dye eFluor780 (eFluor780, Invitrogen, Thermo Fisher Scientific)

Intracellular IFN-γ assay

Spleen and BM cells were incubated at 37°C in 5% CO_2 in round-bottom 96-well plates (2×10^6 cells/well) for 5 hours with a pool of gag protein-derived peptides (gag peptide pool, 15mers overlapping by 11 amino acids) at final concentration of 2 μg/ml for each peptide. Dimethyl sulfoxide (DMSO, Sigma-Aldrich, St. Louis, MO, USA), the peptide pool diluent, was used as negative control and phorbol myristate acetate/ionomycin (PMA/Iono, Sigma-Aldrich) at final concentration of 20 ng/ml and 1 μg/ml respectively as positive controls. All incubations were performed in the presence of Golgi plug (BD Biosciences). After stimulation, cells were collected and incubated with Fc block, stained with Live/Dead Fixable Violet Dye (Invitrogen, Thermo Fisher Scientific) for viability, and with the following mAbs against surface markers: anti-CD3ε APC, clone 145-2C11; anti-CD8α PerCP, clone 53-6.7; anti-CD4 PE, clone H129.19 (all from BD Biosciences). Intracellular staining was performed after treatment with Cytofix/Cytoperm and in the presence of PermWash (BD Biosciences) using anti-mouse IFN-γ FITC, clone XMG1.2 (BD Biosciences).

In vivo killing

Female BALB/c mice were primed with ChAd-gag and boosted with MVA-gag as above. At d45 (range 43-50) post-boost, vaccinated mice and control untreated mice were injected intravenously (i.v.) with 20x10^6 spleen cells previously obtained from untreated female BALB/c mice and stained with Carboxyfluorescein succinimidyl ester (CFSE, eBioscience, Thermo Fisher Scientific). In more details, the injected cells consisted in a 1:1 mixture of CFSE^{high} gag-peptide pulsed and CFSE^{low} unpulsed cells. Spleen, LNs and BM cells were obtained 3 hours after injection and analyzed by flow cytometry using a Beckman Coulter Cytoflex instrument. Propidium Iodide (PI) was used for dead cell exclusion. Percentage of gag-specific killing was calculated according to (20).

Flow cytometry analysis

Samples were analyzed by either LSRFortessa flow cytometer (BD Biosciences) or CytoFLEX System B5-R3-V5 (Beckman Coulter, Brea, CA, USA). In some experiments, CD3^{-} cells were gated out when acquiring spleen and BM samples. Data were analysed using FlowJo software, v. 10.7.1 and 10.8.1 (FlowJo, Ashland, OR, USA).

Estimates of absolute cell numbers

Cells from spleen, LNs and BM were counted by trypan blue exclusion under light microscope, after lysis of Red Blood Cells (RBCs) (Sigma-Aldrich). Residual RBCs —identified as Ter119$^+$ CD45^{-} cells by staining with anti-CD45 Alexafluor 488 (clone 30-F11, Biolegend) and anti-Ter119 PerCP-Cy5.5 (clone TER119, eBioscience), and flow cytometry analysis— were found after RBC lysis in spleen (on average 40%) and BM (on average 30%), but not in LNs. Thus, spleen and BM cell counts were multiplied by 0.6 and 0.7, respectively, to obtain nucleated cell counts. Mouse White Blood Cell (WBC) counts/μl and total blood volume were previously reported (21, 22). The absolute numbers of gag-specific CD8 T cells in spleen, LNs, BM and blood, and of IFN-γ$^+$ CD8 T cells in spleen and BM, were estimated based on their percentages determined by flow cytometry and on nucleated cell counts of corresponding organ as previously described (23).

Cell sorting, RNA sequencing, and bioinformatic analysis

Female BALB/c mice were primed with ChAd-gag as above, and analyzed at either d30 (range 28-29) or d100 (range 96-107) post-prime. CD8 T cells were enriched from pooled RBC-lysed spleen cells of 12 primed mice by negative selection with mouse CD8 Dyna Beads magnetic beads (Thermo Fisher Scientific). Enriched CD8 T cells were stained with Tetr-gag APC, Pent-gag PE, anti-CD3ε PerCP-Cy5.5, anti-CD8α FITC mAbs, and eFluor780. Then live Tetr-gag$^+$Pent-gag$^+$CD3$^+$CD8$^+$ cells were sorted by flow cytometry into PBS buffer 1% BSA 2 mM EDTA using a FACSAria III (BD Biosciences) equipped with 488, 561, and 633 nm lasers, and with FACSDiva software (BD Biosciences, v6.1.3). To reduce stress, cells were sorted in gentle FACS-sorting conditions, using a ceramic nozzle of size 100 μm, a low sheet pressure of 19.84 pound-force per square inch (psi) that keeps the sample pressure at 18.96 psi and an acquisition rate of maximum 1500 events/sec. FACS-sorted cells were confirmed to be 92.92 ± 5.70% pure prior to RNA extraction. Cells were centrifuged for 5 minutes at 300x*g* and pellets resuspended in Buffer RLT Plus (RNeasy Plus Mini Kit from Qiagen, Germantown, MD, USA), and frozen at -80°C. Total RNA was isolated, and cDNA libraries prepared using NEBNext Single Cell/Low Input Library Prep Kit (from 2ng RNA normalised input), following manufacturer's instructions. They were then sequenced on Illumina HiSeq 4000 with 100bp single-end reads, following manufacturer's instructions. Read adaptor removal and quality trimming was carried out with Trimmomatic (version 0.36) (24). Reads were then aligned to the mouse genome, using Ensembl GRCm38 - release 95 as reference.

Read alignment and gene level quantification was performed by STAR alignment (v.2.5.2a) (25) together with RSEM package (v.1.2.31) (26). Statistical analyses were performed in the R programming environment (v. 4.0.3). We used DESeq2 (v.1.30.1) to find differential genes using the negative binomial distribution to model counts, with IHW (v.1.18.0) to control the false discovery rate (FDR), and ashr (v. 2.2.47) for effect-size shrinkage. Genes were designated as differentially expressed (DEGs) if FDR ≤ 0.01. All log-fold-changes estimates were regularised using ashr. We used an independent filter of low-signal genes whose effect varied from comparison to comparison, thus the total number of genes was not the same when analyzing down-regulated and up-regulated genes (total number of genes 10,333 and 7,846, respectively) (RNAseq data are available at GEO, access number GSE207389)

Statistical analysis

Student t test was used for comparison between two groups whenever each group had ≥9 samples, after checking that distribution was normal by Shapiro-Wilk test. Non-parametric tests were used for the remaining comparisons. Mann-Whitney test or Wilcoxon test were used for comparison between two groups. Either Kruskal-Wallis or Friedman test with Dunn's correction for multiple comparison were used for comparison among more than two groups. Differences were considered significant when * $P \leq 0.05$; ** $P \leq 0.01$. Statistical analysis was performed using Prism v.6.0f, GraphPad Software (La Jolla, CA, USA).

Results

Kinetics of gag-specific CD8 T cell expansion and re-entry in a resting state after prime

We exploited our recently developed DNA/Ki-67 flow cytometry assay (14, 27, 28) to evaluate the kinetics of response of CD8 T cells specific for the immunodominant $gag_{197-205}$ peptide (gag-specific) in spleen and LNs of BALB/c mice primed with ChAd-gag at about 2 months of age (Figures 1, S1). As depicted in Figure S1A, our strategy of analysis included a DNA-based singlet gate (Step 1), and an unusually "relaxed" FSC-A/SSC-A (FSC-SSC) gate (Step 4, in orange), as opposed to a classical "narrow" gate (Step 4, shown in white for comparison) (14, 27–29). Our strategy was designed to fully detect proliferating cells, following our previous demonstration that T lymphocytes undergoing clonal expansion were only partially included in the commonly used FSC-SSC gates for resting lymphocytes (14, 27–29). Indeed, we previously showed that proliferating lymphocytes had gradually increased FSC and SSC as they progressed into cell cycle, reflecting augmented cell and nucleus size, and mitochondrial dynamics (27).

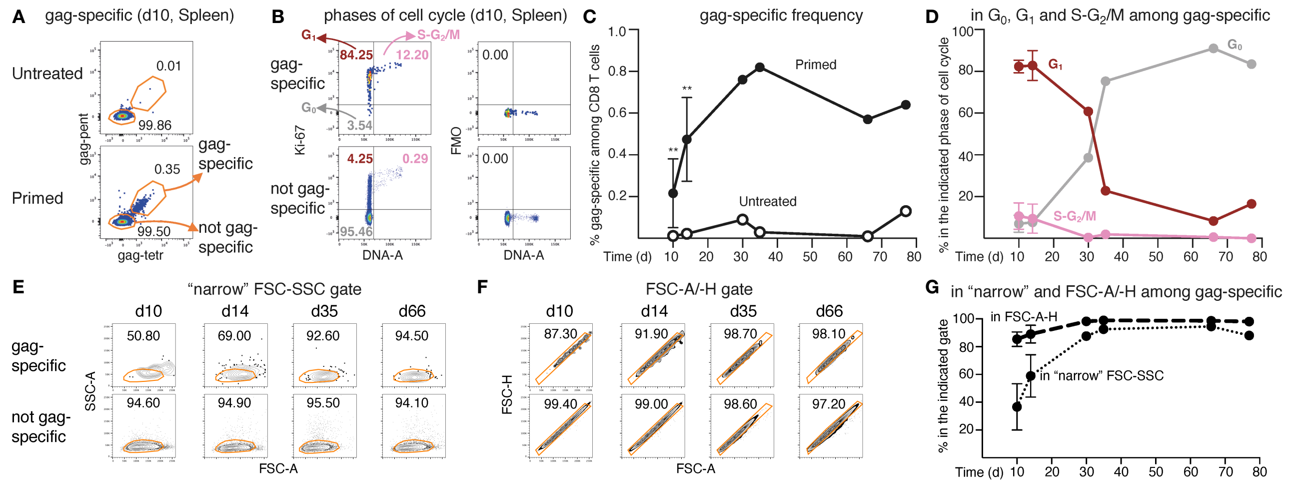

FIGURE 1
Analysis of frequency and cell cycle of gag-specific CD8 T cells from ChAd-gag-primed mice. Female BALB/c mice were primed i.m. in the quadriceps with ChAd-gag (10^7 vp) at d0 and the kinetics of gag-specific CD8 T cell response was tracked by flow cytometry. **(A–G)**. Spleen cells were analysed by membrane and Ki-67/DNA staining at different days (d) post-prime (gating strategy in Figure S1A). Typical plots showing the percentage of "gag-specific" and "not gag-specific cells" from untreated (top) and primed (bottom) mice at d10 **(A)**. gag-specific cells from primed mice were further analyzed on DNA/Ki-67 plots as follows (**B**, top left panel): cells in the G0 phase of cell cycle were identified as DNA 2n/ Ki-67$^-$ (bottom left quadrant); cells in G1 as DNA 2n/ Ki-67$^+$ (upper left quadrant); cells in S-G2/M as DNA>2n/ Ki-67$^+$ (top right quadrant). As a comparison, not gag-specific cells (**B**, bottom left panel) are shown. For each DNA/Ki-67 plot, corresponding Ki-67 Fluorescence Minus One (FMO) control plots (**B**, right panels) are shown. Summary of the kinetics of gag-specific frequency in primed and untreated mice **(C)**, and of cell cycle phases of gag-specific CD8 T cells in primed mice **(D)** (summary of cell cycle phases of not gag-specific CD8 T cells shown in Figure S1B). Kinetics of the percentages of gag-specific and not gag-specific CD8 T cells in the "narrow" FSC-SSC gate (examples in **E**) and in the FSC-A/-H gate (examples in **F**), and summary of gag-specific CD8 T cell results **(G)** (summary of not gag-specific CD8 T cell results shown in Figure S1E). The figure summarizes results of 6 independent prime experiments with a total of 84 mice analyzed at the indicated d post-prime. In flow cytometry plots (in **A, B, E, F**), numbers represent percentages of cells in the indicated regions. In panels **(C, D, G)**, symbols at d10 and d14 represent the mean and bars the Standard Deviations of 5 experiments (each performed with pooled cells from 3 mice per group). At d30, d35, d66 and d77, each symbol represents a pool of 3 mice. Statistical analysis was performed using Mann-Whitney test for comparison between untreated and primed mice at d10 and d14 **(C)**, and Wilcoxon test for comparison between gag-specific CD8 T cells in the "narrow" FSC-SSC gate and in the FSC-A/-H gate at d10 and d14 **(G)**. Statistically significant differences are indicated (** $P \leq 0.01$). This figure includes unpublished data in relation to (14).

We then exploited cell staining with MHC-gag multimers to identify gag-specific and not gag-specific CD8 T cells from untreated and primed mice (Figures 1A, S1, Step 7). Typical examples of DNA/Ki-67 plots of primed spleens are shown in Figure 1B, with gating of gag-specific cells in G_0, G_1 and S-G_2/M phases of cell cycle (top left); not gag-specific cells are shown for comparison (bottom left). Specificity of Ki-67 staining was demonstrated by corresponding Fluorescence Minus One (FMO) plots (Figure 1B, right). The frequency of gag-specific CD8 T cells in primed mice spleens increased from d10 to d30, and then was maintained at a plateau of ~0.7% up to ~ 3 months after prime, with a background of 0.0-0.1% in the spleens of age-matched untreated control mice (Figure 1C). Early after priming 83% and 10% of spleen gag-specific cells were on average in G_1 and in S-G_2/M respectively, with very similar results at d10 and d14. At d30 and later time points, the percentage of cells in S-G_2/M dropped to virtually none, while that of cells in G_1 slowly declined. The G_1 trend was mirrored by the gradual increase of cells in G_0, which represented the majority of gag-specific cells from day 35 onwards (Figure 1D). There was no parallel expansion of not gag-specific cells; in fact, ~93% of these cells was in G_0, ~7% in G_1, and ~0.3% in S-G_2/M at all time points (Figure S1B). We also noticed that changes in membrane expression of two markers of long-term memory, i.e. CD127 (the α chain of IL-7 receptor), and CD62L (a LN homing molecule), tended to be more pronounced in gag-specific spleen cells that were already in G_0 at d30 post-prime, as compared to those that were in G_1 (Figures S1C, D). CD62L results were particularly intriguing, as it is known that this marker is normally high in naïve CD8 T cells, it is down-modulated upon priming, and then re-expressed by memory cells with a T_{CM} phenotype (30, 31), but there is little information about its correlation with the quiescence phase G_0. We thus examined it in more details, as explained in the next paragraphs.

To track the kinetics of proliferation followed by re-entry of spleen gag-specific CD8 T cells into a resting state, we exploited FSC and SSC changes associated with cell cycle (14, 27). As mentioned above, proliferating lymphocytes have FSC and SSC features that place many of them out of the conventional FSC- and SSC-based gates (14, 27). Thus, as a guide to evaluate the kinetics of primary response, we examined the exit and gradual re-entry of proliferating cells into two gates commonly used for resting lymphocytes, i.e., either the “narrow” FSC-SSC (Figure 1E) or the FSC-A/-H gate (Figure 1F). In fact, while these gates are normally applied to total spleen cells for lymphocyte and single cell gating, respectively, we exploited them here to follow Ag-primed T cell changes over time. Only a fraction of spleen gag-specific CD8 T cells was captured by any of these two gates in the second week post-prime (Figures 1E–G), as expected (14). This inadequacy seemed more evident in the case of the “narrow” FSC-SSC gate than in that of the FSC-A/-H gate (Figures 1E–G). One month after priming (d30-d35), the gag-specific cell percentage within the “narrow” FSC-SSC gate raised to ~88-93%, and that within the FSC-A/-H gate to ~98-99%, thus resembling the corresponding percentage of not gag-specific cells; there was no further change at d66 and d77 (Figures 1E–G). This kinetics was not observed in the case of not gag-specific cells that we examined in parallel as a control (Figure S1E). Results were similar in draining LNs (Figures S2A–D). Further analysis demonstrated that only a small percentage of cells in S-G_2/M was captured by the FSC-A/-H gate, and almost none by the “narrow” FSC-SSC gate in both LNs (Figure S2E) and spleen (Figure S2F), in agreement with our previous data (14).

Kinetics of gag-specific T_{CM}-phenotype changes at d30, d60 and d100 post-prime

We then used flow cytometry to track at d30, d60 and d100 post-prime the frequency of gag-specific cells in spleen, LNs, BM and blood, and the proportions among them of CD62L$^+$ cells, i.e. those having a T_{CM} phenotype (30, 31). CD62L staining was also combined with Ki-67 expression analysis, as explained in the next paragraph. It should be noted that in these experiments we did not stain DNA and relied on the typical FSC-A/-H gate to exclude cell aggregates (Figure S3, step 1), since we had observed that gag-specific cells in S-G_2/M were extremely rare after d30 (Figures 1D, S2C) and that 98-99% of gag-specific cells were comprised in the FSC-A/-H gate at d30 and onwards (Figures 1F, G, S2D). We used a “relaxed” FSC-SSC gate (Figure S3, step 4), that was more appropriate than a “narrow” FSC-SSC gate for evaluation of gag-specific cells in G_1 (see Figures S2E, F), even after d30 when G_1 mostly represented a post-mitotic state (Figures 1D, S2C). We found that gag-specific frequency at d30 was on average 5.0% in blood, 3.8% in BM, 1.1% in spleen and 0.2% in LNs from primed mice (examples of flow cytometry plots in Figure 2A, summary of results in Figure 2B). The frequency remained roughly stable at d60 and d100 in the spleen and BM, with a tendency to increase in the LNs. In contrast, a significant decline was observed in the blood from d30 to d100 (Figure 2B). At any time point, and in each organ, primed mice had a significantly higher gag-specific frequency than untreated controls, which always displayed a negligible background (Figures 2A, B). In the primed mice samples, we discriminated between T_{CM} and T_{EM} gag-specific CD8 T cells according to their CD62L expression (Figure 2C). We found that the proportion of T_{CM} tended to be higher in the LNs, and to increase over time in all organs (Figure 2C). Notably, there was a significant rise in T_{CM} proportion among gag-specific CD8 T cells in the blood, from ~2% at d30 to ~21% at d100 on average (Figure 2C), reflecting the contemporary changes in lymphoid organs.

To better investigate the d30-d100 shift, we estimated the absolute numbers of gag-specific cells, and of T_{EM} and T_{CM} gag-specific cells in spleen, LNs, BM and blood (Figures 2D–F). These estimates took into account CD8 T cell abundance in each organ, and the tendency of CD8 T cell percentages to an age-dependent decline in spleen, LNs and blood but not in BM in the time interval of our study (averages: spleen 9.77%; LN 20.85%; blood 9.25%, BM 0.43% at d30, age 11-13 weeks; spleen 7.50%, LNs 15.15%, blood 8.10%, BM 0.50% at d100, age 21-23 weeks). We found that an overall reduction in gag-specific cell numbers coexisted with selective increases of cells belonging to T_{CM} subset and/or found in certain organs (Figures 2D–F). Thus, the sum of gag-specific cells in spleen, LNs, BM and blood at d100 was 88% of that at d30 (Figure 2D), and that of T_{EM} 76% of that at d30 (Figure 2F). In striking contrast, taking the four organs altogether, T_{CM} cells increased 2.5 times from d30 to d100 (Figure 2E). With regards to changes in gag-specific cell distribution, it was remarkable that the sum of cells contained in spleen and blood accounted for ~ ¾ of the cells found in the four organs altogether at d30, and for only ~half of them at d100 (Figure 2D). In fact, from d30 to d100 the

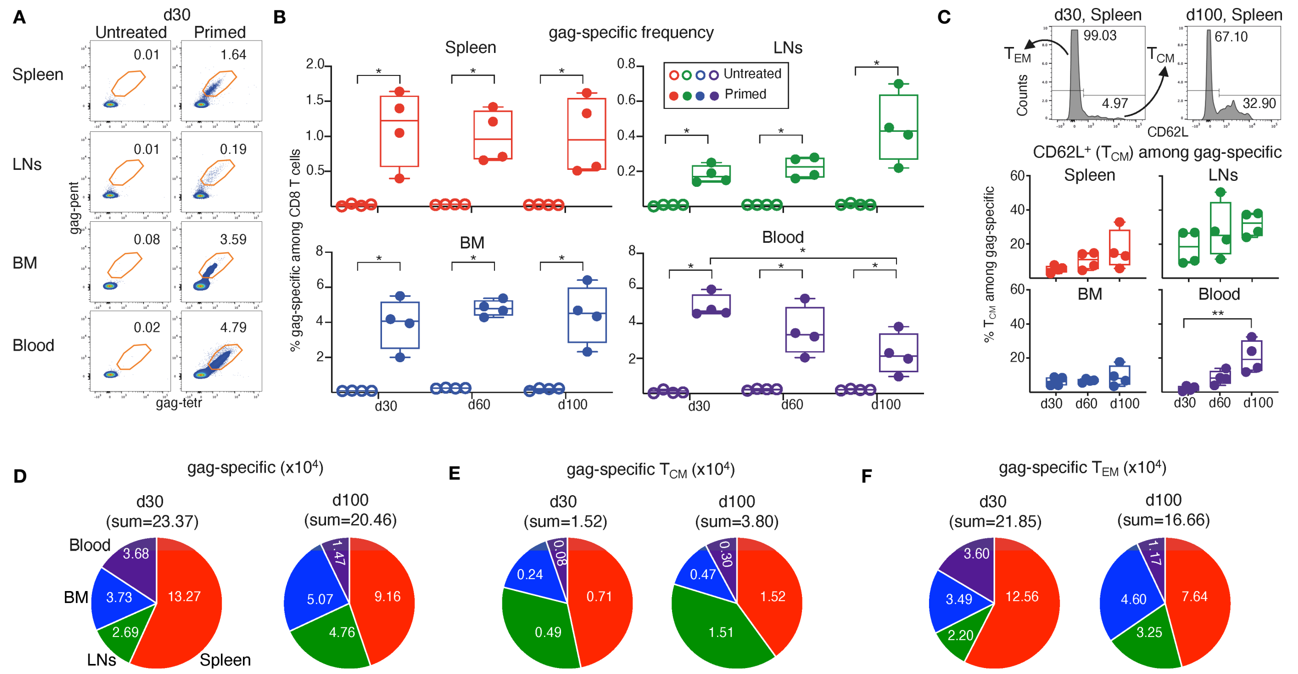

FIGURE 2
Analysis of T_{CM}/T_{EM}-phenotype of gag-specific CD8 T cells from ChAd-gag-primed mice, and estimation of absolute cell numbers. Spleen, lymph nodes (LNs), bone marrow (BM) and blood cells from mice primed as in Figure 1 were analyzed at d30, d60 and d100 post-prime. **(A–C)**. Flow cytometric analysis was performed after membrane and Ki-67 staining (gating strategy in Figure S3, Ki-67 results in Figure 3). Typical plots showing the percentage of gag-specific CD8 T cells at d30 in untreated (left) and primed (right) mice **(A)** and summary of results at d30, d60 and d100 **(B)**. Examples of CD62L histograms of spleen gag-specific CD8 T cells at d30 and d100, showing the gate used to discriminate between TCM (CD62L⁺) and TEM (CD62L⁻) cells (**C**, top). Summary of TCM percentages at d30, d60 and d100 (**C**, bottom). **(D–F)**. Absolute numbers of gag-specific CD8 T cells **(D)**, and of TCM **(E)** and TEM **(F)** gag-specific CD8 T cells, at d30 and d100 in spleen, LNs, BM and blood. The figure summarizes results of 4 independent prime experiments with a total of 72 mice analyzed at the indicated d post-prime. In flow cytometry plots (in **A** and **C**, top), numbers represent percentages of cells in the indicated regions. In panels **(B, C)**, bottom, each symbol represents a pool of 3 mice. Statistical analysis was performed using Mann-Whitney test for comparison between untreated and primed mice **(B)**, and Kruskal-Wallis test with Dunn's correction for multiple comparison for comparison among primed mice at d30, d60 and d100 (**B, C,** bottom). Statistically significant differences are indicated (* $P \leq 0.05$; ** $P \leq 0.01$).

number of gag-specific cells was reduced in blood and spleen, whereas that in LNs and BM increased (Figure 2D). Changes of T_{EM} resembled those of gag-specific cells (Figure 2F), whereas a profound T_{CM} cell increase was observed in each organ (Figure 2E).

Kinetics of re-entry into the G_0 phase of gag-specific CD8 T_{CM} and T_{EM} cells at d30, d60 and d100 post-prime

We reasoned that the reported higher proliferative response to TCR triggering of T_{CM} cells in comparison with T_{EM} cells (30) might be associated with a diverse kinetics of re-entry into the G_0 phase after expansion of the two memory cell types. In other words, we hypothesized that a faster re-entry of T_{CM} cells into the quiescent phase G_0 after priming might be associated with an improved capacity to expand *in vivo* upon antigenic re-exposure, as compared to T_{EM} cells. To identify possible differences in the primary acute response/memory phase transition between the two memory subsets, we tracked Ki-67⁻ (i.e. in G_0) among T_{EM} and T_{CM} gag-specific cells in the primed mice samples described above. At d30, Ki-67⁻ cells were on average ~81% in T_{CM} and ~68% in T_{EM} gag-specific cells from primed spleen (examples of flow cytometry histograms in Figure 3A, top). Both percentages increased over time, being on average ~96% in T_{CM} and ~94% in T_{EM} at d100 (examples in Figure 3A, bottom). The marked Ki-67⁺ cell decline among T_{EM} cells from d30 to d100 was concurrent with a higher representation of T_{CM} cells at d100, as evident in a typical Ki-67/CD62L plot showing an overlay of T_{CM} (gray) and T_{EM} (brown) gag-specific cells (Figure 3B, see also Figures 2C–F). A similar pattern was observed across spleen, LNs, BM and blood, with two points to be highlighted (Figure 3C). First, a statistically significant difference between LNs and blood T_{EM} at d60 (bottom center), not observed at d100 (bottom right), indicating a slow re-entry of LN T_{EM} in G_0. Second, a tendency of BM T_{CM} cells to contain a smaller fraction of Ki-67⁻ than the other organs, both at d60 (top center) and at d100 (top right), indicating a low level of persistent activation of T_{CM} in the BM.

In terms of absolute numbers, the sum of Ki-67⁻ gag-specific cells in spleen, LNs, BM and blood altogether at d100 was 1.2-fold higher than that at d30, as a net result of increase in LNs and BM, almost no change in spleen, and evident reduction in blood (Figure 3D). This was in contrast with the absolute number of Ki-67⁻ T_{CM} found in the four organs altogether, that showed a striking 2.9-fold increase from d30 to d100, with a pronounced rise in each organ, especially in blood and LNs (Figure 3E). The sum of Ki-67⁻ T_{EM} in the four organs at d100 was similar to that at d30 (Figure 3F), in contrast to the above-described reduction of total T_{EM} (Figure 2F). Single organ comparison showed that Ki-67⁻ T_{EM} cells were reduced in blood and spleen, but increased in LNs and BM (Figure 3F).

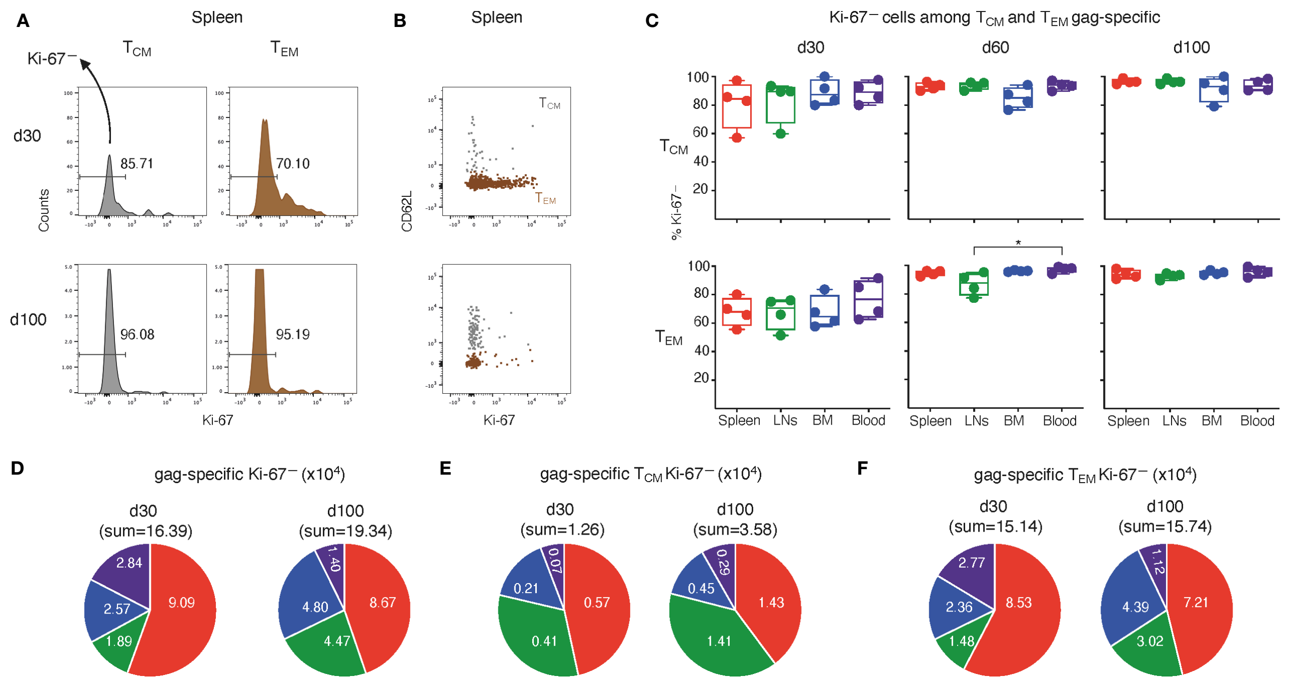

FIGURE 3

Analysis of Ki-67⁻ cells among T_{CM} and T_{EM}-gag-specific CD8 T cells from ChAd-gag-primed mice, and estimation of absolute cell numbers. Spleen, LN, BM and blood cells from primed mice represented in Figure 2 were analyzed for Ki-67 expression by TCM and TEM gag-specific CD8 T cells, gated as in Figure 2. **(A–C)**. Typical histograms showing the percentage of Ki-67⁻ cells among TCM (left) and TEM (right) cells **(A)**, and examples of Ki-67/CD62L plot showing an overlay of TCM (gray) and TEM cells (brown) **(B)**; both panels represent spleen gag-specific CD8 T cells from primed mice at d30 (top) and d100 (bottom). Summary of results of Ki-67⁻ cells among TCM (top) and TEM (bottom) gag-specific CD8 T cells from spleen, LNs, BM and blood at d30, d60 and d100 **(C)**. In **A**, numbers represent percentages of cells in the indicated regions. **(D–F)**. Absolute numbers of gag-specific Ki-67⁻ CD8 T cells **(D)**, and of TCM **(E)** and TEM **(F)** Ki-67⁻ gag-specific CD8 T cells at d30 and d100 in spleen, LNs, BM and blood. Statistical analysis was performed by Friedman test with Dunn's correction for multiple comparison **(C)**. Statistically significant differences are indicated (* $P \leq 0.05$).

RNA sequencing and bioinformatic analysis of spleen gag-specific CD8 T cells at d30 and d100 after prime

A transcriptomic comparison between d100 and d30 spleen gag-specific cells by RNAseq showed that samples of the two groups were easily separated by Principal Component Analysis (Figures 4, S4A). Significant changes at d100 were found in 512 differentially expressed genes (DEGs), 362 of which were down-regulated and 150 up-regulated (Figure 4A). The top 50-up and top 50-down DEGs showed comparable results across samples of each group (Figure S4B).

A striking reduction was observed in a small set of downregulated DEGs, with some of them showing a regularized log-2 Fold Change (LFC) comprised between -5 and -10 (Figure 4A). Among the DEGs that were down to virtually 0 normalized counts, *B-myb* (also known as *Mybl2*) was an already recognized T cell effector player of transition into memory state (32, 33), while others were newly described in this context, e.g. *Ttk*, the gene for Thymidine kinase 1, an IL-2 induced kinase regulating cell cycle progression of T cells (34); *Kif14*, the gene for Kinesin Family Member 14, a positive regulator of cell cycle (35, 36); and *Lrr1*, the gene for Leucine-Rich Repeat Protein 1, an inhibitor of 4-1BB signalling (37) (Figures 4A, B). Notably, about half of the top 50 significantly down-regulated genes (top 50-down) encoded for proteins involved in cell proliferation (Figure S4C, in bold blue). There was a trend of down-regulation of *Mki67*, the gene coding for Ki-67 protein, that did not reach statistical significance (not shown), even though the percentage of Ki-67^+ cells within spleen gag-specific CD8 T cells significantly dropped from 31.50 ± 9.16 at d30 to 5.36 ± 2.56 at d100 (averages ± Standard Deviation, Mann-Whitney test, $P \leq 0.05$). The lack of statistical significance in transcriptomic analysis possibly reflected the correction for multiple tests used for RNAseq data statistical analysis.

In contrast to the dominance of proliferative genes in the top 50-down, the top 50 up-regulated DEGs (top 50-up) were more heterogeneous, and the LFC did not exceed +5 for any of them (Figures 4A, S4C). As expected, the top 50-up DEGs comprised *Ccr7*, *Sell*, and *Il7r* that encode for CCR7, CD62L, and IL-7Rα (CD127) respectively, all recognized markers for T_{CM} phenotype and memory T cell longevity (33, 38), as well as *Bcl2*, a pro-survival gene (33, 39), and *Socs3*, which encodes for a cytokine signalling regulator that controls IL-7Rα re-expression after initial down-regulation in activated T cells (40) (Figures 4A, B). Remarkably, top 50-up DEGs included *Slfn5*, a member of the Schlafen family of genes that has been implicated in T cell quiescence and proliferative potential (41–43), and some genes previously involved in regulating quiescence and maintenance of hematopoietic stem cells (HSCs), i.e. *Ssbp2*, Sequence-specific ssDNA–binding protein 2 (44), and *Myc* (45), often cited for its role in T cell metabolism and memory T cell differentiation (33, 46, 47) (Figures 4A, B). The above mentioned *Socs3* has also been implicated in re-setting quiescence of HSCs after proliferation (48), while the pleiotropic gene *Pros1*, Protein S, also in the top 50-up genes, has been proposed as a regulator of neural stem cell equilibrium between quiescence and proliferation (49)(Figures 4A, B). Altogether, changes in these genes (Figures 4A, B, S4C, in bold

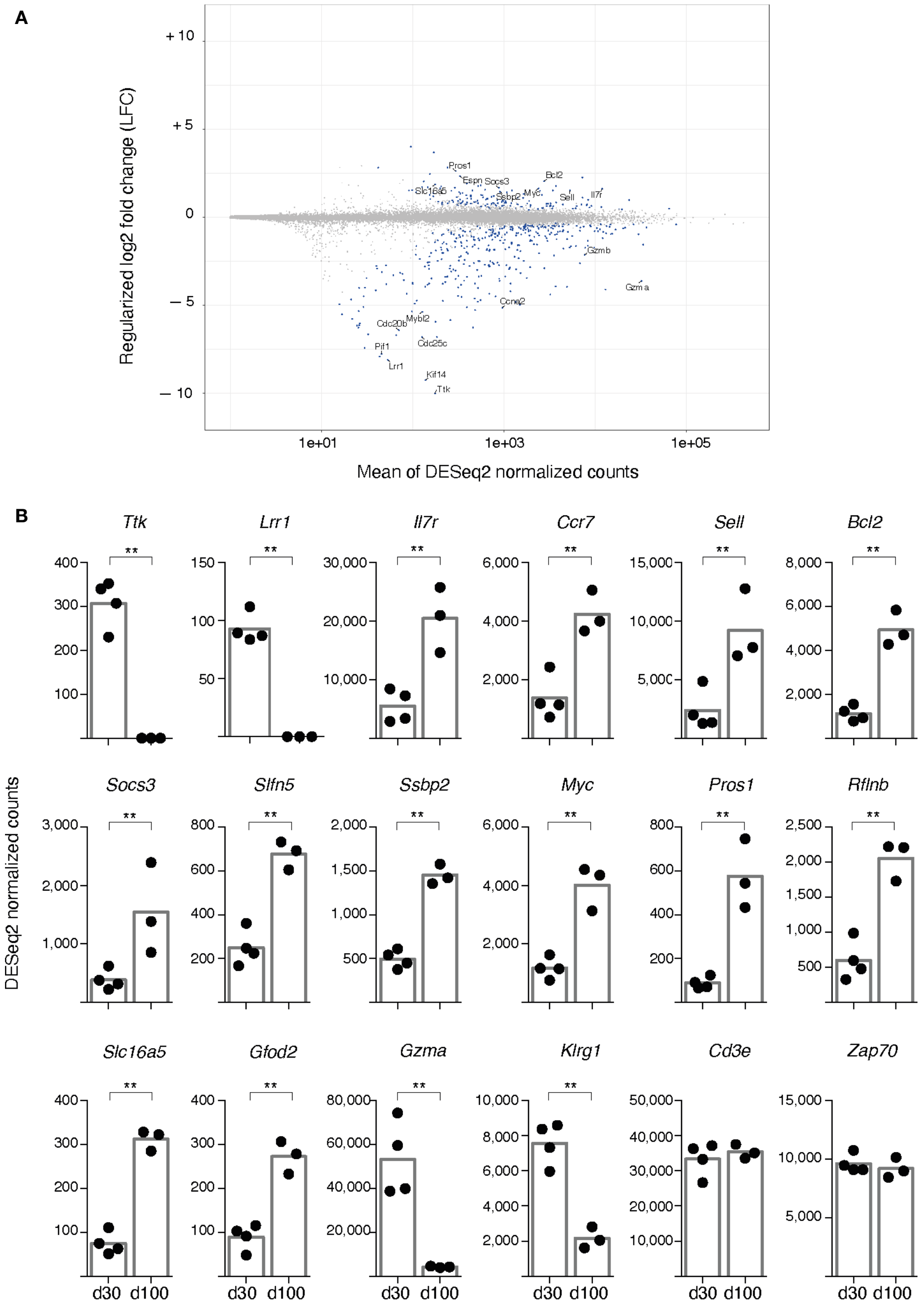

FIGURE 4
RNA seq analysis of spleen gag-specific CD8 T cells at d30 and d100 post-prime. Bulk RNA was sequenced from sorted spleen gag-specific CD8 T cells at d30 and d100 post-prime, in 4 independent prime experiments with a total of 7 samples. Bioinformatic analysis was performed to compare d100 and d30. **(A)**. Scatterplot of genes whose estimated absolute log-2 fold change was < 11. The y-axis represents Log-2 fold changes regularised using an empirical Bayes method, and the x-axis represents means across all samples of the DESeq2-normalised counts. Differentially expressed genes (DEGs) with a statistically significant difference (false discovery rate (FDR) $\leq$ 0.01) are highlighted in blue. Selected gene symbols among the top 50 significantly upregulated (top 50-up) and the top 50 significantly downregulated (top 50-down) genes are indicated (see Figure S4 for full list). **(B)**. DESeq2-normalised counts of representative DEGs having a statistically significant difference between d100 and d30, i.e. Ttk, Lrr1, IL7r, Ccr7, Sell, Bcl2, Socs3, Slfn5, Ssbp2, Myc, Pros1, Rflnb, Slc16a5, Gfod2, Gzma, Klrg1. Analysis of Cd3e and Zap70 is included. Each symbol represents an individual sample; columns represent the mean of d30 and d100 group; statistically significant differences are indicated (** FDR $\leq$ 0.01).

red) support the notion that the quiescent state of gag-specific cells at d100 was actively and finely regulated.

Additional top 50-up DEGs encoded for proteins regulating cell metabolism and redox state (i.e. *Qpct*, *Slc16a5*, *Gfod2*, *Nmnat3*) (Figures 4A, B, S4C, in bold black), pointing to a metabolic change at d100. It is worth noting that *Rflnb*, Refilin B, a TGF-β effector (50) and *Tgfbr3*, TGF-β receptor III, were among the top 50-up DEGs, in agreement with the major role of TGF-β signalling in T cell memory (51), and of TGF-β RI and RII in T cell biology (52, 53), even though the function of TGF-β RIII has been poorly investigated in this context (54). Furthermore, *Cd101* was among the top 50-up DEGs; this gene encodes for a T cell-inhibitory glycoprotein shown to come up in chronic infection (55) (Figures 4B, S4B, C).

Although not listed in the top 50-down, *Gzma*, *Gzmb*, and *Gzmk* were significantly down-regulated, as were *Nkg7* and *Klrg1*, all typical genes of CD8 T cell effector signature (Figures 4A, B). Control genes with no significant changes included *CD3d*, *CD3g*, *CD3e*, *ZAP70*, *Cd8a* and *Cd8b1* (Figure 4B; RNAseq data available at GSE207389).

Kinetics of responsiveness to boost

To compare protocols with different prime/boost intervals, ChAd-gag-primed mice were boosted with MVA-gag either at d30 or at d100 post-prime, and rested for 45d. Then the frequency of gag-specific cells, and that of T_{CM} among gag-specific cells, was measured in spleen, LNs, BM and blood (Figures 5A, B). There was a trend of higher gag-specific frequency when boost was performed at d100 post-prime as compared to boost at d30 in all organs, that reached statistical significance in LNs (Figure 5A). Independently of the time of boost, the organs with the highest frequencies were BM and blood, followed by spleen and then LNs, similarly to the results at d30 and d60 post-prime (see Figure 2B). There was no difference between the two boosts in terms of proportion of T_{CM} among gag-specific cells (Figure 5B). As expected, LNs contained a higher percentage of T_{CM} than any of the other organs, thus resembling post-prime data at d30 and d60 (see Figure 2C).

In vivo killing assay showed that gag-specific cells were functional in spleen, LNs and BM (Figures 5C, D). There was a significantly higher percentage of gag-specific killing in spleen and LNs in the group of mice boosted at d100 post-prime as compared to the group boosted at d30, and a tendency of similarly increased killing in the BM (Figure 5D). Spleen and LNs showed a more prominent killing than BM (Figures 5C, D), possibly reflecting their higher CD8 T cell percentages (see above). Intracellular IFN-γ assay performed at d45 post-boost by stimulating either spleen or BM cells with a pool of gag protein-derived peptides (gag peptide pool) confirmed that boost at d100 post-prime elicited a significantly stronger CD8 T cell response than boost at d30 (Figures S5A–C). Absolute cell number estimation similarly showed that boost at d100 was more effective than boost at

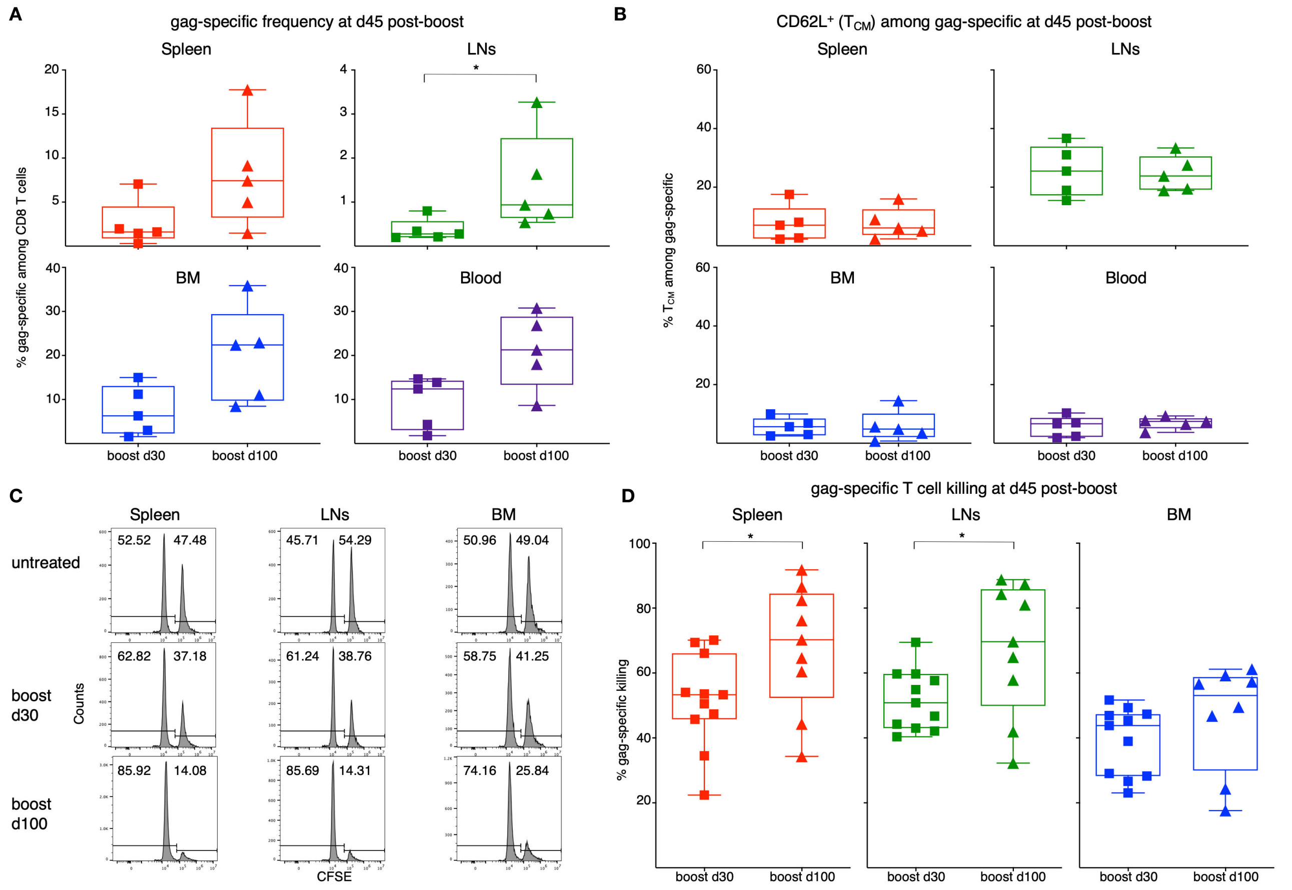

FIGURE 5
Analysis of gag-specific CD8 T cell frequency, T_{CM}-phenotype and *in vivo* killing activity at d45 post-boost. Female BALB/c mice were primed as in Figure 1 at d0. One set of primed mice was boosted with MVA-gag at d30 post-prime, and another at d100 post-prime. For each set, analysis was performed at d45 post-boost. **(A, B)**. Frequency of gag-specific CD8 T cells **(A)** and percentage of TCM among gag-specific CD8 T cells **(B)** in spleen, LNs, BM and blood of primed/boosted mice. **(C, D)**. Primed/boosted and untreated control mice were injected i.v. with a 1:1 mixture of gag-pulsed $CFSE^{high}$ cells and unpulsed $CFSE^{low}$ syngeneic spleen cells (approximately 10x10^6 cells each). After 3 hours, the percentages of $CFSE^{high}$ and $CFSE^{low}$ cells were measured in spleen, LNs and BM, and the percentage of gag-specific killing was determined. Examples of CFSE histograms **(C)** and summary of results **(D)**. **(A, B)** summarize results of 5 independent prime/boost experiments with a total of 60 mice, including control untreated mice (note that at each time point, 3 untreated mice were examined as a control; results were similar to those of untreated control mice shown in Figures 2A, B). Each symbol represents a pool of 3 mice. **(C, D)** summarize results of 4 independent prime/boost experiments with a total of 36 mice, including control untreated mice (see example in panel **C**). In **(C)**, numbers represent percentages of cells in the indicated regions. In **(D)**, each symbol represents a single mouse. Statistical analysis was performed by either Student t test, after checking that distribution was normal by Shapiro-Wilk test, or Mann-Whitney test. Statistically significant differences are indicated (* $P \leq 0.05$).

d30 (Figures S5D–F), and also demonstrated that both boosts yielded tremendously higher numbers of gag-specific CD8 T cells in spleen and BM than those obtained by prime only (compare Figure S5E with Figure 2D). In respect to BM versus spleen comparison, when percentage of IFN-γ^+ among CD8 T cells was evaluated, BM response reached higher levels than that in spleen in both d30 and d100 experimental groups (Figures S5B, C), echoing the gag-specific frequency results (see Figure 5A). In terms of absolute gag-specific cell numbers, spleen contained 2-4-times more cells than BM (Figure S5D–F). Estimations based on IFN-γ^+ assay (Figures S5D, F) were somehow different as compared to those based on MHC-gag multimer staining (Figure S5E), even though cell numbers were in a similar range. This was not surprising, considering that IFN-γ^+ assay measured CD8 T cells producing one cytokine after stimulation with gag peptide pool, whereas MHC-gag multimer staining detected CD8 T cells specific for a single immunodominant peptide, i.e., $\text{gag}_{197\text{-}205}$. Altogether, these results show that boost at d100 was more effective than that at d30.

Discussion

An improved understanding of memory CD8 T cell biology can be highly beneficial for prevention and treatment of human infections, autoimmune diseases and cancers. Long-lived CD8 T cell memory can be established by vaccination protocols based on at least two vaccine doses, however decisions regarding prime/boost time interval have been taken mostly empirically so far (56, 57). In this article we described a splenic memory CD8 T cell signature associated with enhanced response to delayed boost in a model of ChAd-gag/MVA-gag vaccination of BALB/c mice.

In our model, delayed boost at d100 post-prime was more effective than early boost at d30 in terms of frequency and numbers of gag-specific CD8 T cells, *in vivo* gag-specific killing, and IFN-γ production, all measured at d45 post-boost, i.e. in the secondary memory phase. In contrast, delayed and early boost resulted in similar proportions of T_{CM} among gag-specific CD8 T cells in lymphoid organs, suggesting that a more effective response following boost at d100 did not include a change in T_{CM} representation at d45 post-boost.

In our experiments, mice were primed at ~2 months of age, and they reached ~3 and 5 and ½ months when they were boosted at d30 and d100 post-prime, respectively. In agreement with the previously described naïve CD8 T cell decay in aging mice, in relation with reduced thymic output (58, 59), we found here that CD8 T cell percentages tended to decrease at d100 in spleen, LNs and blood, but not in the BM. Nevertheless, considering the limited time frame of our investigation, and that the previously described decay involved naïve cells but not memory CD8 T cells (58), we did not expect any impact of CD8 T cell percentage decrease on gag-specific cell response to boost. As a matter of fact, we found that responsiveness to boost was increased at d100.

We identified a d100 splenic transcriptomic profile of gag-specific memory CD8 T cells, characterized by shut off of several proliferative genes (e.g. *Ccna2*, *Cdc25c*, *Pclaf*), and up-regulation of stem cell genes previously implicated in setting the equilibrium between quiescence and proliferation (e.g. *Slfn5*, *Ssbp2*, *Myc*, *Socs3*). These results are in agreement with the absolute dominance of Ki-67$^-$ cells by flow cytometry analysis, and give granularity to the molecular changes occurring from d30 to d100, i.e. a time interval remarkably characterized by stable numbers of Ki-67$^-$ gag-specific CD8 T cells in the spleen. Transcripts involved in T cell negative regulation and TGF-β pathway (e.g. *Rflnb, Tgfbr3, Cd101*) were also up-regulated, as were some metabolic genes (e.g. *Qpct*, *Gfod2*). Increased expression of T_{CM}/long-lived memory T cell markers (e.g. *Sell*, *Ccr7*, *Il7r*, *Bcl2*), and down-regulation of effector T cell transcripts (e.g. *Gzma, Gzmb, Gzmk*, *Nkg7*, *Klrg1*) were in agreement with previous results (33, 60). At first, T_{CM} marker up-regulation at d100 might appear in contrast with the concurrent strong down-regulation of proliferative genes, considering that T_{CM} phenotype has been associated with increased proliferation potential (30). Nonetheless, these apparent puzzling findings might be reconciliated according to a recent hypothesis suggesting that persistence of memory CD8 T cells in a non-proliferative quiescent state might preserve their potential for prompt expansion upon secondary antigen stimulation (61).

Our flow cytometry analysis and our cell number estimates suggest that gag-specific CD8 T cells migrated from spleen and blood into LNs and BM during the d30-d100 time frame, even though migration in and out of other organs cannot be excluded. Our further findings on gag-specific T_{CM}/T_{EM} phenotypes are consistent with the possibility that T_{CM} had a survival advantage over T_{EM} in all examined organs, and likely self-renewed in the BM (61), while a fraction of T_{EM} up-regulated CD62L, thus acquiring a T_{CM} phenotype. Thus, the transcriptomic differences between d100 and d30 spleen gag-specific CD8 T cells might be due to: i) plasticity of the splenic memory population (e.g. T_{EM} to T_{CM} shift); ii) selective survival of a cell subset (e.g. Ki-67$^-$ T_{CM}); iii) selective cell recirculation in and out of spleen (e.g. T_{EM} migration out of the spleen and accumulation into LNs and BM); iv) a combination of some or all of the above.

In sum, the main features of the d100 versus d30 gag-specific CD8 T cells in the spleen were a selective 2.6-fold increase in Ki-67$^-$ T_{CM} as opposed to a 1.2-fold decrease in Ki-67$^-$ T_{EM}, and a transcriptional switch to a mature memory state (Figure 6). This included, as expected, an increase in T_{CM} phenotype and a decrease in T cell effector genes, plus newly described changes in genes regulating quiescence and proliferation, not implicated before in T cell memory, and in transcripts involved in inhibitory pathways of T cell responses (Figure 6). It is remarkable that in parallel with the d100-d30 molecular shift in the spleen, we measured significant changes in the blood, i.e. a decline in gag-specific frequency within CD8 T cells, and an increase of T_{CM} within gag-specific cells.

Our data are in the same line of previous evidence showing compromised memory T cell longevity with short 14d-prime/boost intervals (62). However, we specifically addressed memory CD8 T cell maturation, as we focused on ≥ 30 d post-prime, after the ending of clonal expansion (63). Some older studies also compared a d30 prime/boost interval with longer ones, using adenoviral vector-based vaccine in mouse models, e.g., d30 versus d60 in ref (9), and ~d30 versus ~d110 in ref (8). Some key features characterize our study as compared to these previous ones. Our choice of d30 versus d100 prime/boost comparison was based on the hypothesis that establishment of quiescence in primed CD8 T cells would be related to improved cells' responsiveness to boosting, and on the experimental results on the kinetics of accumulation of Ki-67$^-$ T_{CM} and T_{EM} gag-specific CD8 T cells in lymphoid organs. In contrast, kinetics of clonal expansion and of re-entry in quiescent phase were not investigated in the above-mentioned studies, nor advanced technologies such as RNAseq were used to characterize the

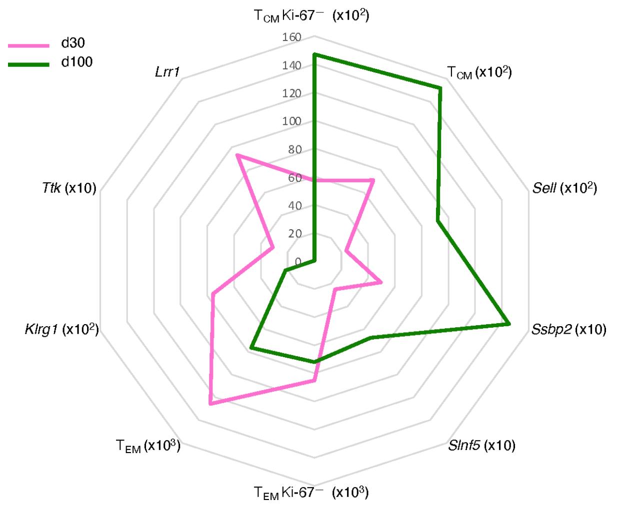

FIGURE 6

Schematic of "quiescent-but highly responsive" memory spleen CD8 T cell signature. Spider plot representing key features of splenic signature of gag-specific CD8 T cells at d30 (pink) and d100 (green) post-prime. Units of measure are the following: absolute cell numbers in the spleen for T_{CM}, T_{EM}, Ki-67⁻ TCM, and Ki-67⁻ TEM gag-specific CD8 T cells (see Figures 2E, F, 3E, F); mean DESeq2-normalized counts for Sell, Ssbp2, Slnf5, Klrg1, Ttk, and Lrr1 (see Figure 4B).

molecular signature of highly responsive memory CD8 T cells at d100 post-prime (8, 9). Furthermore, we compared secondary responses at d45 post-boost, in contrast to the above-mentioned comparative studies that analyzed earlier times post-boost (8, 9). This is because we were interested in established CD8 T cell memory, rather than in changes of the kinetics and/or magnitude of the acute response after boost.

Our data are in agreement with old pioneer studies and more recent ones that altogether emphasize through different approaches the role of a T_{CM}/stem cell molecular profile for long-lived T cell memory (60, 64–67), and are consistent with the hypothesis that lymphoid microenvironments regulate the equilibrium between quiescence and self-renewal in long-term T cell memory (61). Notably, our findings establish a new memory CD8 T cell profile of responsiveness to boost, giving a valuable contribution to the rational design of vaccination protocols. Advancements in this field are much needed, as defining the time interval between vaccine shots represents one of the current challenges after the success of many anti-SARS-CoV-2 vaccination strategies, including those based on adenoviral-vectors and on mRNA (13).

Data availability statement

The datasets presented in this study can be found in online repositories. The name of the repository and accession number can be found below: NCBI Gene Expression Omnibus; GSE207389.

Ethics statement

All experimental procedures were approved by the local animal ethics council and performed in accordance with national and international laws and policies (UE Directive 2010/63/UE; Italian Legislative Decree 26/2014; authorization n. 1065/2015-PR).

Author contributions

ANat and FD conceived the project, designed experiments, interpreted the results, and wrote the paper with help by SS. AF, SC, RS and ANic provided the viral vectors and conducted/supervised mouse immunizations. ANat, SS, GF, LL, AMC performed/analysed flow cytometry experiments. ANat, GP, MM-R, GK performed/analysed cell sorting and RNAseq experiments. AMC, RS, SB performed/analysed intracellular IFN-γ assay. AF, SC, AS and ACH advised on data discussion and paper writing. ACH advised on concepts to prioritize in data analysis and paper writing. All authors contributed to the article and approved the submitted version.

Acknowledgments

The following tetramer was obtained through the NIH Tetramer Facility: APC-conjugated H-2K(d) HIV gag 197–205 AMQMLKETI. We thank The Francis Crick Institute's Advanced Sequencing Facility for RNA sequencing, and Daniel Davies, Silvia Gitto, Magdalene Joseph, Puay Lee, and Alexandru Turcan for useful comments on the manuscript. Work supported by CTN01_00177_962865 (Medintech) grant from Ministero dell'Università e delle Ricerca (MIUR), by MIUR PRIN grant 2017K55HLC_006, by MUR PNRR PE13 INF-ACT grant, by CNR STM 2021, and by the Francis Crick Institute —which receives its core funding from Cancer Research UK (CRUK), the UK Medical Research Council, and the Wellcome Trust— (FC001003).

Conflict of interest

AMC, RS, SB, SC, and AF are employees of ReiThera S.r.l. ANic is named inventor on patent application WO 2005071093 A3 "Chimpanzee adenovirus vaccine carriers". AF and ANic are equity holders in Keires AG. ACH is a board member and equity holder in ImmunoQure, AG., and Gamma Delta Therapeutics, and is an equity holder in Adaptate Biotherapeutics.

The remaining authors declare that the research was conducted in the absence of any commercial or financial relationships that could be construed as a potential conflict of interest.

The authors declare that this study received funding from Reithera. Scientific contribution by co-authors affiliated with Reithera is reported in the co-author contribution section.

Publisher's note

Supplementary material

The Supplementary Material for this article can be found online at: https://www.frontiersin.org/articles/10.3389/fimmu.2023.1043631/full#supplementary-material

References

1. Di Rosa F, Gebhardt T. Bone marrow T cells and the integrated functions of recirculating and tissue-resident memory T cells. *Front Immunol* (2016) 7:51. doi: 10.3389/fimmu.2016.00051

2. Harty JT, Badovinac VP. Shaping and reshaping CD8+ T-cell memory. *Nat Rev Immunol* (2008) 8:107–19. doi: 10.1038/nri2251

3. Appay V, Douek DC, Price DA. CD8+ T cell efficacy in vaccination and disease. *Nat Med* (2008) 14:623–8. doi: 10.1038/nm.f.1774

4. Bolinger B, Sims S, Swadling L, O'Hara G, de Lara C, Baban D, et al. Adenoviral vector vaccination induces a conserved program of CD8(+) T cell memory differentiation in mouse and man. *Cell Rep* (2015) 13:1578–88. doi: 10.1016/j.celrep.2015.10.034

5. Capone S, Reyes-Sandoval A, Naddeo M, Siani L, Ammendola V, Rollier CS, et al. Immune responses against a liver-stage malaria antigen induced by simian adenoviral vector AdCh63 and MVA prime-boost immunisation in non-human primates. *Vaccine.* (2010) 29:256–65. doi: 10.1016/j.vaccine.2010.10.041

6. Majhen D, Calderon H, Chandra N, Fajardo CA, Rajan A, Alemany R, et al. Adenovirus-based vaccines for fighting infectious diseases and cancer: Progress in the field. *Hum Gene Ther* (2014) 25:301–17. doi: 10.1089/hum.2013.235

7. Cagigi A, Loré K. Immune responses induced by mRNA vaccination in mice, monkeys and humans. *Vaccines (Basel)* (2021) 18;9(1):61. doi: 10.3390/vaccines9010061

8. Bruña-Romero O, González-Aseguinolaza G, Hafalla JC, Tsuji M, Nussenzweig RS. Complete, long-lasting protection against malaria of mice primed and boosted with two distinct viral vectors expressing the same plasmodial antigen. *Proc Natl Acad Sci USA* (2001) 98:11491–6. doi: 10.1073/pnas.191380898

9. Tan WG, Jin H-T, West EE, Penaloza-MacMaster P, Wieland A, Zilliox MJ, et al. Comparative analysis of simian immunodeficiency virus gag-specific effector and memory CD8 + T cells induced by different adenovirus vectors. *J Virol* (2013) 87:1359–72. doi: 10.1128/jvi.02055-12

10. Natalini A, Simonetti S, Sher C, D'Oro U, Hayday AC, Di Rosa F. Durable CD8 T cell memory against SARS-CoV-2 by Prime/Boost and multi-dose vaccination: Considerations on inter-dose time intervals. *Int J Mol Sci* (2022) 23:14367. doi: 10.3390/ijms232214367

11. Krammer F. SARS-CoV-2 vaccines in development. *Nature* (2020) 586:516–27. doi: 10.1038/s41586-020-2798-3

12. Lipsitch M, Krammer F, Regev-Yochay G, Lustig Y, Balicer RD. SARS-CoV-2 breakthrough infections in vaccinated individuals: Measurement, causes and impact. *Nat Rev Immunol* (2022) 22:57–65. doi: 10.1038/s41577-021-00662-410.1038/s41577-021-00662-4

13. Payne RP, Longet S, Austin JA, Skelly DT, Dejnirattisai W, Adele S, et al. Immunogenicity of standard and extended dosing intervals of BNT162b2 mRNA vaccine. *Cell.* (2021) 184:5699–5714.e11. doi: 10.1016/j.cell.2021.10.011

14. Simonetti S, Natalini A, Folgori A, Capone S, Nicosia A, Santoni A, et al. Antigen-specific CD8 T cells in cell cycle circulate in the blood after vaccination. *Scand J Immunol* (2019) 89:e12735. doi: 10.1111/sji.12735

15. Colloca S, Barnes E, Folgori A, Ammendola V, Capone S, Cirillo A, et al. Vaccine vectors derived from a large collection of simian adenoviruses induce potent cellular immunity across multiple species. *Sci Transl Med* (2012) 4:115ra2. doi: 10.1126/scitranslmed.3002925

16. Di Lullo G, Soprana E, Panigada M, Palini A, Erfle V, Staib C, et al. Marker gene swapping facilitates recombinant modified vaccinia virus Ankara production by host-range selection. *J Virologic Methods* (2009) 156:37–43. doi: 10.1016/j.jviromet.2008.10.026

17. Di Lullo G, Soprana E, Panigada M, Palini A, Agresti A, Comunian C, et al. The combination of marker gene swapping and fluorescence-activated cell sorting improves the efficiency of recombinant modified vaccinia virus Ankara vaccine production for human use. *J Virol Methods* (2010) 163:195–204. doi: 10.1016/j.jviromet.2009.09.016

18. Quinci AC, Vitale S, Parretta E, Soriani A, Iannitto ML, Cippitelli M, et al. IL-15 inhibits IL-7Ralpha expression by memory-phenotype CD8(+) T cells in the bone marrow. *Eur J Immunol* (2012) 42:1129–39. doi: cyto.a.24509/eji.201142019

19. Abeler-Dörner L, Laing AG, Lorenc A, Ushakov DS, Clare S, Speak AO, et al. High-throughput phenotyping reveals expansive genetic and structural underpinnings of immune variation. *Nat Immunol* (2020) 21:86–100. doi: 10.1038/s41590-019-0549-0

20. Barber DL, Wherry EJ, Ahmed R. Cutting edge: Rapid *in vivo* killing by memory CD8 T cells. *J Immunol* (2003) 171:27–31. doi: 10.4049/jimmunol.171.1.27

21. Nemzek JA, Bolgos GL, Williams BA, Remick DG. Differences in normal values for murine white blood cell counts and other hematological parameters based on sampling site. *Inflammation Res* (2001) 50:523–7. doi: 10.1007/PL00000229

22. Riches AC, Sharp JG, Thomas DB, Smith SV. Blood volume determination in the mouse. *J Physiol* (1973) 228:279–84. doi: 10.1113/jphysiol.1973.sp010086

23. Parretta E, Cassese G, Barba P, Santoni A, Guardiola J, Di Rosa F. CD8 cell division maintaining cytotoxic memory occurs predominantly in the bone marrow. *J Immunol* (2005) 174:7654–64. doi: 10.4049/jimmunol.174.12.7654

24. Bolger AM, Lohse M, Usadel B. Trimmomatic: A flexible trimmer for illumina sequence data. *Bioinformatics.* (2014) 30:2114–20. doi: 10.1093/bioinformatics/btu170

25. Dobin A, Davis CA, Schlesinger F, Drenkow J, Zaleski C, Jha S, et al. STAR: Ultrafast universal RNA-seq aligner. *Bioinformatics* (2013) 29:15–21. doi: 10.1093/bioinformatics/bts635

26. Li B, Dewey CN. RSEM: Accurate transcript quantification from RNA-seq data with or without a reference genome. *BMC Bioinf* (2011) 12:323. doi: 10.1186/1471-2105-12-323

27. Muñoz-Ruiz M, Pujol-Autonell I, Rhys H, Long HM, Greco M, Peakman M, et al. Tracking immunodynamics by identification of s-G2/M-phase T cells in human peripheral blood. *J Autoimmun* (2020) 112:102466. doi: 10.1016/j.jaut.2020.102466

28. Natalini A, Simonetti S, Favaretto G, Peruzzi G, Antonangeli F, Santoni A, et al. OMIP -079: Cell cycle of CD4 + and CD8 + naïve/memory T cell subsets, and of treg cells from mouse spleen. *Cytometry Part A* (2021) 99(12):1171-75. doi: cyto.a.24509/cyto.a.24509

29. Simonetti S, Natalini A, Peruzzi G, Nicosia A, Folgori A, Capone S, et al. A DNA/Ki67-based flow cytometry assay for cell cycle analysis of antigen-specific CD8 T cells in vaccinated mice. *J Visualized Experiments* (2021). doi: 10.3791/61867

30. Sallusto F, Geginat J, Lanzavecchia A. Central memory and effector memory T cell subsets: function, generation, and maintenance. *Annu Rev Immunol* (2004) 22:745–63. doi: 10.1146/annurev.immunol.22.012703.104702

31. Ivetic A, Hoskins Green HL, Hart SJ. L-selectin: A major regulator of leukocyte adhesion, migration and signaling. *Front Immunol* (2019) 10:1068. doi: 10.3389/fimmu.2019.01068

32. Powzaniuk MA, Trotta R, Loza MJ, Harth A, Iozzo RV, Eisenlohr LC, et al. B-myb overexpression results in activation and increased Fas/Fas ligand-mediated cytotoxicity of T and NK cells. *J Immunol* (2001) 167:242–9. doi: 10.4049/jimmunol.167.1.242

33. Chen Y, Zander R, Khatun A, Schauder DM, Cui W. Transcriptional and epigenetic regulation of effector and memory CD8 T cell differentiation. *Front Immunol* (2018) 9:2826. doi: 10.3389/fimmu.2018.02826

34. Schmandt R, Hill M, Amendola A, Mills GB, Hogg D. IL-2-induced expression of TTK, a serine, threonine, tyrosine kinase, correlates with cell cycle progression. *J Immunol* (1994) 152:96.

35. Yang Z, Li C, Yan C, Li J, Yan M, Liu B, et al. KIF14 promotes tumor progression and metastasis and is an independent predictor of poor prognosis in human gastric cancer. *Biochim Biophys Acta Mol Basis Dis* (2019) 1865:181–92. doi: 10.1016/j.bbadis.2018.10.039

36. Zhao Q, Chen S, Chen L. LETM1 (leucine zipper-EF-hand-containing transmembrane protein 1) silence reduces the proliferation, invasion, migration and angiogenesis in esophageal squamous cell carcinoma *via* KIF14 (kinesin family member 14). *Bioengineered.* (2021) 12:7656–65. doi: 10.1080/21655979.2021.1982275

37. Jang LK, Lee ZH, Kim HH, Hill JM, Kim JD, Kwon BS. A novel leucine-rich repeat protein (LRR-1): Potential involvement in 4-1BB-mediated signal transduction. *Mol Cells* (2001) 12:304–12.

38. Kaech SM, Tan JT, Wherry EJ, Konieczny BT, Surh CD, Ahmed R. Selective expression of the interleukin 7 receptor identifies effector CD8 T cells that give rise to long-lived memory cells. *Nat Immunol* (2003) 4:1191–8. doi: 10.1038/ni1009

39. Crauste F, Mafille J, Boucinha L, Djebali S, Gandrillon O, Marvel J, et al. Identification of nascent memory CD8 T cells and modeling of their ontogeny. *Cell Syst* (2017) 4:306–17.e4. doi: 10.1016/j.cels.2017.01.014

40. Güler A, Lopez Venegas M, Adankwah E, Mayatepek E, Nausch N, Jacobsen M. Suppressor of cytokine signalling 3 is crucial for interleukin-7 receptor re-expression after T-cell activation and interleukin-7 dependent proliferation. *Eur J Immunol* (2020) 50:234–44. doi: cyto.a.24509/eji.201948302

41. Geserick P, Kaiser F, Klemm U, Kaufmann SH, Zerrahn J. Modulation of T cell development and activation by novel members of the schlafen (slfn) gene family harbouring an RNA helicase-like motif. *Int Immunol* (2004) 16:1535–48. doi: 10.1093/intimm/dxh155

42. Puck A, Hopf S, Modak M, Majdic O, Cejka P, Blüml S, et al. The soluble cytoplasmic tail of CD45 (ct-CD45) in human plasma contributes to keep T cells in a quiescent state. *Eur J Immunol* (2017) 47:193–205. doi: cyto.a.24509/eji.201646405

43. Metzner FJ, Huber E, Hopfner KP, Lammens K. Structural and biochemical characterization of human schlafen 5. *Nucleic Acids Res* (2022) 50:1147–61. doi: 10.1093/nar/gkab1278

44. Li J, Kurasawa Y, Wang Y, Clise-Dwyer K, Klumpp SA, Liang H, et al. Requirement for ssbp2 in hematopoietic stem cell maintenance and stress response. *J Immunol* (2014) 193:4654–62. doi: 10.4049/jimmunol.1300337

45. Wilson A, Murphy MJ, Oskarsson T, Kaloulis K, Bettess MD, Oser GM, et al. C-myc controls the balance between hematopoietic stem cell self-renewal and differentiation. *Genes Dev* (2004) 18:2747–63. doi: 10.1101/gad.313104

46. Marchingo JM, Sinclair LV, Howden AJ, Cantrell DA. Quantitative analysis of how myc controls T cell proteomes and metabolic pathways during T cell activation. *Elife.* (2020) 9:e53725. doi: 10.7554/eLife.53725

47. Nozais M, Loosveld M, Pankaew S, Grosjean C, Gentil N, Quessada J, et al. MYC deficiency impairs the development of effector/memory T lymphocytes. *iScience* (2021) 24:102761. doi: 10.1016/j.isci.2021.102761

48. Venezia TA, Merchant AA, Ramos CA, Whitehouse NL, Young AS, Shaw CA, et al. Molecular signatures of proliferation and quiescence in hematopoietic stem cells. *PloS Biol* (2004) 2:e301. doi: 10.1371/journal.pbio.0020301

49. Zelentsova K, Talmi Z, Abboud-Jarrous G, Sapir T, Capucha T, Nassar M, et al. Protein s regulates neural stem cell quiescence and neurogenesis. *Stem Cells* (2017) 35:679–93. doi: cyto.a.24509/stem.2522

50. Gay O, Nakamura F, Baudier J. Refilin holds the cap. *Commun Integr Biol* (2011) 4:791–5. doi: 10.4161/cib.17911

51. Ma C, Zhang N. Transforming growth factor-β signaling is constantly shaping memory T-cell population. *Proc Natl Acad Sci USA* (2015) 112:11013–7. doi: 10.1073/pnas.1510119112

52. Takai S, Schlom J, Tucker J, Tsang KY, Greiner JW. Inhibition of TGF-beta1 signaling promotes central memory T cell differentiation. *J Immunol* (2013) 191:2299–307. doi: 10.4049/jimmunol.1300472

53. Ishigame H, Mosaheb MM, Sanjabi S, Flavell RA. Truncated form of TGF-betaRII, but not its absence, induces memory CD8+ T cell expansion and lymphoproliferative disorder in mice. *J Immunol* (2013) 190:6340–50. doi: 10.4049/jimmunol.1300397

54. Kim SK, Henen MA, Hinck AP. Structural biology of betaglycan and endoglin, membrane-bound co-receptors of the TGF-beta family. *Exp Biol Med (Maywood)* (2019) 244:1547–58. doi: 10.1177/1535370219881160

55. Hudson WH, Gensheimer J, Hashimoto M, Wieland A, Valanparambil RM, Li P, et al. Proliferating transitory T cells with an effector-like transcriptional signature emerge from PD-1+ stem-like CD8+ T cells during chronic infection. *Immunity* (2019) 51:1043–1058.e4. doi: 10.1016/j.immuni.2019.11.002

56. Ledgerwood JE, Zephir K, Hu Z, Wei CJ, Chang L, Enama ME, et al. Prime-boost interval matters: A randomized phase 1 study to identify the minimum interval necessary to observe the H5 DNA influenza vaccine priming effect. *J Infect Dis* (2013) 208:418–22. doi: 10.1093/infdis/jit180

57. Pettini E, Pastore G, Fiorino F, Medaglini D, Ciabattini A. Short or long interval between priming and boosting: Does it impact on the vaccine immunogenicity. *Vaccines (Basel)* (2021) 9:289. doi: 10.3390/vaccines9030289

58. Bloom ET, Mostowski HS, Horvath JA. Does the age-related change in CD44-defined T-cell subsets have functional significance for cytotoxic T lymphocyte generation. *Immunol Lett* (1994) 40:251–8. doi: 10.1016/0165-2478(94)00072-7

59. Nikolich-Žugich J. Aging of the T cell compartment in mice and humans: From no naive expectations to foggy memories. *J Immunol* (2014) 193:2622–9. doi: 10.4049/jimmunol.1401174

60. Kaech SM, Hemby S, Kersh E, Ahmed R. Molecular and functional profiling of memory CD8 T cell differentiation. *Cell* (2002) 111:837–51. doi: 10.1016/s0092-8674(02)01139-x

61. Di Rosa F. Two niches in the bone marrow: A hypothesis on life-long T cell memory. *Trends Immunol* (2016) 37:503–12. doi: 10.1016/j.it.2016.05.004

62. Thompson EA, Beura LK, Nelson CE, Anderson KG, Vezys V. Shortened intervals during heterologous boosting preserve memory CD8 T cell function but compromise longevity. *J Immunol* (2016) 196:3054–63. doi: 10.4049/jimmunol.1501797

63. Alvarez-Dominguez JR, Melton DA. Cell maturation: Hallmarks, triggers, and manipulation. *Cell.* (2022) 185:235–49. doi: 10.1016/j.cell.2021.12.012

64. Lugli E, Dominguez MH, Gattinoni L, Chattopadhyay PK, Bolton DL, Song K, et al. Superior T memory stem cell persistence supports long-lived T cell memory. *J Clin Invest* (2013) 123:594–9. doi: 10.1172/JCI66327

65. Graef P, Buchholz VR, Stemberger C, Flossdorf M, Henkel L, Schiemann M, et al. Serial transfer of single-cell-derived immunocompetence reveals stemness of CD8(+) central memory T cells. *Immunity* (2014) 41:116–26. doi: 10.1016/j.immuni.2014.05.018

66. Youngblood B, Hale JS, Kissick HT, Ahn E, Xu X, Wieland A, et al. Effector CD8 T cells dedifferentiate into long-lived memory cells. *Nature* (2017) 552:404–9. doi: 10.1038/nature25144

67. Jung S, Jung JH, Noh JY, Kim WJ, Yoon SY, Jung J, et al. The generation of stem cell-like memory cells early after BNT162b2 vaccination is associated with durability of memory CD8+ T cell responses. *Cell Rep* (2022) 40:111138. doi: 10.1016/j.celrep.2022.111138

Frontiers

Avenue du Tribunal-Fédéral 34
1005 Lausanne, Switzerland
frontiersin.org

Contact us

+41 (0)21 510 17 00
frontiersin.org/about/contact